JOURNAL OF SCIENCE
SAKARYA UNIVERSITY

Sakarya University
Journal of Science



SAKARYA UNIVERSITY
e-issn: 2147-835X

Sakarya University Journal of Science
Volume: 23 Issue: 6 December 2019
Editorial Boards

İrfan Yazıcı, Electrical and Electronics Engineering, Sakarya University (Turkey)

İrfan Yazıcı, Electrical and Electronics Engineering, Sakarya University (Turkey)

İsmail Hakkı Demir, Architecture, Sakarya University (Turkey)

Latif Kelebekli, Chemistry, Ordu University (Turkey)

Latif Kelebekli, Chemistry, Ordu University (Turkey)

Mahmud Tokur, Metallurgical and Materials Engineering, Sakarya University (Turkey)

Mehmet İşleyen, Environmental Engineering, Bursa Technical University (Turkey)

Mehmet İşleyen, Environmental Engineering, Bursa Technical University (Turkey)

Mevlüt Sami Aköz, Civil Engineering, Çukurova University (Turkey)

Miraç Alaf, Metallurgical and Materials Engineering, Bilecik Şeyh Edebali University (Turkey)

Muhammed Maruf Öztürk, Computer Engineering, Süleyman Demirel University (Turkey)

Muhammed Maruf Öztürk, Computer Engineering, Süleyman Demirel University (Turkey)

Murat Sarduvan, Mathematics, Sakarya University (Turkey)

Murat Tuna, Chemistry, Sakarya University (Turkey)

Murat Tuna, Chemistry, Sakarya University (Turkey)

Murat Utkucu, Geophysical Engineering , Sakarya University (Turkey)

Mustafa Akpınar, Software Engineering, Sakarya University (Turkey)

Mustafa Akpınar, Software Engineering, Sakarya University (Turkey)

Nazan Deniz Yön Ertuğ, Biology, Sakarya University (Turkey)

Nazan Deniz Yön Ertuğ, Biology, Sakarya University (Turkey)

Nükhet Sazak, Electrical and Electronics Engineering, Sakarya University (Turkey)

Nükhet Sazak, Electrical and Electronics Engineering, Sakarya University (Turkey)

Osman Kırtel, Civil Engineering, Sakarya University of Applied Sciences (Turkey)

Özer Uygun, Industrial Engineering, Sakarya University (Turkey)

Özer Uygun, Industrial Engineering, Sakarya University (Turkey)

Öznur Özkan Kılıç, Mathematics, Başkent University (Turkey)

Rıfkı Terzioğlu, Electrical and Electronics Engineering, Bolu Abant İzzet Baysal University, (Turkey)

Rıfkı Terzioğlu, Electrical and Electronics Engineering, Bolu Abant İzzet Baysal University, (Turkey)

Sibel Güneş, Mechanical Engineering, Erciyes University (Turkey)

Soley Ersoy, Mathematics, Sakarya University (Turkey)

Soydan Serttaş, Computer Engineering, Dumlupınar University (Turkey)

Soydan Serttaş, Computer Engineering, Dumlupınar University (Turkey)

Tuğrul Çetinkaya, Metallurgical and Materials Engineering, Sakarya University (Turkey)

Turgay Şişman, Biology, Atatürk University (Turkey)

Turgay Şişman, Biology, Atatürk University (Turkey)

SAKARYA UNIVERSITY JOURNAL OF SCIENCE
CONTENTS
Volume: 23 - Issue: 6 (DECEMBER 2019)

RESEARCH ARTICLES

JOURNAL OF SCIENCE
SAKARYA UNIVERSITY

Sakarya University Journal of Science

ISSN 1301-4048 | e-ISSN 2147-835X | Period Bimonthly | Founded: 1997 | Publisher Sakarya University | http://www.saujs.sakarya.edu.tr/

Title: Preparation And Characterization Of Novel Iron (III) HydroxidePaper Mill Sludge Composite Adsorbent For Chromium Removal

Authors: Ali Yaraş, Hasan Arslanoğlu
Recieved: 2018-10-11 13:17:25

Accepted: 2019-01-17 10:30:17

Article Type: Research Article
Volume: 23
Issue: 6
Month: December
Year: 2019
Pages: 1019-1026

How to cite
Ali Yaraş, Hasan Arslanoğlu; (2019), Preparation And Characterization Of Novel Iron (III) HydroxidePaper Mill Sludge Composite Adsorbent For Chromium Removal. Sakarya University Journal of Science, 23(6), 1019-1026, DOI: 10.16984/saufenbilder.469464
Access link
http://www.saujs.sakarya.edu.tr/issue/44246/469464

Sakarya University Journal of Science 23(6), 1019-1026, 2019

Preparation And Characterization Of Novel Iron (III) Hydroxide/Paper Mill Sludge Composite Adsorbent For Chromium Removal

Ali Yaraş*[1], Hasan Arslanoğlu[2]

Abstract

This work deals with the removal of Cr (III) and Cr (VI) from synthetic solutions via a novel composite adsorbent prepared by precipitating iron (III) hydroxide on paper mill sludge (PMS). To obtain $Fe(OH)_3$ loaded PMS, -8+16 mesh fraction of PMS was saponified with NaOH solution, then iron (III) chloride was impregnated, hydrolyzed in NaOH solution and dried. The influences of pH, time, initial concentration and temperature on removal of Cr (III) and Cr (VI) were examined and it was determined that Cr (VI) removal occurs simultaneously with a reduction reaction. Maximum removal yields for Cr (III) and Cr (VI) occurred at approximately pH = 5 and the adsorption achieved equilibrium in 90 min. Cr (VI) adsorption ratio decreases while Cr (III) removal percentage increases with raising in temperature. Experimental results are consistent with Langmuir isotherm. Adsorption capacities of Cr (III) and Cr (VI) were calculated as 8.49, 10.14, 12.62 mg/g and 7.64, 5.39 and 4.17 mg/g for 25, 40 and 55 °C, respectively. Enthalpy changes for Cr (III) and Cr (VI) were calculated as 24.67 kJ/mol and -12.46 kJ/mol, respectively. These results demonstrated that the adsorption phenomenon of Cr (III) and Cr (VI) are endothermic and exothermic.

Keywords: Hexavalent chromium, iron (III) hydroxide, paper mill sludge, adsorption, reduction.

1. INTRODUCTION

Nowadays, water pollution has become an important problem by virtue of increasing technology and human needs. The investigations indicate that a great amount of pollutants is discharged into surface waters. The pollutants such as polycyclic aromatic compounds, pesticides, radioactive substances and toxic heavy metals cause negative influence on human health, in addition they affect water adversely in terms of smell, taste and physical appearance [1].

Since chromium compounds have high toxicity, it is necessary to control the passing to water and treat chromium-containing wastewater. Chromium is discharged from various industries; metal coating, leather, paint, textile, glass and ceramics at high concentrations. Cr is in the form of Cr^{6+} or Cr^{3+} in wastewater and the toxicity of Cr^{6+} is much higher than Cr^{+3} [1], [2].

Cr (VI) is generally first reduced to Cr (III) in the presence of various reducing agents and then removed by precipitation. Adsorption method is most preferred to remove Cr (VI) directly from the wastewater. In this context, there are numerous studies on the utilization of various industrial and agricultural wastes as adsorbents in literature [3].

A large amount of PMS is produced from the paper production plants. Storage and transportation of PMS

* Corresponding Author aliyaras@bartin.edu.tr
[1] Metallurgical and Materials Engineering Department, Bartin University, Turkey ORCID:0000-0003-1725-7788
[2] Chemical Engineering Department, Firat University, Turkey ORCID: 0000-0002-3132-4468

material is very important in terms of reducing the waste load of environment and plants. To eliminate this problem, the storage and composting processes are generally employed [4]. However, strict environmental regulations limit the application of these methods [5], [6]. On the other hand, the incineration treatment is not preferred for PMS as it contains various components [5]. For all these reasons, the researchers focused on the utilization of PMS as an adsorbent in removal toxic and heavy metals from wastewaters [7]–[9].

Previous studies illustrated that iron (III) hydroxide is utilized as an efficient adsorbent for removal chromates from aqueous systems [10], [11]. However, iron (III) hydroxide causes application difficulties due to the collodial properties that it forms in the aqueous medium. In the present study, we plan to produce a composite adsorbent with iron (III) hydroxide precipitated PMS and thus prevent the filtration problem by fixing iron (III) hydroxide. This situation is also probably contribute positively to the problem of swelling by the hydration reaction of PMS in the presence of aqueous solution. Therefore, in this study, adsorption characteristics of Cr (III) and Cr (VI) from synthetic solutions were studied by iron (III) hydroxide precipitated on PMS.

2. MATERIAL METHOD

2.1. Preparation of PMS

PMS was obtained from the OYKA paper factory in Çaycuma/Zonguldak in 2016. It was firstly dried by blowing air with a fan, crushed and sieved to obtain particles with -8+16 mesh ($1.2 < x < 2.4$ mm) size. The prepared sample was dried at 50°C for 12 h.

2.2. Preparation and Characterization of Iron (III) Hydroxide Precipitated PMS

It was obtained by following a process; the iron was saponified with NaOH, treatment with iron (III) chloride and hydrolyzed with NaOH [12].

100 g of PMS was stirred with 0.1 M NaOH solution for 1 h and filtered. The filtrate PMS was washed with purified water until the pH=8 and dried at 50°C for 12 h. Then, it was then stirred in 0.5 M $FeCl_3$ solution for 1 h using a magnetic stirrer, waited for 12 h, filtered and the filtrate was dried at 50°C for 24 h. Lastly, it was hydrolyzed in 0.1 M NaOH solution by stirring, waited for 12 h, then filtered and washed the washing water was until pH 8 was reached. The prepared sample was dried at 50°C for 24 h. As presented in Table 1, some features of the $Fe(OH)_3$-loaded PMS adsorbent prepared are given.

Table 1. Some features of the $Fe(OH)_3$-loaded PMS adsorbent prepared

Characteristics	Value
Bulk density (g/cm^3)	1.36
BET surface area (m^2/g)	4.5
Langmuir surface area (m^2/g)	7.8
Methylene blue sorption capacity (mg/g)	63.6
Mass yield (%, w/w)	78.9
Iron content (%, w/w)	1.77
Ash content (%, w/w)	5.86
Swelling capacity (ml/g)	1.1
Water retention (g/g)	3.42
COD (mg/g)	19.7

Figure 1 and Figure 2 depicts SEM image and EDX spectra analysis of the prepared adsorbent, respectively. EDX spectra results demonstrates the quantitative elemental analysis in weight %; oxygen 55.9, carbon 19.0, iron 17.8, chlorine 6.7 and sodium 0.6. In the light of these findings, it is pointed out that the presence of Fe in the structure is clearly seen.

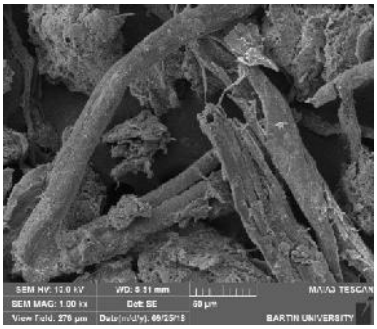

Figure 1. SEM image of $Fe(OH)_3$ loaded PMS

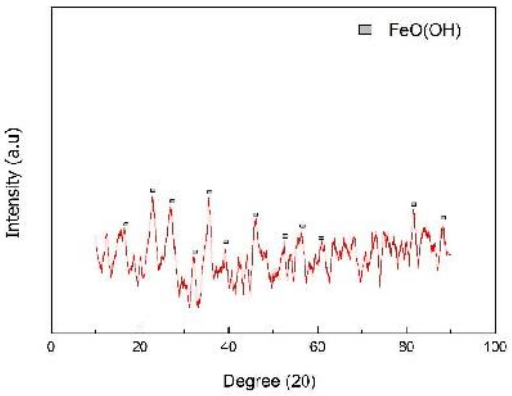

Figure 2. EDX results of $Fe(OH)_3$ loaded PMS

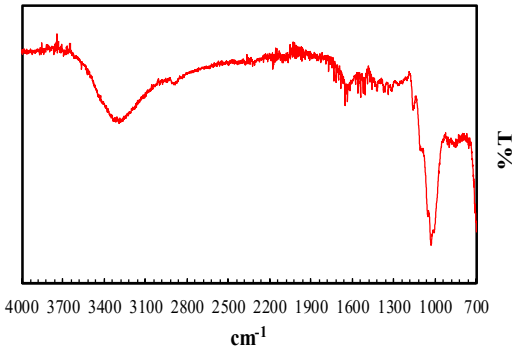

Figure 3. XRD patterns of $Fe(OH)_3$ loaded PMS

The presence of the peaks in Figure 3 clearly demonstrates that the FeO(OH) particles are loaded into the PMS. On the other hand, broad band at 3400 cm^{-1} in Figure 4 pertain to the stretching –OH of cellulose. The weak peak (about 1630 cm^{-1}) was related to deformation vibration of –OH group. The strong peak at 1050 cm^{-1} was attributed to the presence of Fe-OH bonds.

2.3. Preparation of Synthetic Cr Solutions

Synthetic Cr (III) and Cr (VI) solutions were prepared from $Cr_4(SO_4)_5(OH)_2$ and $Na_2Cr_2O_7$ salts. Firstly, the the stock Cr solutions were prepared (1000 ppm) and it was diluted with distilled water. Its pH adjustments were carried out with H_2SO_4 and NaOH solutions.

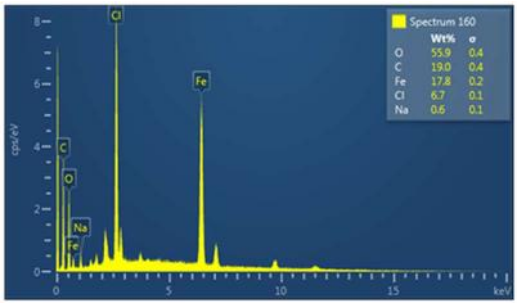

Figure 4. FTIR analysis of Fe(OH)3 loaded PMS

2.4. Adsorption study

All adsorption tests were performed in a 300 ml flask using shaker incubator (Zhcheng ZHWY-200D) with adjustable stirring speed and temperature and samples were taken at the end of the desired times. Cr (VI) amount in supernatant were performed spectrophotometrically by diphenyl carbazide method [13]. Cr (III) and iron analyses were determined by atomic absorption spectrophotometer.

3. RESULT AND DISCUSSION

Figure 5 was demonstrated the impact of pH on removal Cr (III), Cr (VI), total Cr and Fe using $Fe(OH)_3$ loaded PMS. Cr (III) removal is considerably high in varied range from pH=5 to pH=8 and the highest Cr (III) removal value (98.7%) was reached at pH =7. This is due to the tendency of Cr (III) to precipitate by hydrolysis in this pH region. In other words, it can be said that the Cr (III) removal mechanism for this pH range takes place by precipitation. On the other hand, Cr (III) removal is occurred by adsorption process due to Cr (III) concentration values are above 100 mg/l at around pH 4. This result shows that the precipitation of Cr (III) in hydroxide form on depends pH [3]. Above pH=9 values, the removal efficiency decreases and up to 30% at around pH=12. This situation may be attributed to the adsorbent surface being negatively at high pH, the amphoteric properties of Cr (III) and its high tendency to form complexes [14]. In terms of the amount of Fe passing to the solution, as 3.1 mg/l concentration of Fe was passing to the solution at around pH 1.8, this amount decreases to 0.1 mg/l with increasing pH. The pH value was chosen as 4 for subsequent experiments since the removal efficiency is high and Fe concentration passing through the solution is negligible.

The results in Figure 5 indicate that Cr (VI) removal ratio is close to 100% at acidic pH (1-3.5) because of the adsorption comes with the reduction reaction. It is known that Cr (VI) is reduced to Cr (III) using organic material according to the following reaction;

$$Cr_2O_7^{2-} + material + H^+ \rightarrow Cr^{3+} + CO_2, H_2O\ products$$

With increasing pH, the removal values of Cr (VI) and total Cr are approaching each other. Maximum removal percentages for total Cr and Cr (VI) were achieved at 88.85% and 95.55% at pH 4, respectively. This suggests that Cr (VI) is partially reduced and adsorbed

together with Cr (III) because the maximum adsorption of Cr (III) occurs at pH=4.

Based on the results in Figure 6, the removal efficiency increases for both Cr species with increasing of time and the adsorption of Cr (III), Cr (VI) and total Cr reaches the equilibrium after 90 min. At the end of 240 min, 87% of total Cr is removed while the amount of Cr (VI) removed is about 96%.

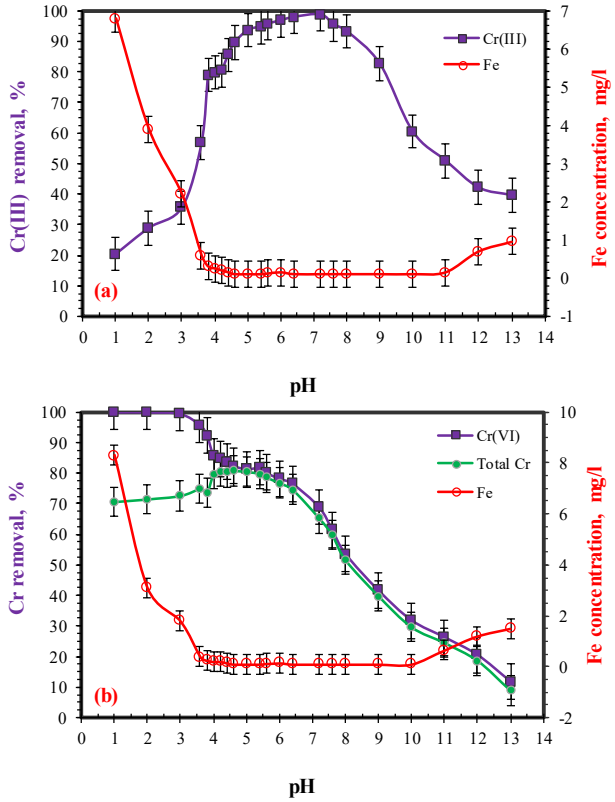

Figure 5. Influence of pH on removal of Cr (III), Cr (VI), total Cr and Fe

To calculate the adsorption kinetics, experimental data were applied to the following Lagergren equation (1) [15];

t is the contact time (min.), k is adsorption rate constant (min^{-1}), qt and qe are amount of substance adsorbed at any time and equilibrium time (mg/g). According to Figure 7, it is seen that the experimental data is good agreement with Lagergren equation for both Cr types. Adsorption rate constants for Cr (III) and Cr (VI) were found to be 0.0456 and 0.0234 min^{-1}, respectively. It can be said that this result is reasonable due to Cr (VI) and Cr (III) are cationic and anionic complex structure in the aqueous solution, respectively. As seen from Figure 8, while Cr (III) removal percentage increases with increase temperature, Cr (VI) removal efficiency decreases. According to the classification by Sposito (1989) [16], above aforementioned nonlinear equilibrium curves correspond to the L type for Cr (III) and Cr (VI).

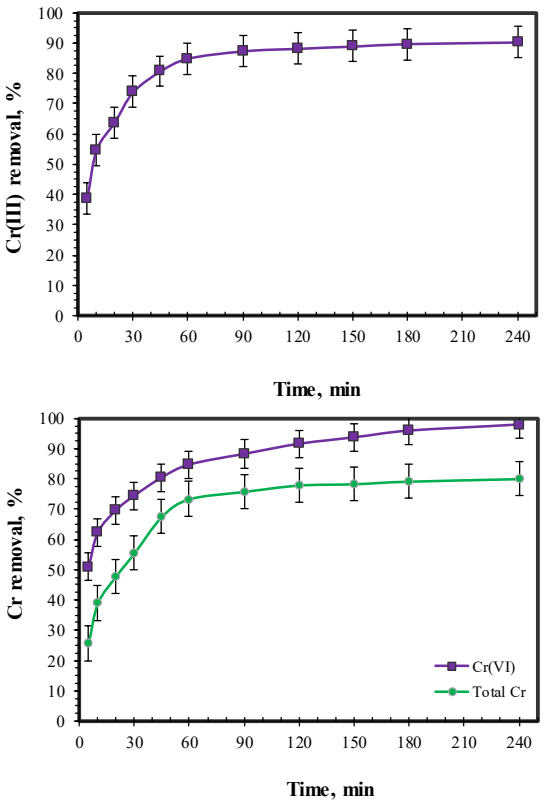

Figure 6. Influence of time on removal of Cr (III), Cr (VI) and total Cr

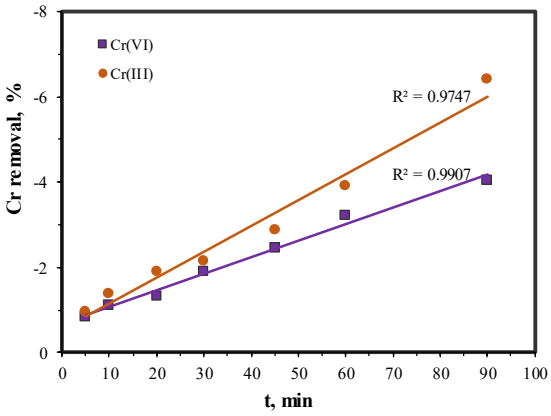

Figure 7. Lagergren graph for adsorption process of Cr (III) and Cr (VI)

$$ln(q_e - q_t) = lnq_e - kt \quad (1)$$

Table 2. Langmuir isotherm constants

Cr type	Temperature, °C	q_{max} (mg/g)	b
Cr (III)	25	8.49	2.65
	40	10.14	1.68
	55	12.62	1.16
Cr (VI)	25	7.64	9.89
	40	5.39	12.28
	55	4.17	17.30

Experimental results were applied to linear Langmuir isotherm equation (2) following as [11];

$$\frac{C_e}{q_e} = \frac{1}{q_{max} b} + \frac{C_e}{q_{max}} \quad (2)$$

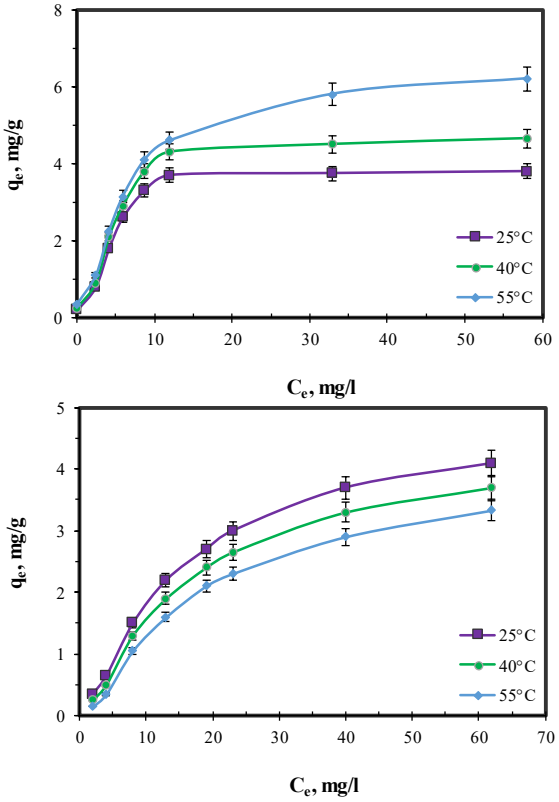

Figure 8. Non-linear adsorption isotherms

Table 3. Thermodynamic parameters

Cr type	Temperature, °C	ΔG (kJ/mol)	ΔS (kJ/molK)	ΔH (kJ/mol)
Cr (III)	25	-2.415	0.091	24.67
	40	-1.350	0.083	
	55	-0.405	0.076	
Cr (VI)	25	-5.680	-0.023	-12.46
	40	-6.531	-0.019	
	55	-7.774	-0.014	

C_e is total Cr concentration at equilibrium (mg/l), qe is amount of Cr adsorbed per unit adsorbent weight, qmax is maximum adsorption capacity (mg/g), b is a constant (mg^{-1}). Langmuir isotherms and the calculated coefficients for Cr (III) and Cr (VI) are illustrated in Figure 9 and Table 2.

The changes of free energy, enthalpy and entropy for adsorption process can be calculated by following equations (3), (4) and (5) [12] ;

$$lnb = lnb^I - \frac{\Delta H}{RT} \quad (3)$$

$$ln(1/b) = \frac{\Delta G}{RT} \quad (4)$$

$$\Delta G = \Delta H - T\Delta S \quad (5)$$

ΔG is free energy (kJ/mol), T is ambient temperature (K), R is universal gas constant (8.314 J/molK), ΔH is enthalpy (kJ/mol) and ΔS is entropy (kJ/molK).

Enthalpy changes for Cr (III) and Cr (VI) were calculated as 24.67 kJ/mol and -12.46 kJ/mol from the slope of the curves in Figure 10, respectively. These results indicated that adsorption phenomenon of Cr (III) and Cr (VI) are endothermic and exothermic, respectively. Free energy and entropy changes of process are given in Table 3. Based on these results, it is seen that Cr (III) adsorption is spontaneously at high temperatures.

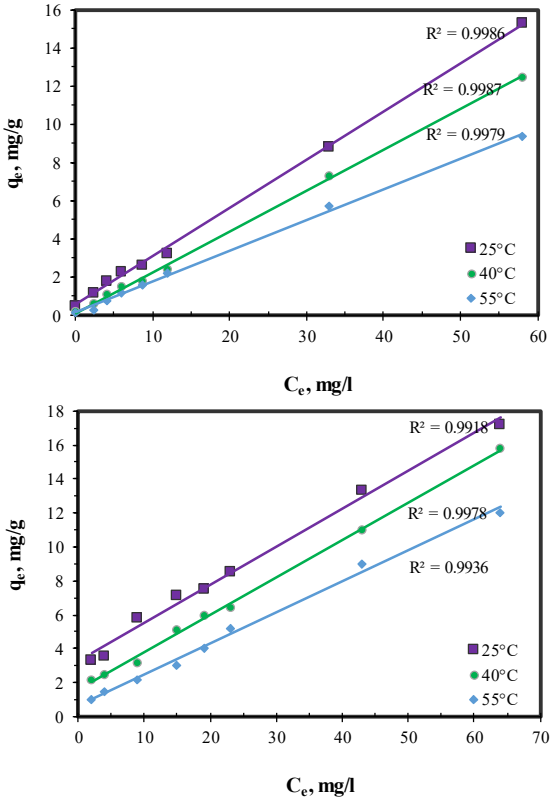

Figure 9. Langmuir isotherms

A slight decrease in entropy change with increasing temperature for Cr (III) indicates that irregularity also decreases with increased adsorption efficiency. This situation is contrary for Cr (VI). Finally, sorption capacities related to chromium reduction via different adsorbents in literature are presented in Table 4. The chromium removal capacity of the $Fe(OH)_3$ loaded PMS was found to be 12.6 mg/g. Therefore, it can be used effectively for removal chromium from synthetic aqueous solutions.

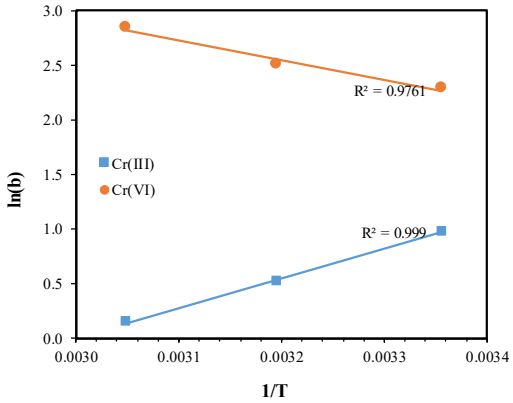

Figure 10. 1/T against lnb

Table 4. Sorption capacities related to chromium reduction with various sorbents in literature

Sorbents	Sorption capacities (mg/g)	Ref.
Grass (*Onopordom Heteracanthom*)	37.3	[17]
Magnetic Chitosan Hydrogel	27.3	[18]
Magnetic activated carbon	51.7	[19]
Walnut shell pyrolysis product	49.8	[20]
Grapefruit shell	39.1	[21]
Carbon / AlOOH composite	32.6	[22]
Biomass waste	53.4	[23]
A kind of flower *(Eupatorium adenophorum)*	89.2	[24]
Activated carbon modified with nitric acid	16.1	[25]
Coconut shell activated carbon	10.9	[26]
Terminalia arjuna nuts activated carbon	28.4	[27]
Peanut shell activated carbon	16.3	[28]
Modified coconut commercial activated carbon	20	[29]
$Fe(OH)_3$-loaded PMS	12.6	This work

4. CONCLUSIONS

Experimental findings demonstrate that the removal of Cr (III) and Cr (VI) using $Fe(OH)_3$ loaded PMS is depending on pH value. It was determined that Cr (III) was removed with a high efficiency at neutral pH and the optimum pH was 4 for Cr (III) adsorption. Cr (III) removal efficiency reached 89% under process conditions; 10 mg/l initial concentration, 10 g/l dosage, 25°C temperature and 120 min. Cr (VI) was substantially removed at acidic pH, and removal efficiencies of Cr (VI) and total Cr were obtained 95%

and 87% under the same conditions at pH 4, respectively.

The results indicate that the adsorption yield increases with increasing time for both Cr species and the process reaches equilibrium in 90 min. Based on Lagergen equation, adsorption rate constants were found as 0.0456 and 0.0234 min^{-1} for Cr (III) and Cr (VI), respectively. Experimental data were determined to be in good agreement with the Langmuir isotherm and adsorption capacities of Cr (III) and Cr (VI) were obtained to be 8.49, 10.14, 12.62 mg/g and 7.64, 5.39 and 4.17 mg/g for 25, 40 and 55°C, respectively.

Enthalpy changes for Cr (III) and Cr (VI) were calculated to be 24.67 and -12.46 kJ/mol and these results indicated that the adsorption phenomenon of Cr (III) and Cr (VI) are endothermic and exothermic, respectively. The entropy value for Cr (III) was found to decrease with temperature while it increased with temperature for Cr (VI). In addition, it is possible to remove Cr (III) and Cr (VI) from synthetic solutions with $Fe(OH)_3$ loaded PMS, but the removal mechanisms for two types of chromium are quite a change from each other. Consequently, PMS can be economically evaluated in the preparation of a composite adsorbent with this proposed process. It means to reduce of PMS load in terms of the environmental and paper production plant. The removal of toxic dyes and heavy metals from wastewater by using PMS or modified PMS can be studied for further study.

REFERENCES

[1] U. Förstner and G. T. W. Wittmann, *Metal pollution in the aquatic environment*. Springer Science & Business Media, 2012.

[2] M. Sittig, "Pollutant removal handbook," 1973.

[3] W. W. Eckenfelder, *Industrial water pollution control*. McGraw-Hill, 1989.

[4] M. Ahmaruzzaman, "Industrial wastes as low-cost potential adsorbents for the treatment of wastewater laden with heavy metals," *Adv. Colloid Interface Sci.*, vol. 166, no. 1–2, pp. 36–59, 2011.

[5] M. C. Monte, E. Fuente, A. Blanco, and C. Negro, "Waste management from pulp and paper production in the European Union," *Waste Manag.*, vol. 29, no. 1, pp. 293–308, 2009.

[6] D. Gavrilescu, "Energy from biomass in pulp and paper mills.," *Environ. Eng. Manag. J.*, vol. 7, no. 5, 2008.

[7] A. Yaras and H. Arslanoğlu, "Valorization of Paper Mill Sludge as Adsorbent in Adsorption Process of Copper (II) Ion from Synthetic Solution: Kinetic, Isotherm and Thermodynamic Studies," *Arab. J. Sci. Eng.*,vol. 43, no. 5, pp. 2393–2402, 2018.

[8] Y. Kalpaklı, Ş. Toygun, G. Köneçoğlu, and M. Akgün, "Equilibrium and kinetic study on the adsorption of basic dye (BY28) onto raw Ca-bentonite," *Desalin. Water Treat.*, vol. 52, no. 37–39, pp. 7389–7399, 2014.

[9] C. I. A. Ferreira, V. Calisto, M. Otero, H. Nadais, and V. I. Esteves, "Removal of tricaine methanesulfonate from aquaculture wastewater by adsorption onto pyrolysed paper mill sludge," *Chemosphere*, vol. 168, pp. 139–146, 2017.

[10] M. Erdem, H. S. Altundogan, A. Özer, and F. Tümen, "Cr (VI) reduction in aqueous solutions by using synthetic iron sulphide," *Environ. Technol.*, vol. 22, no. 10, pp. 1213–1222, 2001.

[11] T. Aoki and M. Munemori, "Recovery of chromium (VI) from wastewaters with iron (III) hydroxide—I: adsorption mechanism of chromium (VI) on iron (III) hydroxide," *Water Res.*, vol. 16, no. 6, pp. 793–796, 1982.

[12] V. M. Dronnet, M. A. V Axelos, C. Renard, and J.-F. Thibault, "Improvement of the binding capacity of metal cations by sugar-beet pulp. 1. Impact of cross-linking treatments on composition, hydration and binding properties," *Carbohydr. Polym.*, vol. 35, no. 1–2, pp. 29–37, 1998.

[13] M. R. Unnithan and T. S. Anirudhan, "The kinetics and thermodynamics of sorption of chromium (VI) onto the iron (III) complex of a carboxylated polyacrylamide-grafted sawdust," *Ind. Eng. Chem. Res.*, vol. 40, no. 12, pp. 2693–2701, 2001.

[14] G. Cimino, A. Passerini, and G. Toscano, "Removal of toxic cations and Cr (VI) from aqueous solution by hazelnut shell," *Water Res.*, vol. 34, no. 11, pp. 2955–2962, 2000.

[15] S. Lagergren, "Zur theorie der sogenannten adsorption geloster stoffe," *K. Sven. vetenskapsakademiens. Handl.*, vol. 24, pp. 1–

39, 1898.

[16] G. Sposito, "Soil particle surface," *The Chemistry of Soils*. Oxford University Press: New York, pp. 136–141, 1989.

[17] S. Ghorbani-Khosrowshahi and M. A. Behnajady, "Chromium (VI) adsorption from aqueous solution by prepared biochar from Onopordom Heteracanthom," *Int. J. Environ. Sci. Technol.*, vol. 13, no. 7, pp. 1803–1814, 2016.

[18] M. Mirabedini, M. Z. Kassaee, and S. Poorsadeghi, "Novel magnetic chitosan hydrogel film, cross-linked with glyoxal as an efficient adsorbent for removal of toxic Cr (VI) from water," *Arab. J. Sci. Eng.*, vol. 42, no. 1, pp. 115–124, 2017.

[19] W. Wang *et al.*, "Cr (VI) removal from aqueous solution with bamboo charcoal chemically modified by iron and cobalt with the assistance of microwave," *J. Environ. Sci.*, vol. 25, no. 9, pp. 1726–1735, 2013.

[20] T. Altun and Y. Kar, "Removal of Cr (VI) from aqueous solution by pyrolytic charcoals," *New Carbon Mater.*, vol. 31, no. 5, pp. 501–509, 2016.

[21] E. Rosales, J. Meijide, T. Tavares, M. Pazos, and M. A. Sanromán, "Grapefruit peelings as a promising biosorbent for the removal of leather dyes and hexavalent chromium," *Process Saf. Environ. Prot.*, vol. 101, pp. 61–71, 2016.

[22] R. Kumar, M. Ehsan, and M. A. Barakat, "Synthesis and characterization of carbon/AlOOH composite for adsorption of chromium (VI) from synthetic wastewater," *J. Ind. Eng. Chem.*, vol. 20, no. 6, pp. 4202–4206, 2014.

[23] M. Jain, V. K. Garg, and K. Kadirvelu, "Adsorption of hexavalent chromium from aqueous medium onto carbonaceous adsorbents prepared from waste biomass," *J. Environ. Manage.*, vol. 91, no. 4, pp. 949–957, 2010.

[24] D. Song *et al.*, "Adsorptive removal of toxic chromium from waste-Water using wheat straw and Eupatorium adenophorum," *PLoS One*, vol. 11, no. 12, p. e0167037, 2016.

[25] G. Huang, J. X. Shi, and T. A. G. Langrish, "Removal of Cr (VI) from aqueous solution using activated carbon modified with nitric acid," *Chem. Eng. J.*, vol. 152, no. 2–3, pp. 434–439, 2009.

[26] S. Babel and T. A. Kurniawan, "Cr (VI) removal from synthetic wastewater using coconut shell charcoal and commercial activated carbon modified with oxidizing agents and/or chitosan," *Chemosphere*, vol. 54, no. 7, pp. 951–967, 2004.

[27] K. Mohanty, M. Jha, B. C. Meikap, and M. N. Biswas, "Removal of chromium (VI) from dilute aqueous solutions by activated carbon developed from Terminalia arjuna nuts activated with zinc chloride," *Chem. Eng. Sci.*, vol. 60, no. 11, pp. 3049–3059, 2005.

[28] Z. A. Al-Othman, R. Ali, and M. Naushad, "Hexavalent chromium removal from aqueous medium by activated carbon prepared from peanut shell: adsorption kinetics, equilibrium and thermodynamic studies," *Chem. Eng. J.*, vol. 184, pp. 238–247, 2012.

[29] G. J. Alaerts, V. Jitjaturunt, and P. Kelderman, "Use of coconut shell-based activated carbon for chromium (VI) removal," *Water Sci. Technol.*, vol. 21, no. 12, pp. 1701–1704, 1989.

JOURNAL OF SCIENCE
SAKARYA UNIVERSITY

Sakarya University Journal of Science

ISSN 1301-4048 | e-ISSN 2147-835X | Period Bimonthly | Founded: 1997 | Publisher Sakarya University | http://www.saujs.sakarya.edu.tr/

Title: Designing and Interpreting a Mathematical Programming Language

Authors: Hüseyin Pehlivan
Recieved: 2018-12-11 06:02:48

Accepted: 2019-04-16 11:50:43

Article Type: Research Article
Volume: 23
Issue: 6
Month: December
Year: 2019
Pages: 1027-1041

How to cite
Hüseyin Pehlivan; (2019), Designing and Interpreting a Mathematical Programming Language. Sakarya University Journal of Science, 23(6), 1027-1041, DOI: 10.16984/saufenbilder.494974
Access link
http://www.saujs.sakarya.edu.tr/issue/44246/494974

Sakarya University Journal of Science 23(6), 1027-1041, 2019

Designing and Interpreting a Mathematical Programming Language

Hüseyin Pehlivan [*1]

Abstract

The syntax of the programming languages has a significant impact on the definition and validation of mathematical calculations. In particular, the management of code identification and validation processes can be made easier and faster, depending on the parametric behavior of the functions. In this article, a programming language that supports the use of mathematical function structures is designed and an interpreter, which can evaluate the source code written in this language, is developed. The language syntax is represented by an LL (k) grammar defined in the BNF notation. The interpreter consists of several basic components such as parser, semantic controller and code evaluator, each of which makes a different kind of code interpretation. The LL (k) parser component used for the syntactic analysis of the language is generated via an automatic code generation tool called JavaCC. The other components work on the abstract syntactic tree that this parser generates. To illustrate the use of the language with code samples, several mathematical algorithms that include calculations on different sequences of numbers, are programmed and interpreted. The paper also performs a comparative analysis of the language with some related ones. The paper also performs a comparative analysis of the language with some related ones based on some design principles and mathematical aspects.

Keywords: programming languages, formal grammars, parsers, interpreters

1. INTRODUCTION

Programming languages are problem solving tools that play a critical role in the development of both computer systems and computer programs which are the most important component of these systems. For programs that can be used in many different service areas such as education, health and safety, it is not only important to edit their source code but also their integration with the target computer systems. A programming language can make it possible to write programs that can easily be integrated into one or several computer systems with different architectures. The efficiency of the development processes of source code depends on design principles adopted by language developers, such as readability, writability, reliability, portability, and

[*] Corresponding Author: pehlivan@ktu.edu.tr

[1] Karadeniz Technical University, Department of Computer Engineering, Trabzon, Turkey. ORCID: 0000-0002-0672-9009

extensibility [1,2]. These principles, increasing the effectiveness and common usage of programming languages, provide an easy adaptation for a wide range of programmers. As each language has its own programming practice or style, some languages are not challenging to use this practice. For example, as in C [3] and Perl [4], very complex coding styles that are subject to international competitions can be developed [5,6].

Programming languages can be divided into two groups as general and special purpose languages. General purpose languages are designed for writing computer applications that can solve different kinds of problems with high level programming structures. They can be classified based on their fundamental features as four main programming paradigms, such as procedural languages (Pascal [7], C [3]), object-oriented languages (Java [8], C# [9]), functional languages (Scheme [10], Haskell [11]) and logical languages (Prolog [12], Ciao [13]). Special purpose languages are developed for programming tasks that require higher performance during compilation, interpretation, or runtime. In these languages, a particular class of problems can be programmed in an easier way, and system security can be increased by hiding the language runtime code. Typical programming areas include text formatting and display (TeX [14], LateX [15]), database interaction (SQL [16], AQL [17]), symbolic mathematics (Matlab [18], Mathematica [19]), hardware identification (Verilog [20], VHDL [21]) and computer games (Maya [22], Unreal Engine [23]).

Functional languages have the syntax similar to the notations of writing mathematical expressions. In these languages, the behavior of mathematical functions play an important role in the definitions made for functions. For example, the scope of the variables is limited to the function bodies and the functions always produce a return value. Since the syntax of the language does not support assignment statements, the variables are single-valued. The behavior of the functions depends only on the parameters given to them. However, some non-mathematical components of the syntax can be used in formal parameter declarations and body definitions of functions.

The literature includes many mathematical programming languages that are basically developed for mathematical modeling and optimization. Typical examples of such languages are AIMMS, AMPL, GAMS, LINGO, LPL, Mosel, MPL, OMNI, OPL and PCOMP, which are all described in [24]. In the modeling languages, the real-world problems are especially represented by mathematical models constructed with a proper set of some relationships such as equalities, inequalities and logical conditions. The main focus is on the provision of programming structures required for mathematical formulations of the problems. The syntax and semantics of these structures contain the code components such as loops and selection statements, as well as strict evaluation, which are not purely mathematical. The same is true for those in special purpose languages such as Matlab and Mathematica.

The design and development processes of programming languages require the coding of a large number of components from syntax definition to code generation in a machine language. One of these components is the language parser that performs syntax analysis. In order to generate the parser code automatically, many compiler-compiler tools (also called parser generators) such as YACC [25], SableCC [26] and JavaCC [27] are developed. Each tool usually uses a different specification file in which the syntax of a particular language is defined in a similar way to the structure of formal grammars [28]. For example, the JavaCC tool that generates the source code of a parser in Java requires the use of two different definition formats adapted from the language grammar for the words and expressions contained in the language syntax.

This paper addresses the development of a mathematical programming language, shortly called MaPL. The mathematical expressions construct the main computational structure of the MaPL language represented by a formal grammar. The interpreter implemented for the language has

several components, such as lexer, parser, semantic controller and code evaluator. The JavaCC tool is used for lexical analysis, syntax analysis and generation of abstract syntax tree (shortly called as AST). The operations of semantic analysis and code evaluation are performed through the syntax tree.

In the design of the syntax of the MaPL language, basic programming structures that meet the requirements of mathematical programming are taken into consideration. Variable declaration, sequential execution, conditional selection, repeated execution and function definition are the most important programming structures. As in functional languages, variable declarations are made without specifying the data type, and repeated calculations are performed with the help of recursive definitions which may be an alternative to the looping statements. Different statements can be executed depending on certain conditions.

2. SYNTAX

Syntax is an issue related to the expression structure of a language. MaPL is designed as a programming language with syntax supporting the notation of writing mathematical expressions. The syntax of the language allows the definition of functions in two different ways, which can be given as follows:

function(p1, p2, …, pn) = body
function(p1, p2, …, pn) : {s1, s2, …, sn} = body

In this syntax, the declarations such as x or x + k (k is an integer) can be made in the formal parameter fields represented by the elements such as p1 and p2. The elements such as s1 and s2, which are specified by opening a code block, can be assignment statements or print statements that display data on the standard output. In the body of the functions, in addition to the ordinary calculation expressions, a sequence of the pairs of expressions and conditions can appear in the following form.

{ expression, condition }

The expressions in this form correspond to the definitions of segmented functions in mathematics. Here are the examples of two functions defined in the MaPL language.

f(x) = 2 * x + 1
g(x+1,y) : { z = x + y; print(z) } = x * y + z

The MaPL language does not include the looping statements provided by the imperative programming languages. In accordance with the mathematical definitions of functions, recursive functions should be used for the calculations that must be made through a looping statement. For example, for the sum of integers between 1 and n, the following function definition can be made, consisting of two equations.

fSum(1) = 1
fSum(n) = fSum (n-1) + n

It is also possible to define in a similar way to the segmented function structure in mathematics. As the function fSum is defined mathematically like

$$f(n) = \begin{cases} 1, & n = 1 \\ f(n-1) + n, & n > 1 \end{cases}$$

the corresponding definition in the MaPL language can be made as follows (instead of the keyword "otherwise", a conditional expression like “n> 1” can also be used to represent the other cases).

fSum(n) = { 1, n == 1 }
{ fSum (n-1) + n, otherwise }

Three types of data can be used in the source file; int, double and string. There is no need to explicitly declare the data types of variables. The type inference of a variable is performed by the language itself, with the type analysis of the first expression that assigns data to that variable. For example, in the following expression, the type inference for the variable x will be made as a string.

x=2 + 3.4 + "5"

Note that the addition operations in this statement associate from left to right. Thus, the value 5.4 calculated by the first operation (i.e., 2 + 3.4) will be of double type and then the data "5.45"

calculated with the next operation (i.e., 5.4 + "5") will be of string type.

The MaPL language has a flat block structure consisting of two levels: global and local. The scope of the function definitions corresponds to the global level, which is the entire source code file. The definitions of formal parameters and local variables have a scope limited only to the body of the relevant function.

As in most programming languages, the evaluation of the source code is initiated by the invocation of the function called main. A source code file can have many syntax components, such as functions, arguments, formal parameters, and segmented function equations. In the language parser, syntax classes are defined using a data structure of linked lists to represent these components. The number of syntax components that can be contained by the source code is determined dynamically by the size of the memory the interpreter uses.

3. PARSING

The parsing process requires the design of a formal grammar for the syntax of a programming language. The JavaCC tool is used to develop the parser for the MaPL language. This section shows how to use a formal grammar in the production of the parser via JavaCC.

3.1. Grammar Design

A formal grammar is specified using a mathematical notation such as BNF and EBNF. The EBNF notation is an extended version of BNF with the addition of some meta-characters (*, +, ?, |, etc.). In these notations, a grammar can consist of one or more syntactic definitions, called rules, which govern the phrase structure of a language. The recursive nature of the rules can always generate an infinite number of possible sentences out of finite number of words. A grammar rule has left and right side definitions separated by symbols such as “=”, “:=” or “->”. The left side of the rule contains a non-terminal and the right side contains a collection of some terminals (also called token) or non-terminals. In the following grammar specifications, the terminals are written in double quotes.

In the syntax analysis, first the source data is scanned from the left to the right and broken into a sequence of terminals. Then the order of terminals in the sequence is examined by means of a grammar. The token examination can be performed from left to right (LL(k) parsing) or from bottom to top (LR(k) parsing), where k is the amount of lookahead the parser needs to select a rule. Since the JavaCC tool can produce only LL(k) parsers, the formal grammar designed for the MaPL language has to consist of a set of rules satisfying the following three properties.

- All the alternatives of a rule (the rules that contain the same non-terminal on the left side) have to produce a k number of different first tokens.
- If there is a rule that may not produce any token, this rule and the rule called after it have to produce a k number of different first tokens.
- The right side of a rule must not contain a left-recursive definition.

Considering the above properties, the LL(1) grammar developed for k = 1 is shown in Table 1, using the EBNF notation. Please note that the grammar does not provide the necessary definitions for id, num, dnum and str rules. The format of the data that is generated by these rules will be defined in the token specification block of the parser.

Table 1. Formal grammar for the MaPL language

```
program -> function ( program )?
function -> header ( block )? "=" ( expr | eqlist )
header -> id "(" ( parlist )? ")"
parlist -> param ( "," parlist )?
param -> id ("+" num)? | num
eqlist -> "{" expr "," bexpr "}" ( eqlist )?
block -> ":" "{" ( stmlist )? "}"
stmlist -> stm ( "," stmlist )?
stm -> id "=" expr
stm -> "print" "(" explist ")"
explist -> expr ( "," explist )?
```

```
expr -> ("+" | "-")? term ( ("+" | "-") term )*
term -> power ( ("*" | "/" | "%") power )*
power -> elem ( "^" power )?
elem -> id ( "(" ( explist )? ")" )? | num | dnum
elem -> str | "(" expr ")" | abs "(" expr ")"
bexpr -> and ( "||" and )*
and -> not ( "&&" not )*
not -> "!" "(" bexpr ")" | belem | "otherwise"
belem -> expr boper expr
boper -> "==" | "/=" | "<" | "<=" | ">=" | ">"
```

The grammar in Table 1 also includes the descriptions of the semantic structure of the MaPL language. The usual precedence and associativity of the operators are two semantic issues, which can be represented by the grammar rules. For example, the expr rule containing the operators "+" and "-" is invoked before the rules (i.e., term and power) containing other operators. The early invocation places these two operators in the nodes close to the root of the parsing tree), giving them a lower priority level. On the other hand, since the power rule is defined in a right-recursive way, the operator "^" contained by the rule is made right-associative.

The JavaCC tool requires three types of definitions for a programming language, such as lexical structure, syntactic structure and generating expressions of abstract syntax tree. All these definitions are stored in the same JavaCC specification file.

3.2. Lexer

The lexical structure of a language is usually defined using regular expressions. In the MaPL-language word set, in addition to 25 functional components consisting of 16 operators, 3 keywords and 6 other symbols, there is an infinite number of data components represented by the rules id, num, dnum and str in Table 1. A separate token class is defined for each of the functional components, while there is only one token class per rule for the others. In the syntax analysis, it is sufficient to make the token class definition for the types since the type of the data is more important than the value.

In Table 2, token class definitions of the MaPL language are given in the TOKEN block in accordance with the JavaCC specification format. No tokens are produced for the words covered by the definitions made within the SKIP block. The token classes whose names begin with the symbol #, such as LETTER and DIGIT, are used as part of other class definitions.

Table 2. Token definitions

```
TOKEN: {
    <PLUS: "+"> | <MINUS: "-">
  | <TIMES: "*"> | <DIVIDE: "/">
  | <MOD: "%"> | <POWER: "^">
  | <AEQ: "="> | <AND: "&&"> | <OR: "||">
  | <NOT: "!"> | <EQ: "=="> | <NE: "/=">
  | <LE: "<"> | <LT: "<="> | <GT: ">=">
  | <GE: ">"> | <COMMA: ",">
  | <COLON: ":"> | <LCURLY: "{">
  | <RCURLY: "}"> | <LPAREN: "(">
  | <RPAREN: ")"> | <ABS: "abs">
  | <PRINT: "print"> | <OTHER: "otherwise">
  | <#LETTER: ["a"-"z","A"-"Z"]>
  | <#DIGIT: [0"-"9"]>
  | <ID: <LETTER>(<LETTER> | <DIGIT>)*>
  | <NUM: (<DIGIT>)+>
  | <DNUM: (<DIGIT>)+"."(<DIGIT>)+>
  | <STR: ("\"" (~["\""] | "\\" "\"")* "\"")>
}
SKIP: { " " | "\t" | "\r" | "\n" }
```

For example, according to the definitions given in Table 2, the sequence of the tokens produced for the statement print (x, y + 1) will be as follows.

PRINT LPAREN ID COMMA ID PLUS NUM RPAREN

This token sequence indicates that the specification order in Table 2 is important. The lexer evaluates all token class definitions from top to bottom, for each word it scans in the source data, and selects the first one matching the word and produces the corresponding token. For example, there are two possible token classes that match the word "print"; PRINT and ID. However, since the print is a keyword in the MaPL language, the PRINT token must be produced. Therefore, the

PRINT definition is placed in one of the lines before the ID definition, with the aim of producing the correct token.

3.3. Parser

The parsers that are used to analyze the syntactic structure of a programming language can be developed by hand or by means of an automated code generating tool like JavaCC. With these tools, the source code of a parser is generated from the method definitions based on the grammar rules of the language. The language of the generated code varies depending on the used tool. For example, the JavaCC tool generates the parser code in the Java programming language.

With the two main deterministic parsing methods called LL(k) and LR(k), the parsing steps are managed by the grammar representing the syntax of the language. An LL(k) parser that performs a leftmost derivation of the code can be configured according to the structure of the grammar rules. It is possible to develop an LL(1) parser for the formal grammar given in Table 1, where a rule can be selected only with one token (i.e., k = 1). In this way, some method definitions are added to the parser to represent each grammar rule, keeping them in the order that the rules call each other in the grammar. Table 3 shows some of typical method definitions for an LL(1) parser using the JavaCC specification format.

Table 3. Parser methods

```
void start() : { } {program() <EOF>}
void program() : { } {function() (program())?}
void function() : { }
  {header() (block())? <AEQ> (expr()|eqlist())}
void header() : { }
  {<ID> <LPAREN> ( parlist )? <RPAREN>}
void parlist() : { }
  { param() (<COMMA> parlist() )? }
void param() : { }
  { <ID> (<PLUS> <NUM> )? | <NUM> }
void eqlist() : { }
  { <LCURLY> expr() <COMMA>
          bexpr() <RCURLY> ( eqlist() )? }
void block() : { }
  { <COLON> <LCURLY>
          ( stmlist() )? <RCURLY> }
void stmlist() : { }
  { stm() ( <COMMA> stmlist() )? }
void stm() : { }
  { <ID> <AEQ> expr()
  | <PRINT> <LPAREN>
          explist() <RPAREN> }
void explist() : { }
  { expr() (<COMMA> explist() )? }
```

As shown in Table 3, start() is the starting method of the parser. A special JavaCC token <EOF> is used to mark the end of source data that can be entered from the standard input or read from a file. The parsing process continues to perform on the source data until this token is encountered.

3.4. Syntax Classes

Syntax classes serve to build a tree-based representation of source data with object-oriented programming structures. The grammar rules of the language have an important role in what syntax classes must be defined. In general, a syntax class is defined for each grammar rule that contains an operator or keyword. The definition of syntax classes representing the rules with the alternatives is made by inheriting from the same super class and thus they can serve as alternatives to each other in a similar way to the rules.

In some cases, a single class is created by combining some of the grammar rules (especially those that are complementary to a certain expression or statement, or invoked by another rule). For example, in the case that a programming language expression is defined by more than one grammar rule, it is adequate to define one syntax class to represent all of these rules. In the grammar in Table 1, the syntax classes for the <block>, <expr>, and <eqlist> rules, which are all invoked by the <function> rule, are not defined.

A syntax class can be given the name of the related grammar rule represented or another name associated with the expression generated by that

rule. The fields of the class are defined by the data types appropriate to the terminals and non-terminals contained in the relevant rule. The classes Var, Num, DNum and Str, for which a rule is not defined, are constructed for id, num, dnum and str non-terminals, respectively. Table 4 shows some of the syntax classes.

Table 4. Syntax classes

```
class Program {
  Function def; Program prog;
  public Program(Function x, Program y)
  { def = x;  prog = y; }
}
class Function {
  Header f;  Stm s;  EList eq;
  public Function(Header x, Stm y, EList z)
  { f = x;  s = y;  eq = z; }
}
class EList {
  Exp e;  BExp b;  EList eq;
  public EList(Exp x, BExp y, EList z)
  { e = x;  b = y;  eq = z; }
}
class Stm { }
class AStm extends Stm {
  String id;  Exp e;
  public AStm(String x, Exp y) {id = x;  e = y;}
}
class PStm extends Stm {
  EList eq;
  public PStm(EList x) { eq = x; }
}
class Exp { }
class Header extends Exp {
  String id; EList eq;
  public Header(String x, EList y)
  { id = x;  eq = y; }
}
```

Although, in most programming languages, the definition expression of a function has a different format or syntax from the invocation expression, both expressions can have the same syntax in the MaPL language. Therefore, the object reference of the Header type added to the Function class will be used to represent both the function definition and calling expressions.

As seen in Table 4, a constructor that is used to create an object of the related class is provided for all the syntax classes. In addition, in the phase of interpreting the source data, a method called accept() for the use of the Visitor interface, described in Section 4, must be defined in the syntax classes as follows.

```
public ..... accept(Visitor v) {
    return v.visit(this);
}
```

The type of the return value for this method should be void for the classes such as Stm, AStm and PStm, and Object for the ones such as Exp, Header and Plus.

3.5. Abstract Syntax Tree

A syntax tree is created as a representation of the source data in the form of a tree data structure by connecting objects derived from syntax classes. The functional components (operators, keywords, etc.) of the source code form the intermediate nodes of the tree, while the data components (constants, variables, etc.) do the leaves. In this way, each node of the tree can contain objects of a different syntax class, depending on the type of the related code component.

Syntax trees are used to perform operations such as type control and code interpretation that are difficult to perform over source data. As in the syntax analysis of the source data, the JavaCC tool can be used in the production of syntax trees. For this purpose, the expressions in Java that will generate the data required for the corresponding node of the syntax tree are added to the special code blocks that are opened in the body of the parser methods. The production of the tree is provided via these expressions that are performed simultaneously with the syntax analysis. In Table 5, some parser methods are shown together with the code blocks added for the generation of the syntax tree.

Table 5. Parser methods that generate abstract syntax tree

```
Program start() : { Program prog; }
  { prog=program() <EOF> { return prog; } }
Program program() :
  { Function def; Program prog = null; }
  { def=function() ( prog=program() )?
    { return new Program(def, prog); } }
Function function() :
  { Header fn; Stm s=null; EList eq; Exp e; }
  { fn=header() ( s=block() )? <AEQ>
   ( e=expr()
    {eq = new EList(e, new BNum(true), null);}
     | eq=eqlist() )
    { return new Function(fn, s, eq); } }
Header header() :
  {Token t; EList eq = null; boolean b = false;}
  { t=<ID> <LPAREN>
       ( eq=parlist() )? <RPAREN>
    { return new Header(t.image, eq); } }
EList parlist() :{ EList eq = null; Exp e; }
  { e=param() ( <COMMA> eq=parlist() )?
    { return new EList(e, null, eq); } }
Exp param() : { Token t, t2; Exp e; }
  { t=<ID> ( <PLUS> t2=<NUM>
     return new Plus(new Var(t.image),
     new Num(Integer.parseInt(t2.image))); } )?
     { return new Var(t.image); }
   | t=<NUM> { return new
            Num(Integer.parseInt(t.image)); } }
EList eqlist() :
  { Exp e; BExp b; EList eq = null; }
  { <LCURLY> e=expr() <COMMA>
    b=bexpr() <RCURLY> ( eq=eqlist() )?
    { return new EList(e, b, eq); } }
Stm block() : { Stm s=null; }
  { <COLON> <LCURLY> ( s=stmlist() )?
    <RCURLY> { return s; } }
```

Since the syntax analysis starts with a call to the start() method, the root node of the syntax tree always has an object of the Program type. Other methods called during the analysis produce different types of objects. For example, using the class definitions in Table 4 and the method definitions in Table 5, the syntax tree produced by the parser for the expression print (x, y + 1) would be as follows.

```
PStm p = new PStm(new EList(new Var("x"),
null,
                new EList(new Plus(new Var("y"),
                  new Num(1)), null, null)));
```

The EList class, defined as a linked list, is used in object construction through several parser methods. The list of function formal parameters, the argument lists of both the print function and user-defined functions, and the list of segmented functions are created as an object of the EList class. The related list element is given as the first argument to this class constructor, the other argument is either the condition expression of the segmented function list or null for the other lists.

4. EVALUATION

The two components, the semantic controller and the code evaluator, need to interpret the source code, using the syntax tree. The implementation of these components that interpret the AST data in different forms is based on the Visitor design pattern, which is one of the behavioral design patterns [29].

4.1. Visitor Interface

The Visitor interface, which provides the type information of visit() methods, corresponds to one of the two components of the Visitor design pattern. The other component is the Accept interface and involves the definition of accept() methods within all syntax classes. The visit() and accept() methods together constitute a double dispatch mechanism that is used to evaluate the objects found in the AST data. Table 6 lists some of the methods that are described in the Visitor interface.

Table 1. Visitor interface

```
interface Visitor {
  public Object visit(Exp e);
  public Object visit(Fn e);
  public Object visit(Plus e);
```

```
    public Object visit(Minus e);
    public Object visit(Times e);
    public Object visit(Divide e);
    public Object visit(Mod e);
    public Object visit(Power e);
    public Object visit(Var e);
    public Object visit(Num e);
    public Object visit(DNum e);
    public Object visit(Str e);
    public void visit(Stm s);
    public void visit(AStm s);
    public void visit(PStm s);
 …….
 }
```

For some method declarations in Table 6, the type of the return value is specified as Object. This kind of method declarations allows the use of the same Visitor interface for different evaluation requirements (type control, interpretation, etc.) of the abstract syntax tree.

4.2. Semantic Controller

For type control operations performed with the semantic controller, a symbol table is created using the definitions in the source code. All formal parameters and local variables defined in the body of the functions are added as symbols to this table. There are some important cases to take into account when an entry is added to the symbol table, which are given below.

- The formal parameters of a function must have unique names.
- The type of a formal parameter is inferred from the expression that uses the parameter.
- The names of local variables must be different from formal parameter names.
- The type of a local variable is inferred from the expression that initializes its first value.

Table 7 shows the SymTable class defined to represent the symbol table. During the analysis of a function definition, a new symbol block is created in the symbol table, and all symbols and their types in the related definition are stored in this block. The symbol block is only accessible through the analysis of the function and is released when the analysis is finished.

Table 7. SymTable class

```
class SymTable {
  int size;
  int index = -1;
  Hashtable[] table;
  public SymTable(int s) {
    size = s;
    table = new Hashtable[s];
  }
  public int beginScope() {
    ++ index;
    if (index >= table.length)
      return -1;
    table[index] = new Hashtable();
    return 0;
  }
  public void endScope() {
    -- index;
  }
  public void put(String id, Object obj) {
    if (obj == null)
      return ;
    table[index].put(id, obj);
  }
  public Object get(String id) {
    return table[index].get(id);
  }
}
```

The semantic analysis of the source code focuses on the syntax tree created by the parser. First, traversing all nodes of the tree, the symbol definitions are determined. For each symbol defined in the source code, a pair (name, type) is stored in the symbol table. For example, the pair ("x", new Num (0)) for a variable x of type int and the pair ("y", new Str ("")) for a variable y of type string are added to the symbol table. When the use of a symbol is encountered during the traversal, the symbol table is looked up and their types are obtained. The following cases are considered for the type inspection performed through the symbol table.

- The data type, order and number of formal parameters as well as the type of returned data must be the same in all equations of a function.
- The actual parameters passed to a function must match the formal parameters in type, order and number.
- The type of a formal parameter or a local variable must be compatible with the use in all expressions, or with the type of value re-assigned to it.
- All local variables must be initialized before being used.
- Each called function must have a definition.
- All operators must be applied to the correct type of data.

The TypeVisitor class, which is implemented from the Visitor interface, is defined to represent the semantic controller. Table 8 shows a part of the TypeVisitor class with the visit() methods defined on some syntax classes.

Table 8. TypeVisitor class

```
Class TypeVisitor implements Visitor {
  Program p;
  SymTable t;
  public TypeVisitor(Program a, SymTable b)
    { p = a;  t = b; }
  public void visit(Stm s) {
    s.accept(this);
  }
  public void visit(LStm s) {
    s.a.accept(this);
    s.b.accept(this);
  }
  public void visit(AStm s) {
    Object a = s.a.accept(this);
    if (a != null) {
      Object b = t.get(s.id);
      if (b == null)
        t.put(s.id, a);
      else if ((a instanceof Num &&
                  !(b instanceof Num)) ||
               (a instanceof DNum &&
                  !(b instanceof DNum)) ||
               (a instanceof Str &&
                  !(b instanceof Str)))
        System.out.println("Consistency error: "
     + s.id + "=" + new PrintVisitor().visit(s.a));
      }
      else
       System.out.println("Inference  error: " +
         s.id + "=" + new PrintVisitor().visit(s.a));
  }
  public Object visit(Var e) {
    return t.get(e.id);
  }
  public Object visit(Num e) {
    return new Num(0);
  }
}
```

In the code fragment shown in Table 8, there is a visit() method defined to analyze a tree node of type AStm that represents an assignment statement. This method checks the compatibility of the type of the variable on the left side of the statement with the type of data calculated by the expression on the right side. If the type cannot be inferred from the expression or the type inconsistency is encountered, then the PrintVisitor class, which is also implemented from the Visitor interface, is used to indicate the relevant expression of the source code.

4.3. Evaluator

The symbol table represented by the SymTable class in the previous section is also used to evaluate the source code. The evaluation process traverses the nodes of the syntax tree and stores the pairs (name, value) for the values assigned to formal parameters or local variables in this table. For example, the pair ("x", new DNum (3.0)) for the expression x = 3.0 is added to the symbol table. If this expression is followed by another expression y = x + 1, then the value of the variable x is queried from the symbol table and a new pair ("y", new DNum (4.0)) is added to the table.

The code evaluator component is represented by the EvalVisitor class implemented from the Visitor

interface. Table 9 shows the EvalVisitor class with some visit() methods.

Table 9. EvalVisitor class

```
class EvalVisitor implements Visitor {
  Program p;
  SymTable t;
  public EvalVisitor(Program a, SymTable b)
    { p = a;  t = b; }
  public void visit(Stm s) {
    s.accept(this);
  }
  public void visit(LStm s) {
    s.a.accept(this);
    s.b.accept(this);
  }
  public void visit(AStm s) {
    t.put(s.id, s.a.accept(this));
  }
  public Object visit(Var e) {
    return t.get(e.id);
  }
  public Object visit(Num e) {
    return new Integer(e.n);
  }
}
```

In all classes implementing the Visitor interface, the data passing between the visit() methods is performed through the objects of type Object. So, in order to be able to use the value wrapped in an object in the calculations, it needs to be converted from the Object type to the primitive data type. For example, given the statement obj=new Integer(x) wrapping the integer x with the object of type Integer, the conversion from the wrapping object to the correct type is performed by the statement x=((Integer)obj).intValue().

5. INTERPRETATION

This section describes the integration of the interpreter components and some examples of programs developed in the MaPL language.

5.1. Integration of Components

The interpreter of the MaPL language is constructed by integrating the Parser, Semantic Controller and Evaluator components introduced in the previous sections. The main() method of the interpreter contained in the Interpreter class is coded as shown in Table 10.

Table 2. Interpreter class

```
public class Interpreter {
 public static void main(String[] args) {
  try {
   Program p =
     new Parser(System.in).Prog();
   SymTable t = new SymTable(10000);
   TypeVisitor type = new TypeVisitor(p, t);
   Object res = type.visit(new Fn("main", null));
   if (res != null) {
     EvalVisitor eval = new EvalVisitor(p, t);
     eval.visit(new Fn("main", null));
   }
  }
  catch(ParseException ex) {
     System.out.println(ex.getMessage());
  }
 }
}
```

There are some source files that the interpreter components depend on. The parser is composed of the JavaCC specifications and the syntax classes for which the files Parser.jj and AST.java are developed, respectively. The type controller is stored in the file TypeVisitor.java, and the code evaluator in the file EvalVisitor.java. Using these files placed in the same directory, the interpreter can be produced as follows.

```
$>  javacc Parser.jj
$>  javac *.java
```

The interpretation of a program written in the MaPL language, which is held in a source file called prog.txt, is started by the following command

```
$>  java Interpreter < prog.txt
```

5.2. Program Examples

To illustrate the syntax of the MaPL language, five examples of programs that generate some popular sequence of numbers are given below.

Program 1: Table 11 shows the source code of a program that finds all the factors of the number 100 and displays it via the show() function.

Table 11. Program that finds the factors of 100

```
main() = factor(100, 1)
factor(n, k) =
    { 0, k > n }
    { show(n, k), n % k ==0 }
    { factor(n, k+1), otherwise }
show(n, k) : { print(k + " ") } = factor(n, k+1)
```

Output 1: The output of the program is as follows:

1 2 4 5 10 20 25 50 100

Program 2: The program in Table 12 shows the prime numbers smaller than 40 in the ascending order; the mod() function checks the divisibility of the number n with the integers k less than the number $\sqrt{n}$.

Table 3. Program that finds the primes up to 40

```
main() = prime(40, 2)
prime(n, k) =
    { 0, k >= n }
    { show(n, k), mod(k, 2)>0 }
    { prime(n, k+1), otherwise }
mod(n, k) =
    { 1, k*k > n }
    { 0, n % k == 0 }
    { mod(n, k+1), otherwise }
show(n, k) : { print(k + " ") } = prime(n, k+1)
```

Output 2: The output of the program is as follows:

2 3 5 7 11 13 17 19 23 29 31 37

Program 3: The program given in Table 13 shows the factorials of positive integers not greater than 5; The fact() function is written in accordance with the mathematical definition. The print() function with no argument writes a new line to the standard output.

Table 43. Program that shows the factorials of 0 to 5

```
main() = show(5, 0)
show(n,k) : { print((k) + "!=" + fact(k)), print()
} =
    { 0, k >= n }
    { show(n, k+1), otherwise }
fact(0) = 1
fact(n) = n * fact(n-1)
```

Output 3: The output of the program is as follows:

0!=1
1!=1
2!=2
3!=6
4!=24
5!=120

Program 4: The program in Table 14 shows the first 15 elements of the fibonacci number sequence, where the fib() function is written in accordance with the mathematical definition.

Table 54. Program that shows the 15 fibonacci numbers

```
main() = show(14, 0)
show(n, k) : { print(fib(k) + " ") } =
  { 0, k >= n }
  { show(n, k+1), otherwise }
fib(0) = 0
fib(1) = 1
fib(k) = fib(k-1) + fib(k-2)
```

Output 4: The output of the program is as follows:

0 1 1 2 3 5 8 13 21 34 55 89 144 233 377

Program 5: The following program in Table 15 shows the first 10 elements of the Catalan number sequence, where the cat() function is written from the mathematical definition. The current syntax of the MaPL language does not allow the use of the

summation symbol (∑), which represents the sum of number sequences.

Table 65. Program that shows the 10 Catalan numbers

```
main() = show(9,0)
show(n, k) : { print(cat(k, 0) + " ") } =
    { 0, k >= n }
    { show(n, k+1), otherwise }
cat(n+1, i) =
    { 1, n < 0 }
    { 0, i > n }
    { cat(i, 0) * cat(n-i, 0) + cat(n+1, i+1),
      otherwise }
```

Output 5: The output of the program is as follows:

1 1 2 5 14 42 132 429 1430 4862

6. COMPARATIVE ANALYSIS

There are several design principles (also known as language metrics) that are introduced for guiding the evaluation of programming languages [30]. For a comparative analysis of the MaPL language, selecting the languages C, C++, Java, Haskell and Matlab, we perform the evaluation based on the metrics of efficiency, extensibility, maintainability, portability, orthogonality, readability, reliability, uniformity and writability. The results are presented in Table 16.

Table 76. Comparison of selected languages via some metrics

Metrics	MaPL	C	C++	Java	Haskell	Matlab
Efficiency	X	X	X	X	X	X
Extensibility		X	X	X	X	X
Maintainability	X	X	X	X	X	X
Orthogonality	X				X	
Portability	X			X		X
Readability	X	X	X	X	X	X
Reliability	X	X	X	X	X	X
Uniformity	X			X	X	
Writability	X	X	X	X	X	X

Another comparison is made for some mathematical languages from the perspective of programming aspects that can support mathematical reasoning. These aspects are generally related to the syntax and semantics of a language; the ones such as referential transparency, non-strict semantics, assignments, recursion, pattern-matching are purely mathematical, as the others such as type annotations, loops, selection statements and side-effects are not. The evaluation focuses on four mathematical languages (i.e., OPL, LPL, AMPL and CMPL) as well as MaPL, considering mathematics as another language called Math. Table 17 shows the analysis results.

Table 87. The aspects of some mathematical languages

Aspect	Math	MaPL	OPL	AMPL	LPL	CMPL
assignments	X	X	X	X	X	X
loops			X	X	X	X
non-strict semantics	X	X				
pattern-matching	X	X	X			
recursion	X	X	X	X		
referential transparency	X	X				
segmented functions	X	X	X		X	
selection statements			X	X	X	X

side-effects	X	X	X	X
type annotations	X	X		X

7. CONCLUSIONS

This study describes the development and interpretation of a programming language (called MaLP) based on the syntax notation of mathematical expressions. The language development process starts with the grammar design and ends with the interpretation stage after various definitions for the syntax. With respect to the syntax, the JavaCC tool is used for the definition of the token and expression structures, and the generation of the abstract syntax tree. During the type control and interpretation stages, two Visitor interfaces that use the abstract syntax tree are implemented. The results of some evaluations of the language interpreter are shown for several examples of MaPL programs.

The syntax of the MaPL language is designed to meet the general programming needs. The language source code supports the use of the basic programming language structures, such as variables, expression sequences, selection (or conditional) expressions, loops, and functions in a mathematical way. In the definitions of mathematical functions based on variables, expressions are written in a polynomial-like form. Different execution paths can be created depending on the selection between two or more statements controlled by conditional expressions. Loop expressions can only be represented by the definitions of recursive functions. These mathematical aspects of the language are supported by the results of the comparative analysis made with some other mathematical languages.

The language syntax needs to be extended to allow the programming of many different mathematical operations during the coding process. For example, it is important that complex numbers and fractional numbers can be represented and basic operations can be performed on these numbers. In addition, there is another need for the operations carried out by the logarithmic and trigonometric functions as well as the summation and product notations used on number sequences. These kinds of operations can be supported by adding new keywords to the language syntax or by developing a language library.

REFERENCES

[1] L. K. C. Louden, “Programming Languages: Principles and Practices", *Cengage Learning*, 2011.

[2] R. Harper, "Practical Principles for Programming Languages", 2nd ed., *Cambridge University Press*, 2016.

[3] B. W. Kernighan and D. M. Ritchie, "The C Programming Language", *Prentice Hall Professional Technical Reference*, 1988.

[4] L. Wall, T. Christiansen and J. Orwant, "Programming Perl", 3rd ed., *O'Reilly Media*, 2000.

[5] M. Mateas and N. Montfort, "A Box, Darkly: Obfuscation, Weird Languages, and Code Aesthetics", In *Digital Arts and Culture: Digital Experience: Design, Aesthetics, Practice (DAC 2005)*, Copenhagen, Denmark, 2005.

[6] International Obfuscated C Code Contest., https://www.ioccc.org/, 2018.

[7] J. Wakerly, "The programming language Pascal", *Microprocessors and Microsystems*, vol. 3, no. 7, pp. 321-326, 1979.

[8] K. Arnold, J. Gosling, and D. Holmes, "The Java programming language", *Addison Wesley Professional*, 2005.

[9] A. Hejlsberg, M. Torgersen, S. Wiltamuth, and P. Golde, "C# Programming Language", *Addison-Wesley Professional*, 2010.

[10] G. Sussman and G. L. Steele, Jr., "Scheme: A interpreter for extended lambda calculus",

Higher-Order and Symbolic Computation, vol. 11, no. 4, pp. 405-439, 1998.

[11] S. P. Jones. "Haskell 98 language and libraries: the revised report", *Cambridge University Press*, 2003.

[12] L. Sterling and E.Y. Shapiro, "The Art of Prolog: Advanced Programming Techniques", 2nd ed., *The MIT Press*, 1994.

[13] M. V. Hermenegildo, F. Bueno, M. Carro, P. López-García, E. Mera, J. F. Morales and G. Puebla, "An overview of Ciao and its design philosophy", *Theory and Practice of Logic Programming - Prolog Systems*, vol.12, no. 1-2, pp. 219-252, 2012.

[14] W. T. Richter, "TEX and Scripting Languages", *Proceedings of the Practical TEX 2004 Conference*, TUGboat, vol. 25, no. 1, pp. 71-88, 2004.

[15] L. Lamport, "LateX : A document preparation system", 2nd ed., *Addison-Wesley*, 1994.

[16] F. Houlette, "SQL: A Beginner's Guide", *McGraw-Hill Education*, New York, US, 2000.

[17] IBM Security QRadar, "Ariel Query Language (AQL) Guide v7.3.1", *IBM Corp.*, 2017.

[18] D. J. Higham , N. J. Higham, The Matlab Guide, 3rd ed., SIAM, 2017.

[19] M. Trott, "The Mathematica guidebook for programming", *Springer*, 2014.

[20] D. E. Thomas, P. R. Moorby, "The Verilog Hardware Description Language", 5th ed., *Springer*, 2002.

[21] D. L. Perry, "VHDL: Programming by Example", *McGraw-Hill Education*, 2002.

[22] M. McKinley, "The Game Animator's Guide to Maya", *Sybex*, 2006.

[23] A. Tavakkoli, "Game Development and Simulation with Unreal Technology", *Routledge*, 2015.

[24] J. Kallrath, "Modeling Languages in Mathematical Optimization", *Springer*, Boston, MA, 2004

[25] J. R. Levine, J. R. Levine, T. Mason and D. Brown, "Lex & Yacc", *O'Reilly Media, Inc*., Sebastopol, CA, USA, 1992.

[26] E. M. Gagnon and L. J. Hendren, "SableCC, an object-oriented compiler framework", In *TOOLS USA 98 (Technology of Object-Oriented Languages and Systems)*, IEEE, 1998.

[27] V. Kodaganallur, "Incorporating language processing into Java applications: A JavaCC tutorial", *IEEE Software*, vol. 21, no. 4, pp. 70–77, 2004.

[28] A. J. Dos Reis, "Compiler Construction Using Java, JavaCC, and Yacc", *IEEE Computer Society, Inc.*, 2012.

[29] E. Gamma, R. Helm, R. Johnson, and J. Vlissides, "Design Patterns: Elements of Reusable Object-Oriented Software", *Addison-Wesley Reading*, MA, 1995.

[30] R. Harper, Practical Principles for Programming Languages, 2nd ed., *Cambridge University Press*, 2016.

JOURNAL OF SCIENCE
SAKARYA UNIVERSITY

Sakarya University Journal of Science

ISSN 1301-4048 | e-ISSN 2147-835X | Period Bimonthly | Founded: 1997 | Publisher Sakarya University | http://www.saujs.sakarya.edu.tr/

Title: Strategic Factors Affecting Green Building Industry: A Macro-Environmental Analysis Using PESTEL Framework

Authors: Serdar Ulubeyli, Oğuzhan Kazancı, Aynur Kazaz, Volkan Arslan
Recieved: 2018-10-25 16:24:02

Accepted: 2019-05-10 18:31:18

Article Type: Research Article
Volume: 23
Issue: 6
Month: December
Year: 2019
Pages: 1042-1055

How to cite
Serdar Ulubeyli, Oğuzhan Kazancı, Aynur Kazaz, Volkan Arslan; (2019), Strategic Factors Affecting Green Building Industry: A Macro-Environmental Analysis Using PESTEL Framework . Sakarya University Journal of Science, 23(6), 1042-1055, DOI: 10.16984/saufenbilder.474824
Access link
http://www.saujs.sakarya.edu.tr/issue/44246/474824

Sakarya University Journal of Science 23(6), 1042-1055, 2019

Strategic Factors Affecting Green Building Industry: A Macro-Environmental Analysis Using PESTEL Framework

Serdar Ulubeyli*[1], Oğuzhan Kazancı[2], Aynur Kazaz[3], Volkan Arslan[4]

Abstract

For the last decade, green buildings have created a new industry of ecological buildings. However, this industry is still newly developing and finds limited implementation opportunities when compared with the traditional building industry. Therefore, for a more preferable green building industry, strategic factors that can have significant effects on the industry should be comprehended. Based on this argument, the present study aims (i) to identify these factors, (ii) to determine their importance levels, and lastly (iii) to find out their current levels of impact on the industry. To this aim, a questionnaire survey was conducted for the Turkish green building industry through 32 industrial practitioners who have an official LEED Credentials. Results obtained were evaluated via the relative importance index method. Consequently, a total of 30 strategic factors were identified. Out of them, 28 were found to be significant while only 16 currently have a significant impact on the industry.

Keywords: Green building, LEED, PESTEL, relative importance index, Turkey

1. INTRODUCTION

Sustainability is one of the major concepts arose due to the increasing population of the world which associated with higher level of demand for water, energy, and natural sources [1]. In addition, it is a fact that buildings and associated construction activities have negative effects on the natural environment and resources [2]. Therefore, there is a growing level of public awareness of green building (GB) [3] and for the last decade, GBs have created a new industry of ecological buildings. In order to promote the transition to a GB sector, many countries, such as the US, the UK, China, etc., are developing GB policies [4]. Nowadays, GB is considered strategically important to firms in the construction sector [5]. Implementation of GB in the construction sector have the potential to promote buildings that are healthy, safe, comfortable, and environmentally friendly [6]. However, this industry is still newly developing and finds limited implementation opportunities when compared with the traditional building industry. Therefore, for a more preferable GB industry, strategic factors that can have significant effects on the industry should be comprehended. In this context, it seems to be important to comprehend strategic factors that can have significant effects on the GB industry. Based on this argument, the present study aims (i) to identify these factors, (ii) to determine their importance levels, and lastly (iii) to find out their current levels of impact on

* Corresponding Author: ulubeyli@beun.edu.tr
[1] Zonguldak Bülent Ecevit University, Department of Civil Engineering, Zonguldak, Turkey. ORCID: 0000-0003-0871-7391
[2] Zonguldak Bülent Ecevit University, Department of Civil Engineering, Zonguldak, Turkey. ORCID: 0000-0001-7926-7178
[3] Akdeniz University, Department of Civil Engineering, Antalya, Turkey. ORCID: 0000-0002-9589-7505
[4] Zonguldak Bülent Ecevit University, Department of Civil Engineering, Zonguldak, Turkey. ORCID: 0000-0002-0368-5653
Bu çalışma ISITES2017'de sunulan bildiriden türetilmiştir.

the industry. To this aim, a questionnaire survey was conducted for the Turkish GB industry through 32 industrial practitioners who have an official LEED Credentials. Consequently, it is expected to attract industrial practitioners' attention to these factors to contribute to the faster development of the GB industry.

2. LITERATURE REVIEW

In the literature, there are numerous studies which have been addressed the GB industry in terms of strategic issues. For example, Teng et al. [7], analyzed the strategies and approaches for the sustainable development of GBs and summarized potential driving forces of them from four aspects, including market development environment, economic value, the degree of social participation, and ecological value. Darko et al. [8], investigated the influences of various types of barriers, drivers, and promotion strategies on GBs adoption in Ghana. Shen et al. [9], revealed the green technical capabilities and barriers to GB in Thailand from the perspectives of consultants, architects, and engineers, using a questionnaire survey and a case study. Teng et al. [10] investigated GB development in China and they proposed three strategies for three problems such as (i) slow-paced GB development, (ii) imbalanced GB supply and demand, and (iii) low overall green level. Wang et al.[11], examined the factors that affect the adoption of green specifications in China. Deng et al. [12] aimed to identify the key barriers to GB development in Ningbo China and suggested policy improvements to the local government. In addition, there are severeal researches conducted in Turkey on GB technology. Yigit and Ozorhon [13], proposed a methodology to aid designers in satisfying the requirements of government regulations and green building certification programs, while optimizing the energy consumption and maintaining the thermal comfort. Pushkar [14], studied the similarities and differences in performances of LEED 2009 Commercial Interiors and LEED 2009 Core and Shell Development Gold certified projects in Turkey, Spain, and Italy. Ugur and Leblebici [15], conducted a study to assess cost-benefit analysis and payback period of two GBs located in Turkey. Akdag and Beldek [16], aimed to combine the architects green building operations together with the engineers green supply chain management for both reducing the usage of materials, encouraging more effective and efficient usage of energy, water and material currently used, ensure the prevention of any kind of waste, perform environmentally sensible and eco-friendly building design and to be able to reuse, recycle, or recover the waste. Mollaoglu et al. [17], comprehended the ways of knowledge and application of GB guidelines and assessment systems as innovations diffuse in developing countries Architecture Engineering and Construction (AEC) industries.Yigit and Acarkan [18], presented international GB certificate and energy performance certificate (EPC) systems and illustrated the official EPC system for buildings in Turkey with case studies. Suzer [19], examined and underlined the problems regarding the issue of weighting environmental concerns in the Leadership in Energy and Environmental Design (LEED) certification system, which is a US-originated but globally used assessment tool. Aktas and Ozorhon [20], investigated the GB certification process of existing buildings in developing countries. For this purpose, a qualitative case study methodology has been employed to gain a better understanding of the critical success factors of the greening and certification process.

This study differs from past studies as it reveals a sectoral overview of GBs in the macro level and conducts a strategic assessment in terms of GBs.

3. MATERIALS AND METHOD

In order to analyse the external environment of the GB industry, a PESTEL analysis has been utilized. A questionnaire survey was then sent to 168 professionals, who have an official LEED Credentials and extensive knowledge of the industry, via e-mail. Of these professionals, 32 (19.05%) have accepted to respond the survey. Since this number is bigger than 30 ($n \geq 30$), the sample group can be regarded as statistically sufficient to represent the whole.

3.1. Analysis Method

PESTEL is a macro-environmental scanning component in the domain of strategic management used in market research generally. It is also employed to evaluate the profitability and impact of an industry [21]. In other words, it is used to reveal positive and negative factors that can have an impact on an organization by evaluating it in terms of political, economic, social, technological, environmental, and legal aspects.

Political factors focuses on the extent to which a government may affect macro-economy or a certain industry, while economic factors indicate macro- and/or micro-economic performance that has major impacts on a company or an industry. Social factors scrutinize social environment of an industry and gauge theshared beliefs and attitudes of a society. Technological factors pertain to innovative efforts in technology that mayinfluence the operations of a market in a positive or negative manner. Environmental factors comprise the determinants of the surrounding environment. Legal factors point out certain laws and regulations that may affect thebusiness atmosphere in an industry [22].

3.2. Methodology

In this study, a total of 30 sub-factors were categorized under six groups of the external environmental factors, such as (i) political, (ii) economic, (iii) social, (iv) technological, (v) environmental, and (vi) legal, to analyse the green building industry. The required data to determine both the importance level and the current level of impact of these factors were then gathered from respondents via a questionnaire survey. Questions of the survey were designed in the form of a five-point Likert-type scale (Table 1). Respondents determined both the importance level and the current level of impact of factors by choosing one of the options listed in Table 1.

Table 1. Five-point Likert scale

5	4	3	2	1
Very High	High	Moderate	Low	Very Low

The average score of each factor was determined using the following formula of RII where i – category of response, W_i – weight given to ith category ranges from 1 to 5, and X_i – percentage of answers given to i^{th} category (1).

$$RII = \frac{\sum_{i=1}^{S} W_i X_i}{\sum_{i=1}^{S} X_i}, (1 \leq RII \leq 5) \quad (1)$$

The obtained results have been subjected to a different classification during the evaluation process of responses. Because, after the evaluation process, a five-point Likert scale of a question is found to be insufficient to reveal the results. Hence, each expression of the five-point Likert scale was defined at specific intervals as 1.00 ≤ very low (VL) ≤ 1.80, 1.80 < low (L) ≤ 2.60, 2.60 < moderate (M) ≤ 3.40, 3.40 < high (H) ≤ 4.20, and 4.20 < very high (VH) ≤ 5.00. Then, these calculated values were ranked according to their importance indices. If any of these factors have the same scores, percentages of respondents who chose options of 5-4, 3, or 2-1 were determined to rank these factors. These percentages were compared starting from options 5-4 to 1-2, respectively, until determining which factor has a higher percentage.

4. ANALYSIS RESULT

The answers given by 32 industrial practitioners from the Turkish GB industry were analyzed, and the results obtained were evaluated through the PESTEL method. According to these findings, six main factor groups such as political, economic, social, technological, environmental, and legal, were discussed in the following sections in a detailed manner.

4.1. Political Factors

Political factors had a “high” importance level (3.94) and a “moderate” current level of impact (3.37) (Tables 2 and 3). Since subvention’s score was very high for importance level and high for current level of impact, it is one of the most significant factors for the GB construction industry in Turkey. These show that the GB industry in Turkey is in a need of investment and that the industry is a newly emerging market. Although various initiatives to promote the GB investment in Turkey have already been initiated at the industrial and governmental level, main steps, such as tax and duties reduction, bureaucratic process simplification, increase in floor area ratio, grant and low interest loans, have not yet been taken. Thus, the insufficient support of authorities in terms of subvention can be regarded as a factor that slows down the speed of the GB industry.

Table 2. RII and importance levels of political sub-factors

No.	Political factors	RII	Importance level	5	4	3	2	1	Overall ranking	Result
1	Subvention	4.53	VH	68.75	21.88	3.12	6.25	0.00	5	√
2	Tax policy	3.93	H	39.39	27.27	21.21	12.13	0.00	20	
3	Political stability	3.77	H	29.03	35.49	22.58	9.67	3.22	24	
4	Customs policy	3.53	H	25.00	31.25	21.88	15.62	6.25	27	
	General Average	3.94	H							

Table 3. RII and current levels of impact of political sub-factors

No.	Political factors	RII	Current level of impact	5	4	3	2	1	Overall ranking	Result
1	Subvention	3.87	H	50.00	15.62	15.62	9.38	9.38	2	√
2	Tax policy	3.45	H	29.03	25.80	19.35	12.91	12.91	15	
3	Political stability	3.27	M	18.18	30.30	24.24	15.15	12.13	24	
4	Customs policy	2.87	M	15.63	18.75	25.00	18.75	21.87	28	
	General Average	3.37	M							

4.2. Economic Factors

Economic factors had a “high” (3.77) importance level and a “medium” (3.45) current level of impact (Tables 4 and 5). Although economic factors were composed of five sub-factors with a “high” importance level, they remained in the lower order with respect to sub-factors of other groups. In terms of the current level of impact, exchange rates, real estate prices, and interest rates were sub-factors with the “high” current level of impact. The fact that these three sub-factors had a highly variable structure in Turkey for many years can affect the GB industry negatively by creating a distrust effect on investors.

Table 4. RII and importance levels of economic sub-factors

No.	Economic factors	RII	Importance level	5	4	3	2	1	Overall ranking	Result
1	Real estate prices	4.00	H	31.25	43.75	18.75	6.25	0.00	19	
2	Interest rates	3.90	H	37.50	34.38	12.50	12.50	3.12	22	
3	Exchange rates	3.90	H	46.88	15.63	21.87	12.50	3.12	23	
4	Inflation rates	3.59	H	28.13	28.13	25.00	12.50	6.24	25	
5	Average income per capita	3.48	H	22.58	25.80	35.48	9.67	6.45	28	
General Average		3.77	H							

Table 5. RII and current levels of impact of economic sub-factors

No.	Economic factors	RII	Current level of impact	5	4	3	2	1	Overall ranking	Result
1	Exchange rates	3.72	H	40.63	21.87	12.50	18.75	6.25	6	√
2	Real estate prices	3.63	H	18.75	43.75	25.00	6.25	6.25	8	√
3	Interest rates	3.63	H	31.25	25.00	25.00	12.50	6.25	9	√
4	Inflation rate	3.38	M	15.63	34.38	31.25	9.37	9.37	17	
5	Average income per capita	2.88	M	15.63	21.87	15.63	28.12	18.75	27	
General Average		3.45	H							

4.3. Social Factors

The importance level of social factors was “high” (3.79) and the current impact level was “medium” (3.13) (Tables 6 and 7). Considering six sub-factors, the quality of life (comfort) perception was highest in the general ranking with “very high” importance level (4.47) and with “high” current level of impact (3.69). This is because effects of GB on (i) the creation of a popular alternative by accelerating the implementation in the last decade, (ii) the use of advanced technology facilities, (iii) the resemblance to intelligent buildings and sometimes the design of intelligent GB, and (iv) the higher initial investment cost makes the quality of life (comfort) perception for investors more important and creates an expectation in this respect.

Table 6. RII and importance levels of social sub-factors

No.	Social factors	RII	Importance level	5	4	3	2	1	Overall ranking	Result
1	Quality of life (comfort) perception	4.47	VH	53.12	40.63	6.25	0.00	0.00	7	√
2	New customer needs	4.28	VH	37.50	53.12	9.38	0.00	0.00	12	
3	Education level of people	4.09	H	40.62	37.50	15.62	3.13	3.13	15	
4	Customer habits	4.03	H	37.50	34.38	21.87	6.25	0.00	17	
5	Growth rate of population	3.25	M	18.75	21.87	31.25	21.88	6.25	29	
6	Demographic structure of population (age distribution)	2.63	M	6.25	6.25	43.25	31.25	12.5	30	
	General Average	3.79	H							

Table 7. RII and current levels of impact of social sub-factors

No.	Social factors	RII	Current level of impact	5	4	3	2	1	Overall ranking	Result
1	Quality of life (comfort) perception	3.69	H	31.25	37.50	9.38	12.50	9.38	7	√
2	New customer needs	3.53	H	28.13	25.00	28.13	9.37	9.37	12	
3	Education level of people	3.38	M	21.88	28.12	28.12	9.38	12.5	18	
4	Customer habits	3.34	M	25.00	28.13	15.62	18.75	12.5	22	
5	Growth rate of population	2.59	L	12.50	6.25	28.13	34.37	18.75	29	
6	Demographic structure of population (age distribution)	2.25	L	3.12	6.25	34.38	25.00	31.25	30	
	General Average	3.13	M							

4.4. Technological Factors

The second most important group among six factor groups was found as technological factors with “very high” importance level (4.34) and “high” current level of impact (3.53) (Tables 8 and 9).

Table 8. RII and importance levels of technological sub-factors

No.	Technological factors	RII	Importance level	5	4	3	2	1	Overall ranking	Result
1	Presence of qualified construction contractors	4.50	VH	59.37	31.25	9.38	0.00	0.00	6	√
2	Presence of qualified building materials	4.41	VH	53.13	40.62	0.00	6.25	0.00	8	√
3	Advanced technology (automation) facilities	4.34	VH	46.88	40.62	12.50	0.00	0.00	10	√
4	Innovation possibilities	4.28	VH	43.75	40.63	15.62	0.00	0.00	13	
5	Presence of qualified construction workforce	4.19	H	40.63	40.63	15.62	3.12	0.00	14	
	General Average	4.34	VH							

Table 9. RII and current levels of impact of technological sub-factors

No.	Technological factors	RII	Current level of impact	5	4	3	2	1	Overall ranking	Result
1	The presence of qualified construction contractors	3,75	H	31.25	31.25	25.00	6.25	6.25	5	√
2	Advanced technology (automation) facilities	3,59	H	25.00	28.13	31.25	12.50	3.12	10	√
3	Presence of qualified building materials	3,56	H	25.00	34.38	18.75	15.62	6.25	11	
4	Innovation possibilities	3,43	H	15.62	37.50	25.00	18.75	3.13	16	
5	Presence of qualified construction workforce	3,31	M	15.63	34.37	28.12	9.38	12.50	23	
	General Average	3,53	H							

Within this group, presence of qualified construction contractors, presence of qualified construction materials, and advanced technology (automation) facilities were placed in top rankings with their "very high" importance levels. In terms of the current level of impact, presence of qualified construction contractors and advanced technology (automation) facilities found their places among the top ranking. In fact, qualified contractors, qualified materials, and advanced technology (automation) facilities are essential for the GB industry. Nevertheless, the reduction of the existing impact levels of the same factors reveals that there are shortcomings in practice in Turkey. In other words, sufficient qualified contractors, easily accessible and

economical construction materials, and automation facilities in the GB industry in Turkey can be found with difficulty compared to traditional buildings.

4.5. Environmental Factors

Among six main factors, the top group was found to be environmental factors with "very high" importance level (4.46) (Table 10) and "high" current level of impact (3.45) (Table 11). Given that the purpose of GBs is to protect the environment, the importance of this factor group can be easily understood. Sub-factors apart from geographical location were in the top five rankings in terms of the importance level and the current level of impact. However, as in all other factor groups, there was a decrease in the current level of impact of sub-factors in this group. The decrease in (i) local, national, and international applications on environment, (ii) energy infrastructure and efficiency, (iii) recycled / converted construction material market, and (iv) waste management points out shortcomings and difficulties in practice. Although there is proper legislation in terms of applications on the environment side, there are drawbacks especially in the control and supervision of such applications.

Table 10. RII and importance levels of environmental sub-factors

No.	Environmental factors	RII	Importance level	5	4	3	2	1	Overall ranking	Result
1	Energy infrastructure and efficiency	4.75	VH	78.10	18.70	3.10	0.00	0.00	1	√
2	Local, national, and international applications on environment	4.68	VH	71.90	25.00	3.10	0.00	0.00	2	√
3	Ecological sustainability	4.68	VH	75.00	21.80	0.00	3.20	0.00	3	√
4	Waste management	4.41	VH	56.25	31.25	9.40	3.10	0.00	9	√
5	Recycled / converted construction material market	4.31	VH	53.12	31.25	9.38	6.25	0.00	11	
6	Geographic location	3.93	H	34.37	40.63	12.5	9.37	3.13	21	
	General Average	4.46	VH							

The lack of knowledge and experience observed in design and construction in Turkey is a factor that reduces the efficiency level of renewable energy systems. Given recycled / converted materials, the supply and demand of such materials in the industry is very limited, contractors cannot easily reach them, and these materials generally create weak and poor quality perception on customers. Regarding waste management, although a number of legal regulations have been made in Turkey for the construction industry in recent years, it is known that the industry is still far from good waste disposal and recycling practices. In Turkey, there are only a few facilities that recycle construction and demolition wastes. The decline in ecological sustainability may be due to the perception that it may not bring an economic benefit to investors.

Table 11. RII and current levels of impact of environmental sub-factors

No.	Environmental factors	RII	Current level of impact	5	4	3	2	1	Overall ranking	Result
1	Local, national, and international applications on environment	3.81	H	37.50	28.13	21.87	3.12	9.38	3	√
2	Energy infrastructure and efficiency	3.78	H	34.38	34.38	15.62	6.34	9.38	4	√
3	Ecological sustainability	3.47	H	28.12	28.12	18.76	12.50	12.50	14	
4	Recycled / converted construction material market	3.34	M	21.87	31.25	18.75	15.63	12.50	19	
5	Waste management	3.34	M	18.75	31.25	25.00	15.63	9.37	20	
6	Geographic location	2.93	M	9.37	25.00	25.00	31.26	9.37	26	
	General Average	3.45	H							

4.6. Legal Factors

Legal factors were a group with "high" importance level (4.07) (Table 12) and "high" current level of impact (3.44) (Table 13). Among four sub-factors, environmental regulations, which is ranked fourth in terms of the importance level and first in terms of the current level of impact, is significant. This can be explained by the fact that the concept of environment is the most important component of the GB industry and that legal arrangements to be made in this regard are expected to directly and strongly influence the industry. Although some progress has been achieved in legislation in the context of European Union harmonization in Turkey, there are various difficulties in terms of the implementation and adaption of laws. Also, public and private sectors cannot completely perform their own duties due to several reasons (physical disabilities, financial constraints, etc.).

Table 22. RII and importance levels of legal sub-factors

No.	Legal factors	RII	Importance level	5	4	3	2	1	Overall ranking	Result
1	Environmental regulations	4.59	VH	65.63	28.12	6.25	0.00	0.00	4	√
2	Difficulties in adaptation of the certification system	4.06	H	31.25	56.25	6.25	0.00	6.25	16	
3	Consumer related regulations	4.03	H	31.25	46.88	15.63	6.25	0.00	18	
4	Regulations on import	3.59	H	25.00	34.38	18.75	18.75	3.12	26	
	General Average	4.07	H							

Table 13. RII and current levels of impact of legal sub-factors

No.	Legal factors	RII	Current level of impact	5	4	3	2	1	Overall ranking	Result
1	Environmental regulations	3.90	H	37.50	31.25	18.75	9.38	3.12	1	√
2	Difficulties in adaptation of the certification system	3.50	H	21.87	31.25	28.13	12.50	6.25	13	
3	Consumer related regulations	3.34	M	12.50	37.50	25.00	21.88	3.12	21	
4	Regulations on import	3.00	M	18.75	9.38	34.37	27.12	9.38	25	
	General Average	3.44	H							

5. DISCUSSION

Results of the study are shown between Tables 2 and 13. In the Result column, the most significant ten sub-factors were marked with "√". These were four of environmental factors (with "very high" importance level), three of technological factors (with "very high" importance level), and one from each group of political, social, and legal factors (with "very high" importance level). However, none of sub-factors from economic factors with "very high" importance level was placed in this list (Table 14). Among the five groups of factors, environmental factors group is in the first place with its very high importance level on affecting the GB industry. It is followed by group of technological factors again with very high importance level. The other groups of factors have high importance level and were listed as legal factors, political factors, and social factors respectively.

Table 34. A summary of results of importance levels of factors affecting the green building industry

Group of factors	Importance Level	Overall ranking
Political factors	High	4
Subvention	Very High	5
Economic factors	High	6
Social Factors	High	5
Quality of life (comfort) perception	Very High	7
Technological factors	Very High	2
Presence of qualified construction contractors	Very High	6
Presence of qualified building materials	Very High	8
Advanced technology (automation) facilities	Very High	10

Environmental factors	Very High	1
Energy infrastructure and efficiency	Very High	1
Local, national, and international applications on environment	Very High	2
Ecological sustainability	Very High	3
Waste management	Very High	9
Legal factors	High	3
Environmental regulations	Very High	4

Energy infrastructure and efficiency sub-factor covers targets such as energy efficient building desing and construction, clean and renewable energy generation or supply. Table 14 reveals that this sub-factor has the highest importance level on the GB industry. The reason behind this may be the lack of knowledge and experience on design and construction activities of GB technology in Turkey. The second most important sub-factor is local, national, and international applications on environment (Table 14). Although there are not many gaps in the legislation in terms of environmental practices, there may be deficiencies in the control and supervision of GB applications in Turkey. Therefore, scantiness of GB applications may have significant negative affect on investors and practioners of GB techonology. Ecological sustainability is another sub-factor of environmental factors which have very high importance level. However, the common opinion that ecological sustainability has no economic benefit for investors may lead a lack of support of investors on GB technology in Turkey. Environmental regulations represents legal factors as the most important sub-factor affecting the GB industry. This is because, environment is the most suitable concept to represent and affect the GB industry. The sub-factor subvention have the highest importance level score of political factors. The lack of subsidies in an emerging market may result in a poor market demand and therefore subsidies provided for GB applications seem to be useful for investors. Presence of qualified contractors is in the sixth place of the list given in Table 14 and GB contractors should have extra characteristics which may be better communication skills and knowledge concerning GBs. Quality of life (comfort) perception is the only social factor in the list and have very high importance level. This sub-factor covers favorable temperature, air quality, better lighting, less noise, and the overall indoor comfort of the buildings. For the benefit of GB investors, these characteristics may be advertised more with a special emphasis by the marketing experts. Presence of qualified building materials is another technological sub-factor with very high importance level. However, in Turkey, there is no permanent material market which needed for the GB construction. Establishing such a market will probably have a positive effect on the GB industry in Turkey. The last sub-factor of environmental factors in the list is waste management. This is also have very high importance level and recycling/reusing efforts to be made during construction and operation stages should be paid great attention for the sake of the GB industry. The tenth sub-factor in the list presented in Table 14, is advanced technology (automation) facilities with very high importance level. It is clear that GB production should be supported by advanced technology and to achieve this, a domestic and high-tech industry needs to be developed.

According to the results presented in Table 15, three of economic factors (with “high” current level of impact), two from each group of technological and environmental factors (with “high” current level of impact), and one from each group of political, legal, and social factors (with “high” current level of impact) are among ten most effective factors.

Table 45. A summary of results of current impact levels of factors affecting the green building industry

Group of factors	Current level of importance	Overall ranking
Political factors	Moderate	5
Subvention	High	2
Economic factors	High	2
Exchange rates	High	6
Real estate prices	High	8
Interest rates	High	9
Social factors	Moderate	6
Quality of life (comfort) perception	High	7
Technological factors	High	1
Presence of qualified construction contractors	High	5
Advanced technology (automation) facilities	High	10
Environmental factors	High	3
Local, national, and international applications on environment	High	3
Energy infrastructure and efficiency	High	4
Legal factors	High	4
Environmental regulations	High	1

Results of current impact levels of factors affecting the GB industry present that ranking order of group of factors is different from the list in Table 14. In Table 15, group of techonoligical factors is in the first place of the list. After that group of economic factors, environmental factors, legal factors, political factors were ranked respectively. The main difference of lists in Table 14 and Table 15 is sub-factors of the group of economic factors. According to current level of importance of sub-factors, exchange rates, real estate prices, and interest rates were listed as significant sub-factors affecting the GB industry. Exchange rates can be considered as one of the most important prices in any economy due to the potential of affecting all other prices and its importance level is high in Table 15. Therefore, it can be asserted that current exchange rates of an economy may have significant role on GB investments. Sub-factor of real estates prices has high importance level. The reason behing this, a green certification may differentiate the end-product and allow to charge a better price to some customers. Another sub-factor of economic factors, interest rates, has important potential to affect the GB industry. This is because, contractors usually having credits from banks for continuous cashflows of material, equipment, and labor supplies.

6. IMPLICATIONS AND LIMITATIONS

The present study has a number of research implications. In the study, Turkish GB industry was analysed and in different geographical locations the respondents may approach to this topic from another perspective. Therefore, future researches may bring potential differences of results in different geographical areas. In addition, specific conditions of the region under study may change the criteria and their weights.

The study was based on views of professionals and there is always a chance for professionals to change their views over time. Also, professionals from other industries may have different opinion on GB industry so that the other industries should also be investigated.

The research has some practical implications. The results obtained may be utilized as an initial point for further industrial policies and legislative plans by strategy-makers. In addition, the results can also be a trigger to encourage investors and professioanls for GB applications.

Lastly, the current study has some limitations as well. In the sub-factors selection of the PESTEL analysis, only three LEED professionals were interviewed. Therefore, it would be better to m interview more than three professionals during the selection process of sub-factors. In this way, a larger scope of professionals may contribute to the study and offer some different sub-factors. All these limitations should be considered in construing the outcomes.

7. CONCLUSIONS

In this study, among six factor groups, environmental factors were determined as the most important factor according to the importance level. Moreover, this group were ranked as the third most important group regarding its "high" current level of impact. The second most important factor was technological factors with a "very high" importance level. Also, they were found to be in the first place with "high" importance level. Legal factors with "high" importance level and current level of impact took place in third and fourth rankings, respectively. Political factors were ranked fourth and fifth place with their "high" importance level and "moderate" current level of impact. Economic factors was in the sixth place with "high" importance level and second with "high" current impact level. Social factors were ranked fifth with "high" importance level and sixth with "moderate" current level of impact. As a result, it is seen that environment is the forerunner. In addition, the importance of quality materials due to the use of technological elements used in the construction phase of green buildings and the passive systems they contain was revealed by importance indices of technological factors. Economic factors were the least important group although they were in the second rank in terms of the current impact level. Looking at political factors, subsidy (governmental investment incentive) was at the forefront. In terms of social factors, the quality of life (comfort) perception was the forerunner. When legal factors are examined, environmental regulations attract attention. This shows that the most important dynamism of the industry, i.e., the environment concept, is an organic part of the green building industry, and regulations to be made in this regard will further strengthen the industry. In conclusion, it is necessary for industrial professionals to intensify their work on the top ten factors. Similarly, it will be more useful for researchers, who would like to take this topic further, to conduct detailed studies on these ten factors rather than repeating a group and factor analysis.

ACKNOWLEDGMENTS

The authors gratefully acknowledge the surveyed respondents for their generous collaboration and contributions. The authors also thank financial supports provided by Committees on Research Grants of Zonguldak Bülent Ecevit University and Akdeniz University.

References

[1] L. N. Dwaikat and K. N. Ali, "The economic benefits of a green building – Evidence from Malaysia," *J. Build. Eng.*, vol. 18, no. February, pp. 448–453, 2018.

[2] L. Zhang, J. Wu, and H. Liu, "Turning green into gold: A review on the economics of green buildings," *J. Clean. Prod.*, vol. 172, pp. 2234–2245, 2018.

[3] Y. He, T. Kvan, M. Liu, and B. Li, "How green building rating systems affect designing green," *Build. Environ.*, vol. 133, no. February, pp. 19–31, 2018.

[4] Y. Fan and X. Xia, "Energy-efficiency building retrofit planning for green building compliance," *Build. Environ.*, vol. 136, no. March, pp. 312–321, 2018.

[5] H. Nykamp, "A transition to green buildings in Norway," *Environ. Innov. Soc. Transitions*, vol. 24, pp. 83–93, 2017.

[6] Z. Ding, Z. Fan, V. W. Y. Tam, Y. Bian, S. Li, I. M. C. S. Illankoon, and S. Moon, "Green building evaluation system implementation," *Build. Environ.*, vol. 133, no. February, pp. 32–

40, 2018.

[7] J. Teng, X. Mu, W. Wang, C. Xu, and W. Liu, "Strategies for sustainable development of green buildings," *Sustain. Cities Soc.*, vol. 44, no. September 2018, pp. 215–226, 2019.

[8] A. Darko, A. P. C. Chan, Y. Yang, M. Shan, B. J. He, and Z. Gou, "Influences of barriers, drivers, and promotion strategies on green building technologies adoption in developing countries: The Ghanaian case," *J. Clean. Prod.*, vol. 200, pp. 687–703, 2018.

[9] W. Shen, W. Tang, A. Siripanan, Z. Lei, C. Duffield, and F. Hui, "Understanding the Green Technical Capabilities and Barriers to Green Buildings in Developing Countries: A Case Study of Thailand," *Sustainability*, vol. 10, no. 10, p. 3585, 2018.

[10] J. Teng, C. Xu, W. Wang, and X. Wu, "A system dynamics-based decision-making tool and strategy optimization simulation of green building development in China," *Clean Technol. Environ. Policy*, vol. 20, no. 6, pp. 1259–1270, 2018.

[11] W. Wang, S. Zhang, and C. Pasquire, "Factors for the adoption of green building specifications in China," *Int. J. Build. Pathol. Adapt.*, vol. 36, no. 3, pp. 254–267, 2018.

[12] W. Deng, T. Yang, L. Tang, and Y. T. Tang, "Barriers and policy recommendations for developing green buildings from local government perspective: a case study of Ningbo China," *Intell. Build. Int.*, vol. 10, no. 2, pp. 61–77, 2018.

[13] S. Yigit and B. Ozorhon, "A simulation-based optimization method for designing energy efficient buildings," *Energy Build.*, vol. 178, pp. 216–227, 2018.

[14] S. Pushkar, "The effect of regional priority points on the performance of LEED 2009 certified buildings in Turkey, Spain, and Italy," *Sustain.*, vol. 10, no. 10, pp. 1–19, 2018.

[15] L. O. Uğur and N. Leblebici, "An examination of the LEED green building certification system in terms of construction costs," *Renew. Sustain. Energy Rev.*, vol. 81, no. March 2017, pp. 1476–1483, 2018.

[16] H. C. Akdag and T. Beldek, "Waste Management in Green Building Operations Using GSCM," *Int. J. Supply Chain Manag.*, vol. 6, no. 3, pp. 174–180, 2017.

[17] S. Mollaoglu, C. Chergia, E. Ergen, and M. Syal, "Diffusion of green building guidelines as innovation in developing countries," *Constr. Innov.*, vol. 16, no. 1, pp. 11–29, 2016.

[18] K. Yigit and B. Acarkan, "Assessment of energy performance certificate systems: A case study for residential buildings in Turkey," *Turkish J. Electr. Eng. Comput. Sci.*, vol. 24, no. 6, pp. 4839–4848, 2016.

[19] O. Suzer, "A comparative review of environmental concern prioritization: LEED vs other major certification systems," *J. Environ. Manage.*, vol. 154, pp. 266–283, 2015.

[20] B. Aktas and B. Ozorhon, "Green Building Certification Process of Existing Buildings in Developing Countries: Cases from Turkey," *J. Manag. Eng.*, vol. 31, no. 6, 2018.

[21] G. Johnson, R. Whittington, D. Angwin, R. Patrick, and S. Kevan, *Exploring Strategy: Text & Cases*, 11th ed. UK: Pearson Education, 2017.

[22] S. Ulubeyli and O. Kazanci, "Holistic sustainability assessment of green building industry in Turkey," *J. Clean. Prod.*, vol. 202, pp. 197–212, 2018.

JOURNAL OF SCIENCE
SAKARYA UNIVERSITY

Sakarya University Journal of Science

ISSN 1301-4048 | e-ISSN 2147-835X | Period Bimonthly | Founded: 1997 | Publisher Sakarya University | http://www.saujs.sakarya.edu.tr/

Title: Computational Interrogation of The Human Norovirus-Host Cell Interactions Facilitated by A-Type Antigen

Authors: Abdulkadir Kocak, Muslum Yildiz
Recieved: 2019-02-11 12:34:37

Accepted: 2019-05-20 11:52:50

Article Type: Research Article
Volume: 23
Issue: 6
Month: December
Year: 2019
Pages: 1056-1065

How to cite
Abdulkadir Kocak, Muslum Yildiz; (2019), Computational Interrogation of The Human Norovirus-Host Cell Interactions Facilitated by A-Type Antigen. Sakarya University Journal of Science, 23(6), 1056-1065, DOI: 10.16984/saufenbilder.525430
Access link
http://www.saujs.sakarya.edu.tr/issue/44246/525430

Sakarya University Journal of Science 23(6), 1056-1065, 2019

Computational Interrogation of The Human Norovirus-Host Cell Interactions Facilitated by A-Type Antigen

Muslum Yildiz*[1], Abdulkadir Kocak[2]

Abstract

Norovirus infectivity, which causes norovirus-induced gastroenteritis, depends on the interaction between capsid protein VP1 of the virus and host cell HGBA receptors that tailor the cell membrane surface. The interaction results in VP1-HGBA complex formation prior to infection. The details of this interaction have been provided by x-ray structures of HGBA-VP1 complexes, but the dynamic nature of this interaction is not fully uncovered. Therefore, the dynamics that drive the formation of VP1-HGBA complex, which is crucial for developing new therapeutic approaches to find a cure for gastroenteritis disease, need to be elucidated. Here, we computationally analyzed the wild type VP1 capsid protein in complex with A-type HGBA antigen to unravel interactions that are important for virus to enter inside the host cell during infection. We have found that the ligand binding causes a fluctuation in a distant loop which resides in the interface of capsid building blocks, VP proteins. This fluctuation leads an instability in capsid particle that may be an indication for virus uncoating mechanism during the cell penetration.

Keywords

Norovirus, therapeutic antibody, HBGA blockage, molecular dynamics

1. INTRODUCTION

Norovirus-induced gastroenteritis, which was named hyperemesis hiemis earlier, was first discovered by Dr. John Zahorsky in 1929. It took almost 50 years, until 1972 in Norwalk, Ohio/USA, to find the link between the disease and norovirus [1]. The disease has become one of the greatest health problems of all infectious diseases throughout history. Nearly 90 million people is affected by the virus and virus-related disease and it claims about 1.5 million life annually around the globe and most of them are children [2-7]. Scientific efforts have so far failed to find an effective drug or an approved vaccine [8, 9].

Noroviruses carry the positive-strand RNA as genetic material and they are members of *Caliciviridae* family [10, 11]. There are mainly seven genogroups of noroviruses (GI-GVII) of which the GI, GII and GIV are the ones causing infection in the human [12, 13]. Since the virus develops mutations rapidly during its life cycle, these major groups are differentiated from each other and various genetic genotypes emerge such as GI.7, GII.4, GII.13, GII.17 etc. Although the involvement of factors for virus cell penetration have not fully been elucidated, studies so far have shown that the interaction between VP1 and HGBA on the host cell surface is required for infection [14-16]. This opens an attractive and hot research area that mainly focuses on finding and developing therapeutics which will block the interaction between VP1 and HBGA antigens for treating the disease [17-20]. With this scientific aim; several crystal structures of VP1-HGBA complex have been solved. Although these structures offer valuable information regarding the atomistic details of the interaction between the two entities, they lack of providing any insights about the dynamic changes upon ligand binding [16, 21-23].

* Corresponding Author: muslum@gtu.edu.tr
[1] Gebze Technical University, Department of Molecular Biology and Genetics, Kocaeli, Turkey. ORCID: 0000-0001-8396-1461
[2] Gebze Technical University, Department of Chemistry, Kocaeli, Turkey. ORCID: 0000-0001-6891-6929

In our previous study, we found that the interaction between GI.1 VP1 and an H-type 1 HBGA antigen did not cause significant change in the binding region but showed a drastic change in a distal loop lying at 395-400 region [24].

Here, we computationally assessed the interaction between sugar part of A-type HGBA antigen and VP1 capsid protein utilizing molecular dynamics simulations. We also assessed whether the same type of dynamic changes upon A-type HBGA binding is observed as with our earlier findings.

2. MATERIALS AND COMPUTATIONAL METHODS

2.1. Protein Preparation

We used the Protein Data Bank (PDB id=2ZL7) as starting structures for halo-VP1 (complexed with A-type HBGA) [22]. The protein was prepared in Maestro [25] by assigning bonds, adding H atoms, fixing overlapping atoms and maximizing the number of H-bonds. The unprotonated side chains of Asp and Glu and protonated side chains of Arg and Lys residues were predicted by Propka 3.1 [26] at pH=7. We used the amber99sb-ildn [27] force field for the VP1 protein and GAFF force field for the ligand. The sugar moiety was first optimized using G09 software at B3LYP/6-311++G(d,p) level by fixing the heavy atoms at the x-ray coordinates. Then, the RESP charges and GAFF parameters were generated using antechamber software [28, 29].

2.2. Simulation Protocol

The simulations were performed using Gromacs 5.1 software package [30]. The dodecahedron box with a ~1500 nm^3 volume and the TIP3P model were used for solvation in simulations of both apo- and halo-form of VP1-HBGA complex systems [31]. Each system has ~145,000 atoms and neutralized by addition of 0.15 M NaCl. LINCS algorithm was used to restrain bonds with hydrogen atoms to their equilibrium length.

We minimized the system gently in 13 steps as with our earlier studies [32, 33]. Each step completed in 5000 cycles of two integrators, Steepest Descent and Conjugate Gradient. In the first step, only hydrogen atoms were kept free and relaxed while all heavy atoms including water frozen at a force of 4000 $kJ.mol^{-1}$. nm^{-2}. Then, the water molecules were relaxed. Next, the force on the side chains were slowly released by reducing the force constants in the order of 4000, 2000, 1000, 500, 200, 50 and 0 $kJ.mol^{-1}.nm^{-2}$. The minimization process was ended by releasing the backbone atoms gradually.

Each system was equilibrated within six steps following the minimization. The first step is a 5 ns of canonical ensemble. The system was heated to 310 K (with time constant of 0.1) with a simulated annealing manner in the first step. The temperature value was reached in the first 500 ps by linear heating and kept unchanged for the next 4.5 ns. For the protein-ligand complex and surroundings the V-rescale thermostat was used as the temperature-coupling group separately. Following the heating the system was equilibrated to the 1 atm pressure in a stepwise isobaric-isothermal ensemble. During this stage, the heavy atoms smoothly and progressively released. Five repetitive MD simulations with different initial velocities were run for 1 ns at the constant pressure using Langevin Dynamics.

3. RESULTS AND DISCUSSION

We have monitored the dynamic changes upon HGBA H-type 1 antigen in our previous study and observed a drastic movement in a distant loop [24].

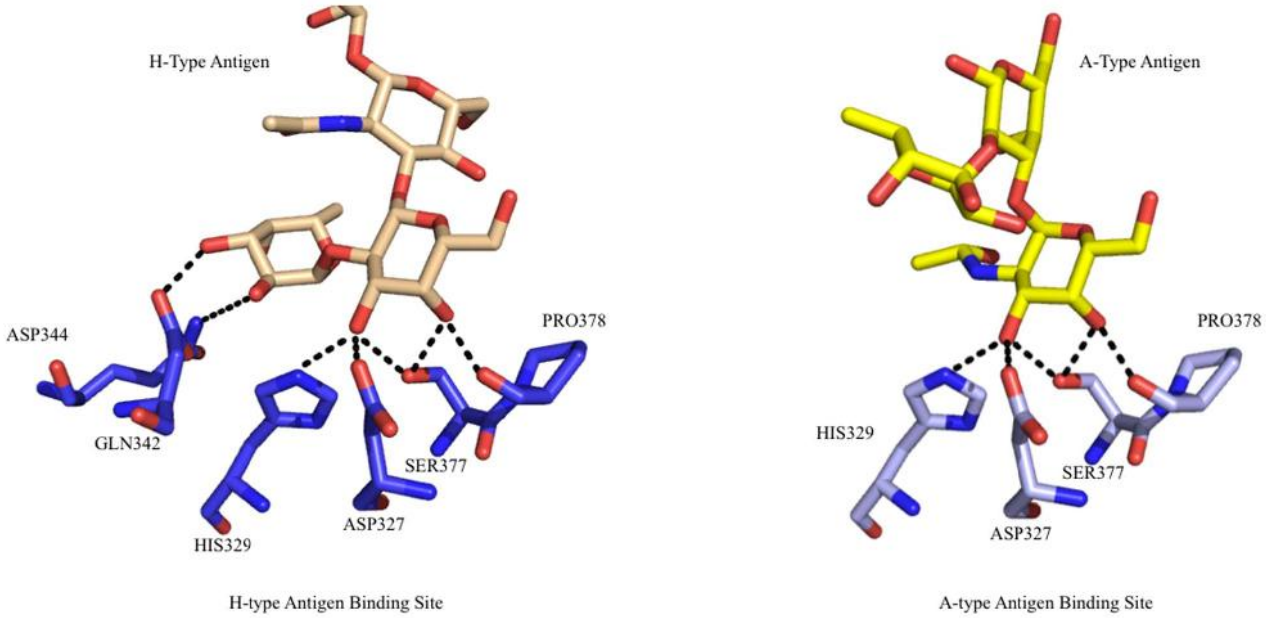

Figure 1 The sugar binding site of VP1 protein. Both A-type and H-type are binding at the same site.

In order to test whether this movement will be observed upon binding to other HBGAs, we simulated the dynamic changes of the complex formed by an A-type antigen and compared with apo form. Here on, all data regarding the apo form of VP1 is adopted from our previous study [24].

The main difference between A-Type and H-type HGBA antigens is that the FUC moiety in A-type antigen has missing interactions with VP1 capsid protein via Asp 344 and Gln 342 residues (Figure 1**).** Thus, it is expected to have a lower affinity in the A-type HBGA binding, which might influence the dynamic behavior.

The overall dynamic behavior of macromolecules can be followed by analyzing the RMSD values over time course of MD simulation. Therefore, we calculated the RMSD of GI.1 VP1 in complex with A type HGBA antigen (PDB id :2ZL7) and compared with apo GI.1 VP1 (PDB id:2ZL5). The ligand binding cause lower RMSD value in VP1 than apo form **(**Figure 2**).**

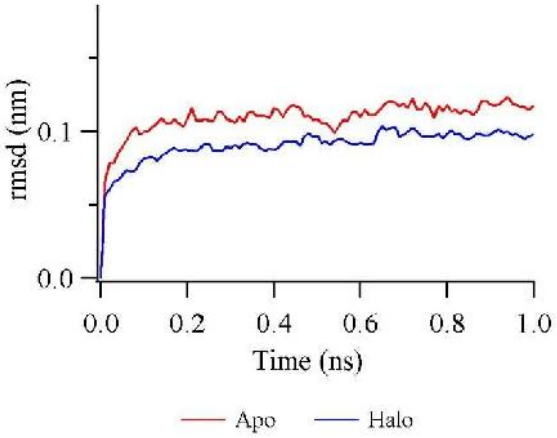

Figure 2 Rmsd values of both apo- and halo- forms of Cα atoms in GI.1 VP1 protein. Both the apo- and halo-forms follow similar trend.

The distances among residues that are near the sugar binding site in the crystal structure and MD simulation were computed for apo and halo form to follow any changes in this region (Table 1). These residues are in a direct contact with the sugar antigen within a distance maximum of 3.50 Å. We followed the deviation in the distances between interacting atoms of His329 and Trp375; Asp327 and Ser380; Trp375 and His329; Asp327 and Ser377; Trp375 and Gln342; Asp327 and Ser377 pairs, respectively, over the course of MD simulation upon sugar binding (Figure 3).

Table 1 Selected distances among the atom pairs of residues in the binding region. All values are in Å. The notation in distance is as follows: the first 3 digits show the residue number, rest shows the atom name in that residue (e.g., 375NE1 refers to Nε1 atom of 375th residue)

	X-ray crystal data		**MD simulation average**	
PDB id	2ZL5[a]	2ZL7[a]	2ZL5[b]	2ZL7[c]
	Apo-	Halo-	Apo-	Halo-
329O- 375N	3.29	3.26	3.48	3.42
327OD2-380OG	2.63	2.60	3.33	3.32
375O-329N	2.90	2.90	2.94	2.95
327O-377N	3.10	3.14	2.93	2.93
375NE1-342OE1	2.96	3.03	6.20	6.23
327N-377O	2.80	2.85	2.98	3.00
[a]: Ref. [22]; [b]:Ref. [24]; [c]: This study				

The distances between these residues are mostly conserved and show slight deviation throughout the simulation (Figure 3). The only notable change upon sugar binding take place in the distance between Asp327 and Ser380 residues. The distance between Asp327_OD2 and Ser380_OG is fluctuating in 1 Å oscillation range but this fluctuation is getting stabilized upon sugar binding (Figure 3b). This is an indication of insignificant dynamic changes due to ligand binding.

We have also analyzed the entire structures to figure out which part of protein gains or lose the flexibility upon ligand binding by analyzing the mean root square fluctuations (RMSF) of every single residue. The residues around the sugar binding site do not show remarkable fluctuations while some residues in a distant loop fluctuate drastically. (Figure 4). These fluctuations are consistent in all repetitive MD simulations for halo form while are not observed for apo protein. This rules out the possibility of a random loop movement.

We have investigated and confirmed this loop movement further by evaluating the principle component analysis (also called covariance analysis). The first eigenvalue from covariance analysis corresponds to this motion and the value in halo-form is very different from that of apo-form (Figure 5a). The rest of the eigenvalues follow similar trend in both proteins. This collective motion is more apparent in the rmsf of eigenvector 1. Comparing the halo-form RMSF with that of apo-form, the dominant factor contributing the 1st eigenvector is the drastic peak lying at 396-402 region. In addition, the residues lying at 303-316, 330-344 and 487-492 contribute to this eigenvector. However, fluctuations of these three regions were already observed in apo-form and thus are not sensitive to ligand binding. In addition, the ones at 294-300 and 303-316 region loses flexibilty upon ligand binding.

The virus genome is encapsulated by virus capsid which is formed by 180'mers (60 x trimer) of VPs. This capsid protects the genome from hostile environment. Once the capsid enters the cell, the capsid must be disassembled for the release of genome. The free genetic material is then translated to critical virus proteins by host cell machinery. Therefore, knowing the detail of capsid disassembly, which is known as uncoating mechanism, is another scientific interest in the field.

We assessed the location of the loop that become more flexible upon ligand binding. We have interestingly found that the loop resides between connection points of monomer VP building blocks that form the virus capsid which protects the virus genome against hostile environment **(Figure 7)**. The mobility of this loop may cause an instability in capsid particle which may be an evidence for uncoating mechanism of the virus.

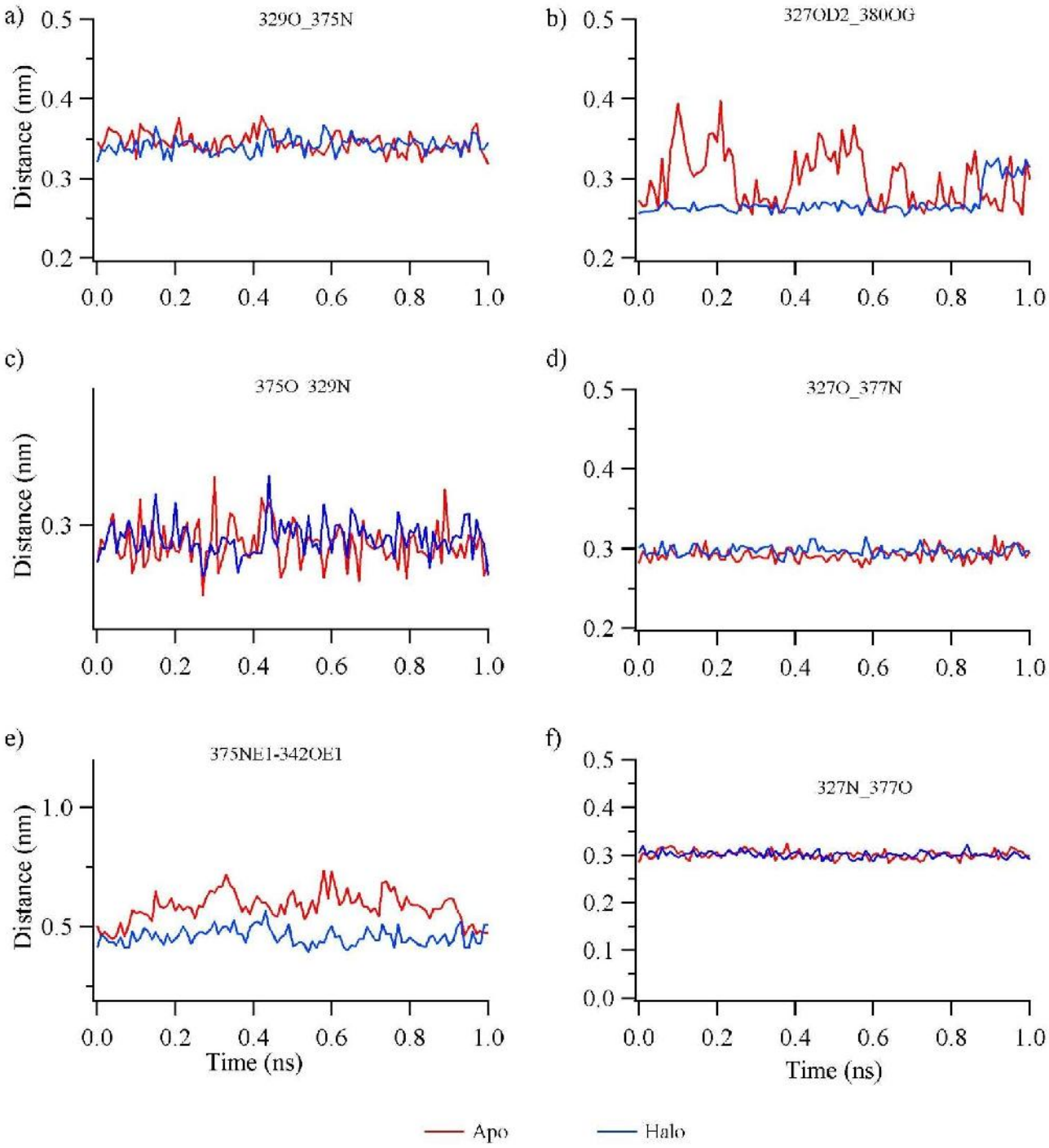

Figure 3 Selected distances among residues in the sugar binding site for halo-form (blue) and apo-form (red) proteins.

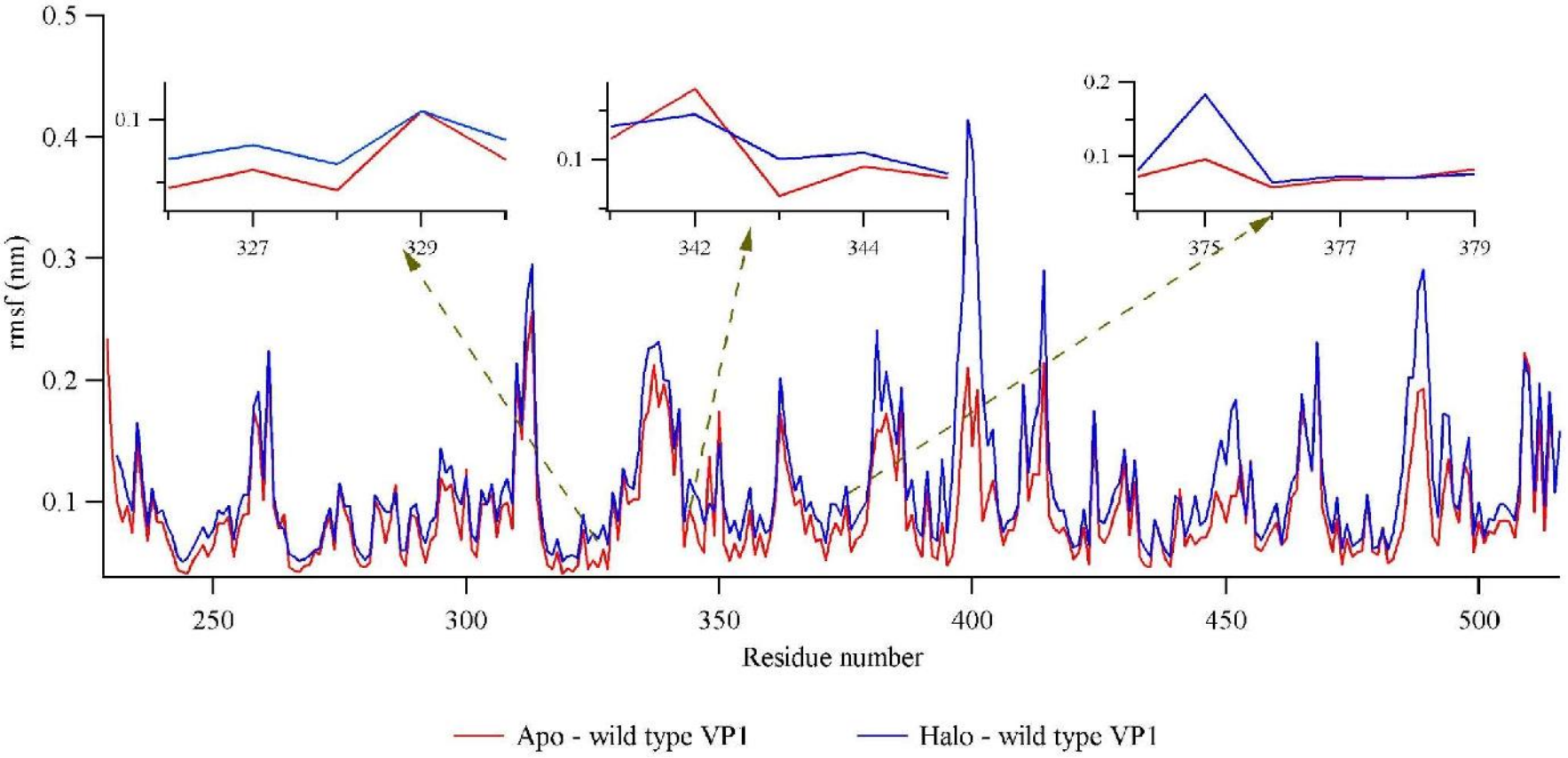

Figure 4 The rmsf of halo-form (blue) and apo-form (red) VP1 residues. The insets are the zoomed of the residues in the sugar binding site. Data do not show any significant rmsf difference at the binding site. The dashed arrows are not part of the data and only meant to show the location of zoomed insets (sugar binding site).

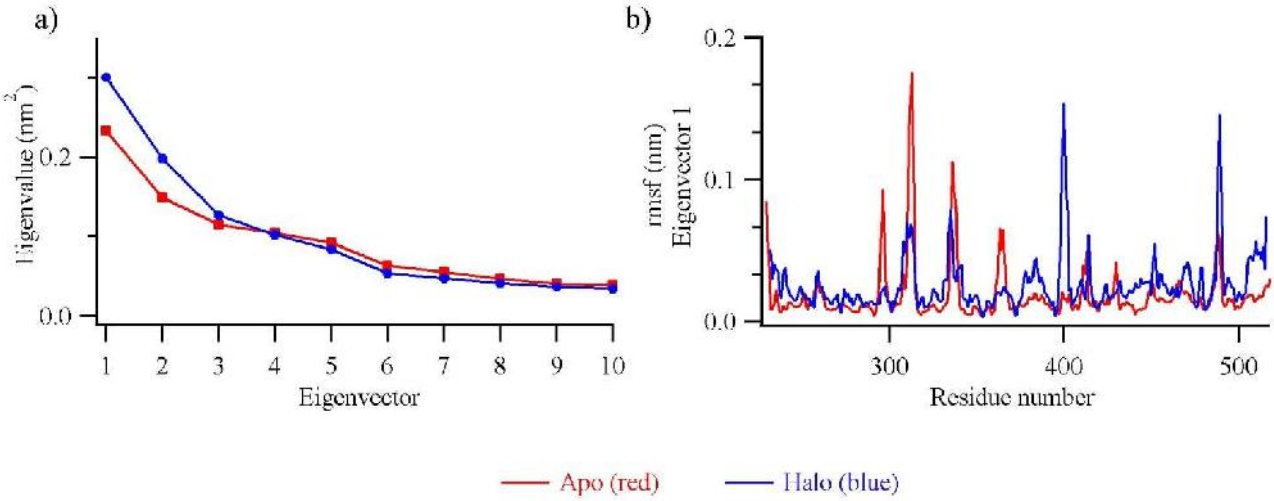

Figure 5 Covariance analysis of apo-form (red) and halo-form (blue) GI.1 VP1 proteins. a) The first 10 eigenvalues showing two proteins differ in only eigenvector 1 and 2. b) rmsf of residues involved in the most dominant collective motion (eigenvector 1)

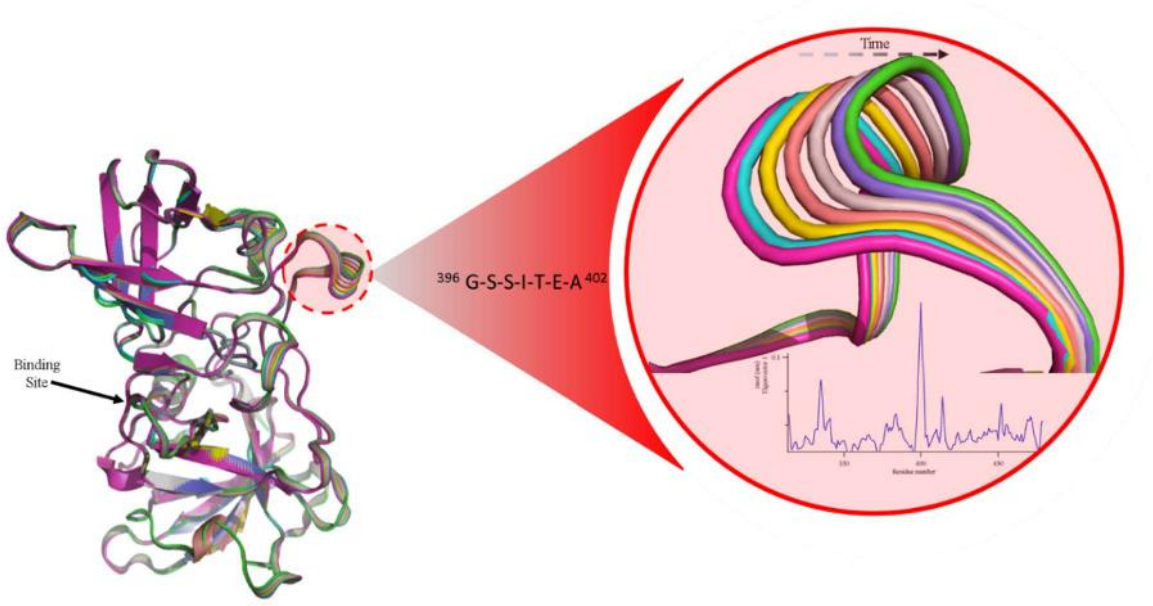

Figure 6 Allosteric loop fluctuation upon ligand binding

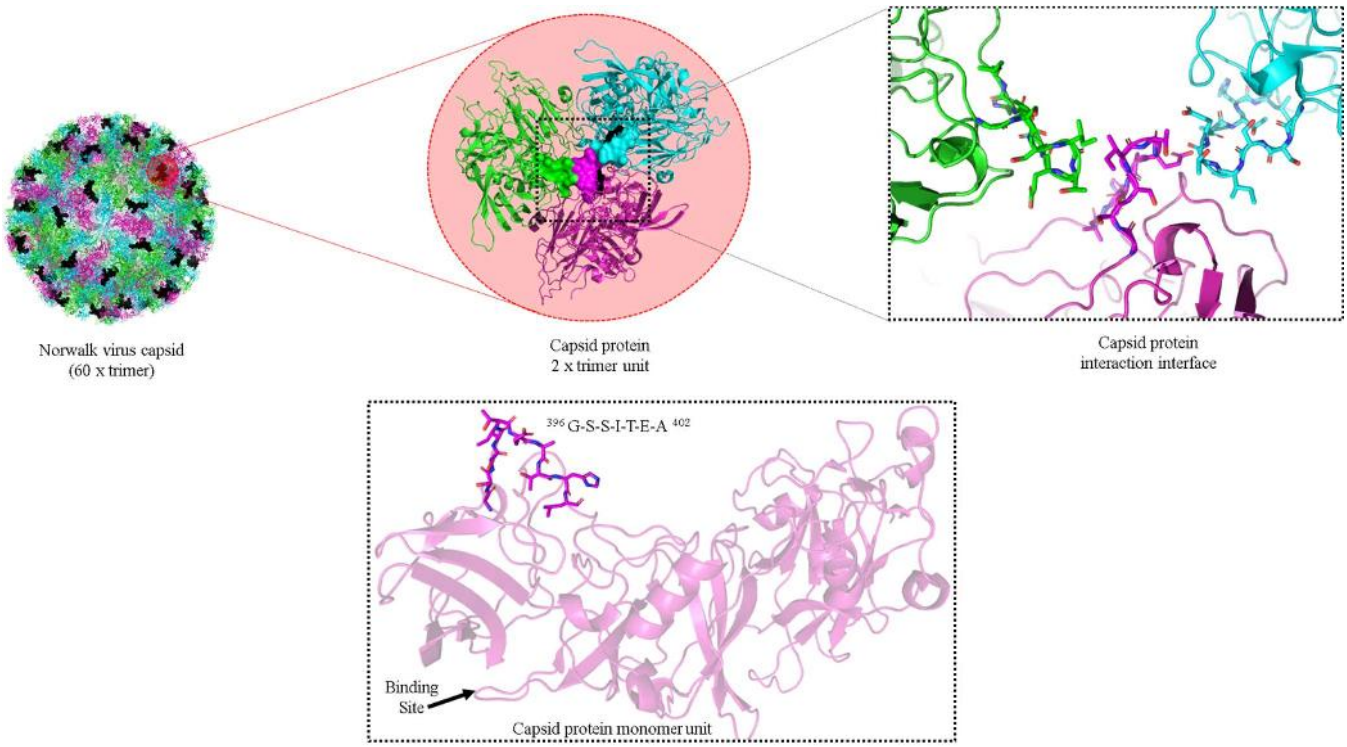

Figure 7 Norwalk virus capsid protein assembling organization from building blocks (PDB id=1IHM). The 396-402 loop stays in the building block interface and make critical interactions for capsid formation. This loop gains flexibility upon ligand binding while it is rigid in apo-form.

CONCLUSION

We have found that the interaction does not cause significant changes in the sugar binding site but stimulates a notable fluctuation in a distant loop. Interestingly this loop mobility also has been observed upon H-type antigen binding which is reported in our previous study. The loop stands in the interface of two VP1 protein that form a capsid for virus. Therefore, we assume that this mobility may help in virus un-coating during infection by destabilizing the capsid packing.

3.1. Appendix a: supplementary data

3.2. Acknowledgements

The numerical calculations reported in this paper were partially performed at TUBITAK ULAKBIM, High Performance and Grid Computing Center (TRUBA resources). This research did not receive any specific grant from funding agencies in the public, commercial, or not-for-profit sectors.

4. REFERENCES

[1] A. Z. Kapikian, R. G. Wyatt, R. Dolin, T. S. Thornhill, A. R. Kalica, and R. M. Chanock, "Visualization by Immune Electron-Microscopy of a 27-Nm Particle Associated with Acute Infectious Nonbacterial Gastroenteritis," *Journal of Virology,* vol. 10, pp. 1075-1081, 1972.

[2] K. L. Kotloff, J. P. Nataro, W. C. Blackwelder, D. Nasrin, T. H. Farag, S. Panchalingam*, et al.*, "Burden and aetiology of diarrhoeal disease in infants and young children in developing countries (the Global Enteric Multicenter Study, GEMS): a prospective, case-control study," *Lancet,* vol. 382, pp. 209-22, Jul 20 2013.

[3] G. Belliot, B. A. Lopman, K. Ambert-Balay, and P. Pothier, "The burden of norovirus gastroenteritis: an important foodborne and healthcare-related infection," *Clin Microbiol Infect,* vol. 20, pp. 724-30, Aug 2014.

[4] A. Kambhampati, M. Koopmans, and B. A. Lopman, "Burden of norovirus in healthcare facilities and strategies for outbreak control," *J Hosp Infect,* vol. 89, pp. 296-301, Apr 2015.

[5] T. N. Hoa Tran, E. Trainor, T. Nakagomi, N. A. Cunliffe, and O. Nakagomi, "Molecular epidemiology of noroviruses associated with acute sporadic gastroenteritis in children: global distribution of genogroups, genotypes and GII.4 variants," *J Clin Virol,* vol. 56, pp. 185-93, Mar 2013.

[6] S. M. Karst, C. E. Wobus, I. G. Goodfellow, K. Y. Green, and H. W. Virgin, "Advances in norovirus biology," *Cell Host Microbe,* vol. 15, pp. 668-80, Jun 11 2014.

[7] J. Rocha-Pereira, J. Neyts, and D. Jochmans, "Norovirus: targets and tools in antiviral drug discovery," *Biochem Pharmacol,* vol. 91, pp. 1-11, Sep 1 2014.

[8] M. Tan and X. Jiang, "Vaccine against norovirus," *Hum Vaccin Immunother,* vol. 10, pp. 1449-56, 2014.

[9] N. Aliabadi, B. A. Lopman, U. D. Parashar, and A. J. Hall, "Progress toward norovirus vaccines: considerations for further development and implementation in potential target populations," *Expert Rev Vaccines,* vol. 14, pp. 1241-53, 2015.

[10] E. Robilotti, S. Deresinski, and B. A. Pinsky, "Norovirus," *Clin Microbiol Rev,* vol. 28, pp. 134-64, Jan 2015.

[11] S. M. Karst, S. Zhu, and I. G. Goodfellow, "The molecular pathology of noroviruses," *J Pathol,* vol. 235, pp. 206-16, Jan 2015.

[12] P. A. White, "Evolution of norovirus," *Clin Microbiol Infect,* vol. 20, pp. 741-5, Aug 2014.

[13] M. M. Patel, A. J. Hall, J. Vinje, and U. D. Parashar, "Noroviruses: a comprehensive review," *J Clin Virol,* vol. 44, pp. 1-8, Jan 2009.

[14] S. Caddy, A. Breiman, J. le Pendu, and I. Goodfellow, "Genogroup IV and VI canine noroviruses interact with histo-blood group antigens," *J Virol,* vol. 88, pp. 10377-91, Sep 2014.

[15] M. de Graaf, J. van Beek, and M. P. Koopmans, "Human norovirus transmission and evolution in a changing world," *Nat Rev Microbiol,* vol. 14, pp. 421-33, Jul 2016.

[16] S. Shanker, R. Czako, B. Sankaran, R. L. Atmar, M. K. Estes, and B. V. Prasad, "Structural analysis of determinants of histo-blood group antigen binding specificity in genogroup I noroviruses," *J Virol,* vol. 88, pp. 6168-80, Jun 2014.

[17] G. Sapparapu, R. Czako, G. Alvarado, S. Shanker, B. V. Prasad, R. L. Atmar*, et al.*, "Frequent Use of the IgA Isotype in Human B Cells Encoding Potent Norovirus-Specific Monoclonal Antibodies That Block HBGA Binding," *PLoS Pathog,* vol. 12, p. e1005719, Jun 2016.

[18] K. Tamminen, M. Malm, T. Vesikari, and V. Blazevic, "Mucosal Antibodies Induced by Intranasal but Not Intramuscular Immunization Block Norovirus GII.4 Virus-Like Particle Receptor Binding," *Viral Immunol,* vol. 29, pp. 315-9, Jun 2016.

[19] L. Garaicoechea, A. Aguilar, G. I. Parra, M. Bok, S. V. Sosnovtsev, G. Canziani*, et al.*, "Llama nanoantibodies with therapeutic potential against human norovirus diarrhea," *PLoS One,* vol. 10, p. e0133665, 2015.

[20] V. P. Lochridge, K. L. Jutila, J. W. Graff, and M. E. Hardy, "Epitopes in the P2 domain of norovirus VP1 recognized by monoclonal antibodies that block cell interactions," *J Gen Virol,* vol. 86, pp. 2799-806, Oct 2005.

[21] B. V. V. Prasad, M. E. Hardy, T. Dokland, J. Bella, M. G. Rossmann, and M. K. Estes, "X-ray crystallographic structure of the Norwalk virus capsid," *Science,* vol. 286, pp. 287-290, Oct 8 1999.

[22] J. M. Choi, A. M. Hutson, M. K. Estes, and B. V. V. Prasad, "Atomic resolution structural characterization of recognition of histo-blood group antigens by Norwalk virus," *Proceedings of the National Academy of Sciences of the United States of America,* vol. 105, pp. 9175-9180, Jul 8 2008.

[23] T. Kubota, A. Kumagai, H. Ito, S. Furukawa, Y. Someya, N. Takeda*, et al.*, "Structural basis for the recognition of Lewis antigens by genogroup I norovirus," *J Virol,* vol. 86, pp. 11138-50, Oct 2012.

[24] A. Kocak and M. Yildiz, "Molecular dynamics studies of the norovirus-host cell interaction mediated by h-type 1 antigen," *Trakya University Journal of Natural Sciences,* vol. ASAP, 2019.

[25] L. Schrödinger, "Maestro," in *Schrödinger Release 2015-2*, ed. New York, NY: Schrödinger, LLC, 2015.

[26] M. H. Olsson, C. R. Sondergaard, M. Rostkowski, and J. H. Jensen, "PROPKA3: Consistent Treatment of Internal and Surface Residues in Empirical pKa Predictions," *J Chem Theory Comput,* vol. 7, pp. 525-37, Feb 8 2011.

[27] K. Lindorff-Larsen, S. Piana, K. Palmo, P. Maragakis, J. L. Klepeis, R. O. Dror*, et al.*, "Improved side-chain torsion potentials for the Amber ff99SB protein force field," *Proteins,* vol. 78, pp. 1950-1958, 2010.

[28] J. Wang, W. Wang, P. A. Kollman, and D. A. Case, "Automatic atom type and bond type perception in molecular mechanical calculations," *Journal of Molecular Graphics and Modelling,* vol. 25, pp. 247-260, 2006/10/01/ 2006.

[29] J. Wang, R. M. Wolf, J. W. Caldwell, P. A. Kollman, and D. A. Case, "Development and testing of a general amber force field," *Journal of Computational Chemistry,* vol. 25, pp. 1157-1174, 2004.

[30] M. J. Abraham, T. Murtola, R. Schulz, S. Páll, J. C. Smith, B. Hess*, et al.*, "GROMACS: High performance molecular simulations through multi-level parallelism from laptops to supercomputers," *SoftwareX,* vol. 1-2, pp. 19-25, 2015.

[31] K. Toukan and A. Rahman, "Molecular-dynamics study of atomic motions in water," *Phys Rev B Condens Matter,* vol. 31, pp. 2643-2648, Mar 1 1985.

[32] A. Kocak, I. Erol, M. Yildiz, and H. Can, "Computational insights into the protonation states of catalytic dyad in BACE1-acyl guanidine based inhibitor complex," *J Mol Graph Model,* vol. 70, pp. 226-235, Nov 2016.

[33] A. Kocak and M. Yildiz, "Docking, molecular dynamics and free energy studies on aspartoacylase mutations involved in Canavan disease," *J Mol Graph Model,* vol. 74, pp. 44-53, Jun 2017.

JOURNAL OF SCIENCE
SAKARYA UNIVERSITY

Sakarya University Journal of Science

ISSN 1301-4048 | e-ISSN 2147-835X | Period Bimonthly | Founded: 1997 | Publisher Sakarya University | http://www.saujs.sakarya.edu.tr/

Title: Green Supplier Selection via an Integrated Multi-Attribute Decision Making Approach

Authors: Ahmet Selcuk Yalcin, Huseyin Selcuk Kilic
Recieved: 2018-09-22 18:04:26

Accepted: 2019-06-26 11:50:17

Article Type: Research Article
Volume: 23
Issue: 6
Month: December
Year: 2019
Pages: 1066-1079

How to cite
Ahmet Selcuk Yalcin, Huseyin Selcuk Kilic; (2019), Green Supplier Selection via an Integrated Multi-Attribute Decision Making Approach. Sakarya University Journal of Science, 23(6), 1066-1079, DOI: 10.16984/saufenbilder.462796
Access link
http://www.saujs.sakarya.edu.tr/issue/44246/462796

Sakarya University Journal of Science 23(6), 1066-1079, 2019

Green Supplier Selection via an Integrated Multi-Attribute Decision Making Approach

Ahmet Selcuk Yalcin[1], Huseyin Selcuk Kilic*[2]

Abstract

The environmental awareness of society and the global competition market has increased significantly due to the environmental problems that happen today. Companies have recognized the importance of focusing on environmental issues in order to be strong in a modern competitive business environment. Therefore, environmental factors are taken into consideration during the supplier selection process, which is an important decision point in the supply chain. In this study, two robust multi-attribute decision making techniques, Intuitionistic Fuzzy AHP (IF-AHP) and PROMETHEE, are used in an integrated way to better handle this selection problem. The steps are clearly explained in the proposed methodology. First, the relative weights of the criteria are determined by IF-AHP, which allows decision makers (DMs) to deal with the uncertainty of the evaluation process. Subsequently, the weights of criteria obtained are used in the PROMETHEE method for the best ranking of alternative suppliers. An application is performed in the air filtration industry to demonstrate the validity of the proposed method.

Keywords: Greenness, IF-AHP, PROMETHEE, Supplier selection

1.INTRODUCTION

The examination and management of industrial wastes has been a serious issue for society since the industrial revolution took place [1]. Especially after 80's, toxic gases and wastes produced by factories have reached serious dimensions which threaten human health. In the 90s, the protection of natural resources and the environment has become a very important global problem at national and international conferences [2]. Suppliers with environmental awareness are preferred by firms because the firms can better adapt to the global environmental trend and create an impressive green image. In addition, another reason is that harmful compounds contained in the raw materials and semi-products provided by the supplier may lead to significant environmental effects in the whole process [3]. Thus, determining the environmentally conscious supplier can be regarded as one of the most significant activities in the supply chain (SC). As globalization grows, supplier selection problem becomes more complex. This problem has become a multi-criteria decision-making problem that requires many variables, environmental and

[1] Okan University, Industrial Engineering, Istanbul, Turkey. ORCID: 0000-0001-8963-0604
* Corresponding Author: huseyin.kilic@marmara.edu.tr
[2] Marmara University, Industrial Engineering, Istanbul, Turkey. ORCID: 0000-0003-3356-0162

traditional criteria and alternatives to be jointly evaluated. DMs may be unsuccessful or reluctant in the assessment stage due to their limited information or the subjectivity of qualitative evaluation criteria. This cause ambiguity and uncertainty in the problem [4,5]. In this paper, IF-AHP is regarded as a suitable method to detect the significance weights of main and sub criteria because it is easy to implement in spite of the ambiguity of human decision. Afterwards, PROMETHEE II method is utilized to rank the alternatives. An implementation is realized in a filtration plant to demonstrate the steps of the suggested model as indicated in Figure 1.

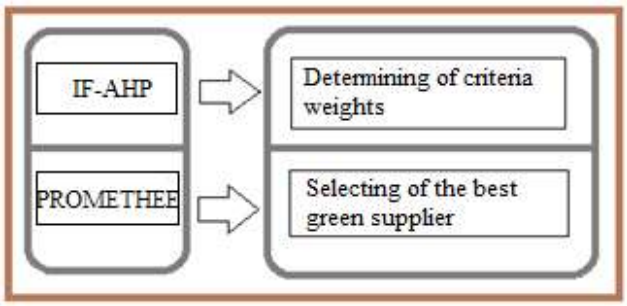

Figure 1. Summary of the study

The objective of the study is to propose a methodology to determine the most appropriate environmentally conscious supplier considering green and conventional criteria. The contributions of this research to the literature are summarized as follows:

- A consensus is made between DMs to prevent time waste when pairwise comparison is made between criteria.
- IF-AHP method which is novel in the literature has been used to weight the criteria
- The proposed methodology has been applied in a case study of the filtration industry, which has never been studied before.
- Since criteria play an important role and change with respect to the sector, the green and classic criteria used in this study were determined considering the filter industry.

The rest of this paper is organized as follows: Section two presents a literature review of green supplier selection methods and criteria. In the third section, the proposed method is explained in detail. In the fourth part, the application of the method suggested in a real case study is introduced. In the last section, the results of the study are discussed and recommendations are given for future studies.

2. LITERATURE REVIEW

In this section, a literature review of the criteria and techniques used in the green supplier selection studies was conducted.

2.1. Green Supplier Selection Criteria

Evaluation of the criteria is the first step in green supplier selection process. The contingency of obtaining misleading and incorrect results increases as long as the criteria are not properly determined. With growing environmental awareness, public and governmental pressures, executives have to buy from suppliers who are able to supply commodities and services with "lower price, higher quality, shorter lead time, and at the same time with focus on stronger environmental responsibility" [6]. In order to achieve long-term success and to select the best green suppliers in the modern market, companies and organizations should pay enough attention to both traditional and environmental factors. In the literature, in the determination of green and traditional criteria, researchers have often benefited from scientific journals, expert opinions and previous researches and so on.

Dickson analyzed 170 negotiations with the procurement directors and ranked 23 traditional criteria which are used in several studies. He introduced quality, delivery, performance history, warranties and claim policies as extremely important [7]. Weber et al. examined the 74 present reports to find out crucial factors in decision making problems and concluded that the most significant factors are price, delivery and quality [8]. Ho et al. illustrated that the most popular criteria are quality, followed by delivery, price/cost, manufacturing capability, service, management, technology, research and development (R&D), finance and flexibility [9]. Environmental management system (EMS), pollution control, green image, green design and solid or water waste are the most frequently used

criteria respectively in the studies published after 2008. Govindan et al. identified EMS as the most important green criterion in the selection of green suppliers [10]. Similarly, Nielsen et al. examined 57 green supplier selection studies, concluded that EMS was used as an environmental criterion in about thirty-five percent of studies [11]. After investigating 34 published articles, Villanueva-Ponce et al. indicated green product design, GSCM, environmental management are the most frequently used ones [12]. Banasik et al. pointed out greenhouse gases as the most popular key performance indicator in the studies [13].

2.2. Green Supplier Selection Methods

An effective supplier selection is the first step of a successful organization and a strong supply chain management (SCM). The success of the supplier selection process has a crucial effect on the productivity and success of the entire SC. However, a large number of previous studies on this subject have indicated that the supplier selection is the most important factor in the achievement of SC. It affects directly the environmental performance of the producer. Nonetheless, as companies increasingly depend on their suppliers, structure and results of green supplier selection problem have become critical [14].

Many different methods have been used in the literature for the selection of green suppliers. After reviewing 123 scientific journals published between 2008 and 2012 in supplier selection, Chai et al. reported that the most frequently utilized decision makings techniques were AHP (24.39%), LP (15.44%), TOPSIS (14.63%), ANP (12.20%) and DEA (10.57%) [15]. In particular, AHP is the most preferred technique by researchers. In the 2005-2009 period, the use of AHP steadily increased and was frequently used in studies [16]. Noci applied the AHP-based approach in five steps to assess the environmental performance of suppliers [17]. Humphreys et al. developed a decision support tool to help organizations integrate environmental factors into the supplier selection process [18]. Lu et al. proposed AHP and fuzzy logic-based model to help the green supply chain designer select the desired design alternative to achieve minimum environmental impact [19]. Lee et al. first applied the Delphi method to differentiate the criteria, then applied fuzzy expanded AHP to assess the uncertainty of the expert opinion [20]. Bai and Sarkis implemented rough set theory to deal with data uncertainty, taking environmental, social and economic factors into account for the selection of green suppliers [21]. Büyüközkan and Çifci proposed a fuzzy group multi-criteria decision model for evaluation of sustainable supplier utilizing fuzzy ANP [22]. Kannan et al. suggested a combined approach for supplier selection and order allocation in the green SC using fuzzy AHP, fuzzy TOPSIS, and multi objective linear programming [23]. Dobos and Vörösmarty introduced an integrated method to select green suppliers using data envelopment analysis and composite indicators [24]. Freeman and Chen developed a combined model for selecting green suppliers in electronic machine manufacturing using the AHP-Entropy model based on the TOPSIS method [25]. Darabi and Haydari suggested an interval valued hesitant fuzzy ranking method based on group decision analysis to evaluate and select green supplier [26]. Yazdani et al. suggested a combined methodology to select the most appropriate supplier, taking into account various environmental performance requirements and criteria. Their methods are based on the DEMATEL, QFD and COPRAS approaches [27]. Banaeian et al. compared the implementation of three popular multi-criteria supplier selection methods (TOPSIS, VIKOR and GRA) in a fuzzy environment. The methods are utilized for green supplier evaluation and selection in agri-food industry [28].

None of the techniques used in supplier selection have been integrated with intuitionistic fuzzy logic, as it has been noticed in the literature review. To address this shortcoming and remove ambiguity in the decision-making process, an approach that incorporates IF-AHP and PROMETHEE techniques in an integrated manner is presented in this study.

3. PROPOSED METHODOLOGY

The proposed methodology for green supplier selection consists of two parts. Firstly, after the criteria used to evaluate the suppliers have been determined, the importance weights of these criteria are found by the IF-AHP approach. Then, the order of suppliers is realized by PROMETHEE method.

3.1. Intuitionistic Fuzzy AHP (IF-AHP)

The IF-AHP method, which results from the integration of the intuitionistic fuzzy (IF) logic and the AHP method, is a method aimed at overcoming the ambiguity caused by the decision maker's subjective decisions. The substantial feature of this method is to have capability to achieve uncertainty which is inherent in decision making problems. Due to the hesitation function, more current results could be effectively obtained. However, IF-AHP is more superior and effective than the other AHP models in the process of removing the uncertainties that emerge from the decision maker [5]. The terms of $\mu_{ij}, v_{ij}, \pi_{ij}$ indicate the degree of membership, non-membership, and hesitation, respectively. The steps of this approach are as follows [29]:

Step 1: The structure of the hierarchy for the assessment of the problem is created. The aim, criteria and alternatives are determined.

Step 2: The pairwise comparative measure of the Intuitionistic Fuzzy-AHP with the novel measure of the decision matrix of triangular intuitionistic fuzzy numbers (TIFNs) is scaled. DMs are asked to detect ratings utilizing the nine AHP linguistic scale from the "equally significant" to the "absolutely more significant" expression on the criteria of the supplier problem. The transformation of the choice numbers of AHP to the TIFNs is shown in Table 1 [29].

Step 3: DMs' weights are determined. The significance of DMs is evaluated as linguistic factors. The linguistic factors of DMs were demonstrated in Table 2. Equation (1) proposed by Boran et al. is utilized to detect the weight of a decision maker weight [30]. It is assumed that $D = (\mu_k, v_k, \pi_k)$ is the IF number of kth DM.

$$\lambda_k = \frac{\left(\mu_k + \pi_k \cdot \left(\frac{\mu_k}{\mu_k + v_k}\right)\right)}{\sum_{k=1}^{m}\left(\mu_k + \pi_k \cdot \left(\frac{\mu_k}{\mu_k + v_k}\right)\right)} \quad (1)$$

Step 4: The unified IF decision matrix based on DM is created. $R^{(k)} = (r_{ij}^k)_{mxn}$ denotes an IF decision matrix of the kth DM. $\lambda = \{\lambda_1, \lambda_2, \dots, \lambda_n\}$ denotes the weight of the all decision-maker and $\sum_{m=1}^{t} \lambda = 1$. Every separate view must be fused into the group idea to form an unified IF decision matrix by implementing intuitionistic fuzzy weighted averaging operator (IFWA) proposed by Xu [31].

$$r_{ij} = IFWA_\lambda\left(r_{ij}^{(1)}, r_{ij}^{(2)}, \dots, r_{ij}^{(t)}\right) =$$

$$\lambda_1 r_{ij}^{(1)} \oplus \lambda_2 r_{ij}^{(2)} \oplus \dots \oplus \lambda_t r_{ij}^{(t)},$$

$$= \begin{bmatrix} 1 - \prod_{k=1}^{t}\left(1 - \mu_{ij}^{(k)}\right)^{\lambda_k}, \\ \prod_{k=1}^{t}\left(v_{ij}^{(k)}\right)^{\lambda_k}, \\ \prod_{k=1}^{t}\left(1 - \mu_{ij}^{(k)}\right)^{\lambda_k} - \\ \prod_{k=1}^{t}\left(v_{ij}^{(k)}\right)^{\lambda_k} \end{bmatrix} \quad (2)$$

$$r_{ij} = (\mu_{ij}, v_{ij}, \pi_{ij},),$$

$$\mu_{ij} = 1 - \prod_{k=1}^{t}\left(1 - \mu_{ij}^{(k)}\right)^{\lambda_k}$$

$$v_{ij} = \prod_{k=1}^{t}\left(v_{ij}^{(k)}\right)^{\lambda_k}$$

$$\pi_{ij} = \prod_{k=1}^{t}\left(1 - \mu_{ij}^{(k)}\right)^{\lambda_k} - \prod_{k=1}^{t}\left(v_{ij}^{(k)}\right)^{\lambda_k}$$

Step 5: The consistency ratio (CR) of the unified IF decision matrix is computed by Equation (3).

$$CR = \frac{((\lambda_{max} - n)/(n-1))}{R.I} \quad (3)$$

in which it is supposed that $(\lambda_{max} - n)$ is the mean valuation of hesitation degree (π_k) of the criteria and n denotes the dimension of matrix in the study. The valuation of random indices (RI) proposed by Saaty is demonstrated on Table 3 [32]. CR can be accepted if it does not pass 0.10. If the ratio is bigger than 0.10, the decision matrix must be evaluated as unstable.

Table 1. Transformation of the AHP choice numbers to TIFNs [29]

Choice on pairwise comparison	AHP Choice Number	Reciprocal Choice Number	TIFNs	Reciprocal TIFNs
Equally important	1	1	(0.02, 0.18, 0.80)	(0.02, 0.18, 0.80)
Intermediate value	2	½	(0.06, 0.23, 0.70)	(0.23, 0.06, 0.70)
Moderately more important	3	1/3	(0.13, 0.27, 0.60)	(0.27, 0.13, 0.60)
Intermediate value	4	¼	(0.22, 0.28, 0.50)	(0.28, 0.22, 0.50)
Strongly more important	5	1/5	(0.33, 0.27, 0.40)	(0.27, 0.33, 0.40)
Intermediate value	6	1/6	(0.47, 0.23, 0.30)	(0.23, 0.47, 0.30)
Very strong more important	7	1/7	(0.62, 0.18, 0.20)	(0.18, 0.62, 0.20)
Intermediate value	8	1/8	(0.80, 0.10, 0.10)	(0.10, 0.80, 0.10)
Extremely more important	9	1/9	(1.0, 0, 0)	(0, 1.0, 0)

Table 2. Linguistic factors for the significance of DMs [30]

Ling. var.	TIFNs
Very significant	(9/10, 5/100, 5/100)
Significant	(75/100, 20/100, 5/100)
Medium	(50/100, 40/100, 10/100)
Insignificant	(25/100, 60/100, 15/100)
Very insignificant	(10/100, 80/100, 10/100)

Table 3. Random indices of sizes of matrices [32]

n	1-2	3	4	5	6	7	8	9
RI	0.0	0.58	0.90	1.12	1.24	1.32	1.41	1.45

Step 6: The IF weight of the unified IF decision matrix is computed. Equation (4) is used to calculate the entropy weight of each criterion.

$$\bar{\bar{w}}_i = -\frac{1}{n \ln 2}[\mu_i \ln \mu_i + v_i \ln v_i - (1-\pi_i)\ln(1-\pi_i) - \pi_i \ln 2] \quad (4)$$

The final entropy weights of each criterion can be calculated using Equation (5). It is assumed that the sum of the criterion weights is equal to one.

$$w_i = \frac{1-\bar{\bar{w}}_i}{n - \sum_i^n \bar{\bar{w}}_i} \quad (5)$$

3.2. PROMETHEE

PROMETHEE (Preference Ranking Organization Method for Enrichment Evaluation) is a multiple decision making method developed by Jean-Pierre Brans in 1982. This method is based on superiority. The steps of the PROMETHEE II method are as follows [33]:

Step 1: The data matrix is created. The data matrix is constructed by weights and alternatives which are evaluated by criteria.

Step 2: The preference functions for criteria are determined. They are determined to show the structure and internal relations of the identified evaluation factors. They are shown in Table 4.

Step 3: The common preference functions for the pair of alternatives based on preference functions are determined. The calculation of common preference function is indicated in Equation (6).

$$P(a,b) = \begin{cases} 0, f(a) \le f(b) \\ p[f(a) - f(b)], f(a) > f(b) \end{cases} \quad (6)$$

Table 4. Preference functions

Type	Parameter	Function
First type	-	$p(d) = \begin{cases} 0, d \leq 0 \\ 1, d > 0 \end{cases}$
Second type	m	$p(d) = \begin{cases} 0, d \leq m \\ 1, d > m \end{cases}$
Third type	k	$p(d) = \begin{cases} d/k, d \leq k \\ 1, d > k \end{cases}$
Fourth type	a, b	$p(d) = \begin{cases} 0, d \leq a \\ 1/2, a < d \leq b \\ 1, d > b \end{cases}$
Fifth type	c, e	$p(d) = \begin{cases} 0, d \leq c \\ d - c/e - c, c < d \leq e \\ 1, d > e \end{cases}$
Sixth type	σ	$P(d) = \begin{cases} 0, d \leq 0 \\ 1 - e^{\frac{d^2}{2\sigma^2}}, d > 0 \end{cases}$

Step 4: The preference index for every pair of alternative is detected. The calculation of preference index for any a and b alternatives evaluated with respect to k criterion is done by using Equation (7).

$$\pi(a,b) = \frac{\sum_{i=1}^{k} W_i * P_i(a,b)}{\sum_{i=1}^{k} W_i} \quad (7)$$

Step 5: Positive and negative superiorities for alternatives are determined. The positive and negative priorities for alternative a could be computed by utilizing Equations (8) and (9) respectively.

$$\Phi^{+}(a) = \frac{1}{n-1} \sum_{i=1}^{n} \pi(a,b) \quad (8)$$

$$\Phi^{-}(a) = \frac{1}{n-1} \sum_{i=1}^{n} \pi(b,a) \quad (9)$$

Step 6: Complete priorities of alternatives with PROMETHEE II are determined. The complete priority of each alternative is calculated by the aid of Equations (10) - (12).

$$\Phi(a) = \Phi^{+}(a) - \Phi^{-}(a) \quad (10)$$

If $\Phi(a) > \Phi(b)$alternative a is more superior. (11)

If $\Phi(a) = \Phi(b)$ alternatives a and b are same. (12)

4. CASE STUDY

This section presents an implementation in the filtration industry to demonstrate the feasibility and validity of the integrated IF-AHP and PROMETHEE approaches. The suppliers in the application provide HEPA air filtration media. Five supplier alternatives were regarded as potential suppliers provided that they have environmental qualifications such as ISO 14001 and EU Eco-Management and Audit Scheme (EMAS). Those suppliers are called as A1, A2, A3, A4 and A5 because of the privacy policy of the companies. The criteria of the study are detected considering the recommendations of the experienced managers in the company. Accordingly, “quality”, “price”, “delivery”, “flexibility” and “green” are the main criteria. “Green image”, “recyclability of raw material”, “design for disassembly and reuse”, “green R & D” and “transportation” are the sub-criteria of “greenness”. Three DMs who are executives of departments of quality, production and R&D have participated in the assessment process.

4.1. IF-AHP

IF-AHP mentioned in Section 3.1 is used to calculate the weights of the main and sub criteria. Only the calculation of the main criteria has been

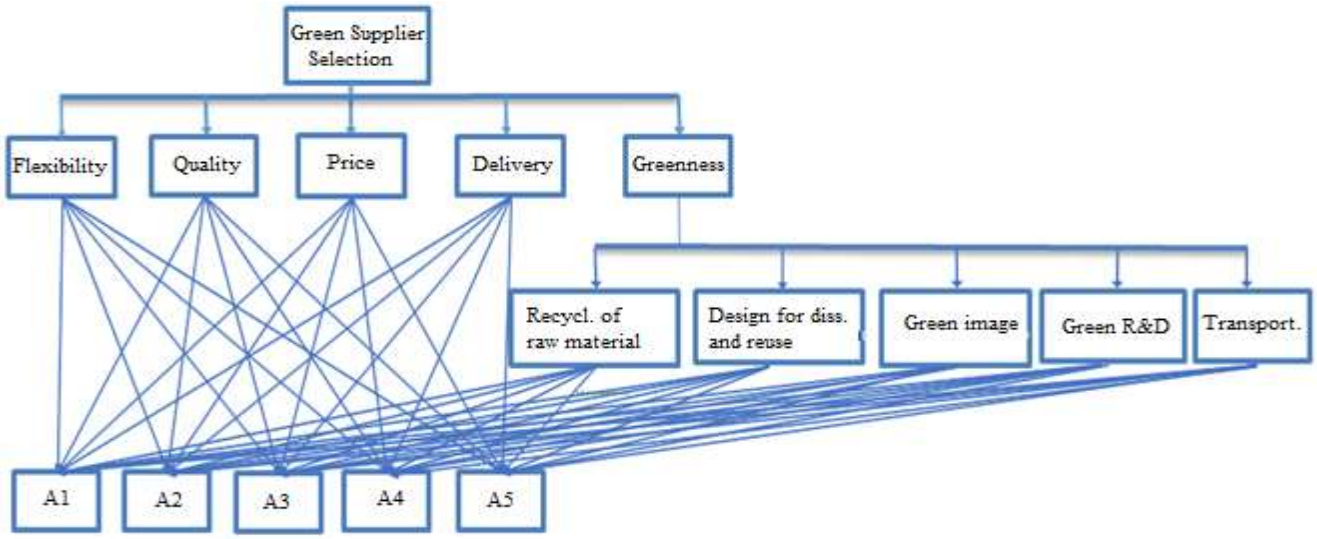

Figure 2. Hierarchical structure of main and sub criteria

shown in detail. The hierarchical diagram of the supplier selection problem is given in Figure 2. The pairwise comparison matrix between criteria mentioned in step 2 is formed by using TIFNs given in Table 1 based on the negotiation between the DMs. The pairwise comparison matrix between the main criteria is shown in Table 5. The step of weighting of DMs mentioned in Step 3 have not implemented because of the compromise between decision makers. The unified fuzzy decision matrix described in step 4 is based on the weight of the compromise evaluation between DMs. In this step, Equation (2) is utilized to unify the whole of transformation of the IF decision matrix of each factor. The results are shown in Table 6. For example, the calculation of unified matrix of greenness criterion considering compromise assessment is shown as follows:

$$= \begin{bmatrix} 1-\prod\begin{pmatrix}(1-0.27)^1*(1-0.27)^1*\\(1-0.22)^1*\\(1-0.02)^1*(1-0.13)^1\end{pmatrix} \\ \prod\begin{pmatrix}(0.33)^1*(0.13)^1*(0.28)^1*\\(0.18)^1*(0.27)^1\end{pmatrix} \\ \prod\begin{pmatrix}(1-0.27)^1*(1-0.27)^1*\\(1-0.22)^1*\\(1-0.02)^1*(1-0.13)^1\end{pmatrix} \\ -\prod\begin{pmatrix}(0.33)^1*(0.13)^1*(0.28)^1*\\(0.18)^1*(0.27)^1\end{pmatrix} \\ = (0.65, 0.001, 0.349) \end{bmatrix}$$

Computation of the CR of the unified IF decision matrix of criterion mentioned in the step 5 is performed using Equation (3).

$$= \frac{\Big(\big((0+0+0.505+0.349+0.369)/5\big)/4\Big)}{1.12} = 0.05$$

As seen in this computation, the CR of the unified IF decision matrix is 0.05. The matrix is stable because this value is less than 0.10. At the last step, entropy weights of every main criteria and final entropy weights are obtained by utilizing Equation (4) and (5), respectively. For instance, calculation of the entropy weight and the final entropy weight of the price as follows:

$$\bar{\bar{w}}_{price} = -\frac{1}{5\ln 2}[0.49\ln 0.49 + 0.005\ln 0.005 - (1-0.505)\ln(1-0.505) - 0.505\ln 2] = 0.1090$$

$$= \frac{1-0.1090}{5-(0+0+0.1090+0.0719+0.0759)} = 0.1878$$

The entropy weights of the quality and delivery criteria are computed as zero. The entropy weights of price, green and flexibility criteria are computed as 0.1090, 0.0719 and 0.0759, respectively. Compromise assessment has also been taken into account when comparing sub-criteria. It is shown in Table 7. The unified matrix of the sub criteria generated by the TIFNs is given in Table 8.

Table 5. Pairwise comparison of main criteria in TIFNs

Main criteria	Quality	Delivery	Price	Greenness	Flexibility
Quality	(0.02,0.18, 0.80)	(0.13,0.27, 0.60)	(1.0,0,0)	(0.33,0.27, 0.40)	(0.62,0.18, 0.20)
Delivery	(0.27, 0.13, 0.60)	(0.02,0.18, 0.80)	(1.0,0,0)	(0.13,0.27, 0.60)	(0.33,0.27, 0.40)
Price	(0,1.0,0)	(0,1.0,0)	(0.02,0.18, 0.80)	(0.28,0.22, 0.50)	(0.27, 0.13, 0.60)
Greenness	(0.27, 0.33, 0.40)	(0.27,0.13, 0.60)	(0.22,0.28, 0.50)	(0.02,0.18, 0.80)	(0.13,0.27, 0.60)
Flexibility	(0.18,0.62, 0.20)	(0.27,0.33, 0.40)	(0.13,0.27, 0,60)	(0.27, 0.13, 0.60)	(0.02,0.18, 0.80)

Table 6. Unified matrix of main criteria in TIFNs

Main criteria	Quality	Delivery	Price	Greenness	Flexibility	Unified matrix
Quality	(0.02,0.18,0.80)	(0.13,0.27, 0.60)	(1.0,0,0)	(0.33,0.27, 0.40)	(0.62,0.18, 0.20)	(1.0,0,0)
Delivery	(0.27,0.13,0.60)	(0.02,0.18, 0.80)	(1.0,0,0)	(0.13,0.27, 0.60)	(0.33,0.27, 0.40)	(1.0,0,0)
Price	(0,1.0,0)	(0,1.0,0)	(0.02,0.18, 0.80)	(0.28,0.22, 0.50)	(0.27, 0.13, 0.60)	(0.49, 0.005, 0.505)
Greenness	(0.27,0.33,0.40)	(0.27, 0.13, 0.60)	(0.22,0.28, 0.50)	(0.02,0.18, 0.80)	(0.13,0.27, 0.60)	(0.65,0.001, 0.349)
Flexibility	(0.18,0.62,0.20)	(0.27,0.33, 0.40)	(0.13,0.27, 0.60)	(0.27, 0.13, 0.60)	(0.02,0.18, 0.80)	(0.63,0.001, 0.369)

Table 7. Pairwise comparison of sub criteria in TIFNs

Sub criteria	Recycl. raw material	Design for diss. and reuse	Green image	Green R&D	Transportation
Recycl. raw material	(0.02,0.18, 0.80)	(0.13,0.27,0.60)	(1.0,0,0)	(0.62,0.18,0.20)	(0.47,0.23,0.30)
Design for diss. and reuse	(0.27,0.13,0.60)	(0.02,0.18,0.80)	(1.0,0,0)	(0.33,0.27,0.40)	(0.33,0.27,0.40)
Green image	(0,1.0,0)	(0,1.0,0)	(0.02,0.18,0.80	(0.23,0.06,0.70	(0.27,0.13,0.60)
Green R&D	(0.18,0.62,0.20)	(0.27,0.33,0.40)	(0.06,0.23,0.70)	(0.02,0.18, 0.80)	(0.27,0.33,0.40)
Transportation	(0.23,0.47,0.30)	(0.27,0.33,0.40)	(0.13,0.27,0.60)	(0.33,0.27,0.40)	(0.02,0.18,0.80)

Table 8. Unified matrix of sub criteria in TIFNs

Sub criteria	Recycl. raw material	Design for dis. and reuse	Green image	Green R&D	Transportation	Unified matrix
Recycl. Raw material.	(0.02,0.18, 0.80)	(0.13,0.27, 0.60)	(1.0,0,0)	(0.62,0.18, 0.20)	(0.47,0.23, 0.30)	(1.0,0,0)
Design for disa. and reuse.	(0.27,0.13, 0.60)	(0.02,0.18, 0.80)	(1.0,0,0)	(0.33,0.27, 0.40)	(0.33,0.27, 0.40)	(1.0,0,0)
Green image	(0,1.0,0)	(0,1.0,0)	(0.02,0.18, 0.80)	(0.23,0.06, 0.70)	(0.27,0.13, 0.60)	(0.45,0.001, 0.549)
Green R&D	(0.18,0.62, 0.20)	(0.27,0.33, 0.40)	(0.06,0.23, 0.70)	(0.02,0.18, 0.80)	(0.27,0.33, 0.40)	(0.60, 0.003, 0.397)
Transportation	(0.23,0.47, 0.40)	(0.27,0.33, 0.40)	(0.13,0.27, 0.60)	(0.33,0.27, 0.40)	(0.02,0.18, 0.80)	(0.68,0.002, 0.318)

The CR of the unified IF decision matrix for sub criteria is also calculated as 0.05. The entropy and final entropy weights of each sub criterion are similarly computed. For instance, calculation the entropy weight and the final entropy weight of the green image are as follows:

$$\bar{\bar{w}}_{g.i.} = -\frac{1}{5\ln 2}[0.45\ln 0.45 + 0.001\ln 0.001 - (1-0.549)\ln(1-0.549) - 0.549\ln 2] = 0.1118$$

$$= \frac{1-0.1118}{5-(0+0+0.1118+0.0848+0.0675)} = 0.1875$$

Final entropy weight of greenness is computed as 0.1956 in the previous step. However, at last, since the green image criterion is a sub-criterion of the greenness criterion, the final entropy weights of greenness and green image are multiplied:

$$w_{greenness} \times w_{green\ image} = 0.1956 \times 0.1875 = 0.0366$$

Final entropy weights of each main and sub criterion are demonstrated in Table 9.

4.2. PROMETHEE

The PROMETHEE method described in Section 3.2 has been used for sorting alternatives considering weights of the criteria. At first, the data matrix created by weights and alternatives assessed by the criteria is given in Table 10. As constructing the data matrix, DMs reconciled and rated alternatives by utilizing a 10-point Likert-type scale considering the criteria.

The preference functions described in step 2 are determined for each criterion. In determining the preference functions for the criteria, the structure of the criterion, the values it can take, and the views of the managers and experts on the criteria are evaluated. Hence, the fifth type preference function is determined as suitable for all the criteria. However, in the price criterion assessment, the supplier offering the lowest price is considered to receive the highest score. The preference function and the related parameters for each of the criteria are given in Table 11. Then, the preference indices for alternatives are calculated by Equation (7) considering common preference functions for the pair of alternatives. Similar calculations are made for other alternative pairs. The results obtained are shown in Table 12.

Table 9. Final entropy weights of main and sub criteria

Criteria	Entropy weights	Final entropy weights
Quality	0	0.2108
Delivery	0	0.2108
Price	0.1090	0.1878
Flexibility	0.0759	0.1948
Recycl. of raw material	0	0.0413
Design for dis. and reuse	0	0.0413
Green image	0.1118	0.0366
Green R&D	0.0848	0.0378
Transportation	0.0675	0.0386

Table 10. Data matrix

Alter.	Criteria								
	Quality (Max)	**Delivery (Max)**	**Price (Max)**	**Flex. (Max)**	**Recycl. of raw mat. (Max)**	**Design for diss. & reuse (Max)**	**Green image (Max)**	**Green R&D (Max)**	**Trans. (Max)**
A	3	2	4	7	5	4	7	4	5
B	6	8	6	5	9	7	9	3	6
C	3	6	9	6	6	8	5	2	4
D	9	4	5	5	5	5	4	2	3
E	5	9	4	8	7	6	2	5	8
Weights	0.2108	0.2108	0.1878	0.1948	0.0413	0.0413	0.0366	0.0378	0.0386

Table 11: Determined preference functions and parameters for each criterion

Criteria	Parameter	Function
Quality (max)	2, 4	$p_{quality}=\begin{cases}0, x \le 2\\ \frac{x-2}{2}, 2<x\le 4\\ 1, x>4\end{cases}$
Delivery (max)	3, 5	$p_{delivery}=\begin{cases}0, x \le 3\\ \frac{x-3}{2}, 3<x\le 5\\ 1, x>5\end{cases}$
Price (max)	2, 4	$p_{price}=\begin{cases}0, x \le 2\\ \frac{x-2}{2}, 2<x\le 4\\ 1, x>4\end{cases}$
Flexibility (max)	1, 3	$p_{flexibility}=\begin{cases}0, x \le 1\\ \frac{x-1}{2}, 1<x\le 3\\ 1, x>3\end{cases}$
Recyclability of raw material (max)	3, 5	$p_{recycl.}=\begin{cases}0, x \le 3\\ \frac{x-3}{2}, 3<x\le 5\\ 1, x>5\end{cases}$
Design for disassembly and reuse (max)	2, 4	$p_{designfordis.}=\begin{cases}0, x \le 2\\ \frac{x-2}{2}, 2<x\le 4\\ 1, x>4\end{cases}$
Green image (max)	3, 5	$p_{greenimage}=\begin{cases}0, x \le 3\\ \frac{x-3}{2}, 3<x\le 5\\ 1, x>5\end{cases}$
Green R&D (max)	1,3	$p_{greenR\&D}=\begin{cases}0, x \le 1\\ \frac{x-1}{2}, 1<x\le 3\\ 1, x>3\end{cases}$
Transportation (max)	2, 4	$p_{transportation}=\begin{cases}0, x \le 2\\ \frac{x-2}{2}, 2<x\le 4\\ 1, x>4\end{cases}$

Table 12. Calculated preference indices for alternative suppliers

	A	B	C	D	E
A	-	0.0974	0.0189	0.1163	0.0366
B	0.3575	-	0.1237	0.1819	0.0366
C	0.3345	0.0939	-	0.2084	0.1878
D	0.2108	0.1054	0.2108	-	0.2108
E	0.2301	0.2137	0.1738	0.4820	-

Table 13. Positive and negative priorities for alternative suppliers

Alternative	**A**	**B**	**C**	**D**	**E**
Φ^+	0.2692	0.6997	0.8246	0.7378	1.0996
Φ^-	1.1329	0.5104	0.5272	0.9886	0.4718

In the next step, positive and negative priorities are calculated for the alternative suppliers by Equations (8) and (9), respectively. Calculation of positive and negative priorities for Alternative A is shown below as an example and the results for the other alternatives are shown in Table 13.

$$\Phi^+(A) = \pi(A,B) + \pi(A,C) + \pi(A,D) + \pi(A,E)$$

=0.0974+0.0189+0.1163+0.0366=0.2692

$$\Phi^-(A) = \pi(B,A) + \pi(C,A) + \pi(D,A) + \pi(E,A)$$

=0.3575+0.3345+0.2108+0.2301=1.1329

Finally, the complete ranking is determined by PROMETHEE II method. The complete priorities of the alternatives are calculated by Equation (10). Equations (11) and (12). The complete ranking is shown in Figure 3. As a result of ranking, supplier E has been identified as the most suitable green supplier for the company. Other suppliers are listed as C-B-D-A respectively.

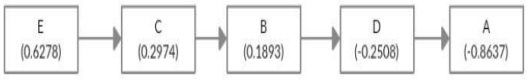

Figure 3. Complete ranking of suppliers

5. CONCLUSION

This paper proposed an integrated model for green supplier selection. IF-AHP is considered as an appropriate method to weigh the criteria since it is easy and robust to implement in spite of the ambiguity of human decision in the assessment period. At first, IF-AHP is applied to determine the criteria weights. Afterwards, PROMETHEE which is regarded as a proper and practical outranking method, is applied to rank the alternative suppliers considering the criteria weights. Eventually, an application is presented for the validation and detailed analysis of the proposed method.

The contribution of this research can be grouped under four headings. First, IF-AHP method which emerges recently in the literature and is powerful enough to remove the ambiguity in decision-making problems is used. The second contribution is to avoid time wasting by providing a consensus assessment between decision makers. The third contribution is that the criterion weight values are obtained without defuzzification operation by the proposed IF-AHP method. The final contribution is that the proposed approach is applied for the first time in the filter industry. Thus, managers and company owners who desire to make green supplier selection in the filter industry can benefit from this study. Green and classical criteria used in this study can also be used in the selection of suppliers in some other

sectors such as automotive, electronics or textile. However, the criteria such as recyclability of raw material design for disassembly and reuse are not suitable for the selection of green suppliers in the service sector.

Although this paper is a comprehensive study, green supplier selection is an appropriate area for development. In order to overcome the uncertainty of the problem in future studies, it can be used to compare the criteria by integrating the intuitionistic fuzzy logic with the Analytical Network Process method which evaluates the feedback between intergroup and intergroup dependencies and criteria. However, Intuitionistic Fuzzy PROMETHEE can be applied to avoid uncertainties in the order of suppliers. Finally, another superiority method, ELECTRE, can be used to rank suppliers and the results can be compared to the results suggested in this study.

REFERENCES

[1] J. Sarkis, Q. Zhu and K. Lai, "An organizational theoretic review of green supply chain management literature" , *International Journal of Production Economics*, vol. 130, pp. 1–15, 2011.

[2] G. Büyüközkan ve Z. Vardaloğlu, "Green supply chain management (Yeşil tedarik zinciri yönetimi)", *Lojistik Dergisi*, Cilt 8, 66-73, 2008.

[3] G. Akman, "Evaluating suppliers to include green supplier development programs via fuzzy c-means and VIKOR methods", *Computers and Industrial Engineering*, vol. 86, pp. 69-82, 2015.

[4] Ö. Bali ve E. Güreşen, "Çoklu Periyotta Çevreci Tedarikçi Seçimi İçin Belirsizlik Etmenli Bir ÇÖKV Yöntemi", *Journal of Defense Science,* vol. 12(1), pp. 43-70, 2013.

[5] Z. Xu and H. Liao, "Intuitionistic Fuzzy Analytic Hierarchy Process", *IEEE transactions on fuzzy systems*, vol. 22(4), pp. 749-761, 2014.

[6] S. Hashemi, A. Karimi and M. Tavana, "An integrated green supplier selection approach with analytic network process and improved Grey relational analysis", *International Journal of Production Economics*, vol. 159, pp. 178-191, 2015.

[7] G.W. Dickson, "An analysis of vendor selection system and decisions", *Journal of Purchasing*, vol. 2(1), pp. 5-17, 1966.

[8] C.A. Weber, J.R. Current and W.C. Benton, "Vendor selection criteria and methods", *European Journal of Operational Research*, vol. 50 (1), pp. 2-18, 1991.

[9] W. Ho, X. Xu, and K.P. Dey, "Multi-criteria decision making approaches for supplier evaluation and selection: A literature review", *European Journal of Operational Research*, vol. 202, pp. 16–24, 2010.

[10] K. Govindan, S. Rajendran, J.Sarkis, and P. Murugesan, "Multi criteria decision making approaches for green supplier evaluation and selection: a literature review", *Journal of Cleaner Production*, vol. 98, pp. 66-83, 2015.

[11] I.E. Nielsen, N. Banaeian, P. Golińska, H. Mobli and M. Omid, "Green Supplier Selection Criteria: From a Literature Review to a Flexible Framework for Determination of Suitable Criteria", *Logistics Operations, Supply Chain Management and Sustainability*, pp. 79-99, 2014.

[12] R. Villanueva-Ponce, L. Avelar-Sosa, A. Alvarado-Iniesta, and V.G. Cruz-Sánchez, "The green supplier selection as a key element in a supply chain: A review of cases studies" *Dyna*, vol. *82*(194), pp. 36-45, 2015.

[13] A. Banasik, J.M. Bloemhof-Ruwaard, A. Kanellopoulos, G.D.H. Claassen and G. A. J. Van der Vorst, " Multi-criteria decision making approaches for green supply chains: a review", *Flexible Services*

and Manufacturing Journal, pp. 1–31, 2016.

[14] O. Gurel, Z. Acar, I. Onden and I. Gumus, "Determinants of the green supplier selection", *Procedia - Social and Behavioral Sciences*, vol. 181, pp. 131 – 139, 2015.

[15] J. Chai, N.K. Liu and W.T. Ngai, "Application of decision-making techniques in supplier selection: A systematic review of literature", *Expert Systems with Applications*, vol. 40, pp. 3872–3885, 2013.

[16] S. Sipahi, and M. Timor, "The analytic hierarchy process and analytic network process: an overview of applications", *Management Decision*, vol. *48*(5), pp. 775-808, 2010.

[17] G. Noci, "Designing green vendor rating systems for the assessment of a supplier's environmental performance", *European Journal of Purchasing & Supply Management*, vol. 3(2), pp. 103–114, 1997.

[18] P.K. Humphreys, Y.K Wong, and F.T.S. Chan, "Integrating environmental criteria into the supplier selection process", *Journal of Materials Processing Technology*, vol. 138, pp. 349-356, 2003.

[19] L.Y.Y. Lu, C.H. Wu and T.C. Kuo, "Environmental principles applicable to green supplier evaluation by using multiobjective decision analysis", *International Journal of Production Research*, vol. 45, pp. 4317-4331, 2007.

[20] A. Lee, H. Kang, C. Hsu and H. Hung, "A green supplier selection model for high-tech industry", *Expert Systems with Applications*, vol. 36, pp. 7917–7927, 2009.

[21] C. Bai and J. Sarkis, "Integrating sustainability into supplier selection with grey system and rough set methodologies", *International Journal of Production Economics*, vol. 124(1), pp. 252-264, 2010.

[22] G. Büyüközkan and G. Çifçi, "A novel fuzzy multi-criteria decision framework for sustainable supplier selection with incomplete information", *Computers in Industry*, vol. 62(2), pp. 164-174, 2011.

[23] D. Kannan, R. Khodaverdi, L. Olfat, A. Jafarian and A. Diabat, "Integrated fuzzy multi criteria decision making method and multi objective programming approach for supplier selection and order allocation in a green supply chain", *Journal of Cleaner Production*, vol. 47, pp. 355-367, 2013.

[24] I. Dobos and G. Vörösmarty, "Green supplier selection and evaluation using DEA-type composite indicators", *International Journal of Production Economics*, vol. 157, pp. 273-278, 2014.

[25] J. Freeman and T. Chen, "Green supplier selection using an AHP-Entropy-TOPSIS framework", *Supply Chain Management: An International Journal*, vol. 20(3), pp. 327–340, 2015.

[26] S. Darabi and J. Heydari, "An interval-valued hesitant fuzzy ranking method based on group decision analysis for green supplier selection, *IFAC-PapersOnLine*, vol. 49(2), pp. 12-17, 2016.

[27] M. Yazdani, P. Chatterjee, E.K. Zavadskas, and S.H. Zolfani, "Integrated QFD-MCDM framework for green supplier selection", *Journal of Cleaner Production*, vol. 142, pp. 3728-3740, 2017.

[28] N. Banaeian, I. Nielsen, B. Fahimnia, H. Hobli and M. Omid, "Green supplier selection using fuzzy group decision making methods: a case study from agri-food industry", *Computers and Operations Research*, vol. 89, pp. 337-347, 2016.

[29] L. Abdullah and L. Najib, "Sustainable energy planning decision using the intuitionistic fuzzy analytic hierarchy process: choosing energy technology in Malaysia" *International Journal of*

Sustainable Energy, vol. 35 (4), pp. 360–377, 2016.

[30] F.E. Boran, S. Genç, M. Kurt and D. Akay, "A multi-criteria intuitionistic fuzzy group decision making for supplier selection with TOPSIS method", *Expert Systems with Applications*, vol. 36(8), pp. 11363-11368, 2009.

[31] Xu, Z. S.. "Intuitionistic Fuzzy Aggregation Operators", *IEEE Transactions on Fuzzy Systems*, vol. 15 (6), pp. 1179–1187, 2007.

[32] T. L Saaty, The Analytical Hierarchy Process, Planning, Priority. Resource Allocation. RWS Publications, USA, 1980.

[33] J.P. Brans ve B. Mareschal, "PROMETHEE methods", *Multiple criteria decision analysis: state of the art surveys* , 163-186, Springer, New York, NY, 2005.

JOURNAL OF SCIENCE
SAKARYA UNIVERSITY

Sakarya University Journal of Science

ISSN 1301-4048 | e-ISSN 2147-835X | Period Bimonthly | Founded: 1997 | Publisher Sakarya University | http://www.saujs.sakarya.edu.tr/

Title: Damage resistance investigation of Armox 500T and Aluminum 7075-T6 plates subjected to drop-weight and ballistic impact loads

Authors: Eyüp Yeter
Recieved: 2019-01-24 09:18:23

Accepted: 2019-06-27 15:21:46

Article Type: Research Article
Volume: 23
Issue: 6
Month: December
Year: 2019
Pages: 1080-1095

How to cite
Eyüp Yeter; (2019), Damage resistance investigation of Armox 500T and Aluminum 7075-T6 plates subjected to drop-weight and ballistic impact loads. Sakarya University Journal of Science, 23(6), 1080-1095, DOI: 10.16984/saufenbilder.517128
Access link
http://www.saujs.sakarya.edu.tr/issue/44246/517128

Sakarya University Journal of Science 23(6), 1080-1095, 2019

Damage resistance investigation of Armox 500T and Aluminum 7075-T6 plates subjected to drop-weight and ballistic impact loads

Eyüp Yeter*[1],

Abstract

The main objective of this paper is to investigate damage resistance of Armox 500T and Aluminum 7075-T6 plates subjected to drop-weight and ballistic impact loads. Investigating the behavior of structures under the low or the high velocity impact loads is an important research topic. The study of materials and their combinations provides fundamental understanding of many engineering structures. In this study, firstly drop weight and ballistic impact resistance of the Armox-500T and Al7075-T6 materials was examined. Ballistic impact analyses were carried out using 7.62 API projectiles with an initial velocity of 800 m/s. During the drop-weight analyses, the drop of 5.5 kg weight from the 800 mm distance was modeled. The situations at which target plates of different thickness can be fully penetrated or not to be fully penetrated by the projectile, the final (residual) velocities in the fully penetrated plates and the amount of energy absorbed by the target plates were investigated. 6.72 API projectiles with an initial velocity of 800 m/s could not fully penetrated the 10 mm Armox-500T target and 26 mm Al7075-T6 target. When drop-weight results are concerned, the maximum impact loads of the Armox-500T target is higher than the Al7075-T6, and the deformation amount is less. In addition, 10 different hybrid models, which consist of various combination of Armox 500T and Al7075-T6 materials in different thicknesses and orientations, have been defined. These models were compared with each other and models that are more resistant to ballistic impact loads were determined. M4, M7, M9, and M10 models were found to be more resistant to the ballistic impact loads than other models.

Keywords: Damage resistance, Drop-weight, Ballistic impact, Armox 500T, Aluminum 7075-T6.

1. INTRODUCTION

Damage resistance investigation of different materials subjected to low or high-velocity impact loads are important to design structures that can withstand to these loads. The study of materials and various combinations of them contribute to the basic understandings of numerous engineering structures that are manufactured using different material choice, such as layered materials,

* Corresponding Author: eyeter@gantep.edu.tr
[1] Gaziantep University, Aircraft and Aerospace Eng. Department, Gaziantep, Turkey. ORCID: 0000-0002-0278-588X

sandwich panels, laminated composites, fiber metal laminates (FML) etc. Since these structures have large surface dimensions and generally used in thin forms, those structures are frequently exposed to impact loads by foreign objects. Also many times these structures are directly designed for the low or high velocity impact loads. In the initial material designs as an armor structure, the main idea or purpose was to prevent damages under the impact loads (especially for ballistic case). But, nowadays designing light-weight structures for the impact-load designs also an important design issue as the case of the other designs.

Damage mechanisms due to low and high velocity impact loads on the different materials and material combinations have been investigated extensively. In general, low velocity impact (LVI) damage is studied under the drop weight impact loadings investigating the effects of a penetrator on a target plate. On the other hand, high velocity impact (HVI) damages are mainly studied as ballistic impact loading considering totally or partial penetration of targets with different types of projectiles. In the drop weight impact event, the maximum penetration loads and deformations of structures with these loads are generally studied. In ballistic cases, the ballistic limit of targets or effects of initial velocity or final velocity of projectile after full or partial penetration of targets have been considered.

Low velocity impact behaviors of different materials have been researched by many researchers. Villavicencio and Guedes Soares [1] investigated drop weight impact characteristics of plates experimentally. From this study, it was seen that the plastic behavior of the samples is directly related to the restraint at the supports. Also, it was shown that in the majority of samples the contribution of the stiffeners to the impact response is unimportant. Liu and Guedes Soares [2] performed Quasi static punch tests and dynamic drop weight impact to investigate damage resistances of tubes. Low velocity impact characteristics of Carbon/Epoxy composites were researched numerically and experimentally by Moura and Marques [3]. Boonkong et al. [4] studied on the low velocity impact characteristics of aluminum sandwich plates using Finite element methods (FEM) to obtain the dynamical responses of these plates. Liu and Liaw [5] performed low velocity impact tests on cast acrylic plates reinforced with aluminum plates using drop-weight impact machine. Impact load characteristics, impact energy and delamination were modeled using experimentally obtained results. Shi et al. [6] researched the impact characteristics of fiber reinforced composite plates by numerically and experimentally. Obtained results from numerical study has close agreement with experimental results. Sevkat et al. [7] studied the progressive damage characteristics of hybrid fiber reinforced laminates (S2 Glass-IM7 graphite /Epoxy) impacting with drop weight loads with various impact velocities. Also, a nonlinear numeric model developed to predict failure behavior. Menna et al. [8] used FEM to predict low velocity impact effects on Glass/Epoxy composites considering orthotropic failure criteria and stress based contact failure between plies. Santiago et al. [9] researched the influences of local impact loads on the fiber-metal laminates which produced with the combinations of aluminum alloys and polypropylene. Soliman et al. [10] studied LVI behaviors of laminated composite plates using 3 different fabric types (2D plain woven, 3D orthogonal and 3D angle interlock having Kevlar 29). The results indicated that the impact characteristics was directly related with the in-plane stiffness of the composites. Feng and Aymerich [11] illustrated the usage of FEM to simulate failure characteristics of sandwich composite plates subjected to LVI loads. The developed model could be used to simulate impact damage size. Rawat et al. [12] studied failure characteristics of laminated composite plates using impactors having various shapes (hemispherical, spherical, oval shape, flat) under the impact loadings. Mass of the used impactors was 5.23 kg and impact velocity was 3 m/sec. Numerical analyses were performed using the LS-DYNA analysis program. Impacting with 23.5 J energy, oval shape impactor caused fiber breakage, but flat impactor caused no fiber damage. Sarasini et al. [13] researched the LVI responses of hybrid E-Glass-Basalt/Epoxy composites. Loads at Various impact energies (5j-12.5j-25J) were applied to the samples which

have different orientation angles. High impact energy capacities obtained using hybrid composites than the composites have glass fibers. Zhang et al. [14] performed a study on the investigation of the mechanic characteristics of honeycomb sandwich panels under LVI.

Ballistic impact behaviors of different materials have also been investigated by many researchers. Deluca et al. [15] tested various dimensions of laminated plates by applying ballistic impact loads at different velocities. The relationship between damage load and the extension of the failure in terms of the average damage fraction was obtained. Meyer and Kleponis [16] studied on the characterization of the titanium alloy by comparing Johnson-Cook and Zerilli-Armstrong numerical models of ballistic experiments. Silva and Chiorean [17] reported results of experiments and numeric study carried out on the Kevlar-29 laminated composites. Close results between numerical and experimental study have been obtained. Ballistic impact characteristics of laminated composites have been investigated using 2D woven fabrics by Naik et al. [18]. Analytic formulation was used to obtain ballistic limit, contact duration at ballistic limit, and the size of the damaged part. Demir et al. [19] investigated impact characteristics of the 7075 and 5083 aluminum, and AISI 4140 steel using 7.62 mm projectile considering the different heat treatments of materials. It was obtained that 7075-T651 have higher impact strength. López-Puente, Jorge Zaera, and Ramón Navarro [20] developed a finite element (FE) numeric model to obtain final velocity and failure characteristics of Carbon/Epoxy composites under the high impact velocities. Experiments were also performed to obtain data to validation of numerical study using a gas gun. The effects of the impact velocity and oblique angle (0° and 45°) were considered. Talib et al. [21] studied the impact behavior of a hybrid Kevlar-Al2O3 powder/Epoxy laminates under the high velocity impact loads. A relationship between the ballistic limit velocity and the thickness of laminates have been given. The parametrical numeric study was done to obtain ballistic performance of sheet steels using Abaqus FE program by Jankowiak, Rusinek, and Wood [22]. A numeric research was performed to obtain ballistic behavior of Kevlar-29/Epoxy under the various types of projectiles using LS – DYNA FE program. Residual velocity and ballistic limit of target plate have been identified. Zhu et al. [23] investigated ballistic performance of the dry-fabrics numerically using LS-DYNA FE program. Absorbed energy, deformation, and extension of damaged zone have been considered. Bandaru et al. [24] performed a detailed study on the hybrid composite armors produced using various combinations of Glass-Carbon-Kevlar fibers. It was obtained that using Kevlar fibers at the rear part, Glass fibers in the exterior and Carbon fibers on the front part gives better ballistic impact response. E-Glass/phenolic composite armors were investigated for their ballistic characteristics by Reddy et al. [25]. The relation between plate thickness and energy absorption capacity of target plates have been given. Experimental and numerical study was performed to investigate ballistic performance of AA6070 aluminum plates by Holmen et al. [26]. Bandaru et al. [27] researched the ballistic characteristics of hybrid composite armors reinforced with Kevlar and basalt fabrics of 2D by experimentally and numerically. It was shown that overall stacking sequence have important effects on the ballistic response of composite armors. Senthil et al. [28] investigated ballistic performance of 2024 aluminum under the ballistic impact loads with 12.7 mm steel projectiles using ABAQUS FE software and JC material model. Sharma et al. [29] investigated impact performance of AA2014-T652 plates by experimentally and numerically using velocities between 800 m/s and 1300 m/s. Johnson-Cook damage model parameters were calibrated using information obtained from stress-strain data. Yeter [30] investigated ballistic impact characteristics of different aluminum alloys hybridized with Kevlar/Epoxy composite. It was concluded that 7075-T6 aluminum alloy has the best ballistic performance among the compared aluminum alloys and hybridization of this alloy with a composite material like Kevlar have some advantages.

In this study, damage resistance of Armox 500T and Aluminum 7075-T6 plates subjected to drop-weight and ballistic impact loads were

investigated. The behavior of plates under the low or high-velocity impact loads are an important concern to the researchers. The study of materials and their combinations provides fundamental understanding of many engineering structures. In this study, firstly drop weight and ballistic impact resistance of the Armox 500T and Al7075-T6 plates were researched for the conditions that they are in single form in the plates. Ballistic impact analyses were carried out using 7.62 API projectiles with an initial velocity of 800 m/s. During the drop-weight analyses, the drop of 5.5 kg weight from the 800 mm distance was modeled. The situations at which target plates of different thickness can be fully penetrated or not to be fully penetrated by the projectile, the final (residual) velocities in the fully penetrated plates and the amount of energy absorbed by the target plates were investigated. Energy absorption of targets in each time interval of ballistic impact and residual velocity of projectiles were determined. Combining different materials in a structure is an important issue to use superior properties of them. Hence, 10 different hybrid models, which consist of various combination of Armox 500T and Al7075-T6 materials in different thicknesses and orientations, have been defined. These models were compared with each other and models that are more resistant to ballistic impact loads were determined.

2. MATERIALS AND METHOD

In the first section of materials and methods, material properties of Armox 500T steel and 7075-T6 aluminum alloys are given. Second, numerical modeling and validation of ballistic impact event used in the study is given. Then, numerical modeling for drop weight impact event is given.

2.1. Material Properties of Plates

In the study, Armox 500T and Aluminum 7075-T6 materials were used as the target plates and their resistance under the low velocity (drop weight) and high velocity (ballistic impact) loads are investigated. The material properties of Armox 500T are taken from a reference study which was carried by Iqbal et al. [31]. The material properties of Armox-500T obtained in this detail study is listed in Table 1.

Aluminum 7075-T6 is the mostly used material in the light weight impact applications and it's material properties are taken from material library of ANSYS [32] and the material parameters are given in Table 2.

Table 1. Material parameters of Armox-500T

Parameter		Value
Young's Modulus (GPa)		201
Poisson's Ratio		0.33
Density(kg/m^3)		7850
Specific Heat (J kg^-1 K^-1)		455
Initial Yield Stress (MPa)		1372.488
Hardening Constant (MPa)		835.022
Hardening Exponent		0.2467
Strain Rate Constant		0.0617
Thermal Softening Exponent		0.84
Melting Temperature (K)		1800
Damage Constants	D1	0.04289
	D2	2.1521
	D3	-2.7575
	D4	-0.0066
	D5	0.86
Reference Strain Rate (/sec)		1

Table 2. Material parameters of Al7075-T6

Parameter	value
Density (kg m^-3)	2804
Specific Heat (J kg^-1 C^-1)	848
Initial Yield Stress Y (MPa)	420
Maximum Yield Stress Ymax (MPa)	810
Hardening Constant B	965
Hardening Exponent n	0.1
Derivative dG/dP G'P	1.741
Derivative dG/dT G'T (Pa C^-1)	-16450000
Derivative dY/dP Y'P	0.02738
Melting Temperature Tmelt (C)	946.85
Gruneisen Coefficient	2.2
Parameter C1 (m s^-1)	5200
Parameter S1	1.36

2.2. Numerical Modeling and Validation of Ballistic Impact

Numerical simulations were performed using ANSYS Finite elements analysis program. The Explicit Dynamics system is used to model the ballistic impact phenomenon which is designed

for simulating of nonlinear structural mechanic applications involving high velocity impact loads, complex material behavior including material damage and failure characteristics, and large deformations and geometric nonlinearities. Explicit Dynamic is the most appropriate for events occurring in a very short time (milliseconds or less). The Johnson-Cook failure model could be used in all element types under the various loads including impact loads. JK model can be used to demonstrate the strength behavior of materials with large strains and high temperatures. With this model, the yield stress depends on the strain, strain rate, and temperature. In the ANSYS, using this model, yield stress can be defined as [31];

$$Y = \left[A + B\varepsilon_p{}^n\right]\left[1 + C\ln\varepsilon_p{}^*\right]\left[1 - T_H{}^m\right] \quad (1)$$

$$T_H = \left(T - T_{room}\right)/\left(T_{melt} - T_{room}\right) \quad (2)$$

In Eq. 1, εp is the effective plastic strain, εp^* is the normalized effective plastic strain rate, A (Initial Yield Stress), B (Hardening Constant), n(Hardening Exponent), C and m are the material constants. The expression in the first parenthesis group gives the stress as a function of strain when εp^* equals to 1.0 s-1 and TH equals to zero. The expressions in the second parenthesis group give the influences of the stress rate on the yield strength of the material. The reference stress rate at which material data is measured is used to normalize the plastic strain rate increase. In Eq. 2, $Tmelt$ and $Troom$ are the melting and room temperatures, respectively.

The target plate used during the ballistic study was taken as 200x200 mm square plate with various thickness. 7.62 Armour-Piercing Incendiary (API) projectile was used during the numerical study. Figure 1 shows the dimensions of the projectile used in this study. Material parameters of the used projectile is given in Table 3. In the FE model of ballistic impact, element erosion was activated. A friction coefficient that equals to 0.2 was considered between the projectile and targets.

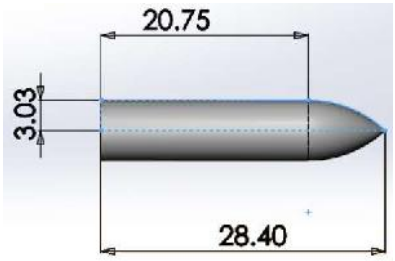

Figure 1. Dimensions of the projectile (in mm)

Table 3. Material parameters of API projectile

Parameter		value
Young's Modulus (GPa)		200
Poisson's Ratio		0.3
Density(kg/m3)		7850
Bulk Modulus (Pa)		1.97059E+11
Shear Modulus (Pa)		75563909774
Specific Heat (J kg^-1 K^-1)		455
Initial Yield Stress (MPa)		1657.71
Hardening Constant (MPa)		20855.6
Hardening Exponent		0.651
Strain Rate Constant		0.0076
Thermal Softening Exponent		0.35
Melting Temperature (K)		1800
Damage Constants	D1	0.0301
	D2	0.0142
	D3	-2.192
	D4	0
	D5	0.35
Reference Strain Rate (/sec)		1

The validation of ballistic numerical model is done comparing the result obtained in the reference study which was performed by Iqbal et al. [30]. Impact velocities of 823.62 m/s and 823.02 are applied against to 8 mm Armox 500T steel target with 7.62 API projectile in the reference study. In Table 4, the comparison of experimental and numerical results taken from reference study, and numerical results of current study are given. Also, projectile velocity reductions during ballistic impact for two different initial projectile velocities of the current study is given in Figure 2. It is seen from Table 4 and Figure 2 that the residual velocity values of current study is close to the experimental and numerical results of reference study and thus, the numerical model can be accepted to investigate the targets under ballistic impact.

Table 4. Ballistic resistance of Armox 500T 8 mm target plate with 7.62 API projectile

Initial velocity (m/s)	Final velocity (m/s)		
	Experimental (ref[31])	Numerical (ref [31])	Numerical (current study)
823.62	334.28	349.6	325.07
823.02	343.74	358.1	341.49

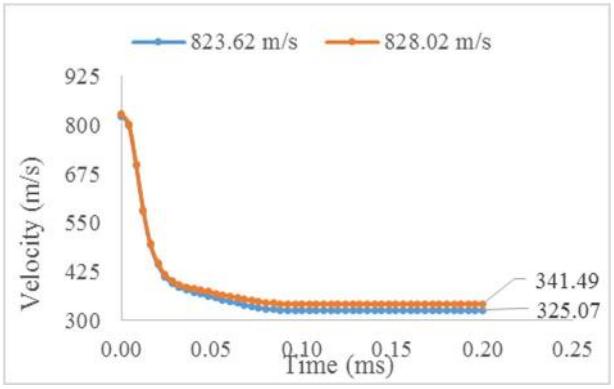

Figure 2. Residual velocities in current simulation

2.3. Numerical Modeling for Drop Weight Impact Event

In this study, the damage resistance of materials to a drop weight impact event is also researched numerically. The numerical models were developed using the transient finite element module of ANSYS. Simulation of the impact event is performed by the collision of two parts, namely, the impactor and the target plate. A hemispherical impactor which has totally 5.5 kg mass and 8mm tip radius are used and as shown in figure 5, the distance between the impactor and target plate is 800 mm. In other words, the impactor is released from 800 mm distance. The target plate dimensions are 150 mm length and 100 mm width. During the analyses, the target plate (as shown in figure 3) fixed from all edges.

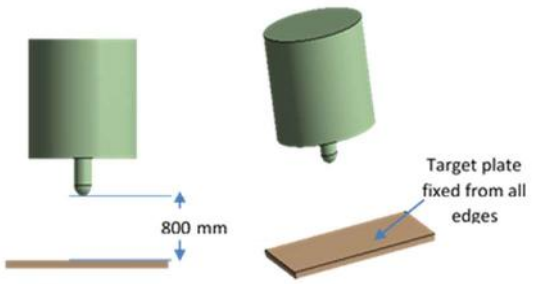

Figure 3. Impactor and target plate properties

3. RESULTS AND DISCUSSION

Results are given in the three section. In the first section, results and discussion of the ballistic impact responses of the Armox 500T and aluminum 7075-T6 are given.

Results are given in the three section. In the first section, results and discussion of the ballistic impact responses of the Armox 500T and aluminum 7075-T6 are given. In the second section, drop weight impact results are given with comparisons of ballistic impact results. In the third section, the ballistic impact responses of the proposed combinations of Armox and Aluminum 7075-T6 are given.

3.1. Ballistic Impact Responses of Armox 500T and Al 7075-T6

During the ballistic impact researches, generally, two conditions are searched. The first condition is the full penetration of target plates, and in this case, the target plates were totally penetrated by the projectile and the projectile has a velocity reduction after total penetration of plates. The second condition is a partial penetration or non-penetration of the target plates. In this case, the projectile has zero final velocity which means that this projectile cannot fully deform these plates. The used initial velocity at which the plates cannot be fully perforated can be called the ballistic limit velocity of this thickness of the plate. Initial and final velocities of projectiles and absorbed energy values of different plates are compared by researchers generally. In this study, the projectile is considered as rigid and an initial velocity of 800 m/s is applied. The target plate is fixed from all edges.

Projectile velocity reduction during ballistic impact for Armox 500T for 1, 3, 6, 9, and 10 mm plate thicknesses are given in Figure 4. As expected, residual velocity decreases with the increase of thickness due to the increased energy absorption capacity in thicker targets. As seen in Figure 4, when the thickness is increased to 10 mm, the final velocity of projectile reduces to the zero. Which means that the plate cannot be perforated when the thickness is 10 mm and the higher. And it is seen that the projectile velocity reduces to zero after 0.05 ms.

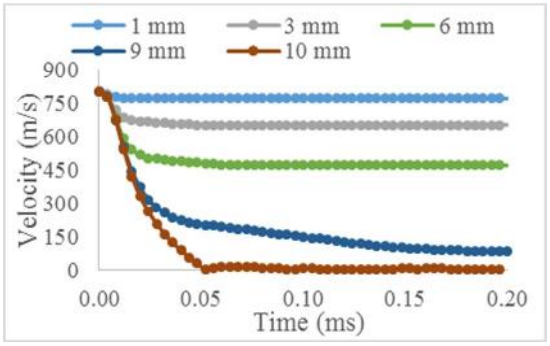

Figure 4. Projectile velocity reduction during ballistic impact for Armox 500T plates for different thicknesses

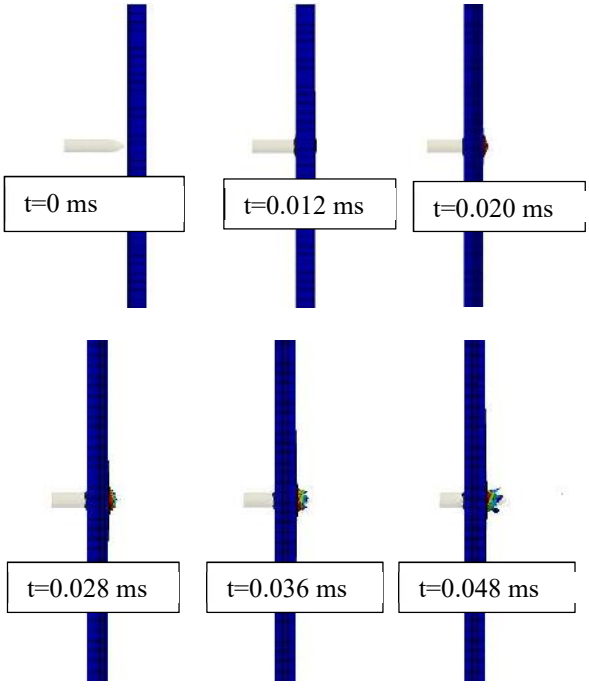

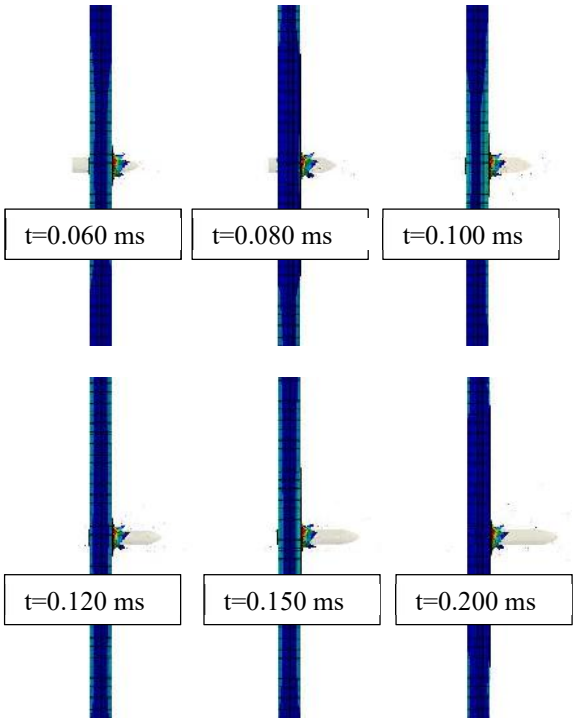

Figure 5. Damage propagation on the 9 mm target (Armox 500T) under the ballistic impact loading

Absorbed energy after ballistic impact event can be calculated by using initial, final velocities of projectile, and mass of the projectile. This equation is given as:

$$E = \frac{1}{2} m(V_i^2 - V_f^2) \quad (3)$$

Where;

E= Absorbed Energy by the target (J); m= Projectile mass (kg); Vi= Projectile initial velocity (m/s); Vf= Projectile final velocity (m/s)

Final velocity of Armox 500T target plate and absorbed energy by the Armox 500T target plate during the ballistic impact event is given in Figure 6 and Table 5 for different thicknesses of target plate. The figure and the Table show that with the increase of the thickness to 10 mm from 1mm, the final velocity is decreased 0 m/s from 769.23 m/s. And amount of absorbed energy is increased to 1811.93 J from 136.70 J.

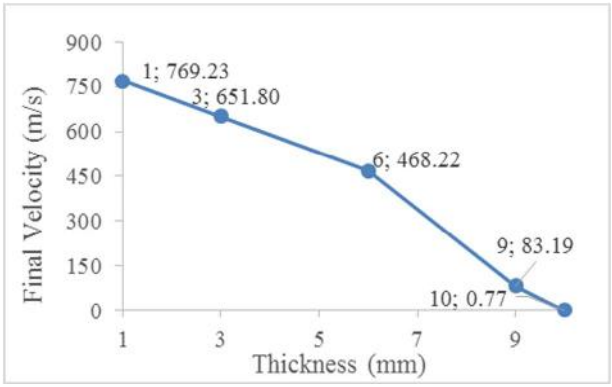

(a)

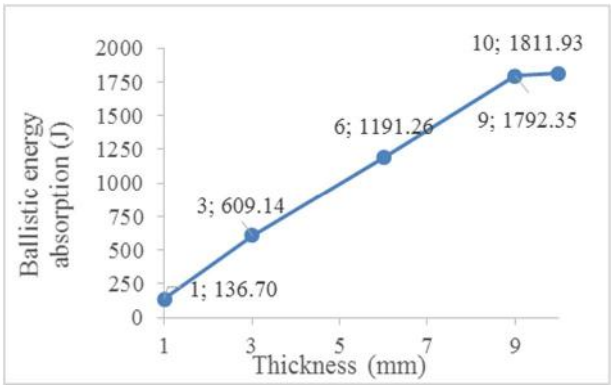

(b)

Figure 6. Variation of Final velocities (a) and Energy absorptions (b) of Armox 500T for different thicknesses

Table 5 Final velocities and Energy absorptions of Armox 500T for different thicknesses

Thickness (mm)	Final velocity (m/s)	Ballistic energy absorption (J)
1	769.23	136.70
3	651.80	609.14
6	468.22	1191.26
9	83.19	1792.35
10	0.77	1811.93

*$V_{initial}$=800 m/s

Projectile velocity reduction during ballistic impact for Aluminum 7075 T6 for 3, 6, 9, 18, and 26 mm thicknesses are given in Figure 7. As seen in figure 7, when the thickness is increased to 26 mm, the final velocity of projectile reduces to the zero. Which means that the plate cannot be fully perforated when the thickness is 26 mm and the higher. And it is seen that the projectile velocity reduces to zero after 0.1 ms. So it is seen that the thickness for Aluminum 7075-T6 at which the target plate cannot be fully perforated 2.6 times higher than the thickness of the Armox 500T. When "velocity first reduction to zero time" of Armox 500T and Aluminum 7075-T6 are compared, it is seen that "velocity first reduction to the zero time" for Aluminum 7075-T6 is 2 times higher than the "velocity first reduction to the zero time" for Armox 500T.

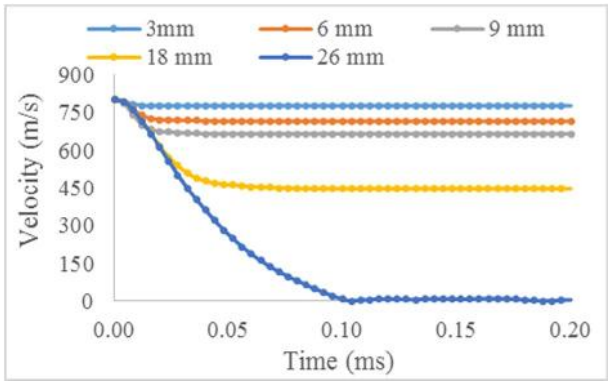

Figure 7. Projectile velocity reduction during ballistic impact for the different thicknesses of AL7075 T6

Final velocity of Al 7075 T6 target plate and absorbed energy by the Al 7075 T6 target plate during the ballistic impact event is given in Figure 8 and Table 6 for different thicknesses of target plate. The figure and the Table show that with the increase of the thickness to 26 mm from 3mm, the final velocity is decreased 0 m/s from 776.57 m/s. And amount of absorbed energy is increased to 1811.93 J from 104.58 J.

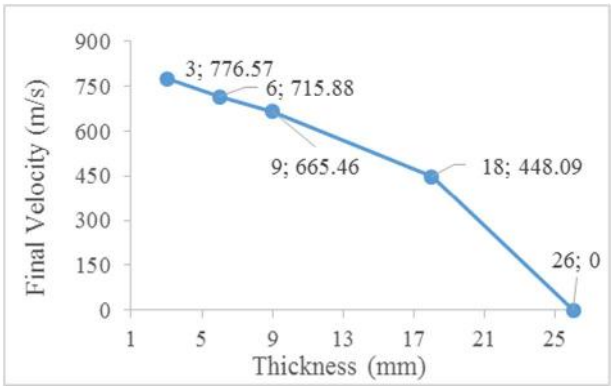

(a)

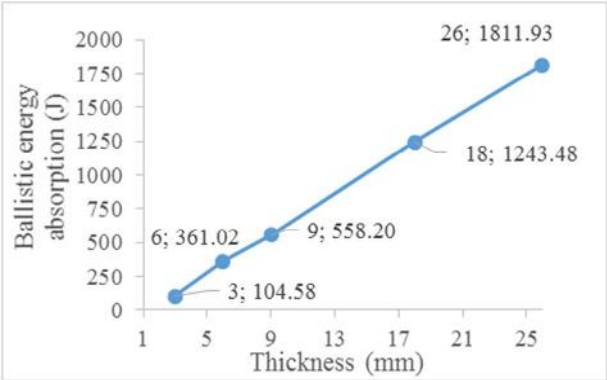

(b)

Figure 8. Variation of final velocities (a) and energy absorptions (b) of Al 7075 T6 for different thicknesses

Table 6. Final velocities and energy absorptions of Al 7075-T6 for different thicknesses

Thickness (mm)	Final velocity (m/s)	Ballistic energy absorption (J)
3	776.57	104.58
6	715.88	361.02
9	665.46	558.20
18	448.09	1243.48
26	0.71	1811.93

*$V_{initial}$=800 m/s

3.2. Drop Weight Impact Results of Armox 500T and Al7075 T6

The damage resistance of materials to a low-velocity loading considering drop weight impact event is given in this section. In this part of the study, both understanding characteristics of Armox 500T and AL7075-t6 plates under the drop-weight loading and comparing the results obtained with this loading and ballistic impact loading is aimed. Deformation comparison of Armox 500T and AL7075-T6 plates are given in Figure 9 for 1-9 mm plate thicknesses. As seen in figure 9 and table 7, maximum deformation of Armox 500T nearly 25% less than maximum deformation of Al7075 T6 for 1mm plate thickness. For 1 mm plate thickness, the impactor and Armox 500T target plate are in contact nearly 4.5 ms and this contact duration is 6 ms for Al 7075-T6.

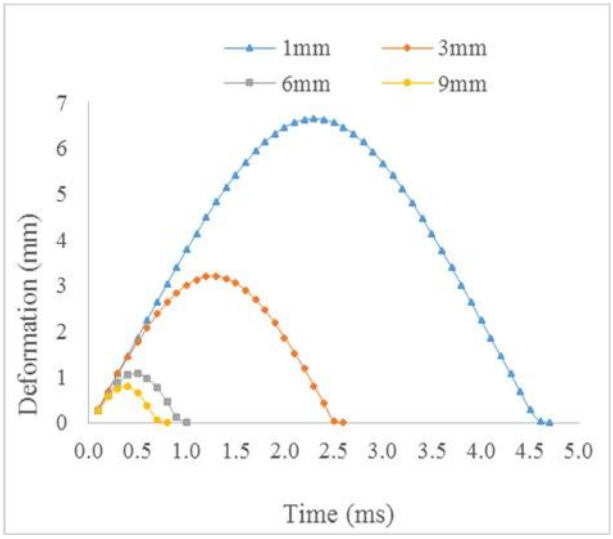

(a)

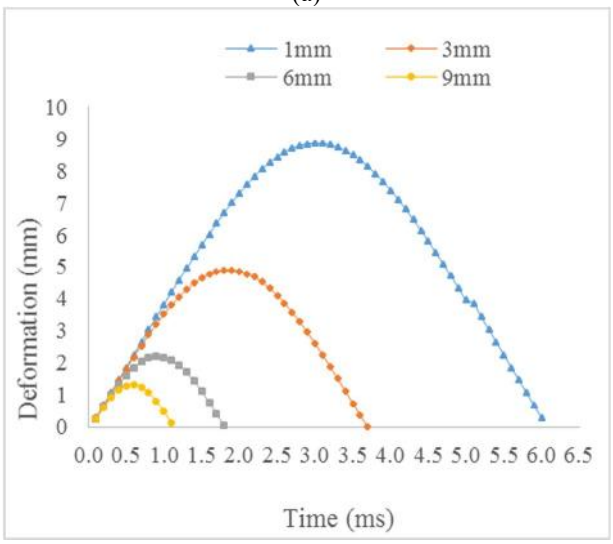

(b)

Figure 9. Deformation graph for different thicknesses of a) Armox 500T b) Al 7075-T6

Table 7. Maximum deformations for Al 7075-T6 and Armox 500T

Thickness (mm)	Al 7075-T6	Armox 500T
1	8.8638	6.6506
3	4.9062	3.2011
6	2.2018	1.0631
9	1.3317	0.77717

Impact force comparison of Armox 500T and AL7075 T6 plates are given in Figure 8 for 1-9 mm plate thicknesses. As seen in figure 10 and table 8 , impact force of Armox 500T nearly 28% less than impact force of Al7075 T6 for 9mm plate thickness.

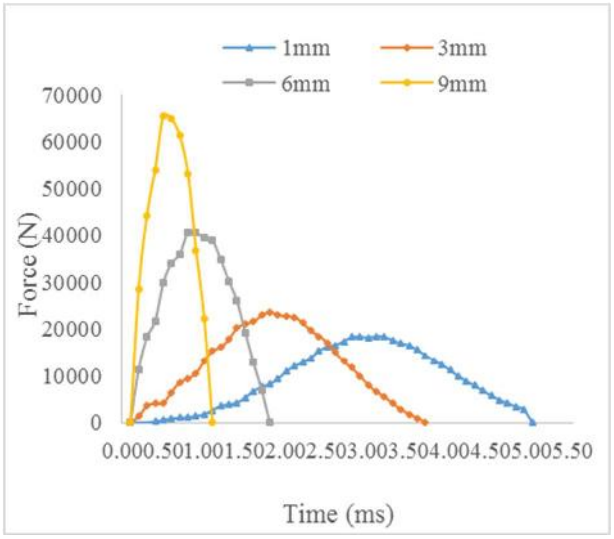

(a)

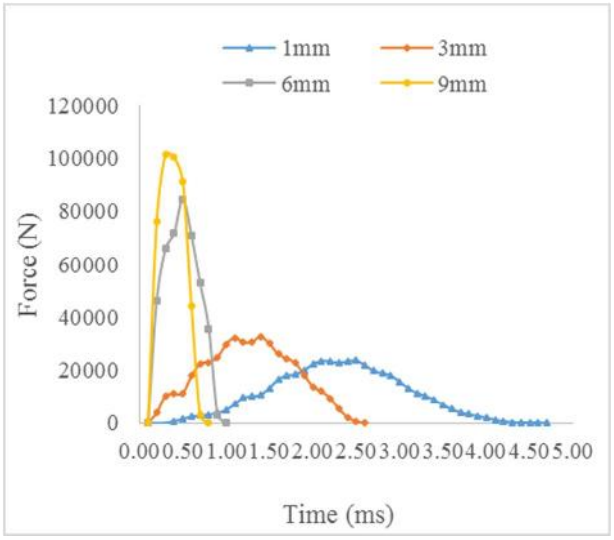

(b)

Figure 10. Impact Force graph for various thickness of a) Al 7075-T6 b) Armox 500T

Table 8. Impact forces for Al 7075-T6 and Armox 500T

Thickness (mm)	Al 7075-T6	Armox 500T
1	18475	23600
3	23640	32583
6	40601	84520
9	65685	101470

"Residual velocity after ballistic impact" versus "impact force after drop-weight" comparison is given in Figure 11 for Al7075 T6 and Armox 500T plates. For aluminum plate, when thickness increased to 3 mm from 1 mm, the residual velocity decreased 776.57 m/s from 790.5 m/s, and impact force increased to 23640 N from 18475 N. So, when the thickness is 3 times increased, residual velocity is 1.018 times decreased and impact force is 1.28 times increased. For steel plate, when thickness increased to 3 mm from 1mm, the residual velocity decreased 651.8 m/s from 769.23 m/s, and impact force increased to 32583 N from 23600 N. So, when the thickness is 3 times increased, residual velocity is 1.18 times decreased and impact force is 1.38 times increased.

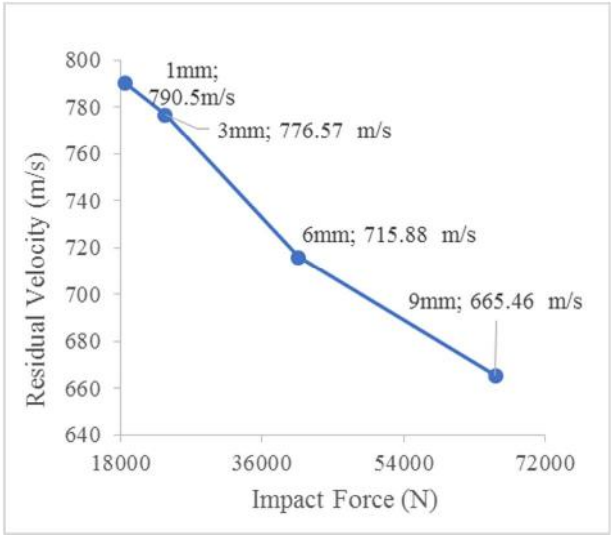

(a)

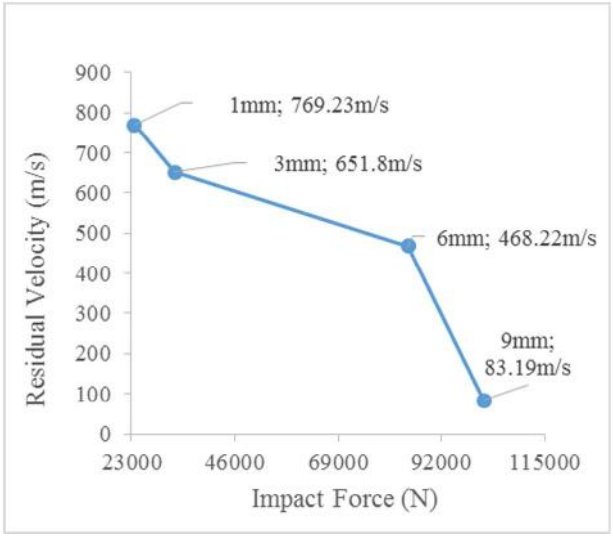

(b)

Figure 11. Residual velocity versus impact force graph for various thickness of a) Al 7075-T6 b) Armox 500T

3.3. Ballistic Impact Responses of Hybrid Models

In the third part of the study, 10 different hybrid models with different combinations of Armox 500T (Ar) and Al 7075 T6 (Al) were proposed. These combinations are 2AR + 13AL+2AR, 2AR + 14AL+2AR, 2AR + 15AL+2AR, 2AR + 16AL+2AR, 3AR + 9AL+3AR, 3AR + 10AL+3AR, 3AR + 11AL+3AR, 4AR + 4AL+4AR, 4AR + 5AL+4AR, and 4AR + 6AL+4AR. These combinations are named as M1, M2, M3, M4, M5, M6, M7, M8, M9, and M10 as shown in Table 9.

Table 9. Schematic representation of different hybrid models

Model	Geometry	Thickness of the individual plate (mm)	Total Thickness (mm)
M1 (2AR + 13AL+2AR)		2+13+2	17
M2 (2AR + 14AL+2AR)		2+14+2	18
M3 (2AR + 15AL+2AR)		2+15+2	19
M4 (2AR + 16AL+2AR)		2+16+2	20
M5 (3AR + 9AL+3AR)		3+9+3	15
M6 (3AR + 10AL+3AR)		3+10+3	16
M7 (3AR + 11AL+3AR)		3+11+3	17
M8 (4AR + 4AL+4AR)		4+4+4	12
M9 (4AR + 5AL+4AR)		4+5+4	13
M10 (4AR + 6AL+4AR)		4+6+4	14

Projectile velocity reductions during ballistic impact event of these proposed models are given in figure 11. M1, M2, M3, and M4, which have 2mm Armox 500T at the left side and right side of the hybrid models, are compared in figure 12(a). Among M1, M2, M3, and M4, residual velocity of M4 decreased to zero. M5, M6, and M7, which have 3mm Armox 500T at the left side and right side of the hybrid models, are compared in figure 12(b). Among M5, M6, and M7, residual velocity of M7 decreased to zero. M8, M9, and M10, which have 4mm Armox 500T at the left side and right side of the hybrid models, are compared in figure 12(c). Residual velocity of M8, M9, and M10 decreased to zero.

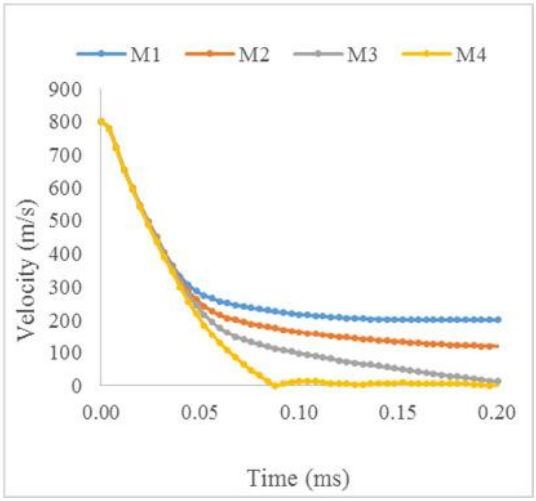

(a)

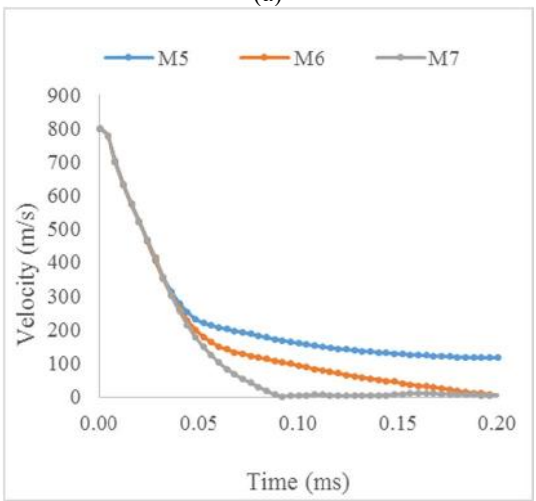

(b)

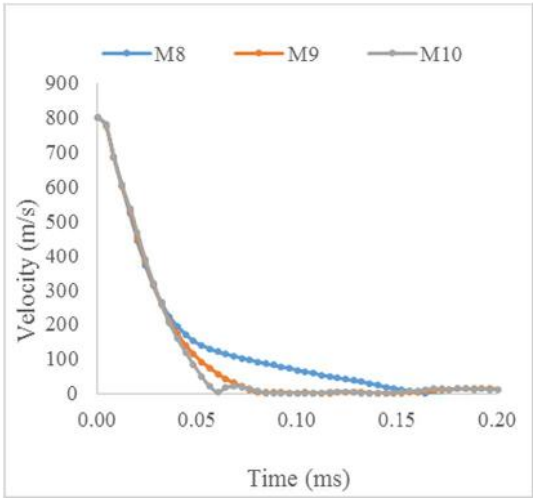

(c)

Figure 12. Projectile velocity reduction during ballistic impact for the hybrid targets

Demir et al. [19] and Yeter [32] has shown that Al7075 has the best ballistic performance among the compared aluminum alloys. So in the current study Al7075 is used for hybridization purpose. Like the reference studies [9, 13, 24, 30], it is seen in the current study that position of materials in different layers directly effects the ballistic performance. And it is also shown that with the correct position of different materials, same ballistic performance can be obtained with less thickness.

Comparisons of residual velocities and absorbed energies of all hybrid models are given in Figure 13 and Table 10. As seen in this figure and table, residual velocities of M4, M6, M7, M8, M9, and M10 are zero or very close to zero. Also absorbed energies of these models are nearly same to each others. Considering these models, targets exhibited approximately identical responses in terms of residual velocity of the projectile.

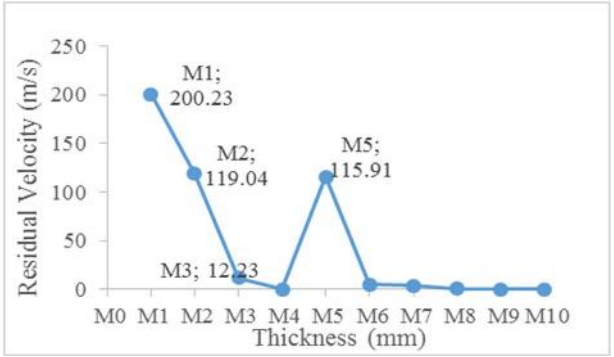

(a)

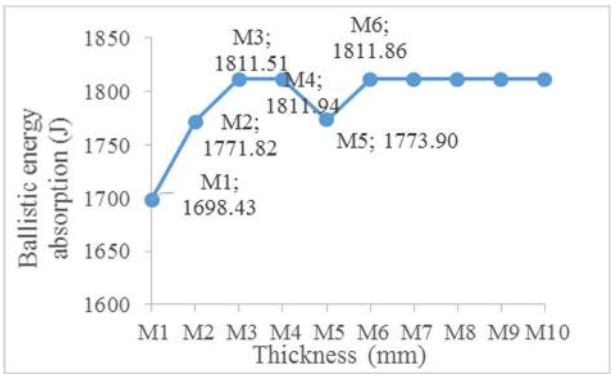

(b)

Figure 13. Variation of residual velocities (a) and energy absorptions (b) of hybrid models for different thicknesses

Table 10. Residual velocities and Energy absorptions for different material models

Material Models	Residual (Final) velocity (m/s)	Ballistic energy absorption (J)
M1	200.23	1698.43
M2	119.04	1771.82
M3	12.23	1811.51
M4	0.51648	1811.94
M5	115.91	1773.90
M6	5.0448	1811.86
M7	4.0018	1811.89
M8	1.0413	1811.93
M9	0.27063	1811.94
M10	0.058176	1811.94

Weight comparisons of hybrid models and non-hybrid (monolithic) materials are given in Figure 14. As seen in this figure, weight of M4 is 2.87 %, M7 is 0.54 %, and M9 is 2.23 % less than Armox 500T (10mm). Also, weight of M4 is 4.26% higher than Al 7075 T6.

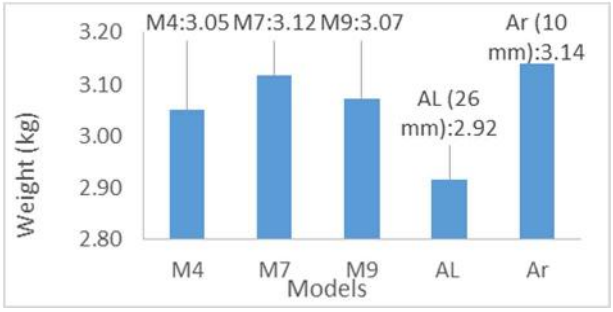

Figure 14. Comparison of Hybrid models and non-hybrid material weight

The front, back and side view of models M1 and M10 are given in Figure 15 to see the damages on the upper and lower surfaces of the layers. As seen

in the figure, in model M1 the outlet part of the projectile (back side of the plates) has higher deformation than inlet part of the projectile. In model M10, outlet part of the projectile has less deformation than inlet part of the projectile since in this model there is partial penetration.

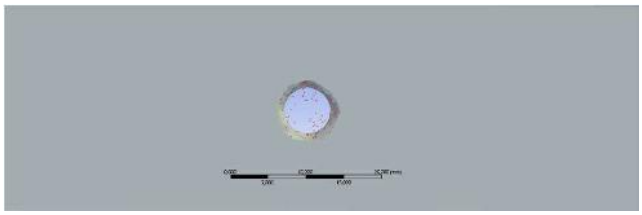

(a)

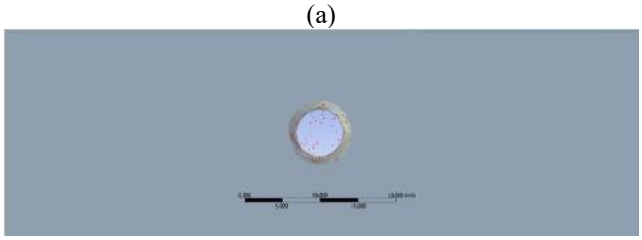

(b)

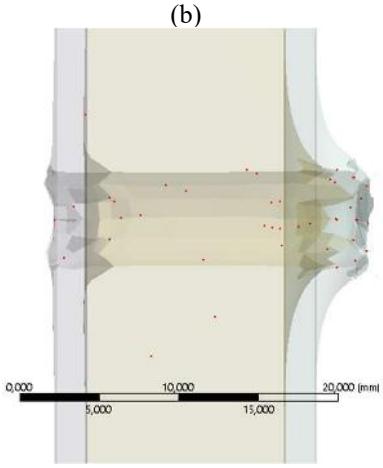

(c)

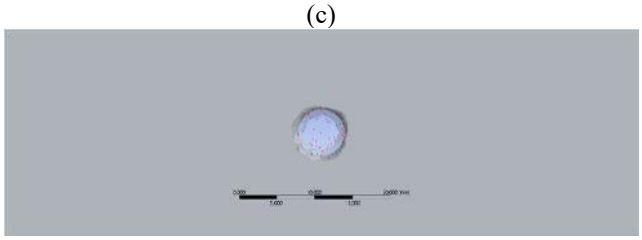

(d)

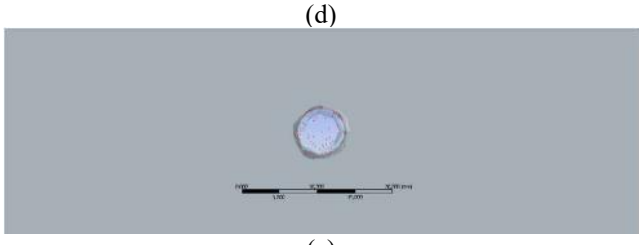

(e)

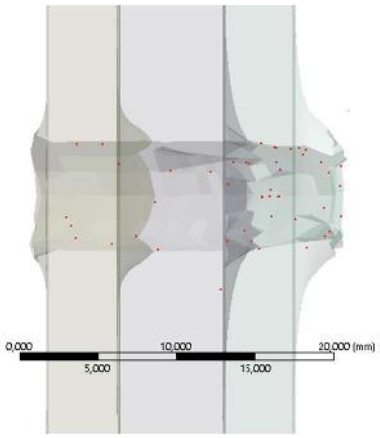

(f)

Figure 15. Deformation on the models (a) M1 front view, (b) M1 back view, (c) M1 side view, d) M10 front view, (e) M10 back view, (f) M10 side view.

4. CONCLUSIONS

In this study, damage resistance of Armox 500T and Aluminum 7075-T6 plates subjected to drop-weight and ballistic impact loads were investigated. The behavior of plates under the low-or high-velocity impact loads are an important concern to the researchers. In this study, firstly drop weight and ballistic impact resistance of the Armox 500T and Al7075-T6 plates are investigated for the conditions that they are in single form in the plates. Combining different materials in a structure is an important issue to use superior properties in a single structure. Then, 10 different models are proposed with different orientations of these materials in a plate. The main specific results are;

- The thickness at which residual velocities of the target plates reduce to the zero is less for Armox 500T than Al 7075 T6. Residual velocity decreases with the increase of thickness due to the increased energy absorption capacity in thicker targets. When the thickness of Armox 500T is increased to 10 mm, the final velocity of projectile reduces to the zero and amount of absorbed energy is increased to 1811.93 J from 136.70 J.
- For Al 7075 T6, when the thickness is increased to 26 mm, the final velocity of projectile reduces to the zero. The

thickness for Aluminum 7075-T6 at which the target plate cannot be fully perforated 2.6 times higher than the thickness of the Armox 500T.

- Under the drop-weight impact loads, maximum deformation of Armox 500T nearly 25% less than maximum deformation of Al7075 T6 for 1mm plate thickness. Contact between the impactor and the target plate, is completed in nearly 4.5 ms for Armox 500T and 6 ms for Al 7075-T6 for 1 mm plate thickness. Impact force of Armox 500T nearly 28% less than Impact force of Al7075 T6 for 9mm plate thickness.
- For aluminum plate, when thickness increased to 3 mm from 1mm, the residual velocity decreased 776.57 m/s from 790.5 m/s, and impact force increased to 23640 N from 18475 N. So, when the thickness is 3 times increased, residual velocity is 1.018 times decreased and impact force is 1.28 times increased. For steel plate, when thickness increased to 3 mm from 1mm, the residual velocity decreased 651.8 m/s from 769.23 m/s, and impact force increased to 32583 N from 23600 N. So, when the thickness is 3 times increased, residual velocity is 1.18 times decreased, and Impact force is 1.38 times increased.
- Residual velocities of M4, M6, M7, M8, M9, and M10 are zero or very close to zero. Also absorbed energies of these models are nearly same to each other's. Considering these models, targets exhibited approximately identical responses in terms of residual velocity of the projectile.

5. REFERENCES

[1] R. Villavicencio and C. G. Soares, "Impact response of rectangular and square stiffened plates supported on two opposite edges," *Thin-Walled Structures,* vol. 68, pp. 164-182, 2013.

[2] B. Liu and C. G. Soares, "Plastic response and failure of rectangular cross-section tubes subjected to transverse quasi-static and low-velocity impact loads," *International Journal of Mechanical Sciences,* vol. 90, pp. 213-227, 2015.

[3] M. De Moura and A. Marques, "Prediction of low velocity impact damage in carbon–epoxy laminates," *Composites Part A: Applied Science and Manufacturing,* vol. 33, no. 3, pp. 361-368, 2002.

[4] T. Boonkong, Y. Shen, Z. Guan, and W. Cantwell, "The low velocity impact response of curvilinear-core sandwich structures," *International Journal of Impact Engineering,* vol. 93, pp. 28-38, 2016.

[5] Y. Liu and B. Liaw, "Drop-weight impact tests and finite element modeling of cast acrylic/aluminum plates," *Polymer Testing,* vol. 28, no. 8, pp. 808-823, 2009.

[6] Y. Shi, T. Swait, and C. Soutis, "Modelling damage evolution in composite laminates subjected to low velocity impact," *Composite Structures,* vol. 94, no. 9, pp. 2902-2913, 2012.

[7] E. Sevkat, B. Liaw, F. Delale, and B. B. Raju, "Drop-weight impact of plain-woven hybrid glass–graphite/toughened epoxy composites," *Composites Part A: Applied Science and Manufacturing,* vol. 40, no. 8, pp. 1090-1110, 2009.

[8] C. Menna, D. Asprone, G. Caprino, V. Lopresto, and A. Prota, "Numerical simulation of impact tests on GFRP composite laminates," *International Journal of Impact Engineering,* vol. 38, no. 8-9, pp. 677-685, 2011.

[9] R. Santiago, W. Cantwell, and M. Alves, "Impact on thermoplastic fibre-metal laminates: experimental observations," *Composite structures,* vol. 159, pp. 800-817, 2017.

[10] E. M. Soliman, M. P. Sheyka, and M. R. Taha, "Low-velocity impact of thin woven carbon fabric composites incorporating

multi-walled carbon nanotubes," *International Journal of Impact Engineering,* vol. 47, pp. 39-47, 2012.

[11] D. Feng and F. Aymerich, "Damage prediction in composite sandwich panels subjected to low-velocity impact," *Composites Part A: Applied Science and Manufacturing,* vol. 52, pp. 12-22, 2013.

[12] P. Rawat, K. Singh, and N. K. Singh, "Numerical investigation of damage area due to different shape of impactors at low velocity impact of GFRP laminate," *Materials Today: Proceedings,* vol. 4, no. 8, pp. 8731-8738, 2017.

[13] F. Sarasini *et al.*, "Effect of basalt fiber hybridization on the impact behavior under low impact velocity of glass/basalt woven fabric/epoxy resin composites," *Composites Part A: Applied Science and Manufacturing,* vol. 47, pp. 109-123, 2013.

[14] D. Zhang, D. Jiang, Q. Fei, and S. Wu, "Experimental and numerical investigation on indentation and energy absorption of a honeycomb sandwich panel under low-velocity impact," *Finite Elements in Analysis and Design,* vol. 117, pp. 21-30, 2016.

[15] E. DeLuca, J. Prifti, W. Betheney, and S. Chou, "Ballistic impact damage of S 2-glass-reinforced plastic structural armor," *Composites Science and Technology,* vol. 58, no. 9, pp. 1453-1461, 1998.

[16] H. W. Meyer and D. S. Kleponis, "Modeling the high strain rate behavior of titanium undergoing ballistic impact and penetration," *International Journal of Impact Engineering,* vol. 26, no. 1, pp. 509-521, 2001.

[17] M. A. Silva, C. Cismaşiu, and C. Chiorean, "Numerical simulation of ballistic impact on composite laminates," *International Journal of Impact Engineering,* vol. 31, no. 3, pp. 289-306, 2005.

[18] N. Naik, P. Shrirao, and B. Reddy, "Ballistic impact behaviour of woven fabric composites: Formulation," *International Journal of Impact Engineering,* vol. 32, no. 9, pp. 1521-1552, 2006.

[19] T. Demir, M. Übeyli, and R. O. Yıldırım, "Investigation on the ballistic impact behavior of various alloys against 7.62 mm armor piercing projectile," *Materials & Design,* vol. 29, no. 10, pp. 2009-2016, 2008.

[20] J. López-Puente, R. Zaera, and C. Navarro, "Experimental and numerical analysis of normal and oblique ballistic impacts on thin carbon/epoxy woven laminates," *Composites Part A: applied science and manufacturing,* vol. 39, no. 2, pp. 374-387, 2008.

[21] A. A. Talib, L. Abbud, A. Ali, and F. Mustapha, "Ballistic impact performance of Kevlar-29 and Al 2 O 3 powder/epoxy targets under high velocity impact," *Materials & Design,* vol. 35, pp. 12-19, 2012.

[22] T. Jankowiak, A. Rusinek, and P. Wood, "A numerical analysis of the dynamic behaviour of sheet steel perforated by a conical projectile under ballistic conditions," *Finite Elements in Analysis and Design,* vol. 65, pp. 39-49, 2013.

[23] D. Zhu, A. Vaidya, B. Mobasher, and S. D. Rajan, "Finite element modeling of ballistic impact on multi-layer Kevlar 49 fabrics," *Composites Part B: Engineering,* vol. 56, pp. 254-262, 2014.

[24] A. K. Bandaru, L. Vetiyatil, and S. Ahmad, "The effect of hybridization on the ballistic impact behavior of hybrid composite armors," *Composites Part B: Engineering,* vol. 76, pp. 300-319, 2015.

[25] P. R. S. Reddy, T. S. Reddy, V. Madhu, A. Gogia, and K. V. Rao, "Behavior of E-glass composite laminates under ballistic impact," *Materials & Design,* vol. 84, pp. 79-86, 2015.

[26] J. K. Holmen, J. Johnsen, O. S. Hopperstad, and T. Børvik, "Influence of fragmentation on the capacity of aluminum alloy plates subjected to ballistic impact," *European Journal of Mechanics-A/Solids,* vol. 55, pp. 221-233, 2016.

[27] A. K. Bandaru, S. Ahmad, and N. Bhatnagar, "Ballistic performance of hybrid thermoplastic composite armors reinforced with Kevlar and basalt fabrics," *Composites Part A: Applied Science and Manufacturing,* vol. 97, pp. 151-165, 2017.

[28] K. Senthil, M. Iqbal, B. Arindam, R. Mittal, and N. Gupta, "Ballistic resistance of 2024 aluminium plates against hemispherical, sphere and blunt nose projectiles," *Thin-Walled Structures,* 2017.

[29] P. Sharma, P. Chandel, V. Bhardwaj, M. Singh, and P. Mahajan, "Ballistic impact response of high strength aluminium alloy 2014-T652 subjected to rigid and deformable projectiles," *Thin-Walled Structures,* 2017.

[30] E. Yeter, "Investigation of Ballistic Impact Response of Aluminum Alloys Hybridized with Kevlar/Epoxy Composites," *Politeknik Dergisi,* pp. 219-227, 2019.

[31] M. Iqbal, K. Senthil, P. Sharma, and N. Gupta, "An investigation of the constitutive behavior of Armox 500T steel and armor piercing incendiary projectile material," *International Journal of Impact Engineering,* vol. 96, pp. 146-164, 2016.

[32] https://www.sharcnet.ca/Software/Ansys/16.2.3/en-us/help/wb_sim/ds_explicit_dynamics_analysis_type.html

JOURNAL OF SCIENCE
SAKARYA UNIVERSITY

Sakarya University Journal of Science

ISSN 1301-4048 | e-ISSN 2147-835X | Period Bimonthly | Founded: 1997 | Publisher Sakarya University | http://www.saujs.sakarya.edu.tr/

Title: Feature Selection with Sequential Forward Selection Algorithm from Emotion Estimation based on EEG Signals

Authors: Talha Burak Alakuş, İbrahim Türkoğlu
Recieved: 2018-12-24 19:36:16

Accepted: 2019-06-27 17:04:21

Article Type: Research Article
Volume: 23
Issue: 6
Month: December
Year: 2019
Pages: 1096-1105

How to cite
Talha Burak Alakuş, İbrahim Türkoğlu; (2019), Feature Selection with Sequential Forward Selection Algorithm from Emotion Estimation based on EEG Signals. Sakarya University Journal of Science, 23(6), 1096-1105, DOI: 10.16984/saufenbilder.501799
Access link
http://www.saujs.sakarya.edu.tr/issue/44246/501799

Sakarya University Journal of Science 23(6), 1096-1105, 2019

Feature Selection with Sequential Forward Selection Algorithm from Emotion Estimation Based on EEG Signals

Talha Burak Alakus*[1], Ibrahim Turkoglu[2]

Abstract

In this study, we conducted EEG-based emotion recognition on arousal-valence emotion model. We collected our own EEG data with mobile EEG device Emotiv Epoc+ 14 channel by applying the visual-aural stimulus. After collection we performed information measurement techniques, statistical methods and time-frequency attribute to obtain key features and created feature space. We wanted to observe the effect of features thus, we performed Sequential Forward Selection algorithm to reduce the feature space and compared the performance of accuracies for both all features and diminished features. In the last part, we applied QSVM (Quadratic Support Vector Machines) to classify the features and contrasted the accuracies. We observed that diminishing the feature space increased our average performance accuracy for arousal-valence dimension from 55% to 65%.

Keywords: emotion estimation, feature selection, support vector machines, EEG

1. INTRODUCTION

Emotion can be described as voluntary or involuntary reactions to external factors like an environment or any stimuli. It plays a crucial role in daily lives and effects all the decisions, moral judgements, prejudices all the time. Basic emotions like anger, fear, happiness reflect the conditions of humans in society and determine their statuses. It is observed that people who reflect positive emotions always are more successful in the community [1].

In order to comprehend the nature and behavior of the emotions, many researchers conduct various studies on emotion analysis with different techniques including physical and non-physical ways. Emotion is an abstract thing thus studies do not reach the desired level. Besides, the mentioned techniques require a high level of data and analysis and as a result of that, data can be very complex and examining the data requires time. Consequently, developing a machine learning and a computer-based system is necessary [2]. Emotions can be collected via various methods such as voice signals, facial expressions, physical activities or body language.

* burak.alakuss@gmail.com
[1] Kirklareli University, Department of Software Engineering, Kirklareli, Turkey. ORCID: 0000-0003-3136-3341
[2] Firat University, Department of Software Engineering, Elazig, Turkey. ORCID: 0000-0003-4938-4167

Although all of these methods are used clearly, it can be manipulated by the subjects with intentionally. This makes interpretation of a raw data wrong and can cause misclassification of emotion data. Hereby, more secure and reliable system is needed thus, the importance of physiological signals -Electrodermal Activity (EDA), Galvanic Skin Response (GSR), Blood Pressure (BP), Electrocardiogram (EKG) and Electroencephalography (EEG) is enhanced [3].

1.1. Electroencephalography

Electroencephalography (EEG) is a way to collect brain signals with electrodes which are placed in the scalp of the brain. Because of advancing technology, EEG signals are not only collected from the hospital but also wearable and portable EEG devices via Wi-Fi and Bluetooth. Figure 1 shows the most popular EEG devices.

Figure 1. Wearable and portable EEG devices. a) Emotiv Epoc 14 Channel, b) Emotiv Insight 5 Channel, c) NeuroSky Brainwave 1 Channel [4-6]

Brain signals are monitored and conditions of the brain are controlled with brain rhythms. As can be seen in Table 1 there are five brain rhythms that are named based on their frequency and amplitude.

Table 1. Brain rhythms

EEG Rhythms	Frequency (Hz)	Amplitude (μV)
Delta (δ)	1 Hz – 3 Hz	20 μV – 400 μV
Theta (θ)	4 Hz – 7 Hz	5 μV – 100 μV
Alpha (α)	8 Hz – 13 Hz	2 μV – 10 μV
Beta (β)	14 Hz – 30 Hz	1 μV – 5 μV
Gamma (ɣ)	31 Hz – 50 Hz	<2 μV

It is a well-known fact that best brain rhythms for emotion analysis are beta (β) and gamma (ɣ) since their frequency is high and amplitude is low [7]. Electrodes are placed on the scalp with the 10-20 system which is defined by the International Electroencephalography and Clinical Neurophysiology Federation Union standard. Figure 2 represents the 10-20 electrode system.

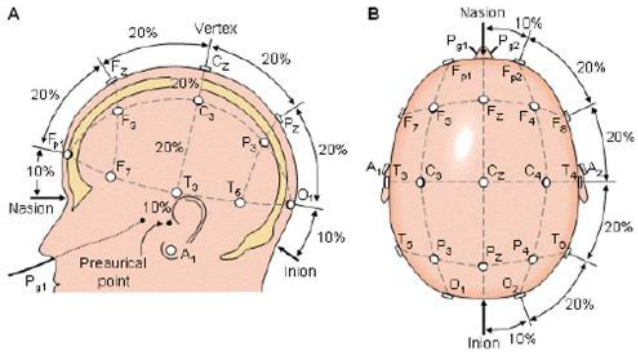

Figure 2. Electrode replacement according to the 10-20 electrode system. a) side of the scalp, b) upside of the scalp [8,9]

Electrodes are disposed on the scalp from nasion to inion and the distances between the electrodes are designated as 10%-20%-20%-20%-10%. The left side of the brain is represented by odd numbers while the right side is represented even numbers. Fp shows the pre-frontal sides of the scalp while F images the frontal parts of the brain. Center side of the brain is specified with 'C' and temporal sides are defined with 'T'. Parietal is the back-side of the brain and specified with 'P' whereas occipital part of the brain is defined 'O'.

1.2. Emotion Models

There are two types of emotion models exist; discrete emotions and dimensional emotions. Discrete feelings consist of positive and negative emotions which include eight basics emotions (anger, anticipation, joy, trust, fear, surprise,

sadness and disgust) [10]. On the other hand, the dimensional model includes both arousal-valence and emotion wheel. In the arousal-valence coordinate system, emotions are separated into four different coordinates. The left side of the coordinate plane represents the negative emotions whereas the right side shows the positive ones. Arousal is specified on the axis of the ordinate and emotions are aligned from calm to excited. Yet, valence is represented on the axis of abscissas and emotions are aligned on this axis as positive and negative. In Figure 3, arousal-valence emotion plane is given.

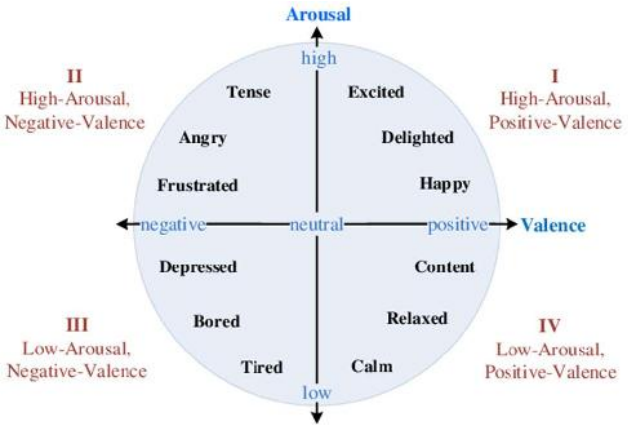

Figure 3. Arousal-valence emotion space [11]

As can be seen in Figure 3 there are four different zones. First two zones are high arousal zones. The first zone includes High Arousal Positive Valence (HAPV) emotions (happy, delighted, excited) and the second zone consists of High Arousal Negative Valence (HANV) emotions (frustrated, angry, tense). Last two zones (3 and 4) are low arousal zones which include Low Arousal Negative Valence (LANV) emotions (depressed, bored, tired) and Low Arousal Positive Valence (LAPV) emotions (content, relaxed, calm). In that model, emotions are not represented by their name but with their arousal-valence coordinate. For example, delighted is not called as delighted but High Arousal Positive Valence (HAPV). Discrete emotions are easier to develop since it classifies and discriminates the specified emotions. However, it is not universal because some of the emotions do not have a definition in some languages [12]. As a result of that, the dimensional model is more common and universal thus many studies applied this model.

1.3. Raw Data Acquisition and Stimulus

In emotion analysis studies, in order to collect raw EEG data and to analyze them some stimuli are used. Stimulus is categorized into three parts; visual, aural and visual-aural.

The visual stimulus includes some images or photographs. The pictures or photographs are shown to the subjects for a certain period of time. During these sessions, EEG signals are collected from subjects. The most popular dataset for visual stimulus is IAPS [13]. Researches can get this dataset by completing the IAPS request form [14].

Aural stimulus consists of sounds or voices. IADS is the well know dataset for aural stimuli [15]. It includes various audio files which are used to stimuli the subjects for a certain period of time. Like IAPS, researchers can obtain this dataset by filling the IADS request form [14].

Visual-aural stimulus contains music clips, short movies, video games etc. which affect the ear and eye at the same time. In the literature, it is observed that DEAP dataset [16] is the most preferred database in studies carried out using both visual-aural stimuli [17]. Like any other databases, researches need to complete the request form and End-User License Agreement [18].

1.4. Evaluation of Stimulus

To evaluate the accuracy of the stimuli, typically SAM (Self-Assessment Manikin) form is used. Generally, in this form, there are four different parameters; valance, arousal, dominance and liking. Subjects rate their feelings according to the parameters after each stimulus session is finished. Each parameter excluding liking has a range of 1 to 9. Figure 4 images a typical SAM form.

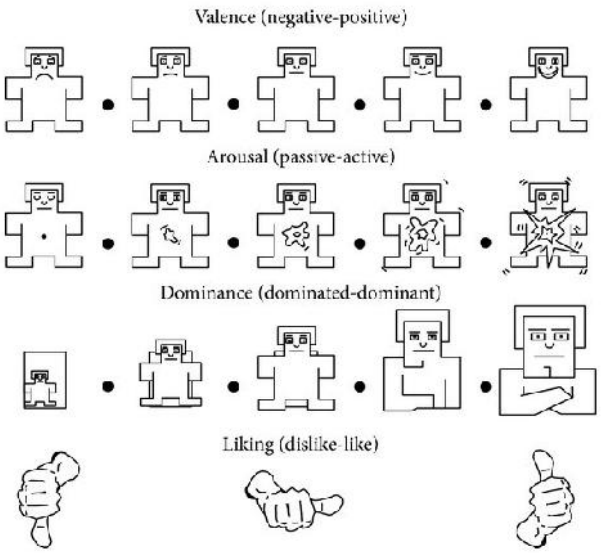

Figure 4. Self-Assessment Manikin [19]

Valence represents the attraction (positive valence) or offensiveness (negative valence) of an event, environment, stimuli or object [20]. In the form, valence is defined from unhappy to happy. If a parameter value is lower than 5 means the subject is unhappy from a given stimulus and represents the low valence. High valence means that the parameter value is higher than 5 and also shows the subject is happy about the stimulus. Considering a parameter value is 5 means that the subject is neutral to the given stimulus.

Arousal is the state of activity against a stimulus. Arousal is identified from calm to excited in SAM. If a parameter value is lower than 5 means the subject is calm from a given stimulus and specifies the low arousal. High arousal refers that the parameter value is higher than 5 and also shows the subject is excited about the stimulus. Considering a parameter value is 5 intends that the subject is neutral to the endowed stimulus.

Dominance shows the submissiveness or prepotency to given stimuli. In the form, dominance is described from obedience to dominance. If a parameter value is lower than 5 means the subject is obedience to a given stimulus and represents the low dominance. High dominance refers that the parameter value is higher than 5 and also shows the subject is dominant to the stimulus. Considering a parameter value is 5 specifies that the subject is neutral to the given stimulus.

The organization of this paper as follows. In Section 2, some studies are explained about EEG based emotion recognition. Their methods, database and classification accuracy also has given. In Section 3, we showed our database, its collection process and technical information about our wearable EEG device. Besides, in this part, feature extraction techniques and feature selection algorithm are mentioned. In the 4th section, we showed the classification accuracy of the EEG channels after the feature selection process. Also, we compared the discrimination accuracy from the original study. In the last section, the study is concluded.

2. RELATED WORKS

In this section, related works about EEG based emotion recognition studies are examined. We observed each study and mentioned their feature extraction methods, classification algorithms, database, and classification performance. According to the literature, the recognition process includes three parts; a) EEG data collection and pre-processing, b) feature extraction and c) feature classification. In some cases, feature selection is also applied to reduce feature matrix into smaller space.

Authors proposed a method based on Kernel Fischer Discrimination Analysis in the study of [21]. They used the IADS database to stimulate 10 different subjects to collect aural stimuli-based EEG data. They applied various feature extraction methods and used the KNN (K Nearest Neighbor) classifier algorithm to discriminate the emotions. They applied dimensional emotion model and classification accuracy is observed 78% from valance plane and 82% from arousal plane.

In the study of [22], researchers used visual-aural stimuli to collect raw EEG data from subjects. They tried to observe and compare the classification accuracy for both 3 electrodes and 8 electrodes system. They applied Higuchi's Fractal Dimension to collect and determine the key features. In order to classify dimensional model

emotions, SVM (Support Vector Machines) classification algorithm is used. At the end of the study, they found the average classification accuracy 51,94% and 77,38% for 3 electrodes and 8 electrodes system respectively. The study showed that increasing the number of electrodes makes classification performance high.

Authors in [23] applied Multivariate Synchrosqueezing Transform (MST) to collect key features from EEG signals. By using MST, they removed vibrations from signals then they applied Independent Component Analysis (ICA) to reduce feature vector. In their study, DEAP dataset is handled. For classification ANN (Artificial Neural Networks) is used. At the end of the study, classification performance is observed from arousal 82,11% and from valence 82,03%.

In the study of [24], authors applied Relevance Vector Machines (RVM) to discriminate the positive-negative emotions. DEAP dataset is utilized in that work and for classification. In the feature extraction phase, they applied sample entropy and multi-scale entropy. After this phase, they used both RVM and SVM to classify the emotions. In conclusion, they observed average classification performance with SVM 78,67% and 93,33% with RVM. It showed that RVM is superior from SVM according to the proposed feature extraction methods.

In this study, we performed SVM classifier and different feature extraction methods including statistical analysis, time-frequency domain and chaotic features. They are all generally used for emotion estimation process in the literature yet there are some differences in our study;

- We collected our own EEG data from a portable EEG device by applying our own stimuli. In the literature ordinarily, publicly available datasets or stimuli applied.
- Second, generally datasets obtained from traditional EEG devices. In our study, we performed a wearable and portable EEG device. With this way, we can compare the performance of this device between traditional devices.

3. MATERIAL AND METHODS

3.1. Technical Information About EEG Device

In this study, we used the Emotiv Epoc+ 14 channel EEG device. EEG channels are AF3, F7, F3, FC5, T7, P7, O1, O2, P8, T8, FC6, F4, F8 and AF4. Figure 5 shows the electrode and sensor locations of the device. It has a sequential sampling method and sampling rate can be down sampled both to 128 SPS and 256 SPS. The bandwidth of the device changes from 0.16 Hz to 43 Hz and digital notch filters at 50 Hz and 60 Hz. It has a build in filter which is 5th order Sinc Filter.

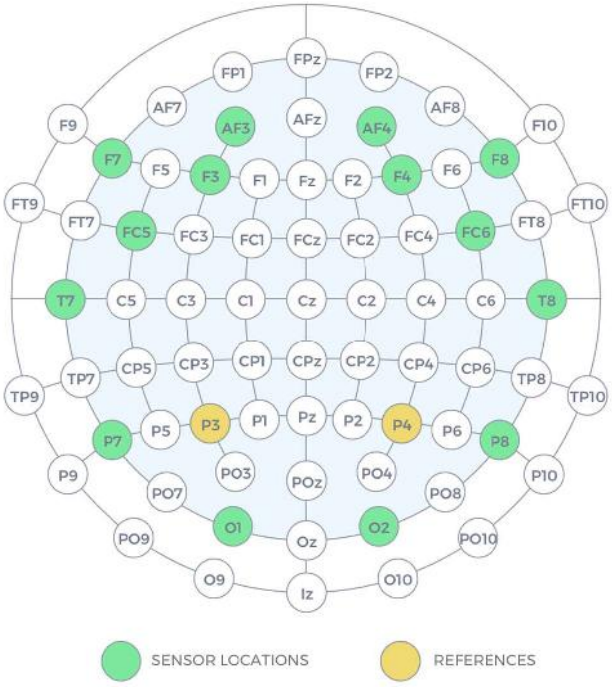

Figure 5. Emotiv Epoc+ sensor and reference locations [4]

In this work, we considered every EEG channel and used the built-in filter to remove artefacts from the device. Also, we configured the sampling rate to 128 SPS.

3.2. EEG Data Collection Process

We collected EEG data from 28 various students from Firat University, Faculty of Technology, Department of Software Engineering. In order to collect the data, we applied 4 different computer

games varied from HAPV, HANV, LANV and LAPV. Before data collection, we informed each subject about the study and their usage since participation was voluntary. Later each subject played each computer game for 5 minutes. During that time, we collected EEG signals for every game. After each session, we applied SAM form to analyze the EEG signals. Figure 6 images the proposed data collection process. We collected 20 minutes long data for each subject thus we have 560 minutes long EEG data in our database.

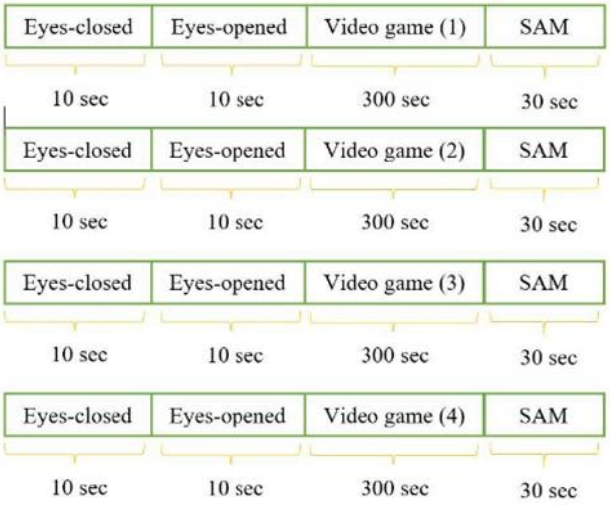

Figure 6. Data collection process

As shown in Figure 6, the first 20 seconds consist of some eye practices. By doing that, we tried to make the subjects focus the games.

3.3. Feature Extraction Methods

Information measurement methods, some statistical techniques and time-frequency domain attributes are used to collect key features. Firstly, we applied Discrete Wavelet Decomposition (DWD) for 4 levels. To do that, we applied the Daubechies wavelet filter with order 2 and collect sub-signals in different frequencies. Later, we applied Detrended Fluctuation Analysis (DFA), Hjorth parameters (H), the average energy of wavelet coefficients (AvgEng), Shannon Entropy (ShanEn), logarithmic energy entropy (LogEn), sample entropy (SampEn), multi-scale entropy (MSCEn), standard deviation (StdDev), variance (V) and zero-crossings (ZC) for each sub-signal. A more detailed description of these methods can be found in [18]. We collected 50 features for each EEG channel. At the end of the feature extraction phase, our feature vector was 50x14x28. The first one indicates the feature number, the second one shows the EEG channels and the last one means the subject numbers. That implies we collected 700 features from one subject and totally 19600 features are available in our database.

3.4. Feature Selection with Sequential Forward Selection Algorithm

Sequential Forward Selection (SFS) is a greedy search algorithm and searches the set from bottom to up. The algorithm starts from an empty set and this set is filled by features selected by some evaluation functions. Here is the pseudo code for the algorithm.

At every rehearsal, the feature is added to the new

1. Starting with an empty set $X_0 = \{\emptyset\}$
2. Algorithm selects the next best feature $t^+ = arg_{t \notin X_k} \max J(X_k + t)$
3. Update $X_{k+1} = X_k + t^+; k = k + 1$
4. Go to part 2

dataset which is selected from the remaining features from the feature set. It is selected based on the minimum classification error [25]. It is widely used since it is simple and rapid. Detailed information about this algorithm can be found in [26].

In our study, we used Bayesian Classification (BS) as an evaluation function in SFS algorithm. Besides, in order to validate our results, we performed resubstitution method. After the feature selection process, features are diminished from 50 to 4-9 for each EEG channel. It means that our new feature space was changed from 50x14x28 to [4-9]x14x28. Besides, the number of total features were decreased from 19600 to 1218.

4. CLASSIFICATION ACCURACIES AND COMPARISON

During the study, we applied the QSVM (Quadratic Support Vector Machines) to determine the arousal-valence performance of the EEG signals. We selected the penalty parameter (C) as 1. Besides, we determined kernel scale mode as a gamma. For classification validation, we applied 10-fold cross-validation. After we specified the necessary parameters, we classified the arousal-valence emotion zones. Our multiclass output includes four different classes namely (HAPV, HANV, LANV, LAPV). Table 2 shows the average classification accuracies for each EEG channel with 50 features (before feature selection).

Table 2. Classification of arousal-valence performance before feature selection [18]

EEG	Number of Features	Accuracy
AF3	50	54%
AF4	50	50%
F3	50	40%
F4	50	54%
F7	50	70%
F8	50	63%
FC5	50	34%
FC6	50	34%
O1	50	55%
O2	50	54%
P7	50	66%
P8	50	70%
T7	50	47%
T8	50	79%
Average	50	55%

According to Table 2, the best classification performance observed from EEG channel T8 (79%). This channel also gave the best performance on HANV arousal-valence plane with 96% classification accuracy. Here is the plane classification performance;

- HAPV: Best result is observed from F5 (85%)
- HANV: Best result is collected from T8 (96%)
- LANV: Best result is obtained from T8 (72%)
- LAPV: Best result is achieved from O1 (72%)

After the discrimination process, we eliminated some of the features based on SFS algorithm. We observed that average classification accuracy is increased. Besides all of the EEG channels showed more successful average performance. Table 3 specifies the classification accuracy after feature selection.

Table 3. Classification performance after feature selection

EEG	Number of Features	Accuracy
AF3	4	58%
AF4	4	56%
F3	7	57%
F4	6	65%
F7	6	75%
F8	6	72%
FC5	9	40%
FC6	8	61%
O1	6	68%
O2	8	55%
P7	6	68%
P8	6	73%
T7	4	75%
T8	7	80%
Average	6	65%

Table 3 shows that average classification accuracy 65% which is more successful than the previous average classification accuracy (55%). With the algorithm, we reduced the features for each channel and all of the channels demonstrated better results. Again, T8 EEG channel is the most effective channel with 80% performance. Here is the plane classification performance after feature selection process;

- HAPV: Best result is observed from P7 (93%)
- HANV: Best result is collected from F7 (100%)
- LANV: Best result is obtained from O1 (79%)

- LAPV: Best result is achieved from T7 (93%)

Best performance progress observed from both T7 and FC6 EEG channels. Their accuracy reached 75% and 61% from 47% and 34% with a growth rate of 28 and 27 respectively. In Table 4, the number of selected features for each EEG channel and their names are provided.

Table 4. Selected features with SFS algorithm

EEG	Num. of Features	Feature Names
AF3	4	LogEn (2), ShanEn, and StdDev.
AF4	4	MSCEn, SampEn, ShanEn, and V.
F3	7	DFA, AvgEng, MSCEn, SampEn (2), and ShanEn (2).
F4	6	LogEn (2), SampEn, ShanEn, StdDev, and V.
F7	6	LogEn, MSCEn, ShanEn (2), and V (2).
F8	6	H, LogEn, MSCEn, ShanEn (2), and V.
FC5	9	DFA, H, AvgEng (2), LogEn, MSCEn, ShanEn, StdDev, and ZC.
FC6	8	H, AvgEng, LogEn (3), MSCEn, SampEn, and ShanEn.
O1	6	H (2), AvgEng, SampEn, StdDev, and V.
O2	8	DFA, H (2), AvgEng, MSCEn, SampEn (2), and ZC
P7	6	H, LogEn, MSCEn, StdDev, and V (2).
P8	6	DFA, MSCEn, ShanEn (2), StdDev, and V.
T7	4	LogEn (3), and MSCEn.
T8	7	AvgEng, LogEn (2), MSCEn (2), SampEn, and StdDev.

According to Table 4, some EEG channels have multiple similar features. They are obtained from different wavelet coefficients. For instance, T7 channel has 4 features after the feature selection process, and 3 of them are logarithmic energy entropies and the other one is multiscale entropy.

5. RESULTS

In this study, we performed EEG based emotion recognition with dimensional emotion models. Our study includes four parts; a) EEG data collection, b) Feature extraction, c) Feature selection, d) Feature classification. In EEG data collection phase, we collected our data by applying a visual-aural stimulus from 28 different subjects. We used a wearable EEG device (14 channel Emotiv Epoc+) and 4 different computer games. After collection of EEG signals, we composed our database. It consists of 392 (14(channel)x28(subject)) EEG signals with 20 minutes long. In the feature extraction stage, we performed DWT to transform EEG signals into sub-signals. We utilized Daubechies 2nd order wavelet filter and signals are decomposed into 4 levels. In that way, we collected 4 detailed coefficients and 1 approximate coefficient. After that, we applied some information measurement and statistical methods to obtain key features from each coefficient. 50x14x25 matrix size of features are obtained after this phase. In the third part, we applied the SFS algorithm to reduce the features and disposed of unnecessary features. We evaluated Bayes function to do that and our new vector space reduces for each channel with a different number of features. On average, our vector reduced to 6x14x28 from 50x14x28. On the classification part, we demonstrated QSVM classifier for discrimination of emotions. Firstly, QSVM is used for each EEG channel based on their arousal-valence plane before feature selection. After, we classified the EEG channels based on selected features again and compared their results. We observed that reducing the feature space gives better results and our average accuracy is increased from 55% to 65%.

ACKNOWLEDGMENTS

This study is supported by the Firat University Scientific Research Project Unit with Project Number: TEKF.17.21. Authors also thank Asst. Prof. Murat Gonen for valuable contribution for collecting and analyzing EEG signals.

REFERENCES

[1] T. B. Alakus, and I. Turkoglu, ‘’EEG based emotion analysis systems,’’ Türkiye Bilişim Vakfı Bilgisayar Bilimleri ve Mühendisliği Dergisi, vol. 11, no. 1, pp. 26 – 39, 2018.

[2] A. Turnip, A. I. Simbolon, M. F. Amri, P. Sihombing, R. H. Setiadi, and E. Mulyana, ‘’Backpropagation neural networks training for EEG-SSVEP classification of emotion recognition,’’ Internetworking Indonesia Journal, vol. 9, no. 1, pp. 53 – 57, 2017.

[3] W. Szwoch, ‘’Using physiological signals for emotion’’, 2013 6th International Conference on Human System Interaction (HSI*),* pp. 556 – 561, 2013.

[4] Emotiv Epoc+ 14 Channel Mobile EEG Device, Online Link: https://www.emotiv.com/product/emotiv-epoc-14-channel-mobile-eeg/

[5] Emotiv Insight 5 Channel Mobile EEG Device, Online Link: https://www.emotiv.com/product/emotiv-insight-5-channel-mobile-eeg/

[6] Brainwave NeuroSky One Channel EEG Device, Online Link: https://store.neurosky.com/pages/mindwave

[7] J. A. Russel, ‘’Core affect and physiological construction of emotion,’’ Psychological Review, vol. 110, no. 1, pp. 145 – 150, 2003.

[8] R. Cooper, J.W. Osselton, J.C. Shaw, *“EEG Technology,”* 2nd Edition, 1974.

[9] H. H. Jasper, ‘’The ten-twenty electrode system of the international federation,” Electroencephalography and Clinical Neurophysiology, vol. 10, pp. 371 – 375, 1958.

[10] P. Ekman, ‘’An argument for basic emotions,’’ Cognition and Emotion, vol. 6, no. ¾, pp. 169 – 200, 1992.

[11] L. C. Yu, L. H. Lee, S. Hao, J. Wang, Y. He, J. Hu, K. R. Lali, and X. Zhang, ‘’Building chinese affective resources in valence-arousal dimensions,’’ Proceedings of the 15th Annual Conference of the Nort American Chapter of the Association for Computational Linguistics: Human Language Techniques (NAACL-HLT), pp. 540 – 545, 2016.

[12] J. A. Russel, “Culture and the categorization of emotions,” Psychological Bulletin, vol. 110, pp. 425 – 450, 1991.

[13] P. J. Lang, M. M. Bradley, and B. N. Cuthbert, ‘’International affective picture system (IAPS): Affective ratings of pictures and instruction manual,’’ Technical Report A-8, 2008.

[14] IAPS Request Form, Online Link: https://csea.phhp.ufl.edu/media.html#topmedia

[15] M. M. Bradley, and P. J. Lang, “International affective digitized sounds (IADS): Affective ratings of sounds and instruction manual,” Technical Report B-3*,* 2007.

[16] S. Koelstra, C. Mühl, and M. Soleymani, “DEAP: A database for emotion analysis using physiological signals,” IEEE Transactions of Affective Computing, vol. 3, no. 1, pp. 18 – 31, 2012.

[17] T. B. Alakus, and I. Turkoglu, “Emotion Detection Based on EEG Signals by Applying Signal Processing and Classification Techniques,” Master Thesis,

Institute of Science, Department of Software Engineering, 2018.

[18] DEAP Dataset Access, Online Link: http://www.eecs.qmul.ac.uk/mmv/datasets/deap/download.html

[19] S. Jirayucharoensak, S. Pan-Ngum, and P. Israsena, "EEG-based emotion recognition using deep learning network with principal component based covariate shift adaptation," The Scientific World Journal, vol. 2014, 2014.

[20] N. H. Frijda, "The emotions," Cambridge University Press, pp. 207, 1986.

[21] Y. H. Liu, W. T. Cheng, Y. T. Hsiao, C. T. Wu., and M. D. Jeng, "EEG-based emotion recognition based on kernel fishers discriminant analysis and spectral Powers," IEEE International Conference on Systems, Man, and Cybernetics, pp. 5 – 8, 2014.

[22] M. M. Javaid, M. A. Yousaf, Q. Z. Sheikh, M. M. Awais, S. Saleem, and M. Khalid, "Real-time EEG-based human emotion recognition," Neural Information Processing, pp. 182 – 190, 2015.

[23] A. Mert, and A. Akan, "Emotion recognition based on time frequency distribution of EEG signals using multivariate synchrosqueezing transform," Digital Signal Processing, vol. 81, no. 2018, pp. 152 – 157, 2018.

[24] L. Xin, S. Xiao-Qi, Q. Xiao-Ying, and S. Xiao-Feng, "Relevance vector machine-based EEG emotion recognition," 2016 Sixth International Conference on Instrumentation & Measurement, Computer, Communication and Control, pp. 293-297, 2016.

[25] A. Marcano-Cedeno, J. Quintanilla-Dominguez, M. G. Cortina-Januchs, and D. Andina,"Feature selection using sequential forward selection and classification applying artificial metaplasticity neural network," 36th Annual Conference on IEEE Industrial Electronics Society, pp. 2845 – 2850, 2010.

[26] I. A. Basheer, and M. Hajmeer, "Artificial neural networks: Fundamentals, computing, design, and application," Journal of Microbiological Methods, vol. 43, no. 1, pp. 3 – 31.

Sakarya University Journal of Science

ISSN 1301-4048 | e-ISSN 2147-835X | Period Bimonthly | Founded: 1997 | Publisher Sakarya University | http://www.saujs.sakarya.edu.tr/

Title: Earthworm (Clitellata; Megadrili) Records from Adana Province

Authors: İbrahim Mete Mısırlıoğlu, Hristo Valchovski
Recieved: 2018-06-06 08:54:19

Accepted: 2019-07-01 19:06:44

Article Type: Research Article
Volume: 23
Issue: 6
Month: December
Year: 2019
Pages: 1106-1109

How to cite
İbrahim Mete Mısırlıoğlu, Hristo Valchovski ; (2019), Earthworm (Clitellata; Megadrili) Records from Adana Province. Sakarya University Journal of Science, 23(6), 1106-1109, DOI: 10.16984/saufenbilder.431200
Access link
http://www.saujs.sakarya.edu.tr/issue/44246/431200

Sakarya University Journal of Science 23(6), 1106-1109, 2019

Earthworm (Clitellata; Megadrili) Records from Adana Province

İbrahim Mete Mısırlıoğlu*[1], Hristo Valchovski [2]

Abstract

The current study deals with earthworm biodiversity of Adana Province. Identification was made by examining the earthworm specimens collected in 6 different localities. At the end of the study, 5 species belonging to 3 genus were found: *Allolobophora chlorotica* (Savigny, 1826), *Aporrectodea caliginosa* (Savigny, 1826), *Aporrectodea rosea* (Savigny, 1826), *Aporrectodea trapezoides* (Dugès, 1828) and *Octodrilus transpadanus* (Rosa, 1884).

Keywords: Clitellata, Earthworms, Lumbricidae, Megadrili, Fauna of Turkey.

1. INTRODUCTION

Eightythree taxa were registered from Turkey so far. According to this result, Turkey is one of the richest country in terms of earthworm biodiversity in the region. But our knowledge about distribution of the species in Turkey is still limited because there are unsampled areas in the country [7].

Our knowledge about earthworm fauna of the Mediterranean, East and South-East regions of Turkey is also very limited. Also, there is no comprehensive study include earthworm records from Adana and its surroundings. So, this area has been selected as a study area because of scarce information about earthworm biodiversity.

Adana is a city of Turkey located in the south part of the country (Mediterranean region). The whole plain which has very fertile agricultural areas is called Adana Ovası, but the remaining part in the southern part is called Çukurova and the part on the north side is called Upova or Anavarza. The city is located at 350-380 north latitude and 340-360 east longitude on both sides of Seyhan River and has Mediterranean climate which the winters are mild and wet and summers are long, hot and dry [1].

So, the aim of the current study is to present some earthworm records from Adana province.

2. MATERIAL AND METHODS

The earthworms were collected from localities written below by digging and handsorting.

Loc. 1. Adana, Şahintepe quarter, edge of stream Sarıçam, altitude 100 m a.s.l. 06.10.2015.

* Corresponding Author: metem@ogu.edu.tr
[1] Eskişehir Osmangazi University, Faculty of Arts and Sciences Department of Biology, Turkey. ORCID: 0000-0001-9928-8478
[2] Eskişehir Osmangazi University, Faculty of Arts and Sciences Department of Biology. ORCID: 0000-0002-6172-4307

Loc. 2. Adana, Yüreğir, Ali Hocalı village, edge of an irrigation canal near the transformer side, altitude 48 m a.s.l., 19.01.2016.

Loc. 3. Adana, Yüreğir, Mustafa Kemal Paşa Boulevard, altitude 57 m a.s.l. 19.01.2016.

Loc. 4. Adana, Yüreğir, altitude 55 m a.s.l., 10.01.2017.

Loc. 5. Adana Sarıçam altitude 95 m a.s.l. 10.01.2017.

Loc. 6. Adana, Sofulu, altitude 108 m a.s.l. 11.01.2017.

The specimens were killed in 85% ethanol in the field. After that in the laboratoty they were transferred to 96% ethanol. Specimens were described and dissected under stereo microscope. The materials are deposited in Soil Invertebrates Laboratory of Eskişehir Osmangazi University, Faculty of Science and Letters, Biology Department by senior author.

Sims & Gerard 1999, Csuzdi & Zicsi 2003, Mısırlıoğlu 2011 were used for identification.

3. RESULTS

At the end of the study, 5 species belonging to 3 genera were found in Adana Province as follow.

Systematic

Genus: *Allolobophora* Eisen 1873

***Allolobophora chlorotica* (Savigny, 1826)**

Fig.1: *Allolobophora chlorotica.*

Localities species found: Loc. 2.

Distribution in Turkey: Aegean [2, 3, 4, 5]; Inner Anatolia [6]; Marmara [5].

Zoogeographical distribution type: A widely introduced peregrine species, native to the Palearctic [7, 8, 9].

Genus: *Aporrectodea* Orley 1885

***Aporrectodea caliginosa* (Dugès, 1828)**

Fig 2: *Aporrectodea caliginosa.*

Previously *Aporrectodea caliginosa* and *Aporrectodea trapezoides* were considered as a unique species as *Aporrectodea caliginosa trapezoides*. But now they are two separate species. So, probably some of the past records of *Aporrectodea caliginosa trapezoides* were *Aporrectodea caliginosa*.

Localities species found: Loc. 1, loc. 2, loc. 3, loc. 4, loc. 5.

Distribution in Turkey: According to [10, 11] this species is probably distributed in all regions of Turkey.

Zoogeographical distribution type: One of the most widely distributed peregrine earthworms [9].

***Aporrectodea rosea* (Savigny, 1826)**

Fig. 3: *Aporrectodea rosea.*

Localities species found: Loc. 3.

Distribution in Turkey: Distributed in all regions of Turkey [10, 11].

Zoogeographical distribution type: A common peregrine species, native to the Palearctic [9].

***Aporrectodea trapezoides* (Dugès, 1828)**

Fig 4: *Aporrectodea trapezoides.*

Localities species found: Loc. 1, loc. 6.

Distribution in Turkey: Distributed in all regions of Turkey [10, 11].

Zoogeographical distribution type: One of the most widely distributed peregrine earthworms [9].

Genus: *Octodrilus* Omodeo, 1956

***Octodrilus transpadanus* (Rosa, 1884)**

Fig. 5: *Octodrilus transpadanus.*

Localities species found: Loc. 4.

Distribution in Turkey: Marmara [2, 5, 12, 13, 14]; North Anatolia [2, 15] Aegean [4, 15]; Inner Anatolia [6]; Mediterranean [13, 4]; South-East Anatolia [16, 17].

Zoogeographical distribution type: Trans-Aegean [7, 9].

4. DISCUSSION

Among the 5 recorded species from Adana province, four of them are peregrine: *Allolobophora chlorotica, Aporrectodea caliginosa, Aporrectodea rosea, Aporrectodea trapezoides* and one of them is Trans-Agean species: *Octodrilus transpadanus.*

Aporrectodea caliginosa, Aporrectodea rosea, Aporrectodea trapezoides are common species in Turkey [10, 11]. *Aporrectodea rosea* was recorded from Adana Pozantı and Adana Kandil Sırtı previously [15].

Octodrilus transpadanus was recorded from Aegean, Mediterranean, Marmara and Inner Anatolia regions of Turkey [10, 11].

Allolobophora chlorotica is a relatively rare peregrine species in Turkey. It was recorded in several localities in Marmara, Aegean and Inner Anatolia [10, 11]. Now, it is found in Adana-Mediterranean region.

Surely, more comprehensive studies are needed to understand the earthworm fauna of Adana province but it is thought that these results are important because they are additional records from a region which its earthworm fauna is very little-known.

Acknowledgements

We would like to thank our colleague Burcu OR for collecting the specimens.

References

[1] http://www.adana.gov.tr/ Adana governorship official website-date of access 22.01.2017.

[2] P. Omodeo and Rota E. Earthworms of Turkey. *Boll. Zool*., 56, 167-199, 1989.

[3] M. Mısırlıoğlu. A Preliminary Study of Earthworms (Oligochaeta, Lumbricidae) from the City of İzmir, Turkey, *Tr. Jr. of Zool*. 32: 473–475, 2008a.

[4] M. Mısırlıoğlu. Some Earthworm Records from Anatolia (Oligochaeta, Lumbricidae), *Tr. Jr. of Zool.* 32: 469–471, 2008b.

[5] M. Mısırlıoğlu and T. Szederjesi. Contributions to the Earthworm Fauna of Turkey, *Megadrilogica* 18(6): 99-102, 2015.

[6] M. Mısırlıoğlu. The earthworms (Oligochaeta: Lumbricidae) of Eskişehir City, Turkey. *Megadrilogica* 9: 17–20, 2002.

[7] T. S. V. Perel. *The Earthworms of the Fauna of Russia, Cadaster and Key*, (Ed. Prof. N. M. Chernova), Academia Nauka, Moscow, 101 p, 1997.

[8] R.W. Sims and B. M. Gerard. *Earthworms*. Syn. Br. Fauna No. 31. Linn. Soc. Lond., London, 169 p, 1999.

[9] Cs. Csuzdi and A. Zicsi. *Earthworms of Hungary (Annelida: Oligochaeta; Lumbricidae)*. Hungarian Natural History Museum, Budapest, 271 p, 2003.

[10] Cs. Csuzdi, A. Zicsi, M. Mısırlıoğlu. An annotated checklist of the earthworm fauna of Turkey (Oligochaeta: Lumbricidae) *Zootaxa*, 1175: 1–29, 2006.

[11] M. Mısırlıoğlu. *Topraksolucanları, Biyolojileri, Ekolojileri ve Türkiye Türleri*, Nobel Yayınları, Ankara, 92 s, 2011.

[12] A. Zicsi. Regenwürmer (Oligochaeta: Lumbricidae) aus der Türkei. *Acta Zool Hung* 19: 217–232, 1973.

[13] Cs. Csuzdi, T. Pavlíček, M. Mısırlıoğlu. Earthworms (Oligochaeta: Lumbricidae, Criodrilidae and Acanthodrilidae) of Hatay Province, Turkey, with description of three new lumbricids, *Acta Zool Hung* 53: 347–361, 2007.

[14] M. Mısırlıoğlu. The Earthworm Fauna of the Kocaeli (İzmit) City Centre (Oligochaeta, Lumbricidae). *Turk J Zool* 31: 353-356, 2007.

[15] P. Omodeo and E. Rota. Earthworms of Turkey II. *Boll Zool*, 58, 171-181, 1991.

[16] T. Pavlíček, Cs. Csuzdi and Y. Coşkun Y. First earthworm records in Mesopotamia (Oligochaetae), *Zoology in the Middle East*, 48:1, 119-120, 2009.

[17] T. Szederjesi, T. Pavlíček, Y. Coşkun, Cs. Csuzdi. New earthworm records from Turkey, with description of three new species (Oligochaeta: Lumbricidae). *Zootaxa* 3764: 555–570, 2014.

JOURNAL OF SCIENCE
SAKARYA UNIVERSITY

Sakarya University Journal of Science

ISSN 1301-4048 | e-ISSN 2147-835X | Period Bimonthly | Founded: 1997 | Publisher Sakarya University | http://www.saujs.sakarya.edu.tr/

Title: Karyotype features based on diploid number and sex chromosome system of Steatoda grossa (Araneae: Theridiidae) from Turkey

Authors: Zübeyde Kumbıçak
Recieved: 2018-12-01 12:28:34

Accepted: 2019-07-01 19:22:05

Article Type: Research Article
Volume: 23
Issue: 6
Month: December
Year: 2019
Pages: 1110-1114

How to cite
Zübeyde Kumbıçak; (2019), Karyotype features based on diploid number and sex chromosome system of Steatoda grossa (Araneae: Theridiidae) from Turkey. Sakarya University Journal of Science, 23(6), 1110-1114, DOI: 10.16984/saufenbilder.491049
Access link
http://www.saujs.sakarya.edu.tr/issue/44246/491049

Sakarya University Journal of Science 23(6), 1110-1114, 2019

Karyotype features based on diploid number and sex chromosome system of *Steatoda grossa* (Araneae: Theridiidae) from Turkey

Zübeyde Kumbıçak*

Abstract

In this study, karyotypic investigation of *Steatoda grossa* belonging to the family Theridiidae was carried out to contribute cytogenetic relationships of the family. A standard air-drying method was used to obtain chromosome slides including three main steps as hypotonisation, fixation and staining. As a result, the diploid number and sex chromosome system was determined as 2n♂=22 (X_1X_2). All chromosomes were telocentric and gradually decreased in size. Sex chromosomes were positively heteropycnotic in the stages of meiosis I, and isopycnotic in meiosis II. The results showed the similarity with the previous investigations obtained from different populations.

Keywords: Araneae, cytogenetics, karyotype, *Steatoda*, Turkey

1. INTRODUCTION

The genus *Steatoda* Sundevall is one of the most familiar genera in the family of Theridiidae that includes over 125 recognised species, distributed around the world [1]. The coloration of this genus is changed by brown to dark brown and the characterisation of an ivory strip on the anterior portion of the abdomen, and fleshy colulus and species are usually known as false widows because of its resemblance with the true widow spiders in the genus *Latrodectus* Walckenaer, 1805, from which can be differentiated by the presence of cheliceral teeth [2]. Eight theridiid spiders of the genus *Steatoda* are distributed in Turkey, namely *S. albomaculata* (De Geer, 1778), S. bipunctata (Linnaeus, 1758), *S. castanea* (Clerck, 1757), *S. dahli* (Nosek, 1905), *S. grossa* (C. L. Koch, 1838), *S. nobilis* (Thorell, 1875), *S. paykulliana* (Walckenaer, 1806), *S. triangulosa* (Walckenaer, 1802) [3]. *S. grossa* is a very common species in Turkey and it is possible to collect them from different populations.

Spiders are divided into three phylogenetic groups namely Mesothelae, Mygalomorphae and Araneaomorphae [4] and the family Theridiidae belongs to the group of Araneomorphae that has the great number of spider species described upto now. Chromosomal studies have been reported for three of the *Steatoda* species; *Steatoda bipunctata* (Linnaeus, 1758), *Steatoda grossa* (C.L. Koch, 1838) and *Steatoda triangulosa* (Walckenaer, 1802) [5]. In these studies chromosomal data have been reported for *S. bipunctata* 2n♂=22 [6]; *Steatoda grossa* 2n♂=22 [7] and *S. triangulosa* 2n♂=22 [8] or 2n♂=26 [9].

This study includes cytogenetical characteristics of *Steatoda grossa* in the point of karyotype structures (i.e. diploid chromosome number and sex chromosome

* Nevşehir Hacı Bektaş Veli University, zkumbicak@nevsehir.edu.tr ORCID: 0000-0001-5949-1092

system) and basic data of meiotic features for Turkish population.

2. EXPERIMENTAL

A total of 11 male specimens were collected under stones by hand or pitfall traps in various locations during March-May in the year 2016 (Table 1). During the field studies, no application was taken on the spiders and they were transferred directly to the laboratory. Subadult specimens were fed by *Drosophila melanogaster* twice a week until became adult. The used specimens were kept in the collection of Genetic Laboratory, Science and Art Faculty, Nevşehir Hacı Bektaş Veli University.

Table 1. Collection data of *Steatoda grossa* used in this study

Number of specimens	Locality and coordinates	Collection date and museum number
2 ♂♂	Pozantı (Adana) 37°25'3⁰.91"N and 34°51'50.68"E	08.04.2016 TH1605, TH1607
1 ♂	Çamalan (Mersin) 37°11'29.79" N and 34°48'07.05"E	108.04.2016 TH1606
3 ♂♂♂	Pınarbaşı (Kayseri) 38°42'47.64" N and 36°23'26.94"E	12.05.2016 TH1608, TH1609, TH1610
3 ♂♂♂	Gülek (Mersin) 37°15'31.22"N and 34°45'46.98"E	28.03.2016 TH1602, TH1603, TH1604
1 ♂	Alacaşar (Nevşehir) 38°37'15.22" N and 34°35'37.50"E	20.05.2016 TH1611
1 ♂	Göksun (Kahramanmaraş) 38°01'30.67" N and 36°30'46.65"E	21.03.2016 TH1601

Chromosomal preparations were made according to the protocol of Král et al. [10], a standard air drying method includes three main steps as hypotonisation, fixation, and staining, respectively. Gonads were dissected out in a pyhsiological solution for invertebrates under stereomicroscope (Leica EZ4) and transferred into hypotonic solution for 13-15 min and freshly prepared fixative solution (3:1, ethanol: acetic acid) two times (10 min and 20 min) at room temperature (RT). Cell suspensions from gonads was prepared from a piece of tissue in a drop of acetic acid (60 %) on a histological plate (42 °C) and the drop was moved till to evaporated by a tungsten needle. Slides were stained in Sörensens phosphate buffer (pH 6.8) for 50 min at RT.

Chromosome investigations were made under light microscope (Olympus) and best mitotic cells were photographed using DP26 camera attached to the BX53 microscope (Olympus) with CellSens software. Ten spermatogonial metaphases were used for karyotype analysis. Chromosome lengths were measured micrometric system by CellSens software. Homologues chromosomes were paired and sorted by length order except sex chromosomes that located at the end of the chromosomes. Chromosome morphology was classified according to the nomenclature of Levan et al. [11].

3. RESULTS

The diploid chromosome number of *Steatoda grossa* was consisted of 22 chromosomes including 20 autosomes and two univalent sex chromosomes (Fig. 1, Fig. 2a). Relative lengths of chromosomes were changed between 9.14±0.56 to 6.65±0.36 and chromosome lengths were decreased gradually in size (Table 2). Sex chromosomes were middle sized elements and relative lengths of X_1 and X_2 were 8.22±0.28 and 7.56±0.42, respectively. Both X_1 and X_2 were middle-sized elements in the karyotype. All chromosomes were telocentric.

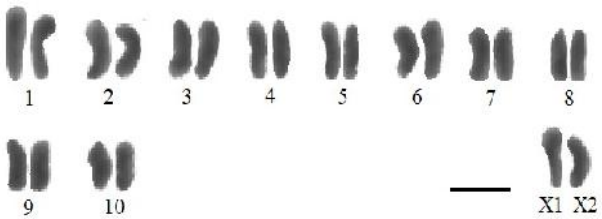

Fig. 1. Karyotype of *Steatoda grossa* from male gonads 2n♂=22 (X_1X_2) (Scale=10 µm)

Leptotene, zygotene and pacythene nuclei showed positively heteropycnotic sex chromosomes as "sex vesicle" located on the periphery of the nucleus (Fig. 2b). Diplotene, diakinesis and metaphase I nuclei obtained 10 autosomal bivalents and two univalent sex chromosomes (Fig. 2c). Autosomal bivalents had usually one chiasma that terminal, interstitial and proximal type. Anaphase I nuclei had two types of

nuclei includes n=10 or n=12 (with sex chromosomes) (Fig. 2d).

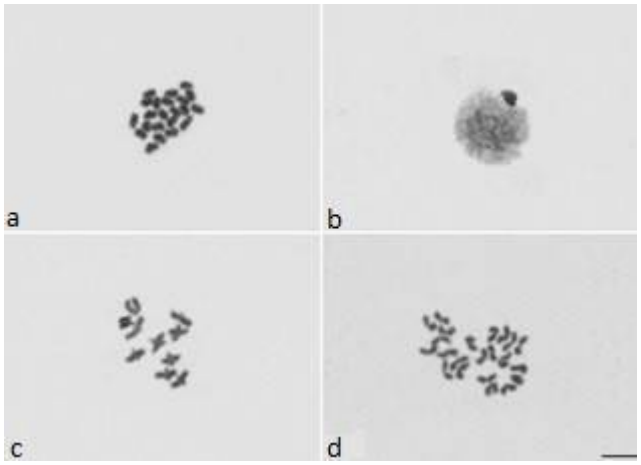

Fig 2. Cell division of *S. grossa* a. mitotic metaphase (2n♂=22), b. leptotene, c. diplotene (10 autosomal bivalents and two univalent sex chromosomes), d. anaphase I (Scale=10 µm)

Table 2. Relative chromosome lengths of haploid set and chromosome morphology of *S. grossa* (±: Standard deviation)

Pair no	Relative Chromosome Length (µm)	Chromosome morphology
1	9.14±0.56	Telocentric
2	8.87±0.12	Telocentric
3	8.60±0.30	Telocentric
4	8.34±0.52	Telocentric
5	8.10±0.67	Telocentric
6	7.79±0.24	Telocentric
7	7.46±0.20	Telocentric
8	7.20±0.47	Telocentric
9	6.92±0.18	Telocentric
10	6.65±0.36	Telocentric
X_1	8.22±0.28	Telocentric
X_2	7.56±0.42	Telocentric

Sex chromosomes were moved together. Prophase II and metaphase II nuclei had isopycnotic sex chromosomes indistinguishable from autosomes by dark staining. Anaphase II nuclei had n=10 or n=12 chromosomes like anaphase I with the exception of chromosome shape which was "V" shaped at anaphase I but "I" shaped at anaphase II.

DISCUSSION

It is known that there are more than 48000 spider species distributed all over the world, In spite of 117 spider families known on the world [1], cytogenetic data have been obtained on 70 families [5], this means that new studies about spider cytogenetics are needed. Thus, all information obtained will contribute to the explanation of topics such as karyotype properties, sex chromosome systems, meiotic division, evolution of chromosomes of spiders. The most studied spider families are the Salticidae and Lycosidae families with 160 and 120 species, respectively. Theridiidae family was studied with 30 species belonging to 15 genera, the most studies genera were listed as *Anelosimus* Simon, 1891 (six species) and *Latrodectus* Walckenaer, 1805 (five species) were the most studied in the family [5]. Although the genus *Steatoda* was represented by 125 species, only three species were investigated by cytogenetically. Previously studies have been showed that the karyotype features were 2n♂=22 (X_1X_20) for both *S. bipunctata* and *S. grossa* and 2n♂=26 (X_1X_20) for *S. triangulosa* [5]. When the karyotypic features of the family are considered, it is observed that the diploid number is mostly 2n♂=22. Except this, samples with diploid number 2n=17 (*Latrodectus geometricus* C.L. Koch, 1841; [12]), 2n=21 (*Argyrodes elevatus* Taczanowski, 1873; [13]), 2n=23 (*Theridion pictum* Walckenaer, 1802; [9]), 2n=24 (*Argyrodes gazingensis* Tikader, 1970; [14], *Chrysso scintillans* Thorell, 1895; [15] and *Nesticodes rufipes* Lucas, 1846; [13]), 2n=26 (*Steatoda triangulosa* Walckenaer, 1802; [9], *Latrodectus hesperus* Chamberlin & Ivie, 1935; [12] and *Latrodectus* gr. *curacaviensis,* [16]) and 2n=29 (*T. pictum*; [9]) were reported. According to [17], a phylogenetic study based on the sequences for two-mitochondrial genes: cytochrome c oxidase subunit I (COI) and ribosomal RNA16S (16S), and three nuclear genes: ribosomal RNAs 18S (18S) and 28S (28S), and histone (H3) on the Theridiidae family, the results of the sequence analysis showed that *Steatoda* and *Latrodectus* were closely related genera. In another study, *Steatoda* and *Latrodectus* species were found to be closed taxa [18]. However, different diploid numbers have been observed in *Steatoda* (2n=22 and 2n=26) and *Latrodectus* (2n=17 and 2n=26) samples,

this indicates an incompatibility on karyotype characteristics among these groups. Studies on other species are needed to explain the karyotype model of the genus *Steatoda*.

ACKNOWLEDGMENTS

I am very grateful to the members of Genetic Laboratory of Nevşehir Hacı Bektaş Veli University who helped in field studies, breeding spiders and laboratory studies. Also, I am grateful to anonymous rewievers for their valuable comments to improve the manuscript.

REFERENCES

[1] World Spider Catalog 2019. The World Spider Catalog. Version 20.0. Natural History Museum Bern. Available at: http://wsc.nmbe.ch Date Accessed: 2019.05.05.

[2] Faúndez, E. I., and M. A. Carvajal, "The spider genus Steatoda Sundevall, 1833 (Arachnida: Theridiidae) in the state of North Dakota (USA)", *Revista Ibérica de Aracnología,* vol. 29, pp. 83-85, 2016.

[3] H. Demir and O. Seyyar, "Annotated checklist of the spiders of Turkey," *Munis Entomology & Zoology*, vol. 12, no. 2, pp. 433-469, 2017.

[4] J.A. Coddington and H.W. Levi, "Systematics and evolution of spiders (Araneae)", *Annual Review Ecology, Evolution and Systematics,* vol. 22, pp. 565-592, 1991.

[5] D. Araujo, M.C. Schneider, E. Paula-Neto and D.M. Cella, "The spider cytogenetic database", Available in, http://www.arthropodacytogenetics.bio.br.spiderdatabase, Jan, 2019.

[6] W. Hackman, "Chromosomenstudien an Araneen mit besonderer berücksichtigung der geschlechtschromosomen", *Acta Zoologica Fennica*, vol. 54, pp. 1-101, 1948.

[7] I. P. Gorlov, O.Yu. Gorlova, And D.V. Logunov, "Cytogenetic studies on Siberian spiders", *Hereditas,* vol. 122, pp. 211-220, 1995.

[8] C. R. Tugmon, J.D. Brown, And N.V. Horner, "Karyotypes of seventeen USA spiders species (Araneae, Araneidae, Gnaphosidae, Loxoscelidae, Lycosidae, Oxyopidae, Philodromidae, Salticidae and Theridiidae)", *The Journal of Arachnology*, vol. 18, pp. 41-48, 1990.

[9] B. Taşdemır, I. Varol, And A. Akpınar, "Cytotaxonomical studies on six species of spiders (Arachnida: Araneae) from Turkey", *Türkiye entomoloji bülteni*, vol. 2, pp. 55-59, 2012.

[10] J. Král, J. Musilová, F. Št`Áhlavský, M. Řezáč, Z. Akan, R. L. Edwards, F.A. Coyle and C.R. Almerje, "Evolution of the karyotype and sex chromosome systems in basal clades of araneomorph spiders (Araneae: Araneomorphae)", *Chromosome Research*, vol. 14, pp. 859-880, 2006.

[11] A. Levan, K. Feradga and A. A. Sandberg, "Nomenclature for centromeric position on chromosomes," *Hereditas*, vol. 52, pp. 201-220, 1964.

[12] Y. Zhao, N.A. Ayoub and C. Y. Hayashi, "Chromosome mapping of dragline silk genes in the genomes of widow spiders (Araneae, Theridiidae)", *PLoS ONE*, vol. 5, no. 9, e12804, pp. 1-8, 2010.

[13] L. M. Stávale, M. C. Schneıder, D. Araujo, A. D. Brescovıt and D. M. Cella, "Chromosomes of Theridiidae spiders (Entelegynae): interspecific karyotype diversity in Argyrodes and diploid number intraspecific variability in Nesticodes rufipes", *Genetics and Molecular Biology*, vol. 33, no. 4, pp. 663-668, 2010.

[14] S. N. Datta and K. Chatterjee, "Chromosome number and sex-determining system in fifty-two species of spiders from North-East India", *Chromosome Information Service,* vol. 35, pp. 6-8, 1983.

[15] A. Kageyama and T. Seto, "Chromosomes of seven species of Japanese theridiid spiders", *Chromosome Information Service*, vol. 27, pp. 10-12, 1979.

[16] D. Araujo, U. M. Maia and A. D. Brescovit, "The first cytogenetic characterization of the

poisonous black widow spider Latrodectus gr. curacaviensis from Brazil, with chromosomal review of the family Theridiidae (Arachnida, Araneae)", *Micron*, vol. 41, pp. 165-168, 2010.

[17] J. Liu, L. J. M. Collado, S. Pekár and I. Agnarsson, "A revised and dated phylogeny of cobweb spiders (Araneae, Araneoidea, Theridiidae): A predatory Cretaceous lineage diversifying in the era of the ants (Hymenoptera, Formicidae)", *Molecular Phylogenetics and Evolution,* vol. 94, pp. 658-675, 2016.

[18] G. Barrantes and W. G. Eberhard, "Ontogeny repeats phylogeny in Steatoda and Latrodectus spiders", *Journal of Arachnology*, vol. 38, no. 3, pp. 485-494, 2010.

JOURNAL OF SCIENCE
SAKARYA UNIVERSITY

Sakarya University Journal of Science

ISSN 1301-4048 | e-ISSN 2147-835X | Period Bimonthly | Founded: 1997 | Publisher Sakarya University | http://www.saujs.sakarya.edu.tr/

Title: Nano Clay Additive Effect on Shear Strength of GFRP Joints

Authors: Ahmet Erkliğ, Mehmet Veysel Çakır, Ömer Yavuz Bozkurt
Recieved: 2019-02-07 14:33:21

Accepted: 2019-07-01 23:18:00

Article Type: Research Article
Volume: 23
Issue: 6
Month: December
Year: 2019
Pages: 1115-1122

How to cite
Ahmet Erkliğ, Mehmet Veysel Çakır, Ömer Yavuz Bozkurt; (2019), Nano Clay Additive Effect on Shear Strength of GFRP Joints. Sakarya University Journal of Science, 23(6), 1115-1122, DOI: 10.16984/saufenbilder.523889
Access link
http://www.saujs.sakarya.edu.tr/issue/44246/523889

Sakarya University Journal of Science 23(6), 1115-1122, 2019

Nano Clay Additive Effect on Shear Strength of GFRP Joints

Ahmet Erkliğ*[1], Mehmet Veysel Çakır [2], Ömer Yavuz Bozkurt[3], Bilal Faaek Ahmed[4]

Abstract

Adhesively bonding joints are widely used in various industries such as aviation, automotive and marine due to its advantages such as lightness, sealing ability, low cost, corrosion resistance and uniform stress distribution. Increasing the quality and durability of adhesives using various methods is a matter of interest both in science and engineering. This study investigates the role of the addition of Nano-clay particles to epoxy resin on the shear strength of single lap GFRP bonding joints. For this aim, Nano-silica particles were added in epoxy resin, 1%, 2%, 3% and 5% by weight. The experimental results obtained from lap shear test showed that the increase in shear strength was about 36, 91 and 63% for 1, 2 and 3 wt. respectively.

Keywords: Single-lap joints, Nano-clay particles, GFRP, shear strength

1. INTRODUCTION

Composite plates made of fiber reinforced polymer have been widely used since four decades ago for major and minor structures in many engineering applications, because they offer significant features over conventional structures made of metals only. These features include considerable reduction in weight, low maintenance and manufacturing costs and hence improving performance [1]. Joining composite materials by adhesives is preferable due to absence of stress concentration emerging in bolted and riveted joints as well as lack of defects induced by machining. The adhesive bonding offers excellent sealing, superior fatigue strength and good performance in raised temperature [2]. Adhesives are, in a simple sense, fluid or semi-fluid liquids which adherent materials using surface or chemical bonds, either natural or synthetic. Adhesion is basically the atomic and molecular interaction between two surfaces [2]. As well as the method's practical and low cost, mechanical, thermal and permeability of epoxy adhesives offer promising developments in an adhesive's properties.

Increasing the quality and durability of adhesives using various methods is a matter of interest both in science and engineering. Among these methods, the use of Nano-particles, such as Nano-fibers, carbon nanotubes, Nano-clays and graphite, as well as practicality and low cost, as well as mechanical, thermal and permeability of

* Corresponding Author: erklig@gantep.edu.tr
[1] Gaziantep University, Mechanical Engineering Department, Gaziantep, Turkey. ORCID: 0000-0003-3906-3415
[2] Kilis 7 Aralık University, Mechanical Engineering Department, Kilis, Turkey. ORCID: 0000-0003-2398-3209
[3] Gaziantep University, Mechanical Engineering Department, Gaziantep, Turkey. ORCID: 0000-0003-0685-8748
[4] Iraqi Ministry of Higher Education and Scientific Research, Al-Nahrain University, Iraq. ORCID:

epoxy adhesives. It offers promising developments in its characteristics [3]. Nanoparticles exhibiting many unique mechanical properties have become one of the most attractive options in recent years to increase the strength of polymer materials and adhesives [4, 5]. In this regard, studies were made on the performance of adhesive bonds by adding many different nanoparticles such as aluminum oxide [6, 7] titanium oxide [8], Nano-graphite [9], carbon nanotube [10] and Nano-clay [11].

Khalili et al. [11] have investigated the mechanical properties of glass fiber composite to composite's single bond connections combined with the Nano-clay addition to the epoxy adhesive under static and dynamic loading in a study they performed, as a result, 1 wt. % of the Nano-clay particles showed maximum strength at tensile load.

Polymer clay nanocomposites (PCN) have recently attracted a great deal of academic and industrial interest, as the clay contribution on the nanometric scale dramatically increases the mechanical and thermal properties [12]. Montmorillonite nano-clay particles have been documented as the best reinforcing materials for PCNs, because they have high aspect ratio, low cost, and they consist of layered silicates that can be placed in separate nano-dimensions with polymer chains [13].

Jeyekumar et al. [14] have produced glass fiber composites using 1, 3, 5, 7% Nano-clay by weight. They supplied homogeny dispersion and observe it in SEM. The samples were subjected to tensile and impact tests. Results show that addition of nano-clay 5% by weight increased tensile strength, flexural strength and impact strength by 23.66%, 53.86% and 29.65%ü, respectively.

Galimberti et al. [15] have investigated mechanical, barrier and thermal properties of composites produced using Nano-clay in a study they have done. It has been specified that the Nano-clay minerals increase the thermal properties of the adhesive.

According to the studies [16-17], if nano-clay addition into the polymer composites is less than 5 % by wt, it could get best result in dispersion, mechanical and thermal properties. Increasing the amount of Nano-clay will also increase the viscosity of the reinforced polymer system, and higher viscosity polymer will cause higher temperature during the sample fabricating.

In the light of progress made in joining technologies, adhesive bonding of composite materials has been become simpler in terms of alignment and consuming time. Many studies have been pointed out the significance of toughening and strengthening adhesives. Studies have shown that the addition of various low concentration Nano-particles to the resins of polymer composites is a good solution to improve mechanical and impact performance without sacrificing toughness or manufacturing process. Although studies on these new nanocomposites are common, there are a limited number of studies on the effect of Nano-clay addition on the adhesive when plate-like materials are combined with adhesive. The mechanical connections and the degradation processes of the adhesively bonded joints are very complex, too. And also many factors such as the type of adhesive, the type of adherent materials, the overlap length and the thickness of the adhesive affect the strength of the connections. Therefore, these effects need to be better understood by using different Nano-particles, different adherents and different adhesives. So, in this study, the effects of adding Nano-clay particles to commercial epoxy resin on the shear strength of GFRP single-lap joints are investigated. The overall aim of this study was to develop a relatively inexpensive and strong adhesive for common engineering applications.

2. EXPERIMENTAL STUDY

2.1. Materials

Clay is known to scientist for centuries; however its application as a reinforcing agent in polymers is relatively recent. Nano-clay type Montmorillonite (MMT) was used as a Nano-filler in this study to reinforce epoxy resin (Figure 1). MMT is hydrated alumina-silica clay

composed of a central alumina octahedral layer and two tetrahedral layers. MMT Nano clay was obtained from Grafen Chemical Industries, Turkey. MMT Nano-clay particles are at 1-10 nanometer sizes with dimethyl dialkylamine and their technical properties are shown in Table 1.

Table 1. Properties of nanoclay particles

Properties	
Loss in Drying (%)	<3
Mass Density (kg/m^3)	200-500
Lateral Width (µm)	0.5-2
Thickness (nm)	1-10

Figure 1. MMT Nano- clay particles

Fiber reinforced polymer (FRP) composite materials are widely used in aerospace, civil and structural industries because of several favorable properties such as low density, high specific strength and stiffness. In addition, the fatigue strength to weight ratios as well as fatigue damage tolerances of many composite laminates is excellent. Thus, FRP composites have emerged as a major class of light-weight structural material. In this study, Glass Fiber Reinforced Polymer G10-FR-4 plate in 2 mm thick was used. G10-FR-4 glass fiber reinforced polymer platters are thermosetting industrial fiberglass composite laminates made of epoxy resin-bonded continuous filament glass fiber material. G10-FR-4 GFRP plates commercially produced were bought from Kupar Pompa, Küçükparmak Mühendislik San. Tic. Ltd. Şti. Turkey. Its mechanical properties are given in Table 2.

MOMENTIVE-MGS L160 epoxy resin and MOMENTIVE-MGS H260S hardener were used as an adhesive material in the experiments which were supplied from DOST Chemical Industrial Raw Materials Industry, Turkey. Resin and hardener mixing ratios are 100:36±2 in weight and 100:43±2 in volume. This adhesive system has an excellent environmental resistance and bonds to a variety of substrates. The original properties, as provided by the manufacturer, are given in Table 3.

Table 2. Properties of GFRP

Properties	
Density (g/cm^3)	17.101
Buckling Strength (MPa)	357.00
Tensile Elastic Modulus (MPa)	23752
Pressure Resistance (N/mm^2)	371.20
Notch Impact Strength (Parallel to Lamination) (kJ/m^2)	117.79

Table 3. Physical properties of laminating resin and hardener (at 25 °C)

	MGS L160 resin	MGS H260 hardener
Density g/cm³	1.13-1.17	0.93-0.97
Viscosity MPa	700-900	80-100
Epoxy equivalent gr/equivalent	166-182	-
Epoxy value equivalent/100gr	0.55-0.60	-
Refractor index	1.5480-1.5530	1.4980-1.4985
Amine value (mgr. KOH / gr)	-	450-500

2.2. Preparation of Adhesive Joint Samples

GFRP composite plates, were wiped with acetone, abraded with an abrasive paper, wiped with a dry cloth to remove released atoms, and then wiped again with acetone. Water proof silicon carbide abrasive paper grade P120D was used to prepare the bonding areas for adhesive bonding.

The epoxy resin was modified by different weight ratios of clay nanoparticles. For lap shear test, clay Nano-particles was added by 1, 2, 3 and 5 % wt. five samples for each epoxy mixture design were prepared and tested. Epoxy resin was firstly put on the cup and after required amount of Clay nanoparticle was added and mixed with mixed with a light load homogenizer at 22,000 rpm for 10 minutes. Hardener was added with 100:40 stoichiometric ratios to the mixture after getting homogeneous mixture and mixed with the same speed for 10 minutes. Finally, mixture was waited for 10 minutes to remove bubbles.

The adherents were prepared from GFRP composite plates by geotine machine as rectangular pieces with appropriate dimensions according to ASTM D5868 – 01 as shown in Figure 2. Single lap joints (SLJ) were created using two thin adherents; each one is 25 mm in wide and 100 mm in long. They were bonded with a 25 mm overlap length, resulting in an overall sample that is 25 mm wide by 175 mm long. The two adherents were of same material. The thickness of the adherents was 2 mm. The adhesive bond-line thickness was 0.1 mm.

Single lap joint is the most popular configuration used in engineering applications such as automotive, wood and plastic, and aerospace industries. Single lap samples are practical, economical and easy to produce. Single lap joints can improve joining efficiency of dissimilar materials. The single lap joint is vastly utilized in adhesive bonding and has been the subject of significant research in the last decades. It also allows easy control and measure of the bond thickness. The simple and efficient design of a single lap joint often enables to evaluate the mechanical properties of the adhesive bonded joints [18].

An aluminum mold (Figure 3) was used to produce SLJs consistent. The mold was machined as stepped base to obtain the required thickness of the bond-line (i.e., 0.1 mm). The aluminum mold was previously coated by release agent to prevent samples from attaching to its surface. SLJs samples were prepared first by applying the adhesive onto one substrate. The second substrate was then placed accordingly to obtain the desired overlap length and excess resin was wiped from the edges. The substrates were then bonded together and carefully cured at a room temperature for 7 days.

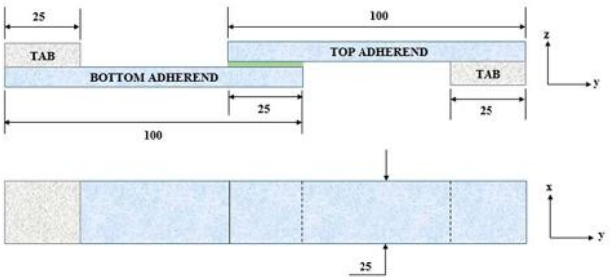

Figure 2. Dimensions of single lap joint according to ASTM D5868 – 01

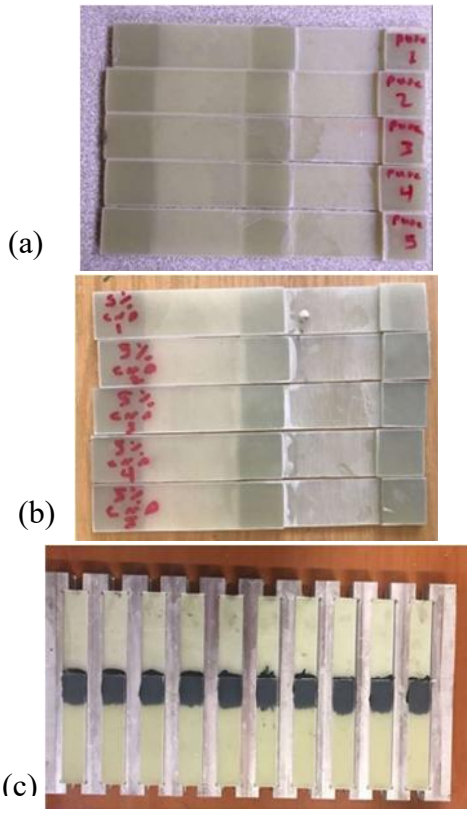

Figure 3. Production of single lap joint samples with the help of aluminum mold (a) Neat epoxy samples, (b) Nano-clay samples, (c) Mold

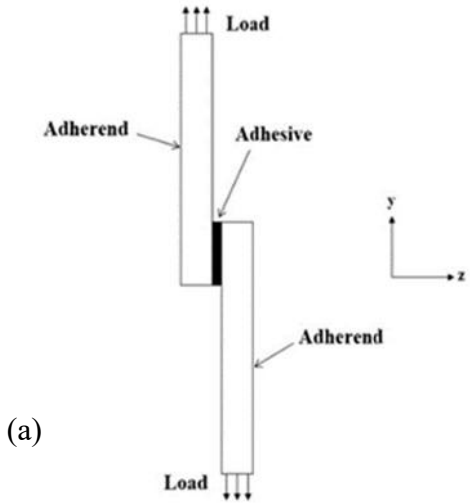

Figure 4. Lap shear test, (a) Schematics of the test set-up, (b) test sample under lap shear loading till fracture

SHIMADZU universal tensile testing machine with 300 kN loading capacity was used to perform tests. Samples were pulled at extension rates of 1.0 mm/min until failure, based on ASTM D3165 – 07 standards as shown in Figure 4.

3. RESULTS AND DISCUSSION

3.1. Shear Test Results

Single lap adhesive bonded joints were prepared with epoxy/Clay nanoparticle (CNP) composite adhesives and tested under lap shear loading in tension. The joints based on different weight ratios of CNP were tested and compared with control samples of neat epoxy. Two parameters fundamentally dominate the adhesive strength: (a) mechanical characteristics of the epoxy resin and CNP and (b) adhesion properties and viscoelastic behavior of epoxy resin. In previous researches on adhesively joints of epoxy [19], it was noticed that the mechanical properties of the joints increased with the increase of Nano particle content, but, at the same time, their viscoelastic behavior has been changed from liquid-like to solid-like. Thus, it was likely that epoxy containing high weight content of CNP will not have good adhesion properties. The results of lap shear tests in tension on the adhesive joints prepared with epoxy containing different amounts of CNP were obtained and presented in load-displacement diagram (Figure 5). The maximum shear strength of SLJs (Figure 6) is estimated using the average maximum shear stress shown in Figure 5.

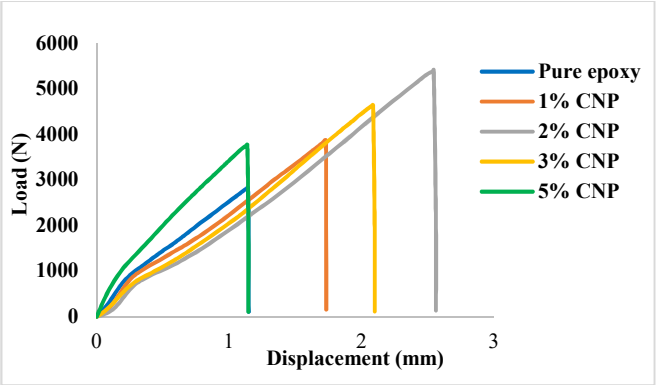

Figure 5 Load-displacement curves for SLJs reinforced with different amounts of CNP and subjected to tensile loading

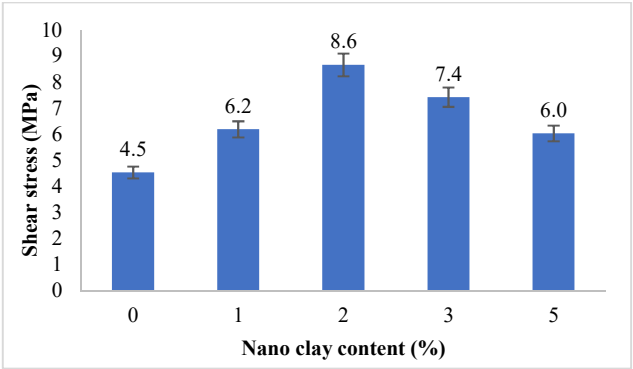

Figure 6. Maximum shear strength of SLJs versus CNP weight content

The variations of standard deviation for the results shown in Figure 6 were 0.276 to 0.661 MPa for composite epoxy. The influence of CNP incorporation into the adhesive layer on the shear

strength of SLJs was studied comparatively by the results of adhesive joints reinforced and unreinforced with CNP. It can be seen that the shear strength of adhesive joints increased with the addition of CNP, but above 2 wt. % of CNP, the shear strength decreased. The shear strength values for pure epoxy and epoxy reinforced with 1, 2, 3, and 5 wt. % of CNP were 4.532, 6.187, 8.653, 7.417, and 6.026 MPa, respectively. The results obtained from the lap shear test can be given in Table 4 1 to 2% by weight of nano-clay was added to the epoxy resin, the shear strength increased by about 36% and 91%, respectively. When CNP content exceeded 2 wt. %, the shear strength of adhesive joints decreased with the increase of Nano clay amount. This can be attributed to the aggregation of particles which causes stress concentration and crack growth in the adhesive layer and lead to sudden failure under lower stresses. However, the results showed that the bonded joints with Nano-clay particle reinforced adhesive, for all epoxy/Nano-clay contents considered in this study, have shear strength higher than that of control samples. The increase in shear strength was about 36, 91, 63, and 33% for 1, 2, 3, and 5 wt. % of CNP.

Table 4. Lap shear test results of SLJs with various amounts of CNP

Sample code	Epoxy + Hardener (%)	Clay (wt. %)	Max. Force (N)	Max. Shear stress (MPa)	Max. Shear strain (%)
T_0	100	0	2832.472	4.532	4.573
T_1	99	1	3867.078	6.187	6.927
T_2	98	2	5408.394	8.653	10.187
T_3	97	3	4635.823	7.417	8.355
T_5	95	5	3766.573	6.026	4.554

3.2. Failure Modes of Adhesively Single Lap Joints

There are two fundamental failure modes in adhesive bonded joints: adhesive failure and cohesive failure. Adhesive failure is an interfacial failure caused by complete separation between the adhesive and the adhered at one side. Cohesive failure is taken place in the adhesive layer only when a thin layer of adhesive still stuck on both sides. A combination between the two modes of failure can be obtained if the joint is neither strong enough to fail cohesively nor very weak to fail adhesively [20]. Nano-particles have the ability to fill micro voids of the substrate surfaces, emerging new points of contact and hence great opportunity to improve the adhesion strength is offered.

After the tensile tests, when the specimens are visually inspected, the difference in adhesion type deterioration is remarkable between the pure epoxy samples and the Nano-clay doped samples see Figure 7. In the unadulterated samples, the adhesiveness of the adhesive is low and there is a large amount of adhesion damage in the sample surfaces. Increasing the ratio of Nano-clay in the adhesive causes the damage type to turn into cohesion damage. While at 1.0 %, 2.0 % and 3 % Nano-clay doped joints, cohesion damage is observed in large proportions, adhesion damage is also present. In the case of 5% Nano-clay doped samples, as can be seen in Figure 7, the roughness on the surface of the adhesive increases, and in this respect, the adhesive property of the adhesive decreases.


0% CNP

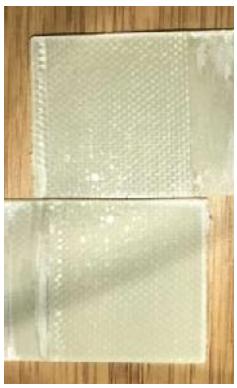
1% CNP

3% CNP


4% CNP

5% CNP

Figure 7. Fracture surfaces of SLJs after shear test

4. CONCLUSION

This work was undertaken primarily to determine the influence of various weight percentages of clay Nano-clay particles utilized to reinforced adhesively bonded single lap joints under shear loads. The overall aim of this study was to develop a relatively inexpensive and strong adhesive for common engineering applications. The experimental results showed excellent improvements in the mechanical properties with addition of the Nano-clay particles. Based on those results, it can be concluded the following:

- The addition of Nano-clay particles efficiently improves the chemical compatibility between epoxy adhesive and composite substrate surfaces and hence more efficient wetting of surface which causes increasing shear strength of the joint.
- The inclusion of Nano-clay particles into the epoxy resin resulted in more ductile behavior and this gives more uniform stress distribution across the joint and results higher strength.
- The maximum shear stresses value 8.653 MPa was obtained with the 2 % by wt addition of CNP, resulting in percentage increase in shear stress of about 91% compared to the neat epoxy resin joints.
- The experiments have shown that there is a powerful correlation between the joints strength and the failure mode. Increasing the ratio of Nano-clay in the adhesive causes the damage type to turn into cohesion damage. While at 1.0 %, 2.0 % and 3 % Nano-clay doped joints, cohesion damage is observed in large proportions, adhesion damage is also present.

5. REFERENCES

[1] A. R. Bunsell, J. Renard, “Fundamentals of fiber reinforced composite materials”, CRC Press, IOP Publishing Ltd, London (2005).

[2] M. D. Banea, L.F. da Silva, “Adhesively bonded joints in composite materials: an overview”, Proceedings of the Institution of Mechanical Engineers, Part L: Journal of Materials: Design and Applications, vol. 223, no. 1, pp. 1-18, 2009.

[3] E. Sancaktar, J. Kuznicki, “Nanocomposite adhesives: Mechanical behaviour with nanoclay”, International Journal of Adhesion and Adhesives, vol. 31, no. 5, pp.286-300, 2011.

[4] A. Tutunchi, R. Kamali, A. Kianvash, “Adhesive strength of steel–epoxy composite joints bonded with structural acrylic adhesives filled with silica nanoparticles”, Journal of Adhesion Science and Technology, vol. 29, no. 3, pp. 195–206, 2015.

[5] D. Guo, X. Guoxin, L. Jianbin, “Mechanical properties of nanoparticles: basics and applications”, Journal of Physics D: Applied Physics, vol. 47, pp.1-25, 2014.

[6] L.Zhai, L. Guoping, L. Jian, Y. Wang, “The effect of nanoparticles on the adhesion of epoxy adhesive”, Materials Letters, vol. 60, pp. 3031–3033, 2006.

[7] P. Ghabezi, M. Farahani, “Composite adhesive-bonded joint reinforcement by incorporation of nano-alumina particles”, Journal of Computational Applied Mechanics, vol. 47, no. 2, pp. 231-239, 2016

[8] S. Akpınar, “Alüminyum oksit ve titanyum dioksit takviyeli yapıştırıcılarla birleştirilmiş bağlantıların mekanik özelliklerinin deneysel olarak belirlenmesi”, Niğde Üniversitesi Mühendislik Bilimleri Dergisi, vol. 5, no. 2, pp. 244-252, 2016.

[9] A.S. Neto, D.T. Lopes da Cruza , A.F. Avila, “Nano-modified adhesive by

graphene: the single lap-joint case", Materials Research, vol. 16, no.3, pp. 592-596, 2013.

[10] Y. Suzhu, M. N. Tong, G. Critchlow, "Use of carbon nanotubes reinforced epoxy as adhesives to join aluminum plates", Materials and Design, vol. 31, pp. 126–129, 2010.

[11] S.M.R. Khalili, M. Tavakolian, A. Sarabi, "Mechanical properties of nanoclay reinforced epoxy adhesive bonded joints made with composite materials", Journal of Adhesion Science and Technology, vol. 24, pp. 1917–1928, 2010.

[12] S. Sinha Ray, M. Okamoto, "Polymer/layered silicate nanocomposites: a review from preparation to processing", Progress in Polymer Science, vol. 28, pp. 1539–1641, 2003.

[13] A. Gu, G. Liang, "Thermal degradation behaviour and kinetic analysis of epoxy/montmorillonite nanocomposites", Polymer Degradation and Stability, vol. 80, pp. 383–391, 2003.

[14] R. Jeyakumar, P.S. Sampath, R. Ramamoorthi, T. Ramakrishnan, "Structural, morphological and mechanical behaviour of glass fibre reinforced epoxy nanoclay composites", International Journal Advanced Manufacturing Technologies, vol. 93, pp. 1-9, 2017.

[15] M. Galimberti, V.R. Cipolletti, M. Coombs, "Applications of clay–polymer nanocomposites", Handbook of Develops in Clay Science, vol. 5, pp. 539-586, 2013.

[16] A. Yasmin, J. L. Abot, I.M. Daniel, "Processing of clay/epoxy nanocomposites by shear mixing", Scripta Materialia, vol. 49, no. 1, pp. 81-86, 2003.

[17] X. Kornmann, H. Lindberg, L.A. Berglund, "Synthesis of epoxy–clay nanocomposites: influence of the nature of the clay on structure", Polymer, vol. 42, no. 4, pp. 1303-1310, 2001.

[18] R.D. Adams, "Adhesive bonding: science, technology and applications", Cambridge: Elsevier, Woodhead Publishing Limited. (2005).

[19] M.B. Saeed, M.S. Zhan, "Adhesive strength of nano-size particles filled thermoplastic polyimides. Part-I: Multi-walled carbon nano-tubes (MWNT)–polyimide composite films", International Journal of Adhesion and Adhesives, vol. 27, no. 4, pp. 306-318, 2007

[20] A. C. Garg, Y. W. Mai, "Failure mechanisms in toughened epoxy resins—A review", Composites Science and Technology, vol. 1, no. 3, pp. 179-223, 1988

JOURNAL OF SCIENCE
SAKARYA UNIVERSITY

Sakarya University Journal of Science

ISSN 1301-4048 | e-ISSN 2147-835X | Period Bimonthly | Founded: 1997 | Publisher Sakarya University | http://www.saujs.sakarya.edu.tr/

Title: Application of Genetic Algorithm for Optimization of Heat-Transfer Parameters

Authors: Mustafa Akpınar
Recieved: 2018-12-21 16:49:36

Accepted: 2019-07-09 13:59:09

Article Type: Research Article
Volume: 23
Issue: 6
Month: December
Year: 2019
Pages: 1123-1130

How to cite
Mustafa Akpınar; (2019), Application of Genetic Algorithm for Optimization of Heat-Transfer Parameters. Sakarya University Journal of Science, 23(6), 1123-1130, DOI: 10.16984/saufenbilder.500643
Access link
http://www.saujs.sakarya.edu.tr/issue/44246/500643

Sakarya University Journal of Science 23(6), 1123-1130, 2019

Application of Genetic Algorithm for Optimization of Heat-Transfer Parameters

Mustafa Akpınar*[1]

Abstract

Nowadays, new materials are developed with the aim to reduce heat transfer and energy loss. Thus, energy can be reduced and heat energy can be transferred efficiently. Many researches on the field of heat transfer have been made in the literature. However, there are few studies on the determination of insulation material thickness using heuristic algorithms and there is no study on finding the thermal boundary layer thickness using heuristic algorithms. One of the heuristic algorithms used in the field of computer science is Genetic Algorithm (GA), which is frequently applied in optimization problems. We propose that GA could be used to solve heat transfer problems of insulation material selection and laminar thermal boundary layer thickness determination. The goal of the proposal is to estimate the optimal parameters using a GA. In the first case, the thickness of insulation material selection and the maximum amount of heat loss that can be caused by different thicknesses of the insulating material under the boundary conditions and assumptions are calculated using GAs. It is shown that, using the heat-transfer coefficient and unit length cylinder, GAs can be used in everyday problems, such as determining the thickness of the insulating material or the outer temperature of the insulating material. In the second case, the boundary layer thickness is determined using GA for air flow with a laminar flow, where its characteristics are constant, irradiation is neglected, and plate and air temperatures are constant in the continuous regime on the plate. For both cases, the GA results are repeated 5 times and it is observed that the results are very close to each other. The experimental results demonstrate that, for both cases GA gives optimal target, minimum and maximum values, thus, GAs are applicable in heat-transfer problems that require optimization.

Keywords: Heat transfer, genetic algorithm, optimization

1. INTRODUCTION

Heat transfer as a science studies to predict the energy transfer that may occur between material bodies as a result of temperature alterations [1]. The heat transfer researches seek not only to explain how heat energy may be transferred but also to estimate the amount of energy will be used under certain specified conditions [1]. Optimization must be determined under certain specified conditions of heat-transfer problems.

* Corresponding Author: akpinar@sakara.edu.tr
[1] Sakarya University, Software Engineering Department, Sakarya, Turkey. ORCID: 0000-0003-4926-3779

The growth of thermal systems, such as those related to material processing, energy conversion, pollution, aerospace, and automobiles, has caused the need to design and optimize thermal systems to grow as well [2]. Thus, optimization on heat transfer and thermal systems becomes more necessary.

There are many studies on heat-transfer optimization. Hayati et al. studied an adaptive neuro-fuzzy inference system (ANFIS) model to estimate the heat-transfer rate of the wire-on-tube type of heat exchanger [3]. Stirling heat engine is applied for optimization with multiple criteria and genetic algorithm (GA) is used for optimization [4]. Shi et al. optimized the inlet part of a microchannel ceramic heat exchanger studying a surrogate model coupled with a GA [5]. Sadeghzadeh demonstrated the GA application in the design of techno-economically optimum shell-and-tube heat exchangers [6]. Anish and Krishnakumar optimized dimensionless parameters, such as the Reynolds number (*Re*), porosity (*p*), perforation perimeter factor (P_f), plate thickness to pore diameter ratio (*l/d*), and spacer thickness to plate thickness ratio (*s/l*) for the maximum Colburn factor and minimum friction factor using a GA [7]. Ge et al. optimized the structure of a minichannel heat sink using a multi-objective GA [8]. Maladi and Balaji applied artificial neural networks (ANNs) and GAs to determine optimal location of three discrete heat sources that could be placed anywhere inside a ventilated cavity and cooled by forced convection [9]. Saruhan and Uygur used genetic algorithm to optimize mechanical system design [10]. They used parameters of speed reducer design for optimization. The condenser heat transfer rate was maximized and pressure drop was minimized using GA in [11]. Another study using GA in heat transfer was optimization of total cost of heat exchanger. In this study, cost was reduced 13.16% and compactness was increased 254% [12]. Another study using GA in energy sector was the thermoelectric generators design [13]. Outpout power of the thermoelectric generators was increased about 51.9% using GA optimization. In another generator design (the heat recovery steam generator) using GA, it is concluded that their approach could be used in existing and new heat recovery steam generators [14]. As stated in the literature review above, heuristic algorithms can be used in heat-transfer problems. For this reason, the objective of this paper is that two sample heat-transfer studies are completed to determine the optimal parameters, using the GA, which is one of the heuristic algorithms used in computer science. The first study includes a heat source that is radially heated and wrapped for insulation purposes to protect the heat with minimum heat loss. In the second study, boundary layer thickness was determined using a GA for air flow with laminar flow.

2. GENETIC ALGORITHM

The GAs are first has applied into the field of neural networks, then into machine learning, and recently into what is now called "evolutionary computation" [15]. The main objective in all application fields was to evolve a population of candidate solutions to a given problem making calculations inspired by natural genetic variation and natural selection [15]. The GAs are approaches which try to find the optimal solution and are based on evolutionary methodologies such as evolutionary biology, which studies inheritance, learning, selection, and mutation [2], [16]. Figure 1a shows the process flow of a GA. As a first step, the initial population is generated, and the fitness for this population is calculated. The fitness is checked to determine whether it meets the stopping criterion. If the stopping criterion is not met, the selection algorithm is run to find the best solutions. The most commonly used selection algorithms are tournament, roulette wheel, proportionate, rank, and steady-state selection [15]–[17]. The next step is to create new children according to the selected parents. At this stage, a crossover is made and shown along with the process in Figure 1. Crossover is a matter of replacing some of the genes in one parent with the corresponding genes of the other [17]. After the crossover phase, a mutation is made. Mutations consist of flipping the bit at a randomly chosen locus [15]. After this process, the fitness of the generated children is calculated, and the best is selected according to the “Elitism” approach. The error criterion is checked again, and this process is repeated until the desired point is reached.

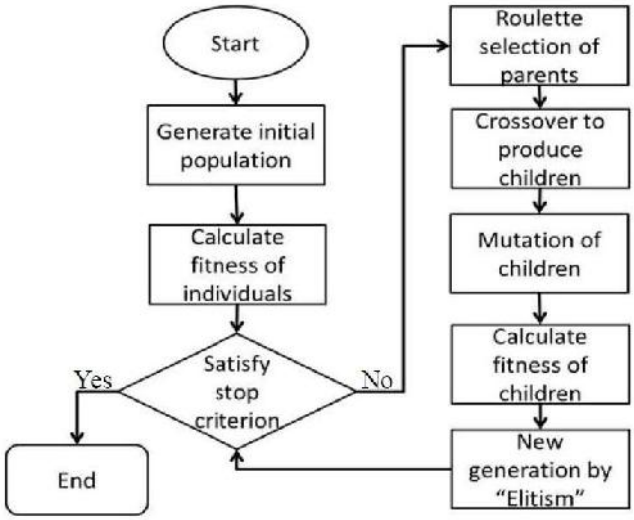

(a)

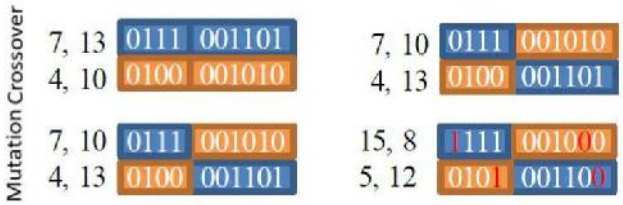

(b)

Figure 1. (a) Genetic algorithm process flow (b) Genetic algorithm crossover and mutation.

Genetic algorithms have a target based on the fitness function. Constraints and design variables are used while the target is found. Constraints are variables that include formulas and ranges and only affect the target function. Design variables are found in a certain range of values, and they are explored by the GA. They are effective on the constraints and target function. The target is the fitness value for which the maximum, minimum, and target values are to be determined

3. CASE STUDIES

In this paper, two sample studies have been defined for optimization. The first of these is the heat transfer in cylindrical surfaces. In this problem, an insulation material surrounds the heat source. The optimization problem is to determine the thickness of the insulation material and the material that will provide the lowest heat loss.

The first study includes a heat source (Figure 2) that is radially heated with a constant/continuous regime and has constant characteristics with no heat generation and is wrapped for insulation purposes to protect the heat with minimum heat loss.

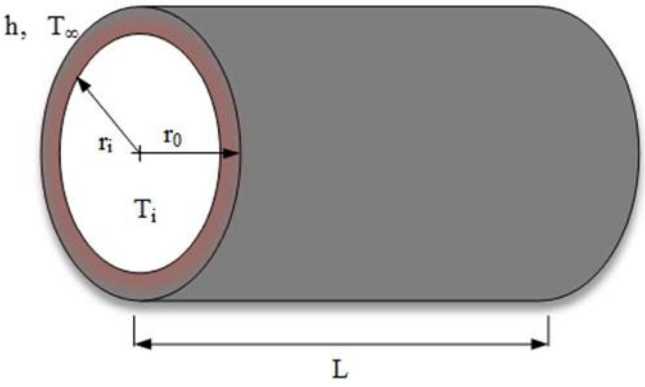

Figure 2. Insulation of a cylinder problem

In the continuous regime and absence of heat generation, the energy balance is equal, and the heat transfer is shown in Eq. (1) [1], [18].

$$Q = 2\pi L\left(T_i - T_\infty\right)\Big/\left(\left(\ln\left(r_o/r_i\right)/k\right) + \left(1/\left(r_o h\right)\right)\right) \quad (1)$$

where Q is the heat flow (heat-transfer amount), T_i is the inner temperature of insulation, T_∞ is the outer surface of insulation, r_o and r_i are the outer and inner radius of insulation, k is the thermal conductivity constant of the material, h is the convection heat transfer coefficients, and L is the length of the cylinder. By taking the derivative of Q according to r_o and equating to zero, the value of r_o, maximizing the heat transfer, is found and given in Eq. (2):

$$\begin{aligned} dQ/dr_o &= 0 \\ &= F\Big/\left(\ln\left(r_o/r_i\right)/k + 1/r_o h\right)^2 \ where \\ F &= -2\pi L\left(T_i - T_\infty\right)\left[\left(1/\left(kr_o\right)\right) - \left(1/\left(kr_o^2\right)\right)\right] \end{aligned} \quad (2)$$

In the second case study, the thermal boundary layer thickness was determined for air flow with the laminar flow, where its characteristics are constant, irradiation is neglected, and plate and air temperatures are constant in the continuous regime on the plate. There are three types of flow

regions on a flat plate [1], [18]. These are laminar, transition, and turbulent regions (Figure 3).

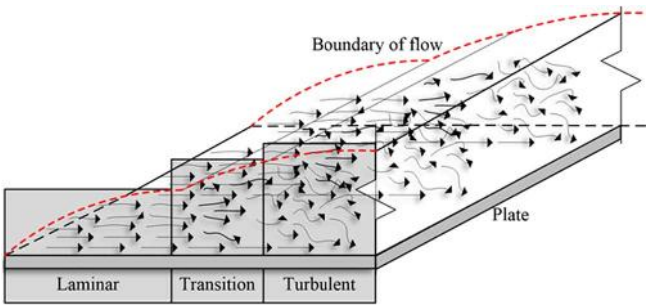

Figure 3. Thermal boundary layer problem

The transition from laminar to turbulent flow occurs when Eq. (3) represented:

$$Re = u_\infty x/v = \rho u_\infty x/\mu > 5 \cdot 10^5 \quad (3)$$

In this equation, u_∞ is the free-stream velocity, x is the distance from leading edge, v is the kinematic viscosity. Kinematic viscosity (v) is dynamic viscosity (μ) divided by the density (ρ) [1]. The Nusselt number, Nu, is the dimensionless variable that identifies the convective heat transfer [18], [19]. In the case in which the flow is laminar (Re<$5 \cdot 10^5$), the Nusselt number is expressed as:

$$Nu_x = 0.332 Re^{1/2} Pr^{1/3} \quad (4)$$

Where Pr is the Prandtl number, which is a dimensionless parameter representing the ratio of the diffusion of momentum to the diffusion of heat in a fluid [20] and is given in Eq. (5):

$$Pr = v/\alpha = v/\left(k/\rho c_p\right) \quad (5)$$

where c_p is the specific heat at a constant pressure (kJ/kg°C), k is the thermal conductivity (kW/m°C), α is the thermal diffusivity, and v is the kinematic viscosity [1]. Equation (6) shows the heat-transfer coefficient:

$$h = Nu_x k/x \quad (6)$$

Equation (7) gives the average value of the heat-transfer coefficient.

$$\bar{h} = 2h \quad (7)$$

The heat flow is calculated in Eq. (8):

$$Q = \bar{h} A (T_w - T_\infty) \quad (8)$$

where T_∞ is the temperature of the fluid outside the thermal boundary, T_w is the temperature of the wall, and A is the area of the plate [1]. Before finding the thermal boundary layer thickness, the hydrodynamic boundary layer thickness should be calculated as follows:

$$\delta = \left(4.64/\sqrt{Re_x}\right) x \quad (9)$$

Equation (10) shows the thermal boundary layer thickness:

$$\delta_t = \left(0.977/Pr^{1/3}\right) \delta \quad (10)$$

4. RESULTS

The results of two different studies are shown in this section. The first of these problems is the cylindrical insulating that has two cases. The first of these two cases is to find the insulation material that is to be used at a predetermined thickness for the allowed maximum heat loss. In the second case, we determine the thickness, given the maximum thermal conductivity constant and insulation material, for the highest heat loss allowed. In both cases, the heat loss (Q) is taken as a constraint. Inner and outer temperature of insulation cylinder is 500°C and 75°C, respectively. Heat sources radius is 30mm. In the first case, Q is a maximum of 100 W and in the second case; Q is a maximum of 120 W. For all tests in both cases, optimization started with k = 1 W/m°C and t = 1 mm. In the first case, optimization was initiated as a design variable at a maximum of 200 mm and a minimum of 25 mm t, and k was determined. In the second case, k is taken as a design variable so that a maximum 0.084 W/m°C and the lowest t-thickness are determined. The main reason why k is different, is that Q is increased from 100W to 120W. Q and k are directly proportional. The fitness function of the cases is given in formula (1). In the case that

the first fitness function is found with t left alone in the equation and, the second fitness function is when k is left alone. The chromosome structure has five values that are t, k and three random generated numbers. Table 1 shows the results and the processing times for the five tests of the two cases.

In the two cases, the following parameters (max 100 generations) were used for optimization: 16 chromosomes in the population, 0.9 crossover probability, 0.1 chromosome mutation probability, and 0.1 random selection probability. The average of the optimization process was performed in approximately one minute. Process steps of the GA optimization is given in Figure 4. Although the GA is a heuristic approach, there are different results, but these values are very close to each other. The results of evolving for each different generation and chromosome are getting close in each iteration. We tried to figure out two situations of the same problem could be solved using GA. Thus, we tried to change design variable and target (k and t) in both model and numeric values and it is clearly seen that GA finds nearly optimum values.

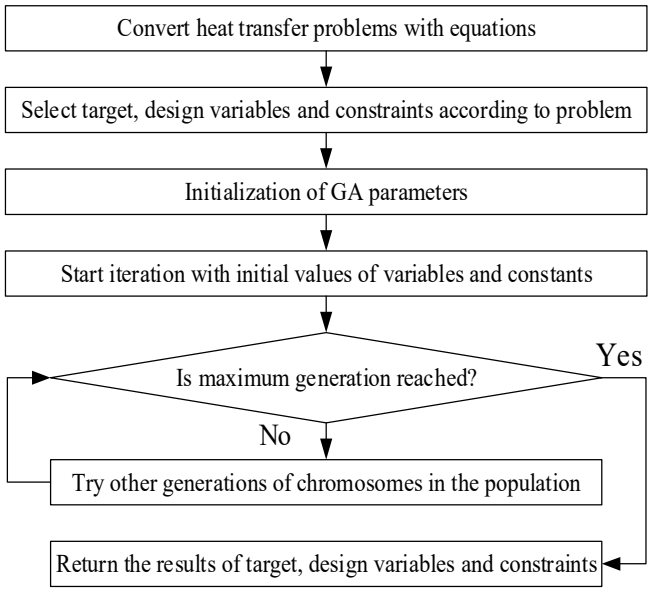

Figure 4. Process steps of the GA optimization

We found that cellulose cotton material (k = 0.071 W/ m°C) could be used as insulation material for the first case, where the material is unknown. In the second case, window glass material (k = 0.078 W/m°C) can be used, and the lowest thickness of insulation material is found to be 137.1 mm.

Table 1. Insulation material and thickness problem results

	Target: Material Type (k - W/m°C)				**Target: Thickness of Insulation (t - mm)**			
Test	***k* (kW/m°C)**	***t* (mm)**	***Q* (W)**	**time (s)**	***k* (kW/m°C)**	***t* (mm)**	***Q* (W)**	**time (s)**
1	0.082	200	99.948	75	0.084	145	117.016	36
2	0.080	200	97.226	59	0.084	137.1	119.994	58
3	0.077	200	93.802	51	0.084	150	115.272	55
4	0.076	200	92.365	57	0.084	137.2	119.955	54
5	0.080	200	97.226	52	0.084	137.1	119.994	59
Avg.	0.079	200	96.113	58.8	0.084	141.28	118.446	52.4

Table 2. Constraints and design variables of different targets with different cases

Case	**Type**	**Goal - Range**
Case 1	Goal	Maximum, minimum, and target (19.6 mm) values of thermal boundary layer thickness (δt)
	Constraints	$Re < 50 \times 10^3$, 140 W $\leq Q \leq$ 190 W
	Design Variables	0.2 m $\leq x \leq$ 1 m, 80°C $\leq T \leq$ 130°C
Case 2	Goal	Maximum, minimum, and target (160.43 W) values of heat flow (Q)
	Constraints	$Re < 50 \times 10^3$
	Design Variables	0.2 m $\leq x \leq$ 1 m, 80°C $\leq T \leq$ 130°C, 0.01 mm $\leq \delta t \leq$ 20 mm
Case 3	Goal	Maximum, minimum, and target (0.61 m) values of distance from leading edge (x)
	Constraints	140 W $\leq Q \leq$ 190 W, 0.01 mm $\leq \delta t \leq$ 20 mm
	Design Variables	$0.01 \leq Re \leq 50 \times 10^3$, 80°C $\leq T \leq$ 130°C

The second study is a problem regarding laminar flow on a hot plate. In this problem, the air at a certain speed flows over the plate, which is hotter than the air. It is aimed so that the flowing air is laminar. In the problem with the laminar boundary layer, three different target variables were determined. Targeted variables for three different cases and relations of these cases with constraints and design variables are given in Table 2. For these three cases, the problems were studied at the minimum, maximum, and target values. Each study was repeated five times, and the average results are shown in Table 3. In all cases of the second study, the temperature of the air is 65.6°C. The temperature in the region of the heat flow is taken as the average of the temperature of the plate and air. The properties of air at atmospheric pressure, given in the table in [1], are used to calculate variables such as the density (ρ), thermal conductivity (k), specific heat at constant pressure (c_p), and velocity of the air (u_∞) in the flow area, which vary according to the plate temperature in the optimization program.

The design variables in the models in Case 1 started at x = 1 m and T = 1°C. In the models in Case 2, the design variables x = 1 m, T = 1°C and δt = 1 mm were initiated. In Case 3, the initial values of the design variables were Re = 1 and T = 1°C. The fitness function of the cases is given in formula (10). In three cases, three fitness functions are evaluated using Eq. (3) to (10). The chromosome structure has five values which are x, T and three random generated numbers for the first case; x, T, δt and two random generated numbers for the second case; Re, T and three random generated numbers for the third case. In all three cases, the following parameters were used for optimization: 16 chromosomes in population, 0.9 crossover probability, 0.1 chromosome mutation probability, 0.1 random selection probability, max 100 generations, and the average of the optimization time is under 85 seconds. The average results for each case are shown in Table 3. In these results, all values in the target rows in the goal column are close when the target values, design variables, and constraints in Cases 1 and 3 are examined. This shows that, while the target variable is found, even though the effect parameters are different in the constraint and design variable states, the results can be found correctly in the global environment. The processing times for the cases were changing an average of 25% (Table 3, t(s) column).

5. CONCLUSION

Parametric equations used in heat transfer are frequently used in the solution of problems. In this study, we attempted to find the most suitable solution in the problems selection of insulation material and determination of laminar boundary layer thickness, which are two different situations used in everyday life. To find the most suitable solution, we proved that the calculations can find the optimum result in the solution space with the help of GA but it does not guarantee to find best solution. It was also found that GAs can be used in more complex problems of heat transfer. As the future work, heuristic algorithms such as simulated annealing, artificial bee colony, ant colony optimization and particle swarm optimization will be applied to determine parameters.

Table 3. Thermal boundary layer problem results

Cases	Goal	x (m)	T_w (°C)	Re	δt (mm)	Q (W)	t (s)
1 - Thermal boundary layer (δt in mm)	Minimum	0.38	128.03	15,189	**15.57**	140.95	77.00
	Target	0.60	123.45	24,507	**19.60**	165.73	94.00
	Maximum	1.00	116.64	41,368	**25.12**	189.60	93.00
2 - Heat flow from plate to air (Q in Watt)	Minimum	0.20	80.00	9,070	20.00	**13.44**	63.20
	Target	0.63	101.11	27,126	13.50	**160.45**	80.60
	Maximum	1.00	130.00	40,084	0.01	**600,936**	77.20
3 - Distance from leading edge (x in m)	Minimum	**0.36**	130.00	14,232	15.14	140.97	78.20
	Target	**0.61**	127.03	24,553	19.76	176.39	92.20
	Maximum	**0.63**	123.33	25,479	19.98	168.54	106.40

6. REFERENCES

[1] J. P. Holman, Heat Transfer, 10th ed. New York, NY: McGraw-Hill, 2010.

[2] Y. Jaluria, Design and Optimization of Thermal Systems, Second Edition, vol. 20071213. CRC Press, 2007.

[3] M. Hayati, A. Rezaei, and M. Seifi, "Prediction of the heat transfer rate of a single layer wire-on-tube type heat exchanger using ANFIS," Int. J. Refrig., vol. 32, no. 8, pp. 1914–1917, Dec. 2009.

[4] R. V. Rao, K. C. More, J. Taler, and P. Ocłoń, "Optimal design of Stirling heat engine using an advanced optimization algorithm," Sādhanā, vol. 41, no. 11, pp. 1321–1331, 2016.

[5] H. Shi, T. Ma, W. Chu, and Q. Wang, "Optimization of inlet part of a microchannel ceramic heat exchanger using surrogate model coupled with genetic algorithm," Energy Convers. Manag., vol. 149, pp. 988–996, Oct. 2017.

[6] H. Sadeghzadeh, M. A. Ehyaei, and M. A. Rosen, "Techno-economic optimization of a shell and tube heat exchanger by genetic and particle swarm algorithms," Energy Convers. Manag., vol. 93, pp. 84–91, Mar. 2015.

[7] A. K. John and K. Krishnakumar, "Performing multiobjective optimization on perforated plate matrix heat exchanger surfaces using genetic algorithm," Int. J. Simul. Multidiscip. Des. Optim., vol. 8, p. A3, Jan. 2017.

[8] Y. Ge, F. Shan, Z. Liu, and W. Liu, "Optimal Structural Design of a Heat Sink With Laminar Single-Phase Flow Using Computational Fluid Dynamics-Based Multi-Objective Genetic Algorithm," J. Heat Transfer, vol. 140, no. 2, p. 022803, Sep. 2017.

[9] R. R. Madadi and C. Balaji, "Optimization of the location of multiple discrete heat sources in a ventilated cavity using artificial neural networks and micro genetic algorithm," Int. J. Heat Mass Transf., vol. 51, no. 9–10, pp. 2299–2312, May 2008.

[10] H. Saruhan and İ. Uygur, "Design Optimization of Mechanical Systems Using Genetic Algorithms," Sak. Univ. J. Sci., vol. 7, no. 2, pp. 77–84, 2003.

[11] S. Sanaye and M. Dehghandokht, "Modeling and multi-objective optimization of parallel flow condenser using evolutionary algorithm," Appl. Energy, vol. 88, no. 5, pp. 1568–1577, May 2011.

[12] K. Baadache and C. Bougriou, "Optimisation of the design of shell and double concentric tubes heat exchanger using the Genetic Algorithm," Heat Mass Transf., vol. 51, no. 10, pp. 1371–1381, Oct. 2015.

[13] W.-H. Chen, P.-H. Wu, and Y.-L. Lin, "Performance optimization of thermoelectric generators designed by multi-objective genetic algorithm," Appl. Energy, vol. 209, pp. 211–223, Jan. 2018.

[14] A. Rezaie, G. Tsatsaronis, and U. Hellwig, "Thermal design and optimization of a heat recovery steam generator in a combined-cycle power plant by applying a genetic algorithm," Energy, vol. 168, pp. 346–357, Feb. 2019.

[15] M. Melanie, An Introduction to Genetic Algorithms, 5th ed. London: MIT Press, 1999.

[16] R. L. Haupt and S. E. Haupt, Practical Genetic Algorithms, 2nd ed. New York, NY, USA: Wiley, 2004.

[17] F. Glover and G. A. Kochenberger, Eds., Handbook of Metaheuristics, vol. 57. Boston: Kluwer Academic Publishers, 2003.

[18] F. Kreith, R. M. Manglik, and S. B. Mark, Principles of Heat Transfer, 7th ed. Stamford, CT: Cengage learning, 2011.

[19] G. L. Shires, "Nusselt Number," in A-to-Z Guide to Thermodynamics, Heat and Mass Transfer, and Fluids Engineering, Begellhouse.

[20] G. L. Shires, "Prandtl Number," in A-to-Z Guide to Thermodynamics, Heat and Mass Transfer, and Fluids Engineering, Begellhouse.

JOURNAL OF SCIENCE
SAKARYA UNIVERSITY

Sakarya University Journal of Science

ISSN 1301-4048 | e-ISSN 2147-835X | Period Bimonthly | Founded: 1997 | Publisher Sakarya University | http://www.saujs.sakarya.edu.tr/

Title: Some results on free Euclidean self-dual codes over F2+vF2

Authors: Refia Aksoy, Fatma Çalışkan
Recieved: 2019-02-11 16:12:09

Accepted: 2019-07-12 09:41:46

Article Type: Research Article
Volume: 23
Issue: 6
Month: December
Year: 2019
Pages: 1131-1136

How to cite
Refia Aksoy, Fatma Çalışkan ; (2019), Some results on free Euclidean self-dual codes over F2+vF2. Sakarya University Journal of Science, 23(6), 1131-1136, DOI: 10.16984/saufenbilder.525606
Access link
http://www.saujs.sakarya.edu.tr/issue/44246/525606

Sakarya University Journal of Science 23(6), 1131-1136, 2019

Some results on free Euclidean self-dual codes over $\mathbb{F}_2 + \upsilon\mathbb{F}_2$

Refia Aksoy [1], Fatma Çalışkan [*2]

Abstract

In this paper, free Euclidean self-dual codes over the ring $\mathbb{F}_2 + \upsilon\mathbb{F}_2$ with $\upsilon^2 = \upsilon$ of order 4 are considered. A necessary and sufficient condition for the form of the generator matrix of a free Euclidean self-dual code is given. By using the distance preserving Gray map from $\mathbb{F}_2 + \upsilon\mathbb{F}_2$ to $\mathbb{F}_2 \times \mathbb{F}_2$, the generator matrix of the binary code which corresponds the code over the ring $\mathbb{F}_2 + \upsilon\mathbb{F}_2$ is obtained. The codes of lengths up to 100 over the ring $\mathbb{F}_2 + \upsilon\mathbb{F}_2$ are found.

Keywords: Euclidean self-dual codes, codes over rings, Chinese remainder theorem

1. INTRODUCTION

Let A be a finite set that is called the alphabet. A code over A is a subset of A^n ($n \in \mathbb{N}$). If A is a field of two elements, then we say that the code is a binary code. Binary codes are used for the computer applications and the digital communications. An electronic information is transmitted through channels as a sequences of zeros and ones. Hence in theory, the binary field has been used as an alphabet. However, mathematicians generalized the alphabet from the binary field to finite fields. Moreover, researchers have studied about codes over finite rings. Codes over finite rings correspond to binary codes via a Gray map.

Linear codes are an important subclass of codes, which are linear subspaces of A^n if A is a field and linear submodules of A^n if A is a ring. If $C = C^{\perp}$, then the linear code C is self-dual. There exist important properties of self-dual codes, because many of the good codes are self-dual such as extended Golay code and they have a powerful algebraic structure. There are a large number of studies about self-dual codes over different finite rings ([5], [7], [12], [16]).

A code has important parameters such as length, dimension and minimum distance. These parameters help us to measure code efficiency and error-correcting capability. The main problem of algebraic coding theory is to find one of these parameters for given values of the other two ([13]). Researchers have investigated bounds which are limits on the parameters of a code ([4], [6], [10]). There are plenty of researches related to obtaining both the minimum distance of a linear

[1] İstanbul University, Institute of Graduate Studies in Sciences, İstanbul, Turkey. ORCID: 0000-0003-3093-0586
[*] Corresponding Author: fatmac@istanbul.edu.tr
[2] İstanbul University, Department of Mathematics, İstanbul, Turkey. ORCID: 0000-0001-7869-870X

code and the linear codes that attain the bounds ([15], [17]).

Constructing new self-dual codes and classifying self-dual codes have been an interesting research subject. Researchers have used different techniques to construct self-dual codes ([9], [11], [14]). In the present paper, we deal with self-dual codes over the ring $\mathbb{F}_2 + \upsilon\mathbb{F}_2$ with $\upsilon^2 = \upsilon$ of order 4. We use several known construction methods to establish free Euclidean self-dual codes. We then obtain self-dual codes over the ring $\mathbb{F}_2 + \upsilon\mathbb{F}_2$ with the highest minimum weights of lengths up to 100.

The rest of the paper is organized as follows. In Section 2, we give some properties of codes over the ring $\mathbb{F}_2 + \upsilon\mathbb{F}_2$. In Section 3, we study free Euclidean self-dual codes over the ring $\mathbb{F}_2 + \upsilon\mathbb{F}_2$ using the Chinese remainder theorem. In Section 4, we find the highest possible minimum weights using the construction methods given in [14].

2. PRELIMINARIES

Let R be the ring $\mathbb{F}_2 + \upsilon\mathbb{F}_2$. A linear code C over R of length n is defined to be an *R-submodule* of R^n. An element of C is called a *codeword* of C. For codes over R, three different weights are considered. These are the *Hamming*, *Lee* and *Bachoc weights*, which are defined in [1] and [7], given in Table 1.

Table 1. The weights of the elements of R

The elements	Hamming Weights	Lee Weights	Bachoc Weights
$\mathbf{0}$	0	0	0
$\mathbf{1}$	1	2	1
$\boldsymbol{\upsilon}$	1	1	2
$\mathbf{1}+\boldsymbol{\upsilon}$	1	1	2

The *minimum Hamming, Lee* and *Bachoc distances*, denoted by d_H, d_L and d_B, of C are the smallest Hamming, Lee and Bachoc weights among all non-zero codewords of C, respectively.

The ring R has two maximal ideals $I_1 = \langle\upsilon\rangle$ and $I_2 = \langle 1+\upsilon\rangle$. Therefore the Gray map $\Phi : R \to R/I_1 \times R/I_2$ is a ring isomorphism via the Chinese remainder theorem, where $\Phi(a+\upsilon b) = (a, a+b)$. Also, $\Phi_i : R \to R/I_i$ is a canonical homomorphism and $R/I_i \cong \mathbb{F}_2$ for $i = 1,2$. The Gray map is extended to R^n such that

$$\begin{aligned} \phi: R^n &\to \mathbb{F}_2^n \times \mathbb{F}_2^n \\ \mathbf{x} &\mapsto \phi(\mathbf{x}) = (\mathbf{r}, \mathbf{r}+\mathbf{q}), \end{aligned}$$

where $\mathbf{x} = \mathbf{r} + \upsilon\mathbf{q}$ and $\mathbf{r}, \mathbf{q} \in \mathbb{F}_2^n$. The map ϕ is a weight-preserving map from R^n (Lee weight) to $\mathbb{F}_2^{2n}$ (Hamming weight), which is, $w_L(\mathbf{x}) = w_H(\phi(\mathbf{x}))$ for $\mathbf{x} \in R^n$. The map ϕ is $\mathbb{F}_2$-linear and every element $\mathbf{x}$ of R^n can be written uniquely as $\mathbf{x} = \mathbf{r} + \upsilon\mathbf{q}$ for $\mathbf{r}, \mathbf{q} \in \mathbb{F}_2^n$. Let $C = \phi^{-1}(C_1, C_2)$ be a code over R. In this case, we denote C as $CRT(C_1, C_2)$, where C_1 and C_2 are uniquely determined for each C.

The *Euclidean inner product* on R^n is given by $(\mathbf{x}, \mathbf{y}) = \sum_{i=1}^n x_i y_i$ and the *Hermitian inner product* on R^n is $\langle \mathbf{x}, \mathbf{y} \rangle = \sum_{i=1}^n x_i \overline{y_i}$ where $\mathbf{x}, \mathbf{y} \in R^n$, with $\mathbf{x} = (x_1, x_2, \dots, x_n)$ and $\mathbf{y} = (y_1, y_2, \dots, y_n)$, and $\overline{0} = 0$, $\overline{1} = 1$, $\overline{\upsilon} = 1+\upsilon$, $\overline{1+\upsilon} = \upsilon$.

The *Euclidean dual* of an $[n,k]$-code C is the $[n, n-k]$-code

$$C^{\perp} = \{\mathbf{x} \in R^n | (\mathbf{x}, \mathbf{c}) = 0 \text{ for all } \mathbf{c} \in C\}$$

and the *Hermitian dual* is the code

$$C^{*} = \{\mathbf{x} \in R^n | \langle \mathbf{x}, \mathbf{c} \rangle = 0 \text{ for all } \mathbf{c} \in C\}.$$

C is *Euclidean self-orthogonal* if $C \subseteq C^{\perp}$ and *Hermitian self-orthogonal* if $C \subseteq C^{*}$. C is *Euclidean self-dual* if $C = C^{\perp}$ and *Hermitian self-dual* $C = C^{*}$.

Two codes are *equivalent* if one can be obtained from the other by permuting the coordinates. A code C is called *isodual* if it is equivalent to its dual. A code C is called *formally self-dual* if C and the dual code of C have the same weight enumerators. Both self-dual codes and isodual codes are formally self-dual codes.

A Euclidean self-dual code is *Type IV* if the Hamming weights of all codewords are even. A Euclidean self-dual code is called *Type I* if it has at least one codeword of odd weight.

Proposition 2.1. ([8]) A code $C = CRT(C_1, C_2)$ is Euclidean self-dual if and only if C_1 and C_2 are both binary self-dual codes.

Remark 2.2. Binary self-dual codes of length n exist if and only if n is even. Moreover, binary self-dual codes have even weights.

Corollary 2.3. ([7]) A Euclidean self-dual code of length n exists if and only if n is even.

Proposition 2.4. ([7]) A code $C = CRT(C_1, C_2)$ is Euclidean Type IV self-dual if and only if $C_1 = C_2$.

Proposition 2.5. ([2]) Let d_H and d_L be the minimum Hamming distance and the minimum Lee distance of a code $C = CRT(C_1, C_2)$, respectively. Then

$$d_H(C) = d_L(C) = min\{d(C_1), d(C_2)\},$$

where $d(C_1)$ and $d(C_2)$ denote the minimum distances of the binary codes C_1 and C_2, respectively.

3. FREE EUCLIDEAN SELF-DUAL CODES

In our study, we consider free Euclidean self-dual codes over R. In this section, we present a general information about the structure of the generator matrix of a free Euclidean self-dual code over R and then we give a necessary and sufficient condition for the form of the generator matrix of a free Euclidean self-dual code.

The generator matrix G of a code C is a matrix whose rows generate C. We say that a code that is generated as a free R-module is called a *free code* over R. The row operations and the properties of R imply that any free code over R can be brought to an equivalent form which is generated by the rows of the matrix $[I_k, A + vB]$, where A and B are $k \times k$ binary matrices and I_k is the $k \times k$ identity matrix.

In general, a non-zero linear code C over R is permutation equivalent to a code with generator matrix of the form

$$G = \begin{bmatrix} I_{k_1} & A_1 & B_1 & D_1 + vD_2 \\ 0 & vI_{k_2} & 0 & vC_1 \\ 0 & 0 & (1+v)I_{k_3} & (1+v)E_1 \end{bmatrix},$$

where A_1, B_1, C_1, D_1, D_2 and E_1 are binary matrices and $|C| = 4^{k_1}2^{k_2}2^{k_3}$ [18].

Proposition 3.1. Let C be the free code given by $CRT(C_1, C_2)$. If $G = [I_k, A + vB]$ generates C, then the corresponding binary codes C_1 and C_2 have generator matrices $G_1 = [I_k, A]$ and $G_2 = [I_k, A + B]$, respectively, and vice versa.

Proof: From Corollary 3.2 in [18], we obtain that the Gray image of C is generated by

$$G' = \begin{bmatrix} \phi(G) \\ \phi(vG) \end{bmatrix} = \begin{bmatrix} I_k & A & 0 & 0 \\ 0 & 0 & I_k & A + B \end{bmatrix}.$$

Theorem 3.2. The matrix $G = [I_k, A + vB]$ generates a Euclidean self-dual code over R of length $2k$ if and only if A is an orthogonal matrix and $AB^T + BA^T + BB^T = 0$, where A and B are $k \times k$ binary matrices.

Proof: Let G be the generator matrix of a Euclidean self-dual code. Then

$$G \cdot G^T = 0.$$

Since

$$G \cdot G^T = [I_k, A + vB] \cdot \begin{bmatrix} I_k \\ A^T + vB^T \end{bmatrix},$$

we find

$$(I_k + AA^T) + v(AB^T + BA^T + BB^T) = 0.$$

Hence

$$AA^T = I_k$$

and

$$AB^T + BA^T + BB^T = 0.$$

Conversely, assume that $AA^T = I_k$ and $AB^T + BA^T + BB^T = 0$. Then $G \cdot G^T = 0$ which implies G generates a Euclidean self-dual code.

Remark 3.3. Let C be a free Euclidean self-dual code with the generator matrix $G = [I_k, A + \upsilon B]$, where A and B are $k \times k$ binary matrices. According to Theorem 3.2, B cannot be equal to A. Otherwise we would obtain $I_k = 0$ which is a contradiction.

Corollary 3.4. A Euclidean self-dual code which is generated by the matrix $G = [I_k, A + \upsilon B]$ is of Type IV if and only if the matrix B is a zero matrix.

4. THE CONSTRUCTION METHODS

In this section, we state three construction methods given in the following. By using these construction methods, we obtain Euclidean self-dual codes satisfying the conditions given in Theorem 3.2. All the computations were done with MAGMA Package [3].

Theorem 4.1. ([14]) Let A be a binary matrix and let I_k be the $k \times k$ identity matrix, then the following assertions hold:

a) A code with a double-circulant construction, i.e., a code with generating matrix $[I_k, A]$, where A is a circulant matrix, is isodual.
b) A code with a bordered double-circulant construction, i.e., a code with generating matrix

$$G = \left[\begin{array}{c|ccc} & \alpha & \beta & \cdots & \beta \\ I_k & \gamma & & & \\ & \vdots & & A & \\ & \gamma & & & \end{array}\right],$$

where A is a $(k-1) \times (k-1)$ circulant matrix, is isodual provided that $\beta = \gamma = 0$ or both β and γ are non-zero.

c) A code with a symmetric construction, i.e., a code with generating matrix $[I_k, A]$, where A is a symmetric matrix, is isodual.

4.1. The Double-Circulant Construction

Let A be a $k \times k$ orthogonal circulant matrix. The code C_1 whose generator matrix is of the form $[I_k, A]$ is a $[2k, k, d_1]$-code. Since C_1 is binary self-dual, we find the matrix B which satisfies the condition given in Theorem 3.2. The code C_2 whose generator matrix is of the form $[I_k, A + B]$ is a $[2k, k, d_2]$-code. Since C_2 is binary self-dual, we obtain the code C over the ring R, where C is a $[2k, k, min\{d_1, d_2\}]$-code. The minimum weights of the Euclidean self-dual codes that are obtained by using this construction method are given in Table 2.

In Table 2, $d_{max}(n)$ is the highest minimum weight of a binary linear code of length n and of dimension $n/2$, $d_{DC}(n)$ is the minimum weight of a Euclidean self-dual code of length n obtained by applying the double-circulant construction.

Table 2. The Euclidean self-dual codes obtained by using the double-circulant construction

length n	$d_{max}(n)$	$d_{DC}(n)$	length n	$d_{max}(n)$	$d_{DC}(n)$
2	2	2	**52**	10-12	10
4	2	2	**54**	11-13	10
6	3	2	**56**	12-14	8
8	4	4	**58**	12-14	10
10	4	2	**60**	12-14	12
12	4	4	**62**	12-15	10
14	4	2	**64**	12-16	12
16	5	4	**66**	12-16	12
18	6	4	**68**	13-16	12
20	6	4	**70**	14-16	10
22	7	6	**72**	15-17	12
24	8	8	**74**	14-18	12
26	7	6	**76**	14-18	12
28	8	4	**78**	15-18	12
30	8	6	**80**	16-19	16
32	8	8	**82**	14-20	14
34	8	6	**84**	15-20	12
36	8	6	**86**	16-20	14
38	8-9	8	**88**	17-20	16
40	9-10	8	**90**	18-21	14
42	10	6	**92**	16-22	14
44	10	8	**94**	16-22	14
46	11	10	**96**	16-22	16
48	12	12	**98**	17-22	14
50	10-12	10	**100**	18-23	14

4.2. The Bordered Double-Circulant Construction

While applying this construction, when k is even, we take $\beta = \gamma = 1$ and $\alpha = 0$. In this case, we may obtain codes whose minimum distance is greater than 2. When k is odd, we take $\beta = \gamma = 0$

and $\alpha = 1$. Since the first row of the matrix G has the minimum weight, this row determines the minimum distance of the code, which is 2. Otherwise, the generator matrix cannot generate a self-dual code. The minimum weights of the Euclidean self-dual codes that are obtained by using this construction method can be seen in Table 3.

In Table 3, $d_{BDC}(n)$ is the minimum weight of a Euclidean self-dual code of length n obtained by applying the bordered double-circulant construction.

Table 3. The Euclidean self-dual codes obtained by using the bordered double-circulant construction

length n	$d_{max}(n)$	$d_{BDC}(n)$	length n	$d_{max}(n)$	$d_{BDC}(n)$
4	2	2	**56**	12-14	12
8	4	4	**60**	12-14	12
12	4	4	**64**	12-16	12
16	5	4	**68**	13-16	12
20	6	4	**72**	15-17	12
24	8	8	**76**	14-18	12
28	8	6	**80**	16-19	12
32	8	8	**84**	15-20	12
36	8	8	**88**	17-20	16
40	9-10	8	**92**	16-22	14
44	10	8	**96**	16-22	16
48	12	12	**100**	18-23	16
52	10-12	10			

4.3. The Symmetric Construction

In this construction, we find all orthogonal symmetric $k \times k$ matrices for $k \leq 8$. When $k \geq 9$, the search field is too big for obtaining all orthogonal symmetric $k \times k$ matrices. We use random orthogonal symmetric 9×9 matrices to obtain a Euclidean self-dual code of length 18. Since investigating a matrix which is both orthogonal and symmetric is a restrictive criterion, we do our search up to length 18.

The minimum weights of the Euclidean self-dual codes that are obtained by using this construction method are given in Table 4. In this table, $d_S(n)$ is the minimum weight of a Euclidean self-dual code of length n obtained by applying the symmetric construction.

Table 4. The Euclidean self-dual codes obtained by using the symmetric construction

length n	$d_{max}(n)$	$d_{BDC}(n)$
2	2	2
4	2	2
6	3	2
8	4	4
10	4	2
12	4	4
14	4	4
16	5	4
18	6	4

5. CONCLUSION

Our aim in this work was to apply construction methods mentioned above for obtaining Euclidean self-dual codes over the ring $\mathbb{F}_2 + v\mathbb{F}_2$. Comparing our results with $d_{max}(n)$, we see that our results are slightly close to $d_{max}(n)$ when we use the double-circulant construction. Our results are mostly close to $d_{max}(n)$ except when $n \equiv 2(mod\ 4)$ in the bordered double-circulant construction. The limited results obtained in the symmetric construction are coincide with the results obtained in the double-circulant construction except when $n = 14$.

ACKNOWLEDGMENTS

We sincerely thank to all colleagues who have inspired and supported us during the preparation of the manuscript. This work was supported by İstanbul University Scientific Research Projects Coordination Unit. Project Number: 29539.

REFERENCES

[1] C. Bachoc, "Applications of coding theory to the construction of modular lattices," *J. Combin. Theory Ser. A,* vol. 78, pp. 92-119, 1997.

[2] K. Betsumiya and M. Harada, "Optimal self-dual codes over $\mathbb{F}_2 \times \mathbb{F}_2$ with respect to the Hamming weight," *IEEE Trans. Inform. Theory*, vol. 50, pp. 356-358, 2004.

[3] W. Bosma, J. Cannon and C. Playoust, "The Magma algebra system I: The user

language," *J Symbolic Comput.*, vol. 24, pp. 235-265, 1997.

[4] A. E. Brouwer, Bounds on the size of linear codes, in: V. S. Pless, W. C. Huffman (Eds.), Handbook of Coding Theory, Elsevier, Amsterdam, pp. 295-461, 1998.

[5] Y. Cengellenmis, A. Dertli and S. T. Dougherty, "Codes over an infinite family of rings with a Gray map," *Des. Codes Cryptogr.*, vol. 72, pp. 559-580, 2014.

[6] J. H. Conway, N. J. A. Sloane, "A New Upper Bound on Minimal Distance of Self-Dual Codes," *IEEE Trans. Inform. Theory*, vol. 36, pp. 1319-1333, 1990.

[7] S. T. Dougherty, P. Gaborit, M. Harada, A. Munemasa and P. Solé, "Type IV self-dual codes over rings," *IEEE Trans. Inform. Theory,* vol. 45, pp. 2345-2360, 1999.

[8] S. T. Dougherty, M. Harada and P. Solé, "Self-dual codes over rings and the Chinese remainder theorem," *Hokkaido Math. J.*, vol. 28, pp. 253-283, 1999.

[9] S. T. Dougherty, J. L. Kim, H. Liu, "Constructions of self-dual codes over finite commutative chain rings*," Int. J. Inf. Coding Theory 1*, vol. 2, pp. 171-190, 2010.

[10] J. Gao, Y. Wang, J. Li, "Bounds on covering radius of linear codes with Chinese Euclidean distance over the finite non chain ring $\mathbb{F}_2 + \upsilon\mathbb{F}_2$," *Inf. Process. Lett.*, vol. 138, pp. 22-26, 2018.

[11] J. Gildea, A. Kaya, R. Taylor, B. Yildiz, "Constructions for self-dual codes induced from group rings," *Finite Fields Appl.*, vol. 51, pp. 71—92, 2018.

[12] C. A. Castillo-Guillén, C. Rentería-Márquez, H. Tapia-Recillas, "Duals of constacyclic codes over finite local Frobenius non-chain rings of length 4," *Discrete Math.*, vol. 341, pp. 919-933, 2018.

[13] R. Hill, A First Course in Coding Theory, Oxford University Press, 1986.

[14] S. Karadeniz, S. T. Dougherty and B. Yildiz, "Constructing formally self-dual codes over R_k," *Discrete Appl. Math.*, vol. 167, pp. 188-196, 2014.

[15] B. Kim, Y. Lee, "Lee Weights of Cyclic Self-Dual Codes over Galois Rings of Characteristic p^2," *Finite Fields Appl.*, vol. 45, pp. 107-130, 2017.

[16] J. L. Kim, Y. Lee, "An Efficient Construction of Self-Dual Codes," *Bull. Korean Math. Soc.*, vol. 52, pp. 915-923, 2015.

[17] J. Li, A. Zhang, K. Feng, "Linear Codes over $\mathbb{F}_q[x]/(x^2)$ and $GR(p^2, m)$ Reaching the Griesmer Bound," *Des. Codes Cryptogr.*, vol. 86, pp. 2837-2855, 2018.

[18] S. Zhu, Y. Wang and M. Shi, "Some results on cyclic codes over $\mathbb{F}_2 + \upsilon\mathbb{F}_2$," *IEEE Trans. Inform. Theory*, vol. 56, pp. 1680-1684, 2010.

JOURNAL OF SCIENCE
SAKARYA UNIVERSITY

Sakarya University Journal of Science

ISSN 1301-4048 | e-ISSN 2147-835X | Period Bimonthly | Founded: 1997 | Publisher Sakarya University | http://www.saujs.sakarya.edu.tr/

Title: Characterization of Functionally Graded Bronze Matrix Ceramic Reinforced Composite Materials

Authors: Serkan Islak, Aimen Mohamed Abushraıda
Recieved: 2019-06-09 22:40:54

Accepted: 2019-07-15 12:42:15

Article Type: Research Article
Volume: 23
Issue: 6
Month: December
Year: 2019
Pages: 1137-1143

How to cite
Serkan Islak, Aimen Mohamed Abushraıda; (2019), Characterization of Functionally Graded Bronze Matrix Ceramic Reinforced Composite Materials. Sakarya University Journal of Science, 23(6), 1137-1143, DOI: 10.16984/saufenbilder.574251
Access link
http://www.saujs.sakarya.edu.tr/issue/44246/574251

Sakarya University Journal of Science 23(6), 1137-1143, 2019

Characterization of Functionally Graded Bronze Matrix Ceramic Reinforced Composite Materials

Serkan Islak*[1], Aimen Mohamed Abushraida[2]

Abstract

In this study, ceramic reinforced bronze matrix functionally graded materials (FGMs) were produced by using powder metallurgy method. B_4C, TiC, Mo_2C and SiC were selected as ceramic reinforcements. The samples with compositions bronze + 10% SiC, bronze + 10% B_4C, bronze + 10% Mo_2C, and bronze + 10% TiC were sintered at 750 °C for 90 minutes. Investigations were carried out to assess the mechanical properties and microstructures of specimens. For this purpose, optical microscope, scanning electron microscope (SEM-EDS), and X-ray diffraction (XRD) analysis were applied for microstructure investigations. Sample hardness testing was carried out with the help of Vickers hardness testing device. Composite layers of ceramic particles were homogeneously distributed. Little pore formation was observed. While the upper and lower composite layers of the FGMs produced were hard, the middle layer was found to be ductile. The highest hardness value was reached in the B_4C reinforced FGM.

Keywords: FGM, bronze, ceramic reinforcements

1. INTRODUCTION

Functionally graded materials (FGMs) are advanced composite materials that are characterized by variations in their composition or microstructure in a specific direction. The desired properties can be achieved in a single bulk material of FGMs, which makes them highly applicable for mechanical and tribological applications [1-3]. FGMs having superior properties are produced by combining different reinforcement phases. This FGM strategy eliminates the use of high cost surface engineering in several applications [4,5]. The selection of the reinforcement helps to achieve a high-level graded performance in these FGMs [6-8]. The development of composite materials with graded properties known as FGMs led to a revolution in the manufacturing of mechanical parts, particularly in the automotive, aviation and biomedical industries [9-11]. FGMs' components have certain useful characteristic properties, which meet the specific needs of certain industrial

* Corresponding Author: serkan@kastamonu.edu.tr
[1] Kastamonu University, Mechanical Engineering, Kastamonu, Turkey. ORCID: 0000-0001-9140-6476
[2] Kastamonu University, Materials Science and Engineering, Kastamonu, Turkey. ORCID: 0000-0002-4475-8417

processes; therefore, they effectively overcome the shortcomings of traditional composite materials. FGMs have many advantages over conventional and composite materials, such as [12-15]: (i) FGMs have an interface layer, that is fully capable of attaching two components made of incompatible materials, which allows them to substantially increase the bond strength. (ii) FGM coating and interfaces can be used to reduce residual and thermal stresses. (iii) FGM coating can be used for connecting materials and eliminating endpoint and interface stresses. (iv) FGM coating not only enhances the strength of connections, as but it can also reduce the crack driving force [16-18].

During recent years, bronze matrix composites have gained widespread importance because they are utilizable in several technological applications. Since they have high conductivity but low mechanical strength, they are taken through dispersion strengthening process, which developed new composite materials with far better properties. Particles including carbides, oxides, and borides are not soluble in the bronze matrix. Moreover, they have high thermal stability to bear high temperatures that makes them a good choice for reinforcement process. Particulate-strengthened copper matrix composites allow making desirable improvements in the mechanical properties such as high temperature tolerance, improved tensile properties, increased stiffness, and better wear resistance [19-21].

In this study, ceramic reinforced bronze matrix FGMs were produced by using powder metallurgy method. Investigations were carried out to evaluate the mechanical properties and microstructures of specimens.

2. MATERIALS AND METHODS

The bronze (Cu-15Sn) powder was selected as the base matrix and the ceramic carbide reinforcements: B_4C, SiC, Mo_2C and TiC are chosen with 10% (mass fraction). The size and purity of the selected powder were: bronze powder (-325 mesh particle size, 99.9% purity), B_4C (-325 mesh particle size, 98% purity), SiC (400 mesh particle size, ≥ 97.5% purity), TiC (-325 mesh particle size, 98% purity), and Mo_2C (-325 mesh particle size, 99.5% purity). Figure 1 shows SEM images of the chosen powders used in the production of FGMs.

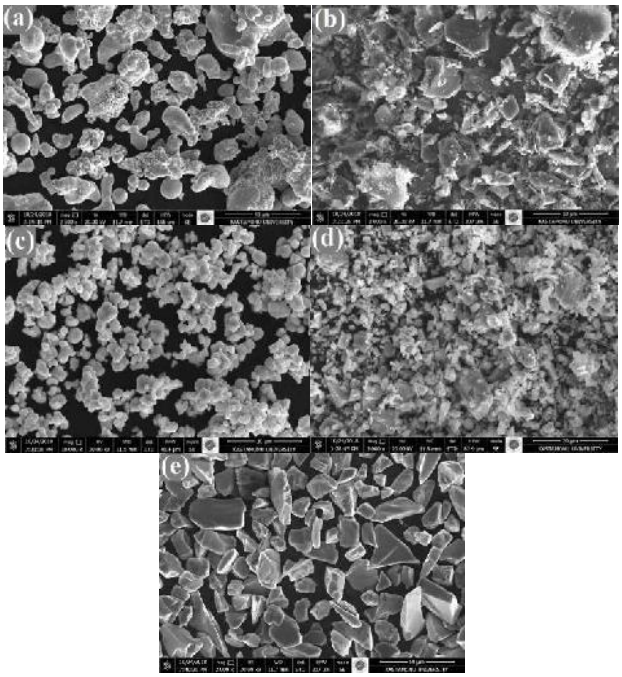

Figure 1. SEM images of powders:(a) bronze, (b) B_4C, (c) Mo_2C, (d) TiC, and (e) SiC

The test samples preparation for different types of reinforcements were carried out in several stages that are summarized in the following steps:

• Mixing: For the mixing process, the powders were subjected to mixing for 45 minutes at speed of 20rpm.

• Compact pressing process: In this process, the powders were placed in a cylindrical mold with a 13mm diameter. The 10% (mass friction) reinforcement powder was added to the powder matrix in lower and upper layers and pressed at 500MPa to produce a 6mm thick cylindrical composite sample with a 13mm diameter (with three 2mm layers), as shown in Figure 2.

• Sintering: The samples were sintered in a tube furnace under a protective argon gas atmosphere. The sintering temperature was 750 ºC and the duration was 90 min. with a heating and cooling

rate of 10 ºC/min. In the literature, the sintering temperature was not exceeded 700 ºC in order to avoid liquid phase sintering for Cu-15Sn [22].

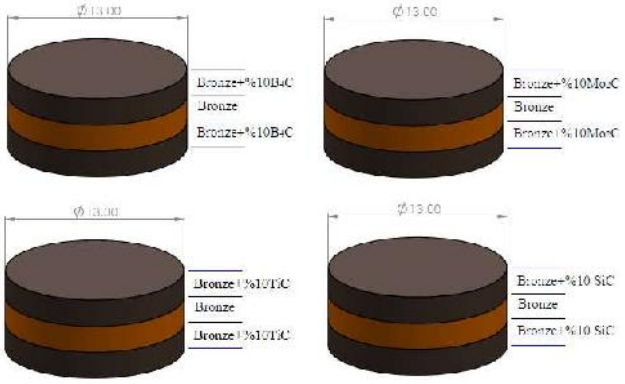

Figure 2. The samples shape and dimensions

For determining the hardness level of the produced samples, we used a Shimadzu HMV-G21 model digital microhardness machine at 200 g load. For accurate determination of hardness, hardness values were measured from the upper, middle, and lower layers of the samples. The hardness values of these layers were taken from different regions and these values were taken into the medium. These different hardness values are given as the error bar in the hardness graph.

For metallographic examinations, the obtained metallography samples were cleaned on 60-1200 mesh papers. Then, the surfaces of the samples were polished with the help of diamond spray. For microstructure investigations, the samples should be etched for 20 seconds in 5 g $FeCl_3$+50ml HCl+100 ml H_2O solution. Energy dispersive spectroscopy (EDS), scanning electron microscopy (SEM), and X-ray diffraction (XRD) were used to understand the phase structures. For SEM analysis, a FEI QUANTA 250 FEG brand SEM device was used. Phases of samples were identified by mean of X-ray diffraction using a Bruker D8 Advance model diffractometer.

3. RESULTS AND DISCUSSION

Figure 3-6 shows the structures of FGMs. In these photographs, triple (composite-middle-composite) layers and enlarged photographs of these regions as well as interface parts are seen in detail. The composite layers and the middle part are clearly distinguished. The B_4C, Mo_2C, TiC and SiC grains were distributed in a similar manner and relatively homogeneously in the bronze matrix. These ceramic particles are located in places where the bronze grains meet. There was no breakage and crack formation at the interface surface. Pore formation was observed in the FGMs.

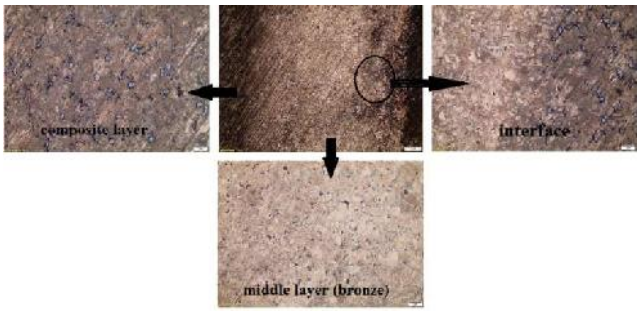

Figure 3. Optical microscope images of B_4C reinforced bronze matrix FGM

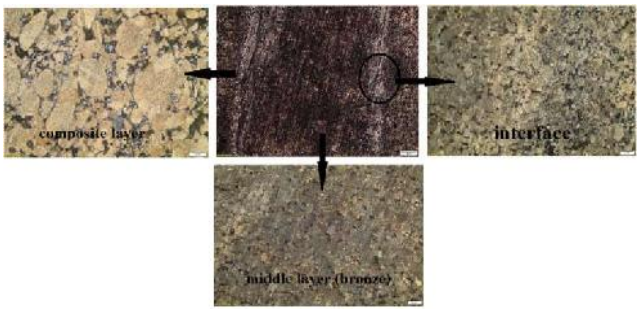

Figure 4. Optical microscope images of Mo_2C reinforced bronze matrix FGM

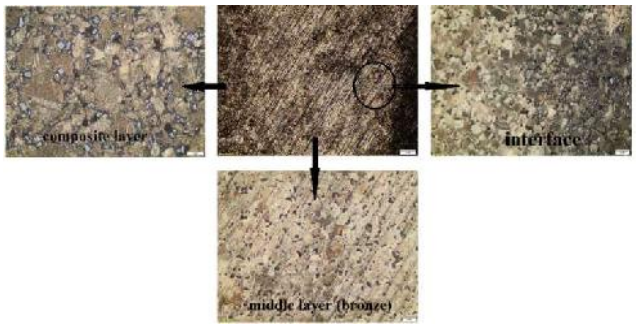

Figure 5. Optical microscope images of TiC reinforced bronze matrix FGM

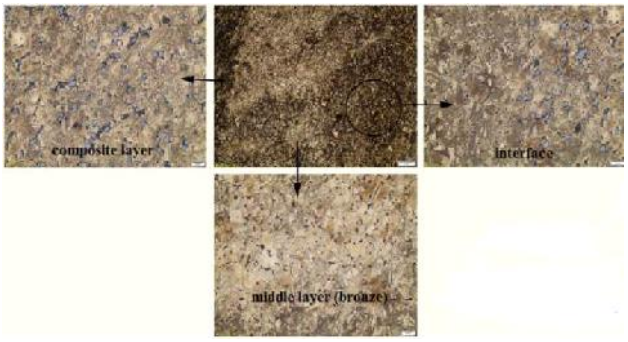

Figure 6. Optical microscope images of SiC reinforced bronze matrix FGM

FGMs have been analyzed by using SEM-MAP analysis to determine the distribution of reinforcing particles (Figure 7). The basic elements are Cu and Sn. The other elements are B, Mo, Ti, Si and C. It is clear that reinforcing particles are distributed uniformly. The homogeneous distribution of the elements has a positive effect on the physical, chemical and mechanical properties of the material [23].

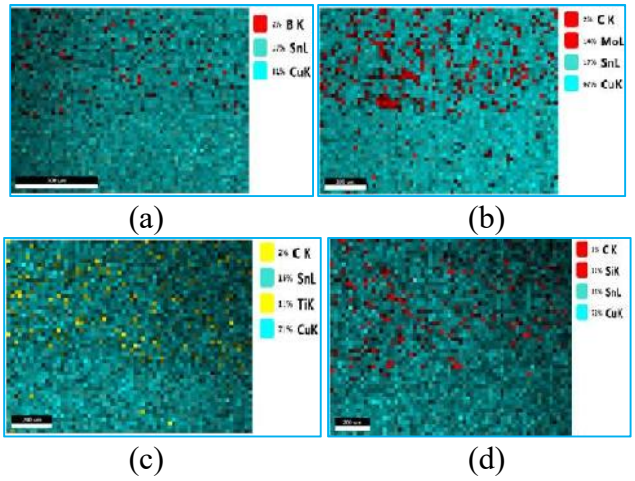

Figure 7. SEM-MAP analysis of FGMs: (a) B_4C, (b) Mo_2C, (c) TiC and (d) SiC

XRD analysis was performed for FGMs to determine whether a phase that would bind the matrix and the carbide particles at the interface. Figures 8 shows the XRD analysis of FGMs. No intermetallic compound was formed between the carbide particles and the matrix. This is due to the absence of any chemical reaction between the matrix and the carbides. In the bronze matrix, α-Cu and Cu_3Sn phases were formed as seen from XRD graphs. These phases were also identified in the literature on bronze [24]. In addition, carbide phases are clearly seen in XRD graphs.

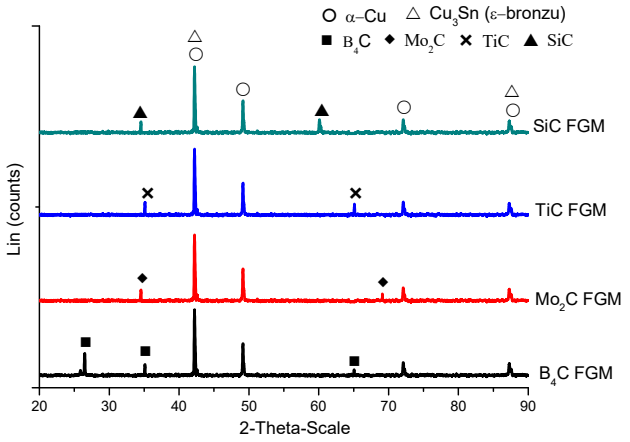

Figure 8. XRD analysis of the FGMs

The hardness graph of FGMs is shown in Figure 9. The hardness value of the middle layer is about 95 $HV_{0.2}$, while the hardness values of composite layers are 210 $HV_{0.2}$ for B_4C, 130 $HV_{0.2}$ for Mo_2C, 176 $HV_{0.2}$ for TiC and 197 $HV_{0.2}$ for SiC. The hardness of the composite layers is very high hardness compared to the middle layer. This rate of increase is about 35% in Mo_2C additive, 100% in SiC additive, 75% in TiC additive and approximately 121% in B_4C additive. Several factors cause a growth in hardness. The hardness of the composite elements, the dispersion strengthening effect and the effect of the hard particles on the movement of dislocations, depending on the mixture rule [25, 26]. Since the composite layers are harder than the middle layer, the wear resistance of the composite layers is expected to increase. This is in agreement with other studies [27-29]. An increase in fatigue strength is expected in FGMs with hard outer layers. This is another effect of high hardness on mechanical properties [30].

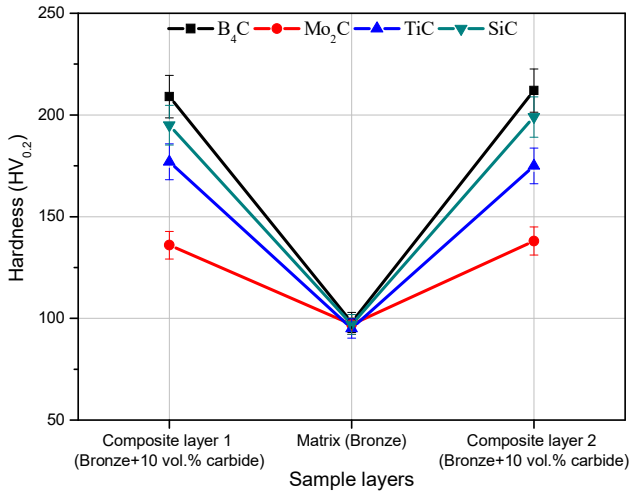

Figure 9. Hardness graph

4. RESULTS

In this study, the microstructure and hardness properties of the FGMs were experimentally investigated in detail. Ceramic reinforced bronze matrix FGMs were successfully produced by using powder metallurgy method. It is seen from both optical photographs and SEM-MAP images that ceramic particles were homogeneously distributed. At the microstructure, little pore formation was observed. The hardness of the FGMs showed an increase with reinforcements. While the hardness of the matrix was about 95 $HV_{0.2}$, the maximum hardness was measured in bronze-10%B_4C composite as 212 $HV_{0.2}$.

REFERENCES

[1] Z. Zhong-tao, L. Ting-ju, Y.Hong-yun, Z. Jian and L. Jie, “Preparation of Al/Si functionally graded materials using ultrasonic separation method”, *China Foundry*, 5, 3, pp. 194−198, 2008.

[2] S.C. Ram, K. Chattopadhyay and I. Chakrabarty, “High temperature tensile properties of centrifugally cast in-situ Al-Mg_2Si functionally graded composites for automotive cylinder block liners”, Journal of Alloys and Compounds, 724, pp. 84-97, 2017.

[3] N. Radhika and R. Raghu, “Development of functionally graded aluminum composites using centrifugal casting and influence of reinforcements on mechanical and wear properties”, *Transactions of Nonferrous Metals Society of China*, 26, pp. 905−916, 2016.

[4] S. Jamian, Y. Watanabe and H. Sato, “Formation of compositional gradient in Al/SiC FGMs fabricated under huge centrifugal forces using solid-particle and mixed-powder methods”, Ceramics International, 45, 7, pp. 9444-9453, 2019

[5] H. Kwon, G.G. Lee, M. Leparoux and A. Kawasaki, “Functionally graded dual-nano particulate-reinforced aluminum matrix composite materials”, *Journal of Physics: Conference Series*, 419, pp. 1−4, 2013.

[6] Y. Miyamoto, W.A. Kaysser, B.H. Rabin, A. Kawasaki and R.G. Ford, (1999). Functionally Graded Materials Design, *Processing and Applications. Springer, US, Boston*, 1999.

[7] S. Heuer, T. Lienig, A. Mohr, T. Weber, G. Pintsuk, J.W. Coenen and C. Linsmeier, “Ultra-fast sintered functionally graded Fe/W composites for the first wall of future fusion reactors”, Composites Part B: Engineering, 164, pp. 205-214, 2019.

[8] Z.L. Chao, L.T. Jiang, G.Q. Chen, J. Qiao, Z.H. Yu, Y.F. Cao and G.H. Wu, “The microstructure and ballistic performance of B_4C/AA2024 functionally graded composites with wide range B_4C volume fraction”, *Composites Part B: Engineering*, 161, pp. 627-638, 2019.

[9] G. Udupa, S.S. Rao and K.V. Gangadharan, “Functionally Graded Composite Materials: An Overview”, *Procedia Materials Science*, 5, pp. 1291-1299, 2014.

[10] S. Decker and L. Krüger, "Mechanical properties of a CrMnNi steel/Mg-PSZ-FGM processed by asymmetric Spark Plasma Sintering", Materials & Design, 115, pp. 8-16, 2017.

[11] A. Toudehdehghan, J.W. Lim, K.E. Foo, M.I.N. Ma'arof and J. Mathews, "A brief review of functionally graded materials", *MATEC Web of Conferences*, 131, EDP Sciences, 2017.

[12] G. Cui, Q. Bi, S. Zhu, L. Fu, J. Yang, Z. Qiao and W. Liu, "Synergistic effect of alumina and graphite on bronze matrix composites: Tribological behaviors in sea water", *Wear*, 303, 1-2, pp. 216-224, 2013.

[13] C. Wu, R. Shi, J. Zhang, G. Luo, Q. Shen, Z. Gan and L. Zhang, "Synthesis of functionally graded AA7075-B4C composite with multi-level gradient structure", Ceramics International, 45, 6, pp. 7761-7766, 2019.

[14] M. Uysal, R. Karslioglu, H. Akbulut and A. Alp, "Characteristics Bronze/Al_2O_3 (Ni) Reinforcement Metal Matrix Composite Produced by Current Activated Sintering", *Proceedings of the 2nd International Congress APMAS2012*, April 26-29, Antalya, Turkey, 2012.

[15] K. Arslan and R. Gunes, "Experimental damage evaluation of honeycomb sandwich structures with Al/B_4C FGM face plates under high velocity impact loads", Composite Structures, 202, pp. 304-312, 2018.

[16] R. Kumar and C.N. Chandrappa, "Synthesis and characterization of Al-SiC functionally graded material composites using powder metallurgy techniques", *International Journal of Innovative Research in Science, Engineering and Technology*, 3, 8, pp. 15464–15471, 2014.

[17] F. Erdemir, A. Canakci and T. Varol, "Microstructural characterization and mechanical properties of functionally graded Al2024/SiC composites prepared by powder metallurgy techniques", *Transactions of Nonferrous Metals Society of China*, 25, pp.3569–3577, 2015.

[18] D.T. Sarathchandra, S.K. Subbu and N. Venkaiah, "Functionally graded materials and processing techniques: An art of review", *Materials today: Proceedings*, 5 10, pp. 21328-21334, 2018.

[19] J. Sobczak and L. Drenchev, "Metallic Functionally Graded Materials: A Specific Class of Advanced Composites", *Journal of Materials Science & Technology*, 29, 4, pp. 297-316, 2013.

[20] M. Naebe and K. Shirvanimoghaddam, "Functionally graded materials: A review of fabrication and properties", *Applied Materials Today*, 5, pp. 223-245, 2016

[21] C.Y. Huang and Y.L. Chen, "Design and impact resistant analysis of functionally graded Al_2O_3–ZrO_2 ceramic composite", Materials & Design, 91, pp. 294-305, 2016.

[22] S. Islak and H. Çelik, "Effect of sintering temperature and boron carbide content on the wear behavior of hot pressed diamond cutting segments", *Science of Sintering*, 47, 2, pp. 131-143, 2015.

[23] S. Buytoz, F. Dagdelen, S. Islak, M. Kok, D. Kir and E. Ercan, "Effect of the TiC content on microstructure and thermal properties of Cu–TiC composites prepared by powder metallurgy", *Journal of Thermal Analysis and Calorimetry*, 117, 3, pp.1277-1283, 2014.

[24] S. Islak, D. Kir and H. Celik, "Investigation of the usability of cubic boron nitride cutting tools as an alternative to diamond cutting tools for the aircraft industry", *Archives of Metallurgy and Materials*, 58, 4, pp. 1119-1123, 2013.

[25] S. Yang, Z. Guo and M. Xia, "Effect of TiB Content on the Properties of Al-TiB

Composites", *Science of Sintering*, 50, 2, pp. 237-244, 2018.

[26] S. Islak, "Mechanical and Corrosion Properties of AlCu Matrix Hybrid Composite Materials", *Science of Sintering*, 51, 1, pp. 81-92, 2019.

[27] O. Carvalho, M. Buciumeanu, S. Madeira, D. Soares, F.S. Silva and G. Miranda, "Optimization of AlSi–CNTs functionally graded material composites for engine piston rings", *Materials & Design*, 80, pp. 163-173, 2015.

[28] S.R. Bakshi, D. Lahiri and A. Agarwal, "Carbon nanotube reinforced metal matrix composites – a review", *International Materials Reviews*, 55, 1, pp. 41–64, 2010.

[29] A.M. Al-Qutub, A. Khalil, N. Saheb and A.S. Hakeem, "Wear and friction behavior of Al6061 alloy reinforced with carbon nanotubes", *Wear*, 297, pp. 752–761, 2013.

[30] A. Bhat, Vamsi K. Balla, S. Bysakh, D. Basu, S. Bose and A. Bandyopadhyay, "Carbon nanotube reinforced Cu–10Sn alloy composites: mechanical and thermal properties", *Materials Science and Engineering: A*, 528, pp. 6727–6732, 2011.

JOURNAL OF SCIENCE
SAKARYA UNIVERSITY

Sakarya University Journal of Science

ISSN 1301-4048 | e-ISSN 2147-835X | Period Bimonthly | Founded: 1997 | Publisher Sakarya University | http://www.saujs.sakarya.edu.tr/

Title: Implementation of Polar Codes in 5G Systems with Different Waveform Modulations by Using USRP

Authors: Marwan Dhuheir, Sıtkı Öztürk
Recieved: 2019-03-06 19:02:23

Accepted: 2019-07-16 15:19:18

Article Type: Research Article
Volume: 23
Issue: 6
Month: December
Year: 2019
Pages: 1144-1153

How to cite
Marwan Dhuheir, Sıtkı Öztürk; (2019), Implementation of Polar Codes in 5G Systems with Different Waveform Modulations by Using USRP. Sakarya University Journal of Science, 23(6), 1144-1153, DOI: 10.16984/saufenbilder.536540
Access link
http://www.saujs.sakarya.edu.tr/issue/44246/536540

Sakarya University Journal of Science 23(6), 1144-1153, 2019

Implementation of Polar Codes in 5G Systems with Different Waveform Modulations by Using USRP

Marwan DHUHEIR*[1], Sıtkı ÖZTÜRK[2]

Abstract

Long Term Evolution (LTE) is an access technique that is used in radio networks. LTE provides high data bandwidth in transmitting data by providing flexibility against noise and interference. Orthogonal Frequency Division Multiplexing (OFDM) technique uses the FDM (Frequency Division Multiplexer) modulation technique to increase the amount of carried information over the wireless network. The OFDM signal is transmitted to the receiver at different frequencies which they are orthogonal to each other by dividing the bandwidth of a signal into smaller sub-carriers. Recently, the use of polar codes as a coding scheme in the new generation 5G systems has come to the communications markets. Polar codes as a channel coding scheme are a promising technique for the future because it is the first codes that reach Shannon capacity limit. The cyclical prefix – OFDM (CP-OFDM), which is used in 4G systems, performs well in many aspects, however, it has much weakness that make the researches look for a new modulation technique to be used in 5G systems. Filtered–OFDM (F-OFDM) is considered one solution to the problems appeared in CP–OFDM. In this paper, the differences between CP-OFDM and F-OFDM regarding advantages and disadvantages of each type are studied in details. The comparison between the two modulations waveforms are done by studying their Error Vector Magnitude (EVM) that deals with measuring the accuracy of the received signals. Furthermore, the comparison between the two modulations waveforms with polar codes in the USRP B210 radio are applied to make our work more practical.

Keywords: Polar Codes, USRP, CP-OFDM, F-OFDM.

1. INTRODUCTION

Coding and modulation are considered the most two important factors in the communication channel coding theorem. Unfortunately, information sent over a noisy channel is inevitably affected by any kind of noise. One of the most important questions in the channel coding theorem is at what rate we can send information reliably through any noisy channel. One way to recover the data sent correctly or with negligible errors is to add redundancy bits. This method is known as channel coding, and it is crucial in communication systems. An effective

* Corresponding Author: aldhuheir2011@gmail.com
[1]Kocaeli University, Electronics and Communication Engineering, Kocaeli, Turkey. ORCID: 0000-0001-8344-2880
[2] Kocaeli University, Electronics and Communication Engineering, Kocaeli, Turkey. ORCID: 0000-0003-3804-5581

coding method is the one that adds redundancy bits in case of having high code rate and gets a low error. Shannon in [1] defined the rate of transmitting data reliably over a channel. This theorem is known as "the channel coding theorem". One important issue is how to design a practical code that achieves the Shannon capacity limit. Polar codes are provably the first codes that achieve the limit of Shannon capacity. Polar codes belong to the class of capacity-achieving linear Forward Error Correction (FEC) block codes with encoding and decoding complexity of $O(NlogN)$, in which N refers to the code block-length. The block error probability of the Successive Cancellation (SC) decoder is approximately less than $2\^(-\sqrt{N})$ [2]. Constructing polar codes is done by transforming the physical channel into virtual channels. The virtual channels are distributed into either good channels or bad channels. In other words, the channels are polarized into perfect channels that have high channel capacities or useless channels that have low channel capacities. Moreover, in this paper, we don't give details about polar codes for an introduction, we recommend referring to [2], [3], [4].

OFDM is an encouraging technique for getting high-data-rate that is required by the telecommunication engineers as it might defeat inter-symbol interference (ISI) that is come from the multipath fading in the wireless channels. OFDM is considered a set of two techniques which are modulation and multiplexing. Modulation refers to the method of mixing the information on changes occurred in the carrier signal. This carrier might be in phase, frequency or amplitude or a combination of them. Multiplexing refers to the signals that are independent of each other and come from various sources; therefore we care about sharing spectrum with many users. In OFDM, the independent signals actually are a sub-set of the main signal. However, the main signal is divided into different channels, then modulated by the data and again go to the multiplexing step in order to get OFDM carrier signal. OFDM is considered a special case of FDM. To explain the concept FDM and OFDM, we can think that a FDM signal is like water flow coming by faucet and OFDM is like water coming from the shower as in Figure 1.

Figure 1. (a) Regular FDM single carrier, all water comes from the single big faucet (b) OFDM, the same amount of water comes from different holes [5]

In case of water coming from the faucet, all water flows through a single big stream which cannot be split into subsets. On the other hand, we can think of the shower is like OFDM which the signal is divided into sub-sets. In the case of the faucet, if we put the thumb over the hole, the water will be stopped from flowing, while in case of the shower, if we do the same though, the water will not be stopped and will be still flowing. This means if there is interference in the FDM, the signal will be obstructed, however in the case of OFDM, it will be possible to send the data.

OFDM is considered one special case of multicarrier modulation technique [6], and it was used firstly in the military section. It was Weinstein in 1971 who carried out OFDM by the means of a Discrete-time Fourier Transform (DFT) [7]. Its computational process was very complicated and it was simplified by a Fast Fourier Transform (FFT). In first days, OFDM was not commonly used because of the expense in FFTs' execution and VLSI technologies offered easy and cheap execution of FFTs and IFFTs. It was Cimini, in the 1980s, who explored the use of OFDM technique in the field of wireless communication [8]. In the years of 1990s, OFDM stated to get in many sides of technologies including by Digital Audio Broadcasting (DAB), Digital Video Broadcasting (DVB), Asymmetric Digital Subscriber Line (ADSL) and IEEE802.11a. The main objective of OFDM is to mitigate the ISI caused by multipath fading, therefore, the whole channel is divided into sub-channels and the total data rate is transmitted in the small sub-channels. This gives

us an advantage of sending data in N times greater compared to a single big carrier channel.

Although the OFDM systems offer the solution for the interference, it has two drawbacks that make us look for another solution to mitigate the interference; the first drawback is the large Peak-to-Average Power Ratio (PAPR). The big difference between OFDM and regular FDM with a single carrier in the PAPR gives us a nonlinear distortion of the sent signal. Therefore this decreases the efficiency of many devices such as power amplifiers. The drawback of OFDM is the sensitivity to two main parameters, one is Doppler frequency and the other is the carrier offset of the signal as they related to the sub-channels bandwidth which the bandwidth between them is very small. Since the space between the sub-channels is very small, any small variation in the OFDM symbol or frequency offset will be destroyed and gives us another problem which is Inter-Carrier Interference (ICI) [9], [10].

One of the main advantages of OFDM over single-carrier patterns is the ability to deal with multiple channel conditions while there is no need for complex equalization filters. In OFDM, the channel equalization is simple because it deals with small modulated narrow-band signals rather than just only one modulated signal as in single carrier schemes. The narrowband carrier rates take the advantage of guard intervals between symbols affordable and this guard helps delete the noise such as ISI, mitigate echoes and time spreading to offer the property of diversity that helps improve Signal to Noise Ratio (SNR).

2. CP-OFDM AND F-OFDM

CP that transmitted during the guard interval contains the copy data of the end of OFDM signal. The advantage of copying the end of OFDM signal is that at the receiver side, the receiver will be able to integrate over a specific number of sinusoid cycles for every multipath signal at OFDM demodulation process with FFT. Figure 2 demonstrates the conventional OFDM in which the input symbols are modulated by using IFFT then CP is added to the output samples.

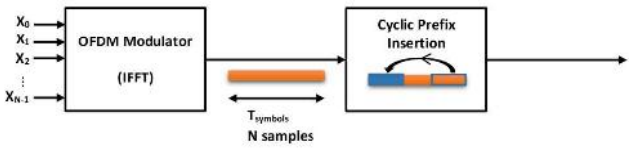

Figure 2. Conventional OFDM

F-OFDM is a technique of using filters to sub-band carriers. This method helps conventional CP-OFDM increase the system flexibility. However, it has a disadvantage of increasing system complexity.

2.1. CP-OFDM

The most important point of OFDM is to use low symbol rate schemes in parallel instead of sending one single symbol modulation scheme which suffer from ISI caused by many sources such as multipath propagations. Each symbol is long and to prevent ISI, it is suggested to insert a guard interval between symbols. This guard has many advantages such as decreasing the sensitivity of devices to time synchronization and eliminating the filters like a pulse shaping filter.

One simple example is that suppose one million symbols per second is sent over a channel by using single carrier modulation, the duration period of symbols is equivalent to one microseconds or less. This exposes that synchronization will be difficult and the interference is high. If the same amount of data is applied to one thousand sub-channels, then duration period of every symbol rate will be longer by amount of a thousand i.e. one millisecond for orthogonal symbols where the bandwidth is the same. Let us suppose that there is 1/8 a guard interval between every symbols. ISI could be mitigated in case of multipath time spreading, which is the measured time between the first received symbol and the last echo signal, is shorter than the guard interval i.e. 125 microseconds. This equivalents to maximum difference of 37.5 km which is the length of the paths [11].

2.2. F-OFDM

Technologies related to physical layer of wireless communication is introduced recently such as

waveform modulation. CP-OFDM has many advantages such as it offers high efficiency, its implementation is simple and it can be combined with MIMO technology easily, etc., so it was adopted in 4G-LTE, Wi-Fi and many wireless communication technologies. However, it has disadvantages such as out-of-band power leakage, it requires high quality requirements for synchronization, and the whole bandwidth could be created by the same waveform parameters, i.e. the subcarrier spacing and CP length.

As 4G, 5G needs to support more diverse traffics shapes. Moreover, in 5G, different scenario of traffics should be considered such as the traffics that come from vehicle to vehicle and the low cost machines' traffics and at the same time it should preserve the same advantages of conventional CP-OFDM.

Therefore F-OFDM was introduced. F-OFDM works by applying sub-band filtering on CP-OFDM in which it could meet the required improvement for 5G systems. The bandwidth is divided to into sub-bands and each band is filtered separately. Each sub-band is configured with various waveforms parameters set according to the existed traffic scenario. During the process of filter configuration, every sub-band is configured independently and creates 5G waveform that has the ability to provide dynamic parameter configuration for the physical layer according to the specific traffic scenario. The frequency spacing between the subcarriers might be different with every sub-band. By using this method, we can get a flexible structure of sub-frames that contain many types of data services in the same sub-frame. It is supposed to adopt this flexible waveform structure to 5G systems. Figure 3 explains the configuration of F-OFDM. The sub-band samples are gathered together in order to add the required filter to them.

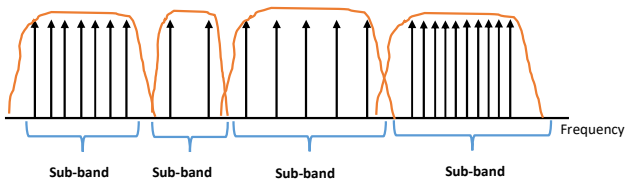

Figure 3. F-OFDM configuration

Figure 4 shows a comparison between conventional CP-OFDM and F-OFDM. In CP-OFDM, the whole band is configured from a single block and the frequency spacing between every sub-carrier is the same. However, in F-OFDM, the whole band is created from various sub-blocks. Moreover, the space frequency between sub-bands is also different i.e. the space frequency of sub-carrier for N_1 is Δf/2 and the space frequency of the sub-carrier N_k is 4Δf. We can see that each sub-band has its own CP and each sub-band has its own filter.

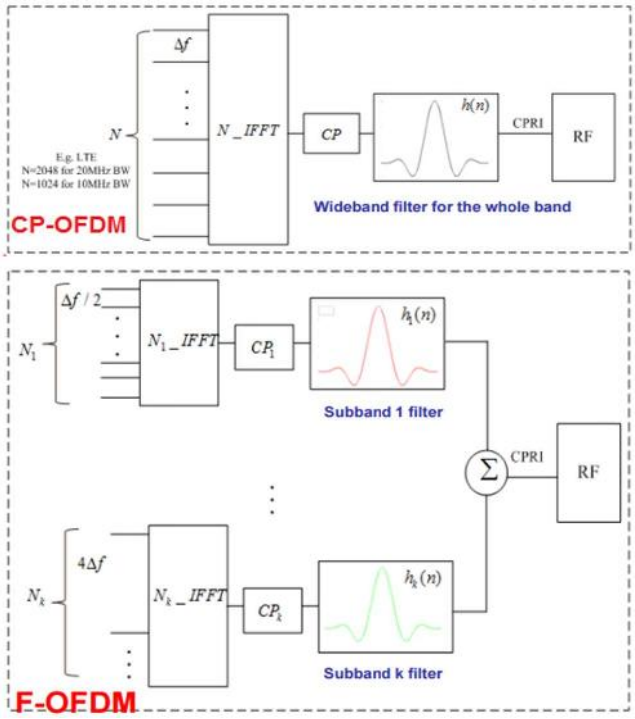

Figure 4. CP-OFDM and F-OFDM comparison [12]

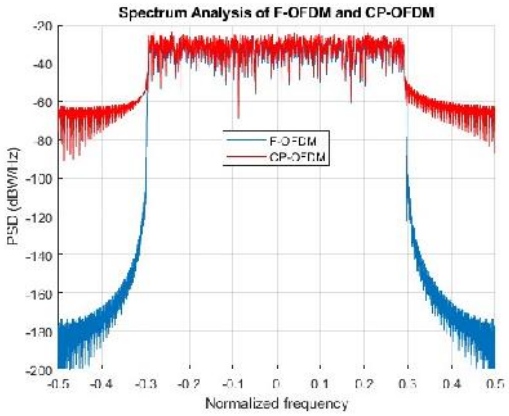

Figure 5. CP-OFDM and F-OFDM spectrum analysis comparison

We can mention that the main advantage of F-OFDM is the flexibility that it provides and the main disadvantage is that its complexity of the structure and implementation is higher than that achieved by CP-OFDM.

Figure 5 shows the comparison between CP-OFDM and F-OFDM in case of spectrum analysis. From the figure, it is clear that F-OFDM has a betterr resistance against noise.

3. TRANSMISSION AND RECEPTION USING POLAR CODES WITH CP-OFDM AND F-OFDM IN USRP RADIO DEVICE

In this part, we used two USRP radios to send data from one device and receive it in the other device with using polar codes as a channel coding scheme. We used LTE- MIMO system to do the experiment in which MIMO 2×2 was used with the diversity property as shown in Figure 6. We sent the string "Kocaeli University" from one USRP device and successfully received it in the other USRP device. We started the work by not introducing any external noise and left the environment noise just only and successfully received the data. In the next step, we added AWGN to the received signal and it was successfully decoded and recovered in the host computer as it is shown in this part.

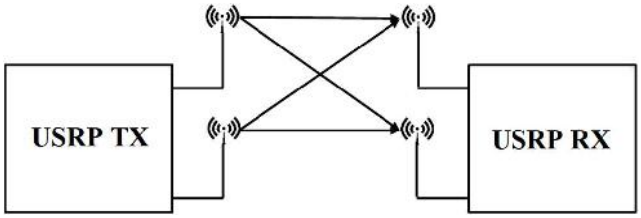

Figure 6. The circuit of USRP MIMO 2×2 antennas

3.1. Universal Software Radio Peripheral (USRP)

USRP is defined as a range of software-defined radios. These software radios allow users to do their experiments with radio waves. USRPs are used by connecting them with host computers through the different speed of links. The software is used to control the hardware in the USRP and transmit or receive data at high-speed links. The USRP B210 hardware works with RF frequencies from 70 MHz to 6 GHz in which it has a Spartan 6 Field Programmable Gate Array (FPGA), and work with USB 3.0 connectivity.

The construction of the USRP platform allows it to work with experiments with a wide range of signals such as FM and TV broadcasting, cellular, Wi-Fi, and so forth. USRP B210 extends the capabilities of B200 by offering more features such as the ability to work with MIMO 2×2, working with a larger FPGA, General Purpose Input/output (GPIO), and it has an external power supply.

The USRP B210 uses an Analog Device RFIC in order to deliver a cost-effective RF experimental platform, and it has the ability to work with 56 MHz of instantaneous bandwidth over a high-bandwidth USB 3.0 connectivity [13].

3.1.1. Transmit blocks

The process of transmission starts when the host computer generates the baseband in-phase (I) and quadrature-phase (Q) signals and sends these signals to the USRP through a USB 3.0 or USB 2.0. Then, the signal needs to be mixed, filtered and interpolated to 64.44 MS/s by the digital up-converter (DUC). The output digital signal is converted to analog by the digital to analog converter (DAC). The output signal is passed through a bandpass filter to mitigate the noise and high-frequency components. The output signal is passed to the mixer in order to up-convert the signal to a user-specified RF frequency. The Phase-Locked Loop (PLL) controls the Voltage-Controlled Oscillator (VCO) in order to make the device clocks and Local Oscillator (LO) will have the ability to be frequency-locked to a reference signal. The final block is the amplifier in which their function is to amplify the signal and transmits it through the antennas [14].

3.1.2. Receiver blocks

The received part starts with the low noise amplifier in which it amplifies the incoming signal. Then the PLL controls the VCO oscillator in order to make the device clocks the LO oscillator can be frequency locked to a reference

signal. After that, the mixer down-converts the signals to I/Q components and pass the signal to the band-pass filter to reduce the noise and high-frequency components from the signal. Then the analog-to-digital converter (ADC) digitizes the (I) and (Q) data. The next block is Digital Down-converter (DDC) and their function is to mixes, filters and decimates the signal to a user-specified rate. The last step is to pass the down-converted samples to the host computer by the USB 3.0 or 2.0 connections.

3.2. LTE Transceiver Application Using Polar Codes as a Channel Coding With MIMO

Figure 7 shows the figure of two computers with the two USRP B210 devices. The parameters of USRP that used in the experiment are shown in Table 1.

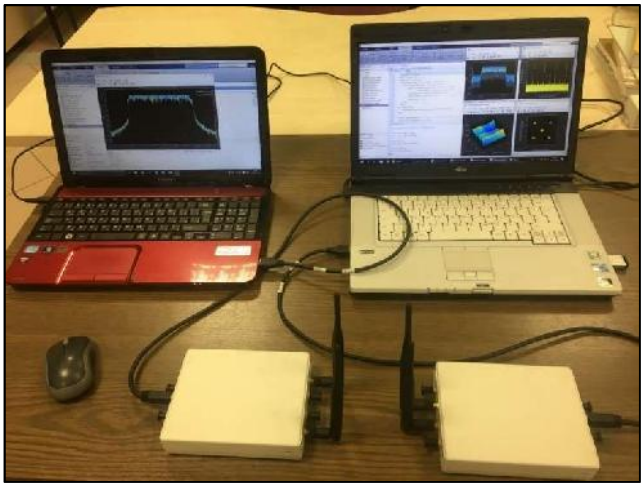

Figure 7. Transmission and reception using two USRP radio devices

The transmission and reception were done by using MIMO 2×2 by using the diversity property in which the data is sent over two antennas to combat the fading and improve the gain of transmission. Moreover, the duplex mode that was used in this transmission is Frequency Division Duplexing (FDD). In the first time, we sent data without adding AWGN as external noise and in the second time, we added noise with SNR is equal to 20dB. We compare between LTE-MIMO system without noise and the same system with AWGN noise in the value of EVM that deals with the accuracy of transmitted symbols within constellation i.e. it measures the quality of signals. In both cases, we were able to recover the transmitted data however the result of EVM was higher with noise and the shape of (I) and (Q) components were not uniform and the antennas were not also uniform in case of adding noise. The following sections explain transmission and reception without noise first then with noise and the comparison between them will be explained as well. In this experiment, we used polar codes as the channel coding scheme and the rate matching polar encoder and the decoder is Successive Cancellation List Decoder with Cyclic Redundancy Check vector (SCL-CRC) that explained in [4].

Table 1. The parameters of the transceiver of USRP radio with LTE-MIMO 2×2

USRP Type	B210
Center Frequency	2.45 GHz
Gain	35 dB
Samples per Frame	19200
Channel Mapping	[1 2]
Master Clock	6×10^6
Interpolation Factor	4
Channel Coding Scheme	Polar Codes
List Size (L)	16
CRC	19

3.2.1. Polar codes implementation in LTE systems with CP-OFDM

In this part, we used LTE systems with polar codes as a channel coding scheme in CP-OFDM waveform type. The parameters used in this transmission are shown in Table 2.

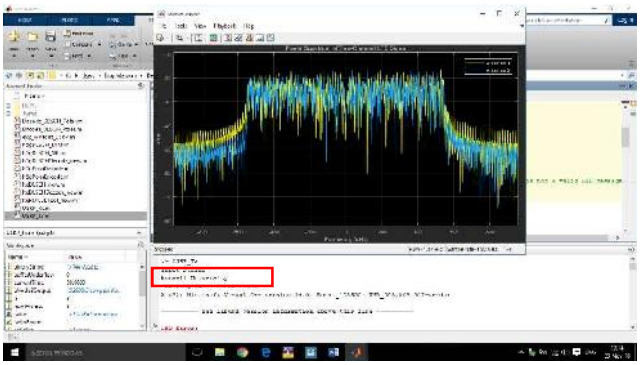

Figure 8. Transmitter spectrum with CP-OFDM and MIMO 2×2

The channels spectrum of the transmitter are shown in Figure 8. Figure 9 shows the reception spectrum of the receiver, constellation diagram, threshold synchronization and channel frequency details. Figure 10 shows MIMO 2×2 antennas channel coefficients. In these figures, we didn't add external noise hence the transmitter spectrum is almost the same of the receiver spectrum. The peak EVM is equal to 21.341dB and the RMS EVM is equal to 8.632dB. The transmitted string is successfully recovered as shown in Figure 9.

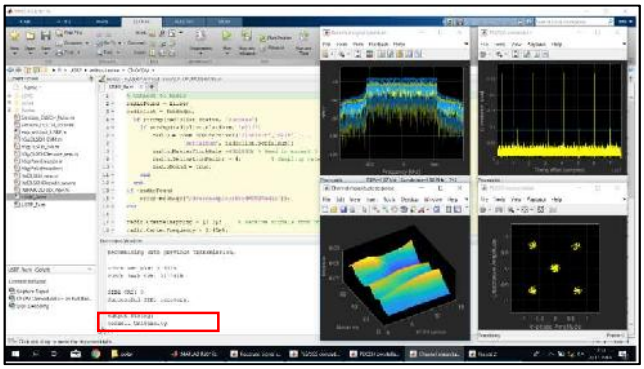

Figure 9. Reception signals with CP-OFDM and MIMO 2×2

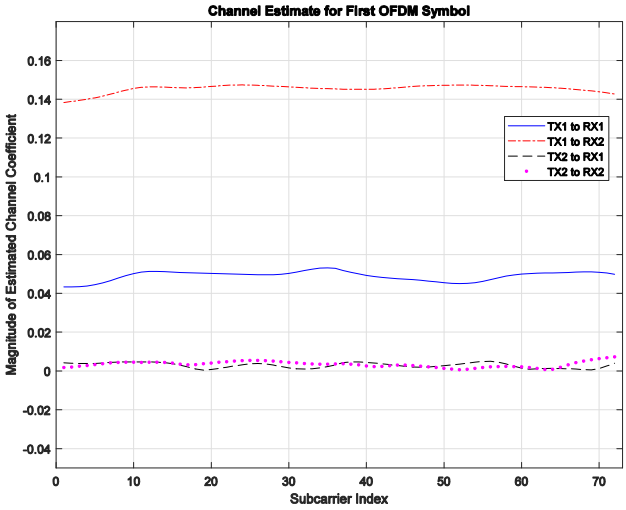

Figure 10. Channel estimation coefficient of MIMO 2×2 and CP-OFDM

Table 2. Configuration of LTE signal with CP-OFDM

Number of resource blocks	6
Cyclic prefix type	Normal
Duplex mode	FDD
Number of cell identity	64
Coding type	QPSK
Transmission Scheme	Transmission diversity
Channel coding scheme	Polar codes
Modulation Type	CP-OFDM
MIMO type	MIMO 2×2

3.2.2. Polar codes implementation in LTE systems with F-OFDM

In this part, we used LTE systems with polar codes as a channel coding scheme in F-OFDM waveform type. The parameters used in this transmission are shown in Table 3. The channels spectrum of the transmitter are shown in Figure 11. Figure 12 shows the reception spectrum of the receiver, constellation diagram, threshold synchronization and channel frequency details. Figure 13 shows MIMO 2×2 antennas channel coefficients. In these figures, we didn't add external noise hence the transmitter spectrum is almost the same of the receiver spectrum. The peak EVM is equal to 59.838dB and the RMS EVM is equal to 9.054dB. The transmitted string is successfully recovered as shown in Figure 12.

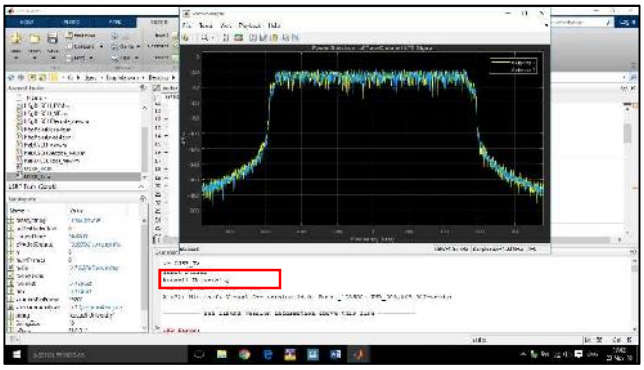

Figure 11. Transmitter spectrum with F-OFDM and MIMO 2×2

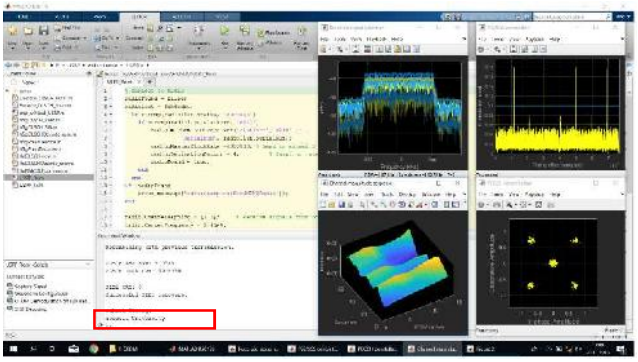

Figure 12. Reception signals with F-OFDM and MIMO 2×2

Table 3. Configuration of LTE signal with F-OFDM

Number of resource blocks	6
Cyclic prefix type	Normal
Duplex mode	FDD
Number of cell identity	64
Coding type	QPSK
Transmission Scheme	Transmission diversity
Channel coding scheme	Polar codes
Modulation Type	F-OFDM
MIMO type	MIMO 2×2

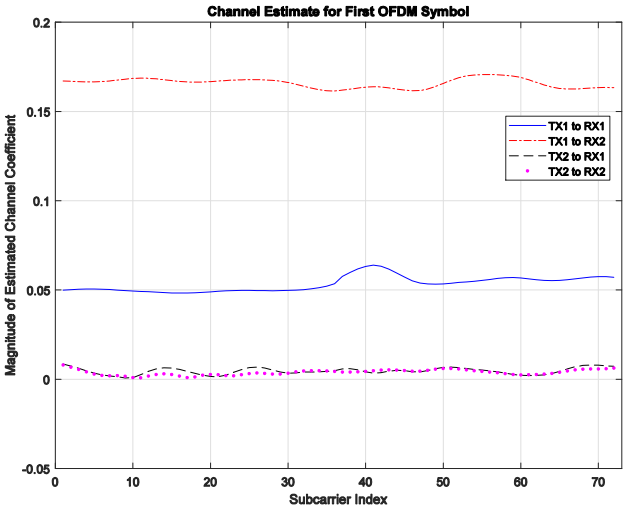

Figure 13. Channel estimation coefficient of MIMO 2×2 and F-OFDM

3.2.3. Polar codes implementation in LTE systems with CP-OFDM and AWGN noise.

In this part, we used LTE systems with polar codes as a channel coding scheme in CP-OFDM waveform type and we added AWGN noise. The parameters used in this transmission are shown in Table 4. The channels spectrum of the transmitter are shown in Figure 8. Figure 14 shows the reception spectrum of the receiver, constellation diagram, threshold synchronization and channel frequency details. Figure 15 shows MIMO 2×2 antennas channel coefficients. In these figures, we added AWGN noise hence the transmitter spectrum is not almost the same of the receiver spectrum. The peak EVM is equal to 135.553dB and the RMS EVM is equal to 60.918dB. The transmitted string is successfully recovered as shown in Figure 14.

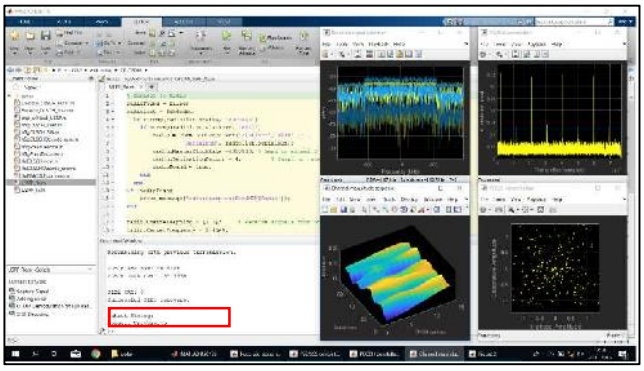

Figure 14. RX signal using MIMO 2×2, CP-OFDM and polar codes with noise

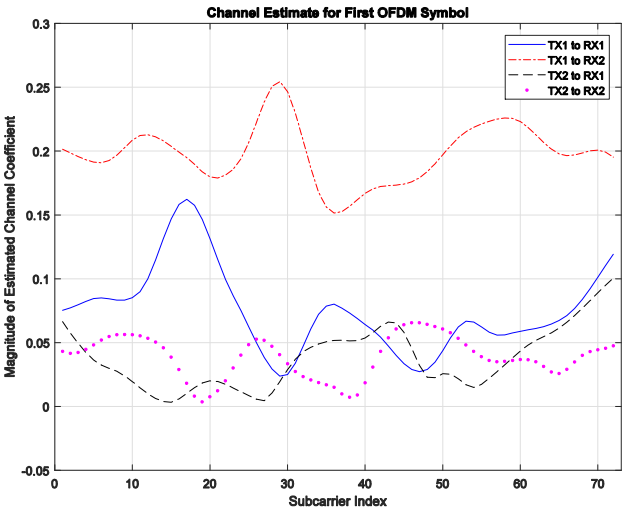

Figure 15. Channel estimation of OFDM symbols

Table 4. Configuration of LTE signal with CP-OFDM

Number of resource blocks	6
Cyclic prefix type	Normal
Duplex mode	FDD
Number of cell identity	64
Coding type	QPSK
Transmission Scheme	Transmission diversity
Channel coding scheme	Polar codes
Modulation Type	CP-OFDM
MIMO type	MIMO 2×2
SNR (for noise)	20 dB

3.2.4. Polar codes implementation in LTE systems with F-OFDM and AWGN noise

In this part, we used LTE systems with polar codes as a channel coding scheme in F-OFDM waveform type and we added AWGN noise. The parameters used in this transmission are shown in Table 5. The channels spectrum of the transmitter are shown in Figure 11. Figure 16 shows the reception spectrum of the receiver, constellation diagram, threshold synchronization and channel frequency details. Figure 17 shows MIMO 2×2 antennas channel coefficients. In these figures, we added AWGN noise hence the transmitter spectrum is not almost the same of the receiver spectrum. The peak EVM is equal to 176.059dB and the RMS EVM is equal to 63.998dB. The transmitted string is successfully recovered as shown in Figure 16.

Table 5. Configuration of LTE signal with F-OFDM

Number of resource blocks	6
Cyclic prefix type	Normal
Duplex mode	FDD
Number of cell identity	64
Coding type	QPSK
Transmission Scheme	Transmission diversity
Channel coding scheme	Polar codes
Modulation Type	F-OFDM
MIMO type	MIMO 2×2
SNR (for noise)	20 dB

Table 6. Comparison between CP-OFDM and F-OFDM

	CP-OFDM	F-OFDM	CP-OFDM	F-OFDM
	(without noise)		(with noise)	
peak EVM (dB)	21.341	59.838	135.55	176.059
RMS EVM (dB)	8.632	9.054	60.918	63.998

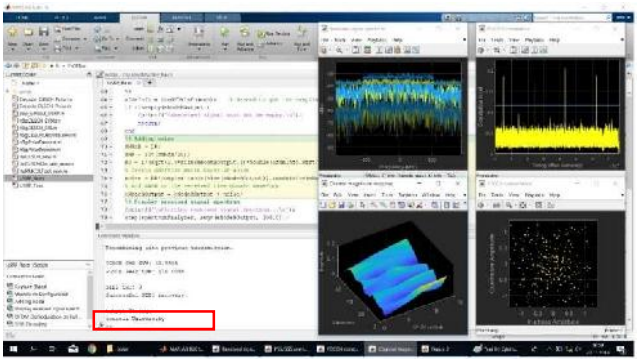

Figure 16. Rx signal using MIMO 2×2, F-OFDM and polar codes with noise

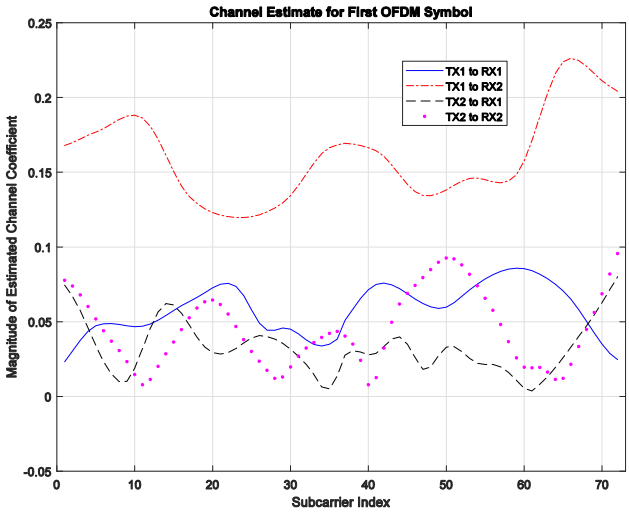

Figure 17. Channel estimation of F-OFDM symbols with noise

4. CONCLUSION

During this study, we studied two different waveforms that are expected to be used in 5G systems. The new coding scheme, polar codes were used in this study to show the transmission and reception process. Firstly, the difference between conventional CP-OFDM and then F-OFDM was presented in details. Then the advantages and disadvantages of using each waveform were mentioned. Although F-OFDM waveform achieves more flexibility than CP-OFDM, it increases the system complexity.

In the practical part of this study, we sent and received data by using LTE-MIMO 2×2 with using polar codes as the channel coding scheme in two USRP radios. A string was sent through one USRP device and successfully received by

another USRP device in all cases. Firstly, we did the experiment by sending and receiving the signal without using external noise and left the noise of the environment and successfully received the signal. In the second time, we added AWG noise to the received signal with SNR = 20 dB and successfully received the signal. We used polar codes with rate-match set and SCL-CRC with L = 16.

Table 6 summarizes the result of transmission and reception among the two USRP radio devices. It can be concluded that the EVM value of CP-OFDM is better than that of F-OFDM in both cases (peak and RMS). This means that the accuracy of received symbols in CP-OFDM is better than that received by F-OFDM.

5. REFERENCES

[1] C. E. Shannon, "A mathematical theory of communication", SIGMOBILE Mob Comput Commun Rev, vol. 5, no. 1, pp. 3–55, 2001.

[2] A. Erdal. "Channel polarization: A method for constructing capacity-achieving codes for symmetric binary-input memoryless channels", IEEE Transactions on Information Theory, vol. 55 no. 7, pp. 3051-73, 2009.

[3] K. Niu, K. Chen , J. Lin, Q. T. Zhang, "Polar codes: Primary concepts and practical decoding algorithms", IEEE Communications magazine, vol. 52, no. 7, pp. 192-203, 2014.

[4] D. Marwan and Ö. Sıtkı, "Polar Codes Applications for 5G Systems", Erciyes University, Journal of Institute Of Science and Technology, vol. 34, no. 3, 2018.

[5] Langton C., "OFDM Tutorial from Complex to Real", December 17, 2012, https://www.rfmentor.com/content/ofdm-tutorial-complex-real, [Accessed Date: 11 Dec. 2018].

[6] R. W. Chang, "Synthesis of band-limited orthogonal signals for multichannel data transmission", Bell Syst. Tech. J., vol. 45, pp. 1775-1796, 1966.

[7] S. B. Weinstein and P. M. Ebert, "Data transmission by frequency-division multiplexing using the discrete Fourier transform," IEEE Trans. on Comm., vol.COM-19, pp. 628-634, 1971.

[8] L. J. Cimini, Jr., "Analysis and simulation of a digital mobile channel using orthogonal frequency division multiplexing," IEEE Trans. on Comm., vol. 33, pp. 665-765, 1985.

[9] M. Russell and G. L. Stüber,"Interchannel interference analysis of OFDM in a mobile environment," in Proc. VTC'95, 1995, pp. 820-824.

[10] Y. G. Li and L. J. Cimini, Jr., "Bounds on the interchannel interference of OFDM in time-varying impairments communications," IEEE Trans. on Comm., vol. 49, pp. 401-404, 2001.

[11] X. Zhang, M. Jia, L Chen, J. Ma, J. Qiu, "Filtered-OFDM-enabler for flexible waveform in the 5th generation cellular networks". InGlobal Communications Conference (GLOBECOM) IEEE, vol. 6, pp. 1-6, 2015.

[12] Altera University Program " 5G : The 1st 5G Algorithm Innovation Competition F - OFDM " , Presentation , May 21 , 2016 .

[13] Ettus Research, http://home.ettus.com/ [Accessed Date: 25 Nov. 2018].

[14] National Instruments, USRP-2901 Block Diagram, http://www.ni.com/documentation/en/usrp-software-defined-radio-device/latest/usrp-2901/block-diagram/ [Accessed Date: 25 Nov. 2018].

JOURNAL OF SCIENCE
SAKARYA UNIVERSITY

Sakarya University Journal of Science

ISSN 1301-4048 | e-ISSN 2147-835X | Period Bimonthly | Founded: 1997 | Publisher Sakarya University | http://www.saujs.sakarya.edu.tr/

Title: On the axial crush performance of PVC foam-filled aluminum/CFRP hybrid circular tube

Authors: Muhammet Muaz Yalçın, Kenan Genel
Recieved: 2019-06-24 10:53:21

Accepted: 2019-08-09 10:51:05

Article Type: Research Article
Volume: 23
Issue: 6
Month: December
Year: 2019
Pages: 1154-1162

How to cite
Muhammet Muaz Yalçın, Kenan Genel; (2019), On the axial crush performance of PVC foam-filled aluminum/CFRP hybrid circular tube. Sakarya University Journal of Science, 23(6), 1154-1162, DOI: 10.16984/saufenbilder.581542
Access link
http://www.saujs.sakarya.edu.tr/issue/44246/581542

Sakarya University Journal of Science 23(6), 1154-1162, 2019

On the axial crush performance of PVC foam-filled aluminum/CFRP hybrid circular tube

Muhammet Muaz Yalçın[1], Kenan Genel[*2]

Abstract

In this study, an experimental investigation was carried out to improve the energy absorption capability of the circular aluminum tubes. For this purpose, different specimen configurations such as polyvinylchloride (PVC) foam-filled, empty hybrid (strengthened with CFRP) and PVC foam-filled hybrid tubes were prepared and tested under axial compression. It is noted from the experiments that the contribution of foam filling maximized when it was used with CFRP together. The results revealed that energy absorption capacity (EAC) of the foam-filled hybrid tube was 2.7 times of the base tube. Moreover, the specific energy absorption (SEA) value enhanced almost 70% compared to that of the base tube and reached 34.9 J/gr.

Keywords: carbon fiber reinforced polymer (CFRP), hybrid composite, interaction effect, aluminum tube

1. INTRODUCTION

There is an ever-increasing interest in the development and utilization of a lightweight structure. In this respect, tubular structures are preferable due to their high strength with low weight, excellent ability to dissipate crash energy by a progressive deformation under the axial compression [1-5]. This interest has resulted in extensive researches on the tubular structures. Pugsley and Macaulay [1] presented an analytical study on the quasi-static axial crushing of circular tubes for axisymmetric and diamond deformation modes. Since then, the axial compressive behavior of different sectioned tubular structures was studied extensively over the last decade [2–4] and has been overviewed by Alghamdi [5].

The ratio of the energy absorption value of the tube to the mass is identified as the specific energy absorption which is often used as a significant measure in most of the studies. As a result, different kind of polymeric foams such as polyurethane (PU) [6], PVC [7], polystyrene (PS) [8] generally used as a filler material. Foams offer high stiffness and strength even with low density. In addition, foams can be fully compressed with almost the same force before the densification. Unlike foam filling tubes, Alia et al.

[1] Sakarya University, Department of Mechanical Engineering, Sakarya, Turkey. ORCID: 0000-0003-4818-7591
[*] Corresponding Author: kgenel@sakarya.edu.tr
[2] Sakarya University, Department of Mechanical Engineering, Sakarya, Turkey. ORCID: 0000-0003-0994-2806

experimentally investigated the tube reinforced PVC foam under different compressive conditions [9]. They reported that the foam filling offers superior properties for aluminum tubes compare to that of steel ones. It is reported for the embedded tube that the foam filling doesn't have any contribution to the energy absorption capability of the tubes. Using fibers for reinforcing the tubes is another way to enhance the crashworthiness of the tubular structure. Therefore different fiber types such as carbon [10–12] and glass [13,14] were used to wrap the tubes in a series of studies. It can be pointed out from the studies that the fiber reinforcing has a significant contribution to the tube wall stability even they increasing embrittlement in tubes. Bambach and Elchalakani [15] experimentally and analytically investigated the effect of CFRP strengthening on deformation process of tubes. They reported that empirical expressions for the plastic collapse were carried out and mean forces are compared well with the result of experiments.

The interaction between the strengthening materials and the tube is another important issue that most of the studies mentioned. It is revealed from the literature that the strengthened tube has higher absorbed energy compare to the summation of the values of the base tube and the strengthening material, separately. This situation is defined as the interaction effect and can be attributed to the contribution to the tube wall stability [16,17]. There are lots of studies on crashworthiness of the strengthened tubular structures and some of them referred briefly to the interaction effect [16,18–21].

The present study aims to improve the energy absorption capability of the aluminum tubes. For this purpose, aluminum tubes were filled with PVC foam and strengthened with CFRP. Different specimen configurations as foam-filled tubes, empty hybrid tubes (CFRP strengthened aluminum tube) and foam-filled hybrid tubes were conducted to axial compression test to evaluate energy absorption performance with respect to SEA.

2. EXPERIMENTAL STUDY

2.1. Material Properties

A6063-T5 aluminum alloy tubes were used for experiments of the present study. In order to determine the mechanical properties of the aluminum tube, the tensile test was carried out according to ASTM-E8/E8M-09 standard for pipes with a diameter higher than 25 mm. The mechanical properties of the aluminum tube are given in Table 1.

Table 1. Mechanical properties of the 6063-T5 aluminium tube

Yield strength (MPa)	Ultimate stress (MPa)	Young's modulus (GPa)	Poisson's ratio
188	212	69	0.33

80 kg/m^3 density of closed-cell PVC foam was used as a foam filler material. Cylindrical PVC foams with the diameter of 56 mm were machined by using CNC to accurate geometrical size. The axial compressive test was conducted to the cylindrical foam and the test result is given in Figure 1. Moreover, the scanning electron microscopy (SEM) examination was carried out to show the cellular structure of the foam. An extra sharp knife was used to cut and prepare PVC foams for SEM analysis. The machined cylindrical foams and SEM image of the foam are given in Figure 2. The approximate cell size of the PVC foam was calculated as 440 μm.

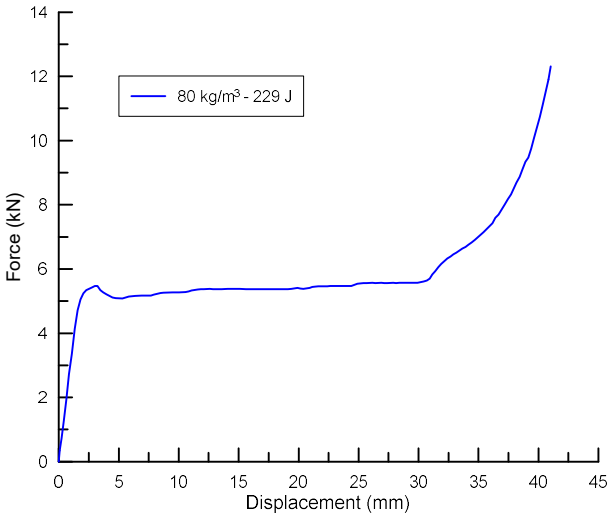

Figure 1. The force-displacement curve of the PVC foam

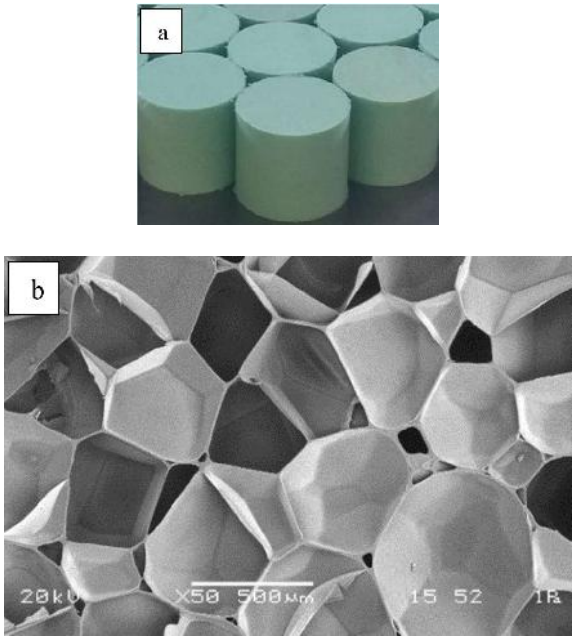

Figure 2. (a) Cylindrical PVC foam and (b) SEM image of the PVC foam

Carbon fiber fabric with a density of 200 g/m^2 was applied to the outside of the aluminum tubes with epoxy. The CFRP has nominally 340 MPa ultimate tensile strength and 42 GPa elasticity modulus. The thickness of the fabric is nominally 0.176 mm.

2.2. Specimen Preparation

The tubes were used in the experimental study have the following geometric properties diameter of 58.5 mm, the wall thickness of 1.25 mm and length of 50 mm. The hardness of all aluminum tubes was measured in the range of 70-72 HV. The commercial aluminum tubes have some imperfections in terms of tube wall thickness along the cross-section which may cause incompatibility of test results. Because of that aluminum tubes were machined both sides of inner and outer to eliminate the inhomogeneity of the wall thickness in cross-section (Figure 3).

Figure 3. Machining process of aluminum tubes

All CFRP reinforced aluminum were cured at least 6 hours at 60°C according to the manufacturer's instructions. Due to the importance of that the aluminum tube and the CFRP should be in contact with the loading platens at the same time, the ends of the hybrid tubes were minimally handed ground. Specimen configuration views of the base, PVC foam-filled, empty hybrid and PVC foam-filled hybrid composite tubes are represented in Figure 4.

Figure 4. Specimen configurations

The tests were performed on a compressive testing machine which has a capacity of 250 kN and 60 mm/min of crosshead speed and the force-displacement data pairs were recorded automatically. Moreover, all of the tests were recorded by a video camera. It is also important that at least three specimens were tested for each specimen combinations.

3. DEFORMATION MODES OF CIRCULAR TUBES

In general, a circular tube starts to deform from one of the ends and the deformation progressively proceeds. There are three different deformation modes for a circular tube namely, i) axisymmetric, ii) diamond and iii) mixed mode. Deformed tube images after axial loading in different modes are given in Figure 5.

Figure 5. Axisymmetric, diamond and mixed deformation modes of tubes (respectively from left)

Andrews et al. [23] and Guillow [18] examined the relation between tube geometry and collapse mode in an extensive range of L/D and D/t. It is deduced from their studies that the deformation would be in axisymmetric mode when D/t and L/D are lower than 50 and 2 respectively. The mix-mode would occur especially for the higher values of L/D. The mix-mode, starting in axisymmetric mode and turning into the diamond mode during the progressive deformation, is generally related to the geometrical imperfections of the tube [3].

A similar test program was carried out for aluminum tubes with different tube geometry to obtain the relationship between geometrical properties and deformation mode. In addition to the previous work, the hardness values of the tubes were also considered. Figure 6 shows a classification chart. It is seen from the chart that the changes in deformation modes with respect to D/t and L/D ratios. It is possible to say that there is a line at the value of L/D=2 which divide the chart into two regions. The axisymmetric mode was observed under this critical ratio. It is pointed out that the hardness has a significant effect on deformation, the tubes were fractured for the higher hardness values [3,18]. It is seen in Figure 7 that the aluminum tube with a hardness value of 75 HV was deformed without folding because of the higher hardness.

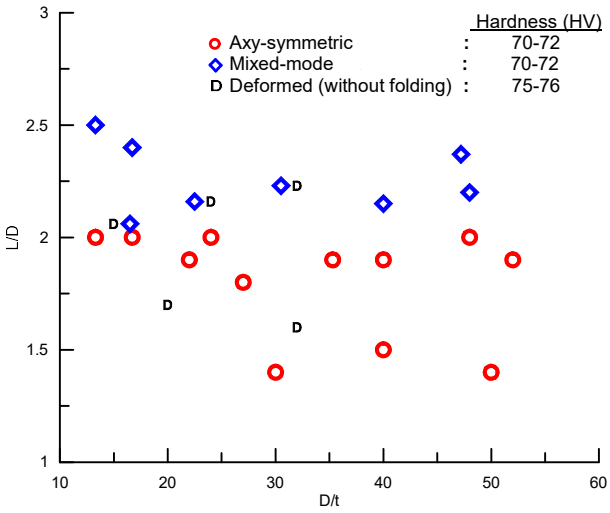

Figure 6. Deformation mode chart of aluminum tubes with different size

Figure 7. Fractured tube

4. RESULTS AND DISCUSSION

At least three experiments were performed for each specimen configurations. The force-displacement curve of the base tube, deformed in axisymmetric mode, is given in Figure 8. It is seen that the curve has a form that oscillates between high and low peak force values. These peak forces are directly related to the inwardly and outwardly movement of the tube wall and each upper peak forces (A-F) were associated with the formation of one fold. Soon after from application of the axial loading, an outward buckle, sometimes two buckles, was seen close to the top or/and bottom ends of the tube. Just before this buckles occurring, the force reached its highest value at point A. All of the other peak forces were lower than A which is because of that the tube was free of all deformations during the first fold formation. Soon after the first fold was completed, the formation of the second fold was already initiated by a local bending produced by the first fold.

Because of that, the other peak forces are lower than that of the peak force at point A.

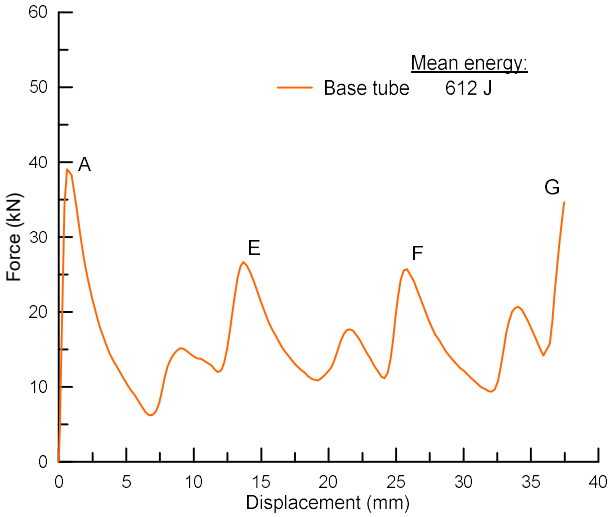

Figure 8 Force-displacement curve of the base tube (t=1.25)

The force-displacement curves of PVC foam-filled specimens are given in Figure 9 shows. It is deduced that foam filling has a decisive role in forces. All upper and lower peak forces were shifted up by foam filling and the specimens almost have the same oscillation form as that of the base tube. Although foam filling was caused an increase in the first peak forces about 6 kN compare to the base tube, the difference reached almost 10 kN for other upper and lower forces. This possibly a result of that the contribution of the foam material is limited at the beginning of the test. During the folding process, the severity of the interaction effect was increased (which is because of the inward movement of the tube wall) and as a result, it was enhanced the other peak forces. The mean absorbed energy value of foam-filled specimens was calculated as 951 J which is almost 55% higher than the base tube.

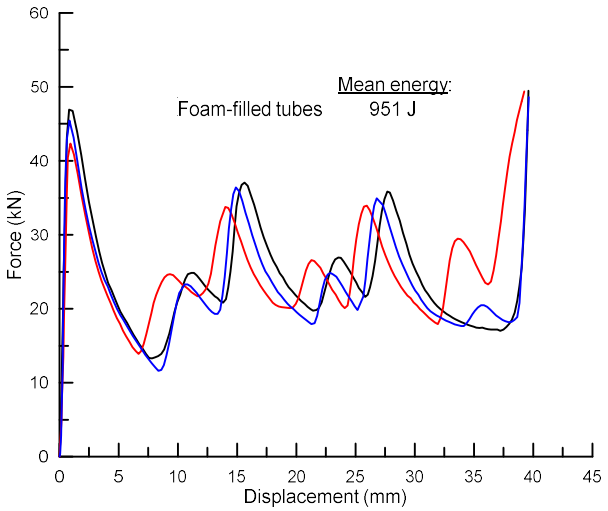

Figure 9 Force-displacement curve of foam-filled tubes

The force-displacement curves of empty hybrid tubes which were produced by reinforcing the aluminum tubes with CFRP are given in Figure 10. It is easily concluded that the CFRP reinforcement changed the oscillation form of the base tube. It is seen that the force-displacement curve, except the start and end parts, has a plateau-like behavior. The first peak force was increased by CFRP reinforcement almost 80% compared to the first peak force of the base tube. It is revealed that the CFRP reinforcement has a more significant effect on the first peak in contrast to foam filling. The absorbed energy of these specimens is almost twice of the base tube and 30% higher than that of the PVC foam-filled specimen.

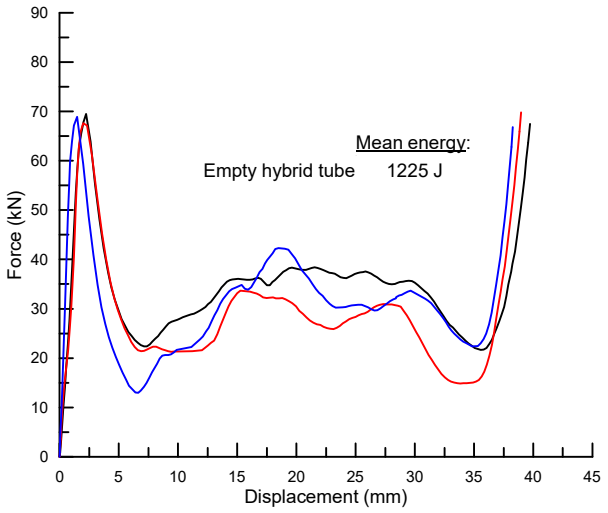

Figure 10 Force-displacement curve of empty hybrid composite tubes

The test results of the PVC foam-filled hybrid specimens under axial loading are represented in Figure 11. When the force-displacement curves are examined, though the characteristic form of the curve is quite similar there is an increase as 10 kN in the first peak force compared to that of empty hybrid tubes. As a result, it can be revealed that the contribution of foam filling was increased when it was used with CFRP reinforcement. When the absorbed energy values of the empty and foam-filled hybrid tubes are compared, it is obvious that the contribution of the foam has a remarkable effect on the energy absorption capability, as well. Foam filling enhanced the energy absorption capacity by almost 34%.

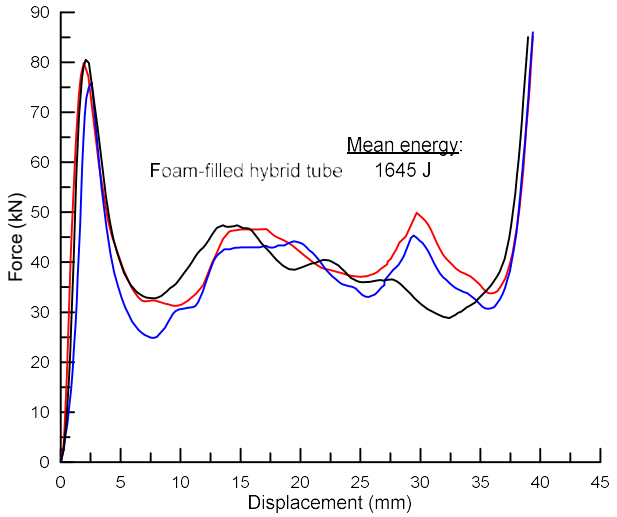

Figure 11. Force-displacement curves of foam-filled hybrid composite tubes

Deformed base tubes and other specimen configurations are given in Figure 12. It is clearly seen that the base tubes were deformed in axisymmetric mode and the mode was the same after foam filling. It can be pointed out that the deformation mode of the empty hybrid tube was changed into diamond mode from axisymmetric by CFRP reinforcement. This could be a result of the restriction of the outward movement of the tube which caused the tube wall tends to move inwardly and diamond mode occurs. The deformation mode was turned into axisymmetric mode again in foam-filled hybrid tubes by foam filling (Figure 13) [2].

Figure 12. Specimen views after test

Figure 13. Changes in deformation modes with different reinforcement materials

4.1. The Interaction Effect

The interaction effect between the tube wall and the foam filler is examined in this section. It is known from the literature that the energy value of the foam-filled tube is higher than the sum of energy values of the base tube and the foam individually. To clarify how the foam filling contributes to the absorbed energy, a graph is given in Figure 14. The difference in absorbed energy is a result of the complex interactions between the tube wall and the foam filler. It is pointed out from the literature that, the wall stability is directly related to these interactions and efficiency of interactions depends on especially the density and type (metallic, polymeric) of the foam [23,24].

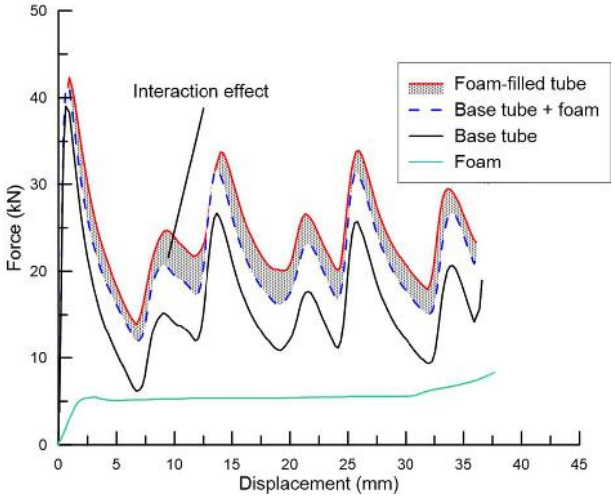

Figure 14. The interaction effect between foam filler and tube by means of absorbed energy

The detailed contributions provided by different strengthening materials such as PVC foam and CFRP is given in Figure 15. It is possible to say that the CFRP strengthening is more effective on absorbed energy than that of foam filling even though it changes the folding mode of the base tube. It is also seen that the contribution of the foam is higher in hybrid specimens compare to that of the base tube. It is because of that the outward movement of the tube wall is restricted in the hybrid tubes which, unlike the base tube. As a result, the tube wall tends to penetrate to the foam filler more than that of the tube without any restriction.

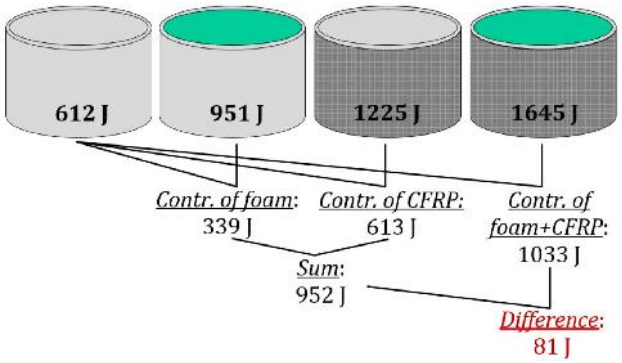

Figure 15. The contributions of reinforcement materials to the absorbed energy

The SEA capabilities for all specimen configurations were calculated. The SEA values were calculated by dividing the energy to the mass and given in Table 2. The results indicate that the foam-filled hybrid structure offers the most effective strengthening model. The SEA of the foam-filled hybrid composite tube was increased by 70% compared to that of the base tube. It is also possible to say that the SEA would obtain higher by using longer tubes.

Table 2. The SEA values of different specimen configurations

Specimen configuration	Energy (J)	Mass (gr)	SEA (J/gr)
Base tube	612	29.9	20.47
Foam-filled	951	40.5	23.48
Empty hybrid	1225	36.7	33.20
Foam-filled hybrid	1645	47.1	34.93

5. CONCLUSIONS

In this study, the EAC and deformation behaviors of the PVC foam-filled aluminum (6063-T5) and hybrid tubes were investigated. For the base tube, the absorbed energy was calculated as 612 J in the axisymmetric mode which was as the same for the foam-filled specimen. Although the hybrid tubes changed the deformation mode from axisymmetric to diamond, it had a significant effect on EAC value. It was also another important point that the improvement in EAC was obtained with lower mass increase compare to that of foam-filled tubes for the hybrid tubes. As a result, the empty hybrid tubes (33.2 J/gr) offered higher SEA values than the foam-filled ones (23.5 J/gr). It is expected that the longer foam-filled hybrid tubes would offer higher EAC and SEA values and they could be used as effective energy absorber devices.

6. REFERENCES

[1] A. Pugsley, “The large-scale crumpling of thin cylindrical columns,” Quarterly Journal of Mechanics and Applied Mathematics, vol. 13, no. 1, pp. 1–9, 1960.

[2] S. R. Reid, T. Y. Reddy, and M. D. Gray, “Static and dynamic axial crushing of foam-filled sheet metal tubes,” International Journal of Mechanical Sciences, vol. 28, no. 5, pp. 295–322, 1986.

[3] D. Al Galib and A. Limam, "Experimental and numerical investigation of static and dynamic axial crushing of circular aluminum tubes," Thin-Walled Structures, vol. 42, no. 8, pp. 1103–1137, 2004.

[4] A. A. Singace, H. Elsobky, and T. Y. Reddy, "On the eccentricity factor in the progressive crushing of tubes," International Journal of Solids and Structures, vol. 32, no. 24, pp. 3589–3602, 1995.

[5] A. A. Alghamdi, "Collapsible impact energy absorbers: an overview," Thin-Walled Structures, vol. 39, no. 2, pp. 189–213, 2001.

[6] J. Zhang, N. Kikuchi, V. Li, A. Yee, and G. Nusholtz, "Constitutive modeling of polymeric foam material subjected to dynamic crash loading," International Journal of Impact Engineering, vol. 21, no. 5, pp. 369–386, 2002.

[7] S. A. Meguid, M. S. Attia, and A. Monfort, "On the crush behaviour of ultralight foam-filled structures," Materials & Design, vol. 25, pp. 183–189, 2004.

[8] A. K. Toksoy and M. Güden, "The strengthening effect of polystyrene foam filling in aluminum thin-walled cylindrical tubes," Thin-Walled Structures, vol. 43, no. 2, pp. 333–350, 2005.

[9] R. A. Alia, Z. W. Guan, A. K. Haldar, and W. J. Cantwell, "A numerical study of the energy-absorption characteristics of metal polymer foams," Journal of Sandwich Structures & Materials, vol. 18, no. 5, pp. 597–623, 2016.

[10] H. C. Kim, D. K. Shin, J. J. Lee, and J. B. Kwon, "Crashworthiness of aluminum/CFRP square hollow section beam under axial impact loading for crash box application," Composite Structure, vol. 112, pp. 1–10, 2014.

[11] Q. Liu, J. Ma, Z. He, Z. Hu, and D. Hui, "Energy absorption of bio-inspired multi-cell CFRP and aluminum square tubes," Composites Part B: Engineering, vol.121, pp. 134–144, 2017.

[12] M. R. Bambach, M. Elchalakani, and X. L. Zhao, "Composite steel – CFRP SHS tubes under axial impact," Composite Structures, vol. 87, no. 3, pp. 282–292, 2009.

[13] M. Guden, S. Yüksel, A. Taşdemirci, and M. Tanoğlu, "Effect of aluminum closed-cell foam filling on the quasi-static axial crush performance of glass fiber reinforced polyester composite and aluminum/composite hybrid tubes," Composite Structures, vol. 81, no. 4, pp. 480–490, 2007.

[14] P. Taylor, N. Swaminathan, and R. C. Averill, "Contribution of failure mechanisms to crush energy absorption in a composite tube," Mechanics of Advanced Materials and Structures, vol. 13, no. 1, pp. 51–59, 2006.

[15] M. R. Bambach and M. Elchalakani, "Plastic mechanism analysis of steel SHS strengthened with CFRP under large axial deformation," vol. 45, pp. 159–170, 2007.

[16] P. Thornton, "Energy absorption by foam filled structures," SAE Technical Paper Series, 1980.

[17] T. Y. Reddy and R. J. Wall, "Axial compression of foam-filled thin-walled circular tubes," International Journal of Impact Engineering, vol. 7, no. 2, pp. 151–166, 1988.

[18] M. Seitzberger, F. G. Rammerstorfer, H. P. Degischer, and R. Gradinger, "Crushing of axially compressed steel tubes filled with aluminium foam," Acta Mechanica, vol. 125, no. 1, pp. 93–105, 1997.

[19] H. R. Zarei and M. Kroger, "Optimization of the foam-filled aluminum tubes for crush

box application," Thin-Walled Structures, vol. 46, no. 2, pp. 214–221, 2008.

[20] A. Darvizeh, M. Darvizeh, R. Ansari, and A. Meshkinzar, "Effect of low density, low strength polyurethane foam on the energy absorption characteristics of circumferentially grooved thick-walled circular tubes," Thin-Walled Structures, vol. 71, pp. 81–90, 2013.

[21] M. Güden, A. K. Toksoy, and H. Kavi, "Experimental investigation of interaction effects in foam-filled thin-walled aluminum tubes," Journal of Materials Science, vol. 41, no. 19, pp. 6417–6424, 2006.

[22] S. R. Guillow, G. Lu, and R. H. Grzebieta, "Quasi-static axial compression of thin-walled circular aluminium tubes," International Journal of Mechanical Sciences, vol. 43, no. 9, pp. 2103–2123, 2001.

[23] S. R. Reid and T. Y. Reddy, "Static and dynamic crushing of tapered sheet metal tubes of rectangular cross-section," International Journal of Mechanical Sciences, vol. 28, no. 9, pp. 623–637, 1986.

JOURNAL OF SCIENCE
SAKARYA UNIVERSITY

Sakarya University Journal of Science

ISSN 1301-4048 | e-ISSN 2147-835X | Period Bimonthly | Founded: 1997 | Publisher Sakarya University | http://www.saujs.sakarya.edu.tr/

Title: Different Approximation To Fuzzy Ring Homomorphisms

Authors: Ümit Deniz
Recieved: 2018-01-16 15:10:16

Accepted: 2019-08-11 14:12:43

Article Type: Research Article
Volume: 23
Issue: 6
Month: December
Year: 2019
Pages: 1163-1172

How to cite
Ümit Deniz; (2019), Different Approximation To Fuzzy Ring Homomorphisms. Sakarya University Journal of Science, 23(6), 1163-1172, DOI: 10.16984/saufenbilder.379634
Access link
http://www.saujs.sakarya.edu.tr/issue/44246/379634

Sakarya University Journal of Science 23(6), 1163-1172, 2019

Different Approximation to Fuzzy Ring Homomorphisms

Ümit Deniz*

Abstract:

In this study we approach the definition of TL −ring homomorphism. In the literature, the definition of fuzzy ring homomorphism is given by Malik and Mordeson by using their fuzzy function definition. In this study, we give the definition of fuzzy ring homomorphism by using the definition of Mustafa Demirci's fuzzy function. Some definition and theorems of ring homomorphism in classic algebra are adapted to fuzzy algebra and proved.

Keywords: Fuzzy sets, Fuzzy Relations, Fuzzy Functions, Fuzzy Ring Homomorphisms.

1. INTRODUCTION

The theory of fuzzy sets was introduced by Zadeh [10]. Fuzzy sets gives opportunity to constitute the uncertain problems in real life to mathematical models. Most of the problems in engineering, economics, medical science etc, have various uncertainties. The fuzzy set theory helps to modelling and solving these problems. Many mathematician tried to transfer the classic set theory to use the definition of Zadeh' s fuzzy set. Rosenfeld [12] gave the definition of fuzzy groups and fuzzy grupoids. Liu [9,10] gave the definition of fuzzy subrings and fuzzy ideals of a ring. Fuzzy relations are playing an important role in fuzzy modelling, fuzzy control and significant applications in relational databases, approximate reasoning, medical diagnosis. Malik and Mordeson gave some conditions to fuzzy relations to define fuzzy function [11]. With this definition, they introduced fuzzy ring homomorphism. In these studies, they used fuzzy subsets $\mu: X \to [0,1]$ and they used infimum for operation on [0,1]. In literature there isn't a certain fuzzy function definition and therefore there isn't a certain fuzzy ring homomorphism definition. In this study, we gave a different definition of fuzzy ring homomorphism. To give this definition, we used the fuzzy function definition of Demirci [2,3] and we used L-subsets $\mu: X \to L$ which L is a complete lattice and T-norms as operation of L.

In this study, we used the definition of fuzzy subrings and fuzzy ideals of a ring from Wang [14,15]. Some definitions and theorems of ring homomorphism in the classic algebra are adapted to fuzzy algebra with this definition and proved.

2. PRELIMINARY

In this section, we have presented the basic definitions and results of fuzzy algebra which may be found in the earlier studies.

Definition 2.1. [1] Let (L, ≤) be a complete lattice with top and bottom elements 1, 0, respectively. *A triangular norm* (briefly t-norm) is a binary operation T on L which is

commutative, associative, monotone and has 1 as a neutral element, i.e., it is a function.

$T: L^2 \to L$ such that for all $x, y, z \in L$

$(T1)\ T(x,y) = T(y,x).$

$(T2)\ T\big(x, T(y,z)\big) = T(T(x,y), z).$

$(T3)\ T(x,y) \leq T(x,z)\ whenever\ y \leq z.$

$(T4)\ T(x,1) = x.$

Definition 2.2. [1]

a) A t-norm T on a lattice L is called ⋁-*distributive* if

$T(a, b_1 \vee b_2) = T(a,b_1) \vee T(a,b_2).$

b) A t-norm T on a complete lattice L is called *infinitely* ⋁*-distributive* if

$$T\left(a, \bigvee_{Q} b_\tau\right) = \bigvee_{Q} T(a, b_\tau)$$

for any subset $\{a, b_\tau \in L, \tau \in Q\}$ of L.

Theorem 2.3. [1] Let L be a complete lattice. If T is a infinitely ⋁-distributive t-norm then

$$\bigvee_{i\in I}\bigvee_{j\in J} T(a_i, b_j) = T\left(\bigvee_{i\in I} a_i, \bigvee_{j\in J} b_j\right).$$

Definition 2.4. [17] Let L be a complete lattice**.** With *a L-subset* of X we mean a function from X into L. We denote all L-subsets set by $F(X,L)$. In particular, when L is [0,1], the L-subsets of X are called *fuzzy subsets*.

Definition 2.5. [3] If X and Y are sets then the function $f: X \times Y \to L$ is called *a L-relation* and the set of all L-relations is denoted by $F(X \times Y, L)$.

Definition 2.6. [2] Let L be a complete lattice. $E: X \times X \to L$ a L-relation E on a set X is *a TL-equivalence relation* if and only if for all $a, b, c \in X$ the following properties are satisfies;

$(E1)\ E(a,a) = 1.$

$(E2)\ E(a,b) = E(b,a).$

$(E3)\ T\big(E(a,b), E(b,c)\big) \leq E(a,c).$

E is called *a separable TL- equivalence relation* or a *TL- equality* if in addition,

$(E4)\ E(a,b) = 1$ implies a=b.

If E is a TL-equivalence relation on X it is shown by (X, E).

Example. [2] Let X be non-empty set and $\alpha \in L$. Then

$i)\ EX_M(x,y) = 1$

$$ii)\ EX_L(x,y) = \begin{cases} 1 & x = y \\ 0 & x \neq y \end{cases}$$

$$iii)\ EX_\propto(x,y) = \begin{cases} 1 & x = y \\ \propto & x \neq y \end{cases}$$

are TL-equivalence relations of X.

Theorem 2.7. [2] Let (X,E) and (Y,F) be two equivalence relations. Then TL-subset $E \times F$

$E \times F: (X \times Y) \times (X \times Y) \to L$ defined by

$(E \times F)\big((x,y),(x',y')\big) = T(E(x,x'), F(y,y'))$

is a TL-equivalence relation.

Definition 2.8. [2] Let E be a TL-equivalence relation on a set X. A L-subset μ of X is *extensional* or *observable* w.r.t. E if and only if

$T\big(\mu(b), E(a,b)\big) \leq \mu(a) \quad \forall a, b \in X.$

Definition 2.9. [13] Let X,Y and Z are sets and $f: X \times Y \to L$ *and* $g: Y \times Z \to L$ be L-relations. Then $g \circ_T f: X \times Z \to L$ L-relation is called composition of f and g such that

$for\ (x,z) \in X \times Z$

$$g \circ_T f(x,z) = \bigvee_{y\in Y} T\big(f(x,y), g(y,z)\big)$$

Definition 2.10. [3] Let $f: X \times Y \to L$ be a L-relation then we call the function

$f^{-1}: Y \times X \to L$ defined by

$f^{-1}(y,x) = f(x,y)$ the inverse of f L-relation.

Definition 2.11. [3] Let $f: X \times Y \to L$ be a L-relation and $A \in F(X,L)\ and\ B \in F(Y,L)$. The L-subsets $f(A)$, $f^{-1}(B)$ defined by for all $x \in X, y \in Y$

$f(A)(y) = \bigvee_{x\in X} T\big(A(x), f(x,y)\big)$ and

$$f^{-1}(B)(x) = \bigvee_{y\in Y} T\big(B(y), f(x,y)\big)$$

are respectively *the image of A* and *the inverse image of B*.

Definition 2.12. [2] Let (X, E), (Y, F) be two TL-equivalence relations and $f \in F(X \times Y, L)$. Then;

a) f is called *an E-extensional* if the inequality T(f(x,y), E(x,x'))≤f(x',y) is satisfied $for\ all\ x, x' \in X\ \ and\ for\ all\ y \in Y$. We call all E-extensional L-relations set as $F(X \times Y, E, L)$.

b) f is called a *F-extensional* if the inequality T(f(x,y), F(y,y')) ≤ f(x,y') Is satisfied $for\ all\ x \in X\ and\ for\ all\ y, y' \in Y$. We denote all F-extensional L-relations set by $F(X \times Y, F, L)$.

c) A L-relation such as f is called *E-F-extensional* if f is E-extensional and F-extensional and denote all E-F- extensional relations set by $F(X \times Y, E, F, L)$..

Definition 2.13. [2] Let (X,E) and (Y,F) be two TL-equivalence relations and $f \in F(X \times Y, E, F, L)$ then;

a) f is called *partial TL-function* if T(f(x,y), f(x,y'))≤F(y,y') is satisfied for all $x \in X$ and for all $y, y' \in Y$.

b) f is called *fully defined* if f fulfills the condition $\bigvee_{z \in Y} f(x,z) = 1$ for all $x \in X$.

c) A fully defined partial TL- function is called *a TL-function*.

Definition 2.14. [3] Let $f \in F(X \times Y, E, F, L)$ be a TL-function;

a) f is called surjective if and only if $\bigvee_{x \in X} f(x,y) = 1$ for all $y \in Y$.

b) f is called injective if and only if $T\big(f(x,y), f(x',y)\big) \le E(x,x')$ for all $x, x' \in X$ and $y \in Y$.

Proposition 2.15. Let (X,E) and (Y,F) be two TL-equivalence relations, $f \in F(X \times Y, E, F, L)$ and $A \in F(X, L)$. If T is a infinitely ⋁- distributive t-norm then $f(A)$ is F-extensional L-subset.

Proof. $For\ x, x' \in X, y, y' \in Y$ and

$$T\big(f(A)(y), F(y,y')\big)$$
$$= T\left(\bigvee_{x \in X} T\big(A(x), f(x,y)\big), F(y,y')\right)$$
$$= \bigvee_{x \in X} T\left(T\big(A(x), f(x,y)\big), F(y,y')\right)$$
$$= \bigvee_{x \in X} T\left(A(x), T\big(f(x,y), F(y,y')\big)\right)$$
$$\le \bigvee_{x \in X} T\big(A(x), f(x,y')\big) = f(A)(y').$$

Proposition 2.16. Let (X,E) and (Y,F) be two TL-equivalence relations, $f \in F(X \times Y, E, F, L)$ and $B \in F(Y, L)$. If T is a infinitely ⋁-distributive t-norm then $f^{-1}(B)$ is E-extensional L-subset.

Proof. $For\ \ x, x' \in X\ y, y' \in Y$ and

$$T\big(f^{-1}(B)(x), E(x,x')\big)$$
$$= T\left(\bigvee_{y \in Y} T\big(B(y), f(x,y)\big), E(x,x')\right)$$
$$= \bigvee_{y \in Y} T\left(T\big(B(y), f(x,y)\big), E(x,x')\right)$$
$$= \bigvee_{y \in Y} T\left(B(y), T\big(f(x,y), E(x,x')\big)\right)$$
$$\le \bigvee_{y \in Y} T\big(B(y), f(x',y)\big) = f^{-1}(B)(x').$$

Theorem 2.17. Let $f \in F(X \times Y, E, F, L)$, $g \in F(Y \times Z, F, G, L)$ be TL-functions and T be a infinitely ⋁-distributive t-norm. Then $g \circ_T f \in F(X \times Z, E, G, L)$ is a TL-function.

Proof. $For\ x, x' \in X\ y, y' \in Y, z, z' \in Z$

$$T\big((g \circ_T f)(x,z), E(x,x')\big)$$
$$= T\left(\bigvee_{y \in Y} T\big(f(x,y), g(y,z)\big), E(x,x')\right)$$
$$= \bigvee_{y \in Y} T\left(T\big(f(x,y), E(x,x')\big), g(y,z)\right)$$
$$\le \bigvee_{y \in Y} T\big(f(x',y), g(y,z)\big) = (g \circ_T f)(x',z)$$

and so $g \circ_T f$ is an E-extensional.

$$T\big((g \circ_T f)(x,z), G(z,z')\big)$$
$$= T\left(\bigvee_{y\in Y} T\big(f(x,y), g(y,z)\big), G(z,z')\right)$$
$$= \bigvee_{y\in Y} T\Big(f(x,y), T\big(G(z,z'), g(y,z)\big)\Big)$$
$$\leq \bigvee_{y\in Y} T\big(f(x,y), g(y,z')\big) = (g \circ_T f)(x,z')$$

Hence $g \circ_T f$ is a G-extensional.

$$T\big((g \circ_T f)(x,z), (g \circ_T f)(x,z')\big)$$
$$= T\left(\bigvee_{y\in Y} T\big(f(x,y), g(y,z)\big), \bigvee_{y'\in Y} T\big(f(x,y'), g(y',z')\big)\right)$$
$$= \bigvee_{y\in Y}\bigvee_{y'\in Y} T\Big(T\big(f(x,y), f(x,y')\big), T\big(g(y,z), g(y',z')\big)\Big)$$
$$\leq \bigvee_{y\in Y}\bigvee_{y'\in Y} T\Big(T\big(F(y,y'), g(y,z)\big), g(y',z')\Big)$$
$$\leq \bigvee_{y'\in Y} T\big(g(y',z), g(y',z')\big)$$
$$\leq \bigvee_{y'\in Y} G(z,z') = G(z,z').$$

Hence $g\circ_T f$ is a partial TL-function.

$$\bigvee_{z\in Y}(g \circ_T f)(x,z) = \bigvee_{z\in Y}\bigvee_{y\in Y} T\big(f(x,y), g(y,z)\big)$$
$$= \bigvee_{z\in Y} T\left(\bigvee_{y\in Y} f(x,y), g(y,z)\right)$$
$$= \bigvee_{z\in Y} T\big(1, g(y,z)\big) = \bigvee_{z\in Y} g(y,z) = 1.$$

Hence $g\circ_T f$ is full defined.

Finally $g\circ_T f$ is TL-function.

Theorem 2.18. Let (R_1, E_1), (R_2, E_2), (S_1, F_1) and (S_2, F_2) be TL-equivalence relations and

$f: R_1 \times S_1 \to L$

$g: R_2 \times S_2 \to L$ be TL-functions. Then the TL-equivalence relation is defined by

$g \times f: (R_1 \times R_2) \times (S_1 \times S_2) \to L$ such that

$$(g \times f)\big((x_1,x_2),(y_1,y_2)\big)$$
$$= T(f(x_1,y_1), g(x_2,y_2))$$

is a TL-function.

Proof.

i) $For\ x_1,\ x_1^* \in R_1\ x_2,\ x_2^* \in R_2\ y_1 \in S_1,\ y_2 \in S_2$

$$T\Big((g \times f)\big((x_1,x_2),(y_1,y_2)\big), (E_1 \times E_2)\big((x_1,x_2),(x_1^*,x_2^*)\big)\Big)$$
$$= T\Big(T\big(f(x_1,y_1), g(x_2,y_2)\big), T\big(E_1(x_1,x_1^*), E_2(x_2,x_2^*)\big)\Big)$$
$$= T\Big(T\big(f(x_1,y_1), E_1(x_1,x_1^*)\big), T\big(g(x_2,y_2), E_2(x_2,x_2^*)\big)\Big)$$
$$\leq T\big(f(x_1^*,y_1), g(x_2^*,y_2)\big)$$
$$= (g \times f)\big((x_1^*,x_2^*),(y_1,y_2)\big).$$ Then, we prove $(g \times f)$ is $(E_1 \times E_2)$ extensional.

ii) $For\ x_1 \in R_1,\ x_2 \in R_2\ ,\ y_1,\ y_1^* \in S_1,\ y_2,\ y_2^* \in S_2$

$$T\Big((g \times f)\big((x_1,x_2),(y_1,y_2)\big), (F_1 \times F_2)\big((y_1,y_2),(y_1^*,y_2^*)\big)\Big)$$
$$= T\Big(T\big(f(x_1,y_1), g(x_2,y_2)\big), T\big(F_1(y_1,y_1^*), F_2(y_2,y_2^*)\big)\Big)$$
$$= T\Big(T\big(f(x_1,y_1), F_1(y_1,y_1^*)\big), T\big(g(x_2,y_2), F_2(y_2,y_2^*)\big)\Big)$$
$$\leq T\big(f(x_1,y_1^*), g(x_2,y_2^*)\big)$$
$$= (g \times f)\big((x_1,x_2),(y_1^*,y_2^*)\big).$$Then, we prove $(g \times f)$ is $(F_1 \times F_2)$ extensional.

iii) $For\ x_1 \in R_1,\ x_2 \in R_2,\ y_1, y_1^* \in S_1\ y_2,$ $y_2^* \in S_2$

$$T\Big((g \times f)\big((x_1,x_2),(y_1,y_2)\big), (g \times f)\big((x_1,x_2),(y_1^*,y_2^*)\big)\Big)$$
$$= T\Big(T\big(f(x_1,y_1), g(x_2,y_2)\big), T\big(f(x_1,y_1^*), g(x_2,y_2^*)\big)\Big)$$
$$= T\Big(T\big(f(x_1,y_1), f(x_1,y_1^*)\big), T\big(g(x_2,y_2), g(x_2,y_2^*)\big)\Big)$$
$$\leq T\big(F_1(y_1,y_1^*), F_2(y_2,y_2^*)\big)$$
$$= (F_1 \times F_2)\big((y_1,y_2),(y_1^*,y_2^*)\big).$$ Then, we prove $(g \times f)$ is partial TL-function.

iv) For each $(x_1,x_2) \in (R_1 \times R_2)$

$$\bigvee_{(y_1,y_2)\in S_1\times S_2} (g\times f)\big((x_1,x_2),(y_1,y_2)\big)$$
$$= \bigvee_{(y_1,y_2)\in S_1\times S_2} T\big(f(x_1,y_1),g(x_2,y_2)\big)$$
$$= T\left(\bigvee_{y_1\in S_1} f(x_1,y_1)\,,\bigvee_{y_2\in S_2} g(x_2,y_2)\right)$$

$= T(1,1) = 1$ (because f and g are fully defined)

Then, we prove $(g\times f)$ is fully defined and so $(g\times f)$ is TL-function.

Definition 2.19. [14] Let R be a ring and $\mu: R\to L$, $\vartheta: R\to L$ are L-subsets. Define $\mu+_T\vartheta, -\mu, \mu-_T\vartheta, \mu._T\,\vartheta \in F(R,L)$ as follows.

$$(\mu+_T\vartheta)(x)$$
$$= \bigvee\{T(\mu(y),\vartheta(z))|y,z\in R, y+z=x\}$$
$$(-\mu)(x) = \mu(-x)$$
$$(\mu-_T\vartheta)(x)$$
$$= \bigvee\{T(\mu(y),\vartheta(z))|y,z\in R, y-z=x\}$$
$$(\mu._T\,\vartheta)(x)$$
$$= \bigvee\{T(\mu(y),\vartheta(z))|y,z\in R, y.z=x\}$$

Where x is any element of R. $\mu+_T\vartheta, \mu-_T\vartheta, \mu._T\,\vartheta$ are called the T-sum, T-difference, and T-. product of μ and ϑ, respectively, and $-\mu$ is called the negative of μ.

Definition 2.21. [14] Let $\mu: R\to L$ such that μ satisfies conditions (R1), (R2) and (R3). Then μ is called *a TL-left ideal of R* if it also satisfies the condition

$(R5)_l$ $\mu(xy)\geq\mu(y)\ \forall x,y\in R$;

a TL-right ideal of R if it also satisfies the condition

$(R5)_r$ $\mu(xy)\geq\mu(x)\ \forall x,y\in R$;

and a TL-two sided ideal or *TL-ideal of R* if it is also satisfies the condition

$(R5)\ \mu(xy)\geq\mu(x)\vee\mu(y)\ \forall x,y\in R.$

In particular, when $T=\wedge$, a TL-left ideal, TL-right ideal and TL-ideal of R are referred to as an L-left ideal, L-right ideal and L-ideal of R, respectively we denote by $TLI_l(R)$, $TLI_r(R)$ and TLI(R), respectively, the set of all TL-left ideals of R, the set of all TL-right ideals of R and the set of all TL-ideals of R.

3. TL-Ring Homomorphisms

In this section we gave the definition of TL-ring homomorphism and carry with this definition the most of the theorems and definitions about ring homomorphisms.

Definition 3.1. Let R and S be rings, $(R,E),(S,F)$ be TL-equivalence relations and $f\in F(R\times S,E,F,L)$ be TL-function. f is called *TL-ring homomorphism* if it satisfies the following conditions

$for\ all\ x,x'\in R\ \ and\ \ y,y'\in S.$

(H1) $f(x+x',y+y')\geq T\big(f(x,y),f(x',y')\big)$

(H2) $f(x.x',y.y')\geq T\big(f(x,y),f(x',y')\big)$

Definition 3.2. Let $f\in F(R\times S,E,F,L)$ be a TL-ring homomorphism

a) If $f(0,0)=1$ then f is called *a perfect TL-ring homomorphism*.

b) If $f(-x,-y)\geq f(x,y)\ for\ all\ x\in R\ and\ y\in S$, then f is called *a strong TL-ring homomorphism*.

c) If f is both perfect and strong TL-ring homomorphism, then it is called *as a complete TL-ring homomorphism.*

Theorem 3.3. Let $f\in F(R\times S,E,F,L)$ and $g\in F(S\times K,F,G,L)$ be TL-ring homomor-phisms and T be a infinitely ⋁-distributive t-norm. Then $g\circ_T f\in F(R\times K,E,G,L)$ TL-function is a TL-ring homomorphism.

Proof From theorem 2.17 $g\circ_T f$ is TL-function. Now we show that only $g\circ_T f$ satisfies the TL-ring homomorphism conditions.

i) $For\ x,x'\in R\ \ y,y'\in S\ and\ z,z'\in K$

$$(g\circ_T f)(x+x',z+z')$$
$$= \bigvee_{y\in S} T\big(f(x+x',y),g(y,z+z')\big)$$
$$= \bigvee_{y,y'\in S} T\big(f(x+x',y+y'),g(y+y',z+z')\big)$$

$$\geq \bigvee_{y,y\prime\in S} T\left(T\big(f(x,y),f(x',y')\big),T\big(g(y,z),g(y',z')\big)\right)$$

$$= T\left(\bigvee_{y\in S} T\big(f(x,y),g(y,z)\big),\bigvee_{y\prime\in S} T\big(f(x',y'),g(y',z')\big)\right)$$

$$= T\big((g\circ_T f)(x,z),(g\circ_T f)(x',z')\big).$$

ii) $For\ x,x'\in R\ \ y,y'\in S\ and\ z,z'\in K$

$$(g\circ_T f)(x.x',z.z')$$

$$= \bigvee_{y,y\prime\in S} T\big(f(x.x',y),g(y,z.z')\big)$$

$$= \bigvee_{y,y\prime\in S} T\big(f(x.x',y.y'),g(y.y',z.z')\big)$$

$$\geq \bigvee_{y,y\prime\in S} T\left(T\big(f(x,y),f(x',y')\big),T\big(g(y,z),g(y',z')\big)\right)$$

$$= T\left(\bigvee_{y\in S} T\big(f(x,y),g(y,z)\big),\bigvee_{y\prime\in S} T\big(f(x',y'),g(y',z')\big)\right)$$

$$= T\big((g\circ_T f)(x,z),(g\circ_T f)(x',z')\big).$$

Theorem 3.4. Let $f\in F(R\times S,E,F,L)$ be a perfect TL-ring homomorphism and T be a infinitely ⋁-distributive t-norm. If $A: R\to L$ is a TL-subring of R, then $f(A): S\to L$ is a TL-subring of S.

Proof. $For\ x,\ x'\in R\ \ y,y'\in S$

$\boldsymbol{R1})\ Since\ for\ x=0$

$T\big(A(0),f(0,0)\big)=1\ then$

$$f(A)(0)=\bigvee_{x\in R} T\big(A(x),f(x,0)\big)\ =1$$

R2) $f(A)(-y)=\big(-f(A)\big)(y)$

$$= -\bigvee_{x\in R} T\big(A(x),f(x,y)\big)$$

$$= \bigvee_{x\in R} T\big((-A)(x),f(x,y)\big)$$

$$= \bigvee_{x\in R} T\big(A(-x),f(x,y)\big)$$

$$\geq \bigvee_{x\in R} T\big(A(x),f(x,y)\big)=f(A)(y)$$

R3) $f(A)(y+y')=\bigvee_{x\in R} T\big(A(x),f(x,y+y')\big)$

$$= \bigvee_{x,x'\in R} T\big(A(x+x'),f(x+x',y+y')\big)$$

$$\geq \bigvee_{x,x\prime\in R} T\left(T\big(A(x),A(x')\big),T\big(f(x,y),f(x',y')\big)\right)$$

$$= T\left(\bigvee_{x\in R} T\big(A(x),f(x,y)\big),\bigvee_{x\prime\in R} T\big(A(x'),f(x',y')\big)\right)$$

$$= T\big(f(A)(y),f(A)(y')\big)$$

R4) $f(A)(y.y')=\bigvee_{x\in R} T\big(A(x),f(x,y.y')\big)$

$$= \bigvee_{x,x\prime\in R} T\big(A(x.x'),f(x.x',y.y')\big)$$

$$\geq \bigvee_{x,x\prime\in R} T\left(T\big(A(x),A(x')\big),T\big(f(x,y),f(x',y')\big)\right)$$

$$= T\left(\bigvee_{x\in R} T\big(A(x),f(x,y)\big),\bigvee_{x\prime\in R} T\big(A(x'),f(x',y')\big)\right)$$

$$= T\big(f(A)(y),f(A)(y')\big)$$

Theorem 3.5. Let $f\in F(R\times S,E,F,L)$ be a perfect TL-ring homomorphism and T be a infinitely ⋁-distributive t-norm. If $B: S\to L$ is a TL-subring of S, then $f^{-1}(B): R\to L$ is a TL-subring of R.

Proof. $For\ x,\ x'\in R\ \ y,y'\in S$

R1) $f^{-1}(B)(0)=\bigvee_{y\in S} T\big(B(y),f(0,y)\big)$

for $y=0\ \ T\big(B(0),f(0,0)\big)=1$ then

$f^{-1}(B)(0)=1.$

R2) $f^{-1}(B)(-x)=-f^{-1}(B)(x)$

$$= -\bigvee_{y\in S} T\big(B(y),f(x,y)\big)$$

$$= \bigvee_{y\in S} T\big((-B)(y),f(x,y)\big)$$

$$= \bigvee_{y\in S} T\big(B(-y),f(x,y)\big)$$

$$\geq \bigvee_{y\in S} T\big(B(y),f(x,y)\big)=f^{-1}(B)(x).$$

R3) $f^{-1}(B)(x+x') = \bigvee_{y\in S} T\big(B(y), f(x+x', y)\big)$

$= \bigvee_{y,y'\in S} T\big(B(y+y'), f(x+x', y+y')\big)$

$\geq \bigvee_{y,y'\in S} T\Big(T\big(B(y), B(y')\big), T\big(f(x,y), f(x',y')\big)\Big)$

$= T\left(\bigvee_{y\in S} T\big(B(y), f(x,y)\big), \bigvee_{y'\in S} T\big(B(y'), f(x',y')\big)\right)$

$= T\big(f^{-1}(B)(x), f^{-1}(B)(x')\big).$

R4) $f^{-1}(B)(x.x') = \bigvee_{y\in S} T\big(B(y), f(x.x', y)\big)$

$= \bigvee_{y,y'\in S} T\big(B(y.y'), f(x.x', y.y')\big)$

$\geq \bigvee_{y,y'\in S} T\Big(T\big(B(y), B(y')\big), T\big(f(x,y), f(x',y')\big)\Big)$

$= T\left(\bigvee_{y\in S} T\big(B(y), f(x,y)\big), \bigvee_{y'\in S} T\big(B(y'), f(x',y')\big)\right)$

$= T\big(f^{-1}(B)(x), f^{-1}(B)(x')\big).$

Theorem 3.6. Let $f \in F(R\times S, E, F, L)$ be a surjective perfect TL-ring homomorphism and T be a infinitely $\bigvee$-distributive t-norm. If $A: R \to L$ is a TL-ideal of R, then $f(A): S \to L$ is a TL-ideal of S.

Proof. The conditions R1, R2 and R3 are provided by Theorem 3.4.

R5)$_l$ $f(A)(y.y') = \bigvee_{x\in R} T\big(A(x), f(x, y.y')\big)$

$= \bigvee_{x,x'\in R} T\big(A(x.x'), f(x.x', y.y')\big)$

$\geq \bigvee_{x,x'\in R} T\Big(A(x), T\big(f(x,y), f(x',y')\big)\Big)$

$= T\left(\bigvee_{x\in R} T\big(A(x), f(x,y)\big), \bigvee_{x'\in R} f(x',y')\right)$

(f is surjective then $\bigvee_{x'\in R} f(x',y') = 1$)

$= \bigvee_{x\in R} T\big(A(x), f(x,y)\big) = f(A)(y).$

R5)$_r$ $f(A)(y.y') = \bigvee_{x\in R} T\big(A(x), f(x, y.y')\big)$

$= \bigvee_{x,x'\in R} T\Big(A\big(x.x', f(x.x', y.y')\big)\Big)$

$\geq \bigvee_{x,x'\in R} T\Big(A(x'), T\big(f(x,y), f(x',y')\big)\Big).$

Theorem 3.7. Let $f \in F(R\times S, E, F, L)$ be a perfect TL-ring homomorphism and T be a infinitely $\bigvee$-distributive t-norm. If $B: S \to L$ is a TL-ideal of S, then $f^{-1}(B): R \to L$ is a TL-ideal of R.

Proof. The conditions R1, R2 and R3 are provided by Theorem 3.5.

For $x, x' \in R \;\; y, y' \in S$

R5)$_l$ $f^{-1}(B)(x.x') = \bigvee_{y\in S} T\big(B(y), f(x.x', y)\big)$

$= \bigvee_{y,y'\in S} T\big(B(y.y'), f(x.x', y.y')\big)$

$= T\left(\bigvee_{y\in S} T\big(B(y), f(x,y)\big), \bigvee_{y'\in S} f(x',y')\right)$

$\left(\bigvee_{y'\in S} f(x',y') = 1 \text{ for all } x' \in R \text{ because f is TL} - \text{function. Then}\right)$

$= T\left(\bigvee_{y\in S} T\big(B(y), f(x,y)\big), 1\right)$

$= \bigvee_{y\in S} T\big(B(y), f(x,y)\big) = f^{-1}(B)(x).$

R5)$_r$ $f^{-1}(B)(x.x') = \bigvee_{y\in S} T\big(B(y), f(x.x', y)\big)$

$= \bigvee_{y,y'\in S} T\big(B(y.y'), f(x.x', y.y')\big)$

$\geq \bigvee_{y,y'\in S} T\Big(B(y'), T\big(f(x,y), f(x',y')\big)\Big)$

$= T\left(\bigvee_{y\in S} f(x,y), \bigvee_{y'\in S} T\big(B(y'), f(x',y')\big)\right)$

$$\left(\bigvee_{y\in S} f(x,y) = 1 \; for \; all \; x \in R\right)$$

because f is TL-function. Then

$$= \bigvee_{y'\in S} T\big(B(y'), f(x',y')\big) = f^{-1}(B)(x').$$

Definition 3.8. Let $f \in F(R\times S, E, F, L)$ be a TL-ring homomorphism. Define Kerf $\in F(R,L)$ and Imf $\in F(S,L)$ as follows.

$(Kerf)(x) = f(x,0)$ and

$$(Imf)(y) = \bigvee_{x\in R} f(x,y)$$

where $x \in R \; and \; y \in S$. Kerf is called *the kernel of f* and Imf is called *the image of f*.

Theorem 3.9. Let $f \in F(R\times S, E, F, L)$ be a complete TL-ring homomorphism then Kerf $\in F(R,L)$ is a TL-subring of R.

Proof. $For \; x, y \in R$

R1) $Kerf(0) = f(0,0) = 1$ because f is complete TL-ring homomorphism.

R2) $Kerf(-x) = f(-x,0) \geq f(x,0)$

$= Kerf(x)$.

R3) $Kerf(x+y) = f(x+y,0)$

$= f(x+y, 0+0) \geq T\big(f(x,0), f(y,0)\big)$

$= T\big(Kerf(x), Kerf(y)\big)$.

R4) $Kerf(xy) = f(xy,0) = f(xy,00)$

$\geq T\big(f(x,0), f(y,0)\big) = T\big(Kerf(x), Kerf(y)\big)$.

Theorem 3.10. Let $f \in F(R\times S, E, F, L)$ be a complete TL-ring homomorphism and T be a infinitely $\bigvee$-distributive t-norm. Then Imf $\in F(S,L)$ is a TL-subring of S.

Proof. $For \; x, x' \in R \;\; y, y' \in S$

R1) It follows $(Imf)(0)$

$$= \bigvee_{x\in R} f(x,0) = 1 \text{ because for x} = 0$$

$f(0,0) = 1$.

R2) $(Imf)(-y) = \bigvee_{x\in R} f(x,-y) \geq \bigvee_{x\in R} f(x,y)$

$= (Imf)(y)$ (because f is complete).

R3) $(Imf)(y+y') = \bigvee_{x\in R} f(x, y+y')$

$$= \bigvee_{x,x'\in R} f(x+x', y+y')$$

$$\geq \bigvee_{x,x'\in R} T\big(f(x,y), f(x',y')\big)$$

$$= T\left(\bigvee_{x\in R} f(x,y), \bigvee_{x'\in R} f(x',y')\right)$$

$= T\big(Imf(y), Imf(y')\big)$.

R4) $(Imf)(yy') = \bigvee_{x\in R} f(x, yy')$

$$= \bigvee_{x,x'\in R} f(xx', yy')$$

$$\geq \bigvee_{x,x'\in R} T\big(f(x,y), f(x',y')\big)$$

$$T\left(\bigvee_{x\in R} f(x,y), \bigvee_{x'\in R} f(x',y')\right)$$

$= T\big(Imf(y), Imf(y')\big)$.

Theorem 3.11. Let R and S be rings, (R,ER_L) and (S,FS_L) be TL-equalities and $f: R \to S$ function be a ring homomorphism. Then TL-function $\bar{f} \in F(R\times S, E, F, L)$ $\bar{f}: R\times S \to L$ defined by

$$\bar{f}(x,y) = \begin{cases} 1 & f(x) = y \\ 0 & f(x) \neq y \end{cases}$$

is a TL-ring homomorphism.

Proof. It is clear that $\bar{f}$ is a TL-function. Let obtain the TL-ring homomorphism conditions.

a) $\bar{f}(x+x', y+y')$

$$= \begin{cases} 1 & f(x+x') = y+y' \\ 0 & f(x+x') \neq y+y' \end{cases}$$

$$= \begin{cases} 1 & f(x)+f(x') = y+y' \\ 0 & f(x)+f(x') \neq y+y' \end{cases}$$

i) If $f(x+x') = y+y'$ then

$\bar{f}(x+x', y+y') = 1$ and the inequality

$\bar{f}(x+x', y+y') \geq T\left(\bar{f}(x,y), \bar{f}(x',y')\right)$

is satisfied.

ii) If $f(x+x') \neq y+y'$ then
$f(x)=y$ and $f(x')=y'$ can't be both because if it can
$f(x)+f(x')=y+y' \Rightarrow f(x+x')=y+y'$
so one of them doesn't exist then
$T\left(\bar{f}(x,y),\bar{f}(x',y')\right)=T(0,1)=0$
and the inequality
$\bar{f}(x+x',y+y') \geq T\left(\bar{f}(x,y),\bar{f}(x',y')\right)$
is satisfied.

b) $\bar{f}(xx',yy')=\begin{cases}1 & f(xx')=yy' \\ 0 & f(xx')\neq yy'\end{cases}$
$=\begin{cases}1 & f(x)f(x')=yy' \\ 0 & f(x)f(x')\neq yy'\end{cases}$

i) If $f(xx')=yy'$ then
$\bar{f}(xx',yy')=1$ and $\bar{f}(xx',yy')$
$\geq T\left(\bar{f}(x,y),\bar{f}(x',y')\right)$ is satisfied.

ii) If $f(xx')\neq yy'$ then
$f(x)=y$ and $f(x')=y'$ can't be both because if it can
$f(x)f(x')=yy' \Rightarrow f(xx')=yy'$
so one of them doesn't exist then

$T\left(\bar{f}(x,y),\bar{f}(x',y')\right)=T(0,1)=0$ and the inequality

$\bar{f}(xx',yy') \geq T\left(\bar{f}(x,y),\bar{f}(x',y')\right)$ is satisfied.

Theorem 3.12. Let $f \in F(R\times S,E,F,L)$ and $g \in F(S\times K,F,G,L)$ be TL-ring homomorphisms. Then

a) $Ker(g\circ_T f)=f^{-1}(Kerg)$.
b) $Im(g\circ_T f)=g(Imf)$.

Proof. a) $Ker(g\circ_T f)=(g\circ_T f)(x,0)$
$=\bigvee_{y\in S} T\big(f(x,y),g(y,0)\big)$
$=\bigvee_{y\in S} T\big(f(x,y),Kerg(y)\big)=f^{-1}(Kerg)(x).$

b) $Im(g\circ_T f)(z)=\bigvee_{x\in R}(g\circ_T f)(x,z)$
$=\bigvee_{x\in R}\left(\bigvee_{y\in S} T\big(f(x,y),g(y,z)\big)\right)$
$=\bigvee_{y\in S} T\left(\bigvee_{x\in R} f(x,y),g(y,z)\right)$
$=\bigvee_{y\in S} T\big((Imf)(y),g(y,z)\big)=g(Imf)(z).$

Theorem 3.13. Let $f \in F(R\times S,E,F,L)$ be a strong TL-ring homomorphism and T be a infinitely ∨-distributive t-norm. Then for $A \in F(R,L)$,

$f^{-1}\big(f(A)\big) \leq A+Kerf.$

Proof.

$f^{-1}\big(f(A)\big)(x)=\bigvee_{y\in S} T\big(f(A)(y),f(x,y)\big)$
$=\bigvee_{y\in S}\left(T\left(\bigvee_{x'\in R} T\big(A(x'),f(x',y)\big)\right),f(x,y)\right)$
$=\bigvee_{y\in S}\bigvee_{x'\in R} T\left(T\big(A(x'),f(x',y)\big),f(x,y)\right)$
$\leq \bigvee_{y\in S}\bigvee_{x'\in R} T\left(T\big(A(x'),f(x',y)\big),f(-x,-y)\right)$
$=\bigvee_{y\in S}\bigvee_{x'\in R} T\left(A(x'),T\big(f(x',y),f(-x,-y)\big)\right)$
$\leq \bigvee_{y\in S}\bigvee_{x'\in R} T\big(A(x'),f(x'-x,y-y)\big)$
$\leq \bigvee T\big(A(x'),f(x-x',0)\big)$
$=\bigvee T\big(A(x'),(Kerf)(x-x')\big)$

$(by\ x'+(x-x')=x)=(A+Kerf)(x).$

Theorem 3.14. Let (R_1, E_1), (R_2, E_2), (S_1, F_1) and (S_2, F_2) be TL-equivalence relations and

$f: R_1\times S_1 \to L$ $g: R_2\times S_2 \to L$ be TL-ring homomorphisms. Then the TL-function defined by

$g\times f: (R_1\times R_2)\times(S_1\times S_2)\to L$
$(g\times f)\big((x_1,x_2),(y_1,y_2)\big)=T(f(x_1,y_1),g(x_2,y_2))$
is a TL-ring homomorphism.

Proof. We proved that $(g\times f)$ is a TL-function in Theorem 2.18. Now we will prove the TL-ring homomorphism conditions.

H1. $x_1,x_1^*\in R_1, x_2,x_2^*\in R_2, y_1,y_1^*\in S_1$

$, y_2, y_2^* \in S_2$

$$(g \times f)\big((x_1, x_2) + (x_1^*, x_2^*), (y_1, y_2) + (y_1^*, y_2^*)\big)$$
$$= (g \times f)\big((x_1 + x_1^*, x_2 + x_2^*), (y_1 + y_1^*, y_2 + y_2^*)\big)$$
$$= T\big(f(x_1 + x_1^*, y_1 + y_1^*), g(x_2 + x_2^*, y_2 + y_2^*)\big)$$
$$\geq T\Big(T\big(f(x_1, y_1), f(x_1^*, y_1^*)\big), T\big(g(x_2, y_2), g(x_2^*, y_2^*)\big)\Big)$$
$$= T\Big(T\big(f(x_1, y_1), g(x_2, y_2)\big), T\big(f(x_1^*, y_1^*), g(x_2^*, y_2^*)\big)\Big)$$
$$= T\Big((g \times f)\big((x_1, x_2), (y_1, y_2)\big), (g \times f)\big((x_1^*, x_2^*), (y_1^*, y_2^*)\big)\Big).$$

H2. $x_1, x_1^* \in R_1, x_2, x_2^* \in R_2, y_1, y_1^* \in S_1,$ $y_2, y_2^* \in S_2$

$$(g \times f)\big((x_1, x_2).(x_1^*, x_2^*), (y_1, y_2).(y_1^*, y_2^*)\big)$$
$$= (g \times f)\big((x_1.x_1^*, x_2.x_2^*), (y_1.y_1^*, y_2.y_2^*)\big)$$
$$= T\big(f(x_1.x_1^*, y_1.y_1^*), g(x_2.x_2^*, y_2.y_2^*)\big)$$
$$\geq T\Big(T\big(f(x_1, y_1), f(x_1^*, y_1^*)\big), T\big(g(x_2, y_2), g(x_2^*, y_2^*)\big)\Big)$$
$$= T\Big(T\big(f(x_1, y_1), g(x_2, y_2)\big), T\big(f(x_1^*, y_1^*), g(x_2^*, y_2^*)\big)\Big)$$
$$= T\Big((g \times f)\big((x_1, x_2), (y_1, y_2)\big), (g \times f)\big((x_1^*, x_2^*), (y_1^*, y_2^*)\big)\Big).$$

4. References

[1] Baets B. De, Mesiar R., Triangular norms on product lattices, *Fuzzy Sets and Systems* 104 (1999) 61-75

[2] Demirci M. and Recasens J., Fuzzy Groups, Fuzzy Functions and Fuzzy Equivalence Relations, *Fuzzy Sets and Systems* 144 (2004) 441-458.

[3] Demirci M., Fuzzy Functions and Their Applications, *Journal of .Mathematical Analysis and Applications*_252 (2000) 495-517.

[4] Demirci M., Fundamentals of M-vague Algebra and M-Vague Arithmetic Operations, *Int. J. Uncertainly, Fuzziness Knowledge-Based Systems* 10, 1 (2002) 25-75.

[5] Karaçal F. and Khadjiev D, ∨-Distributive and infinetly ∨-distributive t-norms on complete lattice, *Fuzzy Sets and Systems* 151 (2005) 341-352

[6] Klement E.P., Mesiar R. and Pap E., Triangular Norms. Position Paper I: Basic Analytical and Algebraic Properties, *Fuzzy Sets and Systems* 143(2004) 5-26.

[7] Klement E.P., Mesiar R. and Pap E., Triangular Norms. Position Paper II: General Constructions and Parameterized Families, *Fuzzy Sets and Systems* 145 (2004) 411-438.

[8] Klement E.P., Mesiar R. and Pap E., Triangular Norms. Position Paper III: Continuous t-Norms, *Fuzzy Sets and Systems* 145 (2004) 439-454.

[9] Liu W.J., Fuzzy Invariant supgroups and fuzzy ideals, *Fuzzy Sets and Systems* 8 (1982) 133-139

[10] Liu W.J., Operations on fuzzy ideals, *Fuzzy Sets and Systems* 11 (1983) 31-41

[11] Malik D.S., Mordeson J.N., Fuzzy homomorphisms of rings, *Fuzzy Sets and Systems*, 46 (1992) 139-146

[12] Rosenfeld A., Fuzzy groups, *J. Math. Anal. Appl.* 35 (1971) 512-517

[13] S̆ostak A. P., Fuzzy Functions and an Extension of the Category L-Top of Chang-Goguen L-Topological Spaces, *Proceedings of the Ninth Prague Symposium*, pp. 271-294, Topology Atlas, Toronto, 2002

[14] Wang Z. D. and Yu Y. D., TL-subrings and TL-ideals, Part 2: Generated TL-ideals, *Fuzzy Sets and Systems* 87 (1997) 209-217.

[15] Wang Z. D. and Yu Y. D., TL-subrings and TL-ideals, Part 1: Basic concepts, *Fuzzy Sets and Systems* 68 (1994) 93-103.

[16]Yamak, S., Fuzzy Algebraic Structure and Fuzzy Representations, Postgraduate Thesis, Karadeniz Technical University, Institute of Science and Technology, 1995.

[17] Zadeh L. A., Fuzzy Sets, *Information and Control*, 8 (1965) 338-353.

JOURNAL OF SCIENCE
SAKARYA UNIVERSITY

Sakarya University Journal of Science

ISSN 1301-4048 | e-ISSN 2147-835X | Period Bimonthly | Founded: 1997 | Publisher Sakarya University | http://www.saujs.sakarya.edu.tr/

Title: Determination Of Environmental Radiation İn The Beach Sand Of Tatvan, Ahlat And Adilcevaz

Authors: Şule Karatepe, Muhammed Fatih Kuluöztürk
Recieved: 2018-12-28 17:49:02

Accepted: 2019-08-15 10:18:18

Article Type: Research Article
Volume: 23
Issue: 6
Month: December
Year: 2019
Pages: 1173-1176

How to cite
Şule Karatepe, Muhammed Fatih Kuluöztürk; (2019), Determination Of Environmental Radiation İn The Beach Sand Of Tatvan, Ahlat And Adilcevaz. Sakarya University Journal of Science, 23(6), 1173-1176, DOI: 10.16984/saufenbilder.504822
Access link
http://www.saujs.sakarya.edu.tr/issue/44246/504822

Sakarya University Journal of Science 23(6), 1173-1176, 2019

Gamma Dose Measurements in the Beach Sands of Tatvan, Ahlat and Adilcevaz

Şule KARATEPE*[1] and M. Fatih KULUÖZTÜRK[2]

Abstract

The determination of radiation level is important in living areas for human health. The aim of this study is to determine environmental radiation in the beach sands of Tatvan, Ahlat and Adilcevaz. Environmental gamma radiation and alpha-beta concentrations determined for 15 different points. It has used portable gamma survey meter which is NaI(TI) scintillation detector. It has also used portable alpha-beta survey meter which consist of ZnS(Ag) scintillator adhered to 0.25 cm (0.010 in) thick plastic scintillator. For α/β emission measurements mean value was measured 81.2 cpm. The mean gamma dose rate value was measured as 0.149 µSv/h for ground level and 0.130 µSv/h for 1 m above the ground. The annual effective dose equivalent was obtained as 261.0 µSv/y. The obtained results were compared with literature.

Keywords: radiation, beach sand, environment gamma

1. INTRODUCTION

People are exposed to ionizing radiation throughout their lives. therefore, determining the risks of gamma radiation is important for health physics. The main sources of background radiation are cosmic radiation and terrestrial radiation [1, 2, 3]. The cause of terrestrial radioactivity is natural or artificial radioactive elements in the soil, air, sand, water and rocks. exposed radioactive elements are commonly ^{238}U, ^{232}Th and ^{40}K for natural radioactivity, ^{137}Cs, ^{90}Sr and $^{239}+^{240}Pu$ for artificial radioactivity [4, 5]. Cosmic radiation can also have a significant effect on high altitude areas [6].

In the recent years; in many countries, determining the level and risk of radiation has become important. Therefore, many researches have been done associated with radiation levels and risks in these countries [4, 5, 6, 7, 8] and in Turkey [9, 10, 11].

The beach sands are mineral deposits formed through weathering and erosion of either igneous or metamorphic rocks [4, 8]. The radiation hazards arising from sand are known that natural radiation is the important contributor to external radiation dose [8]. The most important point in radiation protection is the determination of the radiation dose from external sources.

The coastline of Lake Van is especially used by local residents to swim in the lake and to sunbathe in summer. Therefore, the objective of this paper is to determine the radiological hazards due to natural radioactivity associated with beach sands by measuring environmental gamma dose and α/β emissions. Radiological studies were made on sand of beach locations in Tatvan, Ahlat and Adilcevaz. The obtained results were compared with limit values determined by UNSCEAR [2].

* Corresponding Author: shulekaratepe@beu.edu.tr
[1] Bitlis Eren University, Hizan Vocational School, Bitlis, TURKEY. ORCID: 0000-0001-8125-2231
[2] Bitlis Eren University, Hizan Electrical and Electronics Engineering Department, Bitlis, TURKEY. ORCID:0000-0001-8581-2179

2. MATERIAL AND METHOD

Figure.1 Location of study area in Turkey and Van Lake (Google Maps).

Tatvan, Ahlat and Adilcevaz are located in the north western part of Van Lake (Figure 1). 15 different points were determined for measurement of radioactivity in Tatvan, Ahlat and Adilcevaz beachs where covers almost 100 km of Van Lake coastline and locations of these points were fixed by GPS device. Because of these regions are also located in Nemrut and Süphan volcanic mountains, beach sands have different types from each other. The measurements were recorded in autumn.

Gamma dose levels and α/β emissions of sample points were determined at the site. The environmental gamma measurements were made by Dose Rate Meter (LUDLUM Model 2241 Digital Scaler/Ratemeter + LUDLUM Model 44-10 Prob) that it is containing scintillation counter having to 2"x2" NaI (Tl) crystal at ground and 1m above the ground. Also α/β measurements were made portable (LUDLUM Model 2224-1 alpha/beta Scaler/Ratemeter + LUDLUM Model 43-2-2 Prob) alpha-beta survey meter which consist of ZnS(Ag) scintillator adhered to 0.25 cm (0.010 in) thick plastic scintillator at ground [12]. Readings are represented in terms of R/hr, Sv/h, cpm, or cps. Uncertainty in reading was less than 20% at maximum sensitivity (using manufacturer's calibration) [12].

The locations of the sample points were given in Figure 1 and coordinates of locations were given in Table 1. Measurements were made on-site in areas. Gamma dose rates were recorded as μSv/h. The obtained results are average of five measurements.

The annual effective dose equivalent (AEDE);

$$AEDE = ADRA * OF * T \quad (1)$$

where ADRA is absorbed dose rate in air, OF is outdoor occupancy factor (0.2) and T is the time (8760 hy^{-1}) [2].

3. RESULTS AND DISCUSSION

Environmental gamma measurements were taken on the sand ground and 1m above the ground levels. α/β concentration measurements were also taken on the sand ground and the results were given in Table 1 and are shown Figure 2 and Figure 3.

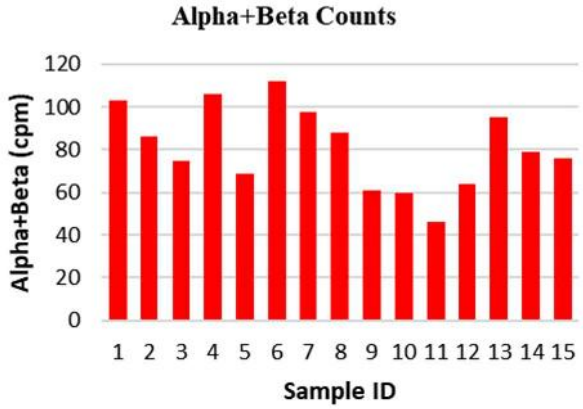

Figure.2 Alpha+Beta count results for each sampling points

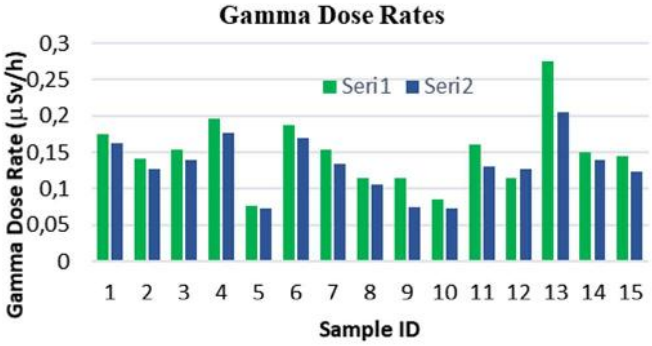

Figure.3 Gamma dose rates on ground and above 1 m for each sampling points

As shown in Table 1 and Figure 2; in the environmental gamma measurement, values in sand ground level are higher than values that were measured at 1 m level.

Table.1 Environmental gamma dose rate and α/β emissions measurement results and coordinates of sampling points.

Sample ID	Latitude	Longitude	Alpha+Beta (cpm)	Gamma (ground) μSv/h	Gamma (1m above) μSv/h
TTVN-01	38°28'53.03"N	42°18'26.44"E	103	0.174	0.162
TTVN-02	38°31'43.03"N	42°18'49.12"E	86	0.142	0.127
TTVN-03	38°31'39.89"N	42°19'00.49"E	75	0.154	0.139
TTVN-04	38°32'58.31"N	42°21'23.19"E	106	0.196	0.177
TTVN-05	38°35'07.15"N	42°23'22.20"E	69	0.076	0.072
AHLT-01	38°37'01.63"N	42°24'16.66"E	112	0.187	0.170
AHLT-02	38°37'40.06"N	42°27'28.43"E	98	0.154	0.134
AHLT-03	38°43'04.30"N	42°25'50.35"E	88	0.115	0.106
AHLT-04	38°45'17.12"N	42°30'36.56"E	61	0.115	0.075
AHLT-05	38°45'22.11"N	42°31'05.65"E	60	0.085	0.073
ADCZ-01	38°46'48.90"N	42°36'28.33"E	46	0.160	0.130
ADCZ-02	38°47'51.83"N	42°44'10.30"E	64	0.115	0.127
ADCZ-03	38°47'41.31"N	42°44'52.58"E	95	0.275	0.205
ADCZ-04	38°47'05.48"N	42°50'34.60"E	79	0.150	0.140
ADCZ-05	38°47'13.43"N	42°50'42.51"E	76	0.145	0.124
Min.			**46**	**0.076**	**0.072**
Max.			**112**	**0.275**	**0.205**
Mean			**81.2**	**0.149**	**0.130**

Maximum value is 0.275 μSv/h in sample ADCZ-03 and minimum value is 0.076 μSv/h for sample TTVN-05 in ground level. Likewise, for 1 m above the sand level, maximum value is 0.205 μSv/h in sample ADCZ-03 and minimum value is 0.072 μSv/h in sample TTVN-05 as ground level. The mean gamma dose rate value is 0.149 μSv/h for ground level and 0.130 μSv/h for 1 m above the ground. Ground levels are lower than 1 m above sand levels. But 1 m above sand level is higher than ground level for ADCZ-03. This sample point is area of beach sports.

As shown in Table 1 and Figure 3; for α/β emission measurements, maximum alpha+beta emission value is 112 cpm in sample AHLT-01, minimum value is 45 cpm in ADCZ-01 and the mean value is 81.2 cpm.

Table.2 The annual effective gamma dose equivalent value of different area in the literature.

Area	Annual effective dose equivalent (μSv/y)
Artvin, Turkey [13]	214.5
Pahang State, Malesia [14]	215.8
Kashmir, Pakistan [15]	497.0
Bushehr, Iran [16]	360
İstanbul, Turkey [17]	75
Present study	261.0
World average [2]	73.6

As shown Table 2, when the obtained results were compared with the literature, it was determined that the results were higher than the world average. However, these results are approximately the same as other studies.

4. CONCLUSION

When the radioactivity values in these regions are evaluated in themselves; Tatvan region has the maximum average alpha+beta emission value as 87.8 cpm and Adilcevaz region has the minimum average alpha+beta emission value as 72 cpm. Beta background levels on floors range from 250 to 450 cpm and alpha background level is 1 cpm in the literature [18]. Hence, the obtained results are lower than the litarature.

For annual gamma dose values; Adilcevaz region has the maximum average gamma dose rate value as 481.8 μSv/y and Ahlat region has the minimum average gamma dose rate value as 126.1 μSv/y.

The mean annual effective dose equivalent is 261.0 μSv/y. This mean obtained result for Tatvan, Ahlat and Adilcevaz beaches is approximately two times bigger than the world average, 73.6 μSv/y [2]. But the radiation received by the population due to beach sands is mainly the result of the spent time on the beach during summer. Therefore, the results show that Tatvan, Ahlat and Adilcevaz beaches can't be considered as an unsafe area with natural background radiation. The higher dose of the gamma radiation dose

of the Tatvan, Ahlat and Adilcevaz beaches can be related to the geological soils and rocks of the Nemrut and Süphan volcanic mountains.

Acknowledgements
This work is supported by Bitlis Eren University Scientific Research Project Support Unit. Project number: 2018.09.

REFERENCES

[1] UNSCEAR: Sources and effects of ionizing radiation, annex B: exposure of the public and workers from various sources of radiation. New York: United Nations Scientific Committee on the Effect of Atomic Radiations; 2010.

[2] UNSCEAR: REPORT Vol. I sources and effects of ionizing radiation, annex a: dose assessment methodologies. New York: United Nations Scientific Committee on the effects of atomic radiation; 2000.

[3] A. M. Pashazadeh, M. Aghajani, I. Nabipour and M. Assadi, "Annual effective dose from environmental gamma radiation in Bushehr city. Journal of Environmental Health Science & Engineering," *Journal of Environmental Health Sciences & Engineering*, 12:4, 2014.

[4] M. SureshGandhi, R. Ravisankar, A. Rajalakshmi, S. Sivakumar, A. Chandrasekaran, D. Pream Anand, "Measurements of natural gamma radiation in beach sediments of north east coast of Tamilnadu, India by gamma ray spectrometry with multivariate statistical approach. Journal of Radiation Research and Applied Sciences," *Journal of Radiation Research and Applied Sciences,* vol.7, no. 1, pp. 7-17, 2014.

[5] S. Şahin Bal, Ş. Karatepe, M. F. Kuluöztürk, E. Yılmaz, M. Kurşat, "The annual change of environmental gamma radiation in Bitlis," *Bitlis Eren University Journal of Science and Technology*, vol. 8, no. 1, pp. 19–23, 2018.

[6] A.K. Mohanty, D. Sengupta, S.K. Das, S.K. Saha, K.V. Van. "Natural radioactivity and radiation exposure in the high background area at Chhatrapur beach placer deposit of Orissa, India" *Journal of Environmental Radioactivity,* vol. 75, pp. 15–33, 2004.

[7] H. K. Shuaibu, M. U. Khandaker, T. Alrefae, D.A. Bradley, "Assessment of natural radioactivity and gamma-ray dose in monazite rich black Sand Beach of Penang Island, Malaysia," *Marine Pollution Bulletin* vol.119, 423–428, 2017.

[8] A. Papadopoulos, A. Koroneos, G. Christofides, and S. Stoulos, "Natural radioactivity distribution and gamma radiation exposure of beach sands close to Kavala pluton, Greece," *Open Geosci*ences, 1 pp. 407–422, 2015.

[9] Z. Korkulu, N. Özkan, "Determination of natural radioactivity levels of beach sand samples in the black sea coast of Kocaeli (Turkey)," *Radiation Physics and Chemistry* vol. 88, pp. 27–31, 2013.

[10] S.F. Özmen, A. Cesur, I. Boztosun, M. Yavuz, "Distribution of natural and anthropogenic radionuclides in beach sand samples from Mediterranean Coast of Turkey," *Radiation Physics and Chemistry,* vol. 103, pp. 37–44, 2014.

[11] H. Kayakökü, Ş. Karatepe, M. Doğru, "Measurements of radioactivity and dose assessments in some building materials in Bitlis, Turkey," *Applied Radiation and Isotopes,* vol. 115, pp. 172–179, 2016.

[12] LUDLUM, Model 44-10 Gamma Scintillator, Ludlum Measurements, Inc., Texas, 2012.

[13] Y. Kobya et al. " Evaluation of Outdoor Gamma Dose Rate and Cancer Risk in Artvin Province, Turkey," *Human and Ecological Risk Assessment: An International Journal*, vol.21:8, pp. 2077-2085, 2015.

[14] H. T. Gabdo et al. " Terrestrial gamma dose rate in Pahang state Malaysia," *J Radioanal Nucl Chem,* vol. 299 pp.1793–1798, 2014.

[15] M. Rafique, " Ambient indoor/outdoor gamma radiation dose rates in the city and at high altitudes of Muzaffarabad (Azad Kashmir)" *Environ Earth Sci*, vol.70, pp.1783–1790, 2013.

[16] A. M. Pashazadeh, M. Aghajani, I. Nabipour and M. Assadi, " Annual effective dose from environmental gamma radiation in Bushehr city,"Jour*nal Of Environmental Health Science & Engineering*, vol.12:4, 2014.

[17] O. Günay, "Assessment of lifetime cancer risk from natural radioactivity levels in Kadikoy and Uskudar District of Istanbul," *Arabian Journal of Geosciences,* vol.11 pp. 782, 2018.

[18] J. R. Morton,"Radıologıcal assessment survey of the vance road facılıty source vault buıldıng materıals oak rıdge ınstıtute for scıence and educatıon oak rıdge, Tennessee," *Vance Road Facility, Source Vault Area,* 0531, 2000.

JOURNAL OF SCIENCE
SAKARYA UNIVERSITY

Sakarya University Journal of Science

ISSN 1301-4048 | e-ISSN 2147-835X | Period Bimonthly | Founded: 1997 | Publisher Sakarya University | http://www.saujs.sakarya.edu.tr/

Title: NMR and DSC studies on the reactions of pentanedioxy spiro-ansa cyclochlorotriphosphazene and pentanedioxy triple-bridged cylochlorotriphosphazene with monofunctional nucleophiles

Authors: Rafig Gurbanov, Murat Tuna, Sedat Türe

Recieved: 2019-03-15 00:17:29

Accepted: 2019-08-16 17:01:11

Article Type: Research Article
Volume: 23
Issue: 6
Month: December
Year: 2019
Pages: 1177-1189

How to cite
Rafig Gurbanov, Murat Tuna, Sedat Türe; (2019), NMR and DSC studies on the reactions of pentanedioxy spiro-ansa cyclochlorotriphosphazene and pentanedioxy triple-bridged cylochlorotriphosphazene with monofunctional nucleophiles. Sakarya University Journal of Science, 23(6), 1177-1189, DOI: 10.16984/saufenbilder.540276
Access link
http://www.saujs.sakarya.edu.tr/issue/44246/540276

Sakarya University Journal of Science 23(6), 1177-1189, 2019

NMR and DSC studies on the reactions of pentanedioxy spiro-ansa cyclochlorotriphosphazene and pentanedioxy triple-bridged cylochlorotriphosphazene with monofunctional nucleophiles

Rafig Gurbanov[1]*[2], Murat Tuna[3], Sedat Türe[4]

Abstract

In this study, the reactions of 2-(2-hydroxyethyl) thiophene (**2**) and benzyl alcohol (**3**) with pentanedioxycyclochlorotriphosphazene (**1**) and pentanedioxy triple-bridged cylochlorotriphosphazene (**6**) were studied. The novel cyclotriphosphazene compounds: two di-substituted spiro-ansa, $N_3P_3[O(CH_2)_5O]$-$(C_6H_7OS)]_2$ (**4**) and $N_3P_3[O(CH_2)_5O$-$(C_6H_5CH_2O)]_2$ (**5**); and two fully substituted triple-bridged, $N_3P_3[O(CH_2)_5O]_3$-$(C_6H_7OS)_6N_3P_3$ (**7**) and $N_3P_3[O(CH_2)_5O]_3$-$(C_6H_5CH_2O)_6N_3P_3$ (**8**) derivatives were formed in THF solvent by using NaH base at ambient conditions. Because of their variety of applications, there is a great deal of interest in the preparation of aromatic macrocyclic derivatives of cyclophosphazenes. The main purpose of these studies is to develop bioactive cyclophosphazene derivatives in the search for new effective drug candidates for the treatment of various diseases, in particular, anticancer and antimicrobials. The synthesized compounds (**4, 5, 7, 8**) were defined using analytical techniques namely Element analysis, TLC/MS system, and NMR spectroscopy. Thermal stabilities, crystal purity, and recrystallization properties and corresponding enthalpies of synthesized derivatives were analyzed in the course of heating and cooling cycles of DSC.

Keywords: Cyclophosphazene, spiro-ansa compounds, triple-bridged compounds, monofunctional nucleophilic reagents, Nuclear magnetic resonance spectroscopy, Differential scanning calorimetry

1. INTRODUCTION

Cyclic phosphazene compounds demonstrate unique thermal features which are composed of interspersing phosphorus and nitrogen atoms with two substituents attached to the phosphorus atoms [1]. Alongside, cyclotriphosphazene-based materials are of special interest not only because of their stable chemical properties but also due to their flame-retardant features [1]. Due to these properties, there are military programs carrying out basic research on the synthesis and properties of polyphosphazenes and phosphazene fluids for the army, navy, other governmental, and commercial applications [2].

The biological activities of phosphazene derivatives are also at the target of current research due to their medicinal applications in the therapy of microbial, fungal and oncological diseases [3]–[7]. In this, special attention should be again given to cyclophosphazene ring carrying various groups of atoms, since they demonstrate antitumor features [8], [9]. The cytotoxicity of cyclotriphosphazenes against blood, lung, cervix, larynx, colon, bladder, prostate, and breast cancer cell lines have been shown in many studies [9]–[13].

Valuable molecular information on different cyclotriphosphazene derivatives can be extracted using thermo-analytical and spectroscopic

characterization techniques [14]–[19]. In brief, DSC presents quantitative and qualitative information about endothermic and exothermic chemical processes, by directly measuring the melting behavior of compound [14], [20], [21]. On the other hand, spectroscopic techniques yield a spectrum representing the unique molecular fingerprint of any substance [22].

The hexachlorocyclophosphazatrienes (**1**) reacting with functional substitutive atoms are of special interest [23]–[32]. In this, the diols are seemed to be the most important [13], [27], [33]–[38], in which spiro, ansa, linear, and bridged chain molecules were identified. The previous studies have shown the heat-induced conversion of bridged-chain fluorophosphazine into a spiro form along with the catalyst-induced remodeling of eight-membered ansa derivatives into six-membered spiro isomers [23], [39], [40]. The mentioned findings are in agreement with the evidence pronouncing the thermodynamic stability of spiro compounds over bridged-chains and/ or ansa ones [41], [42].

The aim of this work was to probe the arrangement profiles of spiro-ansa replaced cyclophosphazene compounds (**1**) with monofunctional nucleophiles. The expansion of the presented work in terms of the antitumor and antimicrobial activities will be executed in the short run.

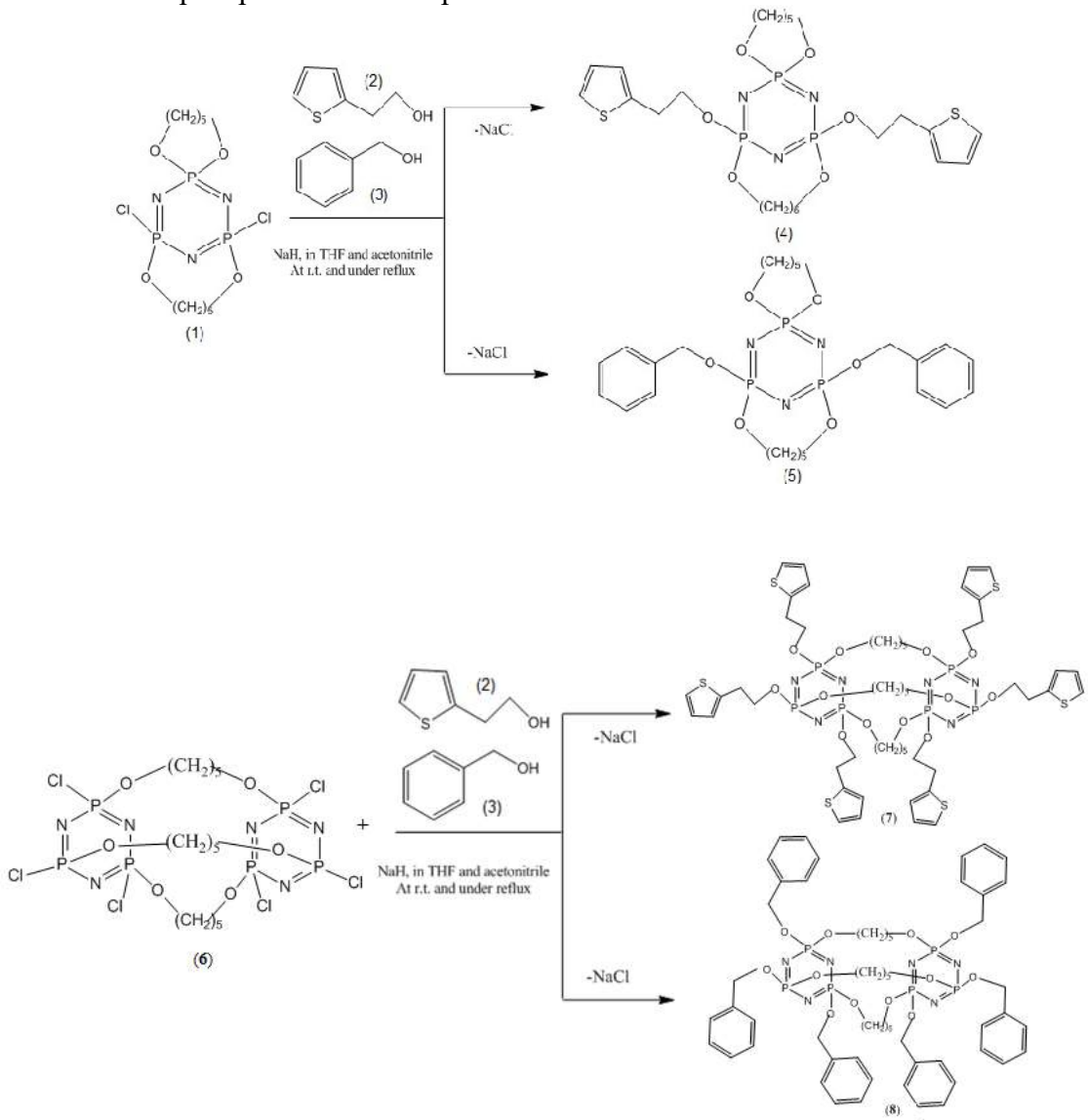

Figure 1. Chemical reaction flowchart for derived products (**4, 5, 7, 8**).

2. EXPERIMENTAL

2.1. Materials

Reagent-grade solvents; THF, dichloromethane, diethyl ether, chloroform, benzene, petroleum (b.p. 40-60^0 C) were obtained from May & Baker Ltd., UK. Deuterated $CDCl_3$ (using as an NMR lock) for NMR spectroscopy, benzyl alcohol, 2-thiophenethanol, 1,4-butanediol, and 1,5-pentanediol were obtained from Aldrich Chem. Co. Ltd. Chemicals leftover from our previous works: $NaBH_4$/NaH and hexachlorocyclotriphosphazatriene were obtained from Sigma & Aldrich Chem. Co. Ltd. TLC plates and silica gel (60, 0.063–0.200 mm), for chromatographic applications, were acquired from Merck Merck & Co., Inc., Solvents were dried by known basic methods. Dichloromethane and THF were distilled on a sodium-potassium alloy under a dry argon atmosphere. Hexachlorocyclotriphosphazene was purified by fractional crystallization technique from n-hexane.

2.2. Methods

Reactions were followed up by using Kieselgel 60^0 254 with pre-coated TLC plates and sprayed with Ninhydrin (0,5% w/v) in a butanol solution and elaborated about at 130^0 C.

The products were separated by column chromatography using Kieselgel 60 (Merck 60, 0.063–0.200 mm). Melting points were established with a Hot Stage Microscopy connected to an FP 800 central processor attached to a polarizing microscope. Elemental analyses were achieved by using a Thermo Finnigan Flash 1112 Instrument. Mass spectra were recorded using a TLC/MS Advion Mass Spectrometer.

^{1}H NMR spectra were recorded using a Varian INOVA 500 MHz and a Bruker DRX spectrometer operating at 499 MHz. and at 500 MHz. respectively. Measurements were performed by using a $CDCl_3$ lock, TMS was used as an internal reference in sample concentrations of 15-20 mg cm^3. ^{31}P NMR spectra were performed by using a Bruker AVII and AVIIIHD 400 MHz spectrometer, operating at 161.97 MHz. (measurements were carried out in $CDCl_3$ using 85%, H_3PO_4 as an external reference.

For thermal analysis, Differential Scanning Calorimetry (DSC) was used according to our previous study [43]. The compounds in crystal form were placed in special DSC containers (aluminum hermetic pans) and sealed using Sample Encapsulating Press. The experiment was conducted through heating and cooling cycles, in which the specimen was heated from -30 °C to 250 °C and then cooled down with a ramp of 5 °C/min. The melting and crystallization events were identified on the basis of corresponding peak locations. The integrated peak area was divided linearly to the specimen mass to determine the enthalpy changes (ΔH° J/g) were calculated by dividing the integrating peak area to the sample weight.

Experimental details together with product types and the relative yields are summarized in Table 1, whereas the NMR data may be found in Tables 2 and 3. The calorimetric characterization of compounds (**4, 5, 7, and 8**) is illustrated in Table 4.

2.3. Synthesis

(**a**) The reactions of pentanedioxycyclochlorotriphosphazene (**1**) with 2-Thiophen ethanol (**2**): Two equivalents of **2**, in excess of NaH, in THF at room temperature: Pentanedioxycyclochlorotriphosphazene (**1**, 0.5 g, 1.2 mmol) was dissolved in dry chloroform (30 mL) in a 250 mL three-necked round-bottomed flask under an argon atmosphere and the reaction mixture was cooled to 0^0 C in ice-bath. NaH (0.115 g, 4.8 mmol) was dissolved in chloroform (10 mL) and the reaction mixture was stirred for half an hour on a magnetic stirrer. After, 2-Thiophen ethanol (**2**, 0.30 g, 2.4 mmol) was dissolved in dry chloroform (20 mL) added dropwise into the stirred solution under an argon atmosphere. Then the reaction mixture was kept stirring for about 48 h at room temperature.

The reaction was followed by TLC silica gel plates using dichloromethane-diethyl ether (5:1) as the eluent for completion of the reaction. Except in small quantity of starting material (**1**) one spot was observed on TLC, using dichloromethane-diethyl ether (5:1) as the mobile phase. The reaction mixture was filtered to remove the NaCl salts and some other insoluble balky materials. The solvent was removed from

the reaction mixture under reduced pressure and the resulting white-colored solid was subjected to column chromatography using the same solvent system as described above. Di-substituted spiro-ansa, $N_3P_3[O(CH_2)_5O]$-$(C_6H_7OS)]_2$ (**4**) derivative was synthesized and characterized. Yield 0.34 g, 78%, m.p.109 °C. Anal. Calc. for $N_3P_3C_{22}H_{34}O_6S_2$: C, 44.52; H, 5.77; N, 7.08, M, 593.505. Found: C, 44.51; H, 5.80; N, 7.08, M^+, 594.39.

(**b**) The reactions of pentanedioxycyclochlorotriphosphazene (1) with Benzyl alcohol (**2**). Two equivalents of **3**, in excess of NaH, in THF at room temperature: Pentanedioxycyclochlorotriphosphazene (1, 0.5 g, 1.2 mmol) was dissolved in dry chloroform (30 mL) in a 250 mL three-necked round-bottomed flask under an argon atmosphere and the reaction mixture was cooled to 0^0 C in ice-bath. NaH (0.115 g, 4.8 mmol) was dissolved in chloroform (10 mL) and the reaction mixture was stirred for half an hour on a magnetic stirrer. After, Benzyl alcohol (**3**, 0.25 g, 2.4 mmol) was dissolved in dry chloroform (20 mL) and added dropwise into the stirred solution under an argon atmosphere. Then the reaction mixture was kept stirring for about 48 h at room temperature.

For completion of the reaction, the reaction was followed by TLC silica gel plates using dichloromethane-diethyl ether (3:1) as the eluent. Except in small quantity of starting material (**1**) one spot was observed on TLC, using dichloromethane-hexane (3:1) as the mobile phase. The reaction mixture was filtered to remove the NaCl salts and some other insoluble balky materials. The solvent was removed from the reaction mixture under reduced pressure and the resulting white-colored solid was subjected to column chromatography using the same solvent system as described above. Except for some glue type insoluble resinous materials, di-substituted spiro-ansa, $N_3P_3[O(CH_2)_5O$-$(C_6H_5CH_2O)]_2$ (**5**) was synthesized and characterized. Yield 0.40 g, 82%, m.p.109 °C. Anal. Calc. for $N_3P_3C_{24}H_{34}O_6$: C, 52.08; H, 6.19; N, 7.59, M, 553.407. Found: C, 53.0; H, 6.23; N, 7.59, M^+, 554.43.

(**c**) The reactions of pentanedioxy triple-bridged cylochlorotriphosphazene (**6**) with 2-Thiophen ethanol (**2**). Six equivalents of **2**, in excess of NaH, in chloroform at room temperature: pentanedioxy triple-bridged cylochlorotriphosphazene (**6**, 0.5 g, 0.6 mmol) was dissolved in dry chloroform (40 mL) in a 250 mL three-necked round-bottomed flask under an argon atmosphere and the reaction mixture was cooled to 0^0 C in ice-bath. NaH (0.172 g, 7.2 mmol) was dissolved in 10 mL of the above-mentioned solvent system and the reaction mixture was stirred for half an hour on a magnetic stirrer. After, 2-Thiophen ethanol (**2**, 0.46 g, 3.6 mmol) was dissolved in dry chloroform (20 mL) and added dropwise into the stirred solution under an argon atmosphere. Then the reaction mixture was kept stirring for about 96 h at room temperature. The reaction was followed by TLC silica gel plates using dichloromethane-hexane (2:1) as the eluent. One spot was observed on TLC, using dichloromethane-hexane (2:1) as the mobile phase. The reaction mixture was filtered to remove the NaCl salts and some other insoluble balky materials. The solvent was removed from the reaction mixture under reduced pressure and the resulting white-colored solid was subjected to column chromatography using the same solvent system as described above. The synthesized product was recrystallized from benzene-hexane (1:5) to give white crystals of Hexa-substituted tripel-bridged, $N_3P_3[O(CH_2)_5O]_3$-$(C_6H_7OS)_6N_3P_3$ (**7**) derivative, yield 0.30 g, 71%, m.p. 206 °C. Anal. Calc. for $N_6P_6C_{51}H_{72}O_{12}S_6$: C, 45.73; H, 5.41; N, 6.27, M, 1339.239. Found: C, 45.75; H, 5.46; N, 6.27, M^+, 1340.29.

(**d**) The reactions of hexachlorocyclotriphosphazatriene (1) with Benzyl alcohol (**2**). Six equivalents of **3**, in excess of NaH, in Chloroform at room temperature: Cyclotriphosphazene (**1**, 0.5 g, 0.6 mmol) was dissolved in dry chloroform (40 mL) in a 250 mL three-necked round-bottomed flask under an argon atmosphere and the reaction mixture was cooled to 0^0 C in ice-bath. NaH (0.172 g, 7.2 mmol) was dissolved in 10 mL of the above-mentioned solvent system and the reaction mixture was stirred for half an hour on a magnetic stirrer. After, Benzyl alcohol (**3**, 0.38 g, 3.6 mmol) was dissolved in dry chloroform (20 mL) and added dropwise into the stirred solution under an argon atmosphere. Then the reaction mixture was kept stirring for about 96 h at room temperature. The reaction was followed by TLC silica gel

plates using dichloromethane-diethyl ether (3:1) as the eluent for completion of the reaction. Except in small quantity of starting material (**6**) one spot was observed on TLC, using dichloromethane-diethyl ether (3:1) as the mobile phase. The reaction mixture was filtered to remove the NaCl salts and some other insoluble resinous materials. The solvent was removed under reduced pressure and the resulting white-colored solid was subjected to column chromatography using the same solvent system as described above. The product was recrystallized from benzene-hexane (1:6) to give white crystals of Hexa substituted tripel-bridged, $N_3P_3[O(CH_2)_5O]_3$-$(C_6H_5CH_2O)_6N_3P_3$ (**8**) derivative. Yield 0.32 g, 83%, m.p. 208 °C. Anal. Calc. for $N_6P_6C_{57}H_{72}O_{12}$: C, 48.49; H, 5.14; N, 5.95, M, 1411.785. Found: C, 48.51; H, 5.17; N, 5.95, M^+, 1412.81.

Table 1. Elemental analysis and the percentage yields of compounds (**4, 5, 7, 8**).

Classification (%)	**Calculated**				**Found**			
Compound	H (%)	C (%)	N (%)	M	H (%)	C (%)	N (%)	$[M^+H]^+$
4 (78%)	5.77	44.52	7.08	593.505	5.80	44.51	7.08	594.39
5 (82%)	6.19	52.08	7.59	553.407	6.23	53.00	7.59	554.43
7 (71%)	5.41	45.73	6.27	1339.239	5.46	45.75	6.27	1340.29
8 (83%)	5.14	48.49	5.95	1411.785	5.17	48.51	5.95	1412.81

3. RESULTS AND DISCUSSION

The interaction between pentanedioxycyclochlorotriphosphazene (**1**) and pentanedioxy triple-bridged cylochlorotriphosphazene (**6**) and 2-(2-hydroxyethyl) thiophene (**2**) and benzyl alcohol (**3**) gave rise to 4 novel synthesized products: two di-substituted spiro-ansa, $N_3P_3[O(CH_2)_5O]$-$(C_6H_7OS)]_2$ (**4**, 78%), and $N_3P_3[O(CH_2)_5O$-$(C_6H_5CH_2O)]_2$ (**5**, 82%); and two hexa-substituted tripel-bridged, $N_3P_3[O(CH_2)_5O]_3$-$(C_6H_7OS)_6N_3P_3$ (**7**, 71%), and $N_3P_3[O(CH_2)_5O]_3$-$(C_6H_5CH_2O)_6N_3P_3$ (**8**, 83%) derivatives.

Analytical techniques namely, Elemental analysis, TLC-MS, ^1H, and ^{31}P NMR spectroscopy were utilized for the characterization of synthesized derivatives. Thermal properties, such as thermal stabilities, crystal purity, and crystallization features were determined using DSC technique. All of the synthesized compounds are thermally stable and water-soluble. The structures of the derived compounds (**4, 5, 7, 8**) are shown in Figure 1.

The spiro-ansa compounds (**4**) and (**5**) replaced with 2-thiophene ethanol and benzyl alcohol, respectively displayed A_2X type NMR spectra. Because of the ≡P spiro and ≡P(OR)OR groups, the ^{31}P NMR spectrum of spiro-ansa derivative permitted characterization of the lines, where each group divide into further lines. Comparison of the results with the previous findings on spiro-ansa structures [44], provided clear identification of the derivatives. The yield proportions of the substances are discussed above.

The spectra of the triple-bridged derivatives (**7** and **8**), were found as spin A_3 type emerging from equal or resembling surroundings at the end of bridges among phosphorus nuclei. One single line is identified for these derivatives, due to the similar nature of the bounded groups and chemically and magnetically identical surroundings of ≡P(OR)OR groups.

The spectra of compound **4**, $N_3P_3[O(CH_2)_5O]$-$(C_6H_7OS)]_2$ is illustrated in Figure 2. Whereas, Table 2 shows the selected criteria (chemical shifts and coupling constants).

Table 2. ^{31}P NMR spectral data from the synthesized derivatives (**4, 5, 7, 8**)[a]

Compound	δP(OR)$_2$[b]	δP(OR)OR[b]	^2J[P(OR)$_2$-P(OR)OR][c]	
(**1**)				[44]
(**6**)				[44]
(**4**)	17.73	25.11	63.72	
(**5**)	18.40	24.60	64.13	
(**7**)		17.73		
(**8**)		17.90		

[a]In $CDCl_3$, relative to 85% H_3PO_4 standard at 161.97 MHz
[b]In ppm
[c]In Hz

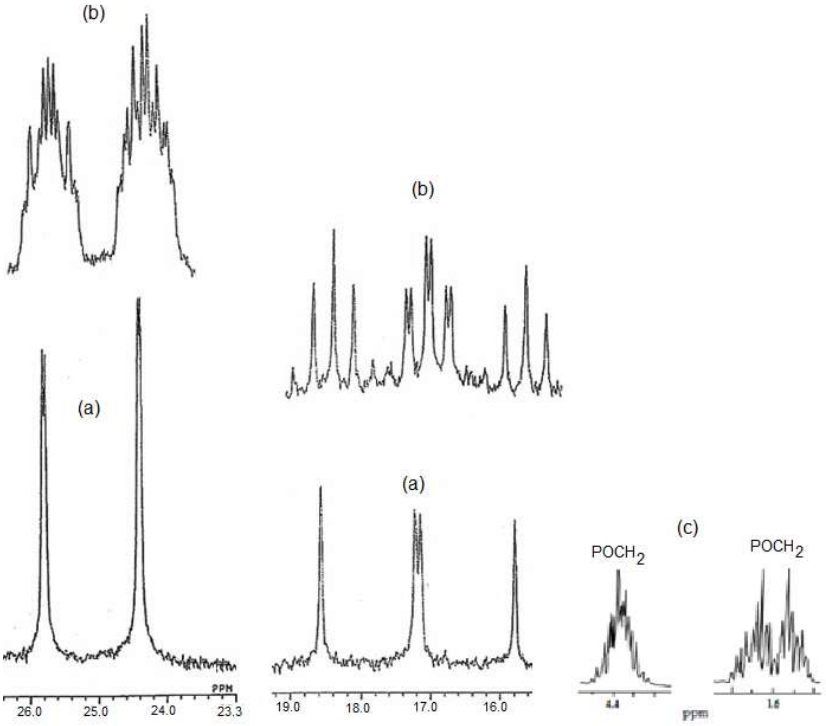

Figure 2. ^{31}P NMR proton decoupled (a) and coupled (b) spectra of compound (**4**): in $CDCl_3$, at 161.97 MHz, ambient temperature and relative to 85% H_3PO_4; and (c) its ^{1}H NMR spectrum, at ambient temperature, in $CDCl_3$ (TMS as internal reference) and at 399.95 MHz.

The α- and β- or aromatic ring protons of methylene may appear in various chemical surroundings depending on their positions relative to the oxygen atoms and aromatic rings. Because of the disproportional locations of the protons, the ^{1}H NMR spectra of compounds **4**, **5**, **7** and **8** demonstrate intricate spectra. The findings are compatible with earlier reported 2-thiophene and benzyl alcohol-substituted ansa derivatives [34]. The interplay between the interchangeable protons in particular groups causes the formation of multiplets specifically AB quartet. This pattern will be future cleaved/ segmented by the adjacent protons and phosphorus nuclei causing the formation of the intricate NMR spectrum. Consequently, different overlapping multiplets may be seen for the protons of $POCH_2$ and the $POCCH_2$. ^{1}H NMR spectral measurements are shown in Table 3 and ^{1}H NMR spectra of α- and β methylene protons of compound **4** are shown in Figure 2.

Table 3. ^{1}H NMR spectral data from the synthesized derivatives (**4, 5, 7, 8**)[a]

Compound		δPOC$\underline{H}_2$[b]	δPCC$\underline{H}_2$[b]		
δPCCC$\underline{H}_2$[b]		^{3}J($\underline{PH}$)[c]			
(**1**)		[44]			
(**6**)		[44]			
(**4**)	Spiro	4.44/4.35	1.75/1.68	1.34	10.90
	Ansa	4.26/4.17	1.59/1.54	1.27	10.60
(**5**)	Spiro	4.38/4.30	1.74/1.67	1.34	13.05
	Ansa	4.25/4.13	1.62/1.55	1.26	13.70
(**7**)		4.29	1.66	1.20	13.01
(**8**)		4.26	1.63	1.23	13.55

δBenzyl-H: 7.30-7.45
δThiophen-H: 6.75-6.90

[a]In $CDCl_3$ (with reference to internal TMS) at 399.95 MHz.
[b]In ppm. [c]In Hz.

In this study, thermal characteristics, i.e. thermal stabilities, crystal purity and recrystallization properties of synthesized derivatives were analyzed in the course of heating and cooling cycles. DSC thermograms have been shown in Figures 3-4. The obtained thermal peaks were numbered and thermal properties of these peaks were characterized in Table 4. Figure 3A and 3B represent the thermograms of compounds **4** and **5**, respectively. For both compounds, two endothermic (1 and 2) and one exothermic peak (1) were found during the heating and cooling cycles, respectively. In the course of heating cycles, endothermic peaks at 109 °C (compound 4 ΔH° 079, compound 5 ΔH° 054) position was assigned to the main melting process for both compounds. Additional melting events happened in these compounds at 205 °C (ΔH° 001) and 231 °C (ΔH° 002) positions, respectively. Recrystallization events occurred at 65 °C (ΔH° 008) and 85 °C (ΔH° 042) positions during the cooling cycles in both compounds (Figure 3A and 3B, Table 4).

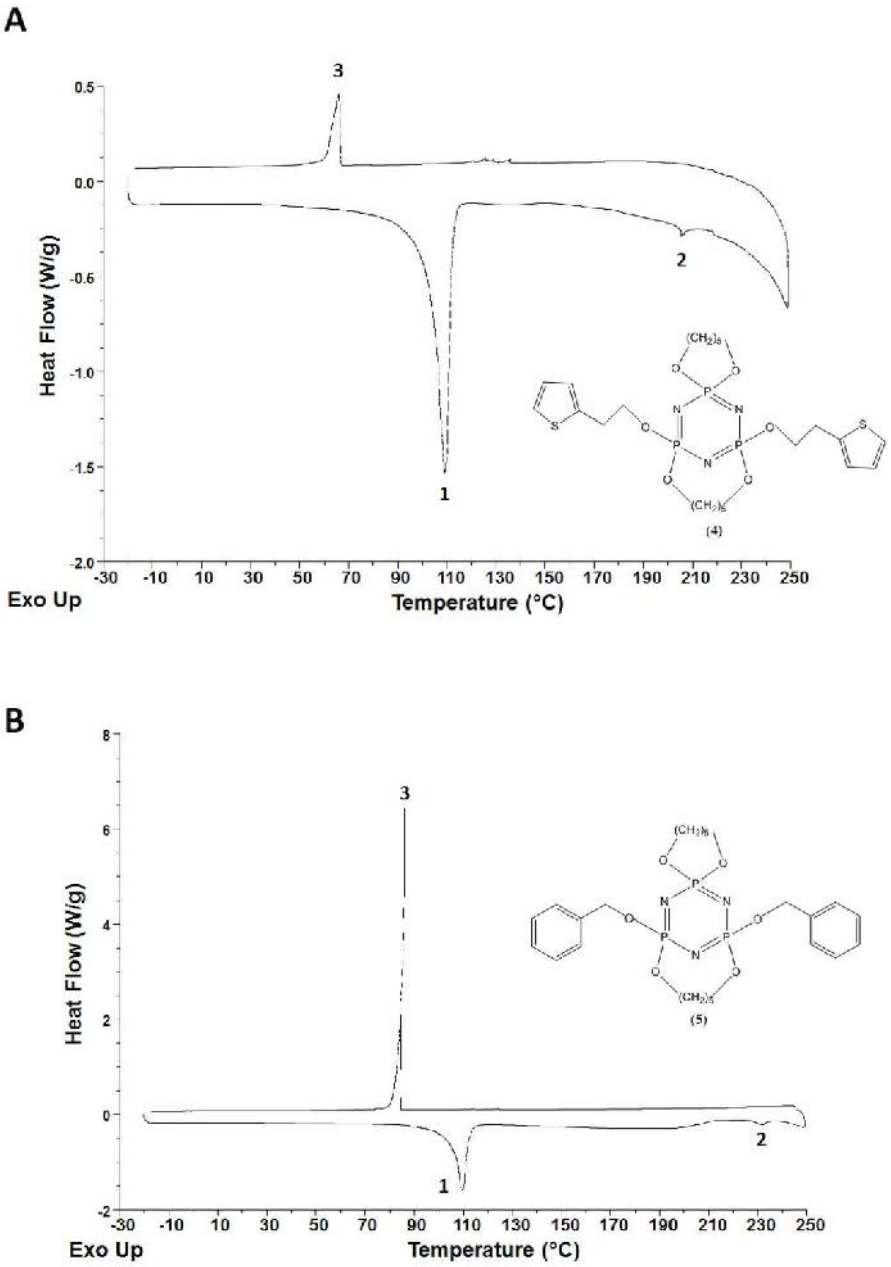

Figure 3. DSC thermograms of compounds **4** (A) and **5** (B).

Thermograms for compounds **7** and **8** have been shown in Figure 4A and 4B, respectively. During the heating cycle, compound **7** gave totally three peaks at positions of 161 °C (ΔH° 097), 206 °C (ΔH° 147), and 213 °C (ΔH° 050), respectively. In this figure, the first exothermic peak (1) was due to the crystallization event, while the other two endothermic peaks (2 and 3) were identified as an indicator of melting events. No thermal event was encountered during the cooling cycle (Figure 4A, Table 4). In total, three peaks appeared again for compound **8**. These peaks were measured in the course of heating and cooling cycle at positions of 195 °C (ΔH° 009), 208 °C (ΔH° 018), and 246 °C (ΔH° 037), respectively. Over the heating cycle, exothermic peak (1) has arisen as a result of crystallization event, while the endothermic one (2) was assigned to the main melting process. Throughout the cooling cycle, a single exothermic peak (3) was assigned to the recrystallization event (Figure 4B, Table 4).

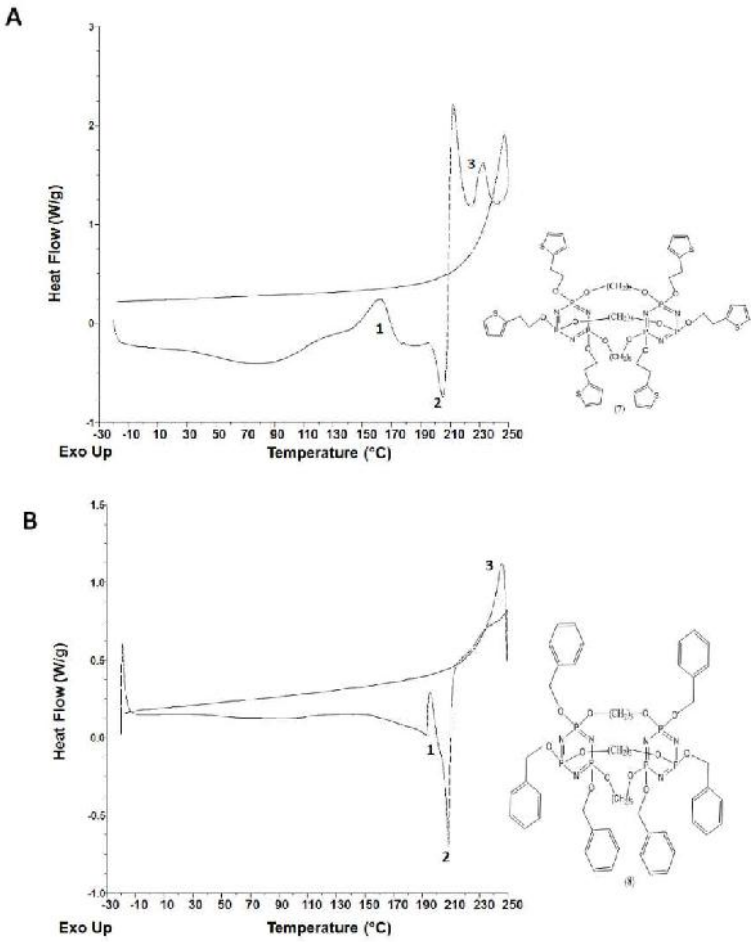

Figure 4. DSC thermograms of compounds **7** (A) and **8** (B).

Table 4. Calorimetric characterization of compounds (**4, 5, 7, 8**).

Compound	Cycle	# Peak	Peak character	Peaks (°C)	Enthalpy ΔH° (J/g)	Phase Transitions
(4)	Heating	1	Endothermic	109	079	Main melting p.
		2	Endothermic	205	001	Melting p.
	Cooling	3	Exothermic	065	008	Recrystallization p.
(5)	Heating	1	Endothermic	109	054	Main melting p.
		2	Endothermic	231	002	Melting p.
	Cooling	3	Exothermic	085	042	Recrystallization p.
(7)	Heating	1	Exothermic	161	097	Crystallization p.
		2	Endothermic	206	147	Main melting p.
		3	Endothermic	213	050	Melting p.
(8)	Heating	1	Exothermic	195	009	Crystallization p.
		2	Endothermic	208	018	Main melting p.
	Cooling	3	Exothermic	246	037	Recrystallization p.

4. CONCLUSIONS

All 2-thiophene ethanol and benzyl alcohol-replaced spiro-ansa and triple-bridged cyclotriphosphazene derivatives were purified using column chromatography and illuminated by several independent analytical tools. Thermal properties such as crystallization and melting behavior and corresponding enthalpies were identified by the DSC technique. Neutral 2-thiophene ethanol and benzyl alcohol with anionic reagents (NaH or $NaBH_4$) were used as the hydrogen chloride acceptor, and the reaction in THF and at room temperature was accomplished. The relatively large and virtually identical yields of spiro-ansa and triple-bridged entities were noted. The novel synthesized cyclophosphazene derivatives (**4, 5, 7, 8**) with aromatic reagents is very important due to their antimicrobial and antitumor activities.

REFERENCES

[1] M. El Gouri, A. El Bachiri, S. E. Hegazi, M. Rafik, and A. El Harfi, "Thermal degradation of a reactive flame retardant based on cyclotriphosphazene and its blend with DGEBA epoxy resin," *Polym Degrad Stab.*, vol. 94, no. 11, pp. 2101–2106, 2009.

[2] R. E. Singler, "Historical overview of the army contributions to phosphazene chemistry," *J Inorg Organomet Polym Mater.*, vol. 16, no. 4. pp. 307–309, 2006.

[3] M. Işklan *et al.*, "Phosphorus-nitrogen compounds. 21. Syntheses, structural investigations, biological activities, and DNA interactions of new N/O spirocyclic phosphazene derivatives. the NMR behaviors of chiral phosphazenes with stereogenic centers upon the addition of chi," *Inorg Chem.*, vol. 49, no. 15, pp. 7057–7071, 2010.

[4] N. Asmafiliz *et al.*, "Phosphorus-nitrogen compounds. Part 23: Syntheses, structural investigations, biological activities, and DNA interactions of new N/O spirocyclotriphosphazenes," *Spectrochim Acta A Mol Biomol Spectrosc.*, vol. 86, pp. 214–223, 2012.

[5] H. Akbaş, A. Karadağ, A. Aydın, A. Destegül, and Z. Kılıç, "Synthesis, structural and thermal properties of the hexapyrrolidinocyclotriphosphazenes-based protic molten salts: Antiproliferative effects against HT29, HeLa, and C6 cancer cell lines," *J Mol Liq.*, vol. 230, pp. 482–495, 2017.

[6] E. Cil, M. A. Tanyildizi, F. Ozen, M. Boybay, M. Arslan, and A. O. Gorgulu, "Synthesis, characterization, and biological-pharmacological evaluation of new phosphazenes bearing dioxybiphenyl and Schiff base groups," *Arch Pharm.*, vol. 345, no. 6, pp. 476–485, 2012.

[7] D. Erdener Çıralı, Z. Uyar, İ. Koyuncu, and N. Hacıoğlu, "Synthesis , characterization and catalytic , cytotoxic and antimicrobial activities of two novel cyclotriphosphazene-based multisite ligands and their Ru (II) complexes," *Appl Organomet Chem.*, vol. 29, no. 8, pp. 536–542, 2015.

[8] A. Uslu, E. Özcan, S. Dural, and F. Yuksel, "Synthesis and characterization of cyclotriphosphazene derivatives bearing azole groups," *Polyhedron*, vol. 117, pp. 394–403, 2016.

[9] M. Siwy *et al.*, "Synthesis and in vitro antileukemic activity of some new 1,3-(oxytetraethylenoxy)cyclotriphosphazene derivatives," *J Med Chem.*, vol. 49, no. 2, pp. 806–810, 2006.

[10] S. S. Machakanur, B. R. Patil, G. N. Naik, R. P. Bakale, S. W. Annie Bligh, and K. B. Gudasi, "Synthesis, characterization and antiproliferative activity of hexa arm star shaped thiosemicarbazones derived from cyclotriphosphazene core," *Inorganica Chim. Acta*, vol. 421, pp. 459–464, 2014.

[11] T. Yildirim *et al.*, "Synthesis, cytotoxicity and apoptosis of cyclotriphosphazene

compounds as anti-cancer agents," *Eur J Med Chem.*, vol. 52, pp. 213–220, 2012.

[12] H. Akbaş *et al.*, "Phosphorus-nitrogen compounds part 27. Syntheses, structural characterizations, antimicrobial and cytotoxic activities, and DNA interactions of new phosphazenes bearing secondary amino and pendant (4-fluorobenzyl)spiro groups," *Eur J Med Chem.*, vol. 70, pp. 294–307, 2013.

[13] A. O. Görgülü, K. Koran, F. Özen, S. Tekin, and S. Sandal, "Synthesis, structural characterization and anti-carcinogenic activity of new cyclotriphosphazenes containing dioxybiphenyl and chalcone groups," *J Mol Struct.*, vol. 1087, pp. 1–10, 2015.

[14] S. V. Levchik, G. Camino, M. P. Luda, L. Costa, A. Lindsay, and D. Stevenson, "Thermal decomposition of cyclotriphosphazenes. I. Alkyl-aminoaryl ethers," *J Appl Polym Sci.*, vol. 67, no. 3, pp. 461–472, 1998.

[15] R. Liu and X. Wang, "Synthesis, characterization, thermal properties and flame retardancy of a novel nonflammable phosphazene-based epoxy resin," *Polym Degrad Stab.*, vol. 94, no. 4, pp. 617–624, 2009.

[16] R. Horvath, C. A. Otter, K. C. Gordon, A. M. Brodie, and E. W. Ainscough, "Excited states of Ru(II) and Re(I) bipyridyl complexes attached to cyclotriphosphazenes: A synthetic, spectroscopic, and computational study," *Inorg Chem.*, vol. 49, no. 9, pp. 4073–4083, 2010.

[17] S. Devaraju, M. Selvi, and M. Alagar, "Synthesis and characterization of thermally stable and flame retardant hexakis (4- polyimide matrices," *Int J Polym Anal Charact.*, vol. 23, no. 1, pp. 29–37, 2018.

[18] S. Zhang *et al.*, "Preparation of Poly(bis(phenoxy)phosphazene) and 31P NMR Analysis of Its Structural Defects under Various Synthesis Conditions," *J Phys Chem B.*, vol. 120, no. 43, pp. 11307–11316, 2016.

[19] H. A. Alidağı, F. Hacıvelioğlu, S. O. Tümay, B. Çoşut, and S. Yeşilot, "Synthesis and spectral properties of fluorene substituted cyclic and polymeric phosphazenes," *Inorg Chim Acta.*, vol. 457, pp. 95–102, 2017.

[20] K. Krishnadevi, V. Selvaraj, and D. Prasanna, "Thermal, mechanical and antibacterial properties of cyclophosphazene incorporated benzoxazine blended bismaleimide composites," *RSC Adv.*, vol. 5, pp. 913–921, 2015.

[21] B. P. Woods and T. R. Hoye, "Differential scanning calorimetry (DSC) as a tool for probing the reactivity of polyynes relevant to hexadehydro-diels-alder (HDDA) cascades," *Org Lett.*, vol. 16, no. 24, pp. 6370–6373, 2014.

[22] Z. S. Eren, S. Tunçer, G. Gezer, L. T. Yildirim, S. Banerjee, and A. Yilmaz, "Improved solubility of celecoxib by inclusion in SBA-15 mesoporous silica: Drug loading in different solvents and release," *Microporous Mesoporous Mater.*, vol. 235, pp. 211–223, 2016.

[23] S. Beşli, S. J. Coles, D. B. Davies, M. B. Hursthouse, A. Kiliç, and R. a Shaw, "A spiro to ansa rearrangement in cyclotriphosphazene derivatives.," *Dalt. Trans.*, vol. 14, no. 26, pp. 2792–2801, 2007.

[24] D. Palabıyık, C. Mutlu Balcı, and S. Beşli, "The role of the substituted group on competitive formation of ansa and spiro isomers," *Inorg Chim Acta.*, vol. 487, pp. 15–23, 2019.

[25] S. Beşli *et al.*, "Competitive formation of cis and trans derivatives in the nucleophilic substitution reactions of cyclophosphazenes having a mono-spiro

P-NHR group," *Dalt. Trans.*, vol. 40, no. 18, pp. 4959–4969, 2011.

[26] G. Guerch, L. Jean-François, R. Lahana, R. Roques, and F. Sournies, "An answer to the spiro versus ansa dilemma in cyclophosphazenes. Part III. N3P3Cl5[HN(CH2)4NH]Cl5P3N3. A serendipitous two-ring bridged-assembly phosphazene," *J Mol Struct.*, vol. 99, no. 3–4, pp. 275–282, 1983.

[27] P. Castera *et al.*, "An answer to the SPIRO versus ANSA dilemma in cyclophosphazenes. Part VII. Neither SPIRO nor ANSA: the BINOdicyclotriphosphazenes, N3P3Cl5 [HN(CH2)nNH] Cl5P3N3," *Inorganica Chim. Acta*, vol. 108, no. 1, pp. 29–33, 1985.

[28] H. A. Al-Madfa, R. A. Shaw, and S. Ture, "Phosphorus-Nitrogen compounds. part 64.1 the reactions of hexachlorocyclotriphosphazatriene with 2, 2-dimethylpropane-l, 3-diol. nuclear magnetic resonance studies of the products," *Phosphorus Sulfur Silicon Relat Elem.*, vol. 53, no. 1–4, pp. 333–338, 1990.

[29] A. S. Freund, M. Calichman, and C. W. Allen, "The reactions of hexafluorocyclotriphosphazene with sodium phenoxide," *Z Anorg Allg Chem.*, vol. 630, no. 12, pp. 2059–2062, 2004.

[30] S. Beşli, S. Doğan, C. Mutlu Balcı, and F. Yuksel, "The reaction of N,N-spiro bridged octachlorobis(cyclotriphosphazene) with 1,3-propanediol: Comparison with 1,2-ethanediol," *Polyhedron*, vol. 122, pp. 61–70, 2017.

[31] S. Ture and R. Gurbanov, "Synthesis and structural characterization of geminal and non-geminal 1,1,3,3-tetramethylguanidine substituted derivatives of cyclotriphosphazene: Thermal and spectroscopic investigations of the products," *Phosphorus Sulfur Silicon Relat Elem.*, vol. 193, no. 10, pp. 620–629, 2018.

[32] S. Ture, R. Gurbanov, and M. Tuna, "Reactions of cyclochlorotriphosphazatriene with 2-mercaptoethanol. Calorimetric and spectroscopic investigations of the derived products," *Phosphorus Sulfur Silicon Relat Elem.*, vol. 193, no. 9, pp. 600–610, 2018.

[33] J. Barberá *et al.*, "Columnar mesomorphic organizations in cyclotriphosphazenes," *J Am Chem Soc.*, vol. 127, no. 25, pp. 8994–9002, 2005.

[34] S. Ture and Ö. Kücük, "The reactions of non-gem-hexanedioxytetrachlorocyclotriphosphazene with 2- (2-hydroxyethyl) thiophene , benzyl alcohol," *Phosphorus Sulfur Silicon Relat Elem.*, vol. 0, no. 0, pp. 1–8, 2019.

[35] E. E. Ilter *et al.*, "Phosphorus-nitrogen compounds: Part 19. Syntheses, structural and electrochemical investigations, biological activities, and DNA interactions of new spirocyclic monoferrocenylcyclotriphosphazenes," *Polyhedron*, vol. 29, no. 15, pp. 2933–2944, 2010.

[36] S. Ture, "Phosphorus-nitrogen compounds: Reinvestigation of the reactions of hexachlorocyclotriphosphazene with 1,4-butane- and 1,6-hexane-diols—NMR studies of the products," *Phosphorus Sulfur Silicon Relat Elem.*, vol. 191, no. 8, pp. 1174–1182, 2016.

[37] S. Ture, "The Reactions of Octachlorocyclotetraphosphazene with Difunctional Bis(2-Hydroxyethyl) Ether. Nuclear Magnetic Studies of the Products," *Phosphorus Sulfur Silicon Relat Elem.*, vol. 189, no. 11, pp. 1746–1767, 2014.

[38] R. A. Shaw and S. Ture, "Phosphorus-nitrogen compounds. part 711. the reactions of hexachlorocyclotriphosphazatriene with bis (2-hydroxyethyl) ether. nuclear magnetic resonance spectroscopic studies of the products," *Phosphorus Sulfur*

Silicon Relat Elem., vol. 57, no. 1–2, pp. 103–109, 1991.

[39] S. Beşli, H. Ibişoğlu, A. Kiliç, I. Ün, and F. Yuksel, "Spiro, ansa-derivatives of cyclotetraphosphazenes with a tetrafluorobutane-1,4-diol," *Polyhedron*, vol. 29, no. 17, pp. 3220–3228, 2010.

[40] S. Beşli *et al.*, "A cis-directing effect towards diols by an exocyclic P-NHR moiety in cyclotriphosphazenes," *Inorg Chem Commun.*, vol. 12, no. 8, pp. 773–777, 2009.

[41] E. T. Eçik, S. Beşli, G. Y. Çiftçi, D. B. Davies, A. Kiliç, and F. Yuksel, "Stereo-selectivity in a cyclotriphosphazene derivative bearing an exocyclic P-O moiety," *Dalt. Trans.*, vol. 41, no. 22, pp. 6715–6725, 2012.

[42] S. Beşli, S. J. Coles, L. S. Coles, D. B. Davies, and A. Kiliç, "Investigation of a spiro to ansa rearrangement with di-functional alcohols in cyclotriphosphazene derivatives," *Polyhedron*, vol. 43, no. 1, pp. 176–184, 2012.

[43] R. Gurbanov and F. Yıldız, "Molecular profile of oral probiotic bacteria to be used with functional foods," *J. Food Heal. Sci.*, vol. 3, pp. 117–131, 2017.

[44] S. Ture, "Phosphorus-Nitrogen Compounds: The Reactions of Hexachlorocyclotriphosphazatriene with Pentane-1,5-Diol. Nuclear Magnetic Resonance Studies of The Products," *Phosphorus Sulfur Silicon Relat Elem.*, vol. 188, no. 9, pp. 1156–1171, 2013.

JOURNAL OF SCIENCE
SAKARYA UNIVERSITY

Sakarya University Journal of Science

ISSN 1301-4048 | e-ISSN 2147-835X | Period Bimonthly | Founded: 1997 | Publisher Sakarya University | http://www.saujs.sakarya.edu.tr/

Title: Analysis Of Silicon Solar Cell Device Parameters Using Pc1D

Authors: Al-Montazer Mandong, Abdullah Üzüm
Recieved: 2019-04-24 10:09:10

Accepted: 2019-08-17 12:04:47

Article Type: Research Article
Volume: 23
Issue: 6
Month: December
Year: 2019
Pages: 1190-1197

How to cite
Al-Montazer Mandong, Abdullah Üzüm; (2019), Analysis Of Silicon Solar Cell Device Parameters Using Pc1D. Sakarya University Journal of Science, 23(6), 1190-1197, DOI: 10.16984/saufenbilder.557490
Access link
http://www.saujs.sakarya.edu.tr/issue/44246/557490

Sakarya University Journal of Science 23(6), 1190-1197, 2019

Analysis of Silicon Solar Cell Device Parameters using PC1D

Al Montazer Mandong[1*], Abdullah Üzüm[2]

Abstract

Analysis of the effects of various physical and electrical parameters in the overall efficiency of a solar cell is critical in designing a high efficiency solar cell. In this work, a computer simulation using PC1D was used to analyze the effects of the most substantial parameters in a silicon solar cell. Absorber layer, emitter layer, antireflection coating layer and back surface field layer were studied especially in terms of doping levels, thicknesses and the optimal values to for these parameters were simulated and obtained. The final simulated solar cells were validated using a measured data of an industrial scale fabricated solar cell with the same parameters and the measured result was in a good conformity with the simulation data. According the performed studies and achieved results, understanding and estimating the effects of these substantial parameters and obtaining their optimal values using a simulation software is both beneficial and the most practical way for designing a high efficiency solar cell structure.

Keywords: PC1D, solar cell, crystalline silicon, simulation, optimization

1. INTRODUCTION

The light energy radiated by the sun incident to the Earth's surface can provide an enormous amount of energy enough to meet the world's energy demands in present and in next generations [1]. Photovoltaic solar cells are one of the most effective options to efficiently harness sunlight by absorbing photons and converting them to a usable electrical energy.

Improving the efficiency of solar cells can significantly contribute to the total generated photovoltaic energy worldwide. A published report from Fraunhofer Institute shows that the solar cell industry is dominated by crystalline silicon (c-Si) solar cells with a global market share of 93% [2]. Currently, the highest confirmed efficiency for mono-crystalline and multi-crystalline are 26.7% and 21.9%, respectively [3-5]. Further improving the efficiency of solar cell requires in depth knowledge of the fundamental working principles of semiconductors. One way to understand the effects for altering physical and electrical properties of each material on the device performance is through an accurate simulation software. Simulation softwares can predict the output behavior of the device with different

* Corresponding Author: montazermandong@gmail.com
[1] Karadeniz Technical University, Department of Electrical-Electronics Engineering, Trabzon, Turkey.
ORCID: 0000-0002-9230-0582
[2] Karadeniz Technical University, Department of Electrical-Electronics Engineering, Trabzon, Turkey.
ORCID: 0000-0001-5324-8892

material properties such as thickness of composing layers, doping levels, etc. Also, they combine both mathematical and experimental data in predicting output behavior of a solar cell. Numerous simulation softwares are available for solar cells such as Silvaco TCAD, Sentaurus TCAD, AFORS-HET and PC1D [6-8]. Sentaurus TCAD is one of the most versatile solar cell simulation software which can predict up to sub-90nm processes with atomic level accuracy [9]. However, its steep price is a major drawback. As an open-source alternative, PC1D can also simulate widely used solar cells such as silicon and germanium. PC1D was created by researchers from Photovoltaics Special Research Centre at University of New South Wales which is a world-renowned institution in solar cell research [8]. Numerous parameters such as temperature, doping levels, parasitic resistance, back surface fields, recombination, carrier lifetime and others can be modified in order to understand their effects on the overall performance of the device. PC1D can provide results including current-voltage (I-V) curves, short circuit current (J_{sc}), open circuit voltage (V_{oc}), etc. in a graphical format. These results can be analyzed and considered in the planning process of the fabrication of an actual device.

Various researchers used PC1D to simulate various types of solar cells before conducting experiment to verify the feasibility of their projects. Sepeai et.al used PC1D to simulate bifacial solar cell [10] while Meenakhshi et.al simulated multi-junction solar cells [11]. Belarbi et.al and Chuan et.al studied silicon solar cells using PC1D [12, 13]. But no validation was presented using a commercial/experimentally fabricated solar cell to verify the simulation software's accuracy and reliability.

In this work, the effects of the most important parameters such as device thickness, doping levels, emitter thickness, back surface field thickness, doping level and antireflection coating on the solar cell performance were studied for crystalline silicon solar cells. PC1D was used in simulating and analyzing performance by modifying device parameters. The result shows the importance of analyzing and obtaining the optimum value of each parameter to obtain the maximum possible device efficiency. Finally, the simulated device with optimized parameters was validated by comparing the results to an industrial scale fabricated solar cell with identical physical and electrical parameters which is other remarkable part of this work.

2. METHODS

The most widely used structure of the silicon solar cell in industry is shown on Figure 1. Understanding the effects of various physical and electrical parameters of each layer is important for achieving high conversion efficiencies. PC1D simulation software was used to study the effects of various device parameters on each layer and achieve the highest possible conversion efficiency.

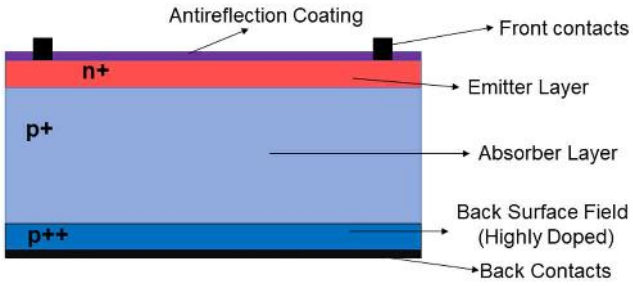

Figure 1. Basic structure of a conventional silicon solar cell with selective emitter

Front contact and back contacts collect mobile charge carriers while the absorber, emitter, and back surface field are responsible in generation and transportation of charge carriers. Antireflection coating minimizes the reflection on the surface of the solar cell and maximizes the light transmission and absorption in order to generate more current. Silicon nitride antireflection coating with refractive index of 1.873 was used in order to minimize reflectance on wavelengths with high spectral irradiance and provide a good surface passivation [14]. Table 1 shows the standard device parameters of the solar cell in this study.

Table 1. Solar cell device parameters using PC1D

Front surface texture depth	3 µm
Internal optical reflectance	Enabled
Shunt Resistance	50000 Ω
Emitter Sheet Resistance	71.85 Ω/sq
Thickness (Absorber Layer)	180 µm
Intrinsic concentration @300k	1×10^{10} cm^{-3}
Front diffusion (N-type)	2×10^{20} cm^{-3} peak
Rear diffusion (P-type)	3×10^{18} cm^{-3} peak
Front SRV	2×10^{5} cm/s
Rear SRV	1×10^{7} cm/s
Bulk recombination	$\tau_n = \tau_p = 30$ µs
Temperature	25°C
Device Area	1 cm^2

2.1. Effects of Absorber Layer Thickness on Solar Cell Performance

One key factor in establishing the feasibility of fabricating a photovoltaic device is the cost of semiconductor materials [14]. Careful selection of materials with optimum thickness is important factor in minimizing expenses while maximizing device efficiency. The absorber layer is the thickest part of commercial silicon solar cells which absorbs light and generates mobile charge carriers that are transported to and collected by the contacts in order to generate electricity [15]. A thicker absorber layer does not mean higher efficiency due to conflicting effects on V_{oc} and J_{sc}. A solar cell with varying absorber layer thickness was studied in this section. Table 2 shows the result of the varying silicon bulk thickness on the device performance. Figure 2 shows the effect of absorber layer thickness on V_{oc}, J_{sc} (Figure 2a) and efficiency (Figure 2b). 'T_{bulk}', 'FF' and 'η' stands for 'bulk thickness', 'fill factor' and 'conversion efficiency', respectively.

Table 2. Device performance depending on absorber thickness

T_{bulk} (µm)	J_{sc} (mA/cm²)	V_{oc} (mV)	FF (%)	η (%)
30	35.50	635.0	78.25	17.64
60	36.66	632.3	78.06	18.09
100	37.10	628.7	77.86	18.16
130	37.20	626.4	77.76	18.12
160	37.21	624.5	77.64	18.04
190	37.18	622.9	77.66	17.99
220	37.11	621.5	77.65	17.91
250	37.03	620.3	77.62	17.83
280	36.94	619.4	77.56	17.75

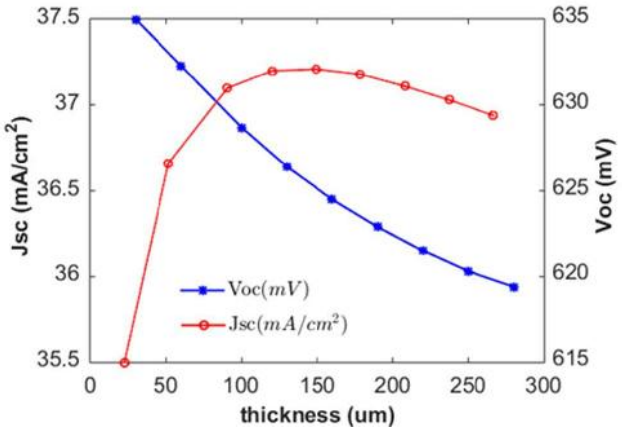

(a)

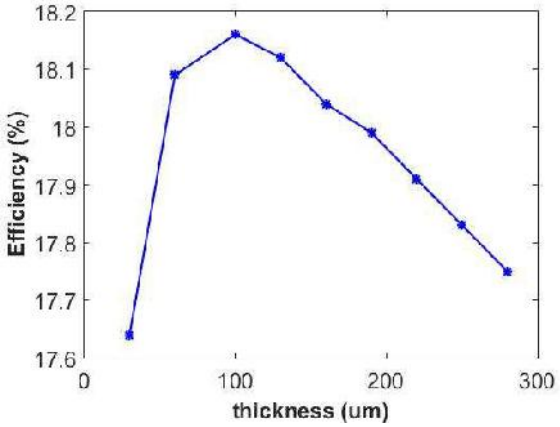

(b)

Figure 2. (a) V_{oc} and J_{sc} as function of bulk thickness, (b) Effect of thickness on efficiency

The J_{sc} is directly proportional to the thickness until bulk thickness of 160µm then reverses after that while the value of the V_{oc} is inversely proportional from 30 to 280µm. The total efficiency of the device is slowly reduced as the device gets thicker more than 100µm. The device with 100µm thickness has the best efficiency of all, but due to difficulty in handling a very thin device and other physical constraints such as bowing effect of standard aluminum back surface field, manufacturers often use device with more than 150µm thickness. Properties including durability, stability, and handling harsh weather conditions should also be considered in manufacturing processes.

2.2. Effects of Emitter Doping Concentration on Device Performance

Large portion of light are absorbed at the surface of the solar cell which results to high generation rate. Doping concentration and the thickness of the emitter should be carefully designed in order to absorb most of incoming light. High doping concentration in these layers can result to a lower overall efficiency due to decreased light transmission, absorption and higher recombination rate [17]. But high enough concentration is also needed in order to aid the drift transport mechanism and achieve lower sheet resistance. Table 3 shows the result of varying doping concentrations on the sheet resistance and overall performance of the device. Figure 3 presents the effect of emitter doping concentration on emitter sheet resistance and V_{oc}. 'C_{dop}' and 'R_{sht}' stands for the 'doping concentration' and 'sheet resistance', respectively.

Table 3.
Influence of emitter doping concentrations on sheet resistance and device performance

C_{dop} (cm^{-3})	J_{sc} (mA/cm^2)	V_{oc} (mV)	FF (%)	R_{sht} (Ω/sq)	η (%)
2×10^{16}	37.52	625.9	77.73	79650	18.25
2×10^{17}	37.52	631.5	77.78	7852	18.43
2×10^{18}	37.52	631.7	77.79	1751	18.44
2×10^{19}	37.49	630.5	77.80	421.7	18.40
2×10^{20}	37.22	623.6	77.70	71.85	18.03
2×10^{21}	34.33	604.3	77.48	8.7	16.08

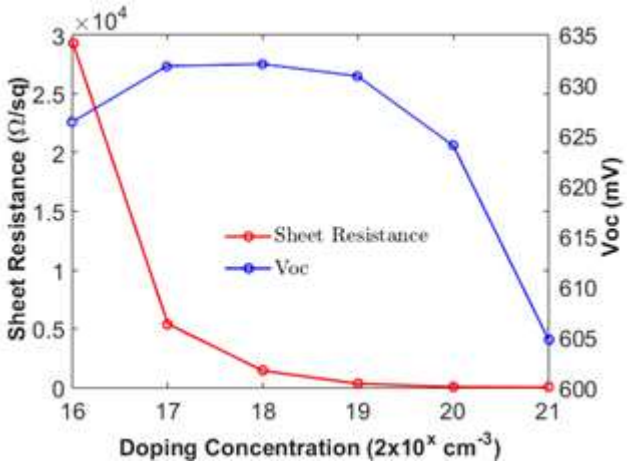

Figure 3. Effect of emitter doping concentration on emitter sheet resistance and on V_{oc}

Device thickness of 150 m was used and emitter doping concentration 2×10^{20} cm^{-3} due to its low sheet resistance. The thickness of the emitter layer can also have a huge impact on the sheet resistance and overall performance of the device. Table 4 shows the device performance with varying emitter thickness. 'T_{emt}' stands for the 'emitter thickness'.

Table 4.
Effect of emitter thickness on device performance

T_{emt} (μm)	J_{sc} (mA/cm^2)	V_{oc} (mV)	FF (%)	R_{sht} (Ω/sq)	η (%)
0.1	36.95	619.7	78.76	71.85	18.03
0.2	36.15	617.0	78.68	35.93	17.55
0.3	34.91	615.3	78.83	23.95	16.93
0.4	33.43	614.3	79.01	17.96	16.23
0.5	31.88	613.6	79.18	14.37	15.49
0.6	30.39	613.0	79.39	11.98	14.79
0.7	29.04	612.5	79.49	10.26	14.14

The J_{sc} and V_{oc} decreases at as the emitter thickness increases while the sheet resistance decreases in value. Lower emitter sheet resistance is desirable in a device, but there are certain drawbacks in having thick emitter. Light hardly penetrates a highly doped and thick emitter layer which affects the generation of charge carrier thus resulting to a lower device efficiency.

2.3. Effect of Back Surface Field Concentration on Device Performance

Back surface field (BSF) is an important part of a modern solar cell which consists of heavily doped layer at the rear of the solar cell. An electric field will be induced to the junction of low and highly doped region which acts as a barrier for minority mobile charge carriers and reduce the recombination at the rear layers of the solar cell [18]. Table 5 shows the result of simulation of varying doping concentration of BSF on sheet resistance and overall device performance. The effects of BSF doping concentration on the overall device performance is shown in Figure 4.

Table 5. Device performance on varying BSF doping concentrations

C_{BSF} (cm^{-3})	J_{sc} (mA/cm^2)	V_{oc} (mV)	FF (%)	R_{sht} (Ω/sq)	η (%)
3×10^{17}	36.72	619.1	77.67	166	17.65
3×10^{18}	37.52	631.7	77.77	36.13	18.44
3×10^{19}	37.11	633.1	77.88	7.175	18.29
3×10^{20}	35.57	626.3	77.81	0.984	17.33
2×10^{21}	35.01	620.7	77.85	0.161	16.92

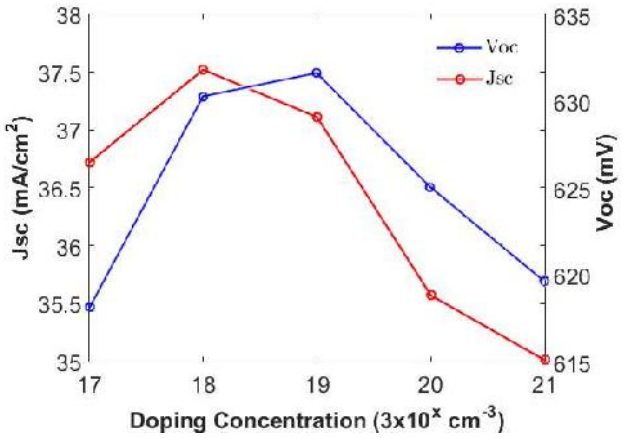

Figure 4. Effects of doping concentration on J_{sc} and V_{oc}

Solar cell with doping concentration of 3×10^{18} cm^{-3} has the highest recorded efficiency. Doping concentration has considerable effect on open circuit voltage of the device from 3×10^{17} to 3×10^{18} cm^{-3}, but after 3×10^{19} cm^{-3} concentration, V_{oc} saturates and then decreases gradually. Similarly, the value of J_{sc} also increases until the doping concentration of 3×10^{18} cm^{-3} but also gradually decreases over higher doping concentrations.

Doping concentration with the highest efficiency was selected and simulated with various thicknesses of BSF. The effects of BSF thickness on the overall device performance is shown on Table 6. The effects of BSF thickness on the V_{oc} and J_{sc} is shown in Figure 5. 'T_{BSF}' stands for the 'BSF thickness'.

Table 6. Device performance of varying BSF thickness

T_{BSF} (µm)	J_{sc} (mA/cm^2)	V_{oc} (mV)	FF (%)	R_{sht} (Ω/sq)	η (%)
5	37.52	631.7	77.77	36.13	18.44
10	37.57	635.3	77.78	18.07	18.57
15	37.52	636.9	77.81	12.04	18.60
20	37.44	638.2	77.87	9.033	18.61
25	37.36	639.1	77.91	7.226	18.61
30	37.36	640.0	77.96	6.022	18.64
35	37.29	640.6	77.97	5.162	18.62
40	37.20	641.4	78.02	4.516	18.61

BSF thickness also has an observable effect on the overall efficiency. As seen on Table 6, a BSF with 30µm thickness produces the highest efficiency.

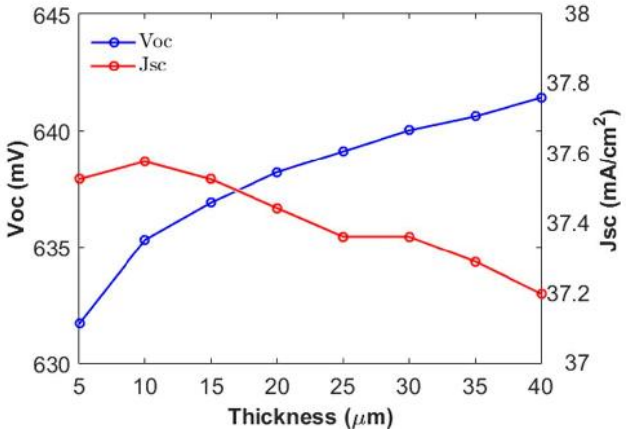

Figure 5. Effect of BSF thickness on J_{sc} and V_{oc}

The value of V_{oc} increases with increasing BSF thickness while the value of J_{sc} is slightly decreasing as the BSF becomes thicker. In addition, the value of the sheet resistance is also inversely proportional with the doping concentration and the thickness of the BSF layer. Higher doping concentration results to a lower resistance but there will be a tradeoff due to significant rise in recombination rate which decreases the collection probability.

2.4. Effect of Antireflection Coating on Device Performance

Antireflection Coating (ARC) is an integral part of high efficiency solar cells. Thin layer of dielectric material is deposited at the surface of solar cell in order to reduce the total reflectance of incoming light and maximize transmission to

generate more charge carriers [16]. ARCs that are used in modern solar cell is composed of single, double or multi-layered dielectric materials with different refractive indices which are stacked one after another. In order to understand the effects of ARC on the device performance, bare silicon, single layer ARC, double layer ARC and triple layer ARC applied silicon surfaces were simulated.

TiO_2 with refractive index of 2.116 and thickness of 67nm was used as single layer ARC (SLARC). MgF_2 and ZnS with refractive indices of 1.39 and 2.371 with thickness of 107nm and 60.5nm respectively was used as double layer ARC (DLARC). MgF_2, SiO_2, TiO_2 with refractive indices of 1.39, 1.48 and 2.453 with thickness of 80nm, 30nm and 60nm was used as triple layer ARC (TLARC). The device performances of each device were given in Table 7. Figure 6a shows the I-V curve of solar cell with and without ARC while Figure 6b shows the reflectance spectra of a device with and without ARC.

Table 7.
Device performance with varying layers of ARC

ARC	J_{sc} (mA/cm^2)	V_{oc} (mV)	FF (%)	□ (%)
None	26.50	619.8	79.79	13.1
SLARC	37.30	628.8	78.88	18.5
DLARC	39.90	630.6	78.56	19.77
TLARC	39.96	630.6	78.53	19.79

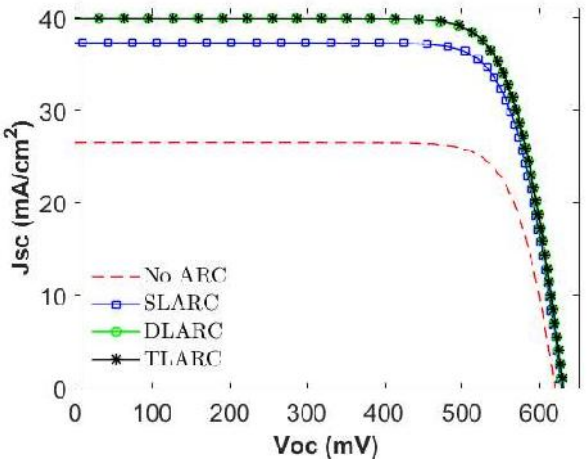

(a)

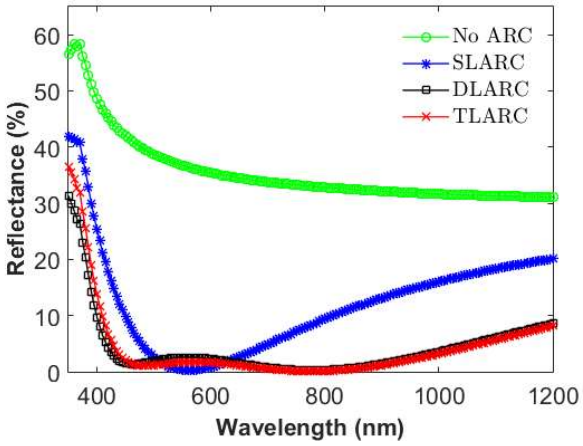

(b)

Figure 6. (a) I-V curve of device with and without ARC, (b) Reflectance spectra of device with and without ARC

2.5. Comparison of Optimal Simulated Solar Cell with a Fabricated Solar Cell

In order to validate simulation data, a simulated device with identical parameters was compared to the measurements of actual solar cell in real application conditions. Table 8 presents the comparison of electrical parameters of simulated solar cell with a real solar cell.

Table 8.
Comparison of electrical parameters of optimal simulated solar cell with a fabricated cell

Data type	J_{sc} (mA/cm^2)	V_{oc} (mV)	FF (%)	□ (%)	Pseudo □ (%)
Real Cell	36.6	617.0	78.30	17.7	18.48
Simulated Cell	37.3	628.8	78.88	18.5	-

According to Table 8, one can observe that the simulation results can predict the actual cell results in a good agreement. Overall, the simulated results were slightly higher than that of the parameters of real cell. Emitter doping of the real cell was 5×10^{20} cm^{-3} where the simulated optimal emitter doping was 2×10^{20} cm^{-3} for a homogenous emitter while the emitter depths of the cells were 0.6□m and 0.1□m, respectively.

Slightly higher performance of simulated cell can be considered in an acceptable range due to lesser recombination losses. On the other hand, the pseudo efficiency of the real cell was measured as 18.48% by Suns-V_{oc} measurement tool which shows the potential efficiency of the cell precisely estimated by the simulation when excluding resistive losses.

3. CONCLUSION

This study highlights the importance of using PC1D simulation software in analyzing and obtaining the optimum values of each device parameter in order to achieve the maximum conversion efficiency. Nonetheless, device properties such as durability, stability, handling harsh weather conditions, and manufacturing process limitations should also be considered when using simulation softwares. Finally, this paper shows the potential of integrating simulation softwares such as PC1D as a practical alternative in research and development stage of fabricating crystalline silicon solar cells due to its accuracy and reliability.

4. REFERENCES

[1] Basic Photovoltaic Principles and Methods, Solar Information Module (1982), SERI/SP-290-1448.

[2] S. Philipps, Photovoltaics Report, Fraunhofer ISE and Werner Warmuth, PSE AG, https://www.ise.fraunhofer.de/content/dam/ise/de/documents/publications/studies/PhotovoltaicsReport.pdf

[3] M. A. Green, Y. Hishikawa, W. Warta, E. D. Dunlop, D. H. Levi, J. Hohl-Ebinger and A. W. H. Ho-Baillie, "Solar Cell Efficiency Tables (version 50)", Prog. Photovoltaics, vol. 25, pp. 668- 676, 2017.

[4] K. Yoshikawa, H. Kawasaki, W. Yoshida, T. Irie, K. Konishi, K. Nakano, T. Uto, D. Adachi, M. Kanematsu, H. Uzu and K. Yamamoto, "Silicon heterojunction solar cell with interdigitated back contacts for a photoconversion efficiency over 26%," Nat. Energy, vol. 2, no. 5, 2017.

[5] J. Benick, A. Richter, R. Müller, H. Hauser, F. Feldmann, P. Krenckel, S. Riepe, F. Schindler, M. C. Schubert, M. Hermle, A. W. Bett and S. W. Glunz "High-Efficiency n-Type HP mc Silicon Solar Cells," IEEE J. Photovoltaics, vol. 7, no. 5, pp.1171–1175,2017.

[6] J. Hofstetter, C. del Cafiizo, S. Ponce-Alcantara and A. Luque, "Optimisation of SiNx:H anti-reflection coatings for silicon solar cells", Spanish Conference on Electron Devices, pp.131-134,2007.

[7] K. Islam, A. Alnuaimi, H. Ally and A. Nayfeh, "ITO, Si3N4 and ZnO:Al Simulation of Different Anti-reflection Coatings (ARC) for Thin Film a-Si:H Solar Cells," 2013 European Modelling Symposium, Manchester, pp. 673-676, 2013.

[8] D. A. Clugston and P. A. Basore, "PC1D Version 5- 32-Bit Solar Cell Modeling on Personal Computers", 26th IEEE Photovoltaics Specialist Conference, Anaheim California, pp. 207–210, 1997.

[9] Synopsis, "Synopsys TCAD Now Offers Atomic-level Accuracy." Online Available: https://news.synopsys.com/index.php?s=20295&item=122584. (Accessed: 23-Nov-2018).

[10] S. Sepeai, M.Y. Sulaiman, M. Khairunaz, A.W. Azhari, K. Sopian, S.H. Zaidi, "Design Optimization of Bifacial Solar Cell by PC1D Simulation," Journal of Energy Technologies and Policy, vol. 3, no. 5, pp. 1–11, 2013.

[11] S. Meenakshi and S. Baskar, "Design of multi-junction solar cells using PC1D," 2013 International Conference on Energy Efficient Technologies for Sustainability, Nagercoil, 2013, pp. 443-449.

[12] M. Belarbi, A. Benyoucef, and B. Benyoucef, "Simulation of the solar cells with PC1D, application to cells based on silicon," Advanced Energy: An International Journal, vol. 1, no.3, 2014.

[13] J. Chuan, L. Tianze, Z. Xia, H. Luan, "Simulation of Silicon Solar Cell using PC1D", Advanced Materials Research, Vols. 383-390, pp 7032-7036, 2012.

[14] B. Liu, S. Zhong, J. Liu, Y. Xia and C. Li, "Silicon nitride film by inline PECVD for black silicon solar cells," International Journal of Photoenergy, vol. 2012, pp. 2–7, 2012.

[15] C.-T. Sah, K.A. Yamakawa, R. Lutwack, "Effects of Thickness on Silicon Solar Cell Efficiency", IEEE Transactions on Electron Devices, vol. 29, no. 5, 1982.

[16] A. Mandong, "Design and Simulation of Single, Double, and Multi-Layer Antireflection Coating for Crystalline Silicon Solar Cell", Master Thesis, Karadeniz Technical University, Trabzon,Turkey,2019.

[17] M. Wolf, "The Influence of Heavy Doping Effects on Silicon Solar Cell Performance", Solar Cells, vol. 17, pp. 53-63, 2018.

[18] R.R. King, K.W. Mitchell and J.M. Gee, "Back Surface Cell Structures for Reducing Recombination in CZ Silicon Solar Cells", Proceedings of 1994 IEEE 1st World Conference on Photovoltaic Energy Conversion - WCPEC (A Joint Conference of PVSC, PVSEC and PSEC), Waikoloa, USA, 1994.

JOURNAL OF SCIENCE
SAKARYA UNIVERSITY

Sakarya University Journal of Science

ISSN 1301-4048 | e-ISSN 2147-835X | Period Bimonthly | Founded: 1997 | Publisher Sakarya University | http://www.saujs.sakarya.edu.tr/

Title: Real Time Performance Comparison Of Buck Converter Circuit Controlled By Discrete Time Pid, Lqr And Smc Controllers İn Continuous-Current Mode

Authors: Ömer Özdemir, İrfan Yazıcı
Recieved: 2018-10-05 15:43:48

Accepted: 2019-08-17 13:56:16

Article Type: Research Article
Volume: 23
Issue: 6
Month: December
Year: 2019
Pages: 1198-1206

How to cite
Ömer Özdemir, İrfan Yazıcı; (2019), Real Time Performance Comparison Of Buck Converter Circuit Controlled By Discrete Time Pid, Lqr And Smc Controllers İn Continuous-Current Mode. Sakarya University Journal of Science, 23(6), 1198-1206, DOI: 10.16984/saufenbilder.467592
Access link
http://www.saujs.sakarya.edu.tr/issue/44246/467592

Sakarya University Journal of Science 23(6), 1198-1206, 2019

Real Time Performance Comparison of Buck Converter Circuit Controlled By Discrete Time PID, LQR and SMC Controllers in Continuous-Current Mode

Ömer ÖZDEMİR*[1], İrfan YAZICI[2]

Abstract

In this study, a DC-DC buck converter circuit which is used to get direct voltage by decreasing the source voltage is researched. Firstly mathematical model for a DC-DC buck converter circuit is obtained and critical inductance value is calculated to make it work in continuous current mode. Then for controlling a DC-DC buck converter, three different controllers in discrete time (sliding mode control, proportional–integral–derivative controller and linear quadratic regulator) are designed. Finally, the performance of these controllers according to changing in the form of step function for input voltage, reference voltage and load conditions are examined and compared with real time studies. According to obtained results, a DC-DC buck converter circuit controlled by sliding mode controller has shown a better performance compared to the other controllers.

Keywords: *DC-DC converter, Buck converter, PID, SMC, LQR*

1. INTRODUCTION

Today, most of the energy consumed is unfortunately derived from fossil fuels. As the technology advances, worldwide energy consumption accelerates day by day [1]. Because the fossil fuels are nonrenewable and their bad effects to the environment, researchers are studying ways to get the maximum efficiency from the used energy [1,2].

Linear regulators are cheap and also have advantages like being robust and durable [3,4]. But also they are large, heavy and have low efficiency between (25% to 60%). Switch mode converters are relatively hard to control and expensive. They can produce electromagnetic interference (EMI). They are light, smaller and have high efficiency between (70% to 95%) [5]. With a right design and control, EMI can be reduced to reasonable values. Switch mode converters can have more than one output and some models have the option to adjust the output voltage poles as desired [6,7].

The DC-DC buck converters are power electronic circuits which get output voltage equal to or less than the input voltage. The DC-DC buck converters have at least one power switch to make a controlled switching. They have inductance and capacitor to filter the current and voltage fluctuations on the load [7,8].

In this study, firstly the DC-DC buck converter is presented and circuit analysis of the DC-DC converter is done. Then for controlling the DC-DC

* Corresponding Author: omerozf@gmail.com
[1] Sakarya University, Electrical and Electronics Engineering, Sakarya, TURKEY. ORCID: 0000-0001-5733-3939
[2] Sakarya University, Electrical and Electronics Engineering, Sakarya, TURKEY. ORCID: 0000-0003-3603-7051

buck converter, in discrete time three different controllers (sliding mode control, proportional–integral–derivative controller, linear quadratic regulator) are designed. Finally, performances of these controllers according to changing input voltage, reference voltage and load conditions are examined and compared with real time studies.

2. DC-DC BUCK CONVERTERS

We have analyzed DC-DC buck converters circuit with the following assumptions.

-Power mosfet and diode are ideal switches.

-The inductor is in continuous current mode.

The structure of the DC-DC buck converters is as shown in Figure 1.

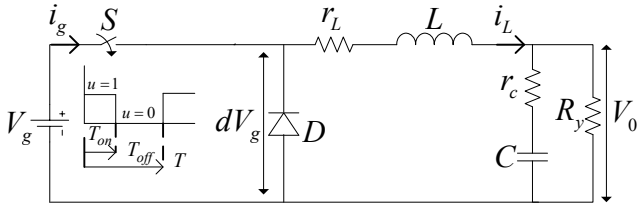

Figure 1. DC-DC buck converter circuit diagram

According to the opening and closing of the switching component which is shown in the Figure 1, as shown in Figure 2 can be analyzed in two modes.

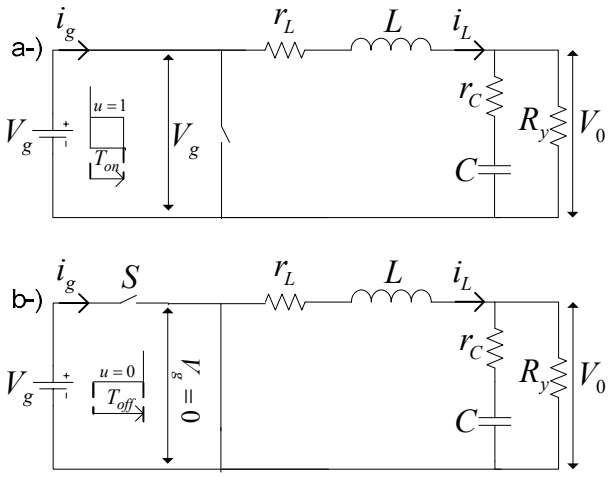

Figure 2. (a) When the switching component is in off mode (b) When the switching component is in on mode.

The ratio of the on time (T_{on}) of switching component to the total switching period (T_s) gives the duty cycle (d) [9,10]

$$d = \frac{T_{on}}{T_{on} + T_{off}} \tag{1}$$

When the switching component is on (dT_s), dynamic representations belonging to the DC-DC buck converters circuit shown in Figure 2.a are given below in equations 2, 3 and 4 [11].

$$v_g = L\frac{di_L}{d_t} + v_0 + r_L i_L \tag{2}$$

$$v_0 = r_C i_C + \frac{1}{C}\int i_C dt \tag{3}$$

$$i_C = i_L - \frac{v_0}{R_Y} \tag{4}$$

Similarly, when the switching component is off $((1-d)T_s)$, dynamic representations belonging to the DC-DC buck converters circuit shown in Figure 2.b are given below equations 5, 6 and 7 [11].

$$0 = L\frac{di_L}{d_t} + v_0 + r_L i_L \tag{5}$$

$$v_0 = r_C i_C + \frac{1}{C}\int i_C dt \tag{6}$$

$$i_C = i_L - \frac{v_0}{R_Y} \tag{7}$$

If selected as inductance current and capacitor voltage state variables. Based on switching components on and off situations, the state space representation of the DC-DC buck converters are given below in equations 8 and 9 [12].

$$\dot{x} = \begin{bmatrix} -\frac{r_L}{L} & \frac{1}{L} \\ \frac{LR_Y - Cr_L r_C R_Y}{LCr_C + R_Y)} & \frac{-L - Cr_C R_Y}{LC(r_C + R_Y)} \end{bmatrix} x + \begin{bmatrix} \frac{V_g}{L} \\ \frac{V_g r_C}{L} \end{bmatrix} u \tag{8}$$

$$\dot{y} = \begin{bmatrix} 0 \\ 1 \end{bmatrix} x \tag{9}$$

Derived from Figure 1, equation 8 and 9, the DC-DC buck converters transfer function between input and output voltages is given below in equation 10 and 11 [13].

$$\frac{V_0(s)}{V_g(s)} = \frac{d(RCr_C s + R)}{(R + r_C)LCs^2 + (m)s + (R + r_L)} \tag{10}$$

$$m = L + Cr_C R + Cr_L R + Cr_C r_L \tag{11}$$

The inductance value must be greater than the critical inductance value, for the buck converter to operate in continuous current mode. The value of critical inductance is given in equation 13 [11,12].

$$2I_Y = \frac{V_0(1-d)}{f_s L} \tag{12}$$

$$L_K = \frac{R(1-d)}{2f_s} = 600\mu H \tag{13}$$

Table 1. The system parameters used in real time studies

Parameter	Value
İnductance	$L = 880\ \mu H, r_L = 1.7\Omega$
Capacitor	$C = 390\ \mu F, r_C = 14m\Omega$
Load	$R = 15\ \Omega$
Input Voltage	$V_g = 13\ V$
Switching Frequency	$f_s = 10\ kHz$

3. CONTROL METHODS OF THE SYSTEM

3.1. Sliding Mode Control

Sliding mode control is a very robust control method under proper conditions indicating the desired dynamic behaviors despite the outer distortions, parasites and parameter changes [15,16]. SMC method is more advantageous than other methods because of its properties like convenience to be used on the system, indifference to parameter uncertainties, damping the noise and endurance [15-18]. Basically, the aim of SMC is reset the difference between the chosen control variables reference and measured value and the derivation of this difference to time and so leading the state variables, to the defined equilibrium point. SMC design is performed in two stages [15-19].

i-) Determining of a stable sliding surface.

ii-) Determining the control signal which will take the system from a starting point to the sliding surface and keep it in there.

In discrete time SMC systems, two types of orbital behavior can be defined as shown in Figure 3. These are [15,20];

i-) Ideal orbit

ii-) Realizable orbit

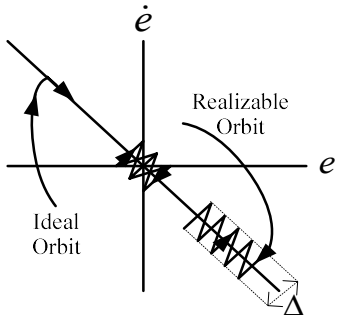

Figure 3. Phase plane for discrete-time SMC

In the SMC systems, for the cases when the system state orbit frequency in discrete time is not infinite, it cannot stay on the sliding surface as in continuous-time SMC systems. It shows a zigzag behavior around sliding surface in a limited band (Δ) which is also called "crackling". Thus,

discrete-time SMC systems are called Quasi-SMC [15,21].

$$2\Delta = 2\frac{\varepsilon T_s}{1-qT_s} \tag{14}$$

For the system to be stable and robust, amplitude of the zigzags and system phase orbit should stay in a limited band as shown in equation 14. Ideal sliding happens when the limited band value is zero $(\Delta = 0)$ [15].

If we rearrange the state variables as $(x_1 = V_0 - V_{ref})$ and $(x_2 = \dot{x}_1)$ to define the DC-DC buck converters SMC control signals, we get the equation 15.

$$\begin{bmatrix}\dot{x}_1\\ \dot{x}_2\end{bmatrix} = \begin{bmatrix}0 & 1\\ -\frac{1}{LC} & -\frac{1}{RC}\end{bmatrix}\begin{bmatrix}x_1\\ x_2\end{bmatrix} + \begin{bmatrix}0\\ \frac{V_{in}}{L}\end{bmatrix}[u] + \begin{bmatrix}0\\ \frac{V_{ref}}{LC}\end{bmatrix} \tag{15}$$

If system parameter values and discrete time state-space model given in Table 1 is discretized by $(T_s = 1/f_s)$ frequency, we get these representations:

$$x(k+1) = Gx(k) + Hu(k) + d_k \tag{16}$$

$$G = \begin{bmatrix}0.9855 & 0.0001\\ -287.49 & 0.9687\end{bmatrix}, H = \begin{bmatrix}0.2\\ 3737.5\end{bmatrix}, d_k = \begin{bmatrix}0\\ -287.5\end{bmatrix} \tag{17}$$

For a DC-DC buck converter circuit we can chose a sliding surface as in equation 18.

$$s(k) = C_g x(k) \tag{18}$$

With the help of Gao access rule, control signal $u(k)$ [22];

$$s(k+1) - s(k) = -qT_s(s(k)) - \varepsilon T_s \operatorname{sgn}(s(k)) \tag{19}$$

$$s(k+1) - s(k) = \begin{Bmatrix} C_g G(x(k)) + C_g H(u(k)) \\ -C_g(x(k)) \end{Bmatrix} \tag{20}$$

Derived from above given Gao access rule equations and using coefficients $C_g = \begin{bmatrix}4 & 10^{-6}\end{bmatrix}$, $e = 200$ and $q = 1500$, for a DC-DC buck converter SMC control signal is as in equation 21.

$$u(k) = ([4\ 10^{-6}]H)^{-1} - [4\ 10^{-6}]Gx(k) - [4\ 10^{-6}]d_k + (1 - 1500T_s)(s(k)) - 200T_s \operatorname{sgn}(s(k))) \tag{21}$$

3.2. Linear Quadratic Regulator

Linear Quadratic Regulator is one of the most suitable control processes based on state feedback method [23,24]. Thus, except some special cases, LQR controlled system response is stable. LQR method is based on obtaining state feedback constants with the help of values which will minimize or maximize the performance index specified for the system. Schematic model controlled with LQR is given in Figure 4 [24].

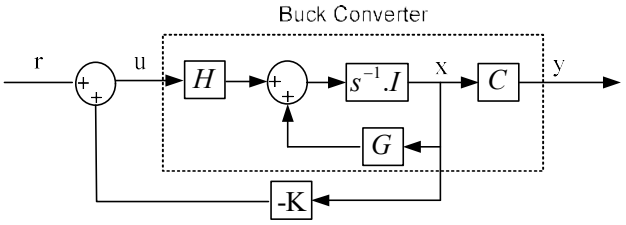

Figure 4. Classical LQR schematic diagram.

As can be seen in the LQR block diagram, LQR method is a state variable feedback structured theory. What is different from LQR method and pole placement method is the way they determine the gain matrix K. In pole placement, designer implants the poles in determined spots to define the gain matrix. But in LQR technique for defining gain matrix K, performance index is used [15,25].

If system is affected from outer parasites and distortions, system deviates from the reference value and regulatory structure only would be insufficient to readjust the system to its reference value [26]. It is possible to eliminate this problem by adding an integral controller to the system. In this study, for making the DC-DC buck converter system immune to outer parasites and distortions and eliminating problems which may cause instability, system state vectors are augmented by appointing a new pole. Schematic model of increased poled LQR controller is given in Figure 5 [24,26].

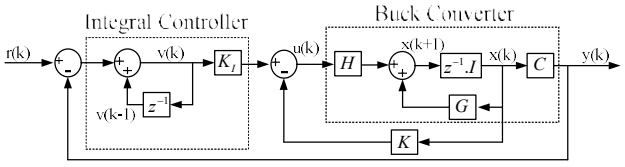

Figure 5. Servo system.

We can write equations augmented poled LQR controller schematic diagram, equation 22 and 23 from in Figure 5 [24].

$$v(k) = v(k\text{-}1) + r(k) - y(k) \tag{22}$$

$$v(k+1) = v(k) + r(k+1) - C(Gx(k) - Hu(k)) \tag{23}$$

Using equations for increased poled discrete-time state space model $x(k+1)$ and $v(k+1)$ we can write;

$$\begin{bmatrix} x(k+1) \\ v(k+1) \end{bmatrix} = \begin{bmatrix} G & 0 \\ -CG & 1 \end{bmatrix} \begin{bmatrix} x(k) \\ v(k) \end{bmatrix} + \begin{bmatrix} H \\ -CH \end{bmatrix} u(k) = + \begin{bmatrix} 0 \\ 1 \end{bmatrix} r(k+1) \tag{24}$$

$$y[k] = \begin{bmatrix} C & 0 \end{bmatrix} \begin{bmatrix} x[k] \\ v[k] \end{bmatrix} \tag{25}$$

And augmented poled LQR controllers control equation would be given in equation 26 [24].

$$u(k) = -Kx(k) + K_i v(k) \tag{26}$$

In equation 27 performance index chosen for DC-DC buck converter is given [15].

$$J = \frac{1}{2} \sum_{k=0}^{\infty} (x^T[k] Q x[k] + u^T[k] R u[k]) \tag{27}$$

In the given performance index, x represents state variables, u represents control variables, Q and R represents positive defined weight matrixes. For increased poled system, gain matrix is given in equation 28 [26].

$$\begin{bmatrix} -K & k_i \end{bmatrix} = (R + \hat{H}^T P \hat{H})^{-1} \hat{H}^T P \hat{G} \tag{28}$$

To obtain gain matrix coefficients, positive defined symmetrical matrix (P) is needed. Using below given equation 29 for discrete-time Ricatti equation, positive defined symmetrical matrix (P) can be obtained [15,26].

$$P = \hat{G}^T P \hat{G} - (\hat{G}^T P \hat{H})(R + \hat{H}^T P \hat{H})^{-1} (\hat{H}^T P \hat{G}) + Q \tag{29}$$

The choice of positive defined weight matrixes Q and R for LQR controller is the preference between density of the control signal and regulation speed. If $Q > R$ is chosen control signals density would be low and system regulation speed would be high. Likewise, if $R > Q$ is chosen, control signals density would be high and system regulation speed would be low. For this study, Q and R are chosen as [25]:

$$Q = \begin{bmatrix} 10 & 0 & 0 \\ 0 & 10 & 0 \\ 0 & 0 & 1 \end{bmatrix}, \quad R = \begin{bmatrix} 1 \end{bmatrix} \tag{30}$$

In this study, gain matrix for augmented poled LQR controlled system is obtained as:

$$K = [0.7094 \quad 1.0248] \text{ ve } k_i = [0.1816] \tag{31}$$

3.3. Proportional Integral Derivative Control

Proportional-integral-derivative (PID), made of a combination of proportional, integral and derivative methods has a relatively simple structure and it is easy to design, thus it is one of the most preferred controller types by the industry which is of classical feedback construction [26,27]. In simple terms, PID controller processes the error value which is the difference between desired reference voltage and system output to produce the control signal which will eliminate the error [28]. While producing the control signal, it processes the error value in three separate mathematical operations (proportional K_P , integral K_I and derivative K_D).Control block diagram for discrete time PID controller system is shown in Figure 6 [29].

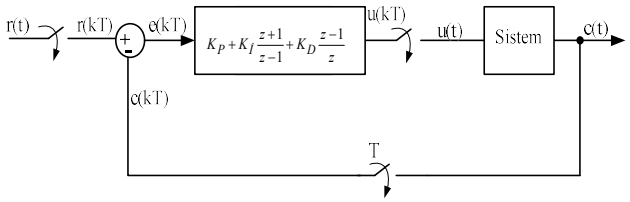

Figure 6. Classical discrete time PID schematic diagram

Mathematically algorithm of PID controller in discrete time is given in equation 32 [29].

$$G_{PID(Z)} = K_P + K_I \frac{z}{z-1} + K_D \frac{z-1}{z} \quad (32)$$

To determine the constants (K_P, K_I and K_D) in above given PID algorithm, there are various methods in literature for time domain and frequency domain. For this study Matlab/Sisotool program is used and K_P, K_I and K_D constants are obtained in equation 33 [24,27].

$$G_{PID(Z)} = 0.17 + +198.117 \frac{z+1}{z-1} + \frac{18.05}{10^6} \frac{z-1}{z} \quad (33)$$

4. REAL TIME STUDIES ON DC-DC BUCK CONVERTER

For real time studies of DC-DC buck converter working in continuous current mode, ARM based Texas Instrument LM4F120 processor is used. Firstly, while working in constant load and constant input voltage, the ability of the DC-DC buck converter controllers to follow reference step function voltage is examined. For this purpose reference voltage is increased to 8V from 7V and then reduced to 6V and again increased to 7V and controller performances are compared. The performances for reference value changes of SMC, PID and LQR are shown below respectively in Table 2 and Figures 7, 8 and 9.

Table 2. Real time performance comparison of the DC-DC buck converter, which is controlled with SMC, LQR and PID controllers for reference voltage change condition

	SMC	LQR	PID	
Settling Time (ms)	0,8	2,9	3,3	**7V→8V**
	1,9	3,7	5,6	**8V→6V**
	0,4	2,9	3,6	**6V→7V**
%Maximum Overshoot	0	0	0,9	**7V→8V**
	0	0	5,6	**8V→6V**
	0	0	1,1	**6V→7V**

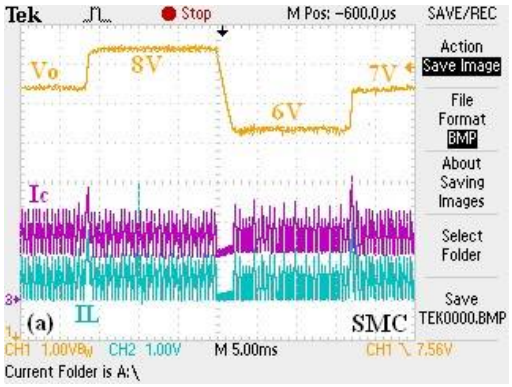

Figure 7. Response curves of SMC examined for reference voltage change condition

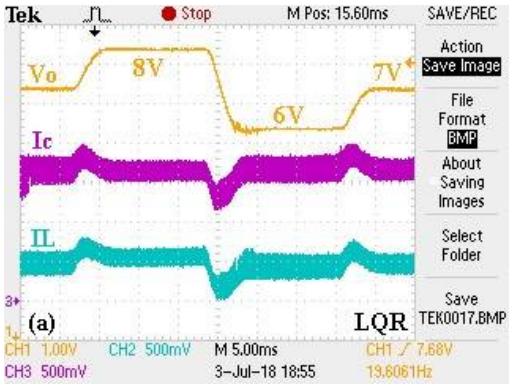

Figure 8. Response curves of LQR controller examined for reference voltage change condition

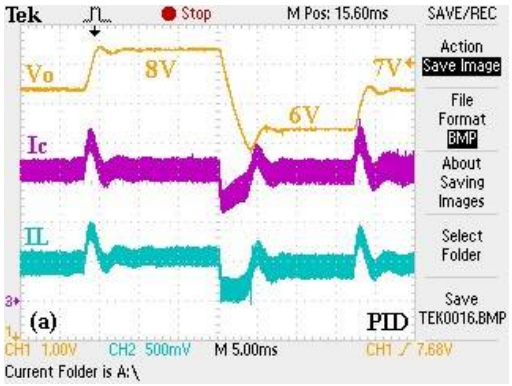

Figure 9. Response curves of PID controller examined for reference voltage change condition

The system with the SMC has performed the fastest follow-up for all change moments and when overflow criteria is taken into account, SMC and LQR systems has the least overflow. However, in the system with the SMC a crackling problem has occurred as can be seen from the inductance and capacitor currents. There are various methods to overcome the crackling problem in literature. In responses of the three controllers, permanent state error wasn't observed.

Secondly, while working in constant load and constant reference voltage, the performances against the changing step functioned input voltage value are examined. For this purpose input voltage value is increased to 18.0 V from 13.0 V to compare the performances of the controllers. Performances belonging to SMC, PID and LQR controllers against the input voltage value change are given below respectively in Table 3 and Figures 10, 11 and 12.

Table 3. Real time performance comparison of the DC-DC buck converter, which is controlled with SMC, LQR and PID controllers for sudden changes of input voltage condition

	13,0V→18,0V		
	SMC	**LQR**	**PID**
Settling Time (ms)	2,6	4,7	6,8
%Maximum Overshoot	11,2	24,5	28,7

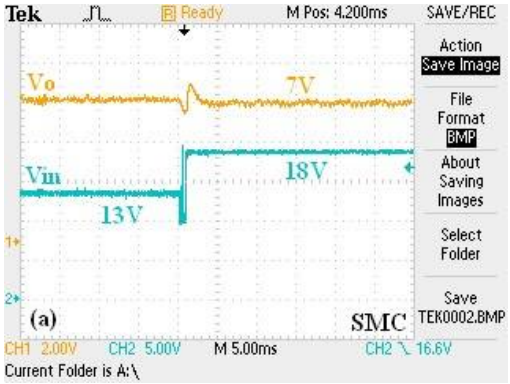

Figure 10. Response curves of SMC examined for sudden changes of input voltage condition

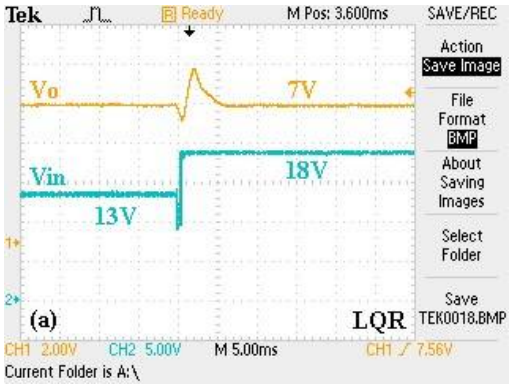

Figure 11. Response curves of LQR controller examined for sudden changes of input voltage condition

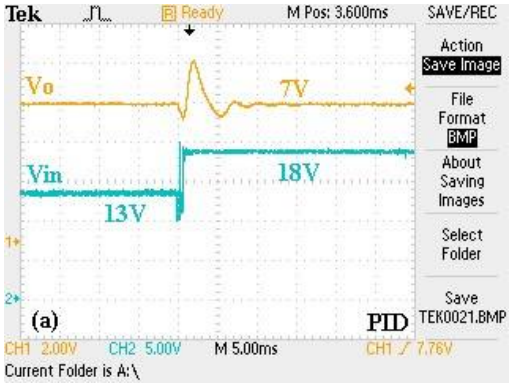

Figure 12. Response curves of PID controller examined for sudden changes of input voltage condition

It is observed that the system with SMC has performed the fastest track and it is the one with the minimum overflow.

Lastly, for a DC-DC buck converter with controllers working in constant input voltage and constant reference voltage, the performances against the changing step functioned load values are examined. For this purpose load value is increased to 15.0 Ω from 7.5 Ω and then reduced to 7.5 Ω again to compare the performances of the controllers. Performances belonging to SMC, PID and LQR controllers against the load value change are given below respectively in Table 4. and Figures 13, 14 and 15.

Table 4. Real time performance comparison of the DC-DC buck converter, which is controlled with SMC, LQR and PID controllers for load change condition

	SMC	LQR	PID	
Settling Time (ms)	0	2,7	2,4	**7,5Ω→15Ω**
	0	3,1	2,1	**15Ω→7,5Ω**
%Maximum Overshoot	0	9,6	9,1	**7,5Ω→15Ω**
	0	9,1	5,7	**15Ω→7,5Ω**

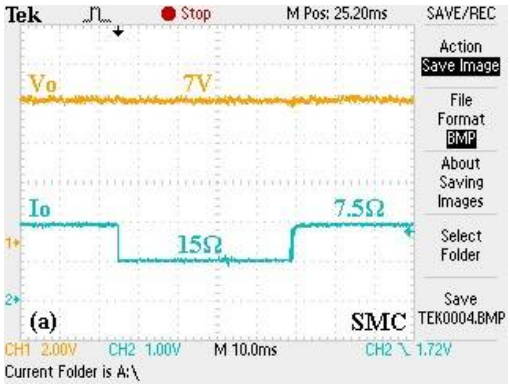

Figure 13. Response curves of SMC examined for load change condition

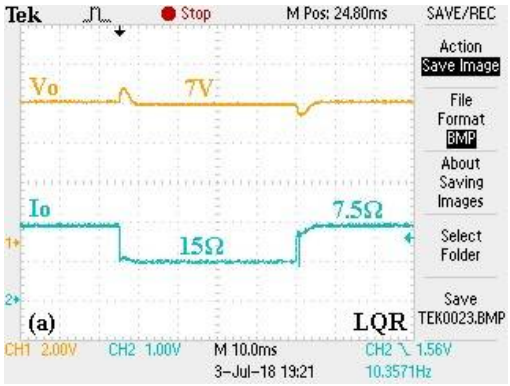

Figure 14. Response curves of LQR controller examined for load change condition

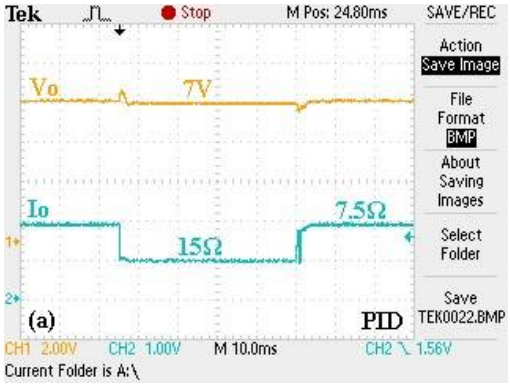

Figure 15. Response curves of PID controller examined for load change condition

5. CONCLUSION

In this study for a DC-DC buck converter working in continuous current mode, SMC, LQR and PID controllers in discrete time are designed and with real time studies, their performances are examined comparatively. As the result of these studies, SMC controlled system is observed to be the least affected system in terms of reference voltage follow-up and distortion inputs like input voltage or load change.

REFERENCES

[1] Adaçayı F. R., "Türkiye İçin Enerji ve Kalkınmada Perspektifler," Aksaray University Journal of Economics and administrative Sciences, vol. 6, pp. 87-103, 2014.

[2] Kadıoğlu S., Tellioğlu Z., "Enerji kaynaklarının kullanımı ve çevreye etkileri", TMMOB Turkey Energy Symposium, s. 55-67, 1996.

[3] Bodur, H., "Güç Elektroniği", BİRSEN Publishing House. 2010.

[4] Mohan N., Undeland T. M., Robbins W.P.,"Power electronics: converters, applications, and design," Literatür Publishing, 2007.

[5] Yıldız M.N., "Güç Elektroniği Ders Notları," Ege University, 2009.

[6] Yanuarsyah Haroen, Pekik Argo Dahonon ve Jasmin Sutanto., "A new type DC-DC converter for rolling stock auxiliary power supply", Electrical Energy Conversion Laboratory, Bandung Institude of Technology, bandung, Indonesia, 2001.

[7] Mamur A., "FPGA Denetimli Düşürücü DA-DA Dönüştürücünün Tasarımı ve Gerçeklemesi" Master's Thesis, Fırat

University, Department of Electrical and Computer Engineering, Eskisehir 2012.

[8] Erdoğan E., "Dijital Kontrollü Çok Fazlı Senkronize DC-DC Alçaltıcı Çevirici Tasarımı", Master's Thesis, Eskisehir Osmangazi University, Graduate School Of Natural And Applied Sciences, Department Of Electronics, Eskişehir, 2010.

[9] Rashid M. H., "Power Electronics: Circuits, Devices, and Applications", Front Cover, 4th Edition 2014.

[10] Alkrunz M., Yazıcı, I., 2016. "Design of discrete time controllers for the DC-DC boost converter". Sakarya University Journal of Science 20 (2016): 75-82.

[11] Arifoğlu U., "Güç Elektroniği Endüstriyel Uygulamaları Ders Notu". Sakarya University, Graduate School Of Natural And Applied Sciences, Sakarya, 2018.

[12] Rashid, M. H., "Power Electronics Handbook", University of West Florida, Pensacola, Florida, 895 p, 2001.

[13] Texas Instruments Incorporated, "AN-1197 Selecting Inductors for Buck Converters" SNVA038B.

[14] Edwards, C., Spurgeon, S.K. 1998. "Sliding mode control, theory and applications", Taylor & Francis, pp.1-65, 2013.

[15] Yazıcı İ., "Model Referans Kayan Kipli Kontrolör Tabanlı Güç Sistem Kararlayıcı Tasarımı", Ph. D. Thesis, Sakarya University, Graduate School

[16] Emelyanov, S.V., "Variable structure control systems" , Moscow, Nauka, 1967.

[17] Itkıs, Y., "Control systems of variable structure", New York, Wiley, 1976.

[18] Utkin, V. I., "Variable structure systems with sliding modes", IEEE Trans. Automat. Contr., AC-22, pp. 212–222, 1977.

[19] Aydın S., "Kayma Kipli Kontrolörlerde Kayma Yüzeyi Tasarımı Yöntemlerinin İncelenmesi ve Sınıflandırılması", Master's Thesis, Pamukkale University Graduate School Of Natural And Applied Sciences, 2008.

[20] Li, H., Song, L., "Discrete variable structure control design and its application to a power system," 2007.

[21] Monsees, G., "Discrete-Time Sliding Mode Control", Ph.D. dissertation, Delft University of Technology, pp.1-130, 2002.

[22] Gao, W., Wang, Y., Homafia, A., "Discrete time variable structure control systems", IEEE Trans. On Ind.Elect., 42, 2, pp. 117-122, 1995.

[23] Kuo BC., "Digital control systems. 2nd ed. Florida: Sounders College Publishing," 1992.

[24] Ogata K., "Discrete Time Control Systems" PrenticeHall,pp.1-580, 1995.

[25] Naidu, D.S., "Optimal control systems", CRC Press, pp.1-120, 2003.

[26] FatihM., http:// web .hitit. edu. tr/ dersn otlari/ mehmet fatih_ 21.03.2014 _4I1U.pdf, Hitit Universty, 2014.

[27] SARIOGLU, K. M., "Dijital Kontrol Sistemleri" Birsen Publishing, İstanbul, 1998.

[28] Burns RS., "Advanced Control Engineering", Butterworth-Heinemann, Oxford-UK, 2001.

[29] Fraser, C. and Milne, J., "Electro-Mechanical Engineering: An Integrated Approach", IEEE Press, New Jersey, 1994.

JOURNAL OF SCIENCE
SAKARYA UNIVERSITY

Sakarya University Journal of Science

ISSN 1301-4048 | e-ISSN 2147-835X | Period Bimonthly | Founded: 1997 | Publisher Sakarya University | http://www.saujs.sakarya.edu.tr/

Title: Evaluation Of Route Optimization Method İn Mobile Ipv6 Networks

Authors: Cemal Koçak, Mohamedi M. Mjahidi
Recieved: 2019-06-26 15:17:11

Accepted: 2019-08-20 14:43:26

Article Type: Research Article
Volume: 23
Issue: 6
Month: December
Year: 2019
Pages: 1207-1217

How to cite
Cemal Koçak, Mohamedi M. Mjahidi; (2019), Evaluation Of Route Optimization Method İn Mobile Ipv6 Networks. Sakarya University Journal of Science, 23(6), 1207-1217, DOI: 10.16984/saufenbilder.582641
Access link
http://www.saujs.sakarya.edu.tr/issue/44246/582641

Sakarya University Journal of Science 23(6), 1207-1217, 2019

Evaluation of Route Optimization Method in Mobile IPv6 Networks

Cemal KOÇAK*[1], Mohamedi M. MJAHIDI [2]

Abstract

With Mobile IPv6 (MIPv6) protocol support, mobile hosts can move from their home networks or one network to another without interrupting ongoing session. In MIPv6 network, packets from CN to MN undergo rectangular routing owing to long delay and tunneling overhead that affect the performance of mobile network. Furthermore, during handover process packet loss due to MN mobility is high which eventually hinder the performance of real application such as video conference, VoIP. Route optimization methods are applied in mobile network to avoid rectangular routing thus reducing delay, tunneling overhead and improving packet delivery. This paper investigated Return Routability Procedure (RRP) as a route optimization method for MIPv6 networks in terms of packets received, tunneling overhead, route optimization overhead and traffic control received. The result showed that video conference received is the same as if no route optimization was applied. However, comparing tunneled control traffics reduced with route optimization control traffic introduced is negligible. Instead, 0.02% of the tunnel and route optimization overheads were more introduced compared to tunneled and route optimization overheads introduced when no route optimization was applied.

Keywords: MIPv6, RRP, CN, MN, Tunneling, MIPv6 Routing Optimization

1. INTRODUCTION

Due to a rapid increase in the use of mobile devices, the need for mobility support has inevitably increased. This led the Internet Engineering Task Force (IETF) to introduce a MIPv6 protocol [1-2] to support the single node mobility when roaming. However, with time sensitive nature of real applications such as video conferencing, Voice over IP (VoIP), music's, online film, movies, gaming and other new applications introduced in recent years, researchers are compelled to pay attention to the Route Optimization methods in mobile networks. Many Route Optimization methods such as Return Routability Procedure (RRP), Enhanced Return Routability Procedure (ERRP), Timely One-Time Procedure (TOTP) etc., have been introduced in the literature.

RRP is a standard route optimization mechanism adopted by IETF in [1-2]. This mechanism was proposed to reduce end-to-end delay, tunneling

* Corresponding Author: ccckocak@gazi.edu.tr
[1] Gazi University, Department of Computer Engineering, Ankara, Turkey. ORCID: 0000-0002-8902-0934
[2] Gazi University, Department of Computer Engineering, Ankara, Turkey. ORCID: 0000-0002-3962-6997

overhead, increase packet delivery and to some extent adding security features to the mobile network. Because of its necessity, it is used as the reference by researchers in the field of mobile network when suggesting a new routing optimization method.

According to [3], the best route optimization scheme is expected to improve packets delivery, to optimize a route between MN and CN, reduce latency owing to MN mobility and tunneling overhead. In addition, when proposing a route optimization method, it is recommend that control signal and route optimization overhead should be reduced as much as possible [4]. The motivation behind this study is to evaluate the RRP route optimization method performance improvement such as end-to-end delay, reduced tunneling overhead with respect to control signal and route optimization overhead introduced.

Route Optimization method is an important phenomenon in the mobile network because bandwidth is typically limited in the wireless medium. Therefore, resources in the wireless network should be used in an economical way to avoid unnecessary overheads and delays. When managing MN mobility in mobile networks, route optimization methods introduce an amount of signaling messages when any mobility management protocol is used. For example, RRP method in MIPv6 exchanges periodic signaling messages even in the absence of MN movement. The signaling overhead is estimated to be 7.16bps when MN communicates with a stationary CN [5]. However, the delay due RRP handover process in the network is undesirable because it can impact performance of real-time applications or interactive applications such as VoIP, video conferencing, and so forth.

The remainder of this paper is organized as follows. In section 2, we discusses the MIPv6 route optimization method as a related works. Section 3 presents the standard MIPv6 network operations while section 4 the focus is given in Return Routability Procedure (RRP) method operations. The definition of network model for this study is depicted in section 5. Performance evaluation including simulation results and discussion are presented in Section 6. Finally, conclusion of the paper is provided in Section 7.

2. RELATED WORKS

Unlike cable network, mobile network suffers sub optimal routing due to the mobility of MNs. MIPv6 was designed for mobile network, hence it suffers from the problem of sub optimal routing. Several methods have been introduced in the literature to optimize a route in the mobile network. However, packet loss may happen in the mobile network because of frequently exchanging access points in the network. Without quantitative measurement of the extent of tunneling reduced, route optimization, level of security added and loss of packet and handover latency in the mobile network, the proposed method would be worthless. The following are literatures that discuss the MIPv6 network route optimization methods that are deemed relevant for this work.

RRP as one of the route optimization method in MIPv6 has an undesirable impact on handover delay, increases overhead and signaling control traffic as it involves signaling among all three nodes (MN, HA, and CN) in the mobile network [5]. With undesirable cost, the result is not what one would expect. This route optimization procedure is the subject of serious discussions concerning its network performance and security implications.

In the literature, several methods tries to improve RRP method by quantifying the weak point as few of the methods based on security messages that authenticate MN and CN such as HoTI, CoTI, HoT and CoT to overcome this weakness. Others try to focus on reducing interaction of messages during handover process and overheads in the network. Although these methods seek to improve RRP method, the majority have not specified the number of features they seek to improve. As this would be important avoiding introducing a route optimization method with a similar effect as RRP or more worse.

In [5, 6, 7, 8] proposes a method based on the security features in the mobile network. Shah, P. A at al., in [5] proposes an enhance route optimization on RRP process which is Time-based; One-Time Password Route Optimization (TOTP-RO). This method uses stateful shared token and maintains original state to use one password to avoid HoTI, CoTI, HoT and CoT messages. Kong, R., and Zhou, H. in [6] Proposes an improvement on the HoTI message to NPT to avoid packet loss if MN is attached or MR. However, [7, 8] focuses on reducing the number of messages to Return Routability Test. For example, in [7] together with IPsec reduces Return Routability Test messages from 6 to 5.

In [9, 10] focuses on the messages exchanged during handover process to reduce latency. Gupta, S., and Gambhir, S. in [9] proposed an architectural structure to minimize the handover latency by removing DAD (one of the most time-consuming processes during handover) and allow the router to configure CoA instead of MN itself. The router maintains two pools of addresses, the used ones and yet to be assigned ones that are free to be given to new connected nodes. Khan, M. Q., & Andresen, S. H. in [10] proposed a MN mobility prediction at CN which is a buffering mechanism. The CN is responsible for calculating the probability movement of MN from one location to another. This solution may suffer from resource problem if mobile CN is communicating with MN. CN buffer memory may be too short to maintain all those computed data and this cause delays.

Cabellos-Aparicio, A., and Domingo-Pascual, J. [11] in their solution introduced a Mobility Agents solution to perform RRP instead of it being done by each mobile client. This solution optimizes a route between MN and CN during handover and reduces the load on CN. The centralized solution (Mobility Agents) that performs Route Optimization on behalf of CN may suffer security threats whenever the Mobility agent is attacked. This will collapse the whole system as all RRP issues are centrally performed. Le, D., & Chang, J., in [12] proposed a tunneling-based route optimization mechanism to reduce per packet overhead compared to standard RRP mechanisms by optimizing packet routing between the MN and CN. It uses tunnel header instead of Type 2 routing header and Home Address option were suggested to carry the MN and CN HoA.

Barbudhe, A. K., et al in [3] stated that Route Optimizations' main problem is handover latency due to signaling control message exchange, which results in severe packet loss. To develop a better route optimization mechanism, they suggested key features to be considered such as minimizing handover latency, CoA Registration time, context establishment time, Binding Registration time, providing security and improve signaling latency. In [13, 14] simulated the MIPv6 network using RRP as a route optimization method. While Al-Saedi, F. A. T., & Asem, M. M., in [14] analyzed the results based on throughput and delay. Le, D., Fu, X., and Hogrefe, D., in [13] outlined and evaluated the results in signaling traffic control and overhead in the mobile network based on the network structure developed by the Institute of Informatics of Goettingen University.

R. Meng, et al in [15] proposed two enhanced schemes for MIPv6 and PMIPv6 so as to achieve low-latency handoff and route optimization method for future mobility oriented applications. In MIPv6, the trustworthiness is merely maintained between MN and HA. In this proposal, once MN attaches to a new Gateway, the MN establishes a trust linkage with the gateway. This route optimization method improves handover delay especially when MN is far away from HA, the handover delay is a half of legacy MIPv6. In other case, the proposed method expected to reduce overhead compared to standard MIPv6 in networks with large amount of short-lifetime connections. This route optimization method is similar to RRP except that the HoTI and HoT messages are exchanged via active gateway instead of HA.

M. Hata, et al. in [16] focused on MIPv6 routing optimization problems and proposed an SDN based end-to-end routing mechanism specified for mobility management instead of RR procedure.

The proposed method optimize an end-to-end delay based on various parameters such as bandwidth, number of domains, and flow operations for mobility after an MN has moved across SDN domains. The nodes in this method communicate with low-delay after inter-domain handovers and avoid disconnection that might occur when switching the route frequently. This method focuses on standard MIPv6 protocol instead of RR method.

Performance evaluation of route optimization in MIPv6 are presented in [17-20]. K. K. Ofosu, et al. evaluated the MIPv6 routing performance by combining MIPv6 and MANET protocols to route packets between the internet and the MANET through gateway agents. The simulation suggested that MANET On-demand routing improved the performance of MIPv6 on MANET regarding the average end-to-end delay, throughput, packet delivery ratio and normalized packet ratio. In the other hand, A. O, Alwer focuses in evaluating MIPv6 route optimization in pure IPv6 and mixed (6to4) network. The result shows that working in pure IPv6 networks was better than working in mixed networks. S. K. Hussein evaluates route optimization security and Quality of service (QoS) requirements of packet streams between MN and CN. These studies did not addresses the main requirement for the better route optimization in MIPv6.

3. MOBILE IPV6 (MIPV6)

MIPv6 was designed for MN to maintain an ongoing connection with CN while changing its location within a topology. While in the home network, a MN is configured with Home Address (HoA) and Care of Address (CoA) when it is in a foreign network. The HoA is assigned to nodes when they are at home subnets and is used for two reason: first, to allow a mobile node to be reachable by having a stable session through the communication and second, to hide the IP layer mobility from the upper layers. The advantage of keeping the HoA permanently to mobile node is that all the Correspondent Nodes (CN) tries to reach the mobile node using HoA without knowing the actual location of the mobile node, the packet will be forwarded to mobile node whether the mobile node is physically attached to a home subnet or not. If the mobile node is not attached to its home subnet, it is the responsibility of home agent to tunnel the packets to the mobile node's CoA.

The CoA is used when the mobile node moves from its home subnet to a foreign subnet, the mobile node acquire a CoA based on the prefix of the foreign subnet. The CoA can be formed based on stateless or stateful mechanisms. Due to the change in position and new address configuration while away from home network, MN must inform Home Agent (HA) of such changes by sending Binding Update (BU) message. In order for the HA to forward packets addressed to MN, it needs to store BU from MN. In this case, HA maintains a Binding Cache (BC) lists which contain all the BU for the MNs it serves. The HA then sends a Binding Acknowledgement (BA) to MN and from this point onward HA acts as a proxy for MN and tunnel all packets destined to MN.

4. RETURN ROUTABILITY PROCEDURE (RRP)

RRP is a Route Optimization method acquired by IETF in [1-2]. It gives CN assurance of the claimed MN CoA to accept a BU from MN. As shown in Figure 1, CN can accept a BU from MN after exchanging Tokens with MN by first MN sending two separate messages; Home Test Init (HoTI) and Care-of Test Init (CoTI), each with its own token encrypted by secret key Kmn (which known only by MN) and then CN uses both tokens to create a secret key Kcn and also sends back two separate messages; Home Test (HoT) and Care-of Test (CoT) to MN each with its own token.

The two messages (HoTI and CoTI) are sent to CN by MN to request HoT and CoT from CN. The HoTI is tunneled to the HA using HoA as a source

address while CoTI is transmitted directly to CN with a CoA as a source address. The HA decapsulates the HoTI from MN and forwards it to CN. The CN replies these two messages with HoT and CoT in the same path. All of these messages are transported inside a mobility header type 1. After this process, the MN can now send a BU using the token shared by CN. On the other side, CN can accept BU from MN with a claimed CoA. From here onward, CN can send all packets directly to MN CoA network.

Before the RR Test process begins, MN uses Router Discovery process to discover that is on a home network or has moved to a new router by acquiring FA CoA. MN sends a Router Solicitation message and in response receives an Agent or Router Advertisement from the router. In some cases, routers are configured to send Agent Advertisement on regular basis or required to respond to any Router Solicitation message received by sending the advertisement. After Router Discovery process, MN performs CoA Registration together with new router Duplicate Address Detection (DAD) to avoid any duplicate address with any host in the foreign network. These three processes (Router Discovery, CoA Registration, and DAD) add some reasonable delay during handover of MN to a new network. To reduce packet drops for all the packets that are directed to the HA, MN sends BU to HA before performing RR Test. Here, the total time required to complete RRP method is shown in the equation 1.

$$T_{rrp} = t_{rd} + t_{cr} + t_{dad} + t_{bha} + t_{rrt} + t_{bcn} \quad (1)$$

Where T_{rrp} = Total latency for RRP

t_{rd} = Router Discovery latency

t_{cr} = CoA Registration latency

t_{bha} = BU with HA latency

t_{rrt} = Return Routability Test latency

t_{bcn} = BU with CN latency

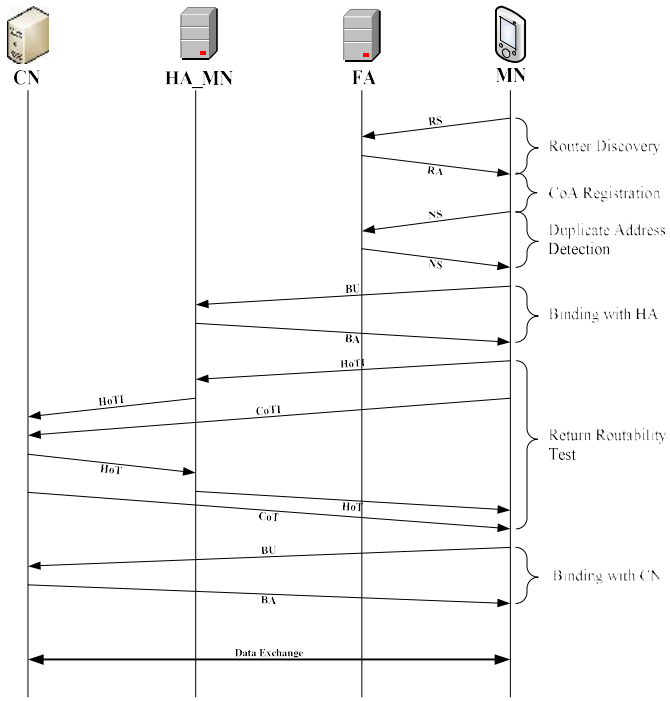

Figure 1. MIPv6 Routing Optimization Using RRP Operational Flows

One objective of MIPv6's RRP was to optimize a route from CN to MN and provide a certainty in the security level of MIPv6 network as opposed to the non-mobile network. RRP-based Route Optimization (RRP-RO) has an advantage that, it is a lightweight mechanism and has no requirements of pre-shared authentication keys. In addition, it does not maintain status at the CN [5]. This is because the home address test and the care-of address test involves message exchange between the MN and the CN, the MN and HA and HA and the CN. The delay during the handover process is high because MN cannot resume a direct communication with CN until both tests are completed.

5. NETWORK MODEL

MIPv6 protocol enables mobile devices to switch between networks and maintain ongoing sessions regardless of the physical location on the internet infrastructure. Figure 2 depicts the simulated network topology for this study. The network topology composed of four routers, CN and MN.

One Router acts as HA for MN while the three Routers act as Foreign Agent (FA) and one of them (FA_2) act as a default gateway for CN. In the network topology, each of the four routers comprises two interfaces; wireless interface which supports IEEE802.11b for roaming connection of MN and wired interface directly connected to the IPv6 internet cloud. FA_2 has one more wired interface to connect to CN. A MN is roaming from its HA passes through FA_1, FA_2, and FA_3 on the way back to its HA in an anti-clockwise direction. Other simulation parameters are shown in Table 1.

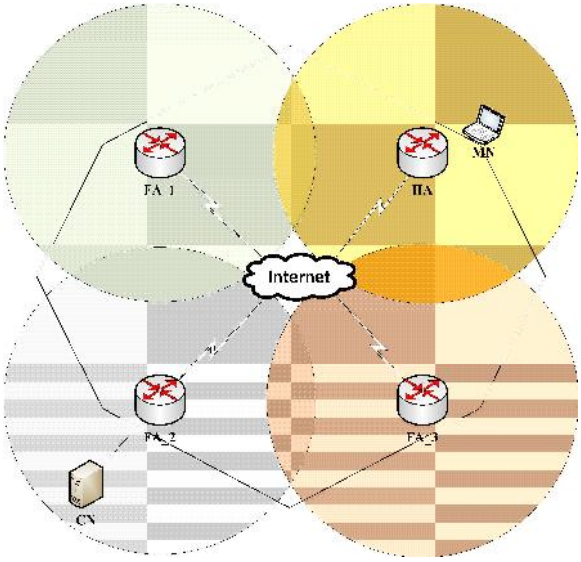

Figure 2 Network Topology

The MN assumes that it has moved to a foreign network if it does not receive agent advertisement from the current agent for a specific period. Once a MN moves to a foreign network, must configures new CoA. The MN movement detection and agent discovery is performed by FA to make itself available to MN by periodically sending Router Advertisement (RA) advertising the FA network prefix. From the advertised network prefix, a new CoA is generated by means of Ipv6 stateless or stateful address autoconfiguration.

On the other hand, if MN needs to configure a new CoA in foreign network but does not need to wait for the periodic RA, it broadcast an Agent Solicitation (AS) message to any available FA. The FA responds to an agent advertisement message with the FA network prefix. To verify the uniqueness of the configured new CoA, MN performs the Dublicate Address Detection (DAD) process before using the CoA. During all this time, MN cannot receive packet directly from CN or in a tunneled via HA.

Table 1. Simulation Parameters

Parameter	**Value**
Topology size	Campus (10km×10km)
Trajectory	Vector
Ground Speed	28mps
Application	Video Conference (light)
Route Optimization Method	RRP
Simulation Time	720 sec

6. EVALUATION OF SIMULATION RESULTS

This section analyses and evaluates the results obtained after the simulated network topology in OPNET Modeler 14.0. Two scenario results were taken from the topology; Route Optimization Enabled and Route Optimization disabled. This paper, analyses and evaluates RRP Route Optimization method in MIPv6 with standard MIPv6 protocol. Video conference packets received, signaling traffic control received and signaling overhead performance results were collected in this study.

6.1. Video Conference Packets Received

Figure 3 shows a video conference received in packets/sec. The results show that the video conference packets received for both cases are the same. In addition, there was a low video conference received around 129.6 to 151.2 sec, 295.2 to 316.8 sec, 460.8 to 482.4 sec and 626.4 to

640.8 sec during the simulation time because of handoff process.

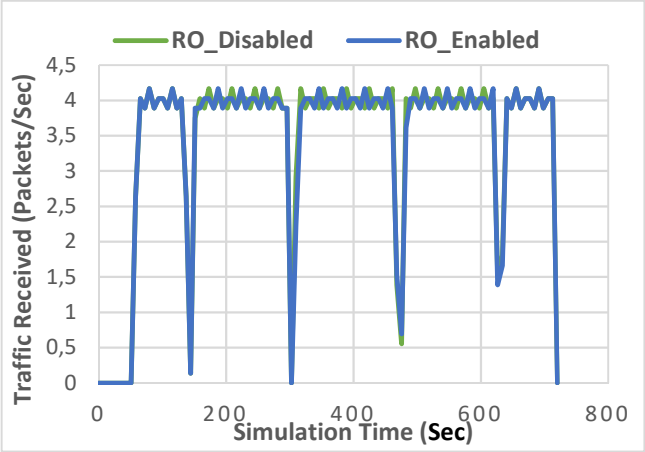

Figure 3. Video Conference Traffic Received

During Router Discovery, CoA Registration, DAD and BU with HA process, MN was not receiving any packet from a CN until the Binding with HA process was completed. The latency values caused by these four process $(t_{rd} + t_{cr} + t_{dad} + t_{bha})$ during handover are shown in Table 2 (i, ii and iii).

Table 2 Latency during Handover Process

No.	Handover	Time Range	Latency
i	HA to FA_1	129.6 to 151.2	21.6 sec
ii	FA_1 to FA_2	295.2 to 316.8	21.6 sec
iii	FA_2 to FA_3	460.8 to 482.4	21.6 sec
iv	FA_3 to HA	626.4 to 640.8	14.4 sec

The latency value during handover for these four process is the same with a value of 21.6 sec. This latency accounted for both scenarios because this was before performing a Return Routability Test. The latency value from FA_3 to HA has a different value of 14.4 sec because MN was returning to its home network. Therefore, no BU with HA process was performed. This is shown in Table 2 (iv). From these latency values, it shows that BU with HA process has a latency value of 21.6 – 14.4 = 7.2 sec. This means the RRP has an undesirable impact on the handover delays which resulted in an undesirable video conference received during this process. This further makes the same results appear as if no route optimization was enabled.

6.2. Signaling Control Traffic Received

Control traffic represents a signaling messages exchanged between MN and HA or MN and CN. It can be a BU or Routability Test messages. Figure 4 shows a control traffic received in packets/sec. It shows that RRP method removes tunneling overhead completely when MN is away from home network and has bonded with CN (from 165.5 to 302.4 sec, 324 to 475.2 sec, 489.6 sec. to the end of simulation time). But this method shows that still there is tunneling exists as shown in Figure 4 with a small interval from 138.8 to 165.5 sec, 302.4 to 324 sec and 475.2 to 489.6 sec of simulation time. This happens when a MN has bound with HA and a Return Routability Test is performed.

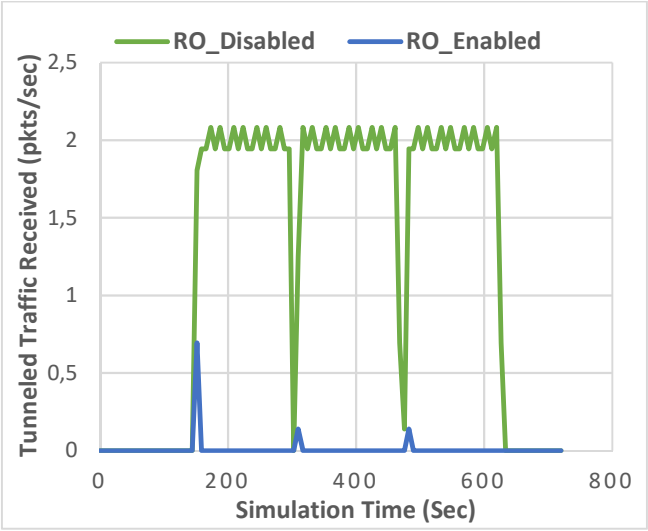

Figure 4. Tunneled Traffic Received

Figure 5 shows Route Optimization Traffic Received in packets/sec. No route optimization overhead was accounted when Route Optimization was disabled. However, during 302.4 sec and 475.2 sec of simulation time, the route optimization overheads were reduced to zero

because of the handover process. During this time MN could not receive any traffic except traffic for registration from a new Foreign Router.

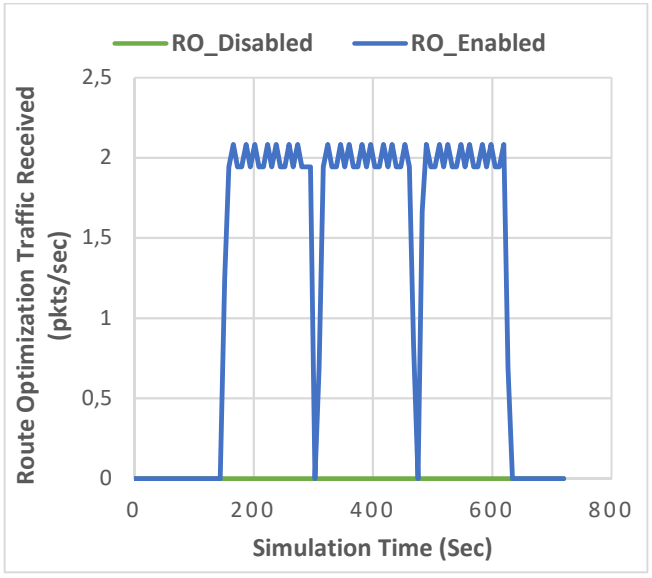

Figure 5. Route Optimization Traffic Received

In Figure 6, Tunneling plus Route Optimization control traffic received in packets/sec were compared for both scenarios. In this figure, it is shown that the Tunneling control traffics and Route Optimization control traffics are the same for both scenarios. This is obvious because RRP reduces tunneling control traffic in the network but introduces an equivalent amount of Route Optimization control traffics in the network.

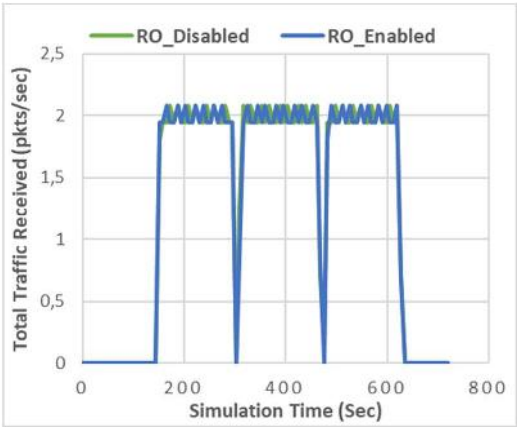

Figure 6. Tunneled and RO Traffic Received

6.3. Signaling Overhead

One objective of Route Optimization is to reduce tunneling traffic overhead as much as possible in the network because it increases the chance of packet fragmentation. Figure 7 shows a tunneling traffic overhead in percentage wise. Tunneling overhead represents an overhead ratio of IPv6 header encapsulation when MN is away from home network and packets for MN are sent to the home network. Upon receiving them HA encapsulates and tunnel them to MN foreign network. Tunnel overheads can be represented by the formula as given in Equation 2.

$$TO = \frac{Outer\ Packet\ IPv6\ hea \quad size}{Inner\ packet\ total\ size} \times 100 \qquad (2)$$

Where, TO is Tunneling Overhead.

From Figure 7 it is shown that, while a MN is away from the HA, if no Route Optimization is enabled, all traffics are tunneled to the MN and this happens at around 150 to 640 sec of simulation time with a value of 0.09%. Where Route Optimization was enabled, tunnel traffic existed for few seconds (around 138.8 to 165.5 sec, 302.4 to 324 sec and 475.2 to 489.6 sec of simulation time) with a value up to 0.36% before MN bound with CN and remove tunneling completely. This is because at these time intervals, the MN bound with HA, finish Return Routability and completing binding with CN.

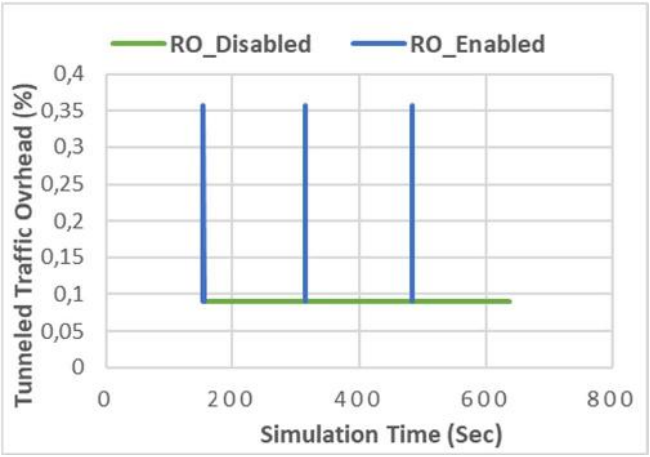

Figure 7. Tunneled Traffic Overhead

In other cases, route optimization overhead represents the overhead ratio of more IPv6 extension header when sending data packets using RRP or any other Route Optimization method. IPv6 packets may have more than one extension headers and there is no limitation of the number of extension headers in the IPv6 protocol. Route optimization overhead can be represented by the formula as given in Equation 3.

$$ROO = \frac{Total\ extension\ hea \quad size}{Original\ packet\ size} \times 100 \qquad (3)$$

Where, ROO is Route Optimization Overhead.

Figure 8 shows route optimization overhead in percentages wise. It shows that no route optimization overhead took place for a case when no Route Optimization was enabled. A route optimization overhead was around 0.11% when MN was away from the HA.

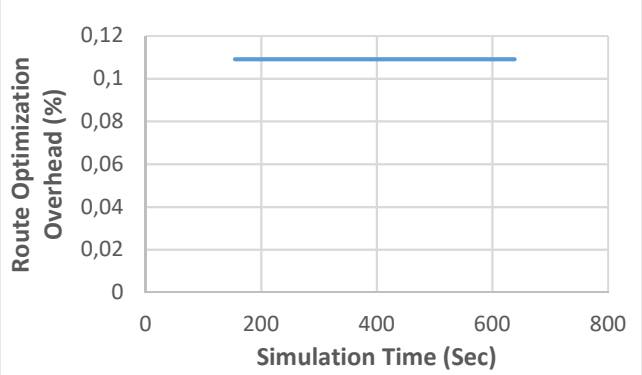

Figure 8. Route Optimization Overhead

Figure 9 shows the sum of Tunnel and route optimization overhead in percentage wise for both scenarios.

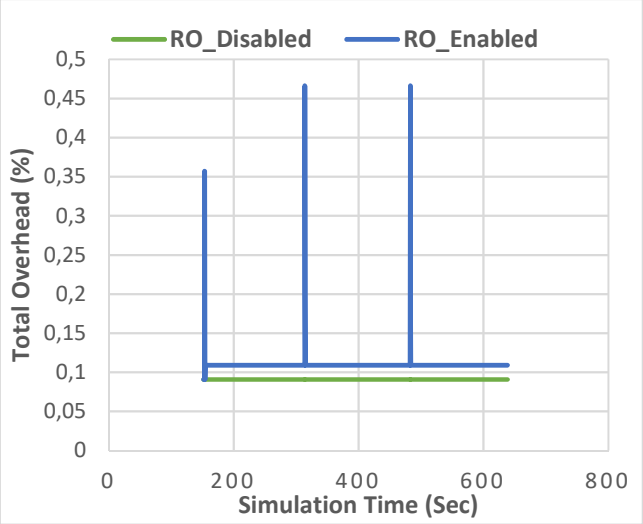

Figure 9. Tunneled and RO Overhead

The total overhead can be calculated as shown in the equation in equation 4.

$$Total\ Overhead = ROO + TO$$

$$Total\ Overhead = \left(\frac{Total\ extension\ heade \quad size}{Original\ packet\ size} + \frac{Outer\ Packet\ IPv6\ header\ size}{Inner\ packet\ total\ size}\right) \times 100 \qquad (4)$$

It is shown that RRP has a higher overhead value of 0.11% compared to normal MIPv6 protocol with no Route Optimization enabled and overhead value of 0.09%. This is because, when no route optimization is enabled, packets are encapsulated with a header length size of 40 Bytes only and forwarded to MN foreign network and for this case, zero route optimization overhead was encountered. Whereas, route optimization enabled using RRP, CN send packets using Type 2 Routing Header and Home Address option with Destination Extension headers, which incurs the overhead cost of both Routing Header and Home Address options. Each extension header has a size of 24 Bytes, which means, two extension headers have a total of 48 Bytes. This makes a difference of 8 Bytes for the data packets from a scenario where no route optimization enabled.

7. CONCLUSION

In this paper, evaluation of RRP Route Optimization method in MIPv6 networks was conducted. Packets received, tunneled traffic received, route optimization control traffic received, tunneled overhead and route optimization overhead performance results for video conference application were collected. Video conference packets received for RRP method were the same as standard MIPv6 protocol. However, results show that packets dropped dramatically during handover process. Compared to tunneling overhead and control traffic received, RRP method adds an equivalent amount of Route Optimization control traffics in the network. The RRP method introduces more overhead to the network compared to legacy MIPv6. Though this method improves End-to-End delay and security in MIPv6 networks, more research is needed for route optimization method in MIPv6 networks. This study serves as a benchmark for proposing route optimization method in MIPv6 networks so that the suggested route optimization method can enhance end-to-end delay, packets delivery, throughput while reducing tunneling, signaling and route optimization overhead.

REFERENCES

[1] D. Johnson, et al., "Mobility support in IPv6," No. RFC 3775, 2004.

[2] C. Perkins, et al., "Mobility support in IPv6," No. RFC 6275, 2011.

[3] A. K. Barbudhe, et al., "Comparison of Mechanisms for Reducing Handover Latency and Packet Loss Problems of Route Optimization in MIPv6," *In Computational Intelligence & Communication Technology (CICT). IEEE International Conference on* 323-329, 2015.

[4] P. A. Shah, et al., "A TOTP-based enhanced route optimization procedure for mobile IPv6 to reduce handover delay and signaling overhead," *The Scientific World Journal*, doi:10.1155/2014/506028, 2014.

[5] R. Kong, H. Zhou, "Analysis and improvement of Return Routability procedure for network mobility," *In Wireless Communications, Networking and Mobile Computing*, WiCOM 2006. International Conference on 1-4. doi:10.1109/WiCOM.2006.306. 2006.

[6] R. Radhakrishnan, et al., "A Robust Return Routability Procedure for Mobile IPv6," *International Journal of Computer Science and Network Security (IJCSNS)*, 8, 243-240, 2008.

[7] A. Z. M. Shahriar, et al., "Route optimization in network mobility: Solutions, classification, comparison, and future research directions," *IEEE Communications Surveys & Tutorials,* 12(1). doi:10.1109/SURV.2010.020110.00087, 2010.

[8] J. Arkko, et al., "Enhanced route optimization for mobile IPv6", No. RFC 4866, 2007.

[9] S. Gupta, S. Gambhir, et al., "An improved architecture for minimizing handover latency in MIPv6," *In Methods and Models in Computer Science (ICM2CS),* International Conference on 106-111. doi: 10.1109/ICM2CS.2010.5706728, 2010.

[10] M. O. Khan, S. H. Andresen, "Pros and cons of route optimization schemes for network mobility and their implications on handovers," *IEEJ Transactions on Electrical and Electronic Engineering*, (6), 622-632, doi: 10.1002/tee.21781, 2012.

[11] A. Cabellos-Aparicio, J. Domingo-Pascual, "Mobility Agents: Avoiding the Signaling of Route Optimization on Large Servers," *In Personal, Indoor and Mobile Radio Communications PIMRC,* IEEE 18th International Symposium on IEEE. pp. 1-5, doi:10.1109/PIMRC.2007.4394606, 2007.

[12] D. Le, J. Chang, "Tunneling-based route optimization for mobile IPv6," *In Wireless Communications, Networking and Information Security (WCNIS),* IEEE International Conference on 509-513, doi:10.1109/WCINS.2010.5544140, 2010.

[13] D. Le, et al., "Evaluation of mobile IPv6 based on an OPNET model," *In Proceedings of the 8th International Conference for Young Computer Scientists (ICYCS'05),* 238-244. 2005.

[14] F. A. T. Al-Saedi, M. M. Asem, "Performance Study of Mobile IPv6 Using OPNET," *International Journal of Engineering, 3*(8), 549-557, 2014.

[15] R. Meng, et al. "IP mobility enhancements for MIPv6 and PMIPv6," Tenth International Conference on Mobile Computing and Ubiquitous Network (ICMU), Toyama, pp. 1-6. doi: 10.23919/ICMU.2017.8330100, 2017.

[16] M. Hata, et al. "SDN Based End-to-End Inter-Domain Routing Mechanism for Mobility Management and Its Evaluation." Sensors (Basel, Switzerland) vol. 18, 12 4228, doi: 10.3390/s18124228, 2018.

[17] K. K. Ofosu, et al., "Performance Evaluation of Mobile IP on Mobile Ad Hoc Networks Using Ns2." Computer Science & Information Technology (CS & IT), 15-27. 2018.

[18] S. K. Hussein, "Performance Evaluation of Mobile Internet Protocol Version 6." International Journal of Management, Information, Technology and Engineering (BEST: IJMITE), Vol. 4, Issue 3, p. 35-52, 2016.

[19] A. O, Alwer, "Performance Evaluation for MIPv6 IN Pure IPv6 Networks vs. 6 TO 4 IP Mechanism Networks using OPNET." International Journal of Electronics, Mechanical and Mechatronics Engineering (IJEMME), Volume 6, Issue 4, p. 1317-1326, 2016.

[20] O. Erunika, et al., "Performance evaluation of host-based mobility management schemes in the internet," *In Mobile Computing and Ubiquitous Networking (ICMU),* Eighth International Conference on IEEE 173-178, doi:10.1109/ICMU.2015.7061062, 2015.

[21] K. M. Al-Farabi, M. H. Kabir, "Reducing packet loss in Mobile IPv6," *In Computer and Information Technology (ICCIT),* 14th International Conference on IEEE 38-43 doi:10.1109/ICCITechn.2011.6164852, 2011.

[22] W. A. A. Alsalihy, M. I. Younis, "Security verification of the return routability protocol by Murphi," *Scientific Research and Essays, 7*(21), 986-1996 doi:10.5897/SRE10.1211, 2012.

[23] A. Dhraief, A. Belghith, "An Experimental Investigation of the Impact of Mobile IPv6 Handover on Transport Protocols," *Smart CR,* 2(1), 1-17, doi:10.6029/smartcr.2012.01.001, 2012.

[24] A. Encarnacao, G. Bayer, "Mobile IPv6 Binding Update-Return Routability Procedure," 2008.

JOURNAL OF SCIENCE
SAKARYA UNIVERSITY

Sakarya University Journal of Science

ISSN 1301-4048 | e-ISSN 2147-835X | Period Bimonthly | Founded: 1997 | Publisher Sakarya University | http://www.saujs.sakarya.edu.tr/

Title: Intelligent Campus Implementation For Smart Cities

Authors: Raşit Cesur, Orhan Torkul, İsmail Hakkı Cedimoğlu, Seda Uçar
Recieved: 2018-01-08 14:59:29

Accepted: 2019-08-21 15:20:46

Article Type: Research Article
Volume: 23
Issue: 6
Month: December
Year: 2019
Pages: 1218-1224

How to cite
Raşit Cesur, Orhan Torkul, İsmail Hakkı Cedimoğlu, Seda Uçar; (2019), Intelligent Campus Implementation For Smart Cities. Sakarya University Journal of Science, 23(6), 1218-1224, DOI: 10.16984/saufenbilder.376218
Access link
http://www.saujs.sakarya.edu.tr/issue/44246/376218

Sakarya University Journal of Science 23(6), 1218-1224, 2019

Intelligent Campus Implementation For Smart Cities

Muhammet Raşit CESUR*[1], Orhan TORKUL[2], İsmail Hakkı CEDİMOĞLU[3], Seda UÇAR[4]

Abstract

Digital transformation has provided the decision-making infrastructure needed to produce custom solutions for each person. Traditional decision support systems have begun to evolve into intelligent systems and mass customization has begun to be applied in many areas of life, such as education, transportation, health, and production. In order to achieve digital transformation in teaching, it is necessary not only to focus on the teaching process but also to focus on environmental factors. The provision of digital content and the performance of the student are carried out in the digital environment with education technologies. It is aimed to maintain sustainability of the environmental quality by following the digital environment by means of digital transformation and to improve the teaching processes with intelligent systems that will interfere immediately in emergency situations.

Keywords: Cyber-physical Systems, Education, Industry 4.0, Artificial Intelligence

1. INTRODUCTION

Digital transformation is an important factor in ensuring mass customization as well as providing flexibility in processes. Providing special content to students is an important factor in increasing the success of teaching by defining individual needs, especially in education systems [1]. The increase in the quality of education is not only about personal content, but also about the quality of educational tools and the environment. Class and campus environment must be monitored in order to follow the environmental conditions in which teaching activities are carried out and to ensure the safety and security of the students. In this process, the classrooms participated by the students and the working environment will be evaluated and a proposal for the determination of the work accidents or emergencies that may occur in the teaching environment or the management of autonomous emergency is proposed.

2. LITERATURE SURVEY

Although different terms such as smart city, digital city, and intelligent cities are used in the literature, different definitions are also made. Albino et al. [2] made firm that concepts such as technology,

* Corresponding Author: cesur@arvasis.com
[1] Sakarya University, Industrial Engineering, Sakarya, Turkey. ORCID: 0000-0001-9941-0517
[2] Yalova University, Industrial Engineering, Yalova, Turkey. ORCID: 0000-0003-2690-7228
[3] Sakarya University, Information Systems Engineering, Sakarya, Turkey. ORCID: 0000-0003-3844-9295
[4] Sakarya University, Computer Engineering, Sakarya, Turkey. ORCID: 0000-0001-5257-7424

infrastructure, knowledge management, connectivity, sustainability, quality of life, and participatory governance have come forward in defining intelligent cities. The key components of urban development for smart cities are smart technology, smart industry, smart services, smart management, and smart life [3]. IoT technology is widely used in smart city implementations all over the world. The main objective of the business partnership between these objects and objects that send data to the cloud computing system via wireless networks is to perform the combined task assigned to them [4]. Wireless sensor networks are one of the most effective tools to use in creating smart cities because of its ease of use and low cost according to Dener and colleagues [5].

These tools are used in a wide range of environments, from emergency training to education. While the use of technology improves productivity, especially the benefits provided in education are greater. The intelligent systems to which human logic is transmitted can provide better performance and metric values than traditional classical approaches [6]. Because education is a process in which people are involved, Mostar University has switched to an intelligent teaching system in education and a digital learning environment for students to reduce administrative costs and save time in education [7]. Infrastructure as a Service (IaaS) is emerging as the most important and fastest growing area in this digital environment [6, 8].

Quality in teaching systems should be improved not only by the process but also by managing emergencies. There are many works in this field. For example, image processing techniques [9, 10, 11], distributed sensor systems [12], object and motion tracking [13, 14, 15], color classification [16] are some of the works in this field. Töreyin and colleagues classified the video data by visualizing fire motion, vibration and irregularity of the video, and increased the fire detection performance [10]. To handle the fire, it is necessary not only to detect the fire, but also to detect its motion. Laugraud and colleagues developed a background subtraction algorithm called LaBGen [15]. In the system developed for this study, these issues were not addressed separately, because various factors like building design, sensor design, and system design affect the digitalization[17].

There are many studies in the literature to solve for single problem. In this study, the knowledge in the scientific literature is transformed into a complete framework. Contribution of the proposed system is that it operates with low cost algorithms, and decrease both network and hardware complexity. By monitoring the teaching environment, a hybrid system has been created that monitors both the emergency management and the quality of the environment as well as the teaching process.

3. INTELLIGENT CAMPUS MODEL

Intelligent campus is an environment in which person-specific data is produced, analyzed and reported in a high-populated environment in order to enable student-specific teaching processes to be maintained. In order to achieve this, it is aimed to follow the operations of working environment by the cloud computing system, to understand the environment with artificial intelligence, and to report with big data systems. Those systems are the main components of Industry 4.0.

3.1. Cloud computing services

The cloud computing system is an important tool for students to follow their work, their connections and the software they use. In addition, the communication infrastructure required for students to be connected to the campus is provided via the cloud system. Cloud model developed for intelligent campus includes:

- Infrastructure as a service (IaaS),
- Software as a service (SaaS).

Because the platform service (PaaS) is effectively used to develop software, the intelligent campus system is not considered as a general part of the cloud. However, it is anticipated that the open platform services will be used independently of the campus cloud system within the scope of the programming lessons.

3.1.1. Infrastructure as a service (IaaS)

IaaS is a cloud service that allows a person or organization to rent infrastructure such as servers and data storage. Within the scope of the infrastructure service, students are provided with a virtual desktop via campus accounts, reporting how long they spend on the virtual desktop and how long they have been using applications. Student accounts have been integrated with the operating system through the Lightweight Directory Access Protocol (LDAP), and it has been determined how long the user remains connected for the specified software. This information is obtained by gathering process information by Power Shell in Windows environment and by Terminal in Linux and Unix environment. How efficiently the application is used can be determined by assignments, but it can be easily measured whether the application is used as much as necessary and how long the given work is performed by the student. For this reason, it is necessary for the instructor to define the minimum usage periods of the applications, to match the applications and assignments, to integrate the student's homework grades into the system and to integrate with application use information.

An advantage provided by the infrastructure service is the sharing of course content, announcements and important information. Information sharing is carried out via web services. Access to the cloud system from any platform is possible. Especially in emergencies, cloud infrastructure is needed to direct people. Two models were designed to guide campus members with cloud service.

- In the first model, the emergency warning will be sent for everyone, and will be redirected if the user accepts it. In this model, floor and partition information will be selected by the user.
- In the second model, the campus member known by face recognition, fingerprint recognition or Radio Frequency Identification (RFID) tag will be directed immediately and no message will be sent to everyone.

Hybrid use of these two models is predicted in terms of application efficiency. This is because the system has to work when there is no tracking system.

3.1.2. Software as a service (SaaS)

Software service differs from infrastructure service in which the software can be run on the students' computers and there is less load on the system. In such a structure there are 2 important issues for students to follow. The first is licensing the software with a server license. Because, the usage times of the software can be reported by a license manager like OpenLM in such a structure. The second important issue is identity verification. This is because the matching of the IP provided by the license manager and the student information is possible. The processes after these operations will continue similar to the infrastructure service.

3.1.3. Internet of things

Monitoring of the conditions in the environment is essential both in terms of teaching quality and management of emergencies. The reports needed in these two processes can be obtained in various and different ways. The data requirements of the model were determined as air quality, ambient temperature, ambient light intensity, noise, RFID tags, fingerprint data, infrared human detection, and image. Air quality, ambient temperature, light intensity, and noise data should be monitored to ensure sustainability in the teaching environment.

RFID tags, fingerprint data, and facial image processing on the image are important for identifying the environment in which campus members are located. Especially in the laboratory environment, it is essential to prevent unauthorized access and to detect casualties at the time of accident. It is also necessary for the detection of activity and direction over the image, the identification of people in the environment, the understanding of human presence with infrared sensors, and the realizing of the priority of intervention in emergencies.

Fire detection via picture and infrared sensors is required for emergency identification. The determination of the activities within the campus and in the building is important for emergency situations in order to evacuate the buildings as soon as possible and with minimum loss. There is

a need for a cloud system to be guided in emergencies.

3.1.4. Sharing sensor data

Data will be collected in different formats from different sensors for realization and reporting ambient conditions. The data will be uploaded to the servers via web services so that the collected data is not saved directly to the server. In particular, high-dimensional data such as images will not be loaded directly to the server, but only the points detected on the image will be stored on the servers. Therefore, all data to be collected for reporting on the server will be text or numbers. Images received are stored on a separate server via the Realtime Streaming Protocol (RTSP) and are mapped to the reporting server. In this way, it is possible to collect data not only from embedded systems, but also from IP cameras. Since the images obtained from the IP cameras will be automatically deleted some time later, the images of the detected exceptional cases are stored in a separate server disk space. In this respect, both disk space saving and evidence relating to the determinations made are stored.

3.1.5. Detection of motion

In-campus motion is analyzed on embedded systems or with images obtained from IP cameras with the RTSP protocol. As the analysis method, background subtraction and image subtraction are used. As a threshold value, the difference between the values of red, green and blue is expected to be at least 10. Two frames of succession taken from the imagery were investigated for difference from each other and background. The midpoints of the points on the binary images obtained are calculated and the closest midpoints are mapped. The amount of slip and direction between these points were determined as the amount and direction of motion. The difference data is normalized by a regression model so that the amount of motion can be understood correctly. Figure 3.1 shows the detection of motion by the system.

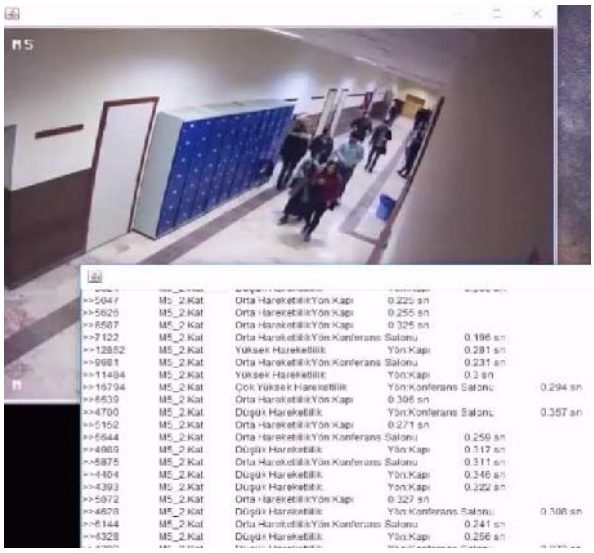

Figure 3.1 Detection of in-building motion

3.1.6. Fire detection

Fire detection and measurement of the fire size were carried out on color and realized by color filters. The neighboring points between the points obtained by filtering the red, green and blue (RGB) and brightness values in the image are determined and the neighboring points are grouped. The size of the fire is interpreted according to the number of points grouped. Detection of fire by image is shown in Figure 3.2.

Figure 3.2 Fire Detection

3.2. Flow of system

The developed system integrates the data collected with student scores related to the learning process through cloud computing. At this point, it is possible to determine how long the students are adapting and their learning speed. The quality of the teaching environment is monitored by sensor data. In emergencies, data collected from the sensors are analyzed and campus residents are guided by an intelligent system via cloud computing.

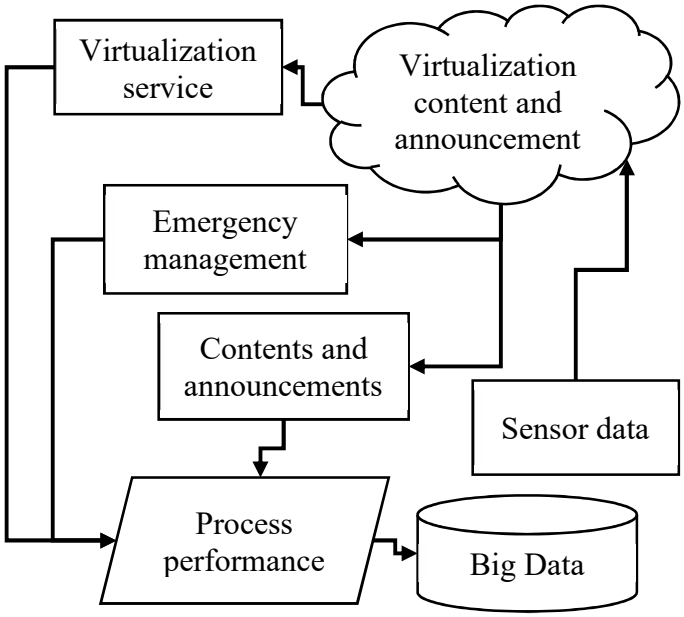

Figure 3.3 Detection of in-building motion

3.3. Mathematical model of the system

Three phases of the system have different objectives, and different performance measures regarding to the objective function. However, there is no need to develop a multi-objective mathematical model to achieve the maximization of the system performance. We develop a cost oriented model with the efficiency and effectiveness constraints, instead of developing a multi-objective model. The objective function of proposed model consists of the setup (SC_h) and maintenance (MC_h) costs of each hardware "h" given in Equation 1. Total cost is calculated by multiplying unit cost with number of each type hardware used "$N_{h,o}$".

$$Min\ (SC_h + MC_h) \sum_{o=1}^{o \in O} N_{h,o} \quad (1)$$

Each hardware will be operated for a specific number of people or a particular zone, which is the operating target of hardware. The index of operating target is noted as "o". Each target must be assigned for at least one hardware, given in Equation 2 and Equation 3.

$$\sum_{h=1}^{h \in H} N_{h,o} \geq 1 \quad (2)$$

$$\sum_{o=1}^{o \in O} N_{h,o} \geq 1 \quad (3)$$

Each system in a zone must satisfy the needs. To actualize it, an effectiveness matrix ($E_{h,o}$) is used for each target and hardware in Equation 4.

$$\sum_{h=1}^{h \in H} E_{h,o} N_{h,o} \geq 1 \quad (4)$$

Efficiency parameter depends on the type of hardware and the process. For instance, the ratio of system timeout to respond time is the efficiency of one emergency sensor. The multiplication of efficiency and the ratio of total area that the sensor covers is the effectiveness. If the effectiveness is smaller than one, we need to use more than one sensors.

4. RESULTS

In order to measure and increase the quality of teaching processes, a model consisting of three phases has been developed. The first part of the developed model follows the learning process through the cloud system. In this process, the students' time to use the software was measured and the learning speeds were revealed together with the scores they have taken from the related assignments. The quality of the teaching environment was measured by sensor data and the identification of possible work accidents for emergency response was determined. When an emergency condition occurs, the cloud system is used to direct the people around and to minimize the losses.

5. RESULTS

The proposed system aims to measure the educational environment to gather the data related to the education process. To manage it, the system is designed as collecting the studying data, environmental conditions, and emergency data.

We proposed a model to minimize the cost, while keeping the effectiveness of the system at a certain level, which we presume that the system will increase the quality of the education process. In the future study, we will try to find out the correlation between the quality of the education process and contribution of the system.

ACKNOWLEDGMENTS

This study is supported by Sakarya University Scientific Research Projects Coordination Unit. Project Number: 2016-01-02-001.

REFERENCES

[1] PACHECO, Edgar; LIPS, Miriam; YOONG, Pak. Transition 2.0: Digital technologies, higher education, and vision impairment. *The Internet and Higher Education*, 37: 1-10, 2018.

[2] V. Albino, U. Berardi and R. M. Dangelico, "Smart Cities: Definitions, Dimensions, Performance and Initiatives", *Journal of Urban Technology*, Vol.22 No:1, s.3-21, 2015.

[3] T. Kim, C. Ramos, S. Mohammed, "Smart City and IoT",*Future Generation Computer Systems,* 79 159–162, 2017.

[4] C. Stergiou, K. E. Psannis, B. Kim, B. Gupta, "Secure integration of IoT and Cloud Computing", *Future Generation Computer Systems,* 78 964–975, 2018.

[5] M. Dener, Y. Özkök, C. Bostancıoğlu, "Fire Detection Systems in Wireless Sensor Networks", *Procedia - Social and Behavioral Sciences,*195 1846 – 1850, 2015.

[6] S. S. Manvi and G. K. Shyam ,"Resource management for Infrastructure as a Service (IaaS) in cloud computing: A survey", *Journal of Network and Computer Applications,*41 424–440, 2014.

[7] R. Kresimir, B. G. Marijana, M. Vlado, "Development of the Intelligent System for the use of University Information System", *Procedia Engineering*, 69 402 – 409, 2014.

[8] J. Gonzalez-Martínez, M. L. Bote-Lorenzo, E. Gomez-Sanchez, R.Cano-Parra, "Cloud computing and education: A state-of-the-art survey", *Computers & Education,* 80 132e151, 2015.

[9] C. Liu and N.Ahuja, "Vision Based Fire Detection", *Pattern Recognition,* 1051-4651, 2014.

[10] B. U. Töreyin, Y. Dedeoğlu, U. Güdükbay, A. E. Çetin, "Computer Vision Based Method for Real-Time Fire and Flame Detection" *Pattern Recognition Letters,* 27, 49–58, 2006.

[11] A. E. Çetin, K. Dimitropoulos, B. Gouverneur, N. Grammalidis, O. Günay, Y. H. Habiboğlu, B. U. Töreyin, S. Verstockt, "Video fire detection – Review", *Digital Signal Processing*, 23, 1827–1843, 2013.

[12] Ç. Döner, G. Şimşek, K.S. Yıldırım, A. Kantarcı, "Kablosuz Algılayıcı Ağları ile Yangın Tespit Sistemi",*Gömülü Sistemler ve Uygulamaları Sempozyumu Gömsis*, İstanbul Teknik Üniversitesi, İstanbul, 2010.

[13] M. Ekinci and E. Gedikli, "Silhouette Based Human Motion Detection and Analysis for Real-Time Automated Video Surveillance", *Turkish Journal of Electrical Engineering and Computer Science*, 13 (2), 199-229. Retrieved from http://dergipark.gov.tr/tbtkelektrik/issue/12091/144525, 2005.

[14] B. Karasulu, "Videolardaki Hareketli Nesnelerin Tespit ve Takibi için Uyarlanabilir Arkaplan Çıkarımı Yaklaşımı Tabanlı Bir Sistem" *Uludağ Üniversitesi Mühendislik-Mimarlık Fakültesi Dergisi*, Cilt 18, Sayı 1, 2013.

[15] B. Laugraud, S. Piérard, M. V. Droogenbroeck, "LaBGen: A Method Based On Motion Detection For Generating The Background Of A Scene", *Pattern Recognition Letters,* 96 12–21, 2017.

[16] F. Yuan, G. Liao, W. Fan, and H. ZHOU, "Vision Based Fire Detection Using Mixture Gaussian Model", *Fire Safety Science,* DOI: 10.3801/IAFSS.FSS.8-1575, 2005.

[17] M. Karima, H. Altan, "Interactive building environments: A case study university building in UAE", *Procedia Engineering*, 180, 1355 – 1362, 2017.

[18] ZHONG, Ray Y., et al. Intelligent Manufacturing in the Context of Industry 4.0: A Review. *Engineering*, 3.5: 616-630, 2017.

JOURNAL OF SCIENCE
SAKARYA UNIVERSITY

Sakarya University Journal of Science

ISSN 1301-4048 | e-ISSN 2147-835X | Period Bimonthly | Founded: 1997 | Publisher Sakarya University | http://www.saujs.sakarya.edu.tr/

Title: Effect Of Imputation Methods İn The Classifier Performance

Authors: Pınar Cihan, Oya Kalıpsız, Erhan Gökçe
Recieved: 2019-01-22 09:13:39

Accepted: 2019-08-23 12:22:04

Article Type: Research Article
Volume: 23
Issue: 6
Month: December
Year: 2019
Pages: 1225-1236

How to cite
Pınar Cihan, Oya Kalıpsız, Erhan Gökçe; (2019), Effect Of Imputation Methods İn The Classifier Performance. Sakarya University Journal of Science, 23(6), 1225-1236, DOI: 10.16984/saufenbilder.515716
Access link
http://www.saujs.sakarya.edu.tr/issue/44246/515716

Sakarya University Journal of Science 23(6), 1225-1236, 2019

Effect of Imputation Methods in the Classifier Performance

Pınar Cihan*[1], Oya Kalıpsız[2], Erhan Gökçe[3]

Abstract

Missing values in a dataset present an important problem for almost any traditional and modern statistical method since most of these methods were developed under the assumption that the dataset was complete. However, in the real world, no complete datasets are available and the issue of missing data is frequently encountered in veterinary field studies as in other fields. While the imputation of missing data is important in veterinary field studies where data mining is newly starting to be implemented, another important issue is how it should be imputed. This is because in many studies observations with any variables having missing values are being removed or they are completed by traditional methods. In recent years, while alternative approaches are widely available to prevent the removal of observations with missing values, they are being used rarely. The aim of this study is to examine mean, median, nearest neighbors, MICE and missForest methods to impute the simulated missing data which is the randomly removed with varying frequencies (5 to 25% by 5%) from the original veterinary dataset. Then highly accurate methods selected to impute the original dataset for observation of influence in classifier performance and to determine the optimal imputation method for the original dataset.

Keywords: missing value, multiple imputation, classification, naive bayes, decision tree, machine learning, veterinary

1. INTRODUCTION

In machine learning, classification is one of the most important tasks [1]. Many machine learning algorithms require a complete dataset and missing values lead to big classification error rates [2].

Missing values are frequently encountered in veterinary field studies. In veterinary; missing value is frequently encountered because collecting the animals for weighing, measuring and other operations or taking and analyzing blood samples are so laborious and costly. During scientific studies, it is quite possible that the researchers might be unable to collect the data in a proper way in terms of completeness due to diseases, deaths, erroneous analysis, the inappropriateness of the measured sample, etc.

* Corresponding Author: pkaya@nku.edu.tr
[1] Namık Kemal University, Computer Engineering Department, Tekirdağ, Turkey. ORCID: 0000-0001-7958-7251
[2] Yıldız Teknik University, Computer Engineering Department, Istanbul, Turkey. ORCID: 0000-0001-9553-669X
[3] Kafkas University, Internal Medicine Department, Kars, Turkey. ORCID: 0000-0003-2674-1010

There are a few alternative methods to overcome missing values in datasets: extending the data with new observations, deleting the observations with the missing value from the dataset and conducting predictions about missing value and substituting the missing value with obtained approximate values [3].

In a number of studies in this field, a complete case analysis is conducted where any observations with missing values are omitted (known as listwise deletion). Even if there are alternative approaches that prevent the removal of observations with missing values, they were rarely used in veterinary field studies. Dohoo et al. [4] have tried to determine which set of results was reliable by imputing missing values in mastitis attitudes data through both deletion and imputation techniques. Ser et al. [5], have first created 10 to 20% missing data in a dataset consisting of 47 sheep and lambs. Then, missing values were imputed using the MI method and the performance of this method was assessed.

Some studies conducted in other fields are as follows; Hron et al. [6] used version of kNN to impute the missing values in compositional data. Liao et al. [7] used four versions of kNN to estimate the missing values in large phenomic data. Tutz and Ramzan [8] used a weighted kNN to impute the missing values in several datasets. Xia et al. [9] used Adjusted Weight Voting Random Forest (AWVRF) for handling missing values. Schmitt et al. [10] compare Mean, K-nearest neighbors (KNN), fuzzy K-means (FKM), singular value decomposition (SVD), bayesian principal component analysis (bPCA) and multiple imputations by chained equations (MICE) imputation methods to impute missing values in four real datasets

The objective of this study is to examine mean, median, kNN, MICE and missForest methods in completing missing data within the veterinary dataset, their influence in classifier accuracy and to determine the optimal imputation method for the dataset. First, five different imputation methods were compared according to criteria of Root Mean Square Error (RMSE), classification error (SCE) and execution time in completing the missing values which were created from 5 to 25% by 5% non-missing part of the original dataset and the most unsuccessful methods were eliminated. Secondly, missing values in the original dataset were imputed using these successful imputation methods and the influence of these methods to the classification performance was observed. Neonatal lambs were classified according to diagnosis using naïve bayes (NB) and decision tree (DT) methods. Accuracy, kappa, recall and precision criteria were taken into consideration during the comparison.

The rest of the study is organized as follows. The second section introduces the imputation methods, datasets, principle of the analysis and evaluation measures criteria. The third section is dedicated to frequency of missingness in dataset, the imputation methods performance, the classification performance and makes a comparison. The last section provides our conclusions.

2. MATERIAL AND METHOD

2.1. Imputation Methods

We compared five commonly used imputation methods that are namely, mean, median, kNN, MICE and MissForest imputation methods. All methods implemented in R programming. Briefly, mean imputation: Mean consists of replacing the missing value for a given variable by the mean of all known values of that variable [11]. Median imputation: Replacing the missing value for a given variable by the median of all known values of that variable [11]. kNN [12]: Algorithm use distances measure such as Euclidean distance for computes the distance between the data point. The missing values are imputed by the average of the non-missing k-nearest neighbors. MICE [13] is an iterative algorithm: First, missing values are estimated using only complete data. Next, missing values are imputed using the complete data and the imputed values from the last iteration. Now, as multiple imputations create multiple predictions for each missing value; they take into account the uncertainty in the imputation and give the best standard errors. If there is not much information on the given data used to prepare the model, the imputations will be highly

variable, leading to high standard errors in the analysis.

MissForest [14]: This method can be used to both impute continuous and categorical values. Given the dataset used to train the random forest model and later this model used to predict the missing values. It yields an out-of-bag imputation error estimate without the need of a test set.

2.2. Dataset

In this study used dataset was collected from 347 lambs in the two sheep flocks in Kars/Turkey. A unique ear tag number was used for registered each lamb. Blood samples, gender, birth weight, parity, health status, etc. information (given in Table 1) are recorded with this ear tag. Clinical examinations were performed as previously defined by our authors [15]. The health status of lambs was regularly monitored by daily visits to farms at the neonatal period and lambs were classified as unhealthy if have any symptoms such as mastitis, pneumonia, enteritis, etc.

2.2.1. Variable Selection from Dataset

Because of placental structure in lambs, the passage of many crucial substances primarily the antibodies from the dam to the lamb does not occur. All substances required for the prevention of diseases in lambs and their normal development are available within the first milk/colostrum produced by the dams after birth. Therefore, taking sufficient colostrum is very important and its inadequacy may be determined by various blood parameters such as IgG measured within 24 hours after the birth. Particularly, the diseases developing at the neonatal period are directly associated with insufficient intake of substances in colostrum. However, it is clear that this effect fades at the post-neonatal period and factors such as the physical and environmental conditions of the plant, vaccination becomes more effective [16]. Therefore, the disease classification shall be performed on neonatal lambs. In order to perform these analyses in an accurate way, features not associated with the disease status or those with direct relation were removed from the dataset. Eventually, 347 samples, 14 features and 1 class label were used in the study. The information and abbreviations of these features are given in Table 1.

Table 1. Dataset features and abbreviations

Features	Abbreviation	Type
Immunoglobulin G	IgG	Numeric { 19 – 5302 }
Gamma Glutamil Trasnfereraz	GGT	Numeric { 38 – 7517 }
Laktoferrin	LT	Numeric { 354 – 2194 }
Total Protein	TP	Numeric { 21 – 117 }
Albumin	ALB	Numeric { 32 – 51 }
Birthweight	BW	Numeric { 2260 – 5900 }
Body weight 28 day after birth	WG28	Numeric { 4364-14016 }
Average Daily Weight Gain	MDG28	Numeric { 17 – 340 }
Healthy status of dams	AH	Nominal { healthy / ill }
Dam's age	AGE	Numeric { 1 - 6 }
Dam's parity	PARITY	Numeric { 1 - 5 }
Type of birth	TWIN	Nominal { twin / single}
Gender	GENDER	Nominal { male / female}
Farm	FARM	Nominal { farm1 / farm2}
Neonatal healthy status of lamb	NGH	Nominal { healthy / ill }

2.3. Principle of the Analysis

Figure 1 shows the general principles of the analysis. The study consists of two-stage. At the first stage; a complete dataset consisting of 259 samples was obtained by removing 88 samples containing missing values from an original dataset consisting of 347 samples. We have implemented a varying percentage of missing values (from 5% to 25% by 5%) generated under an MCAR [17] assumption on the obtained complete dataset. These simulated missing values were imputed using the 5 methods. After measuring 3 evaluation criteria (RMSE, SCE, execution time), they were used to evaluate the differences between original values and replaced ones, the influence of imputed values through the RMSE, SCE criteria, and execution times in seconds, respectively. Two imputation methods with the least successful statistics were removed. In the second stage; missing values within the original dataset were imputed through these more successful three imputation methods. Then, NB and DT algorithms used to diagnosis classification were performed. The classifier performances of accuracy, kappa, recall and precision were compared and the influence of imputation methods on classifiers was observed.

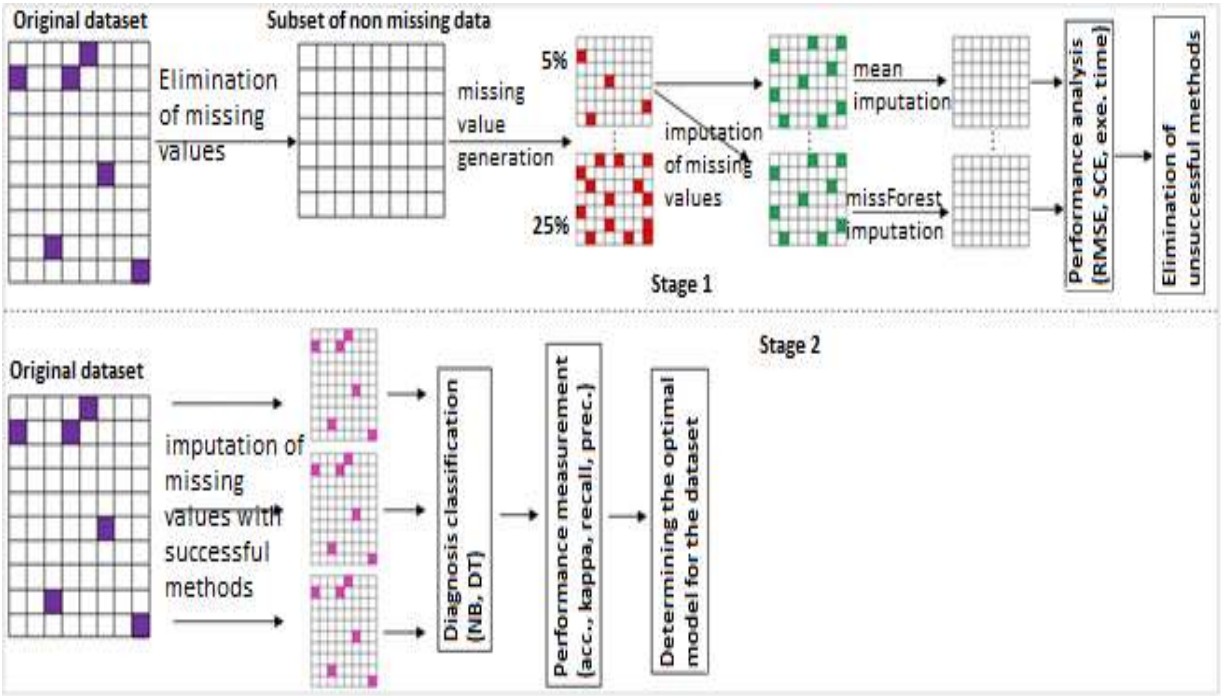

Figure 1. Principle of the method

2.4. Evaluation Metrics

At the first stage of this study, RMSE, SCE and execution time criteria were used, in order to compare the performances of imputation techniques in imputing the missing values within datasets which contain various percentages of missing values.

Root mean square error (RMSE): It measures the difference between the actual value and the estimated value. The smallest RMSE value is always desirable. Basically, the RMSE is defined as:

$$RMSE = \sqrt{\frac{1}{M}\sum_{m=1}^{M}\left(t_{orig}^{m} - t_{reco}^{m}\right)^2} \quad (1)$$

Where t_{orig} and t_{reco} are the m^{th} vectors whose elements are the original values and the reconstructed values, respectively. M denotes the amount of missing value was used.

Supervised classification error (SCE) rate: After imputing the missing data through supervised

classification, this criterion measures the difference between the current subgroups and those which were generated after missing data imputation and assesses if the discriminative or predictive capability is maintained. The approach used for supervised classification is NB algorithm. Classification error defined as:

$$SCE = \frac{\sum False\ positive \quad \sum False\ negative}{\sum Total\ population} \tag{2}$$

Execution time: This criterion indicates the time duration as missing values in datasets are completed by imputation methods. The difference in system time between the start and end of the method gives us this criterion. Particularly in big sized datasets (for example containing videos, images, etc.) the execution time is an important factor and completion in a short time is a desired aspect.

At the second stage of the study, diagnosis classification was performed using NB and DT algorithms, in order to observe the effectiveness of imputation methods and determine the optimal imputation method for the original dataset. Classification accuracy, kappa, recall and precision criteria were used in order to analyze the performances of classifiers. A confusion matrix [18] is used to indicate classification results together on a table where the above measurements may be calculated. A sample confusion matrix is shown in Table 2.

Table 2. A sample confusion matrix for two classes

		Actual	
		Positives (ill)	**Negatives (Healthy)**
Predicted	**Positives (ill)**	*TP (True Positive)*	*FP (False Positive)*
	Negatives (Healthy)	*FN (False Negative)*	*TN (True Negative)*

Classification accuracy: This is the simplest performance measure. It is the proportion of accurately classified samples obtained through any paired classification to the number of all samples. This study indicates how many ill and healthy neonatal lambs may be accurately estimated.

$$\text{Accuracy (Acc)} = \frac{\sum \text{True positive} + \sum \text{True negative}}{\sum \text{Total population}} = \frac{TP+TN}{TP+TN+FP+FN} \tag{3}$$

Recall: Shows the percentage of actually ill lambs which may be estimated by the new method. Namely, this criterion gives the rate of accurate predictability for ill lambs.

$$\text{Recall} = \frac{\sum True\ positive}{\sum Condition\ positive} = \frac{TP}{TP+FN} \tag{4}$$

Precision: Proportion of real ill lambs that are positive (ill) according to the test result.

$$\text{Precision} = \frac{\sum True\ positive}{\sum Test\ outcome\ positive} = \frac{TP}{TP+FP} \tag{5}$$

Kappa statistic: It compares the measurement system with random estimation. High rate of agreement indicates the possibility of more accurate ratings. Poor rates of agreement denote that the ratings may be used in a limited way [19].

$$\text{Kappa} = \frac{(P_{observed} - P_{chance})}{(1 - P_{chanc})} \tag{6}$$

Where $P_{observed}$ is proportion of units classified in which the raters agreed and P_{chance} is proportion of units for which one would expect agreement by chance.

3. RESULTS

3.1. Analysis of Missing Values in Dataset

The dataset used in the study comprises 347 samples, 14 features and 1 label. Some features within the dataset contain missing values. Figure 2(A) shows the percentages of missing values in these features, and Figure 2(B) shows the total missing values of these features.

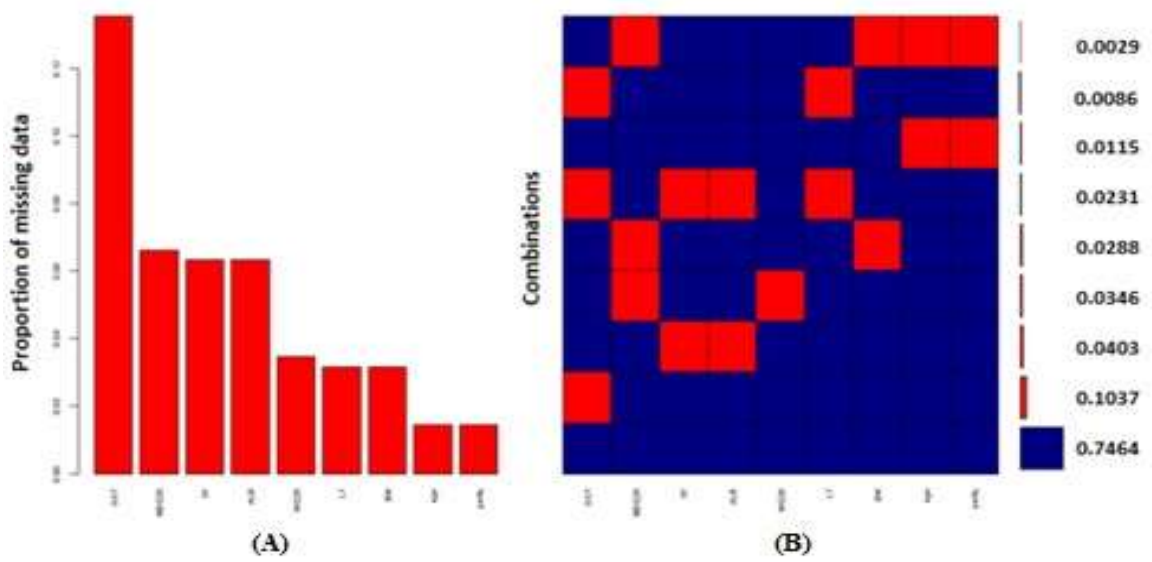

Figure 2. Histogram of missing values and missing rate [20]

When the missing value percentages of features within the dataset are examined (Figure 2(A)) the GGT looks as the one with most missing values, followed by the MDG28, TP, ALB, WG28, LT, BW, age and parity feature. It is obvious that the IgG, AH, twin, gender and farm features do not contain any missing value. When we examined features with missing values, it was clear that 4 out of 5 blood sample features (IgG, GGT, TP LT and ALB) contained missing values and GGT had more than twice missing values in comparison to other blood samples.

On the other hand, dividing each variable into certain ranges Figure 2(B) shows the percentage of missing values for all features in that range. This figure indicates that approx. 75% of samples in this dataset do not contain missing values, 10% miss only the GGT feature, 3% miss four blood samples (GGT, TP, LT, and ALB) together, 3% miss only the age feature. Eventually, missing percentage of the GGT is 2 to 10 times higher than that of other features.

The major part of missing features derives from the GGT. So, it is important to estimate this feature with minimal error, as otherwise it shall be a big source of problem for future analyses. Because IgG levels of <1000 mg/dL taken from ruminants such as lambs or calves with colostrum at the 24th hour after the birth is an important risk factor for the development of diseases in the neonatal period. This is defined as inadequate passive colostral immunity. Utilization of IgG level as a means of detecting passive colostral immunity is limited in farm examination programs, as its measurement is time-consuming and complicated, as it requires comprehensive laboratory conditions and advanced equipment, as it is laborious to send samples routinely to veterinary diagnostic laboratories, and because multiple sample analyses are exhaustive and non-economic. Therefore, detection of passive immunity through indirect test methods such as GGT enzyme activity and total protein (TP) level which are economic, fast and more practicable on field for individual flocks and using direct tests only as validation methods is considered as a better approach. Besides, GGT and TP have a big importance in terms of their adaptability on the field. For these concerns, the estimation of missing values for the GGT feature with a low error rate to determine the association between GGT enzyme activity and IgG levels with high performance is an important issue.

3.2. Evaluation of Imputation Techniques

After generation of missing value from the complete part of the original dataset in percentages of 5%, 10%, 15%, 20% and 25%, the missing values were imputed using mean, median, kNN, MICE and missForest imputation methods. RMSE was calculated for imputed

datasets. The whole process was replicated 10 times and the results are summarized using the box-and-whiskers plots (median/IQR/min-max, including outliers) in Figure 3.

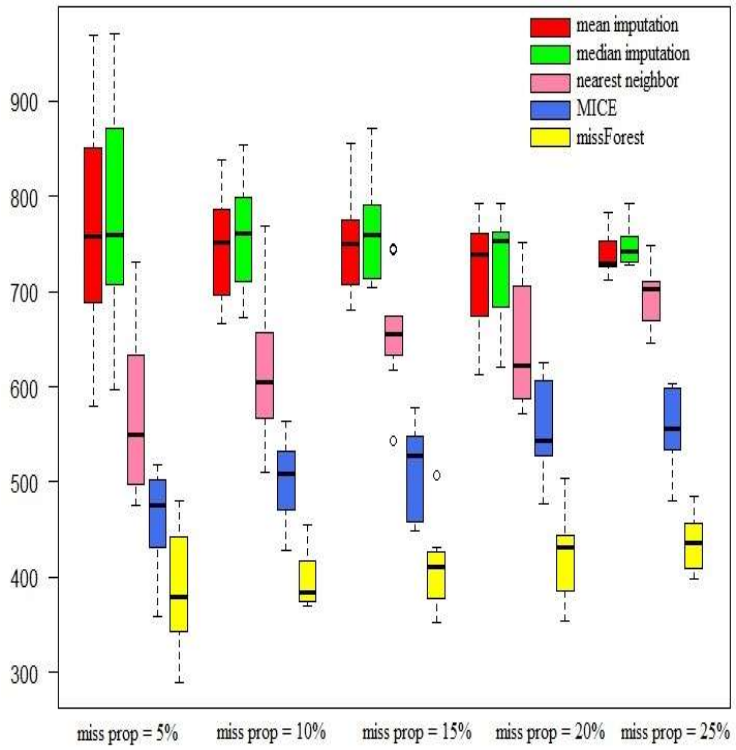

Figure 3. RMSE of imputation methods

RMSE value expresses the error level, so, lower levels indicate the success of the method. Figure 3 shows that the RMSE value of imputed datasets using mean and median method were higher than imputed datasets using kNN, MICE and missForest methods.

According to average RMSE results the most successful method has been missForest (avg. RMSE = 412), followed by respectively MICE (avg. RMSE = 519), kNN (avg. RMSE = 640), mean (avg. RMSE = 747) and median (avg. RMSE = 757) methods. Moreover, the average RMSE value of the missForest method is approx. half of the same for mean, median and kNN methods, so we may infer that it has imputed missing data with approx. 50% lower error rate in comparison to those three methods.

As the missing rate in datasets increase, it is obvious that the average RMSE values of the methods rise near to linear. Therefore, we may conclude those mean and median methods are the most unsuccessful methods in imputing missing values in our dataset for both their high averaged RMSE values and their high deviation from the average.

After imputing the missing values in datasets by 5 different methods, diagnosis classification was performed using NB method. The classification errors and standard deviation values are given in Table 3.

Table 3. Classification error of the five imputation methods.

Method	5%	10%	15%	20%	25%	Average
mean	0.150±0.030	0.113±0.036	0.146±0.046	0.152±0.040	0.146±0.034	0.141±0.037
median	0.141±0.032	0.140±0.033	0.157±0.029	0.133±0.028	0.150±0.043	0.144±0.033
kNN	0.141±0.031	0.154±0.028	0.132±0.031	0.149±0.015	0.125±0.040	0.140±0.029
MICE	0.119±0.024	0.151±0.038	0.155±0.025	0.139±0.031	0.151±0.041	0.143±0.032
missForest	0.137±0.035	0.122±0.029	0.135±0.033	0.139±0.034	0.104±0.024	**0.127±0.031**

While the classification error was 0.121 when the dataset without missing data was classified by the NB classification method, average classification errors of datasets imputed with mean, median, kNN, MICE and missForest imputation methods were 0.141 ± 0.037, 0.144 ± 0.033, 0.140 ± 0.029, 0.143 ± 0.032, and 0.127 ± 0.031 respectively. We have obtained the result that classification errors of imputed datasets using different imputation methods and classification error of the real dataset were quite close. Nevertheless, it is obvious that datasets imputed by the median, MICE and mean imputation methods were those which were classified with the highest error rate and which were the farthest to the real dataset. The dataset imputed by the missForest imputation method was concluded to be the most successful method with the lowest classification error.

When classification errors of imputation methods on average was considered the most successful method has been missForest (error = 0.127 ± 0.031), followed by kNN (error = 0.140 ± 0.029), MICE (error = 0.143 ± 0.032), mean (error = 0.141 ± 0.037) and median (error = 0.144 ± 0.033) methods.

The execution time of imputation method is also a significant factor in completing the missing values within big datasets. While estimation of nearest possible values to real ones by the method, it is also desirable to complete these operations in a short time. Therefore, execution times of methods were calculated and the results were given in Figure 4.

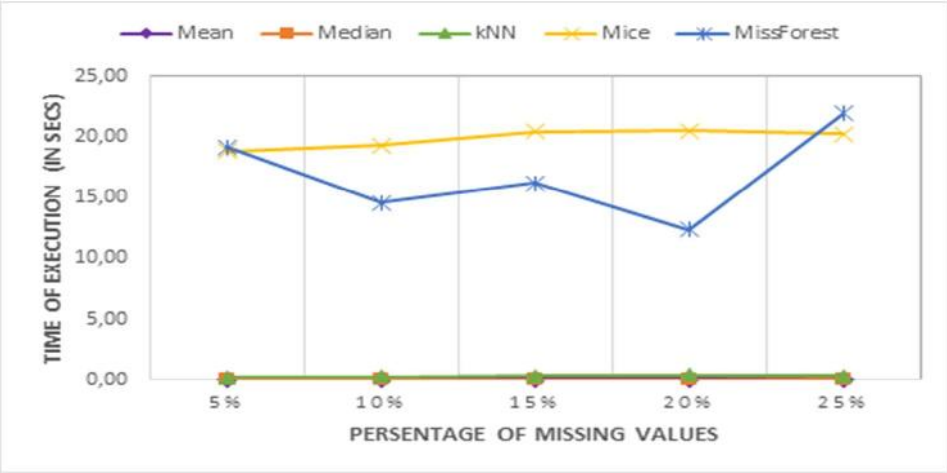

Figure 4. Execution time (secs) of imputation methods

When datasets containing 5-25% missing values were imputed through mean, median, kNN, MICE and missForest imputation methods, the average execution times of these methods were 0.05, 0.03,

0.3, 19.8, and 16.8 seconds respectively. The operation time is quite short for the mean and median methods, because it only places the feature's mean/median value. However, the error rates for datasets imputed with these methods were high (Figure 3 and Table 3).

Because a random forest is created at estimation of missing data through missForest method, and because the MICE method uses regression to estimate missing values, their execution times were longer than other methods. While execution time is important in big datasets, we have focused on success by ignoring execution time, because the dataset used in this study was not an extremely big one and the accurate estimation of the diagnosis was more important.

3.3. Effect in the Classifier Accuracy

Considering the performance of imputation methods and the criteria RMSE, SCE and execution time in imputing datasets, the missing values in an original dataset consisting of 347 samples were imputed through MICE, kNN and missForest imputation methods. Missing values in the original dataset were imputed by the above three methods and the optimal imputation method was determined for the dataset by examining the effect on their classification performances. Neonatal lambs were classified according to diagnosis using NB and DT methods which are frequently used within the literature. While classifying, 70% of the dataset was allocated to trainset, and 30% to test set purposes. During training at model creation, 10-fold cross-validation was performed and the obtained model was tested through a 30% test set. The whole process was replicated 10 times and the accuracy, kappa, recall, precision results are summarized using the box-and-whiskers plots (median/IQR/min-max, including outliers) in Figure 5.

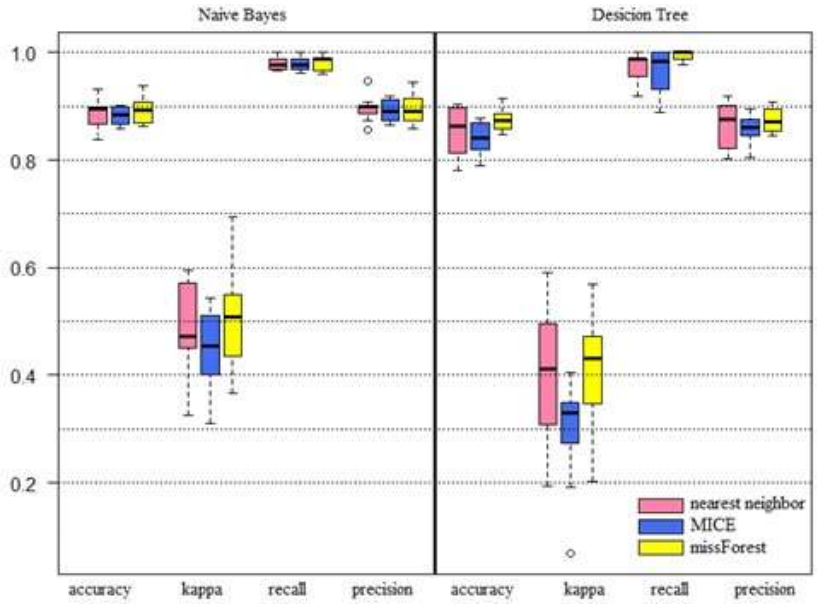

Figure 5. NB and DT classification algorithms results

As shown in Figure 5, the classification performances of datasets imputed by kNN, MICE and missForest methods are quite close to each other. The accuracy criterion indicates how accurately the number of healthy/ill neonatal lambs were estimated. According to this criterion, the classification performance of the dataset imputed by missForest was observed to be more successful than both NB and DT and other imputation methods. Even though the accuracy criterion is a straightforward and important criterion at classification, it should not be assessed alone. Because estimation of ill lambs is crucial in decision support systems along with accurate classification, in general. Therefore, when we examined recall criterion, it was clear that ill lambs were identified with higher success for the dataset imputed by missForest method in both NB and DT methods. Kappa criterion indicates

whether the classification has a chance of success. We can say, the higher this value, the less random was the classification. In our study, it is obvious that missForest method had the highest kappa value for both NB and DT classification methods. On the other way, the precision criterion indicates how good healthy lambs were identified. For both NB and DT methods, it is obvious that the dataset imputed by the kNN method had a higher precision value.

4. CONCLUSION

The used dataset [20] in this study involved 301 ewes and 347 lambs born on two Akkaraman crossbreed sheep farms located in Kars, Turkey. As about approximately 87% of the sheep population in Turkey consist of the fat-tailed breeds mainly Akkaraman, also in veterinary field data mining application is very few and the data mining applications in this area are increasing rapidly. So this dataset has big importance both veterinary and computer science filed. The decrease in the number of ovine animals and livestock products impoverishes the people living in rural parts of our country. Raising the profitability or efficiency is a precondition for the prevention of impoverishment in this sector. This necessitates raising the demand for sheep breeding. Raising the demand for sheep breeding necessitates the reduction of disease and mortality rates. Therefore, estimations and analyses about the diagnosis of the animal is an important issue.

As the missing value within the dataset deprives the opportunity for analyses, they should be imputed. Many methods are being used for the imputation of missing values. The generation of values which are close to real values by the available methods for imputation shall influence the success of analyses positively. So, we have performed an evaluation of five imputation methods for imputing missing values in veterinary data and implemented the classifier accuracy.

At the first stage of the study, missing values were created in datasets in percentages of missing values from 5 to 25% by 5%, after imputing those datasets by mean, median, kNN, MICE and missForest imputation methods, the missing data imputation performances were compared taking the RMSE, SCE and execution time criteria into consideration. According to average RMSE results, the most successful method has been missForest method. When classification errors of imputation methods on average were considered the most successful method has been missForest method. On the other hand, when execution times of imputation methods were examined, the median imputation method is faster than others. The execution time was ignored because our dataset was not too big and also because an accurate estimation of ill lambs was more important. Eventually, at the first stage of the study, mean and median imputation methods were found to be the worst methods to imputing datasets containing 5-25% missing data. Mean and median methods reduce the standard error which invalidates most hypothesis tests. Also, it introduces a wrong representation of the relationship of the variable with other variables in the dataset.

At the second stage, NB and DT algorithm used to diagnosis classification, in order to observe the effect of kNN, MICE and missForest imputation methods on the success of disease classification and to determine the optimal method for the original dataset. To evaluate the classification success the frequently used accuracy, kappa, recall and precision criteria in literature were used. Through NB classification the most successful imputation method was found to be the missForest method. Through the DT classification model the most successful imputation method was again found to be the missForest method. Thus, according to our findings, the missForest imputation method is optimal for our veterinary dataset.

In the veterinary field; collecting the animals for weighing, measuring and other operations or taking and analyzing blood samples is a laborious and costly process. So, generally, a limited number of animal data were used in conducted studies. This study has special importance because it contains multiple features and numerous samplings in comparison to the veterinary field. While researchers might impute

missing data by these tried and true imputation methods, they might also try out different imputation methods that would be compatible with the dataset considering that the performance of methods might differ in different datasets.

Acknowledgments

The dataset used in this study were collected from TUBITAK (Project Code; TOVAG 108 O 847).

5. REFERENCES

[1] J. Han, J. Pei, and M. Kamber, Data mining: concepts and techniques: Elsevier, 2011.

[2] P. J. García-Laencina, J.-L. Sancho-Gómez, and A. R. Figueiras-Vidal, "Pattern classification with missing data: a review," Neural Computing and Applications, vol. 19, pp. 263-282, 2010.

[3] J. L. Schafer, Analysis of incomplete multivariate data: Chapman and Hall/CRC, 1997.

[4] I. R. Dohoo, C. R. Nielsen, and U. Emanuelson, "Multiple imputation in veterinary epidemiological studies: a case study and simulation," Preventive veterinary medicine, vol. 129, pp. 35-47, 2016.

[5] G. Ser and S. Keskin, "Examining of Multiple Imputation Method in Two Missing Observation Mechanisms," JAPS, Journal of Animal and Plant Sciences, vol. 26, pp. 594-598, 2016.

[6] K. Hron, M. Templ, and P. Filzmoser, "Imputation of missing values for compositional data using classical and robust methods," Computational Statistics & Data Analysis, vol. 54, pp. 3095-3107, 2010.

[7] S. G. Liao, Y. Lin, D. D. Kang, D. Chandra, J. Bon, N. Kaminski, et al., "Missing value imputation in high-dimensional phenomic data: imputable or not, and how?," BMC bioinformatics, vol. 15, p. 346, 2014.

[8] G. Tutz and S. Ramzan, "Improved methods for the imputation of missing data by nearest neighbor methods," Computational Statistics & Data Analysis, vol. 90, pp. 84-99, 2015.

[9] J. Xia, S. Zhang, G. Cai, L. Li, Q. Pan, J. Yan, et al., "Adjusted weight voting algorithm for random forests in handling missing values," Pattern Recognition, vol. 69, pp. 52-60, 2017.

[10] P. Schmitt, J. Mandel, and M. Guedj, "A comparison of six methods for missing data imputation," Journal of Biometrics & Biostatistics, vol. 6, p. 1, 2015.

[11] P. Cihan, E. Gökçe, and O. Kalıpsız, "A review of machine learning applications in veterinary field," Kafkas Univ Vet Fak Derg, vol. 23, pp. 673-680, 2017.

[12] O. Troyanskaya, M. Cantor, G. Sherlock, P. Brown, T. Hastie, R. Tibshirani, et al., "Missing value estimation methods for DNA microarrays," Bioinformatics, vol. 17, pp. 520-525, 2001.

[13] S. Van Buuren, H. C. Boshuizen, and D. L. Knook, "Multiple imputation of missing blood pressure covariates in survival analysis," Statistics in medicine, vol. 18, pp. 681-694, 1999.

[14] D. J. Stekhoven and P. Bühlmann, "MissForest—non-parametric missing value imputation for mixed-type data," Bioinformatics, vol. 28, pp. 112-118, 2011.

[15] E. HM, "An epidemiological study on neonatal lamb health," Kafkas Üniversitesi Veteriner Fakültesi Dergisi, vol. 15, 2009.

[16] K. AH and E. HM, "Risk Factors Associated with Passive Immunity, Health, Birth Weight And Growth

Performance in Lambs: III. The Relationship among Passive Immunity, Birth Weight Gender, Birth Type, Parity, Dam," Kafkas Üniversitesi Veteriner Fakültesi Dergisi, vol. 19, 2013.

[17] R. J. Little and D. B. Rubin, Statistical analysis with missing data vol. 333: John Wiley & Sons, 2014.

[18] E. Alpaydin, Introduction to machine learning: MIT press, 2009.

[19] A. J. Viera and J. M. Garrett, "Understanding interobserver agreement: the kappa statistic," Fam Med, vol. 37, pp. 360-363, 2005.

[20] P. Cihan, "Determination of diagnosis, prognosis and risk factors in animal diseases using by data mining methods," Ph.D. dissertation, Comp. Eng., Yildiz Technical Univ., Istanbul, 2018.

JOURNAL OF SCIENCE
SAKARYA UNIVERSITY

Sakarya University Journal of Science

ISSN 1301-4048 | e-ISSN 2147-835X | Period Bimonthly | Founded: 1997 | Publisher Sakarya University | http://www.saujs.sakarya.edu.tr/

Title: The Effect Of Geomagnetic Storms On Fof2 Values At Low Latitude

Authors: Erdinç Timoçin
Recieved: 2019-04-30 14:56:42

Accepted: 2019-08-27 12:53:35

Article Type: Research Article
Volume: 23
Issue: 6
Month: December
Year: 2019
Pages: 1237-1241

How to cite
Erdinç Timoçin; (2019), The Effect Of Geomagnetic Storms On Fof2 Values At Low Latitude. Sakarya University Journal of Science, 23(6), 1237-1241, DOI: 10.16984/saufenbilder.559334
Access link
http://www.saujs.sakarya.edu.tr/issue/44246/559334

Sakarya University Journal of Science 23(6), 1237-1241, 2019

The Effect of Geomagnetic Storms on foF2 Values over Low Latitude Ionosonde Station

Erdinç TİMOÇİN*[1]

Abstract

In this reseach, the changes in the low latitude critical frequencies (foF2) was investigated during the geomagnetically active hours (geomagnetic storms). The critical frequency (foF2) data obtained for 1991 over Manila that is low latitude ionosonde station and the planetary geomagnetic indices (K_p) were used. The superposed epoch analysis was used as a statistical method to investigate the change in the critical frequencies during geomagnetically active hours. The analyzes were conducted separately for the night hours, day hours and all hours of 1991 and they were compared with each other. The results from this research show that the highest change (increase or decrease) in foF2 values during geomagnetically active hours occurs at the event time (zero time) and the local time (day or night) has a significant impact on this change of the foF2 values. The foF2 values increase at local day hours, while the foF2 values decrease at local night hours.

Keywords: Geomagnetic storms, low latitude ionospheric critical frequency, superposed epoch analysis method

1. INTRODUCTION

The ionosphere is the ionized layer of the Earth's atmosphere. Because the ionosphere reflects the radio waves, it is very important for the communication. The electron density in this layer is changed by both the solar activity and geomagnetic storms. Their effects on electron density in the ionosphere layer vary depending on local time, latitude and altitude. Therefore, the solar and geomagnetic activity have different results on the different latitudes, local times, and altitudes [1-6].

The changes in the electron density of the ionosphere during the geomagnetically active hours were defined as ionospheric storms. The positive ionospheric storms increase the electron density, while the negative ionospheric storms decrease electron density [7-9]. Three main mechanisms cause to change in the electron density of the ionosphere region during geomagnetically active hours. The change in the composition of ionosphere is the first mechanism. The atomic oxygen (O) is main source for ionization, while the molecular nitrogen (N_2) is main source for recombination.

*Corresponding Author: erdinctimocin@mersin.edu.tr
[1]Mersin University, Vocational School of Technical Sciences, Mersin, TURKEY. ORCID: 0000-0002-3648-2035

Therefore, the electron density in the ionosphere changes depending on the $n(O)/n(N_2)$ ratio. The increase (decrease) of this ratio cause the positive (negative) storm in the ionosphere [4,10]. The disturbance dynamo electric field (DDEF) is the second mechanism that causes change of electron density in the ionosphere. The DDEF was induced by the thermospheric winds. During the geomagnetically active hours, this electric field is westward during day hours, while it is eastward during night hours. The westward electric field leads to decrease of electron density in the ionosphere during local day hours. The eastward electric field leads to increase of electron density in the ionosphere during local night hours [11]. The prompt penetrating electric fields (PPEFs) are the third mechanism that leads to change of electron density in the ionosphere. During the geomagnetically active hours, this electric field is eastward during the day hours, while it is westward during the night hours. The PPEFs change the electrodynamic structure of the ionosphere. The PPEFs cause to increase of electron density in the ionosphere during local day hours, while they cause decrease of electron density in the ionosphere during local night hours [12-14].

In this research, the effect of the geomagnetic activity on low latitude foF2 values was investigated using by the superposed epoch analysis (SEA) method. I believe that the results from this research will provide to a better understanding of the changes in the low latitude foF2 values observed during the geomagnetically active hours and how local time has an impact on these changes.

2. MATERIAL AND METHOD

To examine the effect of geomagnetic activity on the low latitude foF2 values, the hourly critical frequency data measured during 1991 at Manila (14.7 ^{o}N, 121.1 ^{o}E) were used. The reason for using the 1991 data in the analysis is that solar activity is at its maximum during this year and the geomagnetic activity is higher during this year. Thus, the effect of more geomagnetic storms on foF2 was examined. The global geomagnetic activity index (K_p) were used as geomagnetic activity indicator during 1991. These data were taken from the World Data Center (WDC) [15]. The K_p values were divided into several levels that show the geomagnetic activity levels. These geomagnetic activity levels were given in Table 1.

Table 1. Geomagnetic activity levels

Geomagnetic activity level	**The ranges of K_P**
Quiet	$0^{o}<K_p\leq 2^{+}$
Unsettled	$2^{+}-<K_p\leq 3^{+}$
Active	$3^{+}<K_p\leq 4^{+}$
Minor storm	$4^{+}<K_p\leq 5^{+}$
Moderate storm	$5^{+}<K_p\leq 6^{+}$
Strong storm	$6^{+}<K_p\leq 7^{+}$
Severe storm	$7^{+}<K_p$

In this research, to investigate the effect of the geomagnetic activity on low latitude foF2 values was used superposed epoch analysis (SEA) method. The SEA is a statistical application that is applied to time series. The SEA examines the effect of the geomagnetic activity on the foF2 values and measures the magnitude of response of the foF2 values against geomagnetic activity change. If the events occuring along time series identify properly, the results from the SEA indicate the effects of events on the system. The most important point in the analysis is to decide the concept called the event and to determine this concept as well [5,16,17]. Since the effect of geomagnetic storms on low latitude foF2 values in this study are investigated, the hours with $K_p> 4^{+}$ were chosen as geomagnetic events in the analysis. The 2338 events were detected during all hours of 1991. The 1072 events occurred during the local day hours, while the remaining the 1316 events occurred during the local night hours. After the geomagnetic events was detected, the hourly K_p and the hourly foF2 time series for 1991 were arranged simultaneously. After the two time series, ie, foF2 and K_p, are simultaneously set, a computer program determines the values of K_p greater than 4^{+} in the K_p time series that star at 00:00 on January 01, 1991. When the program finds that K_p value is greater than 4^{+}, it then aligns all foF2 values 50 hours before and 50 hours after

this event in one row. This process continues until the whole period of study is completed by computer. Thus, average foF2 values are obtained for which all events were superposed.

The same method of analysis was then repeated for the data set containing foF2 data at the hours where K_p was equal to 4^+ and smaller than 4^+. This process continues until the whole period of study is completed by computer. Next, the values calculated for the $K_p \leq 4^+$ hours were subtracted from the values calculated for all hours. The results obtained are δfoF2 values. The δfoF2 is defined in following.

$$\delta foF2 = foF2_{(K_p > 4^+)} = foF2_{(All)} - foF2_{(K_p \leq 4^+)} \quad (1)$$

The δfoF2 values indicate the changes in the foF2 values due to the geomagnetic activity change [5,16,17]. To analyze the effect of geomagnetic activity on the low latitude foF2 values depending on local time, this analysis was performed separately for the night hours, daytime and all hours of 1991 and the results were compared.

3. RESULTS

Figure 1 shows the change of δfoF2 values depending on time for all hours of 1991.

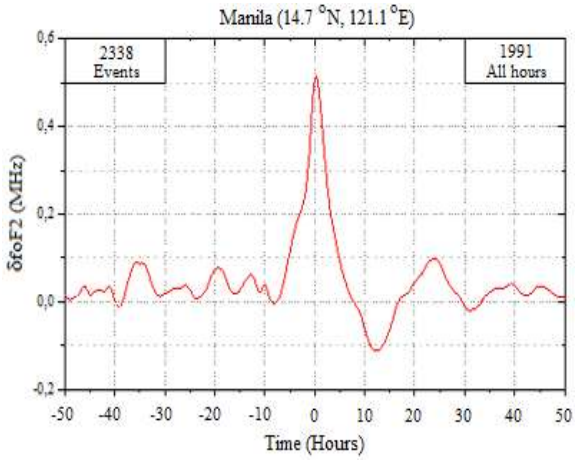

Figure 1. The change of δfoF2 values depending on time for Manila during all hours of 1991

The effect of change in the geomagnetic activity on foF2 values starts about 5 hours before the event moment (time 0) and the their effect on foF2 values reach to maximum at the event moment. The geomagnetic storms cause to increase about 0,5 MHz in the foF2 values. The change in the foF2 values almost disappears after about 30 hours. Figure 2 shows the change of δfoF2 values depending on time for 06-18 local times (LT) of 1991.

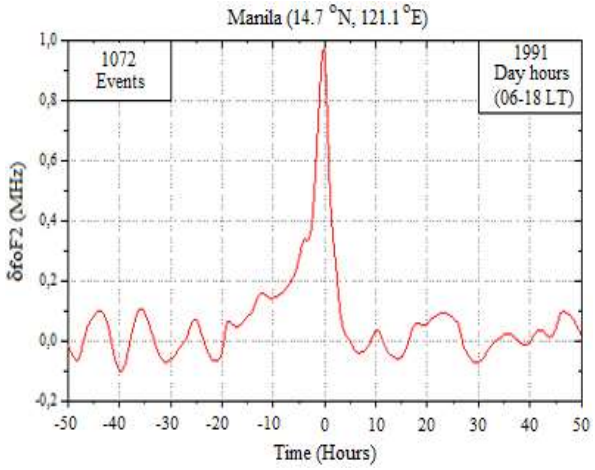

Figure 2. The change of δfoF2 values depending on time for Manila during day hours of 1991

The effect of change in the geomagnetic activity on foF2 values starts about about 10 hours before the event moment (time 0) and the their effect on foF2 values reach to maximum at the event moment. The geomagnetic storms cause to increase about 1 MHz in the foF2 values. That is, geomagnetic storms cause to ionospheric storms in the low latitude foF2 values for day hours. The change in the foF2 values almost disappears after about 5 hours.

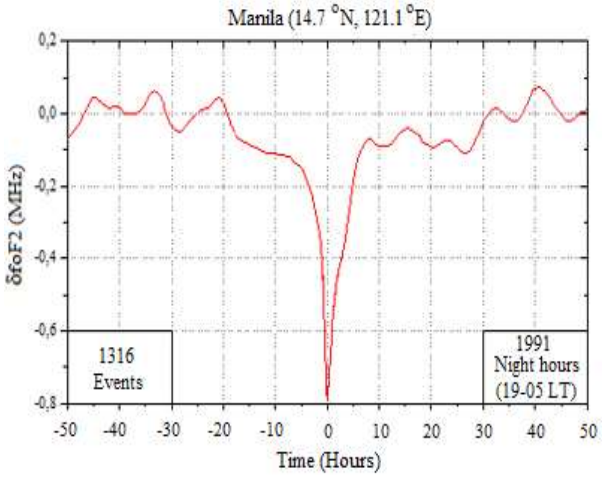

Figure 3. The change of δfoF2 values depending on time for Manila during night hours of 1991

Figure 3 shows the change of δfoF2 values depending on time for 19-05 local times (LT) of 1991. The effect of change in the geomagnetic activity on foF2 values starts about10 hours before the event moment (time 0) and the their effect on foF2 values reach to maximum at the event moment. The geomagnetic storms cause to decrease about 0,8 MHz in the foF2 values. That is, geomagnetic storms cause to negative ionospheric storms in the low latitude foF2 values for night hours. The change in the foF2 values almost disappears after about 10 hours.

4. CONCLUSIONS

The aim of this research is to investigate the effect of geomagnetic activity on low latitude foF2 values. For this, the SEA method was applied to foF2 data obtained during 1991 at Manila. The analyzes were made for different local times and the results were compared with each other. Geomagnetic storms cause significant changes (increase or decrease) in the foF2 values. For all local times, the effect of geomagnetic activity on foF2 values reaches the maximum at the event moment. But, this effect varies depending on local time. For local day hours, the geomagnetic storms cause an increase about 1 MHz in foF2 values at the event moment. The storms cause positive storms in the low latitude foF2 values for local day hours. For local night hours, the geomagnetic storms cause a decrease about 0,8 MHz in the foF2 values at the event moment. That is, the storms cause negative storms in the low latitude foF2 values for local night hours. These results show that the PPEFs are more effective than other mechanisms that cause ionospheric irregularities on low latitude ionosphere.

These results of present study are in good agreement with previous studies that was conducted about foF2 at low latitudes. The previous studies reveal that during geomagnetic storms, the ionospheric critical frequency (foF2) values at low latitudes increase at the day hours and decrease at the night hours [18-23].

5. REFERENCES

[1] J. Lastovička, “Effects of geomagnetic storms in the lower ionosphere, middle atmosphere and troposphere,” Journal of Atmospheric and Terrestrial Physics, vol. 58, no. 7, pp. 831-843, 1996.

[2] R. W. Schunk and A. F. Nagy, “Ionospheres-physics, plasma physics, and chemistry,” Cambridge University Press, 2000.

[3] A. D. Danilov and J. Lastovička, “Effects of Geomagnetic Storms on the Ionosphere and Atmosphere,” Geomagnetism and Aeronomy, vol. 2, no. 3, pp. 209-224, 2001.

[4] G. W. Prölss, “Physics of the Earth's Space Environment,” Berlin-Heidelberg-New York Springer-Verlag Press, 2004.

[5] E. Timoçin, İ. Ünal, Y. Tulunay, and Ü. D. Göker, “The effect of geomagnetic activity changes on the ionospheric critical frequencies (foF2) at magnetic conjugate points,” Advances in Space Research, vol. 62, no. 4, pp. 821-828, 2018.

[6] E. Timoçin, İ. Ünal, and Ü. D. Göker, “A comparison of IRI-2016 foF2 predictions with the observations at different latitudes during geomagnetic storms,” Geomagnetism and Aeronomy, vol. 58, no. 7, pp. 846-856, 2018.

[7] H. Rishbeth, “F-region storms and thermospheric circulation,” Journal of Atmospheric and Terrestrial Physics, vol. 37, no. 7, pp. 1055-1064, 1975.

[8] G. W. Prölss, “Common origin of positive ionospheric storms at middle latitudes and the geomagnetic activity effect at low latitudes,” Journal of Geophysical Research, vol. 98, no. A4, pp. 5981-5991, 1993.

[9] G. W. Prölss, “Handbook of Atmospheric Electrodynamics,” CRC Press, 1995.

[10] G. W. Prölss, "Storm-induced changes in the thermospheric composition at middle latitudes," Planetary Space Science, vol. 35, no. 6, pp. 807-811, 1987.

[11] M. Blanc and A. D. Richmond, "The ionospheric disturbance dynamo," Journal of Geophysical Research, vol. 85, no. A4, pp. 1669-1686, 1980.

[12] B. Tsurutani, A. Mannucci, B. Iijima, M. A. Abdu, J. H. A. Sobral, W. Gonzalez, F. Guarnieri, T. Tsuda, A. Saito, K. Yumoto, B. Fejer, T. J. Fuller-Rowell, J. Kozyra, J. C. Foster, A. Costerand, and V. M. Vasyliunas, "Global dayside ionospheric up lift and enhancement associated with interplanetary electric fields," Journal of Geophysical Research, vol. 109, no. A08302, pp. 1-16, 2004.

[13] A. J. Mannucci, B. T. Tsurutani, B. A. Iijima, A. Komjathy, A. Saito, W. D. Gonzalez, F. L. Guarnieri, J. U. Kozyra, and R. Skoug, "Dayside global ionospheric response to the major interplanetary events of October 29-30, 2003 'Halloween Storms'," Geophysical Research Letters, vol. 32, no. 12, pp. 1-4, 2005.

[14] B. T. Tsurutani, O. P. Verkhoglyadova, A. J. Mannucci, A. Saito, T. Araki, K. Yumoto, T. Tsuda, M. A. Abdu, J. H. A. Sobral, W. D. Gonzalez, H. McCreadie, G. S. Lakhinaand, and V. M. Vasyliunas, "Prompt penetration electric fields (PPEFs) and their ionospheric effects during the great magnetic storm of 30-31 October 2003," Journal of Geophysical Research, vol. 113, no. A5, pp. 1-10, 2008.

[15] World Data Center (WDC), http://www.sws.bom.gov.au/World_Data_Centre.

[16] Y. Tulunay, "Interplanetary magnetic field and its possible effects on the mid latitude ionosphere II," Annali Di Geofisica, vol. 34, no. 2, pp. 193-200, 1994.

[17] Y. Tulunay, "Variability of mid-latitude ionospheric foF2 compared to IMF polarity inversions," Advances in Space Research, vol. 15, no. 2, pp. 35-44, 1995.

[18] X. Wang, J. K. Shi, G. J. Wang, G. A. Zherebtsov, and O. M. Pirog, "Responses of ionospheric foF2 to geomagnetic activities in Hainan," Advances in Space Research, vol. 41, no. 4, pp. 556-561, 2008.

[19] G. A. Mansilla, "Some ionospheric storm effects at equatorial and low latitudes," Advances in Space Research, vol. 53, no. 1, pp. 1329-1336, 2014.

[20] C. Nayak, L. C. Tsai, Y. S. Su, I. A. Galkin, A. T. K. Tan, E. Nofri, and P. Jamjareegulgarn, "Peculiar features of the low-latitude and midlatitude ionospheric response to the St. Patrick's Day geomagnetic storm of 17 March 2015," Journal of Geophysical Research: Space Physics, vol. 121, no. 8, pp. 7941-7960, 2016.

[21] E. Astafyeva, I. Zakharenkova, K. Hozumi, P. Alken, P. Coïsson, M. R. Hairston, and W. R. Coley, "Study of the equatorial and low-latitude electrodynamic and ionospheric disturbances during the 22-23 June 2015 geomagnetic storm using ground-based and spaceborne techniques," Journal of Geophysical Research: Space Physics, vol. 123, no. 3, pp. 2424-2440, 2018.

[22] B. Paul, B. K. De, and A. Guha, "Latitudinal variation of F-region ionospheric response during three strongest geomagnetic storms of 2015," Acta Geodaetica et Geophysica, vol. 53, no. 5, pp. 579-606, 2018.

[23] E. Timoçin, "The north and south symmetry of the ionospheric storms at magnetic conjugate points for low latitudes during the March 1976 severe geomagnetic storms and the relation between daily changes of the storms with geomagnetic activity indices," Advances in Space Research, vol. 63, no. 12, pp. 3965-3977, 2019.

JOURNAL OF SCIENCE
SAKARYA UNIVERSITY

Sakarya University Journal of Science

ISSN 1301-4048 | e-ISSN 2147-835X | Period Bimonthly | Founded: 1997 | Publisher Sakarya University | http://www.saujs.sakarya.edu.tr/

Title: Wi-Fi And Lte-Laa Coexistence Problems, Challenges And Features İn 5Ghz Unlicensed Bandwidth

Authors: Maqsood Sulaimani, Seçkin Arı
Recieved: 2019-04-24 00:46:12

Accepted: 2019-09-03 23:09:17

Article Type: Research Article
Volume: 23
Issue: 6
Month: December
Year: 2019
Pages: 1242-1255

How to cite
Maqsood Sulaimani, Seçkin Arı; (2019), Wi-Fi And Lte-Laa Coexistence Problems, Challenges And Features İn 5Ghz Unlicensed Bandwidth. Sakarya University Journal of Science, 23(6), 1242-1255, DOI: 10.16984/saufenbilder.557409
Access link
http://www.saujs.sakarya.edu.tr/issue/44246/557409

Sakarya University Journal of Science 23(6), 1242-1255, 2019

Wi-Fi and LTE-LAA Coexistence Problems, Challenges and Features in 5GHz Unlicensed Bandwidth

Maqsood Sulaimani*[1], Seçkin Arı[2]

Abstract

The demand for high data rate and stable quality of service from cellular networks' subscribers is a huge challenge for cellular operators. To overcome this issue, while keeping high data rate and stable quality of service more bandwidth is required. The lack of licensed bandwidth and also its high cost make it hard for operators to overcome this issue. To find an effective solution and expand the capacity of cellular networks, operators have started deployment of Long Term Evolution (LTE) in unlicensed bandwidth, exactly utilizing 5GHz unlicensed bandwidth in small cell scenarios. The extension of LTE to the 5GHz unlicensed bandwidth where it is already in used by Wi-Fi will create huge coexistence problems between Wi-Fi and LTE. It results due to different channel access mechanisms of Wi-Fi and LTE. This paper presents the channel access mechanisms of Wi-Fi and LTE-Licensed Assisted Access (LTE-LAA), coexistence problems, challenges, privileges, coexistence features of LTE and Wi-Fi. Finally, simulations are provided for LTE-LAA based Listen Before Talk (LBT) mechanism and Wi-Fi to show that LTE-LAA with LBT mechanism is friendly to the Wi-Fi networks when using the same 5GHz unlicensed channel. The simulation results illustrate that LTE-LAA based-LBT channel access mechanism by alone cannot bring a fair coexistence between these two technologies, and it needs further improvement.

Keywords: LTE, LTE-LAA, Wi-Fi, Coexistence, LBT

1. INTRODUCTION

Based on the rapid growth of internet-based services, the cellular networks need to expand their capacity and respond to the demand of customers accordingly [1]. The cellular networks are facing huge capacity problems due to high load of traffic and the explosion of data hungry applications. As operators using licensed spectrum, due to the lack of licensed spectrum and its high price it will be difficult for operators to overcome the issue of capacity. As operators look for a supplementary

* Corresponding Author: maqsood.sulaimani@ogr.sakarya.edu.tr
[1] Sakarya University, Computer and Information Technology, Sakarya, Turkey, https://orcid.org/0000-0003-2246-4108
[2] Sakarya University, Computer and Information Technology, Sakarya, Turkey, https://orcid.org/0000-0001-7556-8205

best solution to offload their traffic. The only effective solution is to offload cellular network traffic and expand the capacity of unlicensed bandwidth by LTE [2].

Third Generation Partnership Project (3GPP) in Release-13 (R-13) started working on extension of LTE to the 5GHz unlicensed bandwidth. The use of unlicensed bandwidth by LTE will cause serious coexistence issues between Wi-Fi and LTE networks as they use different channel access mechanisms in their Medium Access Control (MAC) protocols. The existing channel access mechanism of LTE is an aggressive mechanism, if it operates in the same operating frequency with Wi-Fi systems; the chance of channel access of Wi-Fi users will be very low even zero when the number of users increase. 3GPP, to fairly share the 5GHz unlicensed bandwidth between Wi-Fi and LTE, they launched LAA[3] based on Listen Before Talk (LBT) channel access mechanism, a similar channel access mechanism to Wi-Fi [3]. LTE-LAA channel access mechanism is based on LBT, a similar mechanism to Wi-Fi Carrier Sense Multiple Access/ Collision Avoidance (CSMA/CA). In LBT channel access mechanism a transmitter will first listen to the channel for a Clear Channel Assessment (CCA) time interval, if the channel is available for CCA time it will send the data, otherwise it will select randomly an Extended-CCA (ECCA) as a back-off time.

The unified structure of the LTE core network for both licensed and unlicensed bandwidth will help the operators to guarantee the valid authentication, high mobility and guarantee Quality of Service (QoS) to the users. In LTE-LAA the unlicensed bandwidth will be used only to increase the data rate in the downlink (DL), but the uplink (UL) and control signal will be carried in licensed bandwidth.

This research study will act as unique point where it will help the researchers and other interested concerns to find coexistence related factors and features related to these two technologies. The study gives an overall idea about the coexistence of LTE-LAA and Wi-Fi.

The rest of the paper is arranged as follows: In part 2, the channel access mechanism of both Wi-Fi and LTE-LAA is explained. In part 3, problems and challenges towards coexistence of Wi-Fi and LTE-LAA are provided. In part 4, coexistence features of both technologies are presented. In part 5, the performance differences of the two technologies are discussed. In part 7, performance degradation of both technologies is reviewed. In part 8, Wi-Fi and LTE-LAA simulation models are given. In part 9, the conducted simulation results are discussed. In part 10, findings and suggestions are found. In part 11, conclusion is given.

2. CHANNEL ACCESS MECHANISMS

2.1. Channel Access Mechanism of Wi-Fi

In Wi-Fi network, medium access of Wi-Fi network station is more complex than a wired one. The station in a Wi-Fi network is unable to detect a collision during its transmission, while sharing the same transmission medium with other stations. The Wireless Local Area Networks (WLANs) are half duplex systems. Therefore, a station cannot transmit and detect the collision at the same time [4].

The 802.11 standard introduced two common MAC protocols, a contention-based, Distributed Coordination Function (DCF) and non-contention based, a centralized protocol, Point Coordination Function (PCF). PCF mechanism is a centralized channel access mechanism. In PCF, the access point (AP) sends the polling message to one station. The station after receiving the polling message from the AP can transmit. The AP when receives the feedback from station, will continue polling another station. In PCF, if a station does not have data to transmit, it will respond with a NULL message to the AP, which causes waste of resources. Even worse, when the number of stations

[3] In this study the LTE-LAA and LAA is used interchangeably

increase in the network, the waiting time for stations to transmit their packets will be also increased due to polling process. PCF mode is not a common mode. Mostly the DCF mode is set as a default MAC protocol.

2.1.1.DCF Channel Access Mechanism

DCF is a non-centralized contention-based mechanism. DCF uses CSMA/CA. The station is only allowed to send the data when it senses the channel and find it free. CSMA/CA uses two channel access methods. Basic and request to send/clear to send (RTS/CTS) methods [5]. The basic approach is a two-way handshaking method. While RTS/CTS as shown in Figure.1 is a four-way handshaking method. In basic approach, the sender will send the Acknowledgement (ACK) frame with original data to the destination. When the receiver gets the data correctly, it will respond back to the sender with confirmation ACK. Hence it will complete the two-way handshaking process. In the RTS/CTS, the sender sends RTS frame to the receiver. If the target user correctly receives the RTS frame and is eligible for receiving, it will respond back to the sender with a CTS frame. The sender after receiving the CTS frame, will send the data frame to the receiver. The receiver after receiving the transmitted data correctly, it will accept the transmitted data frame as a received data frame. Thus, the four-way handshaking is completed.

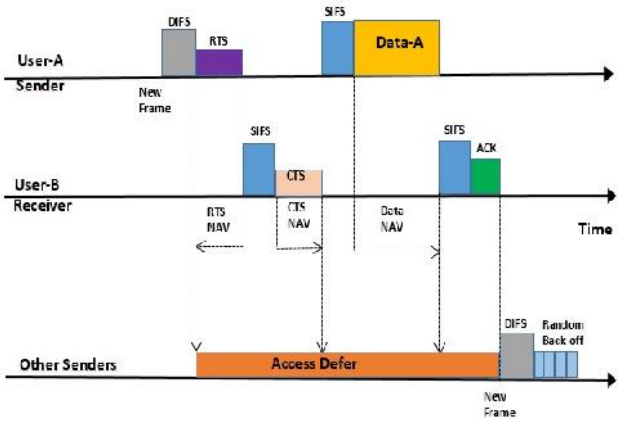

Figure 1. DCF based channel access mechanism

In the second (RTS/CTS) method, if the sender does not receive a CTS frame after sending an RTS frame, RTS/CTS tries to repeat the retransmission process. Network Allocation Vector (NAV) performs virtual carrier sense mechanism [6]. In NAV, each transmitting frame holds a duration value, which specify the required conversation period for a station.

The Figure.2 depicts the flowchart of the CSMA/CA mechanisms. When a station has a new frame to transmit, first it will sense the channel for distributed inter-frame space (DIFS) interval, if the channel is free for DIFS interval it will send the frame immediately, otherwise, the station will postpone its transmission. Again if the channel is sensed free for DIFS interval, the station will select a random back-off number B to further postpone its transmission based on selected random number. The random back-off number or B is selected between (1, CW). The selected random back-off number is decreased by one when the channel is sensed idle for each slot time. The B is frozen when the channel is sensed again busy, and is resumed when the channel is sensed idle again for DIFS interval. When the B reaches zero, the station will transmit the frame. When the receiver receives the frame correctly, after a short inter-frame space (SIFS) interval it will send the ACK frame to the sender to confirm the correct reception of the frame. If the sender receives the ACK message after a SIFS interval, subsequently it will start for a second transmission, otherwise, the sender will start the retransmission procedure for the lost frame.

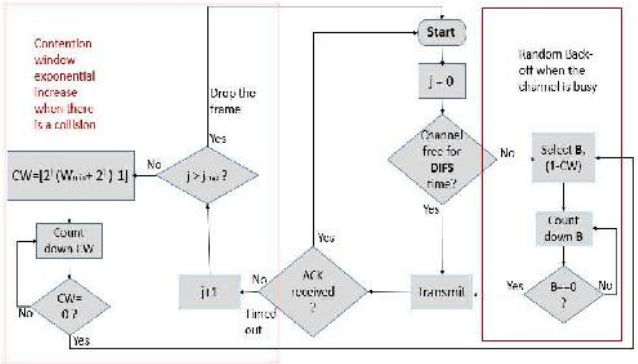

Figure 2. CSMA/CA transmission processes

When there is a time out for ACK frame (sender does not receive the ACK frame after SIFS interval) the sender will start the retransmission procedure. The retransmission procedure is based on contention window (CW) window exponential increase. CW= $[2^j (W_{min}+2^j)-1]$, CW_{min} = 15 and CW_{max} = 1023 and the exponential increase is as (15, 31, 63 ……1023) [7]. j is the number of retransmission and j_{max} is the maximum number of retransmission. When the frame is lost, it means a collision is occurred during the transmission and retransmission procedure will be activated. Each time when there is a collision, the sender will perform a retransmission procedure. The retransmission procedure is repeated until the retransmission number reaches to its maximum number, and after the maximum retransmission if there is again a collision then the frame will be dropped.

2.1. LTE-LAA Channel Access Mechanism

The LTE-LAA standard is introduced by 3GPP in R-13 [8]. The LTE-LAA is an extended version of LTE to the unlicensed bandwidth. In order to provide improved services to the users, LTE-LAA aims to use both licensed and unlicensed bandwidth. LTE-LAA uses carrier aggregation (CA) technology to serve in both licensed and unlicensed bandwidth. The primary cell (Pcell) uses licensed bandwidth which will provide better QoS, mobility and reliability to the users. On the other hand, higher data rate will be provided using unlicensed bandwidth as an additional carrier. LTE-LAA uses the LBT mechanism to share the same channel with other technologies. Where the Node (user) first will listen to the channel for a CCA interval, if it finds the channel clear/free for a CCA time interval, then it will start the transmission. Otherwise, it will select a random back-off until the channel becomes free. Figure.3 shows the channel sharing procedure of LTE-LAA with Wi-Fi. The LTE-LAA is a global standard that aims to provide a single solution to meet legal requirements in all regions [8].

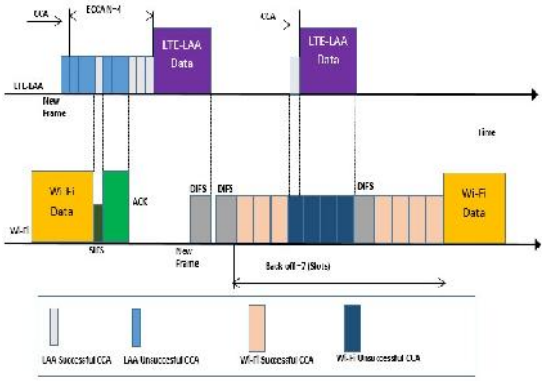

Figure 3. Joint LTE-LAA and Wi-Fi channel access mechanisms

For further clarification the working mechanism of LBT mechanism is shown in Figure.4. The Node will first listen to the channel for CCA interval, if the channel is free for CCA interval it will start the transmission, otherwise, it will select a random back-off number N, an extended-CCA (ECCA). It will count down the N until the N reaches to zero. When the N reaches to zero the Node will start the transmission. After transmission it will take the nack (negative acknowledgement) from hybrid automatic repeat request (HARQ), to see if there is collision during the transmission or not. The collision probability in LTE-LAA is based on HARQ feedback [9].

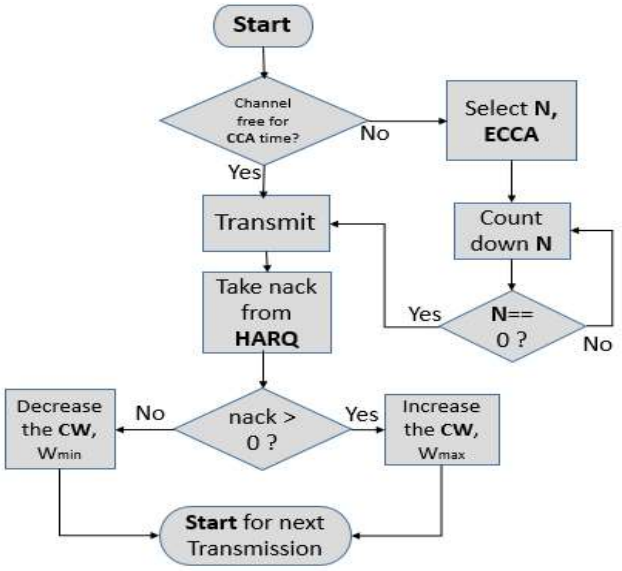

Figure 4. LBT processes for LTE-LAA [10]

The CW is updated based on HARQ feedback. If there is a nack from a recent transmission, the CW will be increased to the maximum, otherwise, the CW will be reset to a minimum and the Node will start for next transmission. The duration of the transmission opportunity (TXOP) depends on the class of CW size. There are four classes of CW [11].

3. Wi-Fi AND LTE COEXISTENCE PROBLEMS AND CHALLENGES

The huge challenge for LTE and Wi-Fi coexistence is that when the LTE uses the same channel in the existence of Wi-Fi, as Wi-Fi uses CSMA/CA channel access mechanism, Wi-Fi users will suffer from high performance degradation. From the other hand, the performance of LTE is almost unaffected. This results from that these two technologies have not the same channel access mechanisms. LTE is designed as a specific controller of a particular bandwidth. LTE transmits the data simultaneously with no delay due to its aggressive channel access mechanism. On the other hand, Wi-Fi is designed using CSMA/CA and a random back-off to fairly coexist with other technologies. Thus, Wi-Fi stations will have little chance of transmission because of its friendly channel access mechanism when sharing the same operating frequency with other technologies.

The lack of inter-technology coordination and mutual interference management mechanisms are the most serious coexistence challenges towards Wi-Fi and LTE technologies. Most broadband wireless access technologies have an interference management mechanism. However, they are used for interference management of their own terminals [12]. These interference management mechanisms cannot respond to the inference issues in heterogeneous wireless networks. Today, the most widely used wireless networks, LTE and Wi-Fi are not only different from each other's, but they are also incompatible when sharing the same operating frequency.

Another problem is the LTE model for deployment of small cells in unlicensed bandwidth as regulatory restricted the effective isotropic radiated power (EIRP) in unlicensed spectrum is too lower than those used in LTE licensed macro cells. In addition, LTE should be able to determine a fair coexistence mechanism when sharing the same unlicensed operating frequency with Wi-Fi networks [12].

The ambient interference in 5GHz unlicensed bandwidth is another serious issue for LTE extension to the 5GHz unlicensed bandwidth. 5GHz unlicensed bandwidth already in used by some other technologies such as Wi-Fi and weather radars. Beside this, Unlicensed-LTE (U-LTE) technologies (LAA, LTE-U and MulteFire) also intended to operate in the same bandwidth. Hence these technologies can have certain interference to each others. The regulatory to fairly use the 5GHz unlicensed bandwidth and reduce the Radio Frequency Interference (RFI) from other Radio Access Networks (RANs) to its minimum they considered some deployment rules and requirements [13]. As U-LTE technologies also intended to use 5GHz unlicensed bandwidth they need to adhere to those rules and requirements same as Wi-Fi. For example, the channels 120-128 in the same time also used by weather radars, the regulatory requirement in some regions such as Europe and Japan to use these channels is to observe the Dynamic Frequency Selection (DFS) and Transmit Power Control (TPC). The Wi-Fi or U-LTE when use these channels and receive the signal from weather radar they must dynamically change the channel. However, this will interrupt the transmission. The interrupt maybe unnoticeable for the non-real time applications such as mail and web browsing, but will certainly have an impact on latency sensitive, real-time applications such as voice and video calls.

In [14] they evaluated the performance of Wi-Fi, LAA and LTE-U in 5GHz unlicensed bandwidth. Based on their simulation results Wi-Fi is found a

good neighbor to LAA and LTE-U. In the same time when LAA and LTE-U coexist their performances are similar. Particularly, LTE-U has better performance when coexist with LAA and Wi-Fi than with LTE-U itself. From other hand, in term of channel occupancy, LAA and LTE-U have more chance of channel occupancy than Wi-Fi. Hence, the performance of Wi-Fi degrades when coexist with LAA and LTE-U.

The study in [15] evaluated the ambient inference effects in 2.4GHz for Wi-Fi networks. They evaluated the impact of six non-Wi-Fi devices (Microwave oven, Bluetooth headset, Analog cordless phone, Digital cordless phone, Analog wireless video camera and Wireless jammer) on Wi-Fi performance. In the presence of these non-Wi-Fi devices the performance of Wi-Fi is certainly affected. This affection is more serious when the non-Wi-Fi devices are found in a near distance to the Wi-Fi networks.

4. COEXISTENCE FEATURES

In below section some of the coexistence features of both technologies are reviewed.

4.1. MAC Protocols

A centralized MAC protocol is used by LTE. It includes a dynamic resource scheduler, which allocates resources dynamically. When the scheduler shares resources between mobile devices, the traffic load, the required QoS, and the status of the channel are taken into account. From other side, Wi-Fi's MAC uses CSMA/CA as a channel access mechanism. Therefore, Wi-Fi systems will be highly affected when LTE starts operating on the same operating frequency without any fair coexistence mechanism.

4.2. Motivation of Sharing the 5GHz Band by Wi-Fi and LAA

The existing cellular networks are facing with huge capacity problems. The promised benefits of the Wi-Fi and LTE networks coexistence has attracted the attention of the researchers [16]. LTE-LAA will provide high data rate and good coverage to the cellular users. From other hand, if a fair coexistence is not found between these two technologies when they share the same operating frequency, traffic load, contention for channel access and network congestion will be increased. The reason to deploy the LTE-LAA in 5GHz bandwidth is not to withdraw the Wi-Fi system, but to further improve utilization of the 5GHz unlicensed bandwidth. To efficiently integrate LTE and Wi-Fi networks, there will be reasonable advantages for both sides. From one side, Wi-Fi networks use only unlicensed bandwidth, the contention of users for channel access causes of low efficiency. Thus, shifting some of the traffic to a well-controlled network (LTE) is needed. From the other hand, to decrease the interference and congestion of the existing LTE network, it is possible to shift a huge amount of the LTE network traffic to the Wi-Fi 5GHz unlicensed bandwidth by deploying LTE-LAA in small cell scenarios.

4.3. Combination of Licensed and Unlicensed Bandwidths

When there is a demand for more capacity, carrier aggregation can be used to manage different capacity carriers. Based on CA deployment mechanism one carrier will serve the Primary Cell (Pcell) and other carriers will serve the Secondary Cells (Scells) [17]. Hence, the second carrier will be only supplemental downlink (SDL) carrier. SDL will be used as a secondary data transmission carrier in downlink, but the uplink and control channel will remain in the licensed bandwidth.

4.4. LTE Carrier Aggregation with Unlicensed Bandwidth

In order to achieve high data rate, it needs to increase the number of carriers, and it is only possible by using CA technology. LTE-Advanced (LTE-A) have started using more than one carrier in the single transmission and CA is the only possible way to use more than one carrier in a single transmission [18]. Therefore, carrier aggregation is one of the most important features to ensure that LTE-LAA technology can use both licensed and unlicensed spectrum together.

4.5. Stable Quality of Service (QoS)

It should be noted that only unlicensed spectrum-based transmission is not stable. Because using only unlicensed bandwidth makes it is difficult to insure acceptable QoS and stable transmission. Therefore, it is not advisable to ignore the use of the licensed bandwidth when extending the LTE to the unlicensed bandwidth. To provide the users to use both spectrums (licensed and unlicensed) LTE-LAA was introduced by 3GPP in R-13.

5. PERFORMANCE DIFFERENCES

Mobile operators evaluate LTE-LAA in 3GPP standardization. Deploying LTE in the unlicensed band can often face a confused decision whether to deploy Wi-Fi or LAA when planning for using small cells (SC) topologies. Considering some practical commercial factors in some deployment scenarios, Wi-Fi or LAA must be used by alone in 5GHz band, regardless of any coexistence mechanism. Some factors that indicate the performance difference between these two technologies are given in below.

5.1. Spectral Efficiency

The following given factors determine LTE-LAA spectral efficiency over Wi-Fi:

5.1.1. Interference Management

Initiative coordination and interference avoidance mechanisms, named, Enhanced Intercellular Interference Coordination (eICIC) and Coordinated Multipoint (CoMP), have been implemented in LTE to minimize interference and increase the spectral efficiency. CoMP transmission and reception refers to a variety of procedures that require coordination between geographically separated eNBs. Where a customer can be served with better resource allocation by multiple eNBs [19]. Hence, as LTE has a robust interference management systems, the management of interference in LAA will be much better than Wi-Fi.

5.1.2. Stable Transmission

As mentioned earlier, LTE implements the centralized MAC protocol. The resources are allocated centrally rather than contention based. For better resource allocation LTE uses the user channel quality feedback report such as channel quality indicator (CQI) and channel state information (CSI).

5.1.3. Good Coverage and Better Mobility Support

The users in LTE-LAA are operated in a single and joined architecture. The core network of LTE can be used for both types of spectrum. Joined architecture means the same core network for both macro and small cells user in licensed and unlicensed spectrums.

5.1.4. HARQ vs ARQ

The retransmission mechanisms in Wi-Fi and LTE are different. HARQ is used by LTE in the MAC layer, having higher efficiency than that of a single loop ARQ used by the Wi-Fi [20] . In ARQ, if there is an error in the received data (when it is detected by the ARQ), the receiver will request the sender for retransmission. In HARQ, however, when there

is an error in the received data, the received data will be buffered and the receiver will request for retransmission of the only lost packets. Then receiver combines the retransmitted packet with the buffered data. When there is succeed decoding by receiver, it will respond with an ACK message to eNB.

5.2. Wi-Fi Privileges vs LTE-LAA

Wi-Fi has many benefits compared to LTE-LAA. Beside to its robust standardization and its established ecosystem, it is widely used and it possesses a wide AP foot print in public and business. This AP foot print can be used as a principle for the distribution and deployment of SC [21]. With the help of APs foot print the deployment of LAA small cells (SCs) can be speed up and also will decrease the cost and complication. On the other hand, an operator may face difficulties getting access to these services when combining the unlicensed and licensed LTE strategy because corporate and commercial places have their own Wi-Fi systems.

6. SUMMARIZING THE FEATURES DISCUSSED ABOVE

a) We found that Wi-Fi and LTE have different MAC adoption. In term of channel access procedure, there is no channel sense and a random back-off mechanism in LTE networks. Instead, LTE systems designed for licensed spectrum actually have a centralized control architecture that allocates a resource unit to the user in each sub-frame. In contrast, a Wi-Fi station that does not need a central controller, first it will sense the channel when there is a pending transmission. Moreover, for Wi-Fi systems it will only occupy the channel when the packets required to be sent.

b) Wi-Fi needs to improve the user mobility, coverage and network competence as LTE offers. LTE network is a well-managed and is properly integrated into the existing operator's cellular networks. Hence, LTE offers valid authentication, stable transmission with guaranteed QoS [22]. Unfortunately, due to the various restrictions on Wi-Fi system, the above mentioned improvements seems hard to be achieved for Wi-Fi systems in the near future.

c) Wi-Fi deployment is easy and widely used in public and business. In addition, the introduction of LTE-LAA will now need to traverse a long journey as Wi-Fi performed. Based on the benefits of both technologies, the selection of LAA or Wi-Fi depends on environmental and also financial factors.

7. PERFORMANCE DEGRADATION

Many coexistence mechanisms are developed for Unlicensed-LTE (U-LTE). Such as, Dynamic Channel Selection (DCS), Carrier Sense Adaptive Transmission (CSAT) for LTE-U and LBT for LTE-LAA. When U-LTE and Wi-Fi share the 5GHz unlicensed bandwidth, these mechanisms were found useful for reducing interference and increasing the efficiency of spectrum utilization. The performance of each mechanism depends to the different factors such as network scale, traffic density, environment, deployment scenario (indoor, outdoor).

The simulation performed in [23], to assess the coexistence results of Wi-Fi and LTE in an indoor environment. Based on simulation results, when LTE shares the same channel with Wi-Fi, and there is no changes to the LTE channel access mechanism, Wi-Fi users seriously suffer from unfairness. By deploying 1 AP per system, LTE users lose only marginal performance (approximately 4% of basic performance), but on the other side, Wi-Fi has lost almost up to 70% of its performance. During the second density deployment, with deploying 5 AP per system, the performance degradation seen by Wi-Fi is around

100%. With increasing the density (APs and Users) channel is totally blocked for Wi-Fi users.

The work in [14] has observations similar to those in [23]. Specifically, by increasing traffic load of the network, it was found that LTE performance was only slightly degraded, but from the other side Wi-Fi performance was seriously dropped. Because Wi-Fi and LTE owned different channel access mechanism. When the channel is occupied, Wi-Fi will postpone its transmission, in contrary, the LTE will always prefer to transmit and in order to deal with high interference it will select a more efficient transmission approach. The aggressive channel access mechanism of LTE causes where LTE users use the major number of transmission opportunities and the Wi-Fi stations will remain in waiting and random back-off mode. By good fortune, the outcomes obtained in [24] showed that the harshness of this adverse effect on Wi-Fi systems could be effectively controlled by limiting LTE aggressive behavior.

The study in [25] presents the coexistence of U-LTE (LTE-U and LTE-LAA) and Wi-Fi in the 5GHz unlicensed bandwidth. Based on the simulation results LTE-U found more unfair to the Wi-Fi due to two factors. First, the incompatibility of LTE-U's duty-cycle to Wi-Fi. Second, lack of an effective coexistence mechanism. Beside this, LTE-LAA with only LBT mechanism cannot guarantee a fair coexistence of LTE with Wi-Fi.

Here in this part we share our simulation results which we conducted for LTE-LAA and Wi-Fi, to find that how LTE-LAA with its LBT mechanism is friendly to Wi-Fi when they share the same 5GHz unlicensed operating channel. We used NS3 [26] with an available LAA and Wi-Fi coexistence model to conduct the results. Based on simulation results, the LBT mechanism which prescribed by 3GPP (European Regulatory) by alone cannot bring fair coexistence between Wi-Fi and LTE-LAA technologies. Still Wi-Fi users suffering from high latency and throughput degradation compared to LAA users.

8. Wi-Fi AND LTE-LAA SIMULATION MODELS

Indoor scenario is deployed for both operators. Each operator deploys four small cells. The four cells or base stations (eNBs for LTE-LAA and APs for Wi-Fi) are equally spaced in a fixed location. The simulation is conducted for two sets of density. First set of density, each operator deploy 5 users per cell, where the total numbers of users for both operators are 40 users (2 operators, 4 cell/operator, 5 user/cell, where total number of users for both operators, 2*4*5=40). In the second set of density, we increased (doubled) the number of users per cell for each operator (2 operators, 4 cell/operator, 10 users/cell, where the total number of users for both operator, 2*4*10=80).

a) Wi-Fi Model

Wi-Fi used 20MHz 802.11n channel. The energy detection threshold (ED) is set to -62dBm for detecting other Radio Access Technologies (RAN). Wi-Fi uses Binary Exponential Back-off (BEB) to update its contention widow (CW). The window (W) is set to (W_{min}=15, W_{max}=1023).

b) LTE-LAA Model

LTE-LAA uses LBT mechanism to fairly share the same 5 GHz unlicensed operating frequency with Wi-Fi users. The energy detection threshold is set same as Wi-Fi (-62dBm). LTE-LAA uses HARQ feedback for collision probability and also updating the CW as defined in [9]. The initial time for CCA is 43 µs, and the slot time of CCA is 9 µs. The maximum TXOP is 8 ms (based on CW window class). In LTE-LAA the collision probability is based on HARQ feedback, if 80% of feedback from recent transmission is negative (nack), the CW will be updated. The CW window is updated between 15-63 for LTE-LAA (W_{min}=15, W_{max}=63).

c) Traffic Model and Performance Metrics

The overall load is same (130Mbps) for both Wi-Fi and LTE-LAA. File Transfer Protocol (FTP) is implemented only for a downlink indoor scenario as recommended in [27]. File transfer rate is based on value of λ. The defined range for λ is between 0.5 to 2.5, here in this simulation, we considered the λ = 0.5. The performance metrics for latency (ms) and for data throughput (Mbps) is considered. The Table 1 lists the concern simulation parameters for both operators.

Table.1 Simulation parameters used for LTE-LAA and Wi-Fi

Parameters	Values
Scenario	Indoor
Number of cell/operator	4
Number of user/cell	5
Packet arrival rate λ	0.5
Traffic model	FTP over UDP
Frequency	5 GHz
Channel bandwidth	20 MHz
Channel High data rate	130 Mbps
W_{min} (Wi-Fi/LAA)	15/15
W_{max} (LTE-LAA/Wi-Fi)	63/1023
ED threshold (Wi-Fi/LAA)	-62 dBm
SIFS	16 µs
DIFS/CCA	50/43 µs
NACKs feedback (LAA)	80%
TXOP	8 ms
Slot time (Wi-Fi/LAA)	9 µs

9. SIMULATION RESULTS

The Figure.5 shows the latency impact for Wi-Fi and LAA users when they share the same 5GHz unlicensed channel. The simulation result is for the first set of density (40 users). The Figure.5 depicts that Wi-Fi users still suffer from high latency (waiting time) when they operate in the same channel with LTE-LAA users. More worse, when the number of users increase the latency (more for Wi-Fi users) also increase. The result for the second set of density (80 users) is shown in Figure.6. Result shows that by increasing the number of users, the latency will be also increased. But the increase of latency is seen much more in Wi-Fi side, Wi-Fi users suffer from a high non-fair coexistence latency. It is due to that when the number of users increase, the contention to access the channel also increase. As discussed earlier that Wi-Fi uses CSMA/CA an innocent channel access mechanism to fairly share the channel. But from other hand, LTE-LAA uses LBT as a coexistence mechanism which still has aggressiveness compare to the Wi-Fi CSMA/CA. Hence, Wi-Fi users loses more time to access the channel.

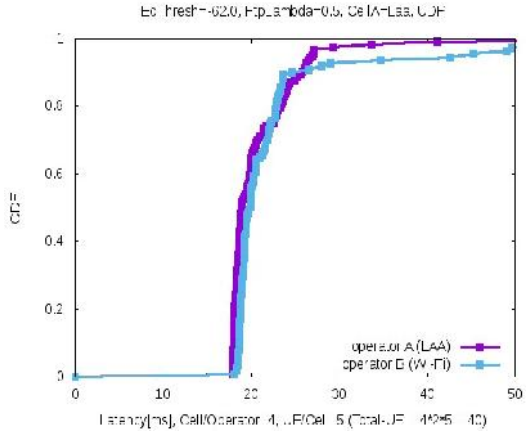

Figure 5. Wi-Fi and LTE-LAA latency (ms) based on LBT mechanism first set of density (40 users)

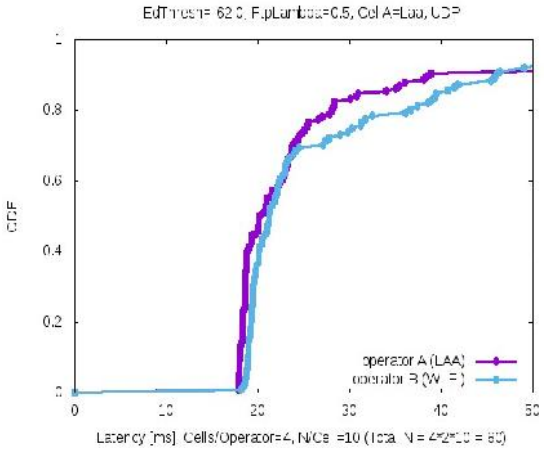

Figure 6. Wi-Fi and LTE-LAA latency (ms) based on LBT mechanism second set of density (80 users)

The second coexistence metrics is throughput. Figure.7 shows the impact of throughput degradation for both LTE-LAA and Wi-Fi users. As

discussed in pervious section that Wi-Fi users suffer from high coexistence latency when they share the same unlicensed channel with LTE-LAA, in the same time also suffer from high data degradation as well. The Figure.7 shows that when the load in the channel increase, the throughput degradation for Wi-Fi users also increase. Same as discussed in previous paragraph, when the number of users increased the latency also increased, same for throughput, by increasing the number of users, the throughput degradation is also increased. The simulation result for the second set of density, where the number of users increased from 40 to 80 users is depicted in Figure No.8. The result obviously shows that when the number of users increased, the throughput degradation is also increased, and Wi-Fi users suffer from high non-fair throughput coexistence issue. In LBT mechanism the collision probability and CW size is updated based on HARQ feedback. The sub-frame associated to the HARQ feedback is received with a delay of 4 ms after its transmission [28].

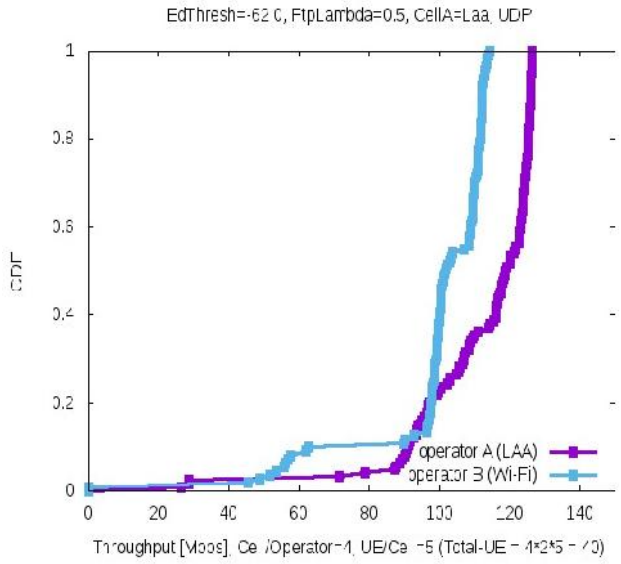

Figure 7. Wi-Fi and LTE-LAA throughput (Mbps) degradation based on LBT mechanism fist set of density (40 users)

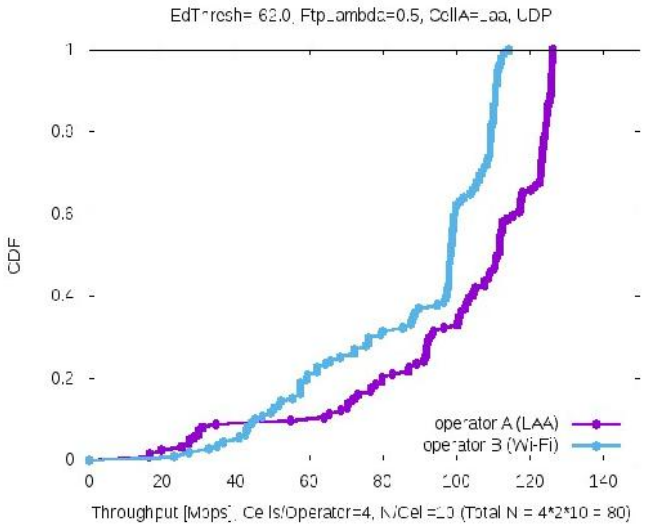

Figure 8. Wi-Fi and LTE-LAA throughput (Mbps) degradation based on LBT mechanism second set of density (80 users)

Hence, this is the main cause for having more collisions in the channel. When the number of collisions increase, both the latency and throughput degradation are also increased. Based on our simulation results and the results conducted in [29] the LBT channel access mechanism as prescribed by 3GPP by alone cannot bring a fair coexistence between Wi-Fi and LTE-LAA users, and still needs more improvement.

10. Findings and Suggestions

The main purpose of this study is to evaluate the coexistence problems, challenges and features of LTE-LAA and Wi-Fi technologies in 5GHz unlicensed bandwidth. In addition to evaluate the LBT coexistence mechanism that how it is friendly to the Wi-Fi. In below we summarize the main findings.

a) We understood if LTE when there is no changes to its air interface protocols coexist with Wi-Fi, Wi-Fi performance is seriously degraded. This is due to that Wi-Fi and LTE owned different channel access mechanisms in their MAC layers. Wi-Fi has an innocent channel access mechanism that

sharing the channel fairly with other concern technologies, while LTE has an aggressive channel access mechanism designed to have always transmission opportunity.

b) To control the aggressive behavior of LTE and coexist in a friendly manner with Wi-Fi, 3GPP developed LTE-LAA technology. LTE-LAA uses LBT coexistence mechanism where the LTE air interface protocols are modified. LBT is a Wi-Fi CSMA/CA like channel access mechanism with channel sense and back-off features.
c) LTE-LAA must also adhere to all those deployment rules and requirements considered for using 5GHz unlicensed bandwidth.
d) The sensitivity of coexistence performance is highly dependent to the channel occupancy factors such as collision probability, back-off algorithm, CW update and HARQ feedback. Due to the scheduling latency of LTE the HARQ feedback associated with sub-frame is arrived with 4 ms delay. Hence, the CW window is updated with delay and it causes to increase the number of collisions in the channel.
e) The density of traffic in the channel has an important on the efficiency of coexistence mechanism. When the number of operators' cells and users increase in the channel the LBT coexistence mechanism is found less efficient.
f) In [14] they found LAA inefficient in terms of resource allocation which effect the coexistence performance negatively. They recommended a smart MAC scheduling approach to improve the inefficiency of LAA scheduling.
g) The coexistence performance is not only affected by the behavior of the MAC layer, we also recommend to investigate the aspects of the upper layers such as Radio Link Layer (RLC).
h) In LTE-LAA the collision probability and CW update is based on HARQ feedback, as HARQ feedback is arrived with long delay, we recommend to reduce this delay to its minimum by giving the priority to the associated sub-frame of HARQ feedback.

11. CONCLUSION

We found that the demand for high data rate and stable QoS is one of the serious issues that cellular networks are facing these days. To overcome these issues they require more bandwidth. Operators are unable to respond to these issues by using existing licensed bandwidth. The lack of licensed bandwidth and its high cost made it hard for cellular operators to provide cost effective services to the customers. Cellular operators seriously in need to offload some of their traffic load to get rid of issue of congested networks. 3GPP in R-13 introduced the LTE-LAA a fair solution for offloading of cellular data from licensed bandwidth to the 5GHz unlicensed bandwidth. However, 5GHz band is already in used by Wi-Fi where it will cause coexistence issue between these two technologies. Along this study we studied and understand the channel access mechanisms of LAA and Wi-Fi. Beside this we also presented the coexistence features, problems and challenges, performance differences and performance degradation of each technology. Last but not least, we conducted the simulation results for both Wi-Fi and LTE-LAA. From simulation results we found that the prescribed LBT mechanism by alone cannot bring a fair coexistence between Wi-Fi and LTE-LAA users when they share the same unlicensed operating frequency. Thus, LBT needs more improvement to bring an acceptable fairness.

12. REFERENCES

[1] N. R. a. I. Guvenc, "Licensed-Assisted Access for WiFi-LTE Coexistence in the Unlicensed Spectrum," in *IEEE Globecom Workshops (GC Wkshps)*, Austin, TX, USA, 2014.

[2] J. A.-F. B. H. Alireza Babaei, "On the Impact of LTE-U on Wi-Fi Performance," in *IEEE 25th IEEE Annual International Symposium on Personal, Indoor, and Mobile Radio Communication (PIMRC)*, Washington, DC, USA, 2014.

[3] Qualcomm, "Progress on LAA and its relationship to LTE-U and MulteFire," Qualcomm Technologies, 2016.

[4] R. v. Steve, Wireless Networking Technology, UK: Newnes, 2007.

[5] S. K. F. H. John D. Matyjas, Spectrum Sharing in Wireless Networks, Florida: CRC Press, 2016.

[6] Devid, Certified Wireless Network Administrator, Indiana: Sybex, 2014.

[7] K. a. H. Matyjas, Spectrum Sharing in Wireless Networks, Florida: CRC Press, 2016.

[8] Qualcomm, "Progress on LAA and its relationship to LTE-U and MulteFire," Qualcomm, 2016.

[9] 3GPP, "Status report for WI: Licensed-Assisted Access to Unlicensed Spectrum," 3GPP, Spain , 2016.

[10] L. N. e. al, "Unified access in licensed and unlicensed bands in LTE-A Pro and 5G," Samsung, Texas, 2017.

[11] h. s. a. p. a. j. c. z. boon loong ng, "Unified access in licensed and unlicensed bands in LTE-A Pro and 5G," 12 Jul 2017. [Online]. Available: https://www.cambridge.org/core/journals/apsipa-transactions-on-signal-and-information-processing/article/unified-access-in-licensed-and-unlicensed-bands-in-ltea-pro-and-5g/3D374A7EDC19D4D84E9EBF20362FC7B8/core-reader#. [Accessed 09 Jul 2019].

[12] A. C. C. V. P. S. C. T. D. Abinader, "Enabling the Coexistence of LTE and Wi-Fi in Unlicensed Bands," *IEEE Communications Magazine,* vol. 52, no. 11, pp. 54-61, 2014.

[13] I. Poole, "Wi-Fi / WLAN Channels, Frequencies, Bands & Bandwidths," Radio-electronic, 21 Nov 2016. [Online]. Available: https://www.radio-electronics.com/info/wireless/wi-fi/80211-channels-number-frequencies-bandwidth.php. [Accessed 23 Aug 2019].

[14] G. A. a. M. BOJOVIC´, "Evaluating Unlicensed LTE Technologies: LAA vs LTE-U," *IEEE Access ,* vol. 7, pp. 89714 - 89751, 2019.

[15] C. W. a. A. Mahanti, "Ambient Interference Effects inWi-Fi Networks," in *9th International IFIP TC 6 Networking Conference (NETWORKING)*, Chennai, 2010.

[16] K. T. L. F. Sadek, "Extending LTE to Unlicensed Band – Merit and Coexistence," in *IEEE International Conference on Communication Workshop (ICCW)*, London, UK, 2015.

[17] J. a. Wannstrom, "Carrier Aggregation explained," 3GPP, 16 June 2013. [Online]. Available: http://www.3gpp.org/technologies/keywords-acronyms/101-carrier-aggregation-explained. [Accessed 24 10 2018].

[18] P. a. Ian, "LTE CA: Carrier Aggregation Tutorial," Radio-electronics, 18 11 2017. [Online]. Available: https://www.radio-electronics.com/info/cellulartelecomms/lte-long-term-evolution/4g-lte-advanced-carrier-channel-aggregation.php. [Accessed 23 10 2018].

[19] C. Cox, An Introduction to LTE, UK: WILEY, 2014.

[20] L. a. pedrini, "What is Retransmission, ARQ and HARQ?," telecomehall, 22 June 2012. [Online]. Available: http://www.telecomhall.com/what-is-retransmission-arq-and-harq.aspx. [Accessed 15 9 2018].

[21] P. a. Monica, "LTE unlicensed and Wi-Fi: moving beyond coexistence," Senza Fili, London, 2015.

[22] B. a. Jay, "The LTE-U Vs. WiFi Debate," Network computing, 05 Dec 2016. [Online]. Available: https://www.networkcomputing.com/wireless-infrastructure/lte-u-vs-wifi-debate/1619382711. [Accessed 01 Nov 2018].

[23] A. V. D. Cavalcante, "Performance Evaluation of LTE and Wi-Fi Coexistence in Unlicensed Bands," in *IEEE 77th Vehicular Technology Conference (VTC Spring)*, Dresden, Germany, 2013.

[24] LTE-Forum, "Coexistence Study for LTE-U SDL V1.0 (2015 -02)," LTE-Forum, Stockholm, 2015.

[25] S. K. ,. Jian, "Coexistence of Wi-Fi and LAA-LTE: Experimental evaluation, analysis and insights," in *IEEE International Conference on Communication Workshop (ICCW)*, London, UK, 2015.

[26] ns3, "Simulator," ns3, [Online]. Available: https://www.nsnam.org/.

[27] 3GPP, "3GPP TR 36.889, Study on Licensed-Assisted Access to Unlicensed Spectrum," 3GPP, 2015.

[28] S. P. J. S. Erik Dahlman, 4G, LTE-Advanced Pro and the Road to 5G, London: Elsevier, 2016.

[29] B. A.-F. Padden, "Overview of EU LBT and its Effectiveness for Coexistence of LAA LTE and Wi-Fi," 04 11 2014. [Online]. Available: https://vdocuments.site/download/submission-doc-ieee-80219-140082r0-november-2014-alireza-babaei-cablelabsslide. [Accessed 13 08 2018].

JOURNAL OF SCIENCE
SAKARYA UNIVERSITY

Sakarya University Journal of Science

ISSN 1301-4048 | e-ISSN 2147-835X | Period Bimonthly | Founded: 1997 | Publisher Sakarya University | http://www.saujs.sakarya.edu.tr/

Title: Gender Prediction From Social Media Comments With Artificial Intelligence

Authors: Özer Çelik, Ahmet Faruk Aslan
Recieved: 2019-04-30 17:42:24

Accepted: 2019-09-03 23:11:19

Article Type: Research Article
Volume: 23
Issue: 6
Month: December
Year: 2019
Pages: 1256-1264

How to cite
Özer Çelik, Ahmet Faruk Aslan; (2019), Gender Prediction From Social Media Comments With Artificial Intelligence. Sakarya University Journal of Science, 23(6), 1256-1264, DOI: 10.16984/saufenbilder.559452
Access link
http://www.saujs.sakarya.edu.tr/issue/44246/559452

Sakarya University Journal of Science 23(6), 1256-1264, 2019

Gender Prediction from Social Media Comments with Machine Learning

Özer ÇELİK*[1], Ahmet Faruk ASLAN[2]

Abstract

In the 21st century, which can be termed as age of artificial intelligence, machine learning (ML) techniques that can become widespread and improve themselves can be given more quality services to humanity in many fields. As a result of these ML developments, nowadays many companies use predictive models to estimate customer behavior. Also, with increasing use of social media, the companies have started to deliver their products and services to their customers via social media accounts. But every customer is not interested in all product or service. Each customer's area of interest is different. Gender is one of the main reasons for this difference. If the gender of a social media user is determined correctly, the amount of sales may be increased by offering the appropriate products or services. The main aim of our study is an estimation of genders of the commenters thanks to machine learning techniques by analyzing the comments of companies posting on Facebook. In context of the study, the genders of the commenters labelled based on commenters' name. The data set is divided into training and test data as 70-30%. As a result of the study, it was seen that machine learning methods predicted with similar accuracy rates, while the highest accuracy rate (74.13%) was obtained by logistic regression method.

Keywords: gender prediction, artificial ıntelligence, machine learning, natural language processing, sentiment analysis

1. INTRODUCTION

The use of social media has made it easier to investigate psychological and social problems [1]. Thus, it is allowed more data-based study beside hypothesis-testing of social science process [2]. With the help of social media, it could be followed up psychological well-being [3, 4, 5], and a host of other behavioral, psychological, medical phenomena [6] and disease rates [7]. Unlike classic hypothesis based on social science, such wide-scale social media researches rarely pay attention to or have access to age and gender information, which can have a significant impact

* Corresponding Author: ozer@ogu.edu.tr
[1] Eskisehir Osmangazi University, Department of Mathematics and Computer Science, Eskisehir, Turkey. ORCID: 0000-0002-4409-3101
[2] Eskisehir Osmangazi University, Department of Mathematics and Computer Science, Eskisehir, Turkey. ORCID: 0000-0003-1583-6508

over many problems. For example, males live nearly five years shorter than females [8]. Men and women differ usually significantly in their interests and work choice [9]. Moreover, social media language change by age [10, 11] and gender [12]. A male could have bias on twitter [13], while social media generally skew towards being young and female.

Today, many companies aim to deliver their services and products to their customers by social media accounts. But a customer is not interested in all product or service. Each customer's product type of interest is different. Gender is one of the main reasons for this difference. If the gender of a social media user is determined correctly, the amount of sales may be increased by offering the appropriate products or services.

Companies measure the satisfaction of their customers upon the physical or online product/service sales from social media. It is quite difficult to analyze the comments for the sharings during a whole day. It can easily be studied context emotion analysis (positive, negative, neutral) in natural language processing which is a subfield of artificial intelligence. In order to consider their services, the companies need to analysis according to the different information of their customers in addition to these analyses. One of the main factors in providing products according to the customers' information is gender.

Online behavior is representative of many aspects of a user's demographics [14, 15]. Many studies have used linguistic cues (such as ngrams) to determine if someone belongs to a certain age group, be it on Twitter or another social media platform [16, 17, 18, 19]. Gender prediction has been studied across blogs [20, 21], Yahoo! search queries [22], and Twitter [15, 18, 20, 23]. Because Twitter does not make gender or age available, such work infers gender and age by leveraging profile information, such as gender-discriminating names or crawling for links to publicly available data (e.g. [20]).

2. MACHINE LEARNING

Machine learning is the algorithm and statistical models used to perform a specific task based on patterns and inferences, instead of using an open instruction of computer systems. It is a sub-topic of artificial intelligence. Machine learning algorithms establish a statistical model of sample data, named as training data, owing to make predictions or decisions without being distinctly programmed [24]. Machine learning is utilized in many applications, such as email filtering and computer vision, where it is not possible to develop appropriate instructions. Machine learning is science of computational statistics, which based on making predictions by using computers. Machine learning focuses on estimations from the learned data based on known features.

Data mining is a field of study within machine learning and focuses on exploratory data analysis through unsupervised learning [25]. Data mining focuses on discovering unknown (historical) features in the data. This is a step in the analysis of information discovery in databases.

In this study, Artificial Neural Networks (ANN), Decision Tree (DT), Support Vector Machine (SVM), Naive Bayes (NB), Logistic Regression (LR), k-Nearest Neighbor (KNN) and Extreme Gradient Boosting (XGBoost) by using machine learning techniques.

2.1. Artificial Neural Networks

The full manuscript must not exceed 20 pages. It must include an abstract of up to 300 words. The 20 pages should include all tables, figures, and references.

2.2. Decision Tree

DT is the decision structure that performs learning from known data classes by inductive method. Decision tree is a learning algorithm that allocates large amounts of data into small data groups utilizing simple decision-making steps. As a result of each accomplished separation, the members in the result group are more like each

other. Decision tree with descriptive and predictive features is one of the most preferred classification algorithms due to its reliable, easy to interpret and integratable into databases [27].

2.3. Support Vector Machine

The support vector machine, also known as support vector network, is one of the supervised classification techniques laid down by Cortes and Rapnik (1995) [28]. SVM is the machine learning algorithm which performs estimate and generalization about new data by performing learning on data that unknown the distribution. The fundamental principle of the SVM is based on the asset of a hyperplane that best distinguishes the data of two classes. SVM is divided into two according to the linear separation and nonlinear separation of the data set [29].

2.4. Naive Bayes

The Naive Bayes classification is a classification by utilizing statistical methods for labeling data. Because it is easy to use, it is often preferred in classification problems. It is generally aimed to calculate the probability values of the effects of each criterion in the Bayesian classification. Naive Bayes calculates the conditional probability of the class to which the data belongs, in order to predict the probability of a class with a data. Bayes theorem is used in this process.

2.5. Logistic Regression

Logistic regression is a method of classifying the relationship between multiple independent variables and dependent variables. Although it has usually been used in medical field in the past, it is an advanced regression method which has gained popularity in social sciences today. Logistic regression is a technique used as an alternative to this method due to the inadequacy of Least Squares Method (LSM) in a multivariate model with dependent and independent variable discrimination. In logistic regression analysis, the probability of the dependent variable with two values is predicted. In addition, the variables in the model are continuous. Because of this feature, it is a technique frequently used for classifying observations.

2.6. k-Nearest Neighbor

The k-nearest neighbor algorithm, which submitted by Fix and Hodges in 1951, are based on the logic that the data closest to each other belong to the same class. The main purpose is to classify the new incoming data by using the data previously classified. The data, which is unknown to which class it belongs to, are called test samples, the previously classified data are called learning samples. In the KNN algorithm, the distance of the test sample from the learning samples is calculated, and then the k-learning sample closest to the test sample is selected. If the selected k samples have mostly belonged to which class; the class of the test sample is also determined as this class [30].

2.7. Extreme Gradient Boosting

XGBoost is a scalable, portable and computationally compiled package of gradient tree strengthening algorithm. While the gradient tree algorithm tries to solve the optimization problem in two basic steps (first determines the direction of the step, then determines the step size), XGBoost finds the step size and direction at one time. Additionally, the XGBoost name refers to the engineering target that pushes the boundary of computing resources for increased tree algorithms. Many researchers use XGBoost due to the reason. The algorithm was designed for performance of compute time and memory resources in the implementation. The design goal is to make the best use of current resources owing to train the model [31].

3. DATA ANALYSIS

3.1. Data Set

Ready package implementations and strong programs in data science are used in machine learning process. The one used in Waikato Environment for Knowledge Analysis (WEKA) machine learning is the most popular open source

coded program.The data sets are in Attribute-Relation File Format (arff) or Comma Separated Values (csv) format for WEKA . So, there is no need to deal with any programming language. The results are gained at training phase by selecting the ready machine learning methods. [32].

Besides, Matlab, Python and R programming languages can be used at machine learning. In our study Python programming language and Scikit Learn library were used. The CountVectorizer method in Scikit Learn library were used in pre-data processing phase. In order to operate Jupyter Notebook and Python and R languages provided by Microsoft for free on cloud Azure Notebook platform were used.

In Python, Scikit Learn library is used at classification in machine learning, clustering and estimation [43]. A total of 8770 comments collected by us have been investigated (1533 female and 7237 male). 1533 female, 1533 male, balanced data set was prepared by stratified sampling. Male and female were coded as 0 and 1, respectively. In addition, the name variable taken part in the data set is also included in the model.

Table 1. Sample Comments in The Data Set

Name	Comment	Gender	Emotion
Furkan Y.	laptop sogutucusu var	0	Neutral
Ziya Y.	ben burda musteriye sunulan avantaji anlayamadim bankadan faizini vererek krediyi cekiyorsun zaten canli para kredi karti pesin fiyati taksitli fiyati olsun	0	Uncertain
Evren G.	hastasiyim telefonun yarin alacagim nasipse	0	Positive
Ferhat U.	ne alacam dandik alana gerizekali derim israf verilen para	0	Negative
Zuhal O.	karlar ulkesi elbisenin fiyati nedir	1	Neutral
Hicran K.	benimkide remington	1	Uncertain
Zeynep K.	benim evimde her sey vestel memnunum	1	Positive
Esin Y.	kesinlikle tavsiye etmiyorum ttelekom olduktan sonra nede telefon hicbisey cekmiyor yer bursa apzima bile almak istemiyorum sozlesmem bitsin bayilerinin onunden dahi gecmem	1	Negative

3.2. Data Processing

In this study, Facebook were selected as a social media platform. The comments of some brands were specified on Facebook. The sharings of the pages, comments, the message text, message transmission date, comments and commenters' information on Facebook can be reached by using several Facebook Application Programming Interfaces (APIs). In order to archive the datas gained via API, SQLite database could be used [17]. By using Ruby programming language, we took the datas via Facebook API and archived on SQLite database.

Then, the arrangement and labelling of the data set before training were done. The comments in data set were cleared from meaningless words and punctuations marks via several pre operations. In order to realize the machine learning, the labelling was done according to the names of users that commented and the gender marks used in Turkish.

A model was created with the data set in our study, Python programming language of Scikit Learn library, KNN and SVM classification algorithms. With the test data reserved in %50 rate, the accuracy rates were calculated on the created model.

The Accuracy Rate (ACC), a commonly used success evaluation method, was used in our study. The accuracy method is the rate of the sample number the system classifies as trues (True Positive (TP) and True Negative (TN)) to all

sample number. And the error rate is the rate of the sample number calculated false (False Positive (FP) and False Negative (FN)) to all sample number. It is expected to have the accuracy rate is higher than the false rate at the end of the study.

Success scores are calculated with the help of the confusion matrix (Table 2).

Table 2. Confusion Matrix

		Actual		**Total (%)**
		0	1	
Predicted	0	TP	FP	Precision Score
	1	FN	TN	Negative Predictive Value (NPV)
Total		Recall Score, Sensitivity	Specificity	ACC

The success measures and formulas used in our study, which were calculated with the help of Confusion Matrix;

$$ACC = (TP + TN)/(TP + TN + FP + FN)$$

$$Precision = TP/(TP + FP)$$

$$NPV = TN/(TP + FP)$$

$$Recall = TP/(TP + FN)$$

$$Specificity = TN/(FP + TN) \quad (1)$$

There are several more accuracy scores calculated with the help of confusion matrix. In addition to, power of the study, type II error, type I error are calculated respectively via TP value, FN value and FP value.

All analysis and processing A computer with Windows 10 64-bit operating system, quad-core Intel Skylake Core i5-6500 CPU with 3.2 GHz 6MB Cache and 8GB 2400MHz DDR4 Ram memory was used.

4. CONCLUSION

The data set is divided into training and test data as 70-30%. It was observed accuracy rates in Table 3 through the results of the study. According to Table 3, the highest accuracy rate was achieved by logistic regression algorithm (74.13%). Approximately 70% accuracy rate was obtained with other algorithms. The comments of the data set were used directly in the training without morphological analysis. It is assumed that if the morphological analysis of these comments is done and then used in the training, the accuracy rates will be higher.

One of the biggest constraints of the analysis developed in order to make predictions on the text is that grammar rules are not frequently observed. This leads to incorrect estimates and therefore low accuracy rates. In similar gender prediction studies in different languages, success rates of approximately 70-80% have been achieved. It is also possible to achieve higher accuracy rates with more data sets.

Table 3. The Accuracy Rates of The Algorithms

Algorithm	**Accuracy Rate (%)**	**Rate of 0 - 1 (%)**
ANN	70.65	77.0-65.0
DT	69.93	79.0-57.0
SVM	72.83	79.0-67.0
NB	70.76	83.0-58.0
LR	74.13	78.8-69.3
KNN	63.04	49.0-77.0
XGBoost	67.39	86.0-49.0

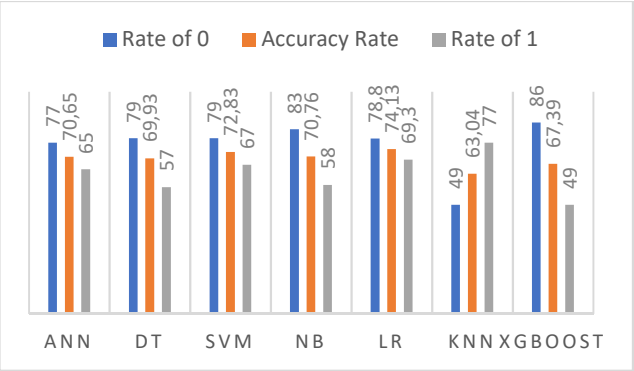

Figure 1. The Accuracy and The Category Rates of The Algorithms

As a result of the research, Receiver Operator Characteristics (ROC) curve graph calculated by confusion matrix data is given in Figure 1. Owing to ROC curve graph, it is possible to see graphically the performances of the models created. It is thought that the reason why the logistic regression algorithm predicts it with higher accuracy rate may be that gender is in binary format.

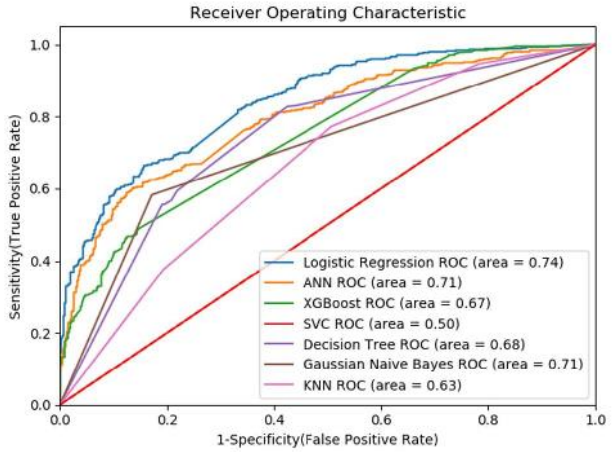

Figure 2. ROC Curve Graph

The results of the logistic regression which gives the highest success rate are given in Table 4.

Table 4. Confusion Matrix of Logistic Regression

		Actual		Total (%)
		Male	Female	
Predicted	Male	368	99	78.80
	Female	139	314	69.32
Total		72.58	76.03	74.13

5. DISCUSSION

For a long time, researchers have investigated for a better understanding of human psychology by examining words people use [34, 35, 36]. According to Tauszczik & Pennebaker say it: Language is the most collective and reliable way for human to convert their inner thoughts and emotions into a form that others can understand. So, language and words are the very items of psychology and communication [37].

There are several studies on the emotion analysis of the sharings on social media and the comments to these sharings. Pang, Lee and Vaithyanatham realized emotional analysis study using SVM and NB machine learning algorithms on English sentences. In this study SVM (%82,9) algorithms gets the highest rate [38]. Similar studies were made for Turkish texts as well. Cetin and Amasyali realized emotion analysis study for Turkish Twitter datas in 2013 using NB, Random Forest, Sequential Minimum Optimizasyon (SMO), KNN and Instance-Based (IB1) learning algorithms [39]. Apart from the comments on social media sites it is also made the emotion analysis of the comments to the cinema, meal order, hotel etc. sites. Sevindi used the machine algorithms of DT, KNN, NB and SVM in 2013 in his Turkish cinema comments emotion analysis studies and had successful results [40]. Nizam and Sakın acquired the best social media emotion analysis performance with %72,33 accuracy rate from SMO using NB, RF, SMO, DT (J48) and IB1- the controlled machine learning methods [41].

Sap et. al. said that demographic lexica have used for widespread in social science, economic, and business applications. A lexica (words and weights) was predicted from words with the demographic tags in Twitter, Facebook, and blog data for age and gender by utilizing classification and regression methods. It was determined the lexica publicly available, was effective technique in language-based age and gender prediction over Facebook and Twitter. Then the lexica were evaluated for generalization across social media

genres as well as in limited message situations [42].

As a result of the literature review, it was seen that at least 72% accuracy was achieved with different ML algorithms in the studies of gender estimation from the comments made on different social media platforms. In our study, the correct prediction rate of 74.13% was achieved with Logistic Regression algorithm. In order to achieve a higher success rate in such studies, it is necessary to have fewer errors such as spelling and grammatical errors in interpretations as suggested in other studies.

6. REFERENCES

[1] D. Lazer, D. Brewer, N. Christakis, J. Fowler, and G. King, "Life in the network: the coming age of computational social science." Science (New York, NY), 323(5915), 721, 2009.

[2] H. A. Schwartz, J. C. Eichstaedt, M. L. Kern, L. Dziurzynski, R. E. Lucas, M. Agrawal, and L. H. Ungar. "Characterizing Geographic Variation in Well-Being Using Tweets." In ICWSM (pp. 583-591), 2013.

[3] P. S. Dodds, K. D. Harris, I. M. Kloumann, C. A. Bliss, and C. M. Danforth. "Temporal patterns of happiness and information in a global social network: Hedonometrics and Twitter." PloS one, 6(12), e26752, 2011.

[4] M. De Choudhury, M. Gamon, S. Counts, and E. Horvitz. "Predicting depression via social media." ICWSM, 13, 1-10, 2013.

[5] H. A. Schwartz, , J. C. Eichstaedt, M. L. Kern, L. Dziurzynski, S. M. Ramones, M. Agrawal, and L. H. Ungar. "Personality, gender, and age in the language of social media: The open-vocabulary approach." PloS one, 8(9), e73791, 2013.

[6] M. Kosinski, D. Stillwell, and T. Graepel. "Private traits and attributes are predictable from digital records of human behavior." Proceedings of the National Academy of Sciences, 201218772, 2013.

[7] M. J. Paul, and M. Dredze. "You are what you Tweet: Analyzing Twitter for public health." Icwsm, 20, 265-272, 2011.

[8] A. Marengoni, S. Angleman, R. Melis, F. Mangialasche, A. Karp, A. Garmen, and L. Fratiglioni. "Aging with multimorbidity: a systematic review of the literature." Ageing research reviews, 10(4), 430-439, 2011.

[9] R. R. McCrae, and P. T. Costa Jr. "A five-factor theory of personality." Handbook of personality: Theory and research, 2(1999), 139-153. 1999.

[10] M. L. Kern, J. C. Eichstaedt, H. A. Schwartz, G. Park, L. H. Ungar, D. J. Stillwell, and M. E. Seligman. "From "Sooo excited!!!" to "So proud": Using language to study development." Developmental psychology, 50(1), 178, 2014.

[11] J. W. Pennebaker, and L. D. Stone. "Words of wisdom: Language use over the life span." Journal of personality and social psychology, 85(2), 291, 2003.

[12] D. A. Huffaker, and S. L. Calvert. "Gender, identity, and language use in teenage blogs." Journal of computer-mediated communication, 10(2), JCMC10211, 2005.

[13] A. Mislove, S. Lehmann, Y. Y. Ahn, J. P. Onnela, and J. N. Rosenquist. "Understanding the Demographics of Twitter Users." ICWSM, 11(5th), 25, 2011.

[14] M. Pennacchiotti, and A. M. Popescu. "A Machine Learning Approach to Twitter User Classification." Icwsm, 11(1), 281-288, 2011.

[15] Rao, D., Yarowsky, D., Shreevats, A., and Gupta, M. (2010, October). Classifying latent user attributes in twitter. In Proceedings of the 2nd international workshop on Search and mining user-generated contents (pp. 37-44). ACM.

[16] F. Al Zamal, W. Liu, and D. Ruths. "Homophily and Latent Attribute Inference:

Inferring Latent Attributes of Twitter Users from Neighbors." ICWSM, 270, 2012.

[17] A. Shlomo K. Moshe, W. P. James, and S. Jonathan. "Automatically profiling the author of an anonymous text." Communications of the ACM, 52(2):119–123, 2009.

[18] D. Nguyen, R. Gravel, D. Trieschnigg, and T. Meder. "" How Old Do You Think I Am?" A Study of Language and Age in Twitter." In ICWSM, 2013.

[19] F. Rangel, and P. Rosso. "Use of language and author profiling: Identification of gender and age." Natural Language Processing and Cognitive Science, 177, 2013.

[20] J. D. Burger, and J. C. Henderson. "An Exploration of Observable Features Related to Blogger Age." In AAAI Spring Symposium: Computational Approaches to Analyzing Weblogs (pp. 15-20), 2006.

[21] S. Goswami, S. Sarkar, and M. Rustagi. "Stylometric analysis of bloggers' age and gender." In Third International AAAI Conference on Weblogs and Social Media, 2009.

[22] R. Jones, R. Kumar, B. Pang, and A. Tomkins. "I know what you did last summer: query logs and user privacy." In Proceedings of the sixteenth ACM conference on Conference on information and knowledge management (pp. 909-914). ACM, 2007.

[23] W. Liu, and D. Ruths. "What's in a Name? Using First Names as Features for Gender Inference in Twitter." In AAAI spring symposium: Analyzing microtext (Vol. 13, No. 1, pp. 10-16), 2013.

[24] M. A. Keane. "Automated Design of Both the Topology and Sizing of Analog Electrical Circuits Using Genetic Programming." Artificial Intelligence in Design '96. Springer, Dordrecht. pp. 151–170, 1996.

[25] J. H. Friedman. "Data Mining and Statistics: What's the connection?" Computing Science and Statistics. 29 (1): 3–9, 1998.

[26] M. Gerven, and S. Bohte. "Artificial neural networks as models of neural information processing." Frontiers Media SA, 2018.

[27] A. S. Albayrak, and O. G. S. K. Yilmaz. "Veri madenciliği: Karar ağacı algoritmaları ve İMKB verileri üzerine bir uygulama." Süleyman Demirel Üniversitesi İktisadi ve İdari Bilimler Fakültesi Dergisi, 14(1), 2009.

[28] O. Celik, and S. S. Altunaydin. "A Research on Machine Learning Methods and Its Applications." Online Learning, 1(3), 2018.

[29] H. Guneren. "Destek vektör makineleri kullanarak gömülü sistem üzerinde yüz tanıma uygulaması", 2015.

[30] H. Ozkan. "K-Means Kümeleme ve K-NN Sınıflandırma Algoritmalarının Öğrenci Notları ve Hastalık Verilerine Uygulanması Bitirme Tezi", İstanbul Teknik Üniversitesi, İstanbul, 2013.

[31] J. Brownlee. "A Gentle Introduction to XGBoost for Applied Machine Learning. Machine Learning Mastery." Available online: http://machinelearningmastery.com/gentle-introduction-xgboost-appliedmachine-learning/ (accessed on 2 March 2018), 2016.

[32] https://www.cs.waikato.ac.nz/ml/weka/, (Access Date: 01.02.2018).

[33] http://scikit-learn.org/, (Access Date: 01.02.2018).

[34] P. Stone, D. Dunphy, M. Smith. "The General Inquirer: A Computer Approach to Content Analysis." MIT press, 1966.

[35] M. Coltheart. "The mrc psycholinguistic database." The Quarterly Journal of Experimental Psychology 33: 497–505, 1981.

[36] J. W. Pennebaker, M. R. Mehl, K. G. Niederhoffer. "Psychological aspects of natural language use: our words, our selves." Annual Review of Psychology 54: 547–77, 2003.

[37] Y. Tausczik, J. Pennebaker. "The psychological meaning of words: Liwc and computerized text analysis methods." Journal of Language and Social Psychology 29: 24–54, 2010.

[38] B. Pang, L. Lee, and S. Vaithyanathan. "Thumbs up?: sentiment classification using machine learning techniques." In Proceedings of the ACL-02 conference on Empirical methods in natural language processing-Volume 10 (pp. 79-86). Association for Computational Linguistics, 2002.

[39] M. Cetin, and M. F. Amasyali. "Supervised and traditional term weighting methods for sentiment analysis." In Signal Processing and Communications Applications Conference (SIU), 2013 21st (pp. 1-4). IEEE, 2013.

[40] B. I. Sevindi. "Comparison of supervised and dictionary based sentiment analysis approaches on Turkish text" (Doctoral dissertation, Master thesis, Gazi University, Turkey), 2013.

[41] H. Nizam, and S. S. Akin. "Machine Learning in Social Media and the Comparison of the Balanced and Non-balanced Data Sets in Emotion Analysis." XIX. Internet Conference in Turkey, 2014.

[42] M. Sap, G. Park, J. Eichstaedt, M. Kern, D. Stillwell, M. Kosinski, and H. A. Schwartz. "Developing age and gender predictive lexica over social media." In Proceedings of the 2014 Conference on Empirical Methods in Natural Language Processing (EMNLP) (pp. 1146-1151), 2014.

JOURNAL OF SCIENCE
SAKARYA UNIVERSITY

Sakarya University Journal of Science

ISSN 1301-4048 | e-ISSN 2147-835X | Period Bimonthly | Founded: 1997 | Publisher Sakarya University | http://www.saujs.sakarya.edu.tr/

Title: A Numerical Investigation Of The Influence Of Semi-Rigid Composite Connections On The Seismic Behavior Of A Building With Steel Concentrically Braced Frames

Authors: Ömer Yönev, Ahmet Necati Yelgin
Recieved: 2019-01-10 14:58:13

Accepted: 2019-09-09 09:37:48

Article Type: Research Article
Volume: 23
Issue: 6
Month: December
Year: 2019
Pages: 1265-1272

How to cite
Ömer Yönev, Ahmet Necati Yelgin; (2019), A Numerical Investigation Of The Influence Of Semi-Rigid Composite Connections On The Seismic Behavior Of A Building With Steel Concentrically Braced Frames. Sakarya University Journal of Science, 23(6), 1265-1272, DOI: 10.16984/saufenbilder.511327
Access link
http://www.saujs.sakarya.edu.tr/issue/44246/511327

Sakarya University Journal of Science 23(6), 1265-1272, 2019

A Numerical Investigation of the Influence of Semi-Rigid Composite Connections on the Seismic Behavior of a Building with Steel Concentrically Braced Frames

Ömer Yönev*[1], Ahmet Necati Yelgin[2]

ABSTRACT

Semi-rigid composite connections are connections which have a certain rotational stiffness and bending strength by means of the slab and its reinforcement. The use of these connections can lead to economic and structurally efficient solutions such as selecting smaller beam sections, reducing deflection and vibration problems. Additionally, they are permitted to use as a secondary lateral resisting system in regions of high seismicity. Therefore, in this study, two investigations were made in terms of seismic behavior evaluation: the influence of semi-rigid composite beam-column connections on interior frames and the influence of shear tab connections. Firstly, a 6-story building with steel special concentrically braced frames is designed according to current seismic design codes. Secondly, 3 models are created using the designed building. In Model 1, all beam-column shear tab connections are assumed as pinned connections. Model 2 and Model 1 are identical except that In Model 2, shear tab connections used in Model 1 are not assumed as pinned connections and their actual behavior is determined and included to the model. In Model 3, all beam-column connections on the interior frames are designed as semi-rigid composite connections. The interior frame sections are reselected and the exterior beam-column connections except for the ones on the braced bays are assumed the same as in Model 2. Lastly, nonlinear static analysis (pushover) is carried out and some comparisons are made with respect to the following aspects: lateral displacement and story drifts under same lateral force and lateral force under the same lateral displacement. As a result, Model 1 and Model 2 showed similar behavior due to the shear tab connections acting almost as pinned while Model 3 showed that using semi-rigid composite connections can increase the base shear capacity by %48 and decrease peak displacements and story drifts by %65.

Keywords: semi-rigid composite connections, concentrically braced frames, nonlinear static analysis, pushover.

* Corresponding Author: omeryonev@gmail.com
[1] Sakarya University, Institute of Natural Sciences, Department of Civil Engineering, Sakarya, Turkey, ORCID: https://orcid.org/0000-0002-2533-7502
[2] Karabük University, Faculty of Engineering, Department of Civil Engineering, Karabük, Turkey, ORCID: https://orcid.org/0000-0002-1879-1459

1. INTRODUCTION

In steel structures, beam-column connections are traditionally assumed either pinned connections or rigid connections to simplify calculations and reduce the complexity of analyses. In analyses, it is assumed that pinned connections have no rotational stiffness and cannot transfer moment while rigid ones have infinite rotational stiffness and can transfer moment. However, in practice all connections have some rotational stiffness and can transfer moment. This behavior, which is called semi-rigid, falls between pinned and rigid behavior.

Semi-rigid connections have been permitted by the AISC Specifications since 1949 but haven't been used widely due to the complexity of analysis required and lack of reliable information of determining moment-rotation characteristics of the connections [1]. However, the moment-rotation characteristics of these connections can be easily achieved thanks to the equations obtained as a result of the studies carried out for many years and various software using finite element analysis method.

Semi-rigid connections that take into account the slab reinforcements in determining of strength and stiffness of connections are called "semi-rigid composite connections" [2]. These connections mostly consist of slab reinforcements which form the top portion of the connection, seat angle for the bottom portion and web angles for shear resistance (Figure 1) [1].

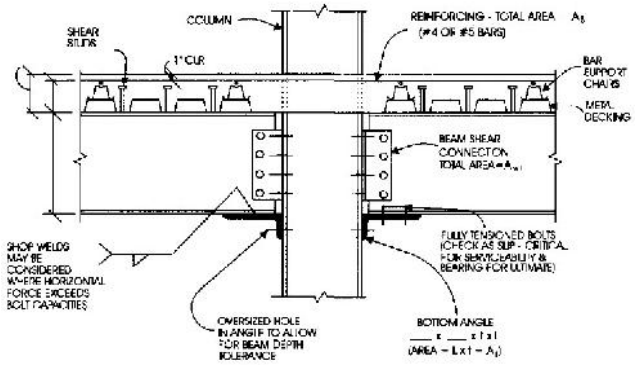

Figure 1 Semi-rigid composite connection [1]

The use of semi-rigid composite connections has many advantages in terms of economy and application. Economically, they can lead to smaller and lighter beam sections. In site, they help reducing erection time and cost when bolted angle connection types are used due to requiring no welding [3].

Apart from these advantages, the structural benefits of the use of these connections are more significant than the ones mentioned above. They help reduces deflection and vibration problems which are an important part of composite beam design [1]. They provide additional strength to structures by having some rotational stiffness and moment capacity [4]. Most importantly, as Leon stated, "they improve the ability of the structure of redistribute loads and survive accidental overloads" [3, p.160].

1.1. Literature Review

In this section, the studies on the influence of semi-rigid connections of seismic behavior of steel structures are mentioned.

Reyes-Salazar et al. [5] investigated the seismic behavior of steel buildings with perimeter moment resisting frames (PMRF) and interior gravity frames (GF). Three steel building models that represent low-, medium- and high-rise buildings were investigated for two cases. The interior connections are assumed as perfectly pinned for Case 1 and then semi-rigid for Case 2. Results show that inter-story shears and inter-story displacement at PMRF reduced for Case 2. It is observed that inter-story shears decreased up to 20, 46 and 11% while the reductions for inter-story displacements are about 14, 44 and 15% for low-, medium- and high-rise buildings, respectively. In conclusion, it was stated that semi-rigid connections have larger stiffness than pinned connections do, and actual behavior of pinned connections should not be neglected in analyses.

Zhang [6] studied the influence of shear tab connections of the behavior of moment frames. Two prototype buildings were designed; one with pinned connections and the other one with semi-

rigid composite connections. Then some comparisons were made in terms of lateral displacement under the same lateral force, lateral force under the same lateral displacement, moment in moment frames and moment in gravity frames. As a result, the building with semi-rigid composite connections showed larger stiffness, moment in moment frames were decreased and it was stated that shear tab connections which are mostly modeled as pinned connections could be used as semi-rigid for providing additional lateral resistance to buildings.

Maison et al. [7] investigated the seismic performance of partially restrained (PR) connections (also known as semi-rigid connections). For this purpose, two buildings (3 and 9 stories) having partially restrained moment frame lateral-force-resisting systems in two different seismic zone were studied. In conclusion, it was stated that PR buildings could be used in regions of moderate and high seismicity.

1.2. Objectives

In the recent researches, there are not many studies which investigate the seismic behavior of semi-rigid composite connections with steel special concentrically frames. Most of the studies have focused on semi-rigid composite connections as a replacement to moment connections or together with moment connections.

In this paper, a 6-story steel office building is designed in compliance with the current seismic design code [8] for three different cases. In the first case (Model 1), all beam-column connections (shear tab connections) are assumed as pinned connections. In the second case (Model 2), the actual behavior of the shear tab connections represented with moment-rotation curves are included to the analyses. In the third case (Model 3), all beam-column connections on the interior frames are designed as semi-rigid composite connections, the interior frame sections are reselected, and the exterior beam-column connections are assumed the same as Model 2. Then nonlinear static analysis (pushover) are carried out in x direction and some comparisons are made with respect to the following aspects: lateral displacement and story drifts under same lateral force and lateral force under the same lateral displacement.

To sum up, the main purpose of this study is to investigate whether replacing pinned connections with semi-rigid composite ones could improve the seismic behavior of structures with steel special concentrically braced frames. The other purpose is to observe the influence of shear tab connections which are assumed as pinned connections in analyses.

1.3. Scope of the Study

Within the scope of this study, some assumptions made in order to simplify the calculations and focus the main variables are listed as follows:

1. Nonlinear properties of the elements are determined according to ASCE 41-13 [9]

2. P-Δ effects are considered in the analyses.

3. Composite decks are assumed to act as rigid diaphragm.

4. All column-base connections are assumed as pinned connections.

5. All beam-beam and brace-column connections are assumed as pinned connections.

6. Element lengths are determined using centerline to centerline dimensioning.

2. BUILDING MODELS

In this chapter, the properties of the designed building are described, and three models are defined briefly.

2.1. Definition of the Building

The building in this paper is assumed to be a 6-story steel office building which has 5 bays in x direction and 4 in y direction. The bay lengths are

equal in each direction and 8 m. in x direction and 7 m. in y direction (Figure 3). The story heights are selected 3,5 m for each story and the height of the building is 21 m. (Figure 4 and Figure 5). The concentrically braces are placed on the perimeter bays of the building and two-story x-braces are selected (Figure 2 and Figure 4).

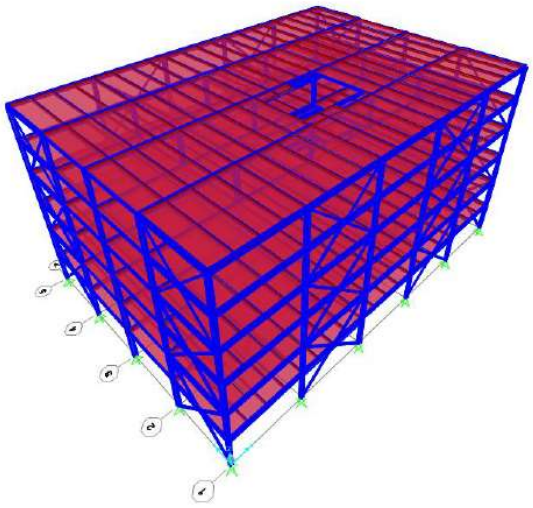

Figure 2 3D view of the building

In the design phase, LRFD method is used and S235 steel grade is selected for all steel structural components except for the steel decking. For secondary beams IPE220 sections are used. For primary beams and columns in braced and unbraced bays different sections are used (Table 1). Column splices are located at 12,00 m. height but are assumed as at 3rd story level in the analyses.

Table 1 Column and beam sections in x direction

Story	Columns		Beams	
	Braced bays	Unbraced bays	Braced bays	Unbraced bays
6	HE320B	HE300B	IPE450	IPE450
5	HE320B	HE300B	HE400B	IPE450
4	HE320B	HE300B	IPE450	IPE450
3	HE300M	HE400B	HE400B	IPE450
2	HE300M	HE400B	IPE450	IPE450
1	HE300M	HE400B	HE400B	IPE450

For determining the earthquake loads Equivalent Lateral Force (EQL) Analysis is performed. Site class ZC is selected and the spectral acceleration parameters used in EQL Analysis are selected as follows; S_s = 0,759, S_1 = 0,217, S_{DS} = 0,911 and S_{D1} = 0,325.

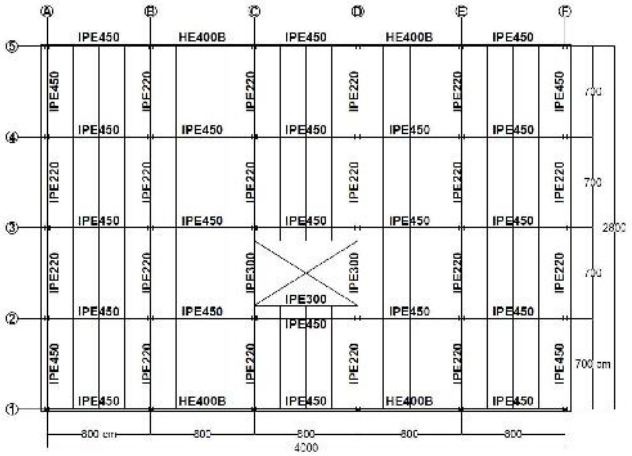

Figure 3 Typical plan view

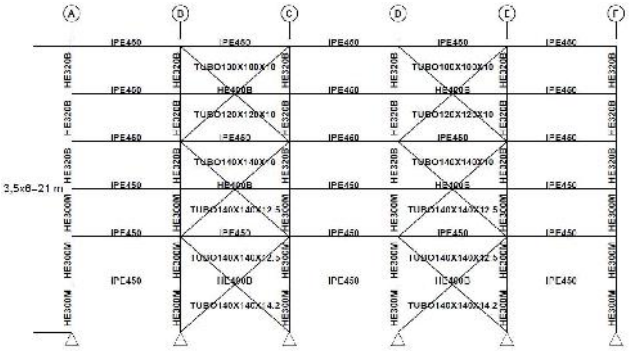

Figure 4 Elevation of the exterior frames (x direction)

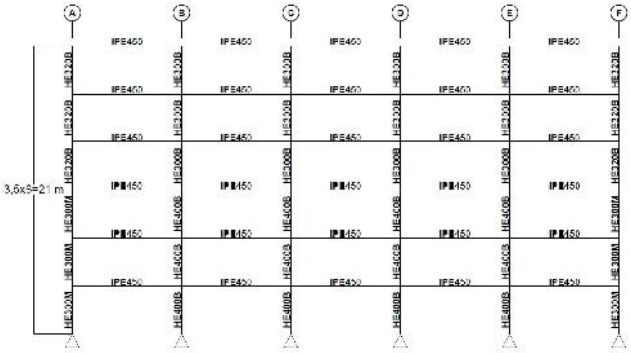

Figure 5 Elevation of the interior frames (x direction)

2.2. Models Used in the Analyses

There are three models used in the analyses. All of them have the same column, brace and secondary beam sections. The only difference between Model 1 and Model 2 is that while beam-

column connections are assumed as pinned connections in Model 1, their actual behavior represented by moment-rotation curves is determined in compliance with Astaneh-asl's study [10] is included in the analysis. The differences between Model 2 and Model 3 are as follows; the interior frame sections are selected IPE400 in Model 3 and the interior connections are designed as semi-rigid composite connections according to American Design Guide 8 [1].

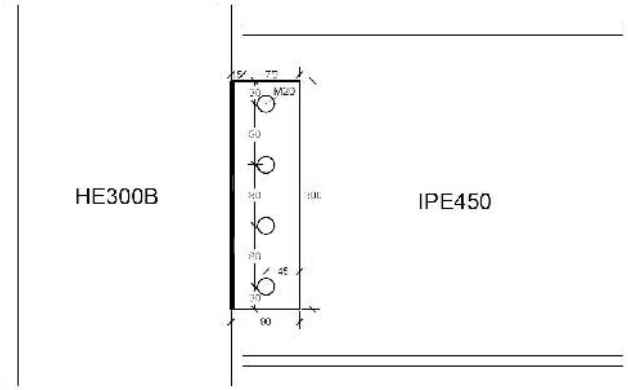

Figure 6 Typical shear tab connection details

There are two types of shear tab connections which have the same configuration and details but different moment capacities. Figure 6 shows typical shear tab connection details and Figure 7 shows moment-rotation behaviors of the connections.

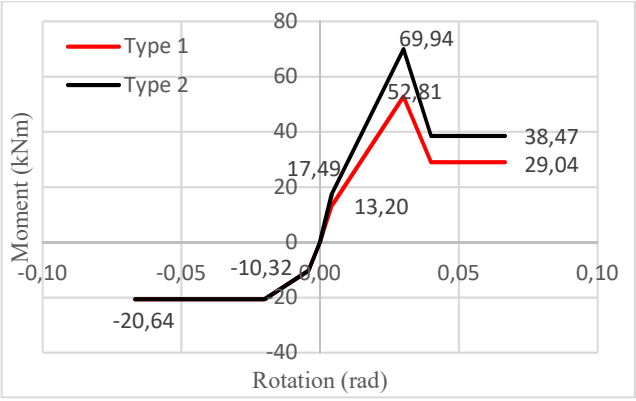

Figure 7 Moment-rotation behavior of the shear tab connections

There is only one type of semi-rigid composite connection used in Model 3 (Figure 8) and its moment-rotation behavior is represented by trilinear model in compliance with Malek's study [11] (Figure9).

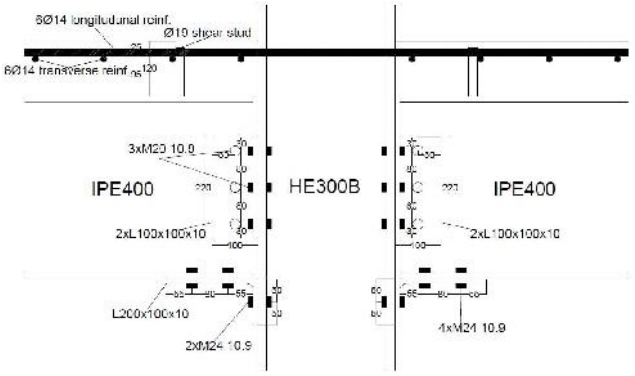

Figure 8 Typical semi-rigid composite connection details

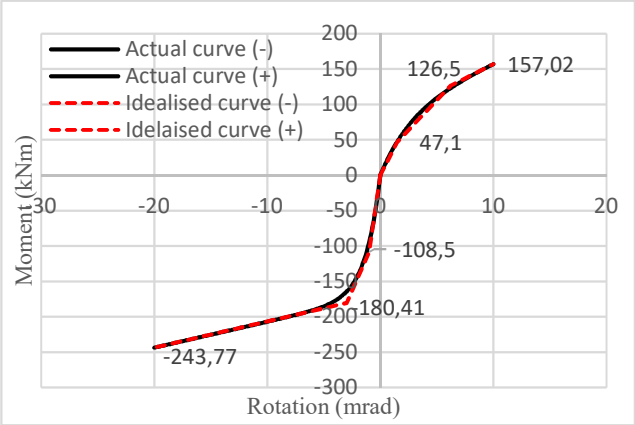

Figure 9 Moment-rotation curve and trilinear idealization of semi-rigid composite connections

3. NUMERICAL ANALYSES OF THE MODELS

In nonlinear static analyses, Sap2000 [12] is used for determining the seismic behavior of the models. Nonlinear moment-rotation behavior of the connections used in Model 2 and Model 3 are represented using nonlinear elastic link elements. These link elements are modeled as 10 cm long (Figure 10) and their properties are defined as seen in Figure 11. Normally the behavior of semi-rigid composite connections are determined for 20 mrad rotation in negative moment, 10 mrad rotation in positive moment and their strength degradation behavior aren't determined but according to ASCE 41-13 [9], strength degradation properties must be included in analyses. Therefore nonlinear link elements for semi-rigid composite connections are modeled

with strength degradation properties (Figure 11), which are determined using nonlinear modeling parameters suggested in ASCE 41-13 [9].

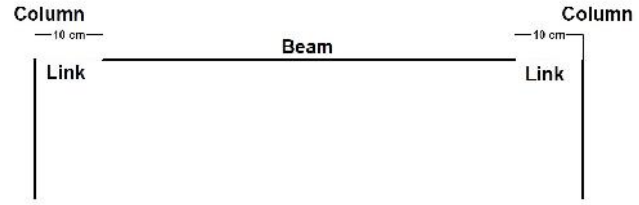

Figure 10 Modeling of nonlinear elastic link elements

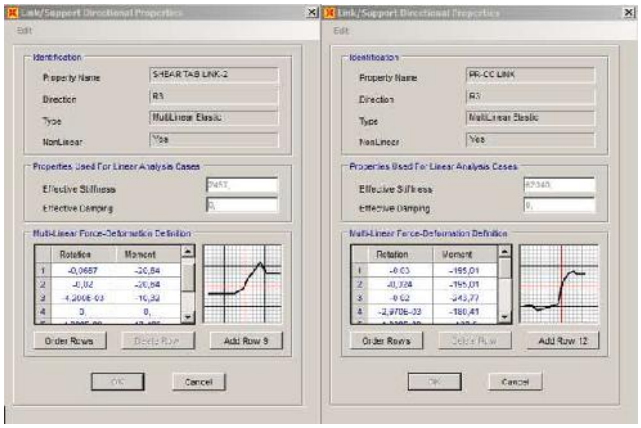

Figure 11 Defining the properties of nonlinear elastic link elements in Sap2000 [12]

Lateral load-bearing system elements are assigned plastic hinges at appropriate locations and the properties of plastic hinges are calculated according to ASCE 41-13 [9]. The types of plastic hinges can be seen on Table 2.

Table 2 Types of plastic hinges assigned

The elements that can go beyond elastic behavior	**Types of plastic hinges**
Braces	P
The columns in the braced bays	P
The beams that intersect the braces	P-M3
The columns linked to the semi-rigid composite connections	P-M3

For determining the seismic behavior of the models, all models are pushed until 50 cm top displacement. Using the pushover curves (Figure 12) base shear and top displacement points are selected for the comparisons (Table 3). Then the models are investigated when they reach the target points.

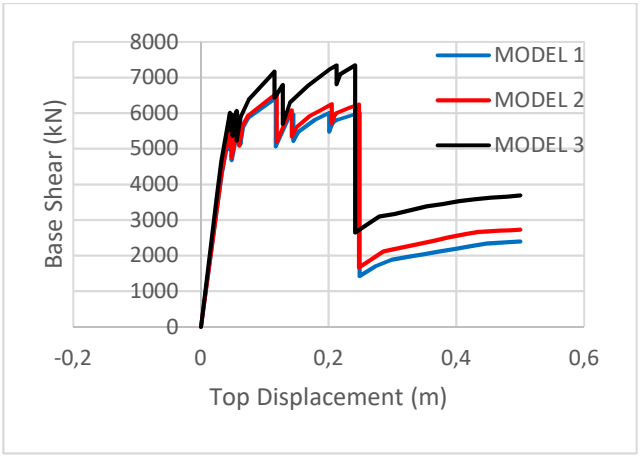

Figure 12 Pushover curves

Table 3 Selected base shear and top displacement values

Base shears (kN)	Top displacements (m)
3000	0,05
4000	0,1
5000	0,15
6000	0,2
6400	0,3

First the models are pushed until target top displacements and base shear capacities are compared. It is observed in Figure 13 that Model 1 and Model 2 have almost the same base shear capacities at the target displacements except that at 0,30 m top displacement Model 2 have larger base shear capacity by 15%. Model 3 have larger base shear capacity than Model 2 at every target displacement. The largest difference between them is 48% at 0,30 m top displacement.

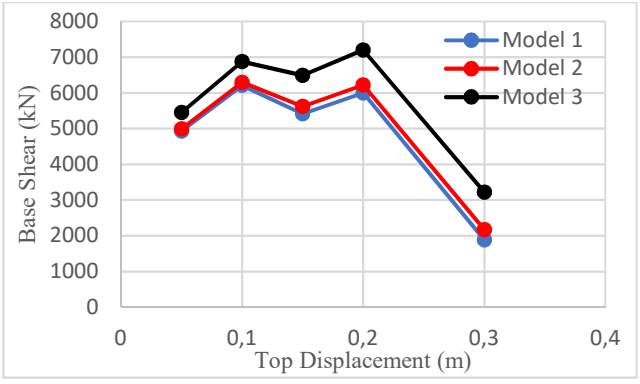

Figure 13 Base shear capacities at the target displacements

Table 4 Top displacements under same lateral force

	Top Displacement (m)				
Base Shear Force (kN)	3000	4000	5000	6000	6400
Model 1	0,023	0,030	0,039	0,083	0,117
Model 2	0,023	0,030	0,039	0,080	0,108
Model 3	0,020	0,027	0,035	0,045	0,076
Model 2/Model 1	0,983	0,980	0,985	0,964	0,922
Model 3/Model 2	0,907	0,919	0,899	0,566	0,704

Under same lateral forces top displacements are close to each other for Model 1 and Model 2. The largest fall in top displacement is observed at 6400 kN lateral force by 8%. On the other hand, Model 3 has smaller top displacements in all cases ranging from %8 to 43% (Table 4).

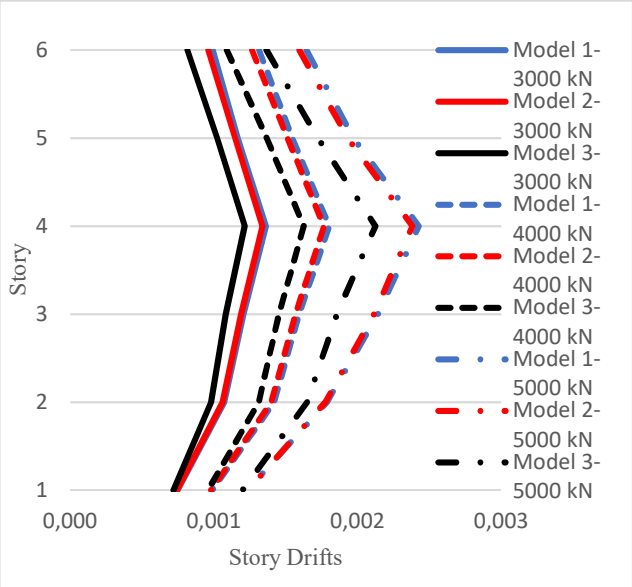

Figure 14 Story drifts under same base shear forces (a)

It is observed from Figure 14 that under 3000, 4000 and 5000 kN base shear forces Model 1 and Model 2 have similar story drifts. The most significant difference between them is that in Model 2 story drifts has decreased by 4%. However, the behavior of Model 2 and Model 3 are explicitly different. Although at first story levels similar results are observed, Model 3 has decreased story drifts by 10% to 15%.

Under 6000 and 6400 kN base shear force while Model 1 and Model 2 has similar story drifts, Model 2 and Model 3 have great differences. Model 2 has smaller story drifts than Model 1 by %10 to 15% and Model 3 has smaller drifts than Model 2 by 20% to 65% (Figure 15). In other words, due to having additional stiffness because of semi-rigid composite connections, Model 3 have smaller story drifts which is the major parameter evaluating the seismic performance of buildings.

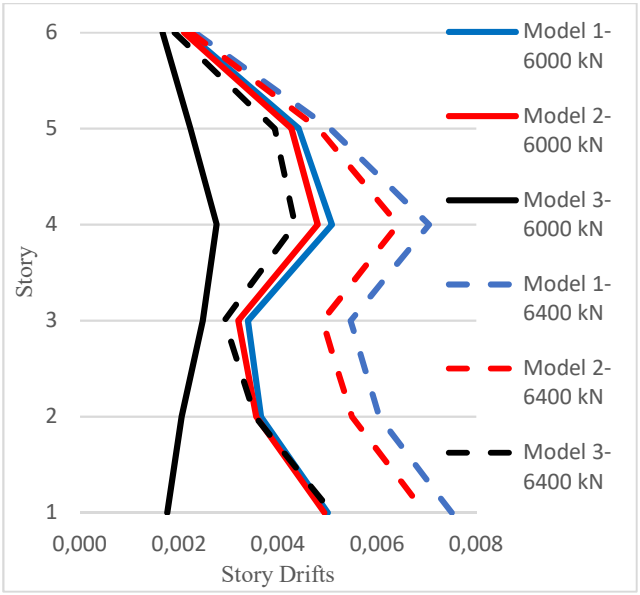

Figure 15 Story drifts under same base shear forces (b)

4. CONCLUSIONS AND FUTURE RECOMMENDATIONS

From the results obtained in this study, the following conclusions can be made:

1. Model 1 and Model 2 showed similar behavior that neglecting actual behavior of shear tab connections doesn't cause significant errors.

2. In every cases Model 3 showed superior performance than Model 2 did in terms of base shear capacity, top displacement and story drifts.

3. The study shows that the use of semi rigid composite connections could lead to better seismic performance and they might be used as an alternative to pinned connections in buildings with steel special concentrically frames.

To obtain more accurate and realistic results, these recommendations can be made for future researches:

1. Target building performance levels could be evaluated and compared.

2. Plastic deformations in braced frames at target displacement could be investigated.

3. Semi-rigid connections having different strength and rotational capacities might be used and compared.

3. Different types of buildings might be selected in terms of story levels, widths, lengths, regularity etc.

4. Nonlinear time history analysis could be used for more accurate structural behavior.

5. REFERENCES

[1] R. T. Leon, J. J. Hoffman, and T. Staeger, Partially restrained composite connections: a design guide. American Institute of Steel Construction, 1996.

[2] 'Eurocode 4: Design of composite steel and concrete structures - Part 1-1: General rules and rules for buildings Eurocode', 2004.

[3] R. T. Leon, 'Composite connections', Prog. Struct. Eng. Mater., vol. 1, no. 2, pp. 159–169, 1998.

[4] Leon, R. "Composite Connections" Structural Engineering Handbook Ed. Chen Wai-Fah Boca Raton: CRC Press LLC, 1999

[5] A. Reyes-Salazar, J. M. Sauceda-Pimentel, S. E. Ruiz, E. Bojórquez, and J. Bojorquez, Seismic response and energy dissipation of 3D complex steel buildings considering the influence of interior semi-rigid connections: low- medium- and high-rise, no. 0123456789. Springer Netherlands, 2018.

[6] W. Zhang, 'Study of the Influence of Gravity Connections on the Lateral Response of Steel-Concrete Composite Moment Frames'. University of Cincinnati, 2012.

[7] B. F. Maison, C. O. Rex, S. D. Lindsey, and K. Kasai, 'Performance of PR Moment Frame Buildings in UBC Seismic Zones 3 and 4', J. Struct. Eng., vol. 126, no. 1, pp. 108–116, 2000.

[8] Afet ve Acil Durum Yönetimi Başkanlığı, Türkiye Bina Deprem Yönetmeliği. Ankara, 2018.

[9] ASCE/SEI, ASCE 41-13 : American Society of Civil Engineers : seismic evaluation and retrofit of existing buildings. 2013.

[10] A. Astaneh-asl, Design of Shear Tab Connections for Gravity and Seismic Loads, no. June. 2005.

[11] A. E. Maleck, 'Second-Order Inelastic and Modified Elastic Analysis and Design Evaluation of Planar Steel Frames', no. April, 2001.

[12] Sap2000 C.S.I, 'Computers and structures Inc', Berkeley, CA, USA, 2005.

JOURNAL OF SCIENCE
SAKARYA UNIVERSITY

Sakarya University Journal of Science

ISSN 1301-4048 | e-ISSN 2147-835X | Period Bimonthly | Founded: 1997 | Publisher Sakarya University | http://www.saujs.sakarya.edu.tr/

Title: High-Temperature Thermostatistical Properties Of Deformed Quantum Gas İn Two Dimensions

Authors: Mustafa Şenay
Recieved: 2019-04-17 17:34:35

Accepted: 2019-09-11 15:48:02

Article Type: Research Article
Volume: 23
Issue: 6
Month: December
Year: 2019
Pages: 1273-1278

How to cite
Mustafa Şenay; (2019), High-Temperature Thermostatistical Properties Of Deformed Quantum Gas İn Two Dimensions. Sakarya University Journal of Science, 23(6), 1273-1278, DOI: 10.16984/saufenbilder.555231
Access link
http://www.saujs.sakarya.edu.tr/issue/44246/555231

Sakarya University Journal of Science 23(6), 1273-1278, 2019

High-temperature thermostatistical properties of deformed quantum gas in two dimensions

Mustafa Senay*

Abstract

In this study, we focus on the high-temperature thermostatistical properties of the q-deformed gas model in two spatial dimensions. Some important thermodynamical functions such as internal energy, entropy, specific heat are calculated depending on deformation parameter q. Moreover, the first five deformed virial coefficients in the equation of state of the model for two dimensions are derived. Also, the results obtained in this work are compared with the results of the undeformed gas model.

Keywords: Virial coefficient, q-deformed boson, q-deformed fermion, thermodynamics

1. INTRODUCTION

The investigation of the quantum groups and the quantum algebras has been become one of the interesting topics for physicsts and mathematicians over the last decades. In order to obtain the quantum groups and the quantum algebras, the usual Lie groups and Lie algebras can be deformed with some real or complex deformation parameters [1]. There are many studies in the literature to understand the physical interpretation of these deformation parameters [2-9]. For instance, in the Ref. [3,4], the q-deformed harmonic oscillators have investigated depending on the q-deformed creation and annihilation operators.

On the other hand, the high and low thermostatistical properties of the q-deformed bosons and fermions have been extensively examined for three dimensional space in the literature [10-17]. In these studies, the q-deformed theory has been found applications in several areas of physics due to its applications in a large variety areas such as Jaynes-Cummings model and the deformed oscillator algebra [10], generalized thermodynamics of q-deformed bosons and fermions [11], Bose-Einstein condensation of a relativistic q-deformed Bose gas [12], thermodynamic geometry of deformed bosons and fermions [13], high-temperature behavior of a deformed Fermi gas obeying interpolating statistics [14], thermal properties of a solid through q-deformed algebra [15], q-deformed Einstein equations [16], thermosize effects in a q-deformed fermion gas model [17]. However, so far, thermostatistics properties of q-deformed bosons and fermions have been less studied for two dimensional space in the literature.

Corresponding Author: mustafasenay86@hotmail.com

*National Defense University, Naval Academy, Istanbul, Turkey. ORCID: 0000-0002-9480-9040

In the view of the above motivations, in this paper, we continue the work of [18] and study the high temperature thermostatistical properties of the q-deformed bosons and fermions for two dimensional space. In the work [18], some thermodynamical functions of such q-deformed bosons and fermions are investigated. We want to find other thermodynamical properties such as the equation of state as a virial expansion. The paper is organized as follows: In Sec. 2, we give a brief of the quantum algebraic properties concerning with the q-deformed algebra of bosons and fermions. In Sec. 3, we investigate some important thermodynamic quantities in the high temperature limit for two dimensional space. In the last Sec., we discuss the effects of fermionic and bosonic q-deformation on the thermodynamic functions and give our conclusions.

2. DEFORMED BOSON AND FERMION ALGEBRA

The symmetric q-deformed algebraic structure of the quantum oscillators is defined by q-deformed Heisenberg algebra in terms of creation and annihilation operators c^* and c, respectively, and the total number operator $\widehat{N}$ as [6-9,11,18]

$$cc^* - \kappa q^{\kappa} c^* c = q^{-N}$$

$$\left[\widehat{N}, c^*\right] = c^*, \quad \left[\widehat{N}, c\right] = -c, \tag{2.1}$$

where q is the real deformation parameter and the constants $\kappa = 1$ and $\kappa = -1$ are related to q-bosons and q-fermions, respectively. In addition, the operators obey the following relations [11]

$$c^* c = \left[\widehat{N}\right], \quad c^* c = \left[1 + \kappa \widehat{N}\right]. \tag{2.2}$$

The basic q-deformed quantum number is defined as

$$[x] = \frac{q^x - q^{-x}}{q - q^{-1}}. \tag{2.3}$$

Moreover, the Jackson derivative (JD) operator for the system is given as

$$D_x^{(q)} f(x) = \frac{1}{x}\left[\frac{f(qx) - f(q^{-1}x)}{q - q^{-1}}\right], \tag{2.4}$$

for any function $f(x)$. This JD operator reduces to the ordinary derivative operator in the limit $q \to 1$ [11].

3. THERMOSTATISTICS OF DEFORMED BOSON AND FERMION

In this section, we present the high temperature thermostatistical properties of deformed bosons and fermions in two dimensonal space. Now, we consider non-interacting q-deformed gas model constructed by Eqs. (2.1)-(2.3) confined in two dimensional space (A). Such non-interacting q-deformed gas model has Hamiltonian in the following [11]

$$H = \sum_i (\varepsilon_i - \mu) N_i, \tag{3.5}$$

where ε_i is the kinetic energy of a particle in the i. state and μ is the chemical potential. In order to investigate the high-temperature properties of the q-deformed gas model in two dimensional space, the logarithm of the grand partition function of the model is given as

$$\ln Z = -\kappa \sum_i \ln(1 - \kappa z e^{-\beta \varepsilon_i}), \tag{3.6}$$

where $z = \exp(\mu / k_B T)$ is the fugacity and $\beta = 1/k_B T$. The total number of particles can be obtained by using JD operator in Eq. (2.4) instead of the standard derivative operator. Therefore, it can be found as

$$N^{(\kappa)} = z D_z^{(q)} \ln Z = \sum_i n_i^{(\kappa)}, \tag{3.7}$$

where $n_i^{(\kappa)}$ is the mean occupation number and expressed by the following form

$$n_i^{(\kappa)} = \frac{1}{q - q^{-1}} \ln\left(\frac{z^{-1} e^{\beta \varepsilon_i} - \kappa q^{-\kappa}}{z^{-1} e^{\beta \varepsilon_i} - \kappa q^{\kappa}}\right). \tag{3.8}$$

From the thermodynamic relation $P^{(\kappa)} A / k_B T = \ln Z$ the equation of state can be written as

$$\frac{P^{(\kappa)} A}{k_B T} = -\kappa \sum_i \ln(1 - \kappa z e^{-\beta \varepsilon_i}). \tag{3.9}$$

When the thermodynamic limit is taken into account, for a large area and a large number of particles, the sum of states can be replaced with the integral. Thus, for two dimensional space, the

equation of state and the total number of particles can be, respectively, expressed as

$$\frac{P^{(\kappa)}}{k_B T} = \frac{1}{\lambda^2}\int_0^\infty dx \ln(1-\kappa z e^{-x}), \quad (3.10)$$

$$\frac{N^{(\kappa)}}{A} = \frac{1}{\lambda}\int_0^\infty \frac{dx}{q-q^{-1}} \ln\left(\frac{1-\kappa q^{-\kappa} z e^{-x}}{1-\kappa q^{\kappa} z e^{-x}}\right), \quad (3.11)$$

where $\lambda = h/(2\pi m k_B T)^{1/2}$ is the thermal wavelength, $x = \beta\varepsilon$ and $\varepsilon = p^2/2m$. Furthermore, these integrals can be expanded with Taylor series for the high temperature limit and defined as

$$\frac{P^{(\kappa)}}{k_B T} = \frac{1}{\lambda^2} h_2^{(\kappa)}(z,q), \quad (3.12)$$

$$\frac{N^{(\kappa)}}{A} = \frac{1}{\lambda^1} h_1^{(\kappa)}(z,q), \quad (3.13)$$

where q-deformed $h_n^{\kappa}(z,q)$ function is defined as [11]

$$h_n^{\kappa}(z,q) = \frac{1}{\Gamma(n)}\int_0^\infty \frac{x^{n-1}dx}{q-q^{-1}} \ln\left(\frac{1-\kappa q^{-\kappa} z e^{-x}}{1-\kappa q^{\kappa} z e^{-x}}\right)$$

$$= \frac{1}{q-q^{-1}}\left[\sum_{l=1}^\infty \frac{(\kappa z^{\kappa})^l}{l^{n+1}} - \sum_{l=1}^\infty \frac{(\kappa z q^{-\kappa})^l}{l^{n+1}}\right], \quad (3.14)$$

where $\Gamma(n) = \int_0^\infty x^{n-1}\exp(-x)$ is the Gamma function [19]. Now, we can find other thermodynamic quantities of the q-deformed gas model. For example, from the thermodynamic relation $U^{(\kappa)} = -(\partial \ln Z/\partial\beta)_{z,A}$, the internal energy of the model can be calculated for two dimensional space. Then, it can be obtained as

$$U^{(\kappa)} = \frac{k_B T A}{\lambda^2} h_2^{(\kappa)}(z,q). \quad (3.15)$$

Moreover, the sepecific heat of the model can be found by the thermodynamic relation $C_A^{(\kappa)} = (\partial U^{(\kappa)}/\partial A)_{N,A}$ in the following form

$$\frac{C_A^{(\kappa)}\lambda^2}{k_B T} = 2z D_z^{(q)} h_3^{(\kappa)}(z,q) - \frac{(z D_z^{(q)} h_2^{(\kappa)}(z,q))^2}{z D_z^{(q)} h_1^{(\kappa)}(z,q)} \quad (3.16)$$

By using the thermodynamic relation $F^{(\kappa)} = \mu N^{(\kappa)} - P^{(\kappa)} A$, the Helmholtz free energy can be determined from Eqs. (3.12) and (3.13) as

$$F^{(\kappa)} = N^{(\kappa)} k_B T\left[\ln z - \frac{h_2^{(\kappa)}(z,q)}{h_1^{(\kappa)}(z,q)}\right]. \quad (3.17)$$

Then, the deformed entropy of the model in two dimensions can be derived from Eqs. (3.15) and (3.17) with the help of the thermodynamic relation $S^{(\kappa)} = (U^{(\kappa)} - F^{(\kappa)})/T$ as

$$\frac{S^{(\kappa)}}{N^{(\kappa)} k_B} = 2\frac{h_2^{(\kappa)}(z,q)}{h_1^{(\kappa)}(z,q)} - \ln z. \quad (3.18)$$

In order to understand the effects of the bosonic and fermionic q-deformation on the q-deformed gas model, in Fig. 1-3, we plot the q-deformed bosonic and fermionic entropy functions and the undeformed entropy function as a function of z for several values deformation parameter q. For both $q < 1$ and $q > 1$ and the same fugacity, the bosonic and fermionic entropy values of the deformed gas model in two dimensional space decrease with the values of the deformation parameter q. Also, at the same fugacity, they are lower than the values of the undeformed bosonic and fermionic entropy values in two dimensional space.

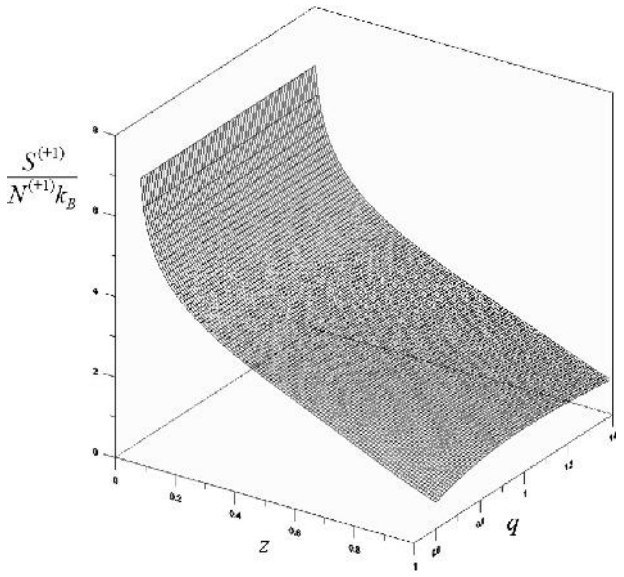

Figure 1. The bosonic entropy function $S^{(+1)}/N^{(+1)}k_B$ with respect to fugacity z and several values of deformation parameter q for boson.

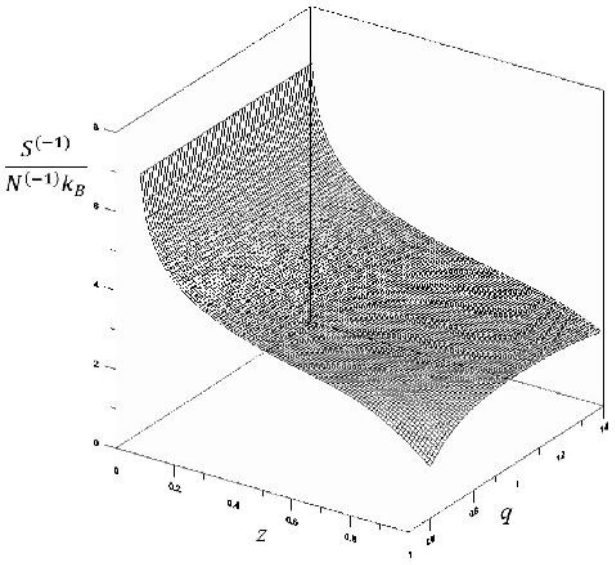

Figure 2. The fermionic entropy function $S^{(-1)}/N^{(-1)}k_B$ with respect to fugacity z and several values of deformation parameter q for fermion.

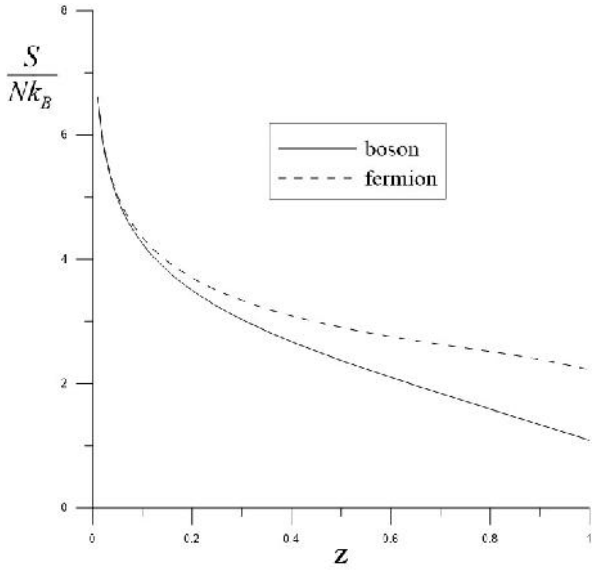

Figure 3. The undeformed bosonic and fermionic entropy function S/Nk_B with respect to fugacity z.

On the other hand, the equation of state of the model can be derived from Eqs. (3.12) and (3.13) as a virial expansion for two dimensional space as

$$\frac{P^{(\kappa)}A}{N^{(\kappa)}k_BT} = a_1^{(\kappa,q)} + a_2^{(\kappa,q)}y + a_3^{(\kappa,q)}y^2 + a_4^{(\kappa,q)}y^3 + a_5^{(\kappa,q)}y^4 + \ldots. \quad (3.19)$$

where $y = (N^{(\kappa)}\lambda^2/A)$ and $a_n^{(\kappa,q)}$ are defined as deformed virial coefficients and the first five of them are found as below

$$a_1^{(\kappa,q)} = 1, \quad (3.20)$$

$$a_2^{(\kappa,q)} = -\kappa\left(\frac{1}{2^3}[2]\right), \quad (3.21)$$

$$a_3^{(\kappa,q)} = -\left(\frac{2}{3}[3] - \frac{1}{2^4}[2]^2\right), \quad (3.22)$$

$$a_4^{(\kappa,q)} = -\kappa\left(\frac{5}{2^7}[2]^3 - \frac{1}{12}[2][3] + \frac{3}{2^6}[4]\right), \quad (3.23)$$

$$a_5^{(\kappa,q)} = -\left(-\frac{7}{2^8}[2]^4 + \frac{1}{12}[2]^2[3] - \frac{1}{2^4}[2][4] - \frac{2}{3^4}[3]^2 + \frac{4}{5^3}[5]\right). \quad (3.24)$$

where $[x]$ q-deformed basic number is defined by Eq. (2.3). In Fig. 4-5, we plot these bosonic and fermionic virial coefficients as a function of deformation parameter q in two dimensional space for the case $q < 1$ and $q > 1$. As it is shown in the Fig. 4, for all values of deformation parameter, the bosonic virial coefficients $a_2^{(+1,q)}$, $a_4^{(+1,q)}$ and $a_5^{(+1,q)}$ have negative values although the bosonic virial coefficient $a_3^{(+1,q)}$ has positive values. As it is shown in the Fig. 5, for all values of deformation parameter, the fermionic virial coefficients $a_2^{(-1,q)}$, $a_3^{(-1,q)}$ and $a_4^{(-1,q)}$ have positive values although the fermionic virial coefficient $a_5^{(-1,q)}$ has negative values.

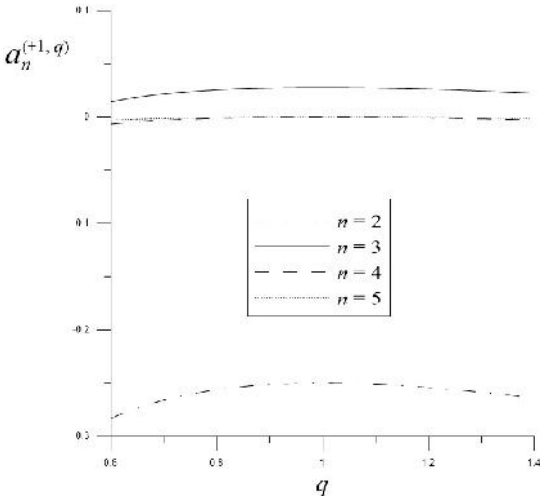

Figure 4. The virial coefficients $a_n^{(+1,q)}$ with respect to several values of deformation parameter q.

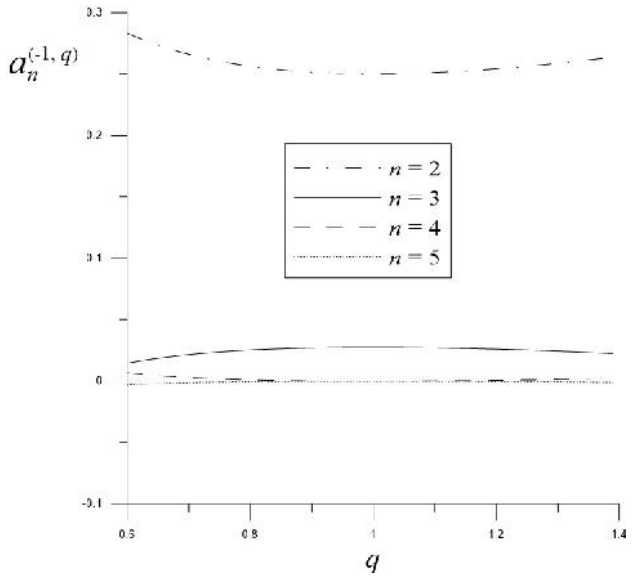

Figure 5. The virial coefficients $a_n^{(-1,q)}$ with respect to several values of deformation parameter q.

4. CONCLUSION

In this paper, we research the effects of the bosonic and fermionic q-deformation on some thermodynamic functions in two dimensional space. For instance, the q-deformed entropy function is obtained in Eq. (3.18). In order to compare, in Fig. 1-3, we demonstrate the plots of the q-deformed entropy functions and undeformed entropy function for boson and fermion. From these graphics, we can conclude that the values of bosonic and fermionic deformed entropy function decrease when the deformation parameter q is increased. Moreover, all thermodyanamic functions found above reduce to undeformed functions in the limit $q \to 1$. The results obtained in this study may be used to investigate properties of some quantum systems in the microelectronic and material sciences.

On the other hand, in the work [20] Pazy and Argaman examined modified Newton theory by using standard Fermi Dirac statistics in two dimensional space. When used this statistics, interaction between particles don't take into account. Therefore, Modified Newton theory can be studied by using the properties of q-deformed fermion in two dimensional instead of standard one and the effects of q-deformation can be researched on this theory. Another important application area can be the investigation of the properties of q-deformation on thermosize effect on Seebeck-like thermosize effect [17,21]. For example, the Seebeck coefficients of the most of metals are negative but some of them are positive such as copper [22]. Free electron theoy is inadequate to explain the behavior of electoron and hole in metals and semicondutors. For this reason, when applied q-deformation on the Seebeck-like thermosize effect, positive and negative Seebeck coefficients of metals and semiconductors may be explained.

The studying of the low temperature thermostatistical properties of the present q-deformed model in two dimensions is one of the open problem.

REFERENCES

[1] M. A. Martin-Delgado, "Planck distribution for a q-boson gas," *Journal of Physics A: Mathematical and General*, vol. 24, pp. L1285-L1291, 1991.

[2] M. Arik, D. D. Coon, "Hilbert spaces of analytic functions and generalized coherent states," *Journal of Mathematical Physics*, vol. 17, pp. 524-527, 1976.

[3] L. C. Biedenharn, "The quantum group $SU_q(2)$ and a q-analogue of the boson operators," *Journal of Physics A: Mathematical and General*, vol. 22, pp. L873-L878, 1989.

[4] A. J. Macfarlane, "On q-analogues of the quantum harmonic oscillator and the quantum group $SU_q(2)$," *Journal of Physics A: Mathematical and General*, vol. 22, pp. 4581-4588, 1989.

[5] K. S. Viswanathan, R. Parthasarathy, .R. Jagannathan, "Generalized q-fermion oscillators and q-coherent states," *Journal of Physics A: Mathematical and General*, vol. 25, pp. L335-L339, 1992.

[6] M. Chaichian, R. Gonzalez Felipe, C. Montonen, "Statistics of q-oscillators quons and relations to fractional statistics,"

Journal of Physics A: Mathematical and General, vol. 26, pp. 4017-4034, 1993.

[7] Y. J. Ng, "Comment on the *q*-analogues of the harmonic oscillator," *Journal of Physics A: Mathematical and Theoretical*, vol. 23, no. 6, pp. 1023-1027, 1990.

[8] C. R. Lee, J. P. Yu, "On *q*-analogues of the statistical distribution," *Physics Letters A*, vol. 150, no. 2, pp. 63-66, 1990.

[9] H. S. Song, S. X. Ding, I. An, "Statistical mechanical properties of the *q*-oscillator system," *Journal of Physics A: Mathematical and Theoretical*, vol. 26, no. 20, pp. 5197-5205, 1993.

[10] J. Crnugelj, M. Martinis, V. Mikuta-Martinis, "Jaynes-Cummings model and the deformed oscillator algebra," *Physics Letters A*, vol. 188, pp. 347-354, 1994.

[11] A. Lavagno, P. Narayana Swamy, "Generalized thermodynamics of *q*-deformed bosons and fermions," *Physical Review E*, vol. 65, pp. 036101-1-036101-5, 2002.

[12] G. Su, S. Cai, H. Chen, "Bose-Einstein condensation of a relativistic *q*-deformed Bose gas," *Journal of Physics A: Mathematical and Theoretical*, vol. 41, pp. 045007, 2008.

[13] B. Mirza, H. Mohammadzadeh, "Thermodynamic geometry of deformed bosons and fermions," *Journal of Physics A: Mathematical and Theoretical*, vol. 44, pp. 0475003, 2011.

[14] A. Algin, M. Senay, "High-temperature behavior of a deformed Fermi gas obeying interpolating statistics," *Physical Review E*, vol. 85, pp. 041123-1-041123-10, 2012.

[15] A. A. Marinho, F. A. Brito, C. Chesman, "Thermal properties of a solid through *q*-deformed algebra," *Physica A*, vol. 391, pp. 3424-3434, 2012.

[16] E. Dil, "Q-Deformed Einstein equations, "*Canadian Journal of Physics*, vol. 93, no. 11, pp. 1274-1278, 2015.

[17] M. Senay, S. Kibaroğlu, "Thermosize effects in a *q*-deformed fermion gas model, "*Modern Physics Letters B*, vol. 32, no. 20, pp. 1850230-1-1850230-9, 2018.

[18] A. Lavagno, P. Narayana Swamy, "Deformed Quantum Statistics in Two Dimensions," *International Journal of Modern Physics B*, vol. 23, no. 2, pp. 235-250, 2009.

[19] G. B. Arfken, H. J. Weber, F. E. Harris, *Mathematical Methods for Physicst* 7rd ed., Amsterdam, Elsevier, 2013.

[20] Pazy, E., Argaman, N., "Quantum particle statistics on the holographic screen leads to modified Newtonian dynamics," *Physical Review D*, vol. 85, no, 10, pp. 104021-1-104021-7, 2012.

[21] T. Lin, G. Su, C. Ou, B. Lin, A. Le Mehaute, Q. A. Wang and J. Chen, "Thermosize effects in confined quantum gas systems," Modern Physics Letter B, vol. 24, no. 15, pp. 1727-1737, 2010.

[22] A. V. Da Rosa, *Fundamentals of Renewable Energy Processes,* Amsterdam, Academic Press, 2009.

Sakarya University Journal of Science

ISSN 1301-4048 | e-ISSN 2147-835X | Period Bimonthly | Founded: 1997 | Publisher Sakarya University | http://www.saujs.sakarya.edu.tr/

Title: Performance And Heat Release Rate Of A Diesel Engine Using Sunflower Methyl Esters And Diesel Fuel Blends İn Experimental Comparison

Authors: Aykut Safa
Recieved: 2019-06-12 14:29:56

Accepted: 2019-09-13 08:49:25

Article Type: Research Article
Volume: 23
Issue: 6
Month: December
Year: 2019
Pages: 1279-1288

How to cite
Aykut Safa; (2019), Performance And Heat Release Rate Of A Diesel Engine Using Sunflower Methyl Esters And Diesel Fuel Blends İn Experimental Comparison. Sakarya University Journal of Science, 23(6), 1279-1288, DOI: 10.16984/saufenbilder.576624
Access link
http://www.saujs.sakarya.edu.tr/issue/44246/576624

Sakarya University Journal of Science 23(6), 1279-1288, 2019

Performance and Heat Release Rate Comparison in a Diesel Engine fueled with Sunflower Methyl Esters/Diesel Fuel Blend

Aykut Safa*[1]

Abstract

Biodiesel fuels are among the leading renewable alternative fuels. And, using biodiesel fuels is available and easy to implement on diesel engines. Biodiesel fuels, methyl/ethyl esters of various oils extracted from vegetables or animals, are being used by many researchers on various types of engines and they were tested at various conditions. Since chemical properties very close to diesel fuel, similar test results for nominal engine performance data with diesel can be obtained by using biodiesel fuels on engines. In this study, effect of sunflower oil methyl esters on engine performance, heat release rate and indicated engine parameters are investigated experimentally on a single cylinder, DI Diesel engine. Tests are performed with diesel fuel and B50 blend fuel, consisting of 50% diesel and 50% biodiesel fuels, at full load condition and at different speeds. Engine brake torque, brake power, brake specific fuel consumption, brake thermal efficiency, heat release rate, and indicated engine parameters are calculated from the test data, and the results obtained by using diesel fuel and B50 blend fuel are compared. Although some worsening on performance data and heat release rate on B50 side, results are very close to each other.

Keywords: Diesel Engine performance, Sunflower Biodiesel Fuel Blends, Heat Release Rate analysis

1. INTRODUCTION

In literature, studies on various biodiesels including Sunflower Methyl Ester (SFME) are present [1-4]. Biodiesel properties and effect on engine performance are investigated in various aspects [5-9]. And studies on heat release data calculated by pressure data can be found in literature [15-18]. In this study, experimental results of a DI CI engine using diesel and biodiesel of SFME and blend fuels are investigated in comparison. Engine performance data, power, torque, and BSFC are revealed and heat release rates obtained from pressure data and engine data are calculated for diesel fuel and B50 blend fuels. The results found close to each other.

* Corresponding Author: safa@yildiz.edu.tr
[1] Yildiz Technical University, Naval Architecture and Marine Engineering Department, Istanbul, Turkey. ORCID: 0000-0002-9650-3651

Biodiesel fuel is a renewable and it can be obtained from waste/raw vegetable oils or animal fats, etc. Since biodiesels are produced by transesterification of fatty acids, they offer high energy density and serve for sustainability through conversion of fatty acids from bio-resources. Thus, the studies on biofuels are increasing in number due to these facts. For widespread usage of biodiesels, standardization is required. However, deviations occur in biodiesel characteristics depending on fuel content [3]. Therefore, for improved insight for correlating biodiesel properties and engine performance and emissions, the corresponding relations should be investigated. Another advantage of biodiesels is the opportunity to be used in a conventional diesel engine easily [9]. [12] Alptekin et al, 2008 reported densities and viscosities of blend fuels, blend of diesel and biodiesel. Experiments on blend fractions, B2-B75, were reported for biodiesel fuels, from sunflower, canola, soybean, cottonseed, corn oils and waste palm oils, according to ASTM test methods. It is reported that, densities and viscosities of the blend fuels increase with the increase of biodiesel fraction in the fuel. [8] Demirbas, 2008, studied viscosity, density, flash point and HHV properties of various biodiesels and concluded aspects to use biodiesels in comparison to conventional fuels of higher viscosity and lower HHV. And also, it is concluded that, viscosity and HHV were highly correlated for vegetable oil methyl esters. [6] Sayin et al, 2009, tested diesel and methanol blends with various fuel injection timings, to improve engine emissions, using a single cylinder CI test engine. As reported, increase in methanol fraction causes decrease in smoke opacity, CO and UHC emissions, but increase in NO_x emissions, and advance in injection timing cause reductions in smoke opacity, CO and UHC, but increase in NO_x and CO_2 emissions. [10] Ozsezen et al, 2011 tested COME and WPOME fuel on a DI diesel engine. Engine with compression ratio, 15.9, and fuel injection of pressure, 197 bar, are used at tests. Heat release analysis is also utilized. Reduction in engine brake power, CO, HC, CO_2, smoke and increase in BSFC and in NO_x emissions are reported compared to diesel fuel results under full load at constant engine speeds [5] Hoekman, 2012 studied 12 common biodiesel feedstocks and presented a detailed report on several properties of biodiesels. [2] Santos et al., 2013 showed the effect of engine parameters and biodiesel fractions on performance and emissions using SFME, SME and neat diesel on two diesel engines. [13] Lahane, 2015 investigated fuel injection, performance, and emissions characteristics of a DI diesel engine at 1500 rpm, using diesel and biodiesel of karanja blend fuels. As reported, ignition delay and pressure rate are lowered for biodiesel fractions. Since biodiesel has a greater cetane number than diesel, CO, HC and smoke emissions are reduced, but NO_x emissions are increased. [4] Pearson et al, 2015 investigated iso-stoichiometric fuel blends and information on chemical properties of hydrous blends, containing water, gasoline, ethanol and methanol is given. [7] Prashant et al, 2016 using diesel and methanol blend fuel studied ignition delay, pressure rate and heat release rate on a dual fuel CI engine. As the methanol fraction is increased, ignition delay, and the angle corresponding to the maximum heat release is increased. [9] Prajapati et al, 2016 studied diesel and biodiesel of sunflower, blend fuels on a single cylinder, DI CI engine at 1500 rpm at various loads. And, for 25% fraction of biodiesel in diesel is concluded to have very close results specific fuel consumption and brake thermal efficiency, compared to neat diesel fuel. [1] Ayhan et al, 2018 proposed conditional blend fuel fractions containing diesel fuel, DEE, biodiesel (SFME) and water. The experimental study done at engine speeds, 1000-2200 rpm, and full load on DI diesel engine is used. The reason of DEE addition is reported to increase blend fuel cetane number and the surfactant addition to obtain a stabilized fuel with water addition. At the maximum torque condition, reductions in engine brake power, brake torque and in CO, NO and smoke levels but increase in brake efficiency and in HC are reported. Fuel injection pressure was 175 bar. [11] Kirankumar et al, 2018 was run a single cylinder diesel engine on neat diesel, B25, B50, B75, and B100 blend fuels of SFME at 1500 rpm. Engine of compression ratio with 16.5 is used in tests. And specific fuel consumption, brake thermal efficiency, exhaust gas temperature increase with brake power has been reported. While, at full load condition using diesel fuel causes lower CO, CO_2,

NO_x and smoke emissions, but using B100 fuel causes the lowest HC emission. In oxygenated fuel blends, complete combustion takes place resulting in high NO_x has also been reported. Because high combustion temperatures occur during the complete combustion, the resulting NO_x formation is high. And also presented that, decrease in the maximum in-cylinder pressure lowers as the blend fraction increases. And it was concluded that the maximum heat release rate for diesel fuel is twice the B100.

Heat release during combustion occur in cylinder is affected by various parameters such as mixture formation, heat loss, engine operational parameters, etc. Therefore, using experimental data, apparent heat release rate can be estimated. [14] Gogoi and Baruah, 2010 studied the effect of biodiesel, blends of karanja oil methyl ester and diesel fuel, on performance through a zero-dimensional cycle simulation model and experimental data. And an increase in brake power for B40 and B60 blend fuels, but a decrease for B20, and also, increase in thermal efficiency for all the biodiesel blends in comparison to neat diesel oil is reported. [15] Asad and Zheng, 2008 investigated heat release mechanisms in compression ignition engines. And they suggest importance of determining combustion parameters based on obtained experimental data. [16] Abbaszadehmosayebi and Ganippa, 2014 calculated the heat release using combustion burnt factor. They concluded, using combustion burnt factor, in comparison to Wiebe function, gives better results. [17] Vipavanich et al., 2018, conducted tests on a CI engine running on gasoline, injected into port, and diesel fuel. Thermal efficiency was evaluated through heat release analysis and combustion parameters are investigated.

This study presents the effect of using biodiesel from sunflower oil on engine performance parameters, brake torque, brake power, brake specific fuel consumption, cumulative heat release and heat release rate. For this reason, test results for fuel blend of diesel fuel and SFME fuel at 50% fraction and neat diesel fuel are given for comparison. And heat release data calculated from engine pressure data are investigated to understand the effect of biodiesel blend fuel better.

2. EXPERIMENTAL SETUP

2.1. Production of Sunflower Oil Methyl Ester

Biodiesel from corn oil is produced by transesterification method. Methanol, with 99% pure alcohol, and KOH, catalyst, are used. Alcohol and catalyst are weighed, and placed in a glass container to dissolve completely. Later, corn oil is heated to the required temperature, and then alcohol and catalyst preparation is added in. The preparation is mixed with a mechanical mixer at a constant temperature for the transesterification reactions to take place. And, glycerin is separated from the ester. Extracted ester is washed with pure water and then taken to drying process. Fuels properties used in the study are given in Table 1.

Table 1 Properties of fuels used in tests

Fuel property	**Diesel** $C_{15}H_{25.5}$	**Biodiesel** $C_{19}H_{35}O_2$	**B50**
Density [kg/m^3]	832	880	862.5
Cetane number	57	46.8	51.9
Lower heating value [MJ/kg]	42.6	39.5	41.05
Kinetic viscosity at 40 °C [mm^2/s]	4.5	4.7	4.6
Self-ignition temperature [°C]	250	125	187.5

As given in Tab.1 mass fractions are compared. Carbon content in biodiesel is lower compared to diesel fuel, 85.4%, and 87.6% respectively. Therefore, carbonaceous pollutants from biodiesel fueled diesel engines will be less than neat diesel. The physicochemical properties given in Tabl.1 is close to the data given by Richard J Pearson [4] et al. And intermediate data [4] are calculated by mass ratios.

2.2. Engine Tests

A single cylinder, 4-stroke, water cooled, direct injection Superstar make test engine is used in the experiments, Table 2.

Table 2 Test Engine specifications

Engine	Super Star 4 stroke CI engine
Aspiration	Atmospheric
Cooling	Water circulation
Injection	DI
Bore [mm]	108
Stroke [mm]	100
Displacement volume [dm^3]	0.92
Connecting rod length [mm]	219
Compression ratio	17
Rated power @2200 rpm, [kW]	13
Injection pressure, [bar]	225
Injection timing, [°CA bTDC]	29
Piston type	Bowl-in-piston

Dynamometer is loaded by a Type, ‘‘S” load cell of 0.1 accuracy, calibrated before the tests, precisely. Test engine specifications are given in Tab.2. Tests are performed at full load condition and at 1200, 1400, 1600, 1800, 2000 and 2200 rpm engine speeds. The optimum static injection advance angle is obtained 29°CA bTDC, as a result of conducting several tests. And the obtained optimum static injection advance angle is used at tests. In Fig. 1, test bed is sketched.

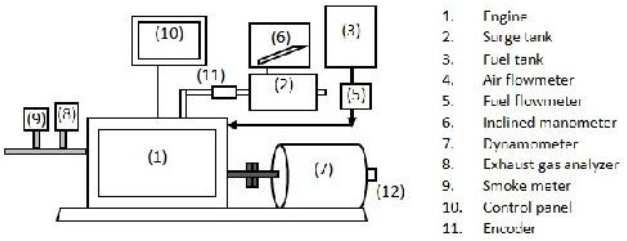

Figure 1 Engine test setup

During experiments, test engine is loaded by a 20 kW capacity electric dynamometer. Before testing, the oil temperature was measured 60 ±2°C. The Heat addition was kept constant, 17.3 mg fuel per cycle at 1100 rpm. Volumetric metering is used for fuel consumption measurements. Prior to experiments, test engine is run sufficient to maintain steady operating temperatures. In the closed circulation cooling system, cooling water outlet temperature was 85°C. Orifice plate – surge tank system is used for air consumption measurements. Kistler 6061B type water cooled piezoelectric sensor, using a Kistler 5011B charge amplifier and AVL make signal conditioner, software for pressure measurements are used for in cylinder pressure measurements, and encoder on the engine crankshaft for angular position detection. Pressure sensor is placed in a bored slot on cylinder head opening to combustion chamber. Pressure sensor technical specifications are given in Tab. 3. For the cylinder pressure and top dead center (TDC) data acquisition, National Instrument PCIe 6251 fast data acquisition card is used for the signals from charge amplifier and the magnetic pick-up.

Table 3 Pressure sensor technical specifications

In-cylinder pressure sensor (6061B, water cooled, piezoelectric type)	
Pressure measuring range [bar]	0-250
Sensitivity	-26.09 pC/bar and +/- %0.3
Stable operating range [°C]	0-350
Natural frequency [kHz]	90
Overload capacity [bar]	300

2.3. Heat Release Analysis

Wiebe function, given in Eq.1, is frequently used in engine heat release analyses [16-17].

$$MFB(\theta) = 1 - e^{-a\left(\frac{\theta-\theta_0}{\theta_b}\right)^{m+1}} \quad (1)$$

where, *MFB* is fraction of burnt fuel, a is form factor, θ is instantaneous crank angle, θ_0 is crank angle for start of combustion, θ_b is engine crank angle for burn duration and m is efficiency factor.

For comparison, modified Wiebe function given in Eq.2, can be used in engine heat release analyses for improved results [16], providing parameter, θ_{50} for burnt fuel fraction at 50% [18]. Instead of form factor, a, θ_{50} is used to obtain closer results.

$$MFB(\theta) = 1 - e^{\ln(0.5)\left(\frac{\theta-\theta_0}{\theta_{50}-\theta_0}\right)^{m+1}} \quad (2)$$

For heat release rate calculations, the first law of thermodynamics is utilized as given in literature [10]. Heat release rate data are obtained using in-cylinder pressure data and engine data as given in

Eq.3. Ratio of specific heats, γ, is considered 1.32 [17].

$$\frac{dQ}{d\theta} = \frac{\gamma}{\gamma - 1} P \frac{dV}{d\theta} + \frac{1}{\gamma - 1} V \frac{dP}{d\theta} \tag{3}$$

where, instantaneous cylinder volume,

$$V(\theta) = V_c + V_d(\theta) \tag{4}$$

and in Eq. 4, clearance volume, V_c is measured from the engine cylinder. Instantaneous cylinder displacement volume [19],

$$V_d(\theta) = \frac{\pi B^2}{4} S(\theta) \tag{5}$$

Instantaneous piston stroke,

$$S(\theta) = R\left((1 - cos(\theta)) + \frac{L}{R}\left(1 - \sqrt{1 - \left(\frac{R}{L}\right)^2 sin^2(\theta)} \right) \right) \tag{6}$$

Derivative of cylinder volume,

$$\frac{dV(\theta)}{d\theta} = \frac{\pi B^2}{4} \frac{dS(\theta)}{d\theta} \tag{7}$$

Derivative of piston stroke,

$$\frac{dS(\theta)}{d\theta} = R\left(sin(\theta) + \frac{R}{2L} \frac{sin(2\theta)}{\sqrt{1 - \left(\frac{R}{L}\right)^2 sin^2(\theta)}} \right) \tag{8}$$

3. RESULTS

In this section, engine performance parameters are investigated at engine speeds of 1200-2400 rpm range. Throughout the experiments, while engine speed increases, fuel mass flow rates decrease, but injection timings are kept constant at 29°bTDC. Experimental results are given in the Figs.2-7.

In Fig.2, engine torques, force times the cantilever arm length from measured on loadcell are given for using diesel and B50 blend fuels at full load condition at testing speeds.

(a)

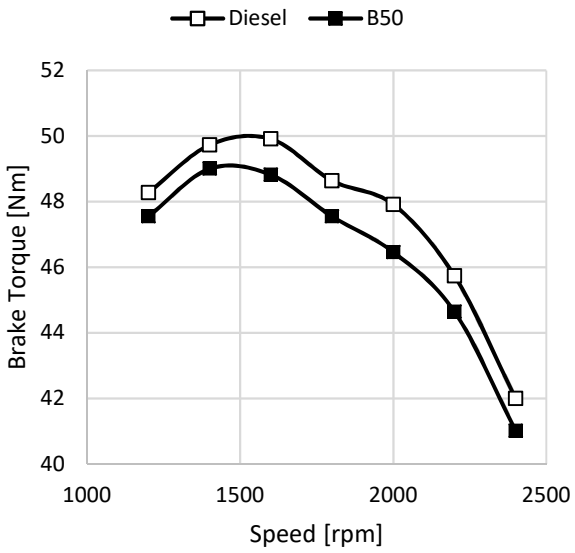

(b)

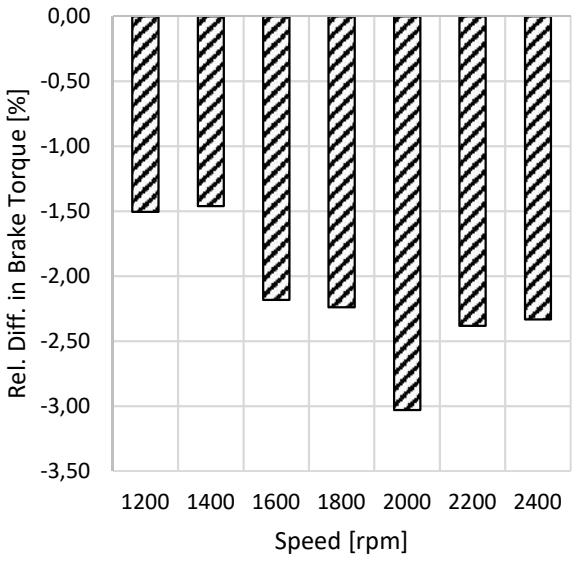

Figure 2 (a) Engine brake torque vs engine speed, (b) % Relative difference vs engine speed

During engine tests, the Maximum Brake Torque (MBT) conditions are sustained. And the results are shown below. At low speeds, engine torque increases, and after reaching a peak value, it starts decreasing. Compared to B50, obtained torques are higher at low speeds for neat diesel fuel and after the maximum value, obtained torques are very close to neat diesel fuel torques. Maximum torque is obtained at 1600 rpm, as given in Fig.2.a. The reasons of decrease in engine torque at low loads are higher heat losses, and degradation in mixture formation and volumetric efficiency. The speed at maximum torque condition also corresponds to the speed at the maximum fuel conversion efficiency condition. Above this speed, engine torque decreases, because of the decrease in volumetric efficiency, increase in mechanical friction loss and insufficient time for combustion to complete. As seen in Fig.2.b, using B50 fuel decreases the torque up to 3%, compared to neat diesel fuel. Highest torque obtained is 49.91 Nm for neat diesel fuel.

As seen in Fig. 3.a, engine power increases with speed, and reaching a peak, then starts decreasing. Slightly higher powers are obtained by using neat diesel fuel, compared to B50 fuel. And, lowest reduction in power is 3% as given in Fig.3.b. Highest power obtained is 10.54 kW for neat diesel fuel.

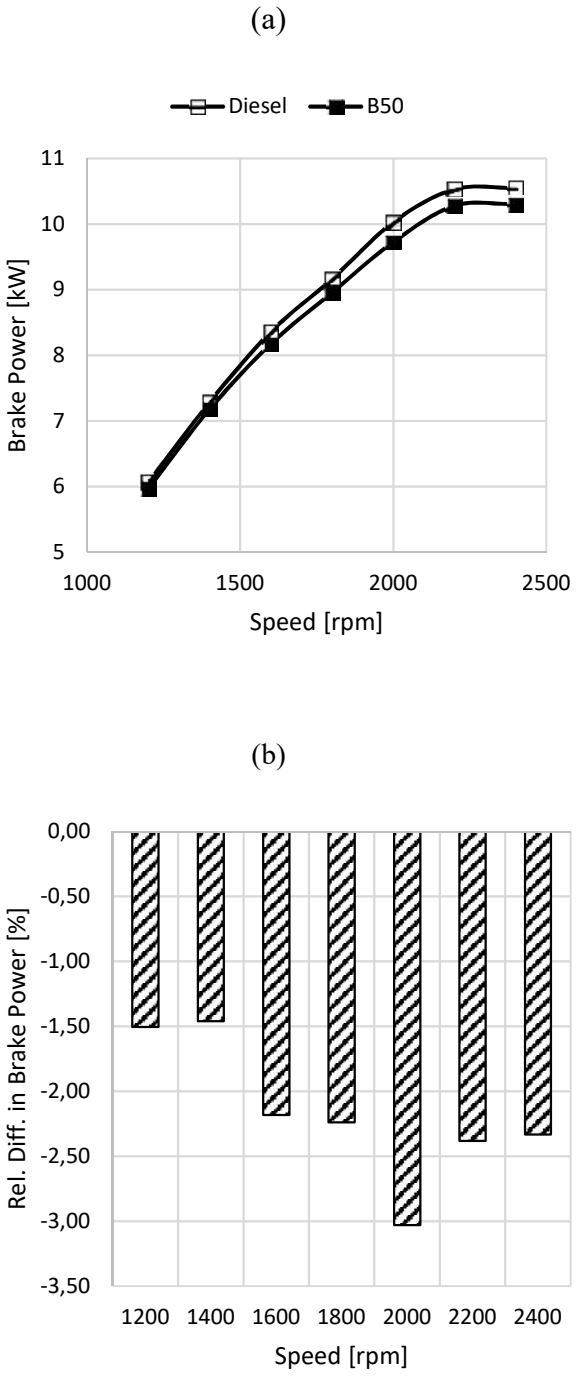

Figure 3 (a) Engine brake power vs engine speed, (b) % Relative difference vs engine speed

Obtained BSFCs are shown in Fig.4.a. For B50 fuel case, more fuel is consumed compared to neat diesel fuel, up to 6.4%. Lowest BSFC obtained is 254.58 g/kWh for neat diesel fuel.

(a)

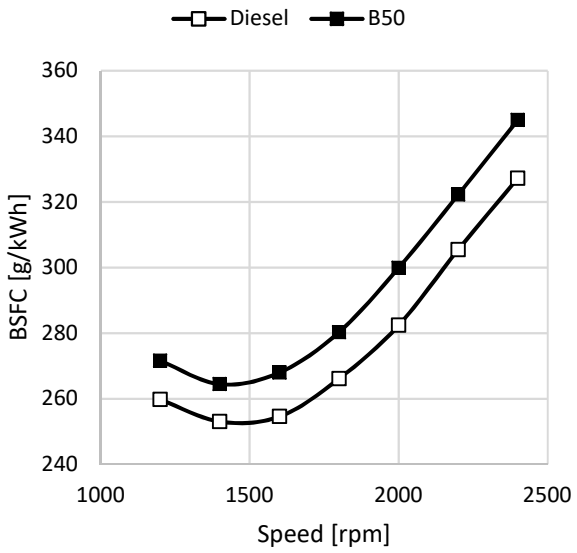

(b)

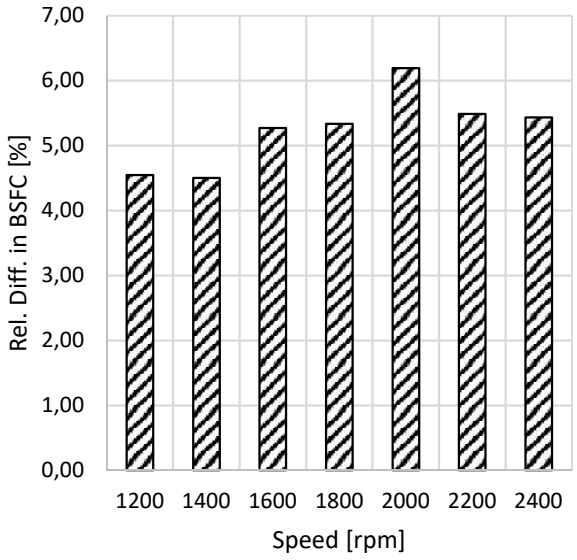

Figure 4 (a) Engine brake torque vs engine speed for the fuels, (b) % Relative difference vs engine speed

In-cylinder pressure data is used in engine performance analyses. In Fig.5a in-cylinder pressure data versus crank angle is shown. When compared, pressure histories are close and similar. And, maximum pressures at MBT condition are depicted in Fig.5.b. Peak values are obtained around 1600 rpm for both fuels, and 79.1 bar for neat diesel fuel.

(a)

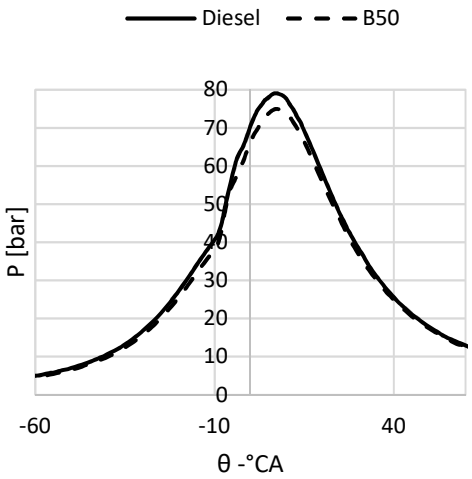

(b)

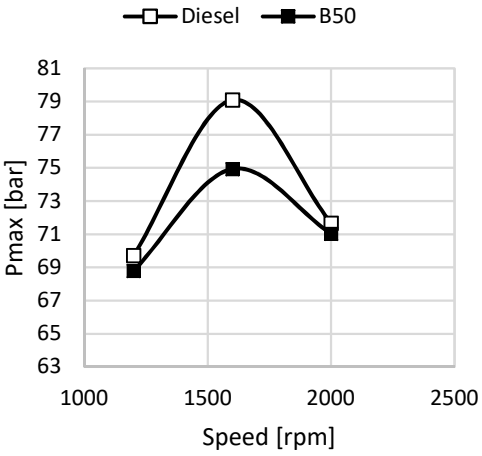

Figure 5 (a) In-cylinder pressure vs crank angle for the fuels, (b) Maximum pressures vs engine speed

In Fig.6, experimental heat release data are presented. Heat release rate curves start from the beginning of ignition and end with combustion. When compared, heat release at premixed combustion stage for neat diesel is less than B50

fuel. Maximum heat release rate is obtained earlier for B50 fuel. As seen Fig.7, the angles for MFB50 are pretty close. However, diesel fuel reaches MFB50 slightly before B50 fuel during combustion at 1600 rpm engine speed. In the evaluation of start and end angles for MFB, θ_5 and θ_{95} are considered, respectively [18]. Cumulative heat release curves are calculated by using equations (3-8).

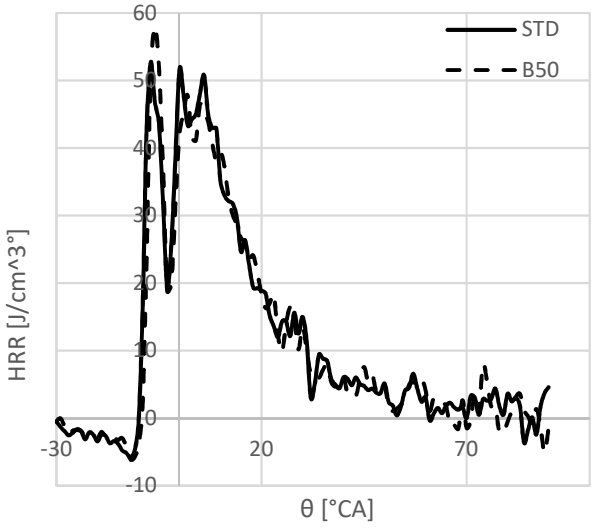

Figure 6 Heat release rate at 1600 rpm vs crank angle for diesel (solid) and B50 (dashed) fuels

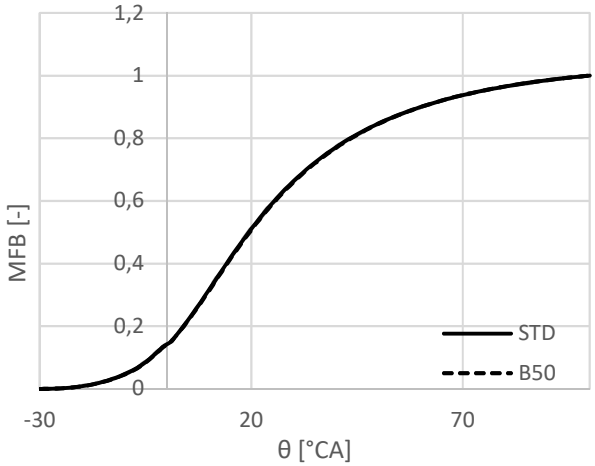

Figure 7 Burned fuel mass vs crank angle for diesel (solid) and B50 (dashed) fuels

4. CONCLUSION

Biodiesels have very high potential to be blended or used as a substitute of diesel fuel. Today, most of the classification societies and legal authorities have issued standards for biodiesels, ASTM, EN etc. Therefore, a gate for a widespread of biodiesels is available.

In this study, biodiesel of sunflower oil, a common vegetable oil, is used to investigate the performance in comparison to neat diesel fuel. It is concluded that, torque, brake power and in-cylinder maximum pressure decrease by using biodiesel blend fuel, B50, and, BSFC increases with biodiesel, since SFME has lower LHV than diesel fuel. However, bearing in mind that, this discrepancy can be overcome by using cheaper biodiesel fuel production methods. Also, using biodiesel fuels is sustainable for being renewable.

Heat release rate data obtained is also presented. And, it is concluded that, for B50 fuel combustion premixed combustion stage is significant compared to neat diesel fuel. Premixed combustion stage is longer in B50 fuel than neat diesel fuel, while, diffusive combustion stage is longer for neat diesel fuel.

As a result, there is a difference in performance parameters compared to diesel fuel. However, this situation is not important considering the economic and diffusive potential of biodiesel fuel.

5. NOMENCLATURE

ASTM	American Society for Testing and Materials
B	Cylinder bore
B10	Blend fuel of 90% Diesel and 10% Biodiesel (by mass)
B20	Blend fuel of 80% Diesel and 20% Biodiesel (by mass)
B5	Blend fuel of 95% Diesel and 5% Biodiesel (by mass)
B50	Blend fuel of 50% Diesel and 50% Biodiesel (by mass)
B75	Blend fuel of 25% Diesel and 75% Biodiesel (by mass)
BSFC	Brake Specific Fuel Consumption
CI	Compression ignition
CO	Carbon monoxide
CO_2	Carbon dioxide
COME	Canola oil methyl ester
DEE	Diethyl ether
DI	Direct injection
EN	European Norm
HC	Hydrocarbons
HHV	Higher heating Value
L	Connecting rod length

LHV	Lower heating Value
m	Wiebe function efficiency factor
NO_x	Nitrogen oxides
P_{inj}	Fuel injection pressure
R	Crank shaft radius
r_c	Compression ratio
S	Stroke
SFME	Sunflower methyl ester
V	Volume
V_c	Clearance volume
V_d	Cylinder displacement volume
WPOME	Waste palm oil methyl ester
ρ	Density
θ	Instantaneous crank angle
θ_0	Crank angle for start of combustion
θ_5	Crank angle for burnt fuel fraction at 5%
θ_{50}	Crank angle for burnt fuel fraction at 50%
θ_b	Burn duration
γ	Ratio of specific heats

6. REFERENCES

[1] Vezir Ayhan, Serdar Tunca, Experimental investigation on using emulsified fuels with different biofuel additives in a DI diesel engine for performance and emissions, Applied Thermal Engineering 129 (2018) 841–854, https://doi.org/10.1016/j.applthermaleng.2017.10.106.

[2] Bjorn S. Santos, Sergio C. Capareda, and Jewel A. Capunitan, Sunflower Methyl Ester as an Engine Fuel: Performance Evaluation and Emissions Analysis, ISRN Renewable Energy, Volume 2013, Article ID 352024, 12 pages, http://dx.doi.org/10.1155/2013/352024

[3] Estelvina Rodríguez Portillo, Araceli Amaya Chávez, Arturo Colín Cruz and Rubí Romero Romero, Biofuels - Status and Perspective: Chapter 13: Qualitative Characteristics of Biodiesel Obtained from Sunflower Oil, IntechOpen, http://dx.doi.org/10.5772/59673.

[4] Richard J Pearson, James WG Turner , Arthur Bell , Stefan de Goede , Chris Woolard and Martin H Davy, Iso-stoichiometric fuel blends: characterisation of physicochemical properties for mixtures of gasoline, ethanol, methanol and water, Proc IMechE Part D: J Automobile Engineering 2015, Vol. 229(1) 111–139 IMechE 2014, DOI: 10.1177/0954407014529424.

[5] S. Kent Hoekman, Amber Broch, Curtis Robbins, Eric Ceniceros, Mani Natarajan, Review of biodiesel composition, properties, and specifications, Renewable and Sustainable Energy Reviews 16 (2012) 143–169, doi:10.1016/j.rser.2011.07.143.

[6] Cenk Sayin, Murat Ilhan, Mustafa Canakci, Metin Gumus, Effect of injection timing on the exhaust emissions of a diesel engine using diesel–methanol blends, Renewable Energy 34 (2009) 1261–1269, 10.1016/j.renene.2008.10.010.

[7] G.K. Prashant, D.B. Lata, P.C. Joshi , Investigations on the effect of methanol blend on the combustion parameters of dual fuel diesel engine, Applied Thermal Engineering 103 (2016) 187–194, 10.1016/j.applthermaleng.2016.04.061.

[8] Ayhan Demirbas, Relationships derived from physical properties of vegetable oil and biodiesel fuels, Fuel 87 (2008) 1743–1748, doi.org/10.1016/j.fuel.2007.08.007.

[9] Ankush Prajapati, Kuladeep Kumar Pandey, Devesh Kumar, Performance and Study of Diesel Engine Using Blends of Sunflower Oil with Diesel, International Journal for Research in Applied Science & Engineering Technology (IJRASET), Volume 4 Issue IV, April 2016.

[10] Ahmet Necati Ozsezen, Mustafa Canakci, Determination of performance and combustion characteristics of a diesel engine fueled with canola and waste palm oil methyl esters, Energy Conversion and Management 52 (2011) 108–116. 10.1016/j.enconman.2010.06.049.

[11] S. Kirankumar, N. Govind, Performance, Emission and Combustion Evaluation of Diesel Engine Using Methyl Esters of Sunflower Oil. Journal of Mechanical Engineering Research and Developments, Vol. 41, No. 1, 2018, pp. 1-8, 10.7508/jmerd.2018.01.001.

[12] Ertan Alptekin, Mustafa Canakci, Determination of the density and the viscosities of biodiesel– diesel fuel blends, Renewable Energy 33 (2008) 2623– 2630, 10.1016/j.renene.2008.02.020.

[13] S. Lahane and K. A. Subramanian, Effect of different percentages of biodiesel–diesel blends on injection, spray, combustion, performance, and emission characteristics of a diesel engine, Fuel, vol. 139, pp. 537–545, Jan. 2015, 10.1016/j.fuel.2014.09.036.
[14] T. K. Gogoi and D. C. Baruah, A cycle simulation model for predicting the performance of a diesel engine fuelled by diesel and biodiesel blends, Energy, vol. 35, no. 3, pp. 1317–1323, Mar. 2010, 10.1016/j.energy.2009.11.014.
[15] Asad and M. Zheng, Fast heat release characterization of a diesel engine, Int. J. Therm. Sci., vol. 47, no. 12, pp. 1688–1700, 2008, 10.1016/j.ijthermalsci.2008.01.009.
[16] G. Abbaszadehmosayebi and L. Ganippa, Characterising Wiebe Equation for Heat Release Analysis based on Combustion Burn Factor (C i), Fuel, vol. 119, pp. 301–307, 2014, 10.1016/j.fuel.2013.11.006.
[17] C. Vipavanich, S. Chuepeng, and S. Skullong, Heat release analysis and thermal efficiency of a single cylinder diesel dual fuel engine with gasoline port injection, Case Stud. Therm. Eng., vol. 12, no. February, pp. 143–148, 2018, 10.1016/j.csite.2018.04.011.
[18] S. Hu, H. Wang, C. Yang, and Y. Wang, Burnt fraction sensitivity analysis and 0-D modelling of common rail diesel engine using Wiebe function, Appl. Therm. Eng., vol. 115, pp. 170–177, Mar. 2017, 10.1016/j.applthermaleng.2016.12.080.
[19] Günter P. Merker, Christian Schwarz, Gunnar Stiesch, Frank Otto, Simulating Combustion Simulation of combustion and pollutant formation for engine-development, Springer-Verlag Berlin Heidelberg, Germany, 2006.